

UNCLASSIFIED

AD NUMBER
AD889396
NEW LIMITATION CHANGE
TO Approved for public release, distribution unlimited
FROM Distribution authorized to U.S. Gov't. agencies only; Test and Evaluation; 19 NOV 1971. Other requests shall be referred to Space and Missile Organization, Los Angeles, CA.
AUTHORITY
USAF ltr, 8 Jul 1980

THIS PAGE IS UNCLASSIFIED

AD 889396

AD No. _____
LCS FILE COPY

SAMSO TR 71-252

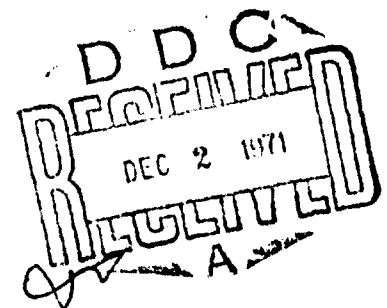
LMSC-B290200-III

19 NOVEMBER 1971



29

**LASER COMMUNICATION
PRELIMINARY SUBSYSTEM DESIGN
FOR THE
SPACE DATA RELAY SUBSYSTEM (U)**



CONTRACT F04701-71-C-0329

SUBMITTED TO DEPARTMENT OF THE AIR FORCE
HEADQUARTERS SPACE AND MISSILE SYSTEMS ORGANIZATION (AFSC)
LOS ANGELES, CALIFORNIA 90045



Distribution limited to U.S. Government agencies only; test and evaluation; 19 November 1971. Other requests for this document must be referred to SAMSO (SYAN).

**FINAL REPORT
VOLUME III
APPENDIXES**

Lockheed Missiles & Space Company, Inc.
A Subsidiary of Lockheed Aircraft Corporation
Palo Alto, California 94304

WHITE SECTION
LATE SECTION

SECTION FOR LATE SECTION

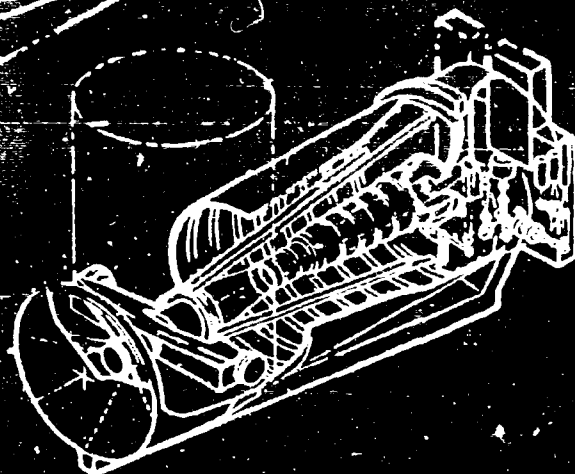
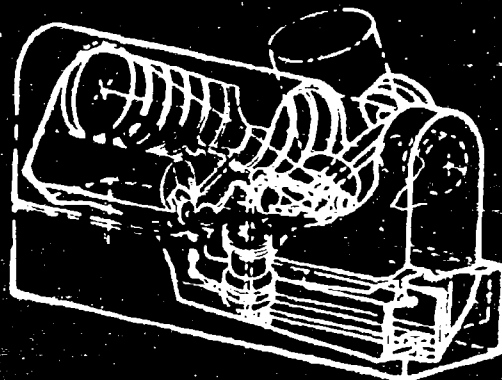
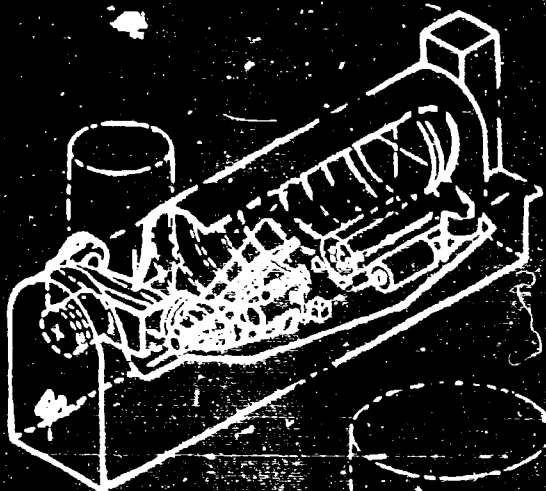
NAME: []

DATE: []

TIME: []

LOCATION: []

REMARKS: []



Distribution limited to U. S. Government agencies only; test and evaluation; 19 November 1971. Other requests for this document must be referred to SAMSO (SYAX).

FINAL REPORT VOLUME III APPENDIXES

Lockheed Missiles & Space Company, Inc.
A Subsidiary of Lockheed Aircraft Corporation
Palo Alto, California 94304

Doc 1-PT 58934-2

PRECEDING PAGE BLANK - NOT FILMED

LMSC-B290200-III

FOREWORD

This Final Laser Communication Subsystem Design Report under Contract F0-4701-71-C-0329 (Laser Communication Preliminary Subsystem Design for the Space Data Relay Subsystem) consists of three volumes:

- Vol. I - Executive Summary
- Vol. II - Task Reports
- Vol. III - Appendixes

Volume I provides a summary of the work performed under the contract. A detailed discussion of the LMSC design is contained in Vol. II. Volume III contains detailed technical discussions of the important aspects of the study which were investigated in order to reach the final design conclusions.

LMSC-B290200-III

ABSTRACT

A preliminary design for a laser communication subsystem (LCS) for a Satellite Data Relay Subsystem is presented in three volumes. The LCS design includes a 1-Gbit/sec data relay system, a 20-kbit/sec command and control system, a ranging system, and the acquisition and tracking system for pointing a 2.4- μ rad beam. Communication links between ground/aircraft/low-orbit satellites and a synchronous relay satellite, between two synchronous relay satellites, and between a synchronous relay satellite and aircraft/ground terminals are treated. The baseline design includes quadriphase-shift-keyed, microwave subcarrier modulation of a 0.53- μ m Nd:YAG laser beam for the high-data-rate subsystem, modulation of a HeNe laser beam for command and control and ranging signals, and a Q-switched Nd:YAG laser for initial acquisition. The optical subsystem design includes 24-in.-diameter and 6-in.-diameter telescopes. The critical components requiring development are evaluated, and a plan and schedule are presented.

CONTENTS

Appendix		Page
A	Requirements Document for the Laser Communications Preliminary Subsystem Design (Mr. M. E. Mauk)	A-1
B	Poisson Noise and Error Probability in Optical Communication Using Bi-Phase Modulated Subcarriers (Dr. G. F. Herrmann)	B-1
C	Bit Error Probability Relationships Used in Modulation Format and Link Parametric Tradeoff Analyses (Dr. H. V. Hance)	C-1
D	Signal-To-Noise Ratio and Bit Error Probability for a Quadri-phase Subcarrier System - Gaussian Statistics Approximation (Dr. H. V. Hance)	D-1
E	Insensitivity of Satellite Orientation on the Reception of Polarization-Modulated Signals (Dr. K. K. Chow)	E-1
F	Transmitting Beam Optics Theory (Drs. R. C. Ohlmann and A. D. MacDonald)	F-1
G	Optical Backgrounds (Mr. W. G. Uplinger)	G-1
H	Brightness of the Image of the Sun Reflected in the Ocean Surface (Dr. D. L. Fried)	H-1
I	Atmospheric Effects on an Optical Data Link; Space-to-Ground (Dr. D. L. Fried)	I-1
J	Antenna Gain Reciprocity for Propagation in a Turbulent Medium (Dr. D. L. Fried)	J-1
K	Atmospheric Turbulence Effects on a Ground-Based Optical Transmitter in a Ground-to-Spacecraft Link (Dr. D. L. Fried)	K-1
L	Effects of Atmospheric Turbulence on Static and Tracking Optical Heterodyne Receivers/Average Antenna Gain and Antenna Gain Variation (Dr. D. L. Fried)	L-1
M	Quantitative Estimates of the Effects of Atmospheric Turbulence on the Performance of a Laser Communication Ground Station (Dr. D. L. Fried)	M-1
N	Computer Programs (Dr. A. D. MacDonald)	N-1
O	Acquisition and Tracking Analysis (Dr. R. C. Ohlmann)	O-1

Appendix A

**REQUIREMENTS DOCUMENT
FOR THE LASER COMMUNICATIONS
PRELIMINARY SUBSYSTEM DESIGN**

by

Mr. M. E. Mauk

(Previously distributed as Technical Memorandum No. 8)

**LOCKHEED PALO ALTO RESEARCH LABORATORY
LOCKHEED MISSILES & SPACE COMPANY
A GROUP DIVISION OF LOCKHEED AIRCRAFT CORPORATION**

Section 1 INTRODUCTION

1.1 PURPOSE

The purpose of this Requirements Document is to set forth all the parameters that direct, influence, or constrain the analysis and design of the Laser Communication Subsystem. This single reference point for requirements will be expanded and revised, as necessary, to maintain completeness and currency.

1.2 SCOPE

This document includes the definition of a postulated set of performance requirements for an operational system application of the Laser Communication Subsystem as well as the subset appropriate for a space experiment support program satellite test. Included also are the progressively more detailed functional and design requirements for the subsystem itself.

1.3 APPLICABLE DOCUMENTS

The documents listed in Section 5 are a part of this Requirements Document to the extent specified herein. In the event of conflicts between any of the listed documents and the requirements set forth in Sections 3, 4, and 5, the requirements of the Contract Statement of Work (Ref. 1) shall take precedence, followed by those set forth in Sections 3, 4, and 5.

Section 2 SYSTEM REQUIREMENTS

The military space data transfer needs of the late 1970's and 80's will require the availability of gigahertz communication bandwidths to accommodate critical high-rate digital and wideband analog information. The Laser Communication Subsystem shall be designed to satisfy these wideband data transfer needs as a part of an operational data relay satellite system. The definition of the operational system and the attendant performance requirements imposed upon the Laser Communication Subsystem are given in the following paragraphs.

2.1 OPERATIONAL SYSTEM

2.1.1 Relay System Definition

The postulated Space Data Relay System consists of three geosynchronous, equatorial satellites equally spaced in their common orbit plane. The selected orbit locations provide the capability for each CONOUS ground terminal to view two relay satellites. The third (or far) relay satellite is connected to the system by means of an intersatellite link to either of the near relay satellites. Operational considerations may make it desirable to consider the following alternatives:

Alternative 1. Relay satellites are so positioned that only one relay satellite is positioned to transmit and receive from the CONUS terminals. This has the advantage that a higher angle of elevation implies less atmospheric propagation loss for the optical links. The disadvantage is that there is some loss of redundancy in that the system depends entirely upon the reliability of the single relay satellite that is in view.

Alternative 2. Each CONUS terminal views two relay satellites, but they are spaced closer than 120° in longitude, for example, one at 50° to 60° W. and the

other at 120° to 130° W. for a spacing of 70°. This provides two satellites in view of CONUS and also has the advantage of a higher angle of elevation. However, this alternative has the disadvantages that (1) the third (far) relay satellite is at a greater range from the near satellites, so a fourth relay satellite may become desirable, and (2) the two relays in view may not be at appropriate longitudes for ideal user viewing.

2.1.2 System User Definition

Three categories of system users can be serviced by the relay system: earth satellites, aircraft, and ground stations. The earth satellite users have been further divided into low-altitude users (satellites with orbit altitudes of less than 1000 nmi and unconstrained inclinations) and synchronous altitude equatorial users (satellites at 19,323-nmi altitudes with east-west stationkeeping capabilities). The aircraft users are identified as jet aircraft operating at altitudes above 30,000 ft. The ground station users are assumed to have favorable geographic locations in order to minimize propagation problems.

2.1.3 Receiving Stations

Communications data receiving stations will be of two types: ground terminals and aircraft terminals. The potential surface terminal deployment pattern is sufficiently varied so that the system design will be capable of completing a communications link under less than favorable propagation conditions. Aircraft terminals will be located in jet aircraft operating at altitudes above 30,000 ft.

2.1.4 Communications Data

The primary data flow paths are from the system users (satellites, aircraft, or ground) to the receiving stations (ground or aircraft) via the relay satellite system, as shown in Fig. 2-1. It is on these paths that the high-rate digital and/or wideband

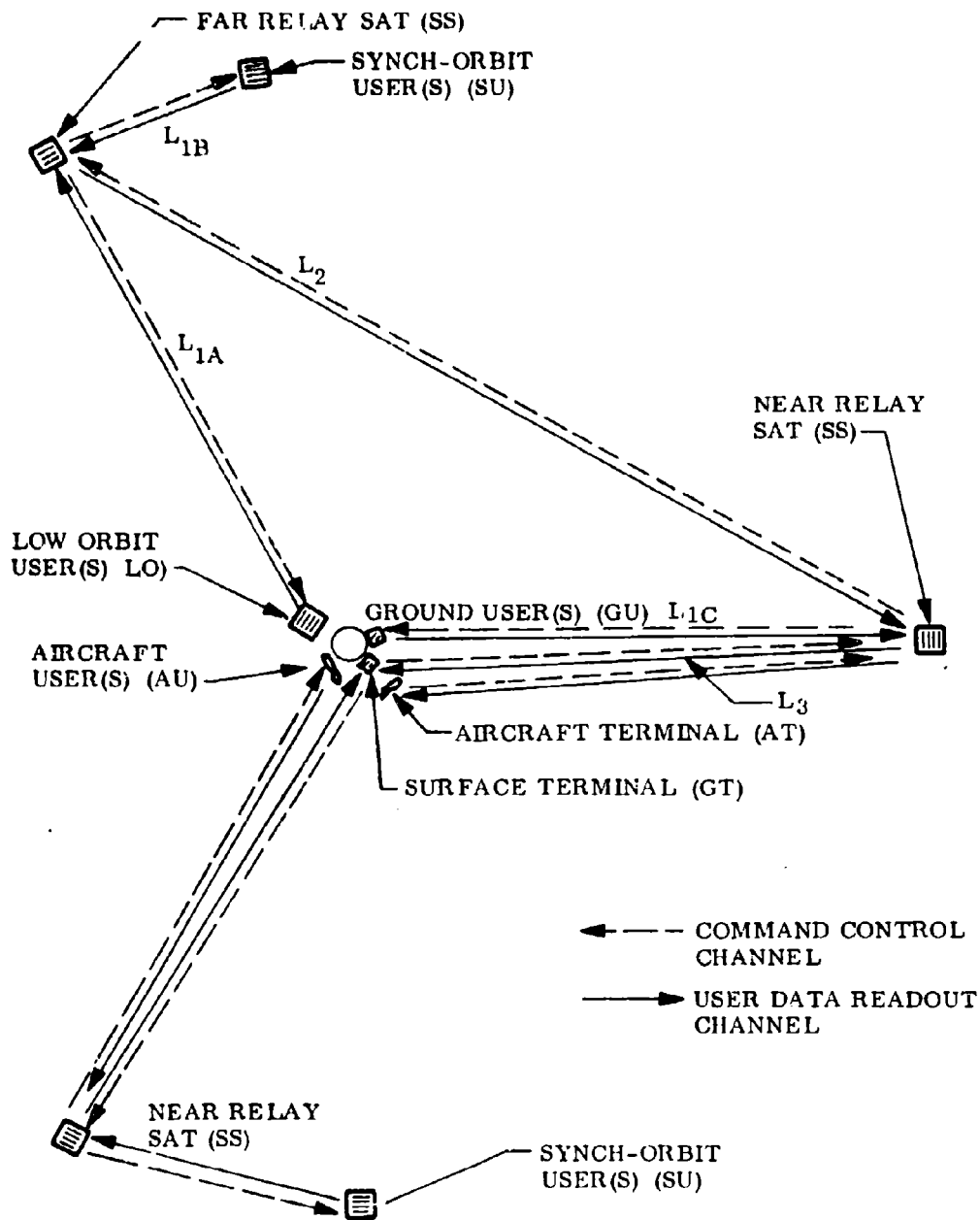


Fig. 2-1 Typical Data Flow Paths Within An Operational Relay Satellite System

analog mission data flow via the laser link to the receiving terminals. In addition, command control data from the receiving site(s) to individual users are also sent over the relay system, as shown. Each relay satellite is capable of simultaneously transferring data directly from any three users to either another relay satellite or a receiving terminal. This yields a system user support capability of up to eight simultaneous user readouts for the postulated system of three relay satellites. Regardless of the user satellite loading of the relay system, no data communications channel can exceed the maximum values specified in sections 2.1.4.1 and 2.1.4.2. All communications between terminals, relays, and users must be accomplished at optical wavelengths utilizing a laser communications subsystem.

2.1.4.1 User Data Readout Channel

The maximum data rate required for individual future user missions is defined as 1 Gbit/sec (10^9 bit/sec). Consistent with this rate, a maximum user analog data rate bandwidth of 1 GHz is established and is also to be considered the minimum bandwidth available within the relay satellite system. The required data channel quality for digital data is specified by a BER of $\leq 10^{-6}$ and for analog data is specified by an output S/N of ≥ 35 dB. The available bandwidth for links L_2 (intersatellite relay) and L_3 (earth readout), as shown in Fig. 2-1, must be a minimum of 1 GHz. When there are multiple users for a given link, such as L_{1A} , L_{1B} , and L_{1C} feeding into links L_2 and/or L_3 , the various users will share the link either by reduced bandwidth by each user or by time multiplexing of a reduced bit rate data.

Narrowband user data identifiable as user telemetry (part of the command and control data), generated separately from the wideband information, must be available continuously from all users linked to the satellites of the relay system. The relay satellite must also transmit housekeeping telemetry. A maximum digital data rate of 50 kbit/sec from each system user, including relay satellites, is specified for this function with a BER of $\leq 10^{-5}$. This error rate is an order of magnitude lower than usual for telemetry but is consistent with the other requirements of the communications subsystem.

2.1.4.2 Command Control Channel

The system (relays and users) command control channel is specified as a digital data channel. The maximum data rate for this channel shall be 20 kbit/sec at a BER of $\leq 10^{-6}$, although the data rate for any particular user will not exceed 10 kbit/sec. Command verification is required and must be provided by the narrowband user data channel (i.e., telemetry channel). As a part of the command control function, the collection of range tracking data characteristics of the spatial position of each relay satellite as well as satellite users shall be provided. Tracking data of users and the far relay shall be collected via the near relay. Range data accuracies will be as follows:

Communications Link	Random Range Error (ft 1σ)	Bias Range Error (ft)
Terminal to Near Relay	5	5
Terminal Direct to User	5	5
Terminal to Far Relay (via Near Relay)	7	7
Terminal to Users (via Near Relay)	7	7

Tracking data are not required on aircraft or surface users.

Both commanding and tracking are periodic functions, but the capability must exist to command any relay satellite or user (in the system) at any time. Tracking data collection shall be on a noninterference basis with command and other telemetry.

2.2 SPACEFLIGHT EXPERIMENTAL PROGRAM

Many of the performance characteristics required for the operational system have been or will be demonstrated prior to deployment of the previously described relay system. There are, however, aspects of the Laser Communication Subsystem that

must be experimentally validated before a commitment can be made to develop the operational system. The experimental program requires the design and development of a space-qualified Laser Communication Subsystem, integration of the subsystem into an STP spacecraft design, and the orbital test and evaluation program utilizing surface and aircraft terminals/users. If practicable, the orbital testing shall include the support of a separate spacecraft user (e. g. , another DoD or NASA satellite with compatible hardware). A synchronous equatorial orbit is required to achieve the objectives of this demonstration.

2.2.1 Space Test Program Satellite Payload Definition

The payload required to satisfy the requirements set forth above must consist of one Package A and one Package B with a limited amount of additional instrumentation. The detailed design requirements for the operational configuration of these packages as defined in Section 4 will apply to the STP model as design goals.

2.2.2 Payload Interface Requirements

The Laser Communication Subsystem design establishes an interface which requires that the STP spacecraft provide the support shown in Table 2-1. In addition, access to a computer is required to perform the acquisition and tracking computations and sequence control. This computer should be a general-purpose binary unit with random access memory. Storage requirements are 6 thousand 16-bit words. Read and write cycle times should be $< 3 \mu\text{sec}$ and access time should be $< 1 \mu\text{sec}$.

2.2.3 Experiment Priorities

The highest priority aspect of the Laser Communication Subsystem experimental program is the demonstration of wideband data readout (i. e. , 1 Gbit/sec) capability from the STP spacecraft to a surface terminal. The priority of the other experiments is shown in Table 2-2. Implicit within each experiment demonstration is the demonstration of the acquisition and tracking function of section 2.2.4.1.

Table 2-1
SUPPORT TO BE PROVIDED BY STP SPACECRAFT

	<u>Package A1</u>	<u>Package B</u>
Experiment Weight	116 lb (100 lb goal)	160 lb (100 lb goal)
28 VDC Power	300 W (140 W goal)	100 W (50 W goal)
Telemetry (1/4 - 1 SPS on all signals)		
Analog	90	80
Discrete	50	50
16-Bit Parallel	10	5
Command		
Discrete	10	10
10-Bit Parallel	35	15
Physical Mounting	See Fig. 2-2	See Fig. 2-3
Attitude Control		
Attitude Acceleration	$\leq 0.01 \text{ rad/sec}^2$	
3σ Attitude Rate Knowledge(a)	$\pm 50^\circ/\text{hr}$	
3σ Attitude Knowledge	$\pm 0.2^\circ$ line-of-sight error	
S/C Position Data		
Altitude Error	$\leq 2 \text{ nmi}$	
Cross-Track Error	$\leq 2 \text{ nmi}$	
In-Track Error	$\leq 2 \text{ nmi}$	
Thermal Constraints - Unobstructed view of deep space by cooling radiator on Package A		

(a) Superimposed on the orbital angular rate.

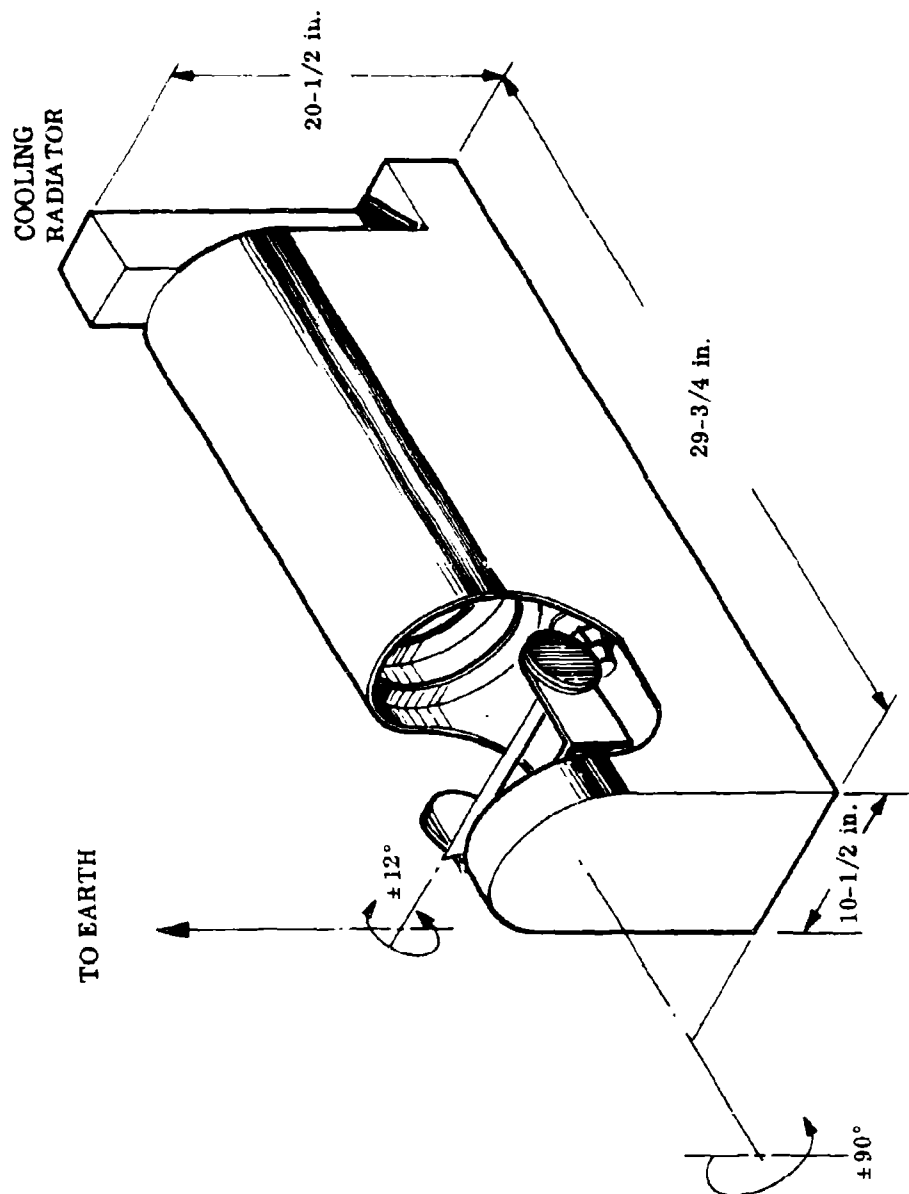


Fig. 2-2 STP Experiment - Package A

A-9

LOCKHEED PALO ALTO RESEARCH LABORATORY
 LOCKHEED MISSILES & SPACE COMPANY
 A GROUP DIVISION OF LOCKHEED AIRCRAFT CORPORATION

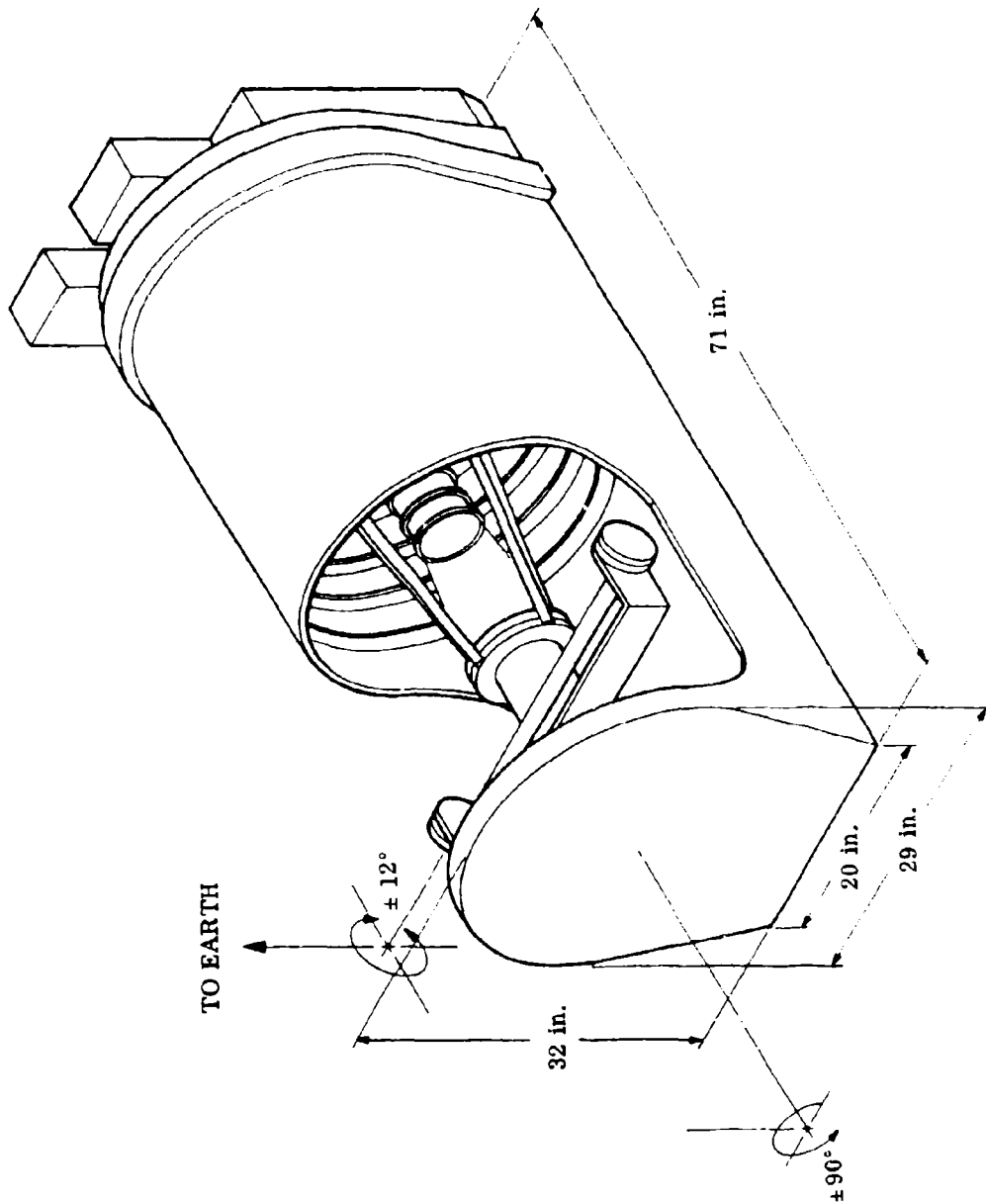


Fig. 2-3 STP Experiment - Package B

A-10

LOCKHEED PALO ALTO RESEARCH LABORATORY
 LOCKHEED MISSILES & SPACE COMPANY
 A GROUP DIVISION OF LOCKHEED AIRCRAFT CORPORATION

Table 2-2
EXPERIMENT PRIORITIES

<u>Priority Level</u>	<u>Demonstration Conditions</u>	<u>Data Type</u>	<u>Section Reference</u>
1	STP to Surface Terminal	1 Gbit/sec	2.2.4.2
2	Surface Terminal to STP	Command & Tracking	2.2.4.4
3	STP to Surface Terminal	Same as No. 1 plus multiplexed digital and analog data, including telemetry	2.2.4.3
4	STP to Aircraft Terminal	1 Gbit/sec	2.2.4.2
5	Aircraft Terminal to STP STP to Aircraft	Command & Tracking	2.2.4.4 2.2.4.3
6	Aircraft User to STP	1 Gbit/sec	2.2.4.2
7	Aircraft User or Another Spacecraft to STP and Re- layed to Surface	1 Gbit/sec	2.2.4.2
8	Ground User to STP	1 Gbit/sec	2.2.4.2

Priorities have been assigned with the following understandings:

- The most important task is to demonstrate transmission of 1 Gbit/sec data from a synchronous satellite to ground. If needed for initial demonstrations, rf links can be employed to assist in the command and control of the sub-system, although the next priority is also high.
- Completing low-bandwidth communication up-link from the ground to the satellite would be the next step, providing command and control over an optical link from the ground.
- The addition of multiplexed data and telemetry to the high-rate data from the satellite would be the next step and would complete a two-way link representative of all basic links in the ultimate system.
- Going through the same steps as above with a high-flying aircraft for the command terminal would be the next most important steps.
- Finally would come the demonstration involving a user satellite, the STP relay, and the ground terminal. This last step could move up in priority, depending on availability and cost.

2.2.4 Communications Experiment Data

The communications experiments shall be designed to provide as close a parallel to the postulated operational data requirements as possible without entailing undue development costs, schedule delays, or risks.

2.2.4.1 Acquisition and Tracking

The acquisition and tracking functions must be initiated under various background conditions in no more than 20 sec. An additional 10 sec may be used to optimize the pointing prior to initiation of communications over the wideband link.

2.2.4.2 Wideband Digital Data

The wideband digital data requirement is for a single 1-Gbit/sec (nominally) data link with the data quality specified by a BER of $\leq 10^{-6}$ in accordance with the experiment priorities of section 2.2.3.

2.2.4.3 Wideband Analog Data

The wideband analog data capability shall be demonstrated by frequency division multiplexing parallel rf subcarriers modulated by digital and/or analog signals over a continuous 1-GHz of rf bandwidth. Analog data may also be transformed by an analog-to-digital (A/D) converter and transformed back to analog after transmission. Such equipment will be peripheral to the main experimental hardware. Actual or simulated digital telemetry data at a maximum rate of 50 kbit/sec shall be included over the wideband links. These data shall be applied as shown in Table 2-2.

2.2.4.4 Command and Tracking Data

The capability of providing a minimum digital command rate of 20 kbit/sec with a BER of $\leq 10^{-6}$ is required; the capability of collecting range tracking data of the accuracy specified in section 2.1.4.2 is required. Both command and tracking data functions shall be exercised in accordance with the priorities shown in Table 2-2.

Section 3 FUNCTIONAL REQUIREMENTS

The following functional requirements associated with the Laser Communication Subsystem were derived from the postulated system requirements defined in Section 2.

3.1 SPATIAL COVERAGE

The required view angles necessary for the initial mutual acquisition of all elements of the system are listed in Table 3-1. These angles are based on the geometric properties of individual acquisition situations in accordance with previous definitions of users and terminals.

3.2 SYSTEM ELEMENT CAPABILITIES

The required functional capabilities of each system element (users, relays and receiving terminals) are set forth in the following paragraphs.

3.2.1 User Capabilities

The generalized user data readout channel (or wideband data channel), for example, at a near relay, will include the capability to handle simultaneously multiple user data together with individual telemetry signals from each user and a common range measurement data signal. The terminal command control channel will include the capability to provide a command signal integrated with a range measurement signal that can be addressed to a specific user at any time. Therefore, the functional capabilities required by a user to function with the relay system are a wideband data transmitter and a narrowband receiver. These elements are to be combined as a single unit called Package A, as shown in Fig. 3-1. In addition, this package must

Table 3-1

REQUIRED VIEW ANGLES

View From \ To	Near Relay	Far Relay	Low-Orbit User	Ground Terminal/ User	Aircraft Terminal/ User	Sync. Satellite User
Near Relay ^(a)	-	$\pm 45^\circ$ CP $\pm 10^\circ$ CP	$\pm 12^\circ$ IP/CP	$\pm 12^\circ$ IP/CP	$\pm 12^\circ$ IP/CP	$\pm 90^\circ$ IP
Far Relay ^(a)	$\pm 45^\circ$ $\pm 10^\circ$ CP	-	$\pm 12^\circ$ IP/CP	$\pm 12^\circ$ IP/CP (User Only) ^(e)	$\pm 12^\circ$ IP/CP (User Only) ^(e)	$\pm 12^\circ$ CP $\pm 90^\circ$ IP $\pm 12^\circ$ CP
Low Orbit User ^(b)	$\pm 110^\circ$ IP/CP $\pm 12^\circ$ CP/IP	$\pm 110^\circ$ IP/CP $\pm 12^\circ$ CP/IP	-	-	-	-
Ground Term/User ^(c)	0-90° EL $\pm 180^\circ$ AZ $\pm 10^\circ$ Yaw/Pitch	0-90° EL (User Only) ^(e) $\pm 180^\circ$ AZ $\pm 10^\circ$ Y/P (User Only) ^(e)	-	-	-	-
Aircraft Term/User ^(d)	$\pm 45^\circ$ Roll $\pm 90^\circ$ IP $\pm 12^\circ$ CP	$\pm 45^\circ$ Roll $\pm 90^\circ$ IP $\pm 12^\circ$ CP	-	-	-	-
Sync. Sat. User ^(a)	-	-	-	-	-	-

(a) View angles in-plane (IP) and cross-plane (CP) referenced to the orbit plane and geocentric radius (nadir line).

(b) View angles IP and CP referenced to orbit plane and negative geocentric radius (zenith line).

(c) View angles azimuth (AZ), referenced to direction toward equator, and elevation (EL) referenced to local tangent plane at the surface.

(d) View angles roll and yaw referenced to negative geocentric radius (zenith line) and a normal to the zenith in the direction of flight.

(e) Far relay not visible from surface terminal.

have the ability to point the required optical antennas (telescopes) in the proper direction for communications link acquisition. After signal acquisition, appropriate auto-tracking and point-ahead capabilities must be included in the designs.

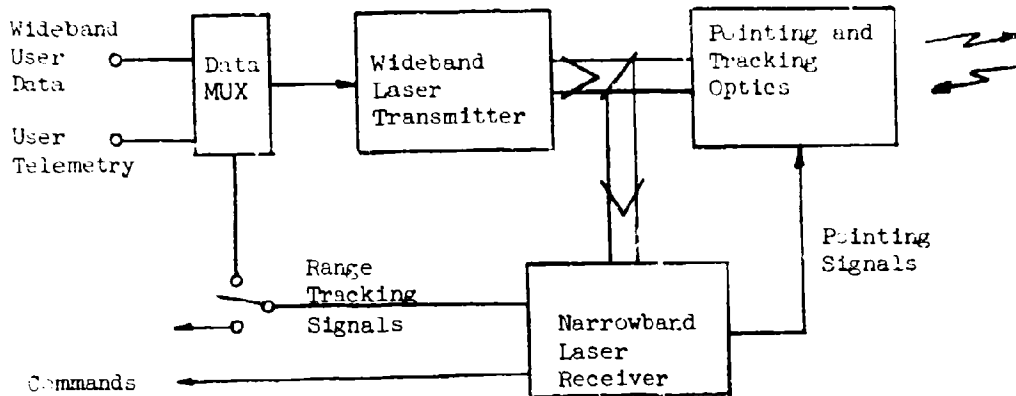


Fig. 3-1 Package A Simplified Functional Diagram

3.2.2 Relay Capabilities

The functional capabilities required on the synchronous relay satellite to communicate with a user are a wideband data receiver and a narrowband data transmitter, which are to be combined as a single unit called Package B. The required functional capability is shown in Fig. 3-2.

The relay satellite must also have the capability to transfer user data to either a second relay satellite or a receiving terminal. This data transfer shall be accomplished by the addition of a Package A to the relay. Two additional Package B's must be introduced into the relay to meet the minimum system support requirements defined in Section 2. Each Package A and B on the relay must have the ability to point the required optical antennas (telescopes) in the proper direction for communications link acquisition. After signal acquisition, appropriate auto-tracking and point-ahead capabilities must be included in the designs. An additional Package A on the relay will not only provide redundancy but will also enable simultaneous transmission to two ground stations which will assist in station switching in case of intermittent cloud cover.

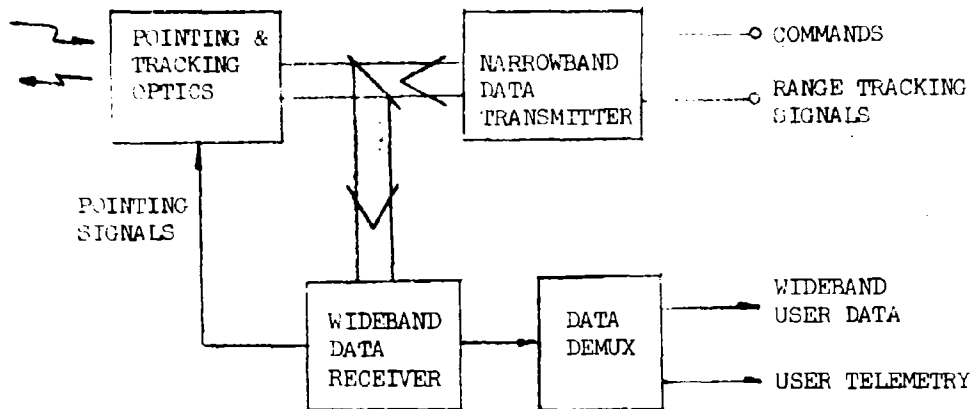


Fig. 3-2 Package B Simplified Functional Diagram

3.2.3 Receiving Terminal

The receiving terminal (surface or aircraft) must have the functional capability to receive and track the wideband data channel from a relay satellite as well as transmitting narrowband command and tracking signals to individually addressed relays or users via the relays. This capability shall be provided by the use of a modified B package. The capability to separate and process user data and telemetry signals (from users and relays) contained on the wideband channel is required. The ability to format commands and generate range tracking signals must also be provided. Command format shall be compatible, through an interface unit, with standard Air Force SGLS system requirements.

3.3 OPERATIONAL SYSTEM CAPABILITIES EXPECTED WITH SUBCARRIER MODULATION OF LASER

The capabilities resulting from the integration of multiple users into a two-hop relay system shall be as shown in Fig. 3-3. The wideband channel data from multiple users shall be combined using both quadriphase shift keying and frequency division multiplex techniques, and the composite signal used to modulate the laser transmitter. These data consist of independent user mission data in analog or digital form and

continuous digital telemetry from each user as well as the relay satellites. The composite modulating signal spectrum could appear as shown in the examples of Fig. 3-4. In this figure, the first spectrum (a) represents the complete signal from a single user, while in (b) the telemetry subcarrier from the relay has been added prior to transmission to a second relay or receiving station. Spectrum (b) can also represent two users, each having ≥ 500 Mbit/sec data rate, or more than two users with digital time division multiplexing up to 500 Mbit/sec in each channel. In Fig. 3-4(c), the composite spectrum represents digital data at a 600 Mbit/sec rate from one user, 200 Mbit/sec from a second user, 50 kbit/sec telemetry signals from the two users as well as from both far and near relay satellites, and the single addressable return ranging signal.

Referring to Fig. 3-3, the narrowband channel must also serve as the optical beacon to aid in the initial optical beam acquisition process. After completion of the acquisition sequence, this beacon becomes the command/tracking data link. A single command data link is required between each cooperating pair of elements of the system. Commanding of a specific user or relay shall be accomplished by the use of a unique destination address for each command recipient. Suitable ranging signals shall be impressed upon the narrowband command channel, on a noninterference basis, for use in a turnaround ranging mode. The desired turnaround point (i.e., the satellite to be tracked) shall be selectable by command from the receiving terminal.

3.4 EXPERIMENTAL PROGRAM CAPABILITIES

The required capabilities of the operational system that shall be demonstrated in the STP Experimental Program are shown in Fig. 3-5. A simulated system user with the Package A capability for transferring wideband data, receiving commands, returning ranging signals, and providing telemetry shall be provided. This user capability shall be applied in the experimental program in accordance with the priorities defined in section 3.2.3 and therefore must be compatible in design and environmentally with the intended applications.

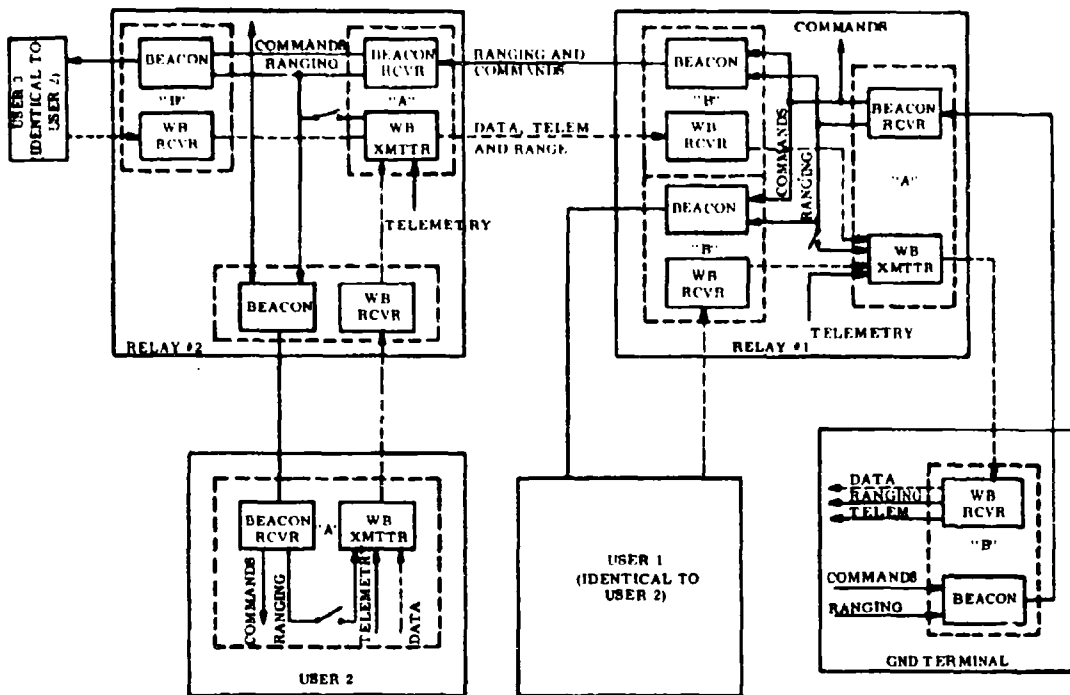


Fig. 3-3 Functional Block Diagram of Operational System

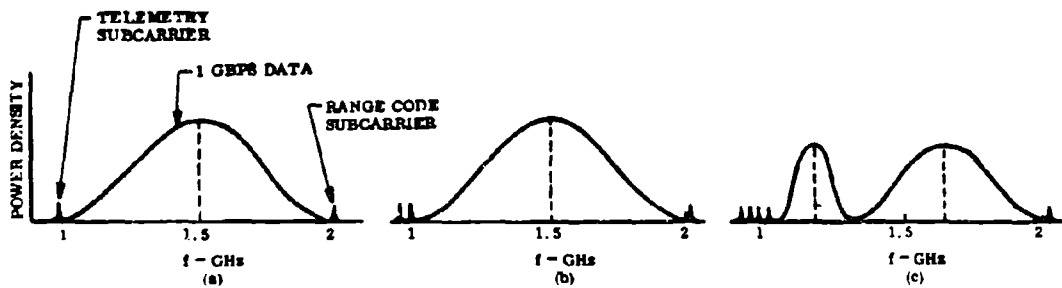


Fig. 3-4 Typical RF Spectra at Optical Modulator Input for Various Data Combinations

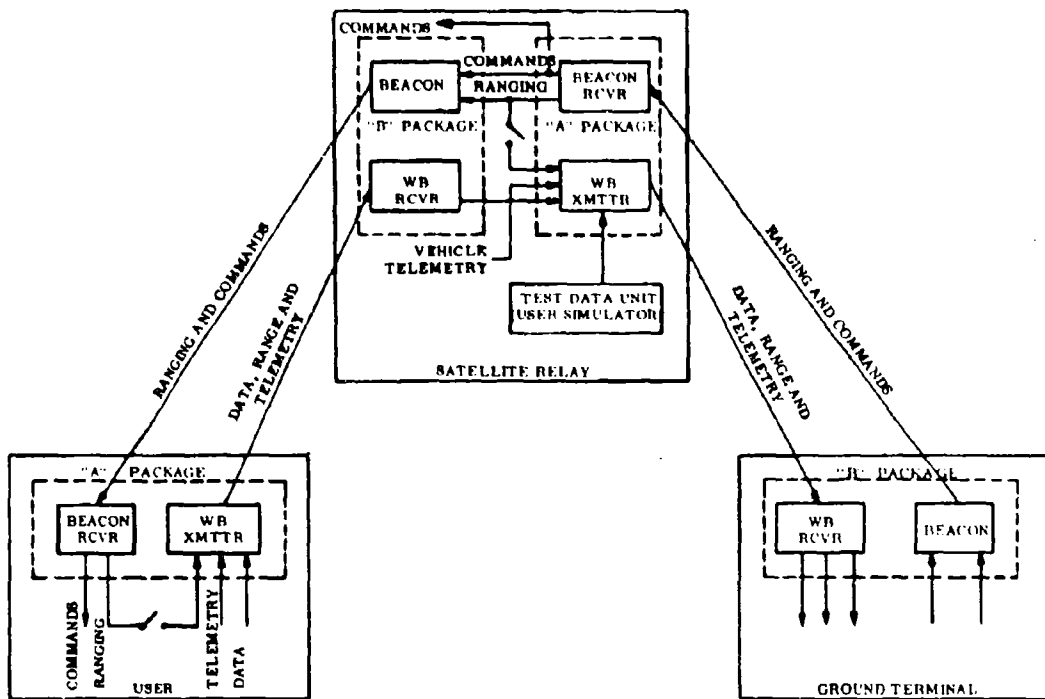


Fig. 3-5 Functional Block Diagram of STP Experimental Program

The STP spacecraft simulating a relay satellite shall provide the capability to forward wideband data (analog and/or digital) received from the simulated system user as well as supplying additional digital data representative of a second system user. This capability provides greater test flexibility, more rigorous testing, and improved reliability. The STP Laser Communication Subsystem shall also provide a command channel through to the user and a command interface with the spacecraft. The commandable capability to turn around range signals and multiplex spacecraft data shall be provided. The Package A view angles from the spacecraft shall provide at least earth coverage, but Package B must have the capability to view either the earth or an experimental synchronous spacecraft user, if available. It may be desirable for Package A also to have the capability of pointing to an experimental synchronous satellite.

The receiving terminal capability shall be compatible with either ground or aircraft deployment options, as required by the priority listing of section 2.2.3. The system performance evaluations shall be performed at the ground installation; the extent of aircraft data processing required is to be determined. The ground and aircraft system may have different antenna systems than either Package A or Package B, but their communication systems must be compatible.

A-20

LOCKHEED PALO ALTO RESEARCH LABORATORY
LOCKHEED MISSILES & SPACE COMPANY
A GROUP DIVISION OF LOCKHEED AIRCRAFT CORPORATION

Section 4

DESIGN REQUIREMENTS

The requirements presented in this section were derived by the translation of functional requirements into practical equipment design concepts that can be evaluated by an STP Experimental Program. The resulting design requirements have been segregated into groups that apply to either Package A or Package B designs and into a general category that pertains to both package designs.

4.1 GENERAL

The following design requirements apply to all aspects of design for a Laser Communication Subsystem whose performance capabilities will be space-flight validated:

- Laser Source: Nd:YAG
- Acquisition Time: ≤ 20 sec
- Pointing Optimization Time: ≤ 10 sec
- Optical Beamwidth: 1 arcsec
- Pointing Accuracy: ± 0.1 beamwidth (1σ)
- Maximum Tracking Rate: $2000 \mu\text{rad/sec}$ (approx.)
- Maximum Point-Ahead Angle: $81 \mu\text{rad}$
- Operating Life: 7-year design life
5-year minimum acceptable life
- Operating Voltage: 28 ± 5 VDC
- Thermal Control: Conduction cooling from components
via space radiators
- Environmental Qualification: (a) Compatible with Titan IIIC launch
(b) Survivable in radiation environment
per SAMSO Exhibit 69-13 and NASA
SP 3024
(c) EMI compatibility with MIL-STD-461A
- Maintainability Level: To be determined
- Vulnerability Level: To be determined
- Data Handling: To be determined

A-21

4.2 PACKAGE A

The following requirements apply only to the Package A design:

- Wideband Transmit Wavelength: 0.53 μm
- Narrowband Receive Wavelength: 1.06- μm Acquisition
0.63- μm Fine Tracking
- Laser Operational Mode: CW
(Wideband)
- Telescope Size: 6 in. diameter
- Line-of-Sight Scan Angles: $\pm 90^\circ \text{ IP} / \pm 12^\circ \text{ CP}^*$
- User Data Characteristics: Digital, single or multiple channel,
synchronous, asynchronous or analog
- User Data Rate/Bandwidth: Digital, 1 Gbit/sec
Analog, 1 GHz
- User Data Interface: To be determined
- User Data Accuracy/Quality: Digital, $\text{BER} \leq 10^{-6}$
Analog $\text{S/N} \geq 35 \text{ dB}$
- Telemetry Data Characteristics: Digital, dual channel
- Telemetry Data Rate: 50 kbit/sec (maximum)
- Telemetry Data Accuracy: $\text{BER} \leq 10^{-5}$
- DC Power Input: 140 W (Design goal)
- Package Weight: 100 lb (Design goal)
- Package Volume: 1 ft^3 (typ.) (excluding telescope
antenna)(Design goal)

* $\pm 110^\circ \text{ IP} / \pm 12^\circ \text{ CP}$ for LOS.

4.3 PACKAGE B

The following requirements apply only to the Package B design:

- Transmit and Receive Wavelengths: 0.53 μm
- Laser Operational Mode (Beacon/Narrowband): 1.06- μm Acquisition beacon
0.63- μm Fine tracking beacon
- Telescope Size: 2 ft diameter (maximum)

- Line-of-Sight Scan Angles: $\pm 90^\circ$ IP* and $\pm 12^\circ$ CP
- Command Data Characteristics: Digital signal, addressable
- Command Rate: ≤ 20 kbit/sec
- Command Data Accuracy: $\text{BER} \leq 10^{-6}$
- Ranging Technique: Compatible with command/beacon implementation
- DC Power Input: 50 W (Design goal)
- Package Weight: 100 lb (Design goal)
- Package Volume: 1 ft^3 (excluding telescope antenna)
(Design goal)

*See section 3.1 for definitions.

Section 5
REFERENCES

1. Contract Statement of Work (SOW) for Space Data Relay Subsystem - Laser Communications, Preliminary Subsystem Design, Contract F04701-71-C-0329
2. Proposal for Laser Communication, Preliminary Subsystem Design for the Space Data Relay Subsystem, LMSC-B273007, Volume I - Technical, Lockheed Missiles & Space Company, 11 Mar 1971
3. Titan III Space Launch Integration Program Plan for a Definition Period, SAMSO-CR-67-110, Revised 14 Feb 1969
4. Titan IIC System Characteristics and Performance for a Near-Synchronous Equatorial Mission, Report No. TOR-0066 (5112-30)-3, Aerospace Corporation, 27 Feb 1970

Appendix B

POISSON NOISE AND ERROR PROBABILITY
IN OPTICAL COMMUNICATION
USING BI-PHASE MODULATED SUBCARRIERS

by

Dr. G. F. Herrmann

(Previously distributed as Technical Memorandum No. 9)

LOCKHEED PALO ALTO RESEARCH LABORATORY
LOCKHEED MISSILES & SPACE COMPANY
A GROUP DIVISION OF LOCKHEED AIRCRAFT CORPORATION

I. Introduction

An optical communication system employing subcarrier bi-phase modulation is currently under consideration.¹ It is the purpose of this note to set a bound on the error rate in this mode of operation. In the simplest system of this kind a light beam is intensity modulated at a single subcarrier frequency ω . The signal, of duration τ , is of the form

$$S_{\pm}(t) = A(1 \pm \mu \sin \omega t) \quad (1)$$

where $S(t)$ is the light intensity, μ the modulation index and the + or - sign applies depending on which of two binary signals is transmitted.

Detection is performed by multiplying the receiver photo-current $I(t)$ by a local oscillator signal of the form $\sin \omega t$ and integrating the product over the time τ . The resulting parameter

$$G = \int_0^{\tau} I(t) \sin \omega t dt \quad (2)$$

provides a criterion for deciding which signal was transmitted. For $G > 0$ one puts $S = S_+$, for $G < 0$, $S = S_-$.

For optimum operation it is desirable for $\omega\tau$ to be a multiple of 2π , and we shall assume this to be the case.

Certain more complicated variants of this system are also contemplated. One procedure consists in the simultaneous transmission of two perpendicularly polarized signals

$$S_{1\pm} = A(1 \pm \mu \sin \omega t) \quad (3a)$$

and

$$S_{2\pm} = A(1 \mp \mu \sin \omega t) \quad (3b)$$

in push-pull relation. This mode of operation is more efficient in the use of power since the total beam intensity, $S_1 + S_2$, remains constant throughout. Detection is performed separately in the two polarizations and the two photo currents are subtracted from each other. The resultant current is then processed as in the simple system by determining G in accordance with Eq. (2).

More generally, the light beam can be made to accommodate several channels through simultaneous modulation by several subcarrier frequencies. Since each frequency allows for two channels in quadrature the typical composite signal is of the form

$$S = A(1 + \sum_1 (\pm \mu_1) \sin \omega_1 t + \sum_1 (\pm \bar{\mu}_1) \cos \omega_1 t) \quad (4)$$

during any given bit-interval τ . Detection is performed by separately multiplying the receiver photo-current by independent local oscillator signals of the form $\sin \omega_1 t$, and $\cos \omega_1 t$ and integrating over τ . In analogy to (2) one obtains a set of parameters $G(\omega_1)$ to serve as estimators for the transmitted digit in each channel.

In any of the above systems detection is assumed to be effected by means of a photo emitter. The photodetector current is a sequence of discrete electrons with generalized Poisson statistics. Because of the binary nature of the decision process very low error rates are accomplished at signal levels corresponding to relatively few photo-electrons per bit. Under these conditions a calculation of the error probability based on the assumption of an additive Gaussian shot-noise is inaccurate. It is the purpose of this note to calculate an upper bound on the error based on a direct statistical analysis of the photo-electron current.

II. Photo Current Statistics

The statistical theory of photo-electron counting is reviewed in a recent article by Karp, O'Neill and Gagliardi¹ which includes a comprehensive list of references on this subject. Photo emission can be described in terms of a semi-classical theory as a Poisson process with a rate that is determined by the intensity of the incident radiation.

Let $S(t)$ represent the intensity of light incident on a photocathode. The photo-emission rate is given by

$$\alpha(t) = CS(t) \quad (5)$$

where C is a constant. The emission rate $\alpha(t)$ is defined as the probability density that an electron be emitted at time t [i.e., $\alpha(t)dt$ is the probability of emission during the interval between t and $t + dt$]. By introducing a variable

$$\bar{n}(\tau) = \int_0^{\tau} \alpha(t)dt \quad (6)$$

the process described by (1) can be represented² as a Poisson process with probability distribution

$$P_n(\bar{n}) = \frac{\bar{n}^n}{n!} e^{-\bar{n}} \quad (7)$$

Here $P_n(\bar{n})$ is the probability of n photo emissions during the interval $0 \leq t \leq \tau$, and \bar{n} represents the mean, or expected value of n .

III. Modulation by Single Subcarrier

The signal in this case is given by (1). The emission rate is accordingly

$$\alpha(t) = \bar{\alpha}(1 + \mu \sin \omega t) \quad (8)$$

where $\bar{\alpha}$ is a constant representing the time average of α . The current is the sum of discrete pulses associated with individual photo electrons. In section VII we show that provided the response time of the system is short compared to τ these pulses can be represented as a series of Dirac delta functions of the form $\delta(t - t_1)$ where the t_1 represent the emission times. Thus

$$I(t) = \sum_1 \delta(t - t_1) \quad (9)$$

and the detector output, in accordance with (2) is

$$G = \sum_1 \sin \omega t_1. \quad (10)$$

G is a random variable with a distribution determined by the distributions of the emission times t_1 .

The problem of determining the probability of an error in the received binary digit is now formulated as follows. Assume that S_+ is the transmitted signal. If $G < 0$ then the receiver will decide that $S = S_-$ and therefore be in error. If the a priori probability for the transmission of S_+ and S_- is equal then the probability of the above occurrence equals the bit error rate.

Our objective is therefore to determine

$$P_E = F_G(0) = \text{Prob} (G < 0) \quad (11)$$

where F_G is the cumulative distribution function of G for a Poisson process with a time varying rate

$$\alpha(t) = \bar{\alpha} (1 + \mu \sin \omega t). \quad (12)$$

The solution is undertaken in two steps. Consider the interval τ . $P_n(\tau)$, as given by (7) represents the probability that exactly n electrons were

emitted during this interval. Let $\bar{F}_G(G/n)$ be the conditional cumulative distribution function for G , given that the number of emitted electrons is exactly n . Then clearly

$$F_G = \sum_n P_n(\bar{n}) \bar{F}_G(G/n) \quad (13)$$

and in particular

$$P_E = \sum_{n=0}^{\infty} P_n(\bar{n}) \bar{F}_G(0/n) \quad (14)$$

The conditional distribution $F_G(G/n)$ can be regarded as representing the cumulative distribution function of the random variable

$$G_n = \sum_{i=1}^n u_i \quad (15)$$

where

$$u_i = \sin \omega t_i \quad (16)$$

and t_i represents the emission time of a particular electron, given that that electron was emitted during the interval $0 \leq t \leq \tau$. Since in a Poisson process individual occurrences (electron emissions in the present case) are independent, the emission time t_i of each specific electron may be regarded as a random variable with a probability density $f_{ti}(t)$ that is proportional to the emission probability $\alpha(t)$ and that is independent of the emission times of the other electrons in the interval. It is given by

$$f_{ti}(t) = \frac{1}{\tau} (1 + \mu \sin \omega t) \quad (17)$$

where the proportionality constant was determined from the condition

$$\int_0^{\tau} f_{ti}(t) dt = 1$$

under the assumption that $\omega\tau$ is a multiple of 2π .

From (17) it follows that the random variable u_1 is characterized by a probability density

$$f_{u1}(u) = \frac{1}{\pi} \frac{1 + \mu u}{\sqrt{1 - u^2}}; \quad -1 \leq u \leq 1. \quad (18)$$

G_n is therefore the sum of n independent identically distributed variables with probability density (18). Exact calculation of the distribution function of G_n for all n appears prohibitively complicated. One can however readily get an upper bound $B(n)$ for the value of $F_G(0/n)$ which we require in Eq. (14). This is provided by the Chernoff-Bound³ which is particularly suitable for problems of this kind. This bound has the form

$$B(n) = b^n \quad (19)$$

with

$$b = E[e^{-\lambda u}] \quad (20)$$

where $E[]$ stands for the expectation. In the present case the parameter λ is obtained by solving the equation

$$E[ue^{-\lambda u}] = 0. \quad (21)$$

In accordance with Eq. (18), Eq. (21) assumes the explicit form

$$\int_{-1}^1 ue^{-\lambda u} \left[\frac{1 + \mu u}{\pi \sqrt{1 - u^2}} \right] du = -I_1(\lambda) + \mu I_0(\lambda) + \mu I_2(\lambda) = 0 \quad (22)$$

where the I_k are modified Bessel functions. Similarly, Eq. (20)

becomes

$$b(\mu) = \int_{-1}^1 e^{-\lambda u} \left[\frac{1 + \mu u}{\pi \sqrt{1 - u^2}} \right] du = I_0(\lambda) - \mu I_1(\lambda). \quad (23)$$

Eq. (22) has been solved numerically to give λ as a function of μ . Substitution into (23) then yielded b as a function of μ .

We are now in a position to establish a bound for the error probability P_E . Since $\bar{F}_G(0, n)$ is bounded by $B(n) = b^n$, Eqs. (14) and (7) yield

$$P_E \leq \sum_{n=0}^{\infty} \frac{\bar{n}^n}{n!} e^{-\bar{n}} b^n = e^{-\bar{n}(1-b)} \quad (24)$$

or

$$P_E(\text{db}) = 10 \log_{10} P_E \leq -10[(1-b) \log_{10} e] \bar{n} \quad (25)$$

The upper bound to $P_E(\text{db})$ is therefore proportional to the mean number \bar{n} of electrons emitted during the bit duration τ . Through its dependence on b it also is a function of the modulation index μ . In Figure 1 the upper bound to $P_E(\text{db})/\bar{n}$, namely $-10(1-b)\log_{10} e$, is plotted against μ and in Figure 2 against μ^2 . The latter figure demonstrates an approximate proportionality between the variables. This is to be expected. μ^2 represents the power associated with the high-frequency modulation and $\mu^2 \bar{n}$ can therefore be regarded as representing the number of electrons specifically associated with the signal.

IV. Push-Pull Operation

In this mode of operation two complementary signals as given by Eq. (3) are transmitted using two perpendicular linearly polarized components of the light beam. The two photo currents $I_1(t)$ and $I_2(t)$ resulting from independent detection of the two polarizations are subtracted from each other and processed in the same manner as above by multiplication with a local oscillator signal of the form $\sin \omega t$. The estimator is given by

$$G = \int_0^{\tau} [I_1(t) - I_2(t)] \sin \omega t \, dt \quad (26)$$

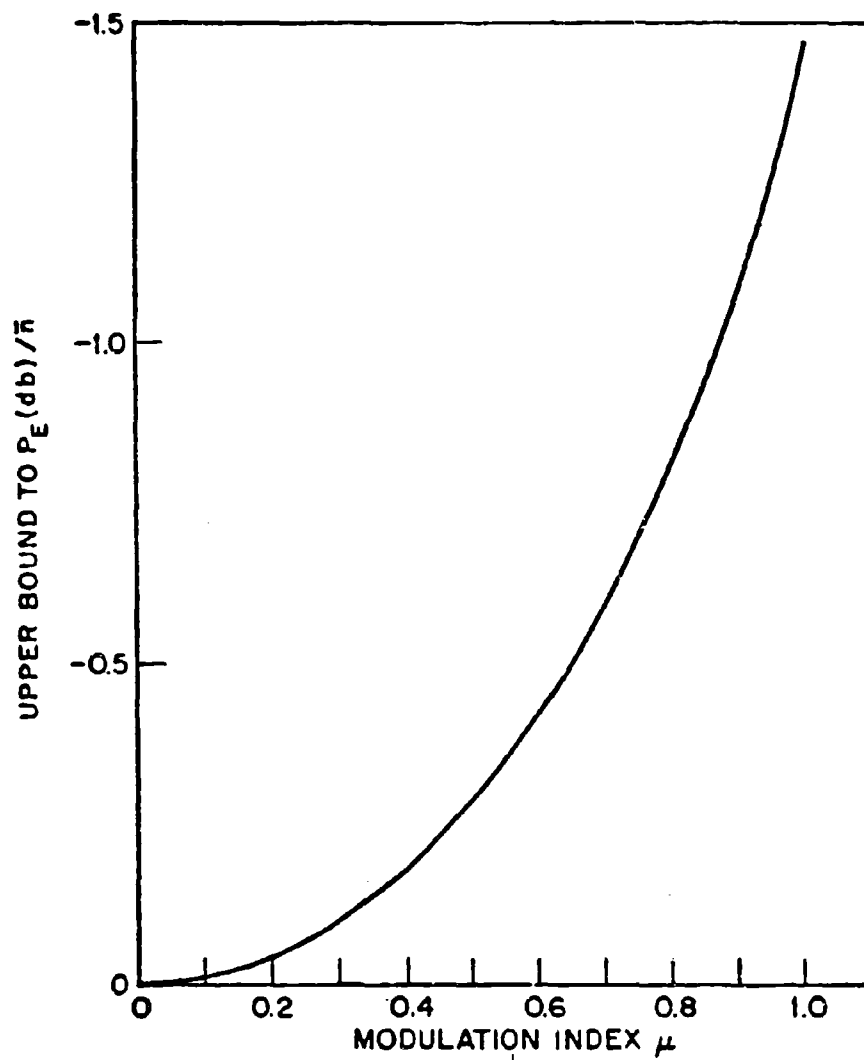


Fig. 1 Upper Bound to Probability of Error (in decibels) as a Function of Modulation Index μ . The term \bar{n} is the mean number of photoelectrons per bit

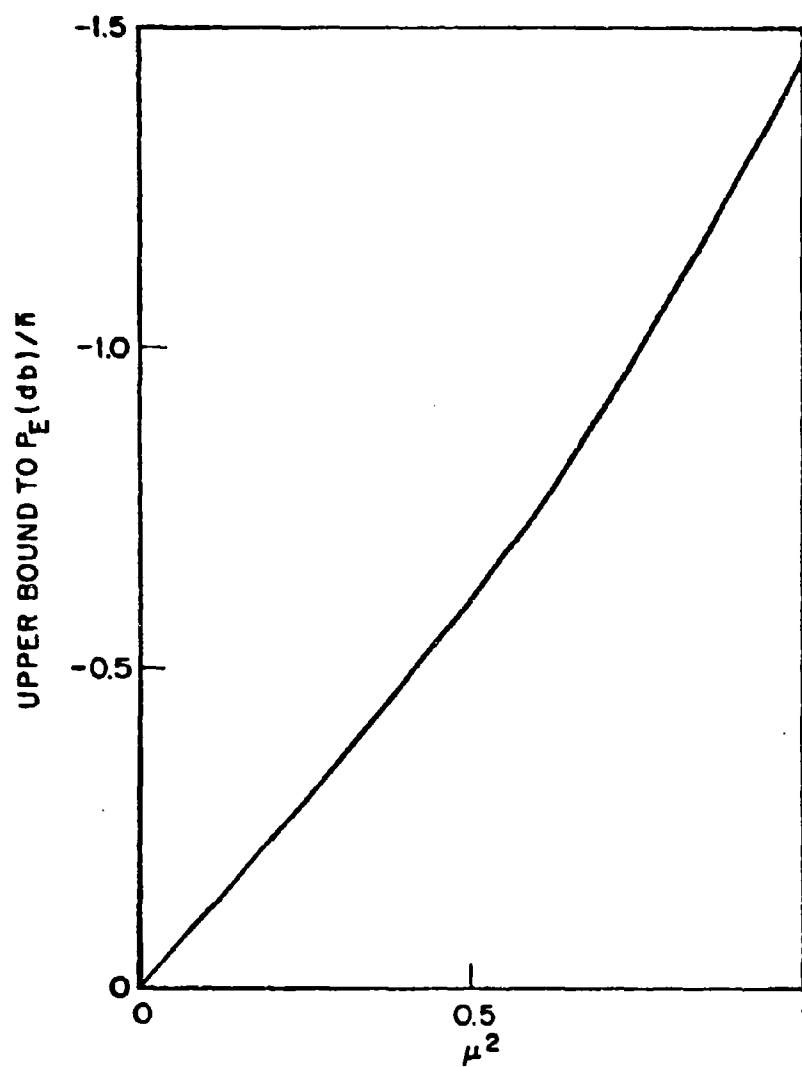


Fig. 2 Upper Bound to Probability of Error (in decibels) as a Function of μ^2

For discretely emitted electrons this yields, in analogy to (10)

$$G = \sum_1 \sin \omega t_{11} - \sum_k \sin \omega t_{2k} \quad (27)$$

where t_{11} is a photo-emission time in the first detector, and t_{2k} in the second detector.

The analysis proceeds exactly along the lines followed in Section III. Assuming

$$S_1 = A(1 + \sin \omega t) \quad (28a)$$

$$S_2 = A(1 - \sin \omega t) \quad (28b)$$

the probability of error equals the probability that $G < 0$.

In analogy to Eq. (12) one has

$$\alpha_1(t) = \bar{\alpha}(1 + \mu \sin \omega t) \quad (29a)$$

and

$$\alpha_2(t) = \bar{\alpha}(1 - \mu \sin \omega t) \quad (29b)$$

where α_1 and α_2 are the emission rates in the first and second detectors, respectively, and $\bar{\alpha}$ is the time averaged emission rate in either detector.

As in Eq. (16) one defines random variables

$$u_{11} = \sin t_{11} \quad u_{2k} = - \sin t_{2k} \quad (30)$$

The probability densities for u_{11} and u_{2k} are easily calculated. They are identical to each other and are again given by Eq. (18). One can therefore discard the subscripts 1 and 2 and write G in the form

$$G = \sum u_i$$

as the sum of independent identically distributed variables. This equation is identical with Eq. (15) and the distribution function for G is

therefore unchanged. Note however, that summation is over all electrons emitted from both cathodes.

One may therefore conclude that the error estimate for the single detector applies to the push-pull system, with the provision that \bar{n} in Eqs. (24) and (25) and in Figs. 1 and 2 refers to the total mean emission rate of the two detectors.

V. Multichannel Operation

The results of Section 3 are easily generalized to the case where several bi-phase signals with different microwave subcarrier frequencies are simultaneously transmitted on a single light beam. At each microwave frequency it is possible to transmit two channels with phase in quadrature. The resulting signal can therefore be represented in the form

$$S = A \left[1 + \sum_i (\pm \mu_i \sin \omega_i t \pm \bar{\mu}_i \cos \omega_i t) \right],$$

assuming that two channels with waveforms $\sin \omega_i t$ and $\cos \omega_i t$, respectively, are transmitted at each frequency.

In order to avoid cross-talk, the bit interval τ is chosen so that $\omega_i \tau$ is a multiple of 2π for all ω_i . Without loss of generality we assume that during the particular bit-interval under consideration the transmitted signal has + signs for all channels in the above equation. In that case

$$\alpha(t) = \bar{\alpha} [1 + \sum (\mu_i \sin \omega_i t + \bar{\mu}_i \cos \omega_i t)] \quad (31)$$

We follow the same procedure as before, and concentrate on the coherent detection of the signal at a particular subcarrier frequency,

say ω_1 . As in Eq. (16) we define

$$u_1 = \sin \omega_1 t_1$$

and employ

$$G = \sum u_1 \quad (38)$$

as estimator for the $\sin \omega_1 t$ channel. It is easily shown that under the assumption $\omega_1 \tau = 2\pi N_1$ where N_1 is an integer, the presence of signals in other channels has no effect on the distribution function of u_1 . As in the case of the single channel it is given simply by (18). The distribution function for G remains, similarly, unchanged.

Eqs. (24) and (25) therefore again provide estimates for the error probability. In applying these equations and in using Figs. 1 and 2, one should substitute μ_1 or $\bar{\mu}_1$, respectively, for μ and interpret \bar{n} as the mean total number of electrons emitted from the photocathode during the interval τ .

VI. The Effect of Background Radiation

An accurate evaluation of the contribution of background radiation to the probability of error is in general quite difficult. In practice, a simplified treatment of this effect which ignores the incoherent nature of the radiation is under most normal conditions not far off the mark.

In the semi-classical model² the background radiation after passing through appropriate optical filters can be viewed as narrow band Gaussian noise whose instantaneous intensity determines the emission rate from the photo-cathode. The distribution of photoelectrons is governed by Bose Einstein Statistics rather than the Poisson statistics

characteristic of coherent radiation. However, under almost all conceivable practical circumstances the regime of operations is one where the Poisson distribution represents an excellent approximation. Crudely stated, the random character of the background radiation is a minor source of noise compared with the shot noise associated with the increased photo-electron current due to this radiation. One may therefore treat the background radiation as if it were of constant intensity. In this approximation the intensity of the incident radiation in the case of single-channel operation is represented by

$$S_{\pm}(t) = B + A(1 \pm \mu \sin \omega t) \quad (33)$$

where B is the background intensity. By defining an effective modulation index

$$\mu_{\text{eff}} = \frac{A}{A+B} \mu \quad (34)$$

one can rewrite this equation in the form

$$S_{\pm}(t) = (B+A)(1 \pm \mu_{\text{eff}} \sin \omega t). \quad (35)$$

From here on, the treatment is identical to that followed in Section III. In the results, as summarized in Eqs. (24) and (25) and in Figs. 1 and 2, μ_{eff} must be substituted for μ , and \bar{n} represents the time average of the total number of emitted photo-electrons.

An identical procedure applies to multichannel operation.

VII. The Effect of a Finite Response Time

A more accurate representation of the photo current than that given by Eq. (9) is

$$I(t) = \sum_i h(t - t_i) \quad (36)$$

where $h(t)$ is the impulse-response function of the system. The accurate expression for G is accordingly

$$G = \sum_1 \int_0^{\tau} h(t - t_1) \sin \omega t dt = \sum_1 g_1 \quad (37)$$

with summation restricted to t_1 within the interval.

If the response time is short compared to τ and if t_1 is not near the interval boundaries then one may assume that $h(t - t_1)$ is effectively zero outside the interval. In that case

$$g_1 = \int_0^{\tau} h(t - t_1) \sin \omega t dt \approx \quad (38)$$

$$\int_{-\infty}^{\infty} h(t - t_1) \sin \omega t dt.$$

g_1 can be represented in terms of the transfer function $H(\omega)$, where

$$H(\omega) = \int_{-\infty}^{\infty} h(t) e^{-i\omega t} dt.$$

Putting $H(\omega)$ in polar form,

$$H(\omega) = R e^{i\theta}$$

one easily obtains

$$g_1 \approx R \sin(\omega t_1 - \theta)$$

and hence

$$G \approx R \sum \sin(\omega t_1 - \theta); \quad 0 \leq t_1 \leq \tau \quad (39)$$

This expression differs from Eq. (10) only in the proportionality factor R and the constant phase delay θ . The delay is easily compensated for electronically, and the proportionality factor does not effect the sign of G . The substitution of $\delta(t - t_1)$ for $h(t - t_1)$ is therefore legitimate

in this approximation.

In making the approximation incorporated in Eq. (38) one in effect neglects the tail of the impulse-response function $h(t - t_1)$ extending beyond τ . The approximation would tend to become increasingly more valid as the response time approaches τ . On the other hand there are no specific requirements that link the response time to the modulation frequency. In fact, $h(t)$ may extend over several cycles of the modulating signal. Although this will cause a reduction in the output signal it in no way affects the statistical properties involved in the decision process.

VIII. Calculation of Error Probability by "Tilted-Probability" Method

The principal advantage of the Chernoff-Bound is that it provides a sense of certitude by setting an absolute upper bound to the probability of error. A more realistic value for the error rate is provided by an approximation technique widely used in Information and in Coding-Theory which employs so-called tilted probabilities.⁴ The values predicted by this method lie in many cases substantially below the Chernoff-Bound.

Recall that the Chernoff-Bound was introduced in the course of evaluating the cumulative distribution function (c.d.f.) $\bar{F}_G(0/n)$ of the random variable G_n . According to Eq. (15), G_n is given by

$$G_n = \sum_{i=1}^n u_i$$

and is thus the sum of n independent, identically distributed random variables u_i . In evaluating the distribution function of such a sum, one is tempted to invoke the central limit theorem (CLT), but such a procedure is not valid if applied in a straightforward manner. The CLT is useful at points that are within a standard deviation or so from the mean of the distribution, and this standard deviation varies roughly as the square root of n . On the other hand, since the mean of G_n is given by

$$E(G_n) = nE(u) \quad (40)$$

The point $G_n = 0$ recedes farther from the center of the distribution in direct proportion to n itself, and, therefore, in the limit of large n , lies outside the range of applicability of the CLT. In the present case, convergence to the central limit merely implies the obvious fact that $F_G(0/n)$ goes to zero as $n \rightarrow \infty$.

This difficulty is circumvented if one addresses oneself to a set of modified random variables that are tailored so as to optimize the application of the CLT.

Let $f_u(u)$ represent the probability density function (p.d.f.) of u . Define a new set of variables $u(\lambda)$, characterized by a parameter λ , such that the p.d.f. of $u(\lambda)$ is

$$f_{u(\lambda)}(x) = e^{-M(\lambda)} f_u(x) e^{-\lambda x} \quad (41)$$

where $M(\lambda)$ is determined from the condition that the integral over a p.d.f. equals one, and is therefore given by

$$M(\lambda) = \lim_{n \rightarrow \infty} E_u[e^{-\lambda u}] \quad (42)$$

Multiplication of $f_u(x)$ by $e^{-\lambda x}$ (for $\lambda > 0$) has the effect of accentuating the probability for small values of x while lowering that of high values. One therefore refers to $f_{u(\lambda)}(x)$ as a "tilted-probability" function. The purpose of the tilting is to create a new variable $u(\lambda)$ whose mean equals zero, and in turn, a new sum

$$G(\lambda) = \sum_{i=1}^n u_i(\lambda) \quad (43)$$

whose mean is also zero. We may now legitimately apply the CLT to these

new "tilted" variables.

In order for $u(\lambda)$ to have zero mean, λ is chosen to satisfy

$$E[u(\lambda)] = e^{-M(\lambda)} \int_{-1}^1 u e^{-\lambda u} f_u(u) du = 0. \quad (44)$$

We shall assume in all subsequent discussion that λ satisfies Eq. (44).

The usefulness of the approach rests on the fact that the new variable $G(S)$ defined in Eq. (43) is itself a tilted variable derived from G_n . In fact, let $f_G(x)$ represent the p.d.f. of G_n and let $f_{G(\lambda)}(x)$ represent the p.d.f. of $G(\lambda)$. Then it is readily proved by complete induction that

$$f_{G(\lambda)}(x) = f_G(x) e^{-\lambda x - nM(\lambda)}. \quad (45)$$

Therefore, conversely

$$f_G(x) = f_{G(\lambda)}(x) e^{\lambda x + nM(\lambda)} \quad (46)$$

and hence, finally,

$$\bar{F}_G(0/n) = \int_{-\infty}^0 f_G(x) dx = e^{nM(\lambda)} \int_{-\infty}^0 e^{\lambda x} f_{G(\lambda)}(x) dx \quad (47)$$

In order to realize what has been gained by the transformation to tilted variables, one should note two points: First, the presence of the factor $e^{\lambda x}$ means that the integral on the right of Eq. (47) depends essentially only on the value of the integrand near $x = 0$ (since integration is over the domain $x \leq 0$). Second, since $G(\lambda)$ is a zero-mean variable, and the sum of independent zero-mean variables, our problem is now one of evaluating the p.d.f. of a function in the neighborhood of its mean, rather than on the outskirts of the distribution as in the case of G_n . This is exactly the optimum regime for the application of the CLT. We therefore proceed to replace $G(\lambda)$ by a zero-mean normally distributed variable with variance equal to the variance of $G(\lambda)$.

Before proceeding we must digress to calculate the variance of $u(\lambda)$. Since $E[u(\lambda)] = 0$, the variance is given by

$$\begin{aligned}\sigma^2 &= \text{Var}[u(\lambda)] = E[(u(\lambda))^2] \\ &= e^{-M(\lambda)} \int_{-\infty}^{\infty} u^2 e^{-\lambda u} f_u(u) du\end{aligned}\quad (48)$$

Since $G(\lambda)$ is the sum of n independent variables u_i ,

$$\text{Var}[G(s)] = n\sigma^2. \quad (49)$$

Hence, we shall represent $f_{G(s)}(x)$ as the Gaussian

$$f_{G(s)}(x) \approx \frac{1}{\sigma\sqrt{2\pi n}} e^{-(x^2/2n\sigma^2)} \quad (50)$$

Substitution of Eq. (50) into Eq. (47) results, after some manipulation, in the equation

$$F_G(0|n) = e^{nM(\lambda)} + \frac{1}{2} \lambda^2 n\sigma^2 \text{erfc}_*(\lambda\sigma\sqrt{n}) \quad (51)$$

Where

$$\text{erfc}_*(x) = \frac{1}{\sqrt{2\pi}} \int_x^{\infty} e^{-(y^2/2)} dy \quad (52)$$

In the regime of interest, the argument of the error function $\text{erfc}_*(x)$ is reasonably large. Relying on the inequality

$$\frac{1}{x\sqrt{2\pi}} \left(1 - \frac{1}{x^2}\right) e^{-(x^2/2)} < \text{erfc}_*(x) < \frac{1}{x\sqrt{2\pi}} e^{-(x^2/2)} \quad (53)$$

We can simplify Eq. (51) by replacing $\text{erfc}_*(x)$ by its upper bound. Equation (53) indicates that $\text{erfc}_*(x)$ differs from this bound by no more than a

factor $1/x^2$, which becomes negligible for large x . The substitution results in

$$F_G(0|n) = \frac{e^{nM(\lambda)}}{\lambda \sigma \sqrt{2\pi n}} \quad (54)$$

Comparison of Eq. (40) with Eq. (20) reveals that

$$M(\lambda) = \ln b$$

and hence

$$F_G(0|n) = \frac{b^n}{\lambda \sigma \sqrt{2\pi n}} \quad (55)$$

The expression on the right thus consists of the Chernoff-bound b , multiplied by a coefficient $1/(\lambda \sigma \sqrt{2\pi n})$. As this coefficient may be quite small for large n , the error rate predicted by Eq. (55) may fall considerably below the Chernoff-bound.

The procedure for evaluating Eq. (55) can be summarized as follows:

- (1) In accordance with Eq. (41), one must evaluate the integral

$$\int_{-1}^1 u e^{-\lambda u} f_u(u) du \quad (56)$$

as a function of λ and determine the value of λ which will cause the function to equal zero.

- (2) Using this value of λ , determine

$$b = \int_{-1}^1 e^{-\lambda u} f_u(u) du \quad (57)$$

and

$$\sigma^2 = b^{-1} \int_{-1}^1 u^2 e^{-\lambda u} f_u(u) du \quad (58)$$

(3) Substitute λ , b , and σ into Eq. (55).

Having calculated $\bar{F}_G(0|n)$ we can now use Eq. (14) to calculate the error-rate P_E . Substitution of Eq. (55) and (7) into Eq. (14) gives

$$\begin{aligned} P_E &= \sum \bar{F}_G(0|n) \frac{e^{-\bar{n}} (\bar{n})^n}{n!} \\ &= \frac{e^{-\bar{n}}}{\lambda \sigma \sqrt{2\pi}} \sum \frac{(\bar{n} b)^n}{n! n} \end{aligned} \quad (59)$$

A few words need to be said concerning the sum in Eq. (59). For low values of n , Eq. (54) represents a poor approximation. On the other hand, in the regime of interest, where $\bar{n} = 50$ to 100 , the coefficients of $\bar{F}_G(0|n)$ in Eq. (59) are negligibly small for $n \ll \bar{n}$, so that the corresponding terms in any case make an insignificant contribution to the sum. In particular, for $n = 0$, the coefficient of $\bar{F}_G(0|0)$ is $e^{-\bar{n}}$, which represents an exceedingly small number. We may therefore simply leave out the first term and sum over n from 1 to ∞ .

In order to evaluate the sum, we introduce the function

$$\varphi(x) = e^{-x} \sqrt{x} \sum_{n=1}^{\infty} \frac{x^n}{n! \sqrt{n}} \quad (60)$$

From the fact that

$$e^x = \sum \frac{x^n}{n!}$$

one might be inclined to suspect that $\varphi(x) \sim 1$, especially for large x . Numerical computation shows that $\varphi(x)$ indeed converges to 1 with amazing rapidity; it assumes a value of 1.08 for $x = 5$, 1.01 for $x = 40$, and 1.004 for $x = 100$.

Using Eq. (60), we can rewrite Eq. (59) in the form

$$P_E = \frac{e^{-\bar{n}(1-b)}}{\lambda \sigma \sqrt{2\pi b \bar{n}}} \varphi(\bar{n}b) \quad (61)$$

In the regime of interest, $\varphi(\bar{n}b) \sim 1$, hence

$$P_E = \frac{e^{-\bar{n}(1-b)}}{\lambda \sigma \sqrt{2\pi b \bar{n}}} \quad (62)$$

By taking the logarithm of Eq. (62) we arrive at an implicit equation for \bar{n}

$$\bar{n} = n_{CB} - A \log \bar{n} - B \quad (63)$$

where

$$n_{CB} = - \frac{\log P_E}{(1-b) \log e} \quad (64)$$

$$A = \frac{1}{2(1-b) \log e} \quad (65)$$

$$B = \frac{\log [2\pi b \lambda^2 \sigma^2]}{2(1-b) \log e} \quad (66)$$

n_{CB} is precisely the mean emission number per digit required to satisfy the Chernoff-bound for a given error rate P_E as can be recognized by comparing Eq. (64) with Eq. (24). The other terms in Eq. (63) effect a reduction of this number, provided that A and B are positive. Like n_{CB} , the coefficients A and B are functions of the modulation index μ through their dependence on b , λ , and σ .

For the present, system $f_u(u)$ is given by Eq. (18). λ and b are calculated as before, from Eqs. (22) and (23). According to Eq. (55), the

remaining parameter, σ , is given by

$$\begin{aligned}\sigma^2 &= b^{-1} \int_{-1}^1 u^2 e^{-\lambda u} \left[\frac{1 - \mu u}{\pi \sqrt{1 - u^2}} \right] du \\ &= b^{-1} \left[I_0(\lambda) \left(1 + \frac{\mu}{\lambda}\right) - I_1(\lambda) \left(\mu + \frac{1}{\lambda} + \frac{2\mu}{\lambda^2}\right) \right]\end{aligned}\quad (67)$$

With the help of Eqs. (22) and (23) this can be put in the simpler form

$$\sigma^2 = 1 - \frac{\mu I_1(\lambda)}{n\lambda^2}$$

Using the values of λ , b , and σ^2 , one can calculate the parameters entering Eq. (63). The value of n_{CB} for a given P_E can be easily read off Fig. 1.

$A(\mu)$ and $B(\mu)$ are presented in Figs. 3, and 4.

Although Eq. (63) is an implicit equation in \bar{n} , it is easily solved by iteration starting with the substitution $\log \bar{n} \rightarrow \log n_{CB}$.

For example, for $\mu = 0.7$ one has $A = 8.4$, $B = 1.8$; hence

$$\bar{n} = n_{CB} - 8.4 \log \bar{n} - 1.8 \quad (68)$$

If the required error rate is $P_E = 10^{-7}$, then

$$n_{CB} = 118$$

For the first iteration, put $\log \bar{n} = \log n_{CB} = \log 118 = 2.07$. Substitution into Eq. (68) results in $\bar{n}_1 \sim 99$. For the second iteration, put $\log \bar{n} = \log \bar{n}_1 = 1.996$. Substitution into Eq. (68) gives $\bar{n}_2 \sim 100$. Further iterations result in negligible corrections.

This example indicates that the actual required photoelectron count for a given error rate may be as much as 15 percent lower than indicated by the Chernoff-bound.

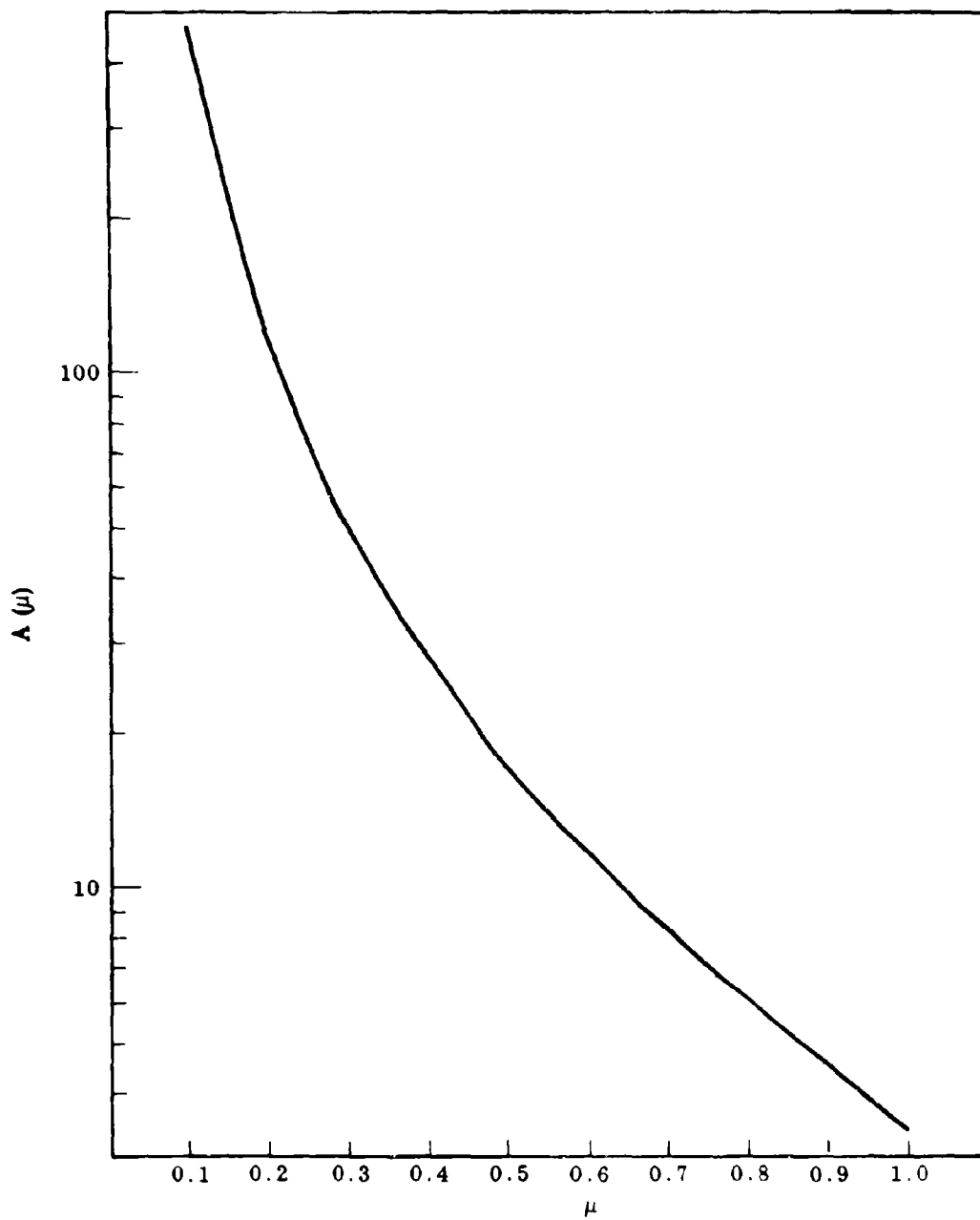


Fig. 3 Plot of the Parameter A as a Function of Effective Modulation Index μ

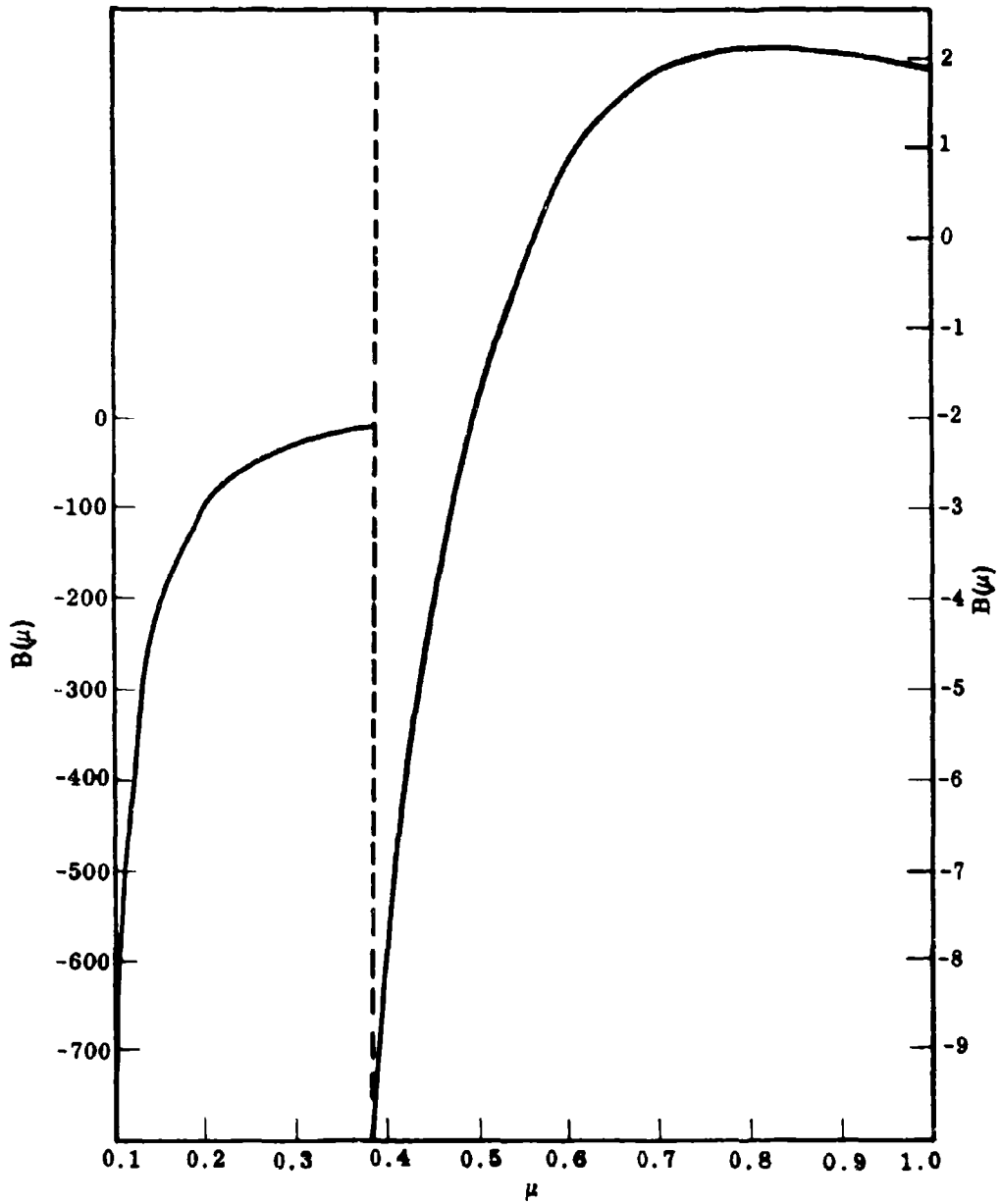


Fig. 4 Plot of the Parameter B as a Function of Effective Modulation Index μ

References

1. P. S. Castro et al., "A One-Gbit/Sec CW Laser Communication Experiment," Digest of Technical Papers, 1971 IEEE/OEA Conference on Laser Engineering and Applications (To be published in IEEE J. Quantum Electronics)
2. S. Karp, E. L. O'Neill, and R. M. Gagliardi, "Communication Theory for the Free-Space Optical Channel," Proc. IEEE 58, 1011-1016 (1970)
3. H. Chernoff, "A Measure of Asymptotic Efficiency for Tests of a Hypothesis Based on the Sum of Observations," Annals Math. Stat. 23, 493-507 (1962)
4. For a detailed discussion of tilted probability techniques, see R. E. Fano, Transmission of Information, M.I.T. Press, Chapter 8 (1961)

Appendix C

BIT ERROR PROBABILITY RELATIONSHIPS USED
IN MODULATION FORMAT AND LINK
PARAMETRIC TRADEOFF ANALYSES

by

Dr. H. V. Hance

LOCKHEED PALO ALTO RESEARCH LABORATORY
LOCKHEED MISSILES & SPACE COMPANY
A GROUP DIVISION OF LOCKHEED AIRCRAFT CORPORATION

Section 1 INTRODUCTION

The primary purpose of this appendix is to develop for each of the candidate modulation formats the basic analytical expressions that are employed in the digital computer programs described in Appendix N and that are used in calculating required received signal power for a specified bit error probability. A further purpose is to provide graphs of these expressions in a form suitable for use in comparing the candidate modulation formats considered in Volume II under Task 2.

The modulation formats analyzed here are as follows:

- (1) Digital quadriphase-modulated microwave subcarrier, polarization modulated cw laser
- (2) Binary baseband intensity (on-off) modulated laser
- (3) Binary baseband polarization modulated laser

In the last two cases, the signal and background parameters that determine bit error probability are defined in such a way that the analytical results obtained are applicable to either cw or pulse laser systems. To apply these results to any particular system, it is necessary only to take account of (1) the influence of receiver gating (if used) on the relationship between background intensity and background photoelectron count per decision time, and (2) any transmitter power loss incidental to optical multiplexing, if resorted to as a means of obtaining a transmitted pulse rate adequate to the information rate to be handled.

In the case of the baseband systems, the exact analytical expressions for bit error probability are given first and the graphical representations of these exact expressions are presented. However, neither the exact analytical expressions nor the graphical plots are convenient as a basis for routine computer calculations. Numerical evaluation

of the analytical expressions involves excessive amounts of computation, while storage and recall of the graphical data in the computer would involve slow and/or expensive "table lookup" methods.

These difficulties can be avoided by developing simplified approximate analytical expressions for bit error probability, using the results of the exact analysis to verify that adequate accuracy is obtained over the range of signal parameters of interest. Suitable approximate expressions for bit error probability are introduced for each of the baseband modulation formats, and their adequacy is demonstrated by the method just described.

Section 2

DIGITAL QUADRIPIHASE SUBCARRIER/POLARIZATION MODULATED LASER

The analysis in this section uses as a starting point the theoretical results obtained in Appendix B. In that appendix, expressions are derived for bit error probability P_E in terms of optical signal and background strengths, and signal modulation index, for a number of subcarrier formats. The quadriphase format to be considered here is covered in Section V of the appendix as a special case of "multichannel operation."

It is important to note at the outset that the analysis in Appendix B does not give "exact" expressions, but rather provides an upper bound for the error probability. That is, the analysis gives approximate results but is carried out in such a way that any error in the predicted value of P_E is in the direction of overestimation. For this reason, and because, as will be evident later, the relationship between P_E and the signal strength parameter K_S is reciprocally monotonic, the calculated value of K_S needed for a specified P_E will also be overestimated. Thus, the number of received signal photons required per data as calculated using this theory will be conservative.

In order to apply the analysis of Appendix B to the quadriphase subcarrier system, we consider first the case of a single-photodetector receiver, treated in Section V of the appendix. Following Eq. B(31),* the output of the photodetector can be characterized by the time-varying photoelectron rate

$$\alpha_1(t) = \bar{\alpha}_1 [1 \pm \mu_A \sin \omega t \pm \mu_B \cos \omega t] \quad (1)$$

*Equations identified by "B" numbers are contained in Appendix B.

Here μ_A and μ_B correspond to μ_1 and $\bar{\mu}_1$ of Eq. B(31) and are the modulation indexes associated with the two input data channels A and B. (See Task 2, Vol. 2, for a description of the quadriphase modulation system.) The term $\bar{\alpha}_1$ is the mean photodetector current in the ensemble-average sense:

$$\bar{\alpha}_1 = \langle \alpha_1(t) \rangle$$

As discussed in Section V, the error probability for channel A depends on $\bar{\alpha}_1$ and μ_A , but not on μ_B , and similarly for channel B. That is, each data train can be recovered without interference from the other. However, this does not mean that the values of μ_A and μ_B can be chosen arbitrarily. In particular, when $\mu_A = \mu_B$, as we assume hereafter, their value is limited to appreciably less than unity. To find the maximum value allowed, we write Eq. (1) in the equivalent form

$$\alpha_1(t) = \bar{\alpha}_1 \left[1 + m \sin \left(\omega t + k \frac{\pi}{2} + \frac{\pi}{4} \right) \right] \quad (2)$$

where

$$m = (\mu_A^2 + \mu_B^2)^{1/2} \quad (3)$$

and k takes one of the four values 0, 1, 2, 3, depending upon the particular combination of \pm signs assumed. In this form, m represents the modulation index of the optical beam at the photodetector input due to the total QPSK microwave subcarrier.

Because of the restriction $\mu_A = \mu_B$ imposed above, we have the following from Eq. (3):

$$\mu_A = \mu_B = \frac{m}{\sqrt{2}} \quad (4)$$

Substituting for μ_A and μ_B in Eq. (1) gives

$$\alpha_1(t) = \bar{\alpha}_1 \left[1 + \left(\frac{m}{\sqrt{2}} \right) \sin \omega t + \left(\frac{m}{\sqrt{2}} \right) \cos \omega t \right] \quad (5)$$

Because the value of m cannot exceed unity [according to Eq. (2), $m > 1$ would imply a negative photoelectron rate during a portion of the modulation cycle], it follows that μ_A and μ_B cannot exceed 0.707.

We now consider the addition of a second photodetector and assume differential summation of their outputs. Because of the independence of the A and B channels, the modification of the analytical formalism needed to take account of the second (push-pull) detector is the same in the two-channel (quadruphase) case as in single-channel (biphase) case analyzed in Section IV of Appendix B. Consequently, the same conclusions apply, namely, that the error probability for each channel is determined by (1) the modulation index for the channel ($\mu_A = \mu_B = m/\sqrt{2}$) and (2) the mean (expected) total number of photoelectrons in both detectors during the bit decision time τ . In the notation of Appendix B, this number is $\bar{n} = \bar{\alpha}_1 + \bar{\alpha}_2$. In the following, we denote this quantity by K_S . Similarly, we use K_B for the expected total number of background photoelectrons in time τ .

Before writing the expression for P_E , we note from Section VI of Appendix B that the effect of background can be fully taken into account by replacing \bar{n} and the μ 's by properly chosen effective values. In our notation, these effective values are

$$\bar{n}_{\text{eff}} = K_S + K_B \quad (6)$$

and

$$\mu_{\text{eff}} = \frac{K_S}{K_S + K_B} \mu = \frac{K_S}{K_S + K_B} \frac{m}{\sqrt{2}} \quad (7)$$

In terms of \bar{n}_{eff} and μ_{eff} , the expression for bit error probability from Eq. B(24) is

$$P_E = e^{-\bar{n}_{\text{eff}} f(\mu_{\text{eff}}^2)} \quad (8)$$

or, in terms of decibel units ($10 \log_{10} P_E$), from Eq. B(25),

$$(P_E)_{\text{dB}} = 10 \log_{10} P_E = -10 \left[f(\mu_{\text{eff}}^2) \log_{10} e \right] \bar{n}_{\text{eff}} \quad (9)$$

where $-10 \left[f(\mu_{\text{eff}}^2) \log_{10} e \right]$ is the function plotted in Appendix B as Fig. 2. Noting that this function is approximately linear with μ_{eff}^2 , we recast Eq. (9) in the form

$$10 \log_{10} P_E = (-1.45) \bar{n}_{\text{eff}} (\mu_{\text{eff}}^2) g(\mu_{\text{eff}}) \quad (10)$$

where the function $g(\mu_{\text{eff}})$ takes account of the slight departure of the graph from linearity; $g(\mu_{\text{eff}})$ is plotted in Fig. 2-1. It is seen that $g(\mu_{\text{eff}}) = 1$ for $\mu_{\text{eff}} = 1$, but decreases to 0.75 at $\mu_{\text{eff}} = 0$.

Equations (6) and (7) can now be used in Eq. (10) to express P_E explicitly in terms of K_S , K_B , and m . The result is

$$10 \log_{10} P_E = (-1.45) \frac{m^2}{2} \frac{K_S}{1 + K_B/K_S} \cdot g \quad (11)$$

where $g = g(\mu_{\text{eff}})$ is obtained from Fig. 2-1* with

$$\mu_{\text{eff}} = \frac{m}{\sqrt{2}} \frac{1}{1 + K_B/K_S} \quad (12)$$

*For purposes of computer calculations using Eq. (11), the function g can be represented with adequate accuracy for most purposes by the empirical approximation $g(\mu_{\text{eff}}) = 3/4 [1 + 1/3 (\mu_{\text{eff}}^2)]$.

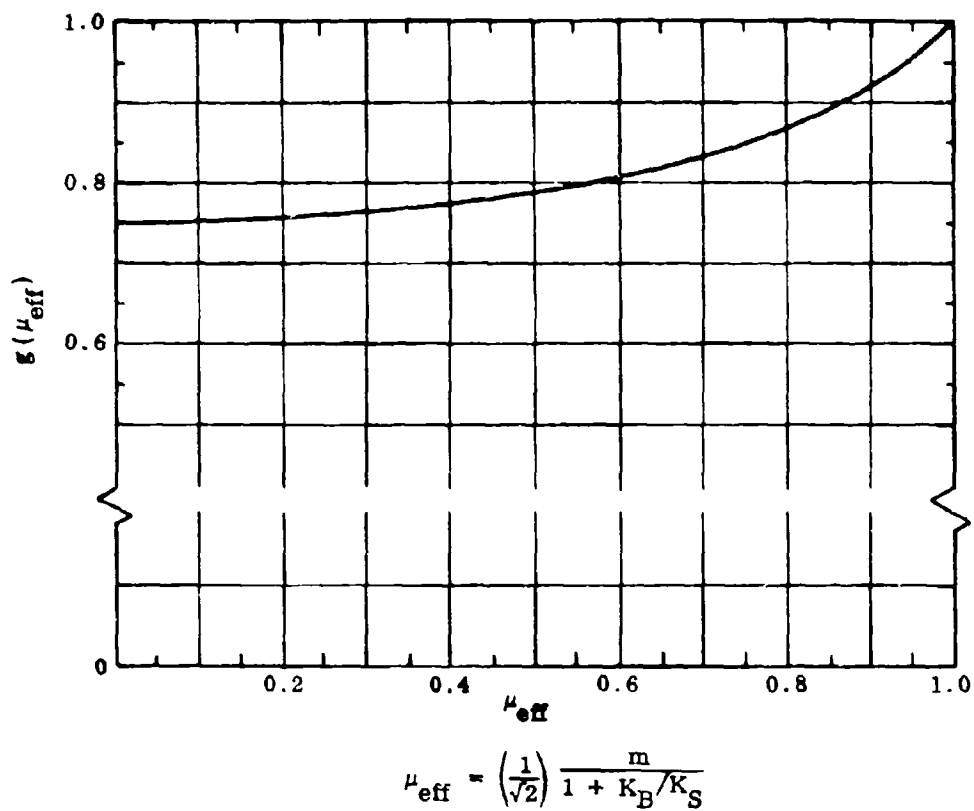


Fig. 2-1 The Factor g in Eqs. (10) and (11)

As an example of the use of Eq. (11), we will calculate the value of K_S required for $P_E = 1 \times 10^{-6}$ when $m = 0.9$ and $K_B = 0$. From Eq. (12),

$$\mu_{eff} = \frac{0.9}{2} = 0.636$$

From Fig. 2-1, for this value of μ_{eff} , $g = 0.82$. Using these values in Eq. (11) and solving for K_S , we obtain $K_S = 125$ photoelectrons per decision interval. The corresponding number of photoelectrons per data bit K_R is obtained by dividing K_S by the number of data bits per decision time, namely, $\log_2 4 = 2$. Thus,

$$K_R = \frac{K_S}{(\log_2 4)} = \frac{K_S}{2} = 62.5$$

In the above example, if the background parameter K_B had been other than zero, the value of μ_{eff} could not have been obtained from Fig. 2-1 without first assigning a value to K_S . As this is the quantity to be found, and because Eq. (11) is an implicit expression for K_S , the correct value of K_S must be arrived at by successive approximations. Using this method, a graph of K_S versus K_B can be constructed for a given value of m , say, $m = 1$. The curve for $m = 1$ in Fig. 2-2 was constructed in this way. Once this has been done, graphs for other $m < 1$ can be constructed from the first by choosing a value of m , say, m' , and using Eqs. (6) and (7) to find new but equivalent values of K_S and K_B . Calling these new values K'_S and K'_B , the combination will be equivalent to the first set if the values of \bar{n}_{eff} and μ_{eff} as given by Eqs. (6) and (7) remain unchanged. Thus, the equivalence conditions are

$$K'_S + K'_B = K_S + K_B$$

and

$$\frac{K'_S}{K'_S + K'_B} \cdot \frac{m'}{\sqrt{2}} = \frac{K_S}{K_S + K_B} \cdot \frac{m}{\sqrt{2}}$$

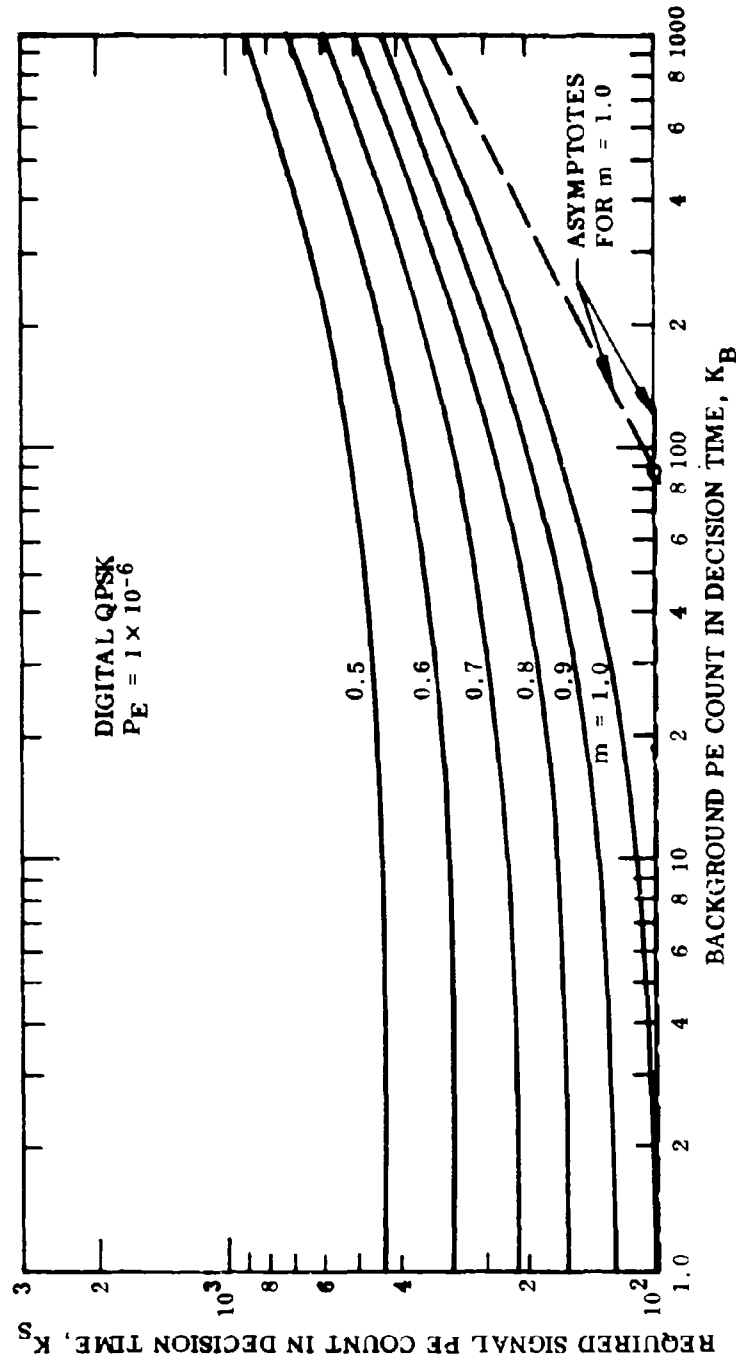


Fig. 2-2 K_S , the Number of Signal Photoelectrons Required per Bit Decision Time τ by a Subcarrier/QPSK/Polarization Modulation Receiver for a Bit Error Probability of 1×10^{-6} as a Function of Background Interference Level for Several Values of Modulation Index, m

Using the first equation in the second to replace $K_S + K_B$ by $K'_S + K'_B$, we obtain the equivalence condition

$$K'_S = \frac{m}{m'} K_S \quad (13)$$

Using this result in the first equation gives a second condition,

$$K'_B = \left(1 - \frac{m}{m'}\right) K_S + K_B \quad (14)$$

The curves in Fig. 2-2 for $m < 1$ were constructed from the curve for $m = 1.0$ by using these equivalence conditions as follows: A series of values of K_B and the associated K_S values for $m = 1$ were tabulated; then for an assigned value of $m' < 1$, pairs of values of K'_S and K'_B were calculated using Eqs. (13) and (14). The curves in Fig. 2-2 for $m < 1$ are plots of these derived or "equivalent" K'_S and K'_B values.

An alternative presentation of the results given in Fig. 2-2, with modulation index as the independent variable rather than background, is obtained by taking vertical cuts at fixed values of background. The resulting cross-plots are given in Fig. 2-3. In this case, the signal and background parameters are expressed on a per-bit basis; i.e., $K_R = K_S / \log_2 4$ is plotted as a function of modulation index m with background photoelectron count per data bit ($= K_B / \log_2 4$) as the parameter.

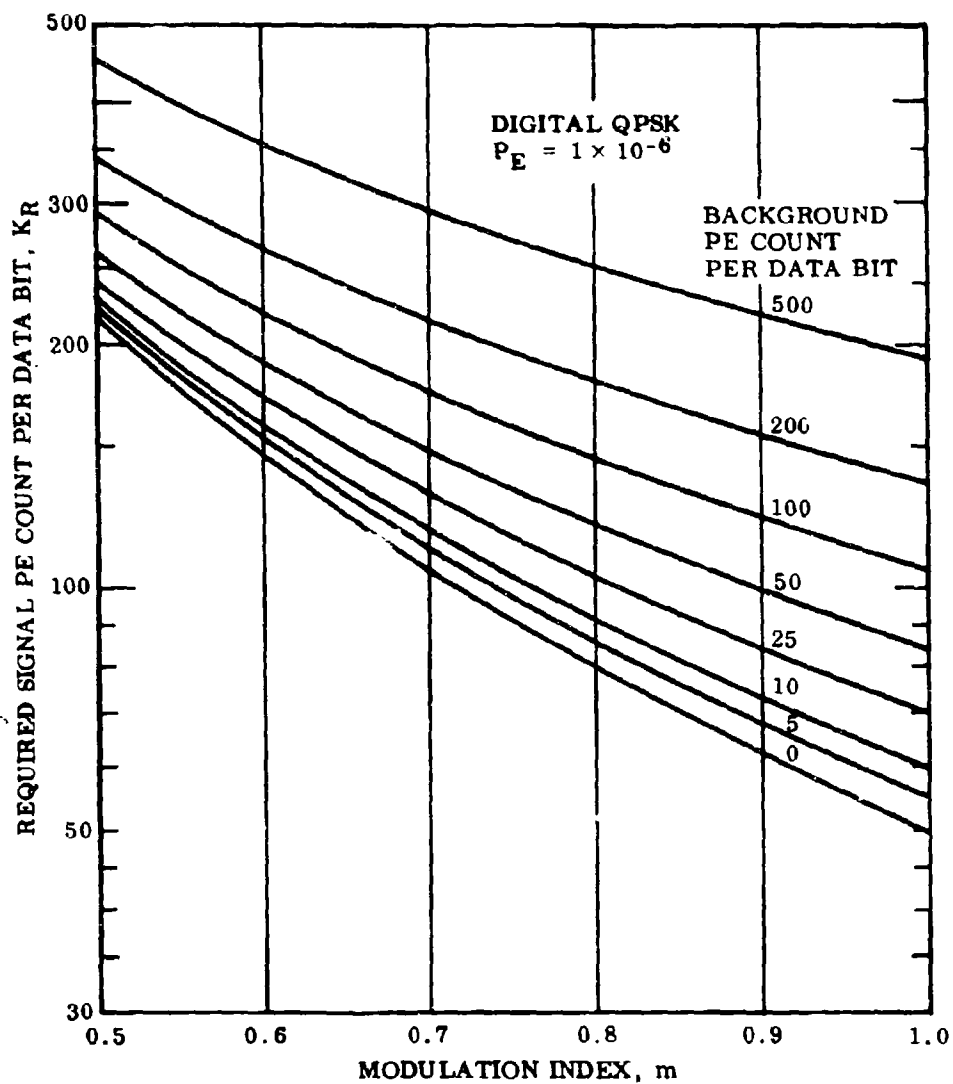


Fig. 2-3 K_R , the Number of Signal Photoelectrons Required per Data Bit by a Subcarrier/QPSK/Polarization Modulation Receiver for a Bit Error Probability of 1×10^{-6} as a Function of Modulation Index, m , for Several Background Interference Levels

Section 3 BINARY BASEBAND ON-OFF MODULATION

3.1 EXACT ANALYSIS

An exact analysis of this system has been given by Curren and Ross (Ref. 1), and graphic results covering a range of conditions of practical interest are given by Ross et al. (Ref. 2). However, the results are presented in a form that is inconvenient for our purposes, and, for some conditions of interest, with insufficient accuracy. Therefore, it was necessary to perform an independent numerical analysis of this modulation scheme.

In this analysis, the theoretical expression of Curren and Ross (Ref. 2) or, equivalently, Pratt (Ref. 3), is first used to calculate bit error probability in terms of the signal and background parameters assuming ideal modulator action (infinite extinction) and an optimum detection threshold. Then, by means of an equivalence argument, we show that a finite extinction ratio can be accounted for by a change of signal and background parameters, as in the case of the subcarrier system. Finally, the equivalence relations derived are used to obtain graphic plots showing the effect of varying the extinction ratio.

Following Pratt (Ref. 3), for an on-off optical modulation system transmitting "one" and "zero" bits with equal probability, and assuming an ideal photon counting receiver, the bit error probability P_E is

$$P_E = \frac{1}{2} \left\{ 1 - \sum_{k=0}^{k_D} \frac{\exp\{-K_B\}}{k!} [K_B]^k + \sum_{k=0}^{k_D} \frac{\exp\{-K_B - K_S\}}{k!} [K_B + K_S]^k \right\} \quad (15)$$

where k_D is the greatest integer contained in the maximum-likelihood threshold given by

$$T = \frac{K_S}{\ln [1 + K_S/K_B]} \quad (16)$$

and where K_S and K_B are, respectively, the expected signal and background photoelectron counts as defined previously. Figure 3-1 shows the variation of P_E with respect to K_S for a wide range of values of K_B .^{*} For a specified value of P_E (say, 1×10^{-6}), a horizontal cut through this family provides pairs of corresponding values of K_B and K_S , which are plotted as the lower curve of Fig. 3-2 ($E = \infty$). We next use this curve to obtain similar curves but for finite values of the extinction ratio E , as defined below.

If the modulator fails to extinguish the transmitter pulse during a binary "zero," leakage of signal power will occur during the time it should be suppressed. Thus, if the signal photoelectron count at the receiver during a binary "one" is K'_S , with unity transmission through the modulator, then during a binary "zero" the count is K'_S/E , where E is defined as the extinction ratio ($1 < E < \infty$). This leakage signal adds to the real background, as shown in Fig. 3-3(b). If the imperfections of the modulator that cause incomplete extinction are optical in nature, they will also tend to reduce the peak transmittance for a binary "one." For completeness, therefore, we postulate an incremental reduction of peak signal by an amount K'_S/E , as shown in Fig. 3-3(b). This reduction is equal in magnitude to the incremental increase in background due to incomplete extinction.

^{*}The scallops that usually appear in graphs of this function have been smoothed for the sake of simplicity, since they are of no practical importance for present purposes.

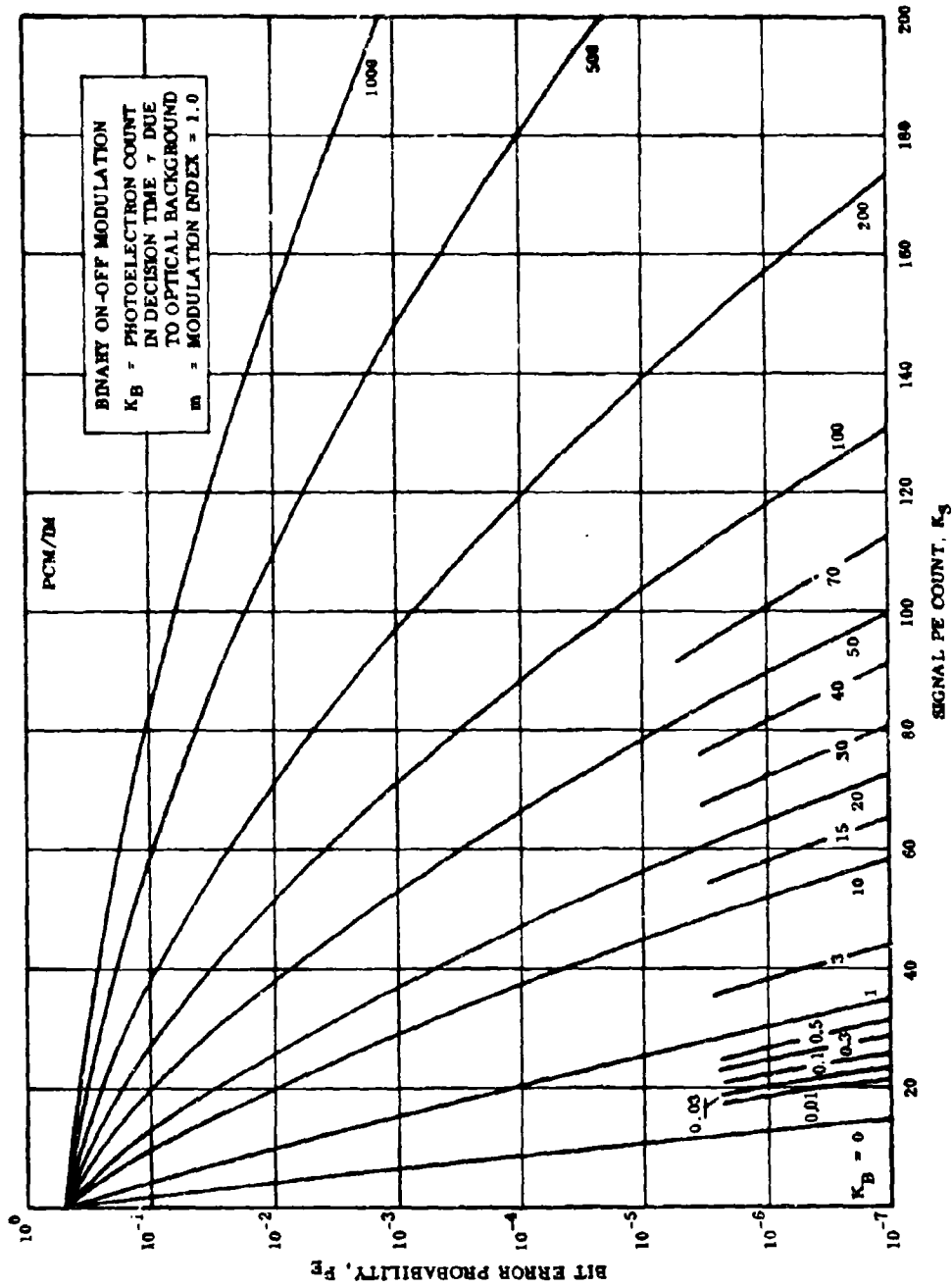


Fig. 3-1 Signal PE Count Versus Bit Error Probability

C-14

LOCKHEED PALO ALTO RESEARCH LABORATORY
 LOCKHEED MISSILES & SPACE COMPANY
 A GROUP DIVISION OF LOCKHEED AIRCRAFT CORPORATION

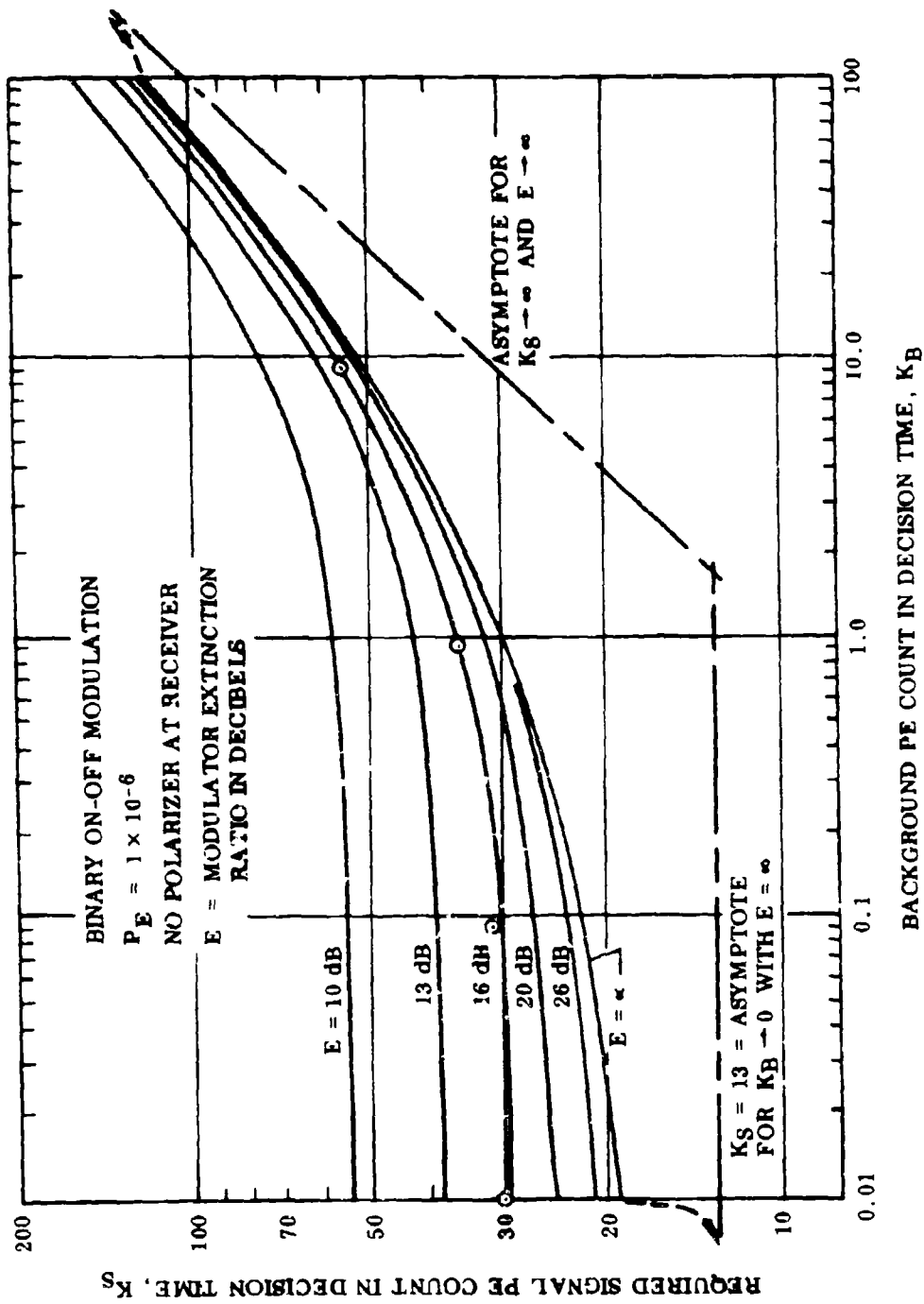


Fig. 3-2 Required Minimum Signal Photoelectron Count in Decision Time τ Versus Background Count in Same Time

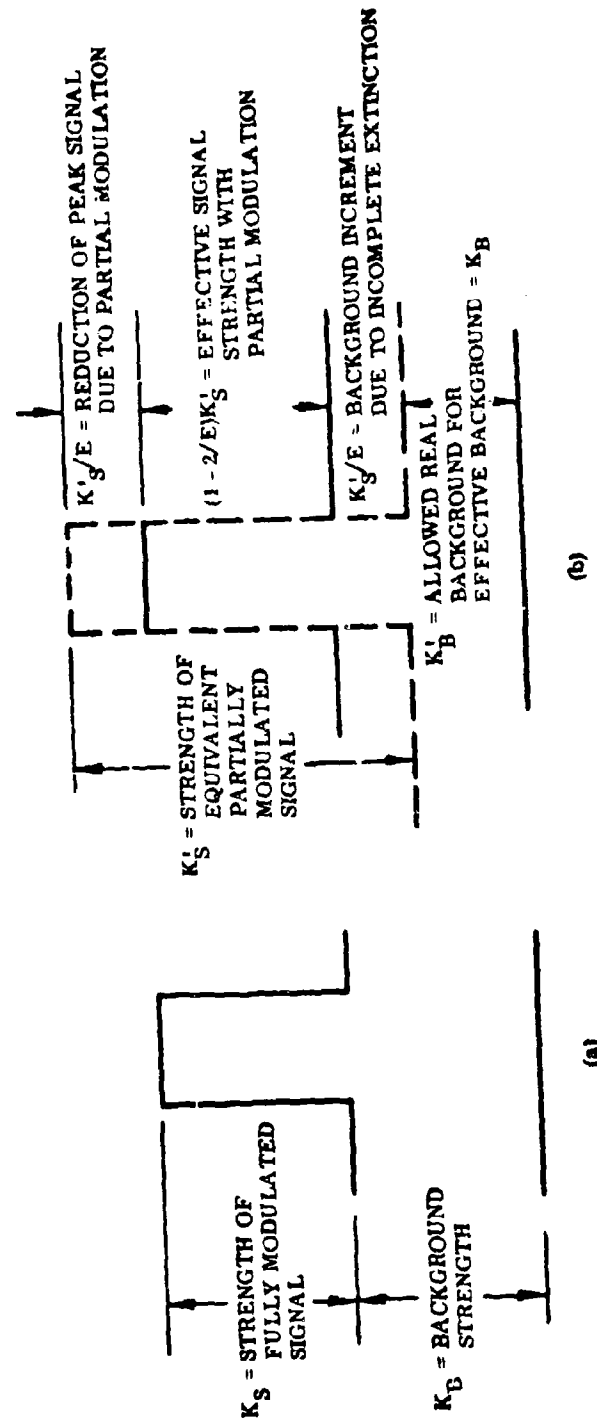


Fig. 3-3 A Fully Modulated Signal With (a) Background and (b) an Equivalent Partially Modulated Signal and Background

The effect of leakage can now be accounted for by defining an effective background $K'_B + K'_S/E$ and a fully modulated effective signal $(1 - 2/E)K'_S$, as illustrated in the figure.* We now ask what values K'_S and K'_B are required to have so that the corresponding effective signal and background values will be equal, respectively, to specified values of K_S (for a fully modulated signal) and K_B . Two such equivalent signal and background conditions are represented in Fig. 3-3, from which it is evident that the conditions to be satisfied for equivalence are

$$(1 - 2/E)K'_S = K_S$$

and

$$K'_B + (1/E)K'_S = K_B$$

These equations can be solved to give explicit expressions for K'_S and K'_B :

$$K'_S = K_S \cdot \frac{1}{1 - 2/E} = K_S \frac{E}{E - 2} \quad (17)$$

$$K'_B = K_B - K_S \cdot \frac{1}{E - 2} \quad (18)$$

Equations (17) and (18) were used to produce the curves in Fig. 3-2 for $E < \infty$ using values of K_S and K_B from the curve for $E = \infty$. (The method used was essentially the same as the one outlined in the previous section for obtaining the curves in Fig. 2-2

*In writing this expression, it is assumed that a polarization analyzer cannot be used in the receiver to reduce the background reaching the photodetector. This will be the case if time division multiplexing in the transmitter (to increase pulse repetition rate) is accomplished with the help of polarization beam splitters and recombiners because then the transmitted signal will be composed of two sets of pulse trains orthogonally polarized with respect to one another. If the transmitted polarization is such as to permit an analyzer to be used in the receiver, then K_B in the following analysis should be replaced by $K_B/2$.

for $m < 1$.) Cuts through the family of Fig. 3-2 for constant values of E then yield the curves of Fig. 3-4. In these plots, extinction ratio is expressed in decibels, defined as $E_{dB} = 10 \log_{10} E$. Also, for consistency with the corresponding graph for the quadriphase system, Fig. 2-3, the signal and background parameters are given on a photoelectron-per-data bit basis.

3.2 ANALYTICAL APPROXIMATION - ON-OFF MODULATION

A simplified approximate analytical expression for bit error probability for the on-off modulation format has been derived by Bucher (Ref. 4) by a technique similar to that used in Appendix B for the subcarrier system, namely, the use of the Chernoff bound. As for the subcarrier system, this method guarantees that calculated values of bit error probability (or, equivalently, signal power required for a specified bit error probability) will be conservative. For this reason, the term "upper bound" is more appropriate than "approximate" in referring to such expressions.

In our notation, Bucher's expression for bit error probability for ideal on-off modulation and a threshold receiver with the threshold optimized in accordance with Eq. (16) is

$$P_E \leq C \exp(-K_S \cdot E_T) \quad (19)$$

where E_T is a function of the ratio K_S/K_B as follows:

$$E_T(K_S/K_B) = \frac{\left(1 + \frac{K_B}{K_S}\right) \ln \left(1 + \frac{K_S}{K_B}\right) - \ln \left(1 + \frac{K_B}{K_S}\right) \ln \left(1 + \frac{K_S}{K_B}\right) - 1}{\ln \left(1 + \frac{K_S}{K_B}\right)} \quad (20)$$

The factor C in Eq. (19) is unity according to Bucher's development. However, since the results of the exact theory are available, we can adjust the value of C to improve the accuracy of Eq. (19). After some experimentation, a value of $C = 1.0$ was selected as best for the range of signal parameters of interest in this study.

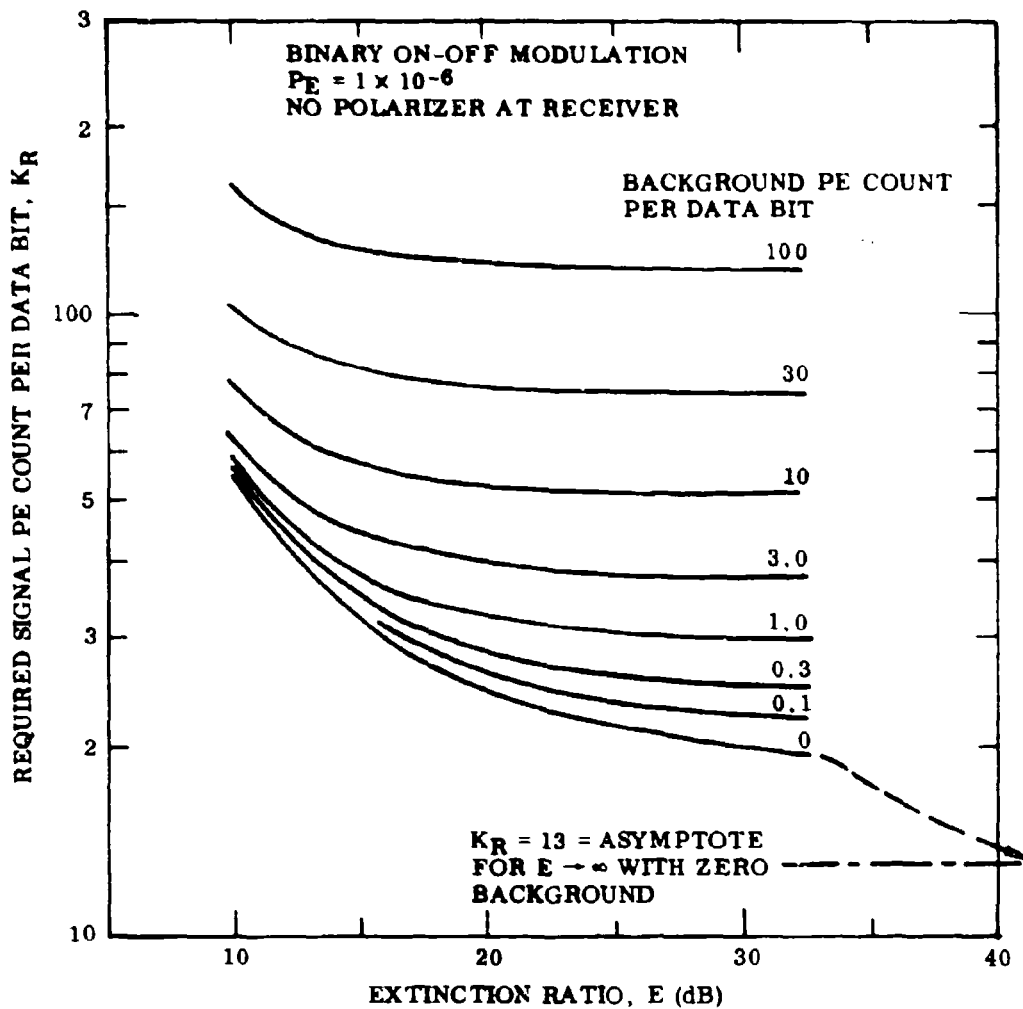


Fig. 3-4 Required Minimum Signal Photoelectron Count per Data Bit, K_R , Versus Extinction Ratio, E

In the case of a nonideal modulator, Eq. (19) is still applicable, provided K_S is now thought of as the strength of an equivalent, fully modulated signal and K_B is regarded as an effective background. To express these effective values in terms of the actual signal and background, we again use the equivalence argument illustrated by Fig. 3-3. We now regard K'_S and K'_B [at (b)] as the actual signal and background parameters and K_S and K_B [at (a)] as the derived or equivalent quantities. Accordingly, we use the equivalence relations derived above to express K_S and K_B in Eqs. (19) and (20) in terms of K'_S and K'_B . Then we drop the primes so that K_S and K_B again denote actual signal and background values, giving

$$P_E \leq C \cdot \exp [-(1 - 2/E) K_S \cdot E_T(\rho)] \quad (21)$$

where $E_T(\rho)$ is the same function as Eq. (20) but with K_B/K_S replaced by ρ where

$$\rho = \frac{(1 - 2/E)K_S}{K_B + (1/E)K_S} \quad (22)$$

To check the accuracy of this approximation method, values of K_S were calculated for $E = 40$ (16 dB) and are plotted in Fig. 3-2. These are seen to be in good agreement with the curves based on the exact theory.

Section 4

BINARY BASEBAND POLARIZATION MODULATION

4.1 EXACT ANALYSIS

Pratt has analyzed this system and derived expressions for bit error probability in terms of Bessel functions; he also gives an alternate expression in terms of Marcum's Q-function (Ref. 5). However, for purposes of machine computation, intermediate results of Pratt's development are more useful. In our notation, the expression for bit error probability that is most convenient to use is

$$P_E = 1 - \left[\sum_{j=0}^{\infty} P(Z = j) - \frac{1}{2} P(Z = 0) \right] \quad (23)$$

where Z is the difference in photocounts between the two detectors. A correct decision is made with unit probability whenever $Z > 0$ and with a probability of $1/2$ when $Z = 0$ since only a guess is possible in the latter case. The probability that a specified value of Z will occur is given by

$$P(Z = j) = \sum_{m=0}^{\infty} p_S(X = j + m) p_B(Y = m) \quad (24)$$

where p_S and p_B are the Poisson probability functions for signal-plus-background and background alone,

$$p_S(X = k) = \frac{\left(K_S + \frac{K_B}{2} \right)^k \exp - \left(K_S + \frac{K_B}{2} \right)}{k!} \quad (25)$$

and

$$p_B(Y = k) = \frac{\left(\frac{K_B}{2}\right)^k \exp\left(-\frac{K_B}{2}\right)}{k!} \quad (26)$$

In these expressions, K_S is the total mean photoelectron count for the two photo-detectors in the decision time and K_B is the background count in the same time. In Eqs. (25) and (26), the term $K_B/2$ is the mean background photocount per detector.

Figure 4-1 is a plot of Eq. (23) for a number of values of the background parameter K_B . Comparing this graph with the corresponding one for on-off modulation (Fig. 3-1), it is seen that for all $K_B > 0$, the polarization modulation system is superior in that it requires a significantly smaller signal photoelectron count to produce a given bit error probability.

The curve for $m = 1$ in Fig. 4-2 was derived from Fig. 4-1 by taking a horizontal cut at $P_E = 1 \times 10^{-6}$. The curves for $m < 1$ were then obtained from this by use of the equivalence relations, Eqs. (13) and (14), in the same way as for the QPSK system.* Vertical cuts through the curves of Fig. 4-2 at fixed values of the background parameter K_B then yield the family of Fig. 4-3. However, the signal and background parameters are expressed in Fig. 4-3 in terms of photoelectrons per data bit, as for the corresponding graphs for the other systems.

4.2 ANALYTICAL APPROXIMATION - BINARY POLARIZATION

The computation of bit error probability using the exact expression, Eq. (23), is again found to be expensive in machine time, and hence an approximate expression in analytical form is desired. For this purpose, we start with an upper bound derived for this modulation method by Bucher (Ref. 4) and applicable when the modulator

*The definition of modulation index m is the same as that given in the discussion of the QPSK system, namely, actual photocurrent swing divided by maximum possible swing for ideal modulation.

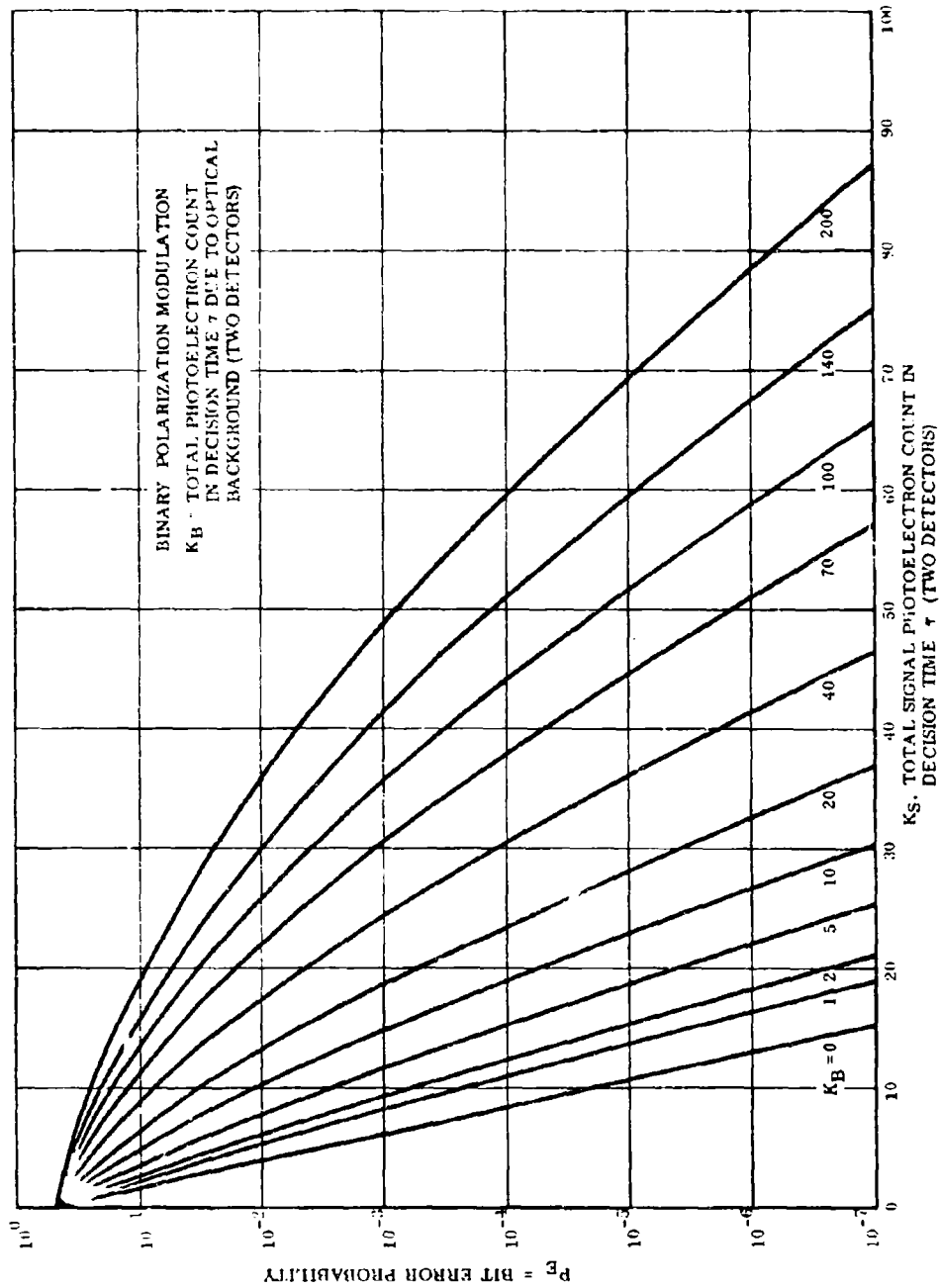


Fig. 4-1 Bit Error Probability, P_E , Versus Signal PE Count per Decision, K_S , for Several Values of Background PE Count, K_B , in the Same Time. Modulation Index, $m = 1.0$.

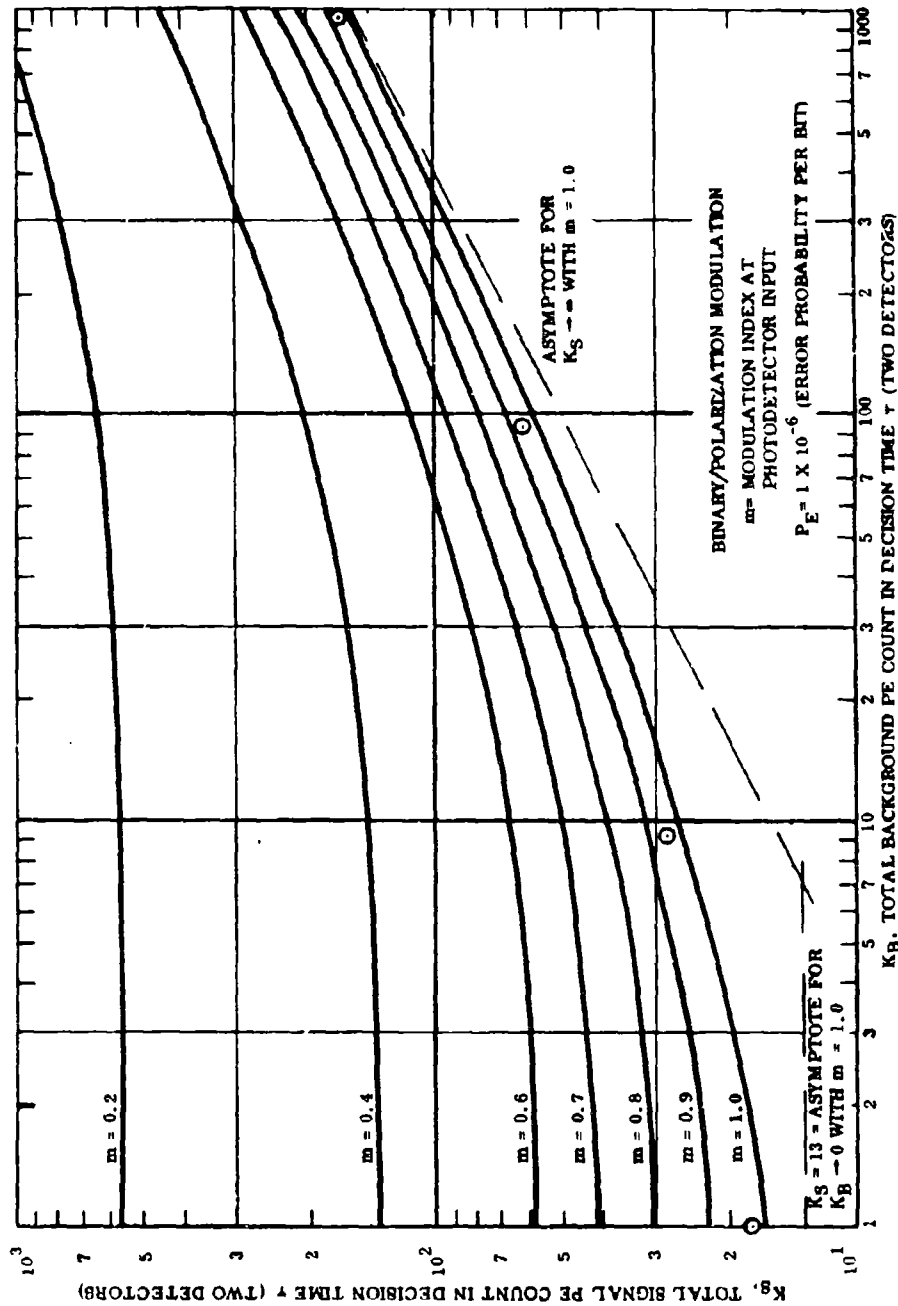


Fig. 4-2 Required Signal PE Count per Decision Versus Background PE Count in Same Time for Several Values of Modulation Index, m

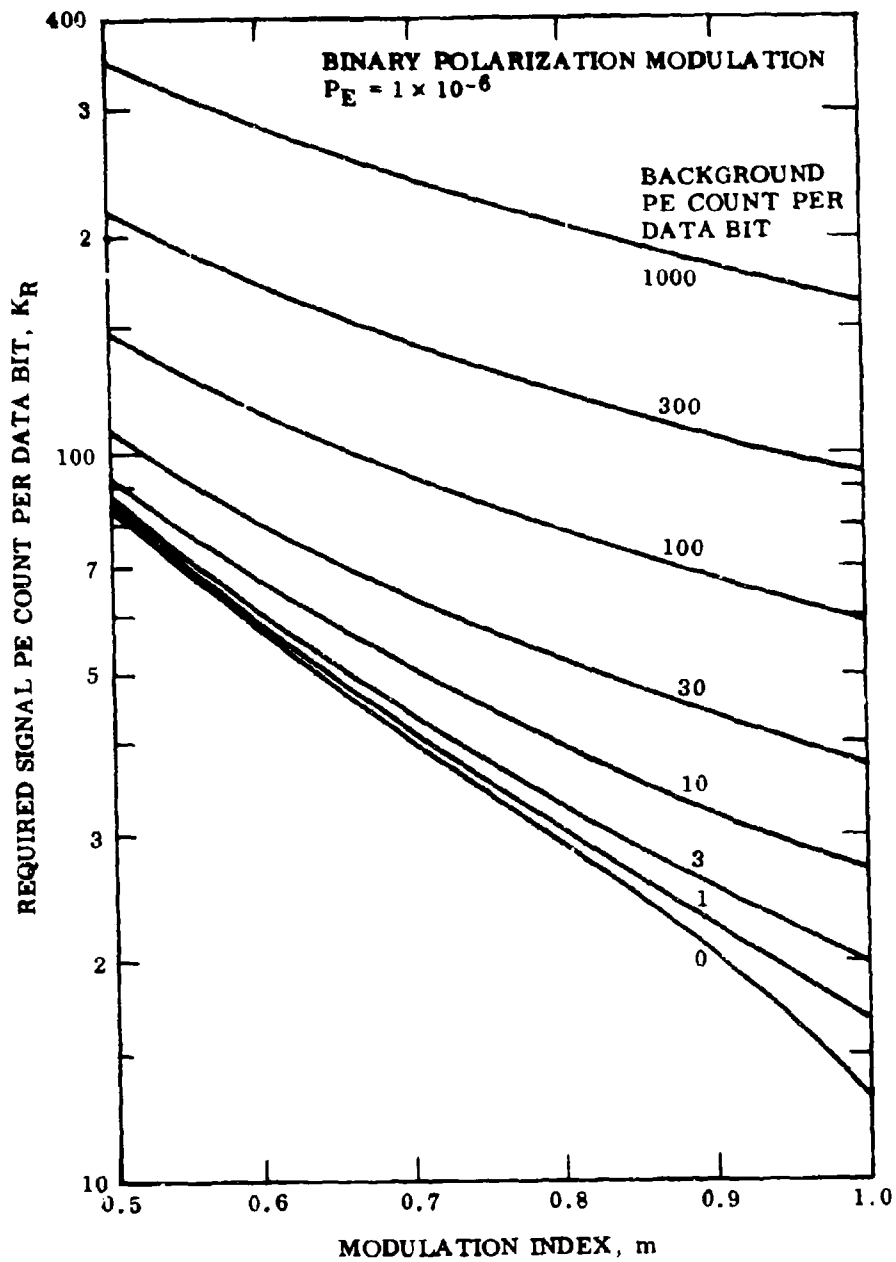


Fig. 4-3 Required Minimum Signal Photoelectron Count per Data Bit, K_R , Versus Modulation Index, m

C-25

LOCKHEED PALO ALTO RESEARCH LABORATORY
LOCKHEED MISSILES & SPACE COMPANY
A GROUP DIVISION OF LOCKHEED AIRCRAFT CORPORATION

action is ideal. That is, when the transmitted polarization is switched between two orthogonal states, the received laser signal all goes to one photodetector or the other according to which binary state was transmitted.

In our notation, Bucher's expression (Ref. 4, Eq. 5) can be written in the form

$$P_E \leq C \exp \{ -K_S \cdot E_C \} \quad (27)$$

where

$$E_C = \frac{\sqrt{1 + 2 K_S/K_B} - 1}{\sqrt{1 + 2 K_S/K_B} + 1} \quad (28)$$

In Bucher's development, the factor C in Eq. (27) is unity, but comparison of numerical values given by the exact expression Eq. (23), indicates that with a value of $C = 0.5$, the accuracy of the expression is improved significantly. Values of K_S calculated with $C = 0.5$ and plotted in Fig. 4-2 along the curve for $m = 1.0$ are seen to agree within a few percent with the "exact" values represented by the curve, but still on the conservative side.

Although somewhat complex at first glance, Eq. (27) can be solved explicitly for K_S in terms of K_B and P_E . The result (with $C = 0.5$) is

$$K_S = -\ln(2P_E) + \sqrt{(-2K_B) \ln(2P_E)} \quad (29)$$

Equation (27) can now be modified to take account of nonideal modulation by the same method as used in the previous section for on-off modulation. However, for the binary polarization system we prefer to specify modulator action in terms of modulation index, as defined for the subcarrier system (see Vol. II, Task 1) rather than in terms of extinction ratio. Using the same reasoning as in the previous section, it is easy to show that the equivalence relations that apply in this case are the same as those for the subcarrier system given by Eqs. (13) and (14). As in that case, modulation

index m is defined as the ratio of peak-to-peak signal current swing (each detector) to total signal current (both detectors). Substituting for K_S and K_B in Eq. (27) and (28) and dropping the primes, as before, we obtain

$$P_E \approx \frac{1}{2} \exp - \{m K_S E_C(m)\} \quad (30)$$

where

$$E_C(m) = \frac{\sqrt{1 + \frac{2mK_S}{K_B + (1-m)K_S} - 1}}{\sqrt{1 + \frac{2mK_S}{K_B + (1-m)K_S} + 1}}$$

Again, the expression for P_E can be inverted to obtain the following explicit expression for K_S :

$$K_S = \frac{-\ln(2P_E)}{m^2} \left[1 + \sqrt{(1-m^2) + 2m^2 \frac{K_B}{-\ln(2P_E)}} \right] \quad (31)$$

Section 5
REFERENCES

1. T. F. Curran and M. Ross, "Optimum Thresholds in Optical Communication," Proc. IEEE (Corresp.), Vol. 53, Nov 1965, pp. 1770-1780
2. M. Ross, J. P. Brand, and G. M. Lee, Short Pulse Laser Modulation Techniques, Technical Report AFAL-TR-70-130, Contract F33615-69-C-1418, Jun 1970
3. W. K. Pratt, Laser Communication Systems, Wiley, New York, 1969, Chap. 11
4. E. A. Bucher, Error Performance Bounds for Two Receivers for Optical Communication and Detection, Air Force Electronic Systems Division Report ESD-TR-70-349, 10 Nov 1970; MIT Lincoln Laboratory Technical Note 1970-18
5. W. K. Pratt, "Binary Detection in an Optical Polarization Modulation Communication Channel," IEEE Trans. Comm. Tech., Vol. COM-14, Oct 1966, pp. 664-665

Appendix D

SIGNAL-TO-NOISE RATIO AND BIT ERROR
PROBABILITY FOR A QUADRI PHASE SUBCARRIER
SYSTEM - GAUSSIAN STATISTICS APPROXIMATION

by

Dr. H. V. Hance

(Based in part on analyses performed under
Contract N00014-71-C-0049 and contained
in LMSC-D243625)

LOCKHEED PALO ALTO RESEARCH LABORATORY
LOCKHEED MISSILES & SPACE COMPANY
A GROUP DIVISION OF LOCKHEED AIRCRAFT CORPORATION

Section 1
INTRODUCTION

This appendix has two purposes: (1) to develop expressions in several forms for signal-to-noise ratio for the microwave subcarrier after photodetection of the polarization-modulated optical beam and bandpass filtering, and (2) to obtain an approximate expression for bit error probability using the S/N expression developed here in conjunction with expressions for bit error probability derived in standard references on rf communication system theory.

Section 2

REPRESENTATION OF SIGNAL AND NOISE PHOTOCURRENTS

We assume that the received optical signal is polarization modulated at a microwave subcarrier frequency ω_m and that it is converted into two intensity-modulated beams by means of a polarization beam splitter in the manner described under Task 2 of Vol. II. Separate photodetectors, one for each beam, then produce output photocurrents given by

$$i_1(t) = \frac{I_O}{2} \left[1 + m \sin \left(\omega_m t + k \frac{\pi}{2} + \frac{\pi}{4} \right) \right] + \frac{I_B}{2} + i_{N1}(t) \quad (1)$$

and

$$i_2(t) = \frac{I_O}{2} \left[1 - m \sin \left(\omega_m t + k \frac{\pi}{2} + \frac{\pi}{4} \right) \right] + \frac{I_B}{2} + i_{N2}(t) \quad (2)$$

where

I_O = total mean photocurrent of both detectors due to the laser signal

I_B = total mean photocurrent of both detectors due to optical background

m = intensity modulation index at photodetector input

k = 0, 1, 2, or 3, depending upon which of four possible phase states is transmitted

and $i_{N1}(t)$ and $i_{N2}(t)$ are, respectively, the random shot currents in the two photodetectors due to the signal and background photocurrents. The factor of 1/2 associated with I_O and I_B accounts for the division of signal and background optical power between the two photodetectors.

These two photodetector currents are represented in Fig. 1. The dashed curves show the ensemble average photocurrents, which are the ideal values that would exist in

the absence of photocurrent shot noise. The magnitude of the shot noise is shown to vary during the subcarrier modulation cycle in accordance with the variation of optical intensity. Also, the mean background photocurrent is shown.

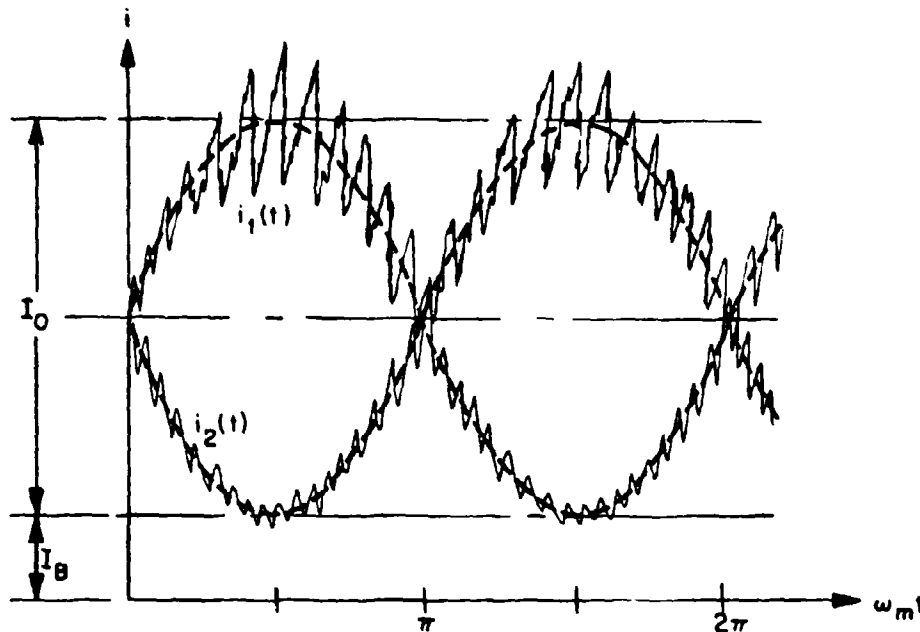


Fig. 1 Photodetector Output Currents. The sinusoidal variation of (ensemble average) photocurrent for one subcarrier cycle is indicated by the dashed lines. Superimposed is a representation of the total current, including the shot noise component. Note the opposite variations of noise magnitude for the two outputs during one cycle

Section 3 SUBCARRIER AND NOISE POWER

We now calculate the variance of the noise currents i_{N1} and i_{N2} by use of the well-known shot current expression (Ref. 1),

$$\langle i_N^2 \rangle = 2q \langle i(t) \rangle B \quad (3)$$

where q is the electronic charge, B is the photodetector output circuit bandwidth, and the brackets denote the expectation or ensemble average value. Using Eqs. (1) and (2) for $i(t)$ gives

$$\langle i_{N1}^2 \rangle = \left\{ \frac{I_0}{2} \left[1 + m \sin \left(\omega_m t + k \frac{\pi}{2} + \frac{\pi}{4} \right) \right] + \frac{I_B}{2} \right\} 2q B \quad (4)$$

$$\langle i_{N2}^2 \rangle = \left\{ \frac{I_0}{2} \left[1 - m \sin \left(\omega_m t + k \frac{\pi}{2} + \frac{\pi}{4} \right) \right] + \frac{I_B}{2} \right\} 2q B \quad (5)$$

It is seen that these variances are time-dependent.

Since the signal currents in the two detectors are phase-coherent, while the shot currents are random relative to one another, an improvement in signal-to-noise ratio can be obtained by combining these two signal currents.

Taking the difference of the signal currents, as given by Eqs. (1) and (2), and disregarding the noise term gives the following for the combined useful subcarrier signal current:

$$i_c(t) = m I_0 \sin \left(\omega_m t + k \frac{\pi}{2} + \frac{\pi}{4} \right) \quad (6)$$

Assuming noiseless current multiplication by a factor M , the corresponding sub-carrier signal power in a load R_L is given by

$$P_{sc} = \overline{i_c^2(t)} M^2 R_L = \frac{1}{2} m^2 I_o^2 M^2 R_L \quad (7)$$

Similarly, the noise power of the combined signal after amplification is obtained by using Eqs. (4) and (5);

$$P_{NS} = \left[\langle i_{N1}^2 \rangle + \langle i_{N2}^2 \rangle \right] M^2 R_L = 2qBR_L M^2 (I_o + I_B) \quad (8)$$

The latter expression is seen to be independent of time even though the variances of the individual noise currents, as given by Eqs. (4) and (5), are functions of time. Thus, the noise power of the combined photocurrents does not vary during the modulation cycle. The subscript S in the noise term P_{NS} denotes noise power due to shot effect.

In practice, the photocurrent multiplication factor will vary from photoelectron to photoelectron and this variation will increase the randomness of the output current. It has been shown (Ref. 2) that this increase in output noise can be represented by application of a noise factor $F_D \geq 1$ to the noise power given by Eq. (8). Also, any load or amplifier following the photodetector and having an effective noise temperature $T_{eff} > 0$ will contribute additional noise power in the amount of $kT_{eff}B$, where k is Boltzmann's constant. Thus, the total output noise of the photodetector and associated amplifier or load is

$$P_{NT} = F_D P_N + kT_{eff}B$$

where the subscript T denotes total noise due to shot and thermal noise components. Using Eq. (8), this becomes

$$P_{NT} = 2qBR_L M^2 F_D (I_o + I_B) + kT_{eff}B \quad (9)$$

For some purposes, it is convenient to write this in the form

$$P_{NT} = 2qBR_L M^2 F_D (I_o + I_B)(1 + F_T) \quad (10)$$

where

$$F_T = \frac{k T_{eff}}{2qBR_L M^2 F_D (I_o + I_B)} \quad (11)$$

The term F_T is the ratio of the thermal noise due to amplifier (or load) following the photodetector to the output noise of the photodetector itself, the two measured in the same bandwidth. Thus, F_T has the significance of an excess noise factor. It should be noted, however, that F_T is not the conventional noise figure of the post-amplifier. Calling the latter noise figure F_A , if the input to the post-amplifier is terminated by a room-temperature resistive load, the effective temperature T_{eff} to be used in Eq. (9) or (11) is given by

$$T_{eff} = 300(1 + F_A) (^{\circ}K) \quad (12)$$

Section 4 CARRIER-TO-NOISE RATIO

The ratio of subcarrier power for a bandwidth B to noise power in the same band is obtained using Eqs. (7) and (9):

$$\frac{P_{sc}}{P_{NT}} = \frac{\frac{1}{2} \cdot m^2 I_o^2 M^2 R_L}{2qBR_L M^2 F_D (I_o + I_B) + k T_{eff} B} \quad (13)$$

An equivalent expression in a simpler form is obtained by using Eqs. (7) and (10),

$$\frac{P_{sc}}{P_{NT}} = \frac{m^2 I_o^2}{4qB(I_o + I_B) F_D (1 + F_T)} \quad (14)$$

where F_T is given by Eq. (11).

Next, we express this signal-to-noise ratio in terms of the laser power and optical background power incident on the photodetectors. Letting P_R and P_B stand for these quantities, we can write

$$I_o = \eta_D \frac{P_R q}{h\nu} \quad (15)$$

and

$$I_B = \eta_D \frac{P_B q}{h\nu} \quad (16)$$

where

- η_D = photodetector quantum efficiency
 h = Planck's constant
 $= 6.625 \times 10^{-34}$ joules-sec
 q = electronic charge
 $= 1.6 \times 10^{-19}$ coulombs
 ν = laser frequency (Hz)

Substituting into Eq. (13) and rearranging slightly gives

$$\frac{P_{sc}}{P_{NT}} = \frac{\left[m M \frac{\eta_D q}{h \nu} \right]^2 P_R^2 R_L}{4 M^2 q F_D \left(\frac{\eta_D q}{h \nu} \right) (P_R + P_B) B R_L + 2 k T_{eff} B} \quad (17)$$

or, equivalently, from Eq. (14),

$$\frac{P_{sc}}{P_{NT}} = \frac{\left[m \frac{\eta_D q}{h \nu} \right]^2 P_R^2}{4 q B F_D \left(\frac{\eta_D q}{h \nu} \right) (P_R + P_B)(1 + F_T)} \quad (18)$$

where, now

$$F_T = \frac{k T_{eff}}{2 q B R_L M^2 F_D \left(\frac{\eta_D q}{h \nu} \right) (P_R + P_B)} \quad (19)$$

For ease of interpretation (in Section 7), we rewrite Eq. (18) in the form

$$\frac{P_{sc}}{P_{NT}} = \frac{P_R}{2 h \nu B} \cdot \frac{\eta_D}{F_D (1 + F_T)} \cdot \frac{m^2}{2} \cdot \frac{1}{1 + P_B/P_R} \quad (20)$$

For some purposes, it is convenient to express signal-to-noise ratio in terms of the signal and background parameters K_S and K_B , defined, respectively, as the mean total signal and background photoelectron counts (two detectors) in τ , the bit decision time. The mean signal and background photocurrents are then given by

$$I_O = \frac{K_S q}{\tau} \quad (21)$$

and

$$I_B = \frac{K_B q}{\tau} \quad (22)$$

Substituting for I_O and I_B in Eq. (14) gives

$$\frac{P_{sc}}{P_{NT}} = \frac{m^2 K_S^2}{4 B \tau (K_S + K_B) F_D (1 + F_T)} \quad (23)$$

Section 5
BIT ERROR PROBABILITY - GAUSSIAN APPROXIMATION

We now wish to obtain an expression for bit error probability using the results derived in textbooks on rf communication theory. In this derivation, we will assume that the noise has Gaussian statistics and that its power spectral density n_o is uniform over the subcarrier band. (The assumption of Gaussian statistics is necessary to permit use of rf communication theory.)

The subcarrier energy in a bit decision time τ is given by

$$E_{\tau} = P_{sc} \tau \quad (24)$$

However, as discussed under Task 2 of Volume II, the quadriphase-modulated subcarrier signal can be regarded as the sum (in phase quadrature) of two biphase-modulated signals carrying independent data streams, each using one-half of the total subcarrier power. It is convenient, therefore, to define the effective subcarrier power per channel as

$$P'_{sc} = \frac{1}{2} P_{sc} \quad (25)$$

and the corresponding effective subcarrier energy per channel, per decision, as

$$E'_{\tau} = P'_{sc} \tau = \frac{1}{2} P_{sc} \tau \quad (26)$$

Under the assumption of uniform noise spectral density over the subcarrier band, we have

$$n_o = P_{NT}/B \quad (27)$$

Therefore

$$\frac{E'_T}{n_0} = (B\tau) \frac{P'_{sc}}{P_{NT}} = \frac{1}{2} (B\tau) \frac{P_{sc}}{P_{NT}} \quad (28)$$

Using Eq. (23) for P_{sc}/P_{NT} , we obtain

$$\frac{E'_T}{n_0} = \frac{1}{8} \cdot \frac{m^2 K_S^2}{(K_S + K_B) F_D (1 + F_T)} \quad (29)$$

The error probability per bit for a coherently detected, biphas-modulated rf carrier with additive Gaussian noise is well known [e.g., Ref. 3, Eq. (7-6-4)]. It is

$$P_E = \frac{1}{2} \text{Erfc} \sqrt{\frac{E}{n_0}} \quad (30)$$

where Erfc is the error function complement, E is the signal energy per data bit, and n_0 is the (one-sided) noise power spectral density. Identifying E in this expression with E'_T , and using Eq. (29) for E/n_0 in Eq. (30), we obtain for the error probability in either biphas channel

$$\begin{aligned} P_E &= \frac{1}{2} \text{Erfc} \sqrt{\frac{E'_T}{n_0}} \\ &= \frac{1}{2} \text{Erfc} \left[\frac{1}{8} \cdot \frac{m^2 K_S^2}{(K_S + K_B) F_D (1 + F_T)} \right]^{\frac{1}{2}} \end{aligned} \quad (31)$$

Assuming that the two channels are identical, they will have the same bit error probability; hence, taken together they will produce twice as many errors per unit time as one would alone. However, they will also transmit twice as much data per unit time. Therefore, the probability of error per bit transmitted (two channels) is the same as for one channel alone. Thus, the error probability per bit for the quadriphase system is given by Eq. (31).

The quantity E'_τ can be given an alternate interpretation to that of subcarrier energy per channel, per decision. For this we define a new parameter E_R as the total subcarrier energy per data bit received. In the quadriphase system, the number of data bits per decision time τ is two, since two independent binary decisions (one for each channel) are made in each interval τ . Since E_τ , as given by Eq. (24), is defined as the (total) subcarrier energy in time τ , we have

$$E_R = \frac{E_\tau}{2} = E'_\tau \quad (32)$$

Therefore,

$$\frac{E_R}{n_o} = \frac{E'_\tau}{n_o} = \frac{1}{2} \cdot \frac{E_\tau}{n_o} = \frac{1}{2} \cdot \frac{P_{sc} \tau}{n_o} \quad (33)$$

and Eq. (31) can be written

$$P_E = \frac{1}{2} \operatorname{Erfc} \sqrt{\frac{E_R}{n_o}} \quad (34)$$

where, in view of Eqs (33) and (31),

$$\frac{E_R}{n_o} = \frac{1}{8} \cdot \frac{m^2 K_S^2}{(K_S + K_B) F_D (1 + F_A)} \quad (35)$$

Thus, E'_τ , the effective energy per bit per (biphase) channel is numerically the same as E_R , the actual (quadriphase) subcarrier energy per bit. This result is not surprising, since it is known that biphase and quadriphase-modulated subcarrier systems are equivalent in terms of subcarrier energy required per data bit for a specified error probability (Ref. 4).

Finally, we give an approximation for Eq. (34) based on the well-known asymptotic expansion for the error function complement (Ref. 5),

$$\operatorname{Erfc} \chi \approx \frac{\exp(-\chi^2)}{(\pi)^{1/2} \chi} \quad (36)$$

Accordingly, we can write

$$P_E \approx \frac{1}{2} \left(\pi \frac{E_R}{n_0} \right)^{-\frac{1}{2}} \exp \left(-\frac{E_R}{n_0} \right) \quad (37)$$

where, as before, E_R/n_0 is given by Eq. (35).

Section 6

MULTILINK CHANNELS WITH NONREGENERATIVE REPEATERS

In this section, we consider the case of a multilink optical channel using the QPSK subcarrier format and simple amplifying repeaters. That is, the baseband data streams are not recovered and regenerated at each relay; the subcarrier is only amplified and then retransmitted over the next link. Specifically, we wish to obtain a relationship between bit error probability and the signal parameters.

Figure 2 shows the channel model to be used. The input signal to link 1 (signal power = S_1) is assumed to be transmitted without distortion through the link, so that the useful output signal power is S_1 . However, in the successive links, noise components $N_1, N_2 \dots N_n$ are added. Thus, the total input signal to Link No. 2 is $S_2 = S_1 + N_1$, and to Link No. 3 is $S_3 = S_2 + N_2 = S_1 + N_1 + N_2$. The total output of Link No. 3 is then $S'_3 = S_3 + N_3 = S_1 + N_1 + N_2 + N_3$; the useful output is S_1 ; and the output signal-to-noise ratio is

$$\text{SNR}_o = \frac{S_1}{N_1 + N_2 + N_3} \quad (33)$$

The generalization to an arbitrary number of links is obvious, but for the sake of simplicity we now concentrate on the three-link channel.

The assumption that the useful signal remains unchanged at the output of each link and that the accumulated noise power is the sum of the noise power of each link is equivalent to postulating linearity of response for each link. For this condition to be valid in a practical sense requires that the signal plus noise in each link be kept moderately below the saturation level of the repeater so that suppression of the useful signal by the noise does not occur.

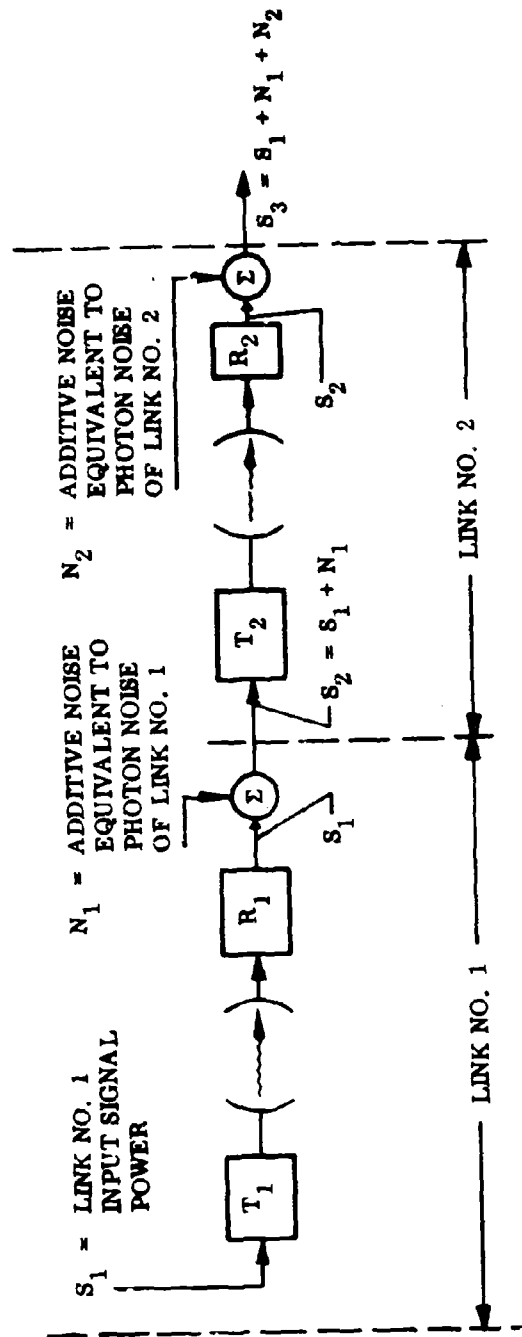


Fig. 2 Link Model Used in Analyzing Multilink, High-Data-Rate Channel Using Nonregenerative Repeaters

Next we define the single-link signal-to-noise ratio for the kth link as

$$\text{SNR}_k = \frac{S_k}{N_k} \quad (39)$$

where S_k is the power of the total input (signal plus noise) from the preceding link; for example,

$$S_2 = S_1 + N_1 \quad (40)$$

and

$$S_3 = S_2 + N_2 = S_1 + N_1 + N_2 \quad (41)$$

We now invert Eq. (38) and rewrite it in the form

$$\frac{1}{\text{SNR}_0} = \frac{N_1}{S_1} + \frac{N_2}{S_1} + \frac{N_3}{S_1} \quad (42)$$

The first term is just $1/\text{SNR}_1$, as given by Eq. (39). The second term can be rewritten in the form

$$\frac{N_2}{S_1} = \frac{N_2}{S_2} \cdot \frac{S_2}{S_1} = \frac{1}{\text{SNR}_2} \cdot \frac{S_1 + N_1}{S_1} \quad (43)$$

or

$$\frac{N_2}{S_1} = \frac{1}{\text{SNR}_2} \left(1 + \frac{1}{\text{SNR}_1} \right)$$

where Eq. (40) has been used for S_2 and Eq. (39) for S_1/N_1 .

Similarly, we can rewrite the third term in Eq. (42) as

$$\frac{N_3}{S_1} = \frac{N_3}{S_3} \cdot \frac{S_3}{S_2} \cdot \frac{S_2}{S_1} = \frac{1}{\text{SNR}_3} \cdot \frac{S_2 + N_2}{S_2} \cdot \frac{S_1 + N_1}{S_1}$$

or

$$\frac{N_3}{S_1} = \frac{1}{\text{SNR}_3} \left(1 + \frac{1}{\text{SNR}_2}\right) \left(1 + \frac{1}{\text{SNR}_1}\right)$$

Substituting Eqs. (43) and (44) in (42) gives

$$\frac{1}{\text{SNR}_0} = \frac{1}{\text{SNR}_1} + \frac{1}{\text{SNR}_2} \left(1 + \frac{1}{\text{SNR}_1}\right) + \frac{1}{\text{SNR}_3} \left(1 + \frac{1}{\text{SNR}_1} + \frac{1}{\text{SNR}_2}\right)$$

In cases where SNR_1 and $\text{SNR}_2 > 100$ and the number of links is small, Eq. (45) can be simplified with negligible error to

$$\frac{1}{\text{SNR}_0} \approx \frac{1}{\text{SNR}_1} + \frac{1}{\text{SNR}_2} + \frac{1}{\text{SNR}_3}$$

We now wish to relate SNR_0 to the ratio (E_τ/n_0) in Eq. (34) in order to obtain an expression for bit error probability. For this purpose, we define $E_{\tau k}$ as the received energy per decision time τ for the k th link; then $S_k = E_{\tau k}/\tau$. Also, we can write $N_k = n_0 B_k$, where B_k is the bandwidth of the k th link. In terms of these quantities, we have

$$\text{SNR}_k = \frac{S_k}{N_k} = \frac{E_{\tau k}}{n_0} \cdot \frac{1}{B_k \tau}$$

Next, we define the normalized link signal-to-noise parameter

$$\gamma_k = E_{\tau k}/n_0$$

Equation (47) can then be rewritten as

$$\text{SNR}_k = \gamma_k / B_k \tau \quad (49)$$

We now substitute this value of SNR_k in Eq. (46), and at the same time set $B_k = 1.0$ since we are concerned in the remainder of this analysis only with the noise power in a 1-Hz bandwidth. We obtain

$$\frac{1}{\gamma_0} = \frac{1}{\gamma_1} + \frac{1}{\gamma_2} + \frac{1}{\gamma_3} \quad (50)$$

Since γ_0 is the output subcarrier energy per decision time τ , we can identify γ_0 with the ratio E_r/n_o in Eq. (33). From this equation, we see that E_r/n_o , the argument of Eq. (34) for bit error probability, is related to γ_0 by $E_r/n_o = \gamma_0/2$. Therefore, we have

$$P_E = \frac{1}{2} \text{Erfc} \left[\frac{\eta_B \gamma_0}{2} \right]^{\frac{1}{2}} \approx \frac{1}{2} \left(\frac{\eta_B \gamma_0}{2} \right)^{-\frac{1}{2}} \exp \left(-\frac{\eta_B \gamma_0}{2} \right) \quad (51)$$

where Erfc is the error function complement defined by

$$\text{Erfc} [z] = \frac{2}{\sqrt{\pi}} \int_z^{\infty} \exp -t^2 dt \quad (52)$$

and the approximate form is obtained by use of Eq. (36). In writing Eq. (51), we have included an efficiency factor η_B to represent nonideal action of the bit synchronizer.

The γ_k for the individual links can be calculated by use of Eq. (24) if we regard S_k as the power of a cw subcarrier equal to the power of the actual subcarrier plus that of the accompanying noise. Defining K_{Sk} and K_{Bk} as the actual signal and background photocounts in a decision time τ for the kth link, we have

$$\gamma_k = \frac{m^2}{4} \frac{K_{Sk}}{1 + K_{Bk}/K_{Sk}} \quad (53)$$

This expression in combination with Eqs. (49) and (50) permits bit error probability to be calculated for a multilink channel, subject to the approximation involved in the representation of the Poisson noise by additive Gaussian noise. As discussed in Section 7, any error in this approximation is on the conservative side in that the predicted bit error probability is too high. Alternatively, if P_E is specified, the calculated minimum required value of the signal-to-noise parameter γ will be greater than the value given by an exact theory.

Section 7

DISCUSSION OF RESULTS

The individual factors in Eq. (20) can each be interpreted physically. The first, $P_R/2h\nu B$, can easily be shown to be just the ratio of photocurrent dc power to shot noise power that would exist if signal shot effect were the only source of noise. The second factor can be regarded as an effective quantum efficiency reduced from the value appropriate for calculation of dc photocurrent by the effect of photomultiplier excess noise and post-amplifier noise. This reduction is used in Vol. II, Task 1 (which is otherwise based on the results for Poisson statistics developed in Appendixes B and C) as the means for taking account of these sources of excess noise. The third factor accounts for the reduction in useful output when the modulation index is less than unity; the factor of 2 in the denominator arises from the assumption of sinusoidal modulation. (If square-wave modulation were used, the denominator would be unity.) Finally, the factor $1/(1 + P_B/P_R)$ accounts for the reduction of signal/noise due to the received background radiation.

It should be noted that in deriving the above expressions for signal-to-noise ratio, no assumptions were required as to the statistical properties of the shot noise current other than that the noise currents in the two photodetectors are statistically independent. As discussed in Appendix B, the photocurrents are well described by Poisson statistics. However, after the photocurrent passes through the subcarrier bandpass filter, these statistics are modified and tend toward Gaussian. Moreover, the differential combining of the photodetector outputs assures that the probability density function of these currents is symmetrical about a mean value of zero, in contrast to the asymmetry of the Poisson density function. This makes for an even closer approach to Gaussian statistics.

If we assume that thermal noise adds negligibly to the shot noise (i.e., if $F_A \ll 1$), the value of Eq. (20) is just twice that of a similar expression derived by Pratt [Ref. 1, Eq. (10-21)] for a single photodetector receiver and a 100% modulated ($m = 1$) optical signal, provided his background term is properly interpreted. The factor of 2 accounts for the doubling of signal-to-noise ratio resulting from addition of the two photodetector outputs. With regard to treatment of background, our analysis assumes that the received background power is divided between the two photodetectors, while in the system considered by Pratt, all the background power (his P_B) is incident on the one photodetector. In that system, it would be possible to reduce the background by one-half by inserting a polarization analyzer ahead of the photodetector and orienting it to match the polarization of the received laser signal. With that arrangement, the background parameter P_B would be replaced by $P_B/2$ and the resulting expression would be in agreement with ours, except for the factor of 2 already discussed.

As an example of the use of Eq. (37), we use the same conditions that were used in the example in Appendix C, Section 2, namely, $P_E = 1 \times 10^{-6}$, $m = 0.9$, $K_B = 0$, $F_D = 1.0$, and $F_T = 0$. From Eq. (37) we find that the required value of E_R/η_o is 11.32. Using this value in Eq. (35) together with the constants given above, we find that the required number of photoelectrons in decision time τ is $K_S = 112$. Accordingly, the number required per data bit K_R (as defined in Appendix C) is $K_R = K_S/2 = 56$. This value is seen to be about 10% smaller than the value obtained in Appendix C by use of the Chernoff-bound statistics developed in Appendix B. It is interesting to note that the alternate analysis of subcarrier systems given in Appendix B, based on the "tilted probability distribution" method indicates that the Chernoff bound method is somewhat more than 10% pessimistic in terms of the required photoelectron count indicated. Therefore, it is believed that the Gaussian statistics approximation, although giving values below those obtained by use of the Chernoff bound method, are still on the conservative side.

Section 8
REFERENCES

1. W. K. Pratt, Optical Communications Systems, John Wiley and Sons, Inc., New York, 1969, Chap. 8
2. L. K. Anderson and M. DiDomenico, Jr., "High-Speed Photodetectors for Microwave Demodulation of Light," Advances in Microwaves, Vol. 5, Leo Young, Ed., Academic Press, New York, 1970
3. M. Schwartz, W. R. Bennett, and S. Stein, Communication Systems and Techniques, McGraw-Hill, Inc., New York, 1966
4. Ira Jacobs, "Comparison of M-ary Modulation Systems," Bell Syst. Tech. J., Vol. 46, Jun 1967, pp. 843 - 864
5. M. Abramowitz and I. A. Stegun, Handbook of Mathematical Functions, U.S. Government Printing Office, Washington, D.C., 1964

Appendix E

INSENSITIVITY OF SATELLITE
ORIENTATION ON THE RECEPTION
OF POLARIZATION-MODULATED SIGNALS

by

Dr. K. K. Chow

LOCKHEED PALO ALTO RESEARCH LABORATORY
LOCKHEED MISSILES & SPACE COMPANY
A GROUP DIVISION OF LOCKHEED AIRCRAFT CORPORATION

Section 1
INTRODUCTION

In a space data relay subsystem (SDRS), the constraints on satellite orientation should be kept to a minimum to ensure ease of operation. Therefore, the modulation format should be so chosen that the received signal is independent of the relative orientation between the transmitter and the receiver.

One such format, the polarization modulation format proposed by LMSC, fulfills this requirement and has been discussed briefly under Task 2, Vol. II, of this final report. There, it is shown through heuristic arguments that the received signal strength is not orientation dependent; however, no analysis is given. In this appendix, detailed analyses of the effects of satellite orientation on received signal, in terms of static optical propagation and microwave modulation, are given. For completeness and ease of reference, a physical description of the transmitter/receiver configuration and a geometrical construction method are also given.

E-1

LOCKHEED PALO ALTO RESEARCH LABORATORY
LOCKHEED MISSILES & SPACE COMPANY
A GROUP DIVISION OF LOCKHEED AIRCRAFT CORPORATION

Section 2

PHYSICAL DESCRIPTION

Using the polarization modulation format, the birefringent electrooptic (EO) modulator crystal is zero- or half-wave biased optically. Thus, without any modulation voltage on the crystal, linearly polarized light, polarized at 45° to the birefringent axes, emerges as linearly polarized light after traversing the modulator. On the other hand, if positive or negative quarter-wave voltage is applied to the crystal, the output at the modulator will be right-hand or left-hand circularly polarized. At the receiver, the combination of a quarter-wave plate and a polarization beam splitter then directs the appropriate amount of optical power to the proper photodetectors according to the modulation voltage. The situation is shown schematically in Fig. 1.

Before going through the detailed analysis, it is interesting to note that geometrical construction may be used to show how the loci of the optical electric vector appear at various points of the transmitter and the receiver at different phases of the modulation cycle. These are shown in Figs. 2, 3, and 4, in which a sinusoidal modulation voltage, of peak value equal to the quarter-wave voltage of the modulator, is assumed. Figure 2 shows the case in which the modulator axes in the transmitter are aligned with the quarter-wave plate axes in the receiver; Fig. 3 shows the case in which the two sets of axes are at 45° to each other; while Fig. 4 shows the general case in which the two sets of axes are at an arbitrary angle θ to each other. The polarizing beam splitter axes are oriented at 45° to the quarter-wave plate axes in all cases, however. The construction is accomplished by considering the polarization states of the optical electric vector at various modulation phases and then taking the projection along the appropriate axes as the light propagates through the quarter-wave plate and the polarization beam splitter. From Figs. 2, 3, and 4, it is clear that, while the polarization states at various components may vary with the relative orientation θ between the transmitter and the receiver, the amplitudes of optical electric vector received at the two photodetectors do not change with orientation θ .

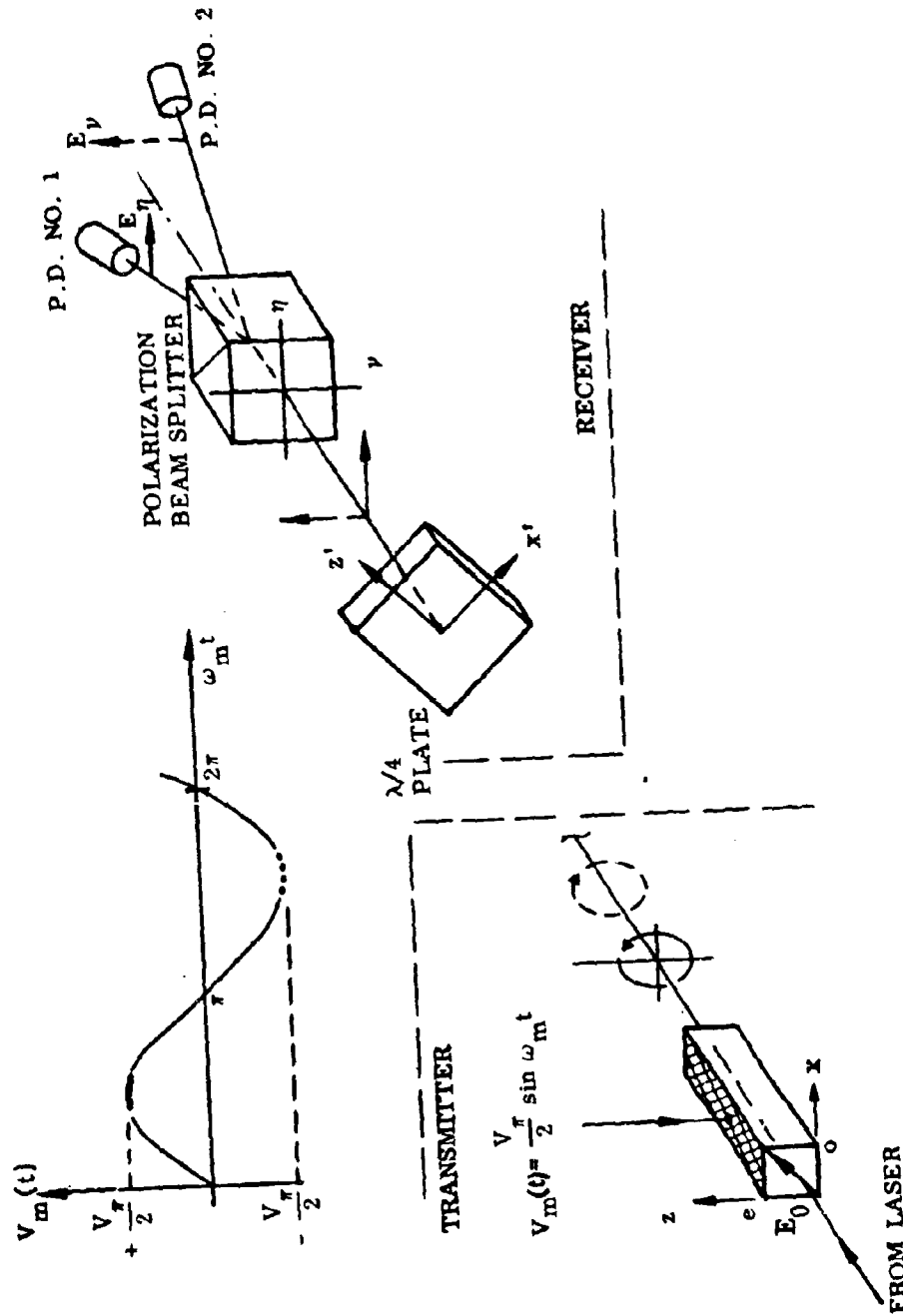
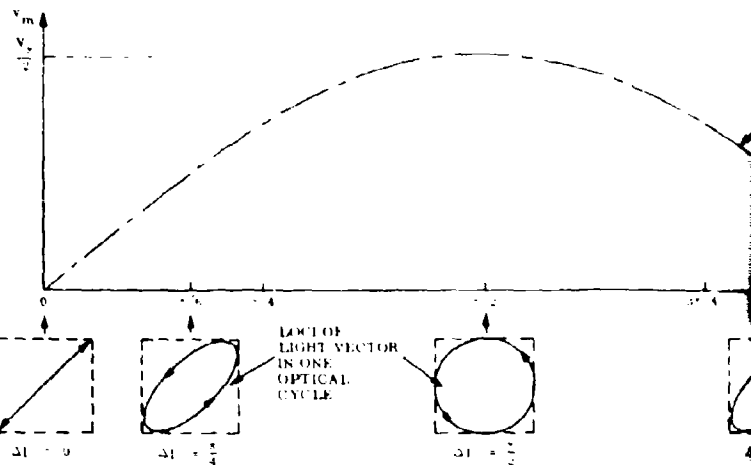


Fig. 1 Schematic View of Various Optical Components and Their Orientations in the Transmitter and the Receiver

This construction has been made by assuming θ to be static; that is, the orientation between the satellites is not time varying. In the next section, a time-varying $\theta = \theta(t)$ will be considered. It will be shown that the results are still the same.

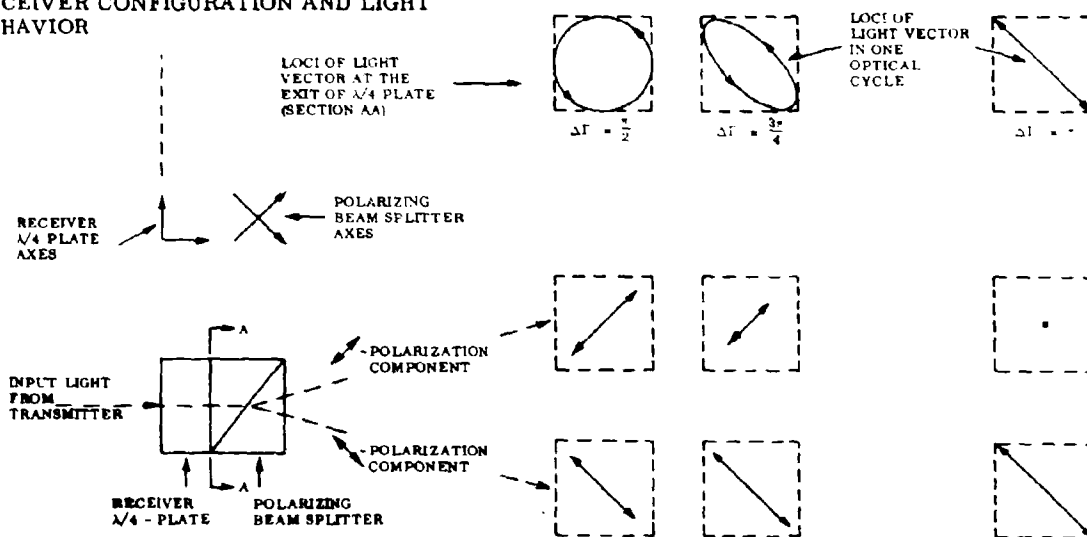
1. MODULATION VOLTAGE CURVE



2. LOCI OF LIGHT VECTOR, AT VARIOUS PHASES OF THE MODULATING VOLTAGE, AT THE EXIT APERTURE OF THE TRANSMITTER: MODULATOR CRYSTAL AXES ALIGNED WITH RECEIVER $\lambda/4$ - PLATE AXES

MODULATOR CRYSTAL e-AXIS
MODULATOR CRYSTAL o-AXIS

3. RECEIVER CONFIGURATION AND LIGHT BEHAVIOR



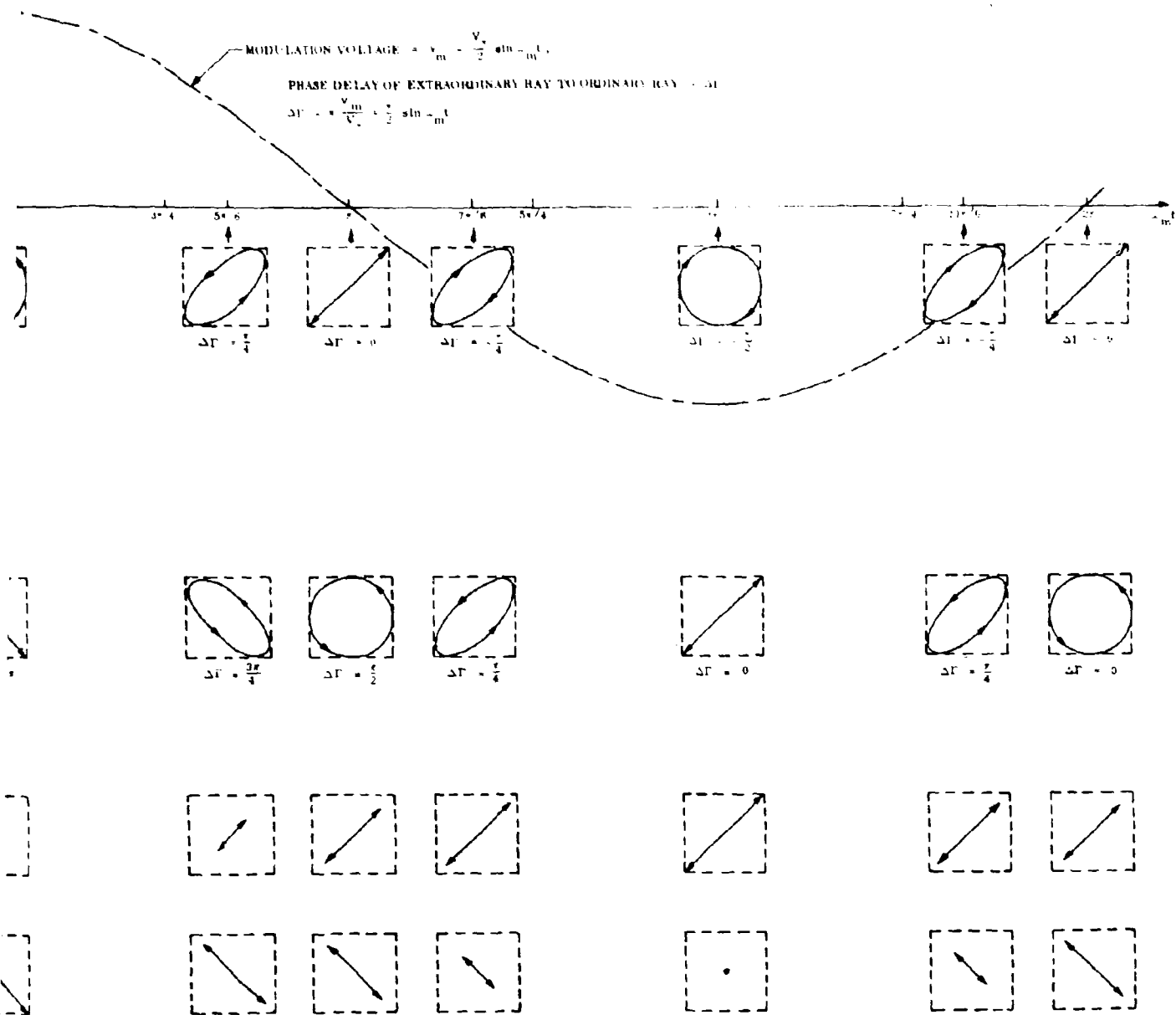
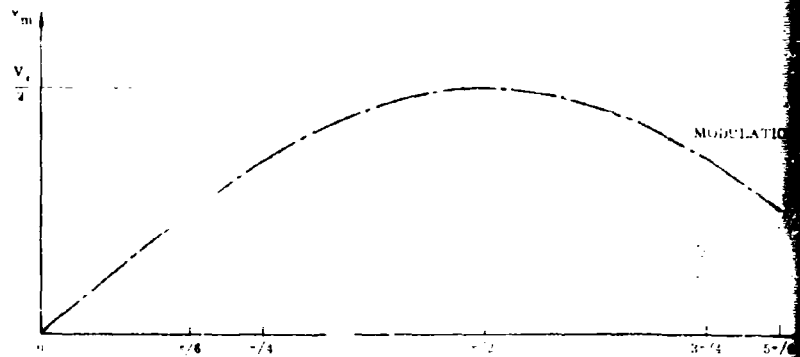


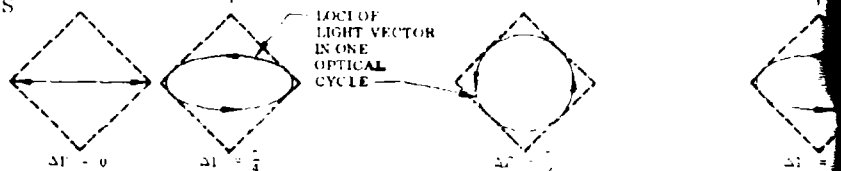
Fig. 2 Behavior of Optical Electric Vectors at Various Transmitter and Receiver Components Over a Modulation Cycle: Modulator Axes in Transmitter Aligned With the Quarter-Wave Plate Axes in the Receiver

1. MODULATION VOLTAGE CURVE



2. LOCI OF LIGHT VECTOR, AT VARIOUS PHASES OF THE MODULATING VOLTAGE, AT THE EXIT APERTURE OF THE TRANSMITTER: MODULATOR CRYSTAL AXES INCLINED AT 45° TO RECEIVER $\lambda/4$ -PLATE AXES

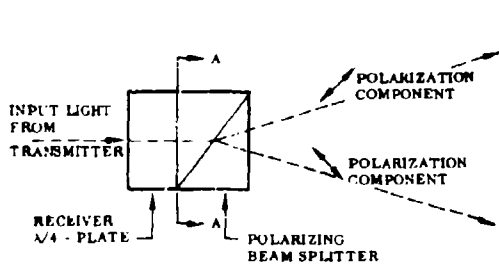
MODULATOR CRYSTAL x -AXIS 45° MODULATOR CRYSTAL y -AXIS



3. RECEIVER CONFIGURATION AND LIGHT BEHAVIOR

LOCI OF LIGHT VECTOR AT THE EXIT OF $\lambda/4$ PLATE (SECTION AA)

RECEIVER $\lambda/4$ PLATE AXES POLARIZING BEAM SPLITTER AXES



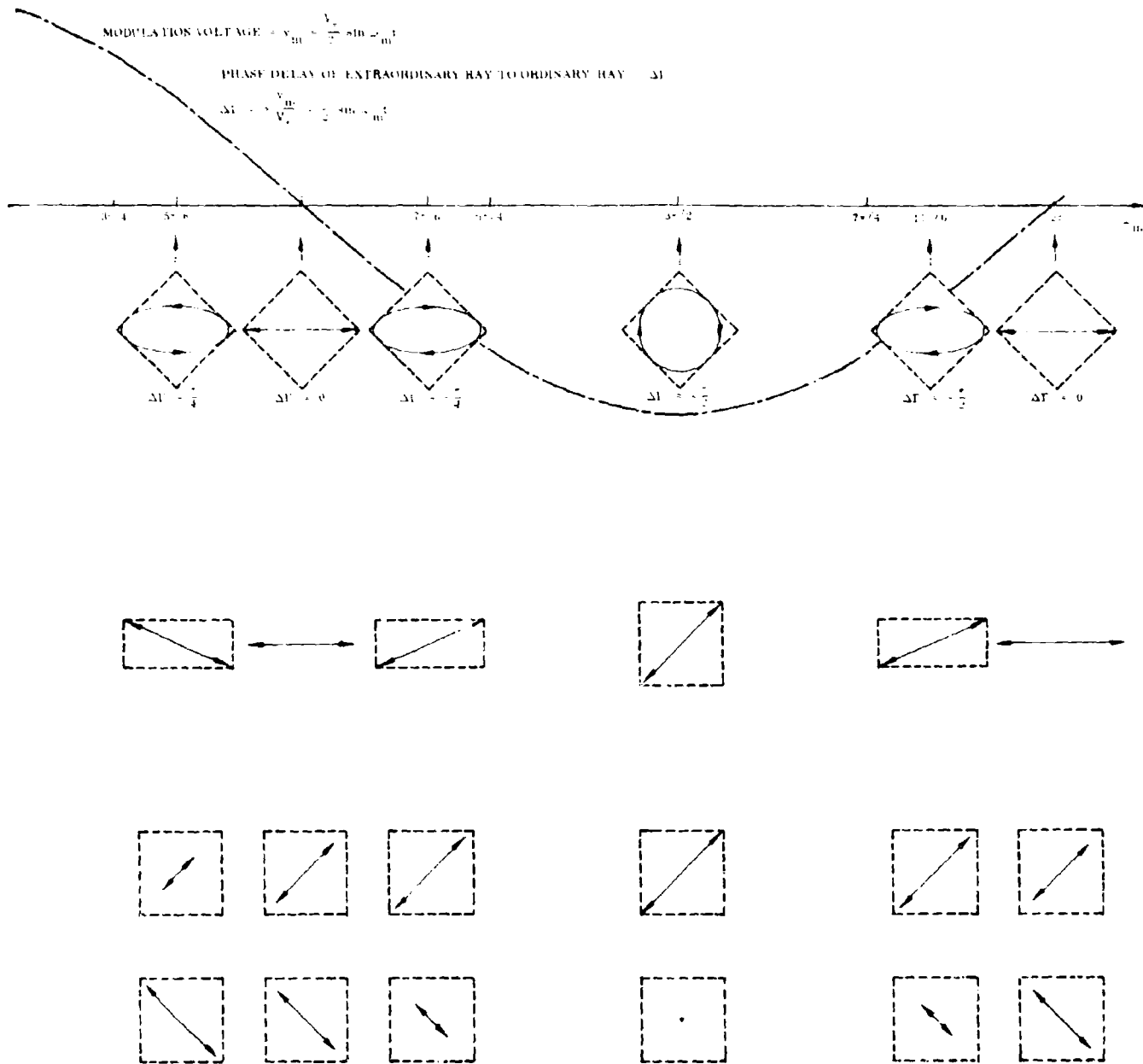
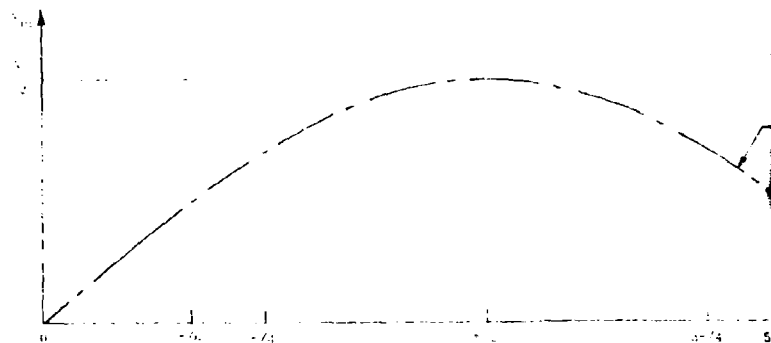
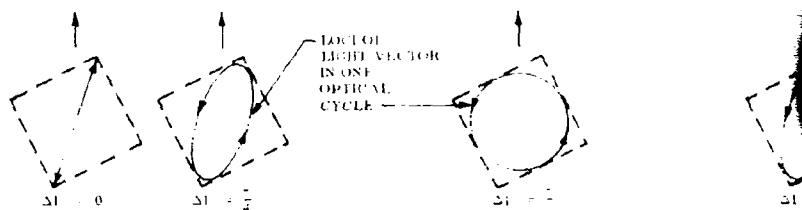


Fig. 3 Behavior of Optical Electric Vectors at Various Transmitter and Receiver Components Over a Modulation Cycle: Modulator Axes in Transmitter Oriented at 45° to the Quarter-Wave Plate Axes in the Receiver

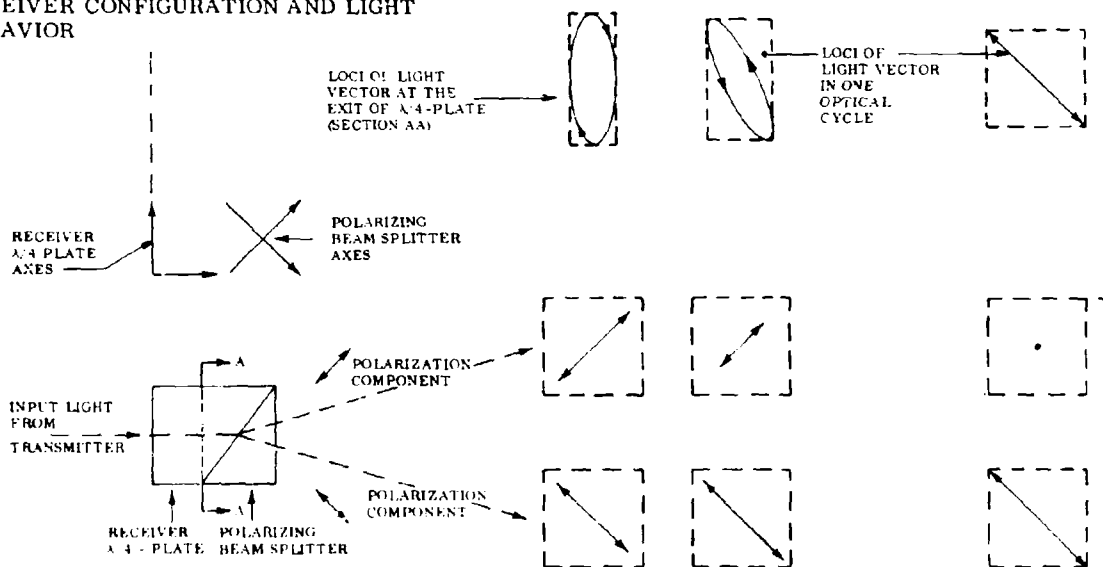
1. MODULATION VOLTAGE CURVE



2. LOCI OF LIGHT VECTOR, AT VARIOUS PHASES OF THE MODULATING VOLTAGE, AT THE EXIT APERTURE OF THE TRANSMITTER: MODULATOR CRYSTAL AXES INCLINED AT ANGLE θ TO RECEIVER $\lambda/4$ -PLATE AXES



3. RECEIVER CONFIGURATION AND LIGHT BEHAVIOR



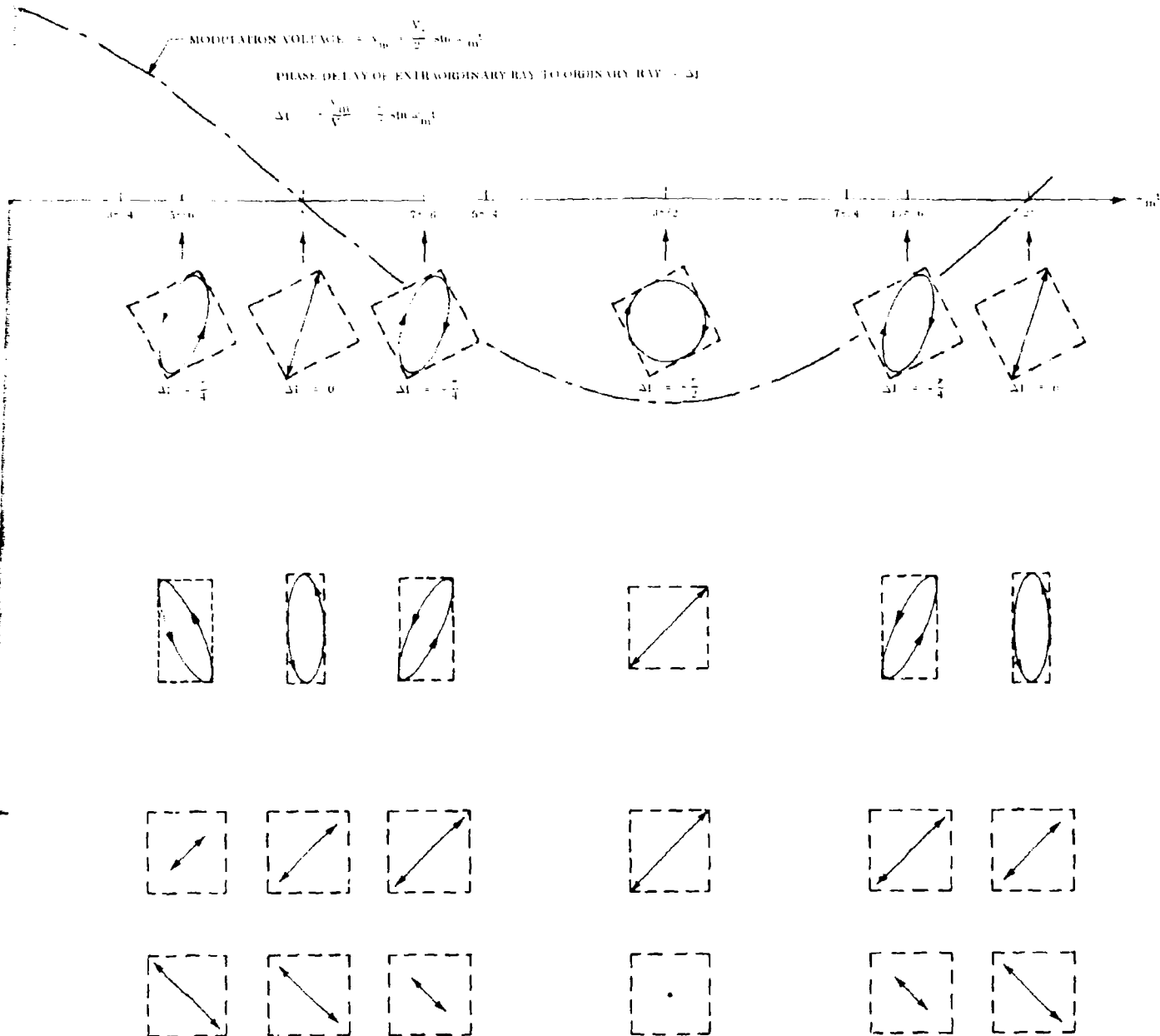


Fig. 4 Behavior of Optical Electric Vectors at Various Transmitter and Receiver Components Over a Modulation Cycle: Modulator Axes in Transmitter Oriented at an Arbitrary Angle θ to the Quarter-Wave Plate Axes in the Receiver

Section 3 ANALYSIS

Consider the EO crystal and the optical E-vector E_o as shown in Fig. 5.

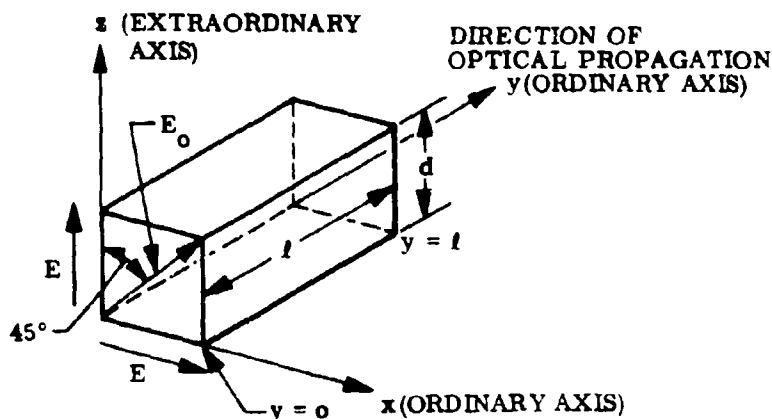


Fig. 5 Relationship Between the Input Light Vector E_o and the Birefringent Axes of the EO Crystal

It is clear that

$$E_o(y) = \hat{i}_z E e^{j(\omega_o t - \beta_z y)} + \hat{i}_x E e^{j(\omega_o t - \beta_x y)} \quad (1)$$

where

\hat{i}_z, \hat{i}_x = unit vectors along z and x directions, respectively

E = component of optical E-vector at the input of the crystal, polarized along x and z axes $= \frac{1}{\sqrt{2}} E_o$

ω_o = optical radian frequency

β_z, β_x = optical propagation constants for light polarized along the z and x axes, respectively, and are functions of modulation voltage

At the output face of the crystal, $y = \ell$, and the light vector is given by

$$E_o(\ell) = E e^{j\omega_o t} \left[\hat{i}_z e^{-j\beta_z \ell} + \hat{i}_x e^{-j\beta_x \ell} \right] \quad (2)$$

Now β_z and β_x are given by

$$\beta_z = \frac{\omega_o}{c} n_e \left[1 - \frac{1}{2} n_e^2 \frac{v_m(t)}{d} r_{33} \right] \quad (3)$$

$$\beta_x = \frac{\omega_o}{c} n_o \left[1 - \frac{1}{2} n_o^2 \frac{v_m(t)}{d} r_{13} \right] \quad (4)$$

where

c = velocity of light in free space

n_e, n_o = refractive indexes of extraordinary and ordinary rays, respectively

$v_m(t)$ = modulation voltage, function of time

d = crystal thickness, as shown in Fig. 2

r_{33}, r_{13} = appropriate EO coefficients of the EO crystal

Therefore, Eq. (2) may be written as

$$E_o(\ell) = E \left[\hat{i}_z + \hat{i}_x \exp(j\Delta\Gamma) \right] \exp \left\{ j \left[\omega_o t - \frac{\omega_o}{c} \left(n_e - \frac{1}{2} n_e^3 \frac{v_m(t)}{d} r_{33} \right) \ell \right] \right\} \quad (5)$$

where $\Delta\Gamma$ = relative phase retardation between the ordinary and extraordinary rays and is given by

$$\Delta\Gamma = (\beta_z - \beta_x) \ell = \frac{\omega_o}{c} \left[(n_e - n_o) \ell - \frac{1}{2} \left(n_e^3 r_{33} - n_o^3 r_{13} \right) \frac{v_m(t)}{d} \ell \right] \quad (6)$$

At 0-bias, $\frac{\omega_0}{c} (n_e - n_o) \ell = 0$ reducing Eq. (6) to

$$\Delta\Gamma = \frac{\omega_0}{2c} \left(n_o^3 r_{13} - n_e^3 r_{33} \right) \frac{\ell}{d} v_m(t) \quad (7)$$

for a sinusoidal modulation voltage $v_m(t) = V_m \sin \omega_m t$ in which the peak voltage V_m is the quarter-wave voltage, i.e.,

$$V_m = \frac{\pi c}{\omega_0 \left(n_o^3 r_{13} - n_e^3 r_{33} \right) \frac{\ell}{d}} = \frac{V_\pi}{2} \quad (8)$$

where V_π is the half-wave voltage, Eq. (7) becomes

$$\Delta\Gamma = \frac{\pi}{2} \sin \omega_m t \quad (9)$$

and Eq. (5) becomes

$$E_o(\ell) = E \left[\hat{1}_z + \hat{1}_x \exp \left(j \frac{\pi}{2} \sin \omega_m t \right) \right] \exp \left\{ j \left[\omega_0 t - \frac{\omega_0}{c} \left(n_e \ell - \frac{1}{2} n_e^3 r_{33} \frac{\ell}{d} \frac{V_\pi}{2} \sin \omega_m t \right) \right] \right\} \quad (10)$$

Since the modulation frequency ω_m is much less than the optical frequency ω_0 , the modulation phase is essentially unchanged in a given short interval of time in which the optical frequency goes through many cycles. Therefore, the second $\sin \omega_m t$ in Eq. (10) appears as a slowly changing optical phase while the first $\sin \omega_m t$ determines the resultant polarization of $E_o(\ell)$. Clearly at $\omega_m t = 0$ and π , $E_o(\ell)$ is linearly polarized at 45° to the z - and x -axes, i.e., polarized in the same way as, or orthogonal to, the input light. At $\omega_m t = \pi/2$ and $3\pi/2$, $\Delta\Gamma$ becomes ± 1 . That is, the x -component of the field (ordinary ray) either leads or lags the z -component (extraordinary ray) by $\pi/2$, resulting in either right-hand or left-hand circular polarization at the output. At intermediate values of $\omega_m t$, the output is elliptically polarized. These polarization states have been shown in the second row of Figs. 2, 3, and 4.

In passing through free space between the transmitter and the receiver, no additional relative phase delay between the ordinary and the extraordinary rays occurs. Therefore, Eq. (10) also describes the field quantities at the input of the receiver, which, for this purpose, may be considered as consisting of a combination of a quarter-wave plate and a polarization beam splitter. The beam splitter axes, η , ν , are oriented at 45° to the quarter-wave axes z' , x' , while z' and x' can be at an arbitrary angle which can be a function of time, $\theta(t)$, to the modulator axes z , x . The situation is as shown in Fig. 6.

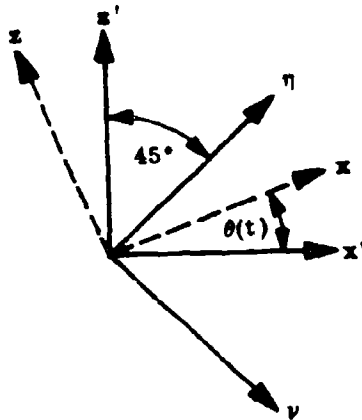


Fig. 6 Angular Relationships Between Various Optical Axes of Transmitter and Receiver Elements.

z, x : Modulator Axes
 z', x' : Quarter-Wave Plate Axes
 η, ν : Polarization Splitter Axes

Rewrite $\frac{\omega_0}{c} \left(n_e \ell - \frac{1}{2} n_e^3 r_{33} \frac{\ell}{d} \frac{V}{2} \sin \omega_m t \right)$ as $A - B \sin \omega_m t$, and combining Eqs. (9) and (10), we find

$$E_o(\ell) = E \left[\hat{i}_z + \hat{i}_x e^{j\Delta\Gamma} \right] \exp \left[j \left(\omega_0 t - A + B \sin \omega_m t \right) \right] \quad (11)$$

Therefore, writing in terms of components along the $z'x'$ axes of the retardation plate, the optical E-field at the input of the receiver is

$$E_o(y') = E \left[\hat{i}_{z'} \left(\cos \theta + \sin \theta e^{j\Delta\Gamma} \right) + \hat{i}_{x'} \left(-\sin \theta + \cos \theta e^{j\Delta\Gamma} \right) \right] \exp \left[j \left(\omega_0 t - A + B \sin \omega_m t \right) \right] \quad (12)$$

where

- y' = coordinate axis along the thickness of the retardation plate
 θ = $\theta(t)$ = angular misorientation (can be a function of time)
 $\hat{i}_{z'}, \hat{i}_{y'}$ = unit vectors along z' and x' axes, respectively

Let the propagation constants for light polarized along the z' and x' axes be $\beta_{z'}$ and $\beta_{x'}$, respectively, and let the retardation plate be of thickness L . Then

$$E_o(L) = E \cos \theta \left\{ \hat{i}_{z'} \left(1 + \tan \theta e^{j\Delta\Gamma} \right) + \hat{i}_{x'} \left(-\tan \theta + e^{j\Delta\Gamma} \right) e^{-j(\beta_{x'} - \beta_{z'})L} \right\} \exp \left[j \left(\omega_o t - A + B \sin \omega_m t - \beta_{z'} L \right) \right] \quad (13)$$

for a quarter-wave plate, $(\beta_{x'} - \beta_{z'})L = \frac{\pi}{2}$, and Eq. (13) simplifies to:

$$E_o(L) = E \cos \theta \left\{ \hat{i}_{z'} \left(1 + \tan \theta e^{j\Delta\Gamma} \right) - j \hat{i}_{x'} \left(-\tan \theta + e^{j\Delta\Gamma} \right) \right\} \exp \left[j \left[\omega_o t - (A + \beta_{z'} L) + B \sin \omega_m t \right] \right] \quad (14)$$

where it should be recalled that $\theta = \theta(t)$ and $\Delta\Gamma = \Delta\Gamma(\omega_m t)$.

As the light enters the polarization splitter, the component along the η axis, E_η , is given by

$$\begin{aligned}
 E_\eta &= E \cos \theta \cdot \cos 45^\circ \left\{ \left(1 + \tan \theta e^{j\Delta\Gamma} \right) - j \left(-\tan \theta + e^{j\Delta\Gamma} \right) \right\} \\
 &\quad \exp \left[j \left[\omega_o t - (A + \beta_{z'} L) + B \sin \omega_m t \right] \right] \\
 &= \frac{E}{\sqrt{2}} \left[\left(1 + \sin \Delta\Gamma \right)^2 + \cos^2 \Delta\Gamma \right]^{\frac{1}{2}} \\
 &\quad \exp \left[j \left[\omega_o t - (A + \beta_{z'} L) + B \sin \omega_m t + \theta + \psi \right] \right] \quad (15)
 \end{aligned}$$

$$\text{where } \xi = \xi(\omega_m t) = \tan^{-1} \left[\frac{-\cos \Delta\Gamma(\omega_m t)}{1 + \sin \Delta\Gamma(\omega_m t)} \right]$$

or

$$\begin{aligned} E_\eta &= \frac{E}{\sqrt{2}} \left[2 \left(1 + \sin \Delta\Gamma \right) \right]^{\frac{1}{2}} \exp \left\{ j \left[\omega_0 t - (A + \beta_z L) + B \sin \omega_m t + \theta + \xi \right] \right\} \\ &= E \left[1 + \sin \left(\frac{\pi}{2} \sin \omega_m t \right) \right]^{\frac{1}{2}} \exp \left\{ j \left[\omega_0 t + B \sin \omega_m t + \theta(t) + \xi(\omega_m t) - (A + \beta_z L) \right] \right\} \end{aligned} \quad (16)$$

Similarly, the component of light along the ν -axis is given by

$$\begin{aligned} E_\nu &= E \cos \theta \cos 45^\circ \left\{ - \left(1 + \tan \theta e^{j\Delta\Gamma} \right) - j \left(-\tan \theta + e^{j\Delta\Gamma} \right) \right\} \\ &\quad \cdot \exp \left\{ j \left[\omega_0 t - (A + \beta_z L) + B \sin \omega_m t \right] \right\} \\ &= \frac{E}{\sqrt{2}} \left[\left(2 - 2 \sin \Delta\Gamma \right) \right]^{\frac{1}{2}} \exp \left\{ j \left[\omega_0 t - (A + \beta_z L) + B \sin \omega_m t + \pi - \theta + \xi' \right] \right\} \end{aligned} \quad (17)$$

$$\text{where } \xi' = \xi'(\omega_m t) = \tan^{-1} \left[\frac{\cos \Delta\Gamma(\omega_m t)}{1 - \sin \Delta\Gamma(\omega_m t)} \right]$$

or

$$\begin{aligned} E_\nu &= E \left[1 - \sin \left(\frac{\pi}{2} \sin \omega_m t \right) \right]^{\frac{1}{2}} \\ &\quad \cdot \exp \left\{ j \left[\omega_0 t + B \sin \omega_m t - \theta(t) + \xi'(\omega_m t) - (A + \beta_z L) + \pi \right] \right\} \end{aligned} \quad (18)$$

From Eqs. (16) and (18), it is clear that the orientation between satellites, $\theta(t)$, will only affect the phase of the optical carrier and not the phase of the microwave sub-carrier. In practice, $\theta(t)$ is a very slowly varying function of time (typically in the Hz range) so that its effect on the optical phase is negligible. The amplitudes of the

electric fields directed to the photodetectors (see Fig. 1), E_η and E_ν , are independent of $\theta(t)$. Since photodetectors respond to intensity only, one detector will receive an intensity of $1/2 E_\eta E_\eta^*$ while the other will receive $E_\nu E_\nu^*$. Now,

$$E_\eta E_\eta^* = E^2 \left[1 + \sin\left(\frac{\pi}{2} \sin \omega_m t\right) \right] = E^2 \left[1 + \sum_{n=1}^{\infty} 2 J_n\left(\frac{\pi}{2}\right) \sin n \omega_m t \right] \quad (19)$$

where J_n is Bessel's function of the first kind, nth order.

$$E_\nu E_\nu^* = E^2 \left[1 - \sin\left(\frac{\pi}{2} \sin \omega_m t\right) \right] = E^2 \left[1 - \sum_{n=1}^{\infty} 2 J_n\left(\frac{\pi}{2}\right) \sin n \omega_m t \right] \quad (20)$$

Equations (19) and (20) give the intensities as seen by photodetectors and contain all the harmonics of the modulating frequency. Subsequent filtering at the receiver allows only the fundamental components to be amplified. That is, the signal from Photodetector No. 1, I_1 , after filtering, may be written as

$$I_1(\omega_m t) = k_1 E^2 \cdot \left[2 J_1\left(\frac{\pi}{2}\right) \sin \omega_m t \right] \quad (21)$$

while that from Photodetector No. 2, I_2 , is given by

$$I_2(\omega_m t) = k_2 E^2 \left[-2 J_1\left(\frac{\pi}{2}\right) \sin \omega_m t \right] \quad (22)$$

where k_1 , k_2 are proportionality constants and ideally, $k_1 = k_2$. It can be seen that the photodetector output currents, I_1 and I_2 , are 180° out of phase. By taking the difference between I_1 and I_2 , the total signal current, I , is

$$I = I_1 - I_2 = 4 k E^2 J_1\left(\frac{\pi}{2}\right) \sin \omega_m t \quad (23)$$

assuming that $k_1 = k_2 = k$. That is, the signal finally used in the receiver is double that from each channel.

It is interesting to note that had a conventional intensity modulation scheme been used, that is, if the modulator had been quarter-wave biased and a polarization analyzer had been placed at the transmitter, a 3-dB loss in the final signal would have resulted. Thus, the polarization modulation proposed here has the 3-dB advantage, as well as being insensitive to orientation.

Returning to the scheme under consideration, if one of the channels becomes degraded, for instance, $k_1 \neq k_2$ in Eqs. (21) and (22), then

$$i = 2 (k_1 + k_2) E^2 J_1\left(\frac{\pi}{2}\right) \sin \omega_m t < 4k E^2 J_1\left(\frac{\pi}{2}\right) \sin \omega_m t \quad (24)$$

Therefore, degradation of one channel only gives rise to degraded overall performance because of the lower received signal, but it does not result in total disruption of the receiver, as has occasionally been thought.

Section 4 CONCLUSIONS

From the geometrical construction and the analysis, it is clear that using this modulation format, the received signals are independent of satellite orientation, so long as in the receiver the relative axes of the quarter-wave plate and the polarization beam splitter are oriented at 45° to each other. Since this is a simple design requirement in the receiver, no problem should ever arise. The only effect of satellite orientation, which in general will be a slowly varying function of time, appears as a slowly varying term in the optical phase, which is not detected at the photodetectors. Therefore, it is concluded that using the modulation format, no special constraint on satellite orientation needs to be applied.

Appendix F

TRANSMITTING BEAM OPTICS THEORY

by

Dr. R. C. Ohlmann

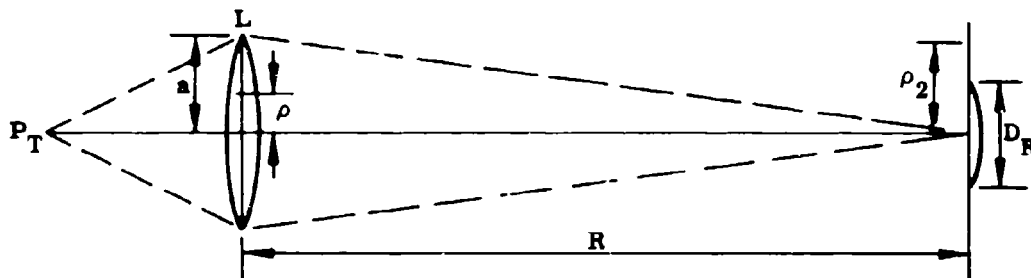
Dr. A. D. MacDonald

(Previously distributed as Technical Memorandum No. 18)

LOCKHEED PALO ALTO RESEARCH LABORATORY
LOCKHEED MISSILES & SPACE COMPANY
A GROUP DIVISION OF LOCKHEED AIRCRAFT CORPORATION

In a calculation of the power received by a distant antenna of diameter D_R , we assume that the laser emits in a TEM_{00} mode with a Gaussian amplitude distribution and plane wavefront. The laser output is expanded without aperturing more than 0.5% until it reaches the transmitting lens of diameter D_T . The following calculation determines the peak intensity I_R , or the power per unit area reaching the receiving antenna, and, for a D_T small compared with the beam diameter at the receiver, also determines the received power P_R in terms of the transmitted power P_T .

The sketch below shows the optical system of the transmitter, simplified to a single lens of radius $a = D_T/2$. We use Kirchhoff's formulation to determine the intensity at the receiver, which requires a definition of the amplitude of the wave U such that $|U|^2 = I$.



The light amplitude on plane L is given by

$$U(\rho) = \begin{cases} \sqrt{\frac{2 P_T}{\pi \omega_o^2}} e^{-\rho^2/\omega_o^2} & \rho \leq a \\ 0 & \rho > a \end{cases} \quad (1)$$

F-1

LOCKHEED PALO ALTO RESEARCH LABORATORY
LOCKHEED MISSILES & SPACE COMPANY
A GROUP DIVISION OF LOCKHEED AIRCRAFT CORPORATION

where ω_0 is the waist radius of the Gaussian beam at the lens. Kirchhoff's formulation then gives the distribution at the receiver, $U_R(\rho_2)$, as

$$U_R(\rho_2) = \frac{1}{\lambda R} \int_0^{2\pi} \int_0^a U(\rho) \exp \left[-\frac{2\pi i \rho \rho_2}{\lambda R} \cos(\phi - \phi_2) \right] \rho d\rho d\phi \quad (2)$$

where ϕ and ϕ_2 are the angle coordinates, R is the range, and λ is the wavelength.

Substituting Eq. (1) and integrating over ϕ gives

$$\begin{aligned} U_R(\rho_2) &= \frac{(8\pi P_T)^{1/2}}{\lambda R \omega_0} \int_0^a J_0 \left(\frac{2\pi \rho \rho_2}{\lambda R} \right) e^{-\rho^2/\omega_0^2} \rho d\rho \\ &= Q \int_0^a J_0(k\rho) e^{-\rho^2/\omega_0^2} \rho d\rho \end{aligned} \quad (3)$$

where $k = (2\pi \rho_2/\lambda R)$.

Equation (3) is solved by successive integration by parts:

$$\begin{aligned} \int_0^a J_0(k\rho) e^{-\rho^2/\omega_0^2} \rho d\rho &= \frac{\omega_0^2}{2} \left[e^{-\rho^2/\omega_0^2} J_0(k\rho) \right]_0^a \\ &\quad - \frac{1}{2} \int_0^a \omega_0^2 e^{-\rho^2/\omega_0^2} \frac{d}{d\rho} [J_0(k\rho)] d\rho \end{aligned} \quad (4)$$

We make use of the relationships among the Bessel functions,

$$\frac{d}{d\rho} J_0(k\rho) = -kJ_1(k\rho)$$

and, in general,

$$\frac{d}{d\rho} \left(\frac{J_n(k\rho)}{\rho^n} \right) = -k\rho^{-n} J_{n+1}(k\rho)$$

to complete the integration of Eq. (3) in the following manner:

$$\begin{aligned} U_R(\rho_2) = & Q \left\{ \frac{\omega_o^2}{2} \left[1 - e^{-a^2/\omega_o^2} J_0(ka) \right] - \frac{k\omega_o^4}{4} \left[\frac{k}{2} - e^{-a^2/\omega_o^2} \frac{J_1(ka)}{a} \right] \right. \\ & + \frac{k^2\omega_o^6}{8} \left[\frac{k^2}{8} - e^{-a^2/\omega_o^2} \frac{J_2(ka)}{a^2} \right] \\ & \left. - \frac{k^3\omega_o^8}{16} \left[\frac{k^3}{2^3 3!} - e^{-a^2/\omega_o^2} \frac{J_3(ka)}{a^3} \right] \right\} + \dots \end{aligned}$$

Rearranging terms, we obtain

$$\begin{aligned} U_R(\rho_2) = & Q \frac{\omega_o^2}{2} \left\{ 1 - \frac{k^2\omega_o^2}{4} + \frac{1}{2} \left(\frac{k^2\omega_o^2}{4} \right)^2 - \dots \right. \\ & - e^{-a^2/\omega_o^2} \left[J_0(ka) - \frac{J_1(ka)}{a} \times \frac{k\omega_o^2}{2} + \frac{k^2\omega_o^4}{4} \frac{J_2(ka)}{a^2} \right. \\ & \left. \left. - \frac{k^3\omega_o^6}{8} \frac{J_3(ka)}{a^3} \right] + \dots \right\} \\ = & Q \frac{\omega_o^2}{2} \left[e^{-k^2\omega_o^2/4} - e^{-a^2/\omega_o^2} \sum_{m=0}^{\infty} (-1)^m S^m J_m(ka) \right] \end{aligned} \quad (5)$$

$$\text{where } S = (k\omega_o^2/2a) = \left[ka (\omega_o^2/2a^2) \right].$$

For a wide range of values of both S and ka , the sum in Eq. (4) is relatively insensitive to changes of variables, so that approximations can readily be made, and in any case the sum is dominated by the first few terms and is easy to calculate. A plot of the function is shown in Fig. 1.

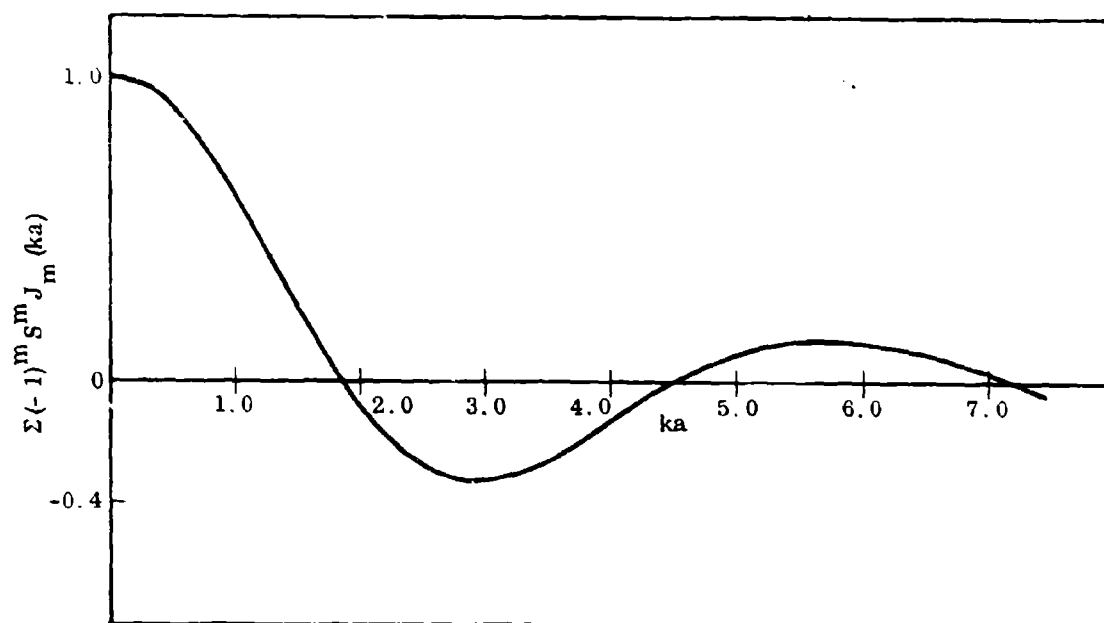


Fig. 1 Plot of $\sum_{m=0}^{\infty} (-1)^m S^m J_m(ka)$ for $S = 0.4 ka$. The coefficient $0.4 = \omega_0^2/2a^2$ corresponds to maximum antenna gain

When ρ_2 approaches zero [$ka \ll 1$ or $\rho_2 \ll (\lambda R/2\pi a)$]

$$U_R(0) = Q \frac{\omega_0^2}{2} \left(1 - e^{-a^2/\omega_0^2} \right) \quad (6)$$

and $U_R(\rho_2)$ may be written

$$U_R(\rho_2) = U_R(0) \frac{\left[e^{-k^2 \omega_0^2/4} - e^{-a^2/\omega_0^2} \sum_{m=0}^{\infty} (-1)^m S^m J_m(ka) \right]}{\left(1 - e^{-a^2/\omega_0^2} \right)} \quad (7)$$

In the special case where $(k\omega_0/2) < 1$ and ω_0 is near optimum so that $\rho_2 a \ll \lambda R$, Eq. (7) becomes

$$U_R(\rho_2) \approx U_R(0) e^{-\rho_2^2/\omega_0^2} \quad (8)$$

where $\omega_2 = \lambda R/\pi\omega_0$.

For a given value of a , the term $U_R(0)$ can be maximized with respect to variations of ω_0 , holding a constant, by solving the equation $(d/d\omega_0) U_R(0) = 0$:

$$U_R(0) = C\omega_0 \left(1 - e^{-a^2/\omega_0^2}\right) \text{ with } C = Q\omega_0$$

$$\frac{d}{d\omega_0} U_R(0) = C \left[\left(1 - e^{-a^2/\omega_0^2}\right) + \omega_0 \left(-\frac{2a^2 e^{-a^2/\omega_0^2}}{\omega_0^3}\right) \right] = 0$$

$$\therefore 1 - e^{-a^2/\omega_0^2} = \frac{2a^2}{\omega_0^2} e^{-a^2/\omega_0^2}$$

$$1 = e^{-a^2/\omega_0^2} \left(2 \frac{a^2}{\omega_0^2} + 1\right) \text{ or } e^{a^2/\omega_0^2} = 1 + 2 \frac{a^2}{\omega_0^2}$$

Numerical solution of the resulting equation yields $\omega_0 = 0.89a \approx 0.445 D_T$. Substitution of this value in Eq. (6) leads to the result

$$U_R(0)_{\text{opt}} = (2.57 P_T)^{1/2} \frac{a}{\lambda R} \quad (9)$$

and the intensity $I_{R(opt)}^{(0)} = |U_R^2(0)|$ is given by

$$I_{R(opt)}^{(0)} = \frac{2.57 P_T a^2}{\lambda^2 R^2} \quad \text{or} \quad 0.642 \frac{P_T D_T^2}{\lambda^2 R^2} \quad (10)$$

The received power is $P_R = \pi/4 D_R^2 I_R$, or

$$P_R = 0.504 \frac{D_R^2 D_T^2}{\lambda^2 R^2} P_T \quad (11)$$

For small ρ_2 , or under the conditions for which Eq. (6) is valid,

$$P_R = \int_0^{D_R/2} I_R(\rho_2) 2\pi \rho_2 d\rho_2$$

or

$$P_R = 0.516 P_T \left(1 - e^{-D_R^2/2\omega_2^2} \right) \quad (12)$$

and when $D_R/2\omega_2$ is large enough so that only the two leading terms of the exponential are needed, Eq. (12) reduces to

$$P_R = 0.504 P_T \frac{D_R^2 D_T^2}{\lambda^2 R^2}$$

the same as Eq. (11). Comparison with the link equation,

$$P_R = \frac{\pi^2}{16} r_T \frac{D_R^2 D_T^2}{\lambda^2 R^2} P_T = G_T G_R \left(\frac{\lambda}{4\pi R} \right)^2 P_T$$

where $G_T = \eta_T (\pi D_T / \lambda)^2$ and $G_R = (\pi D_R / \lambda)^2$, leads to a value of $\eta_T = 0.82$ multiplied by the transmittance of the optical system.

Finally, a beamwidth θ_{FWHP} is defined as the full width at half-intensity of the beam. The angular dependence of intensity can be obtained from Eq. (8) by setting $\theta = \rho_2 / R$. Then

$$I(\theta) \approx I(0) e^{-2\theta^2 / \theta_2^2} \quad (13)$$

where

$$\theta_2 = \frac{\omega_2}{R} = \frac{\lambda}{\pi \omega_0} = 0.714 \frac{\lambda}{D_T} \quad (14)$$

for the optimum case where $\omega_0 = 0.89a = 0.445 D_T$.

The beamwidth θ_{FWHP} is equal to twice the angle θ at which $I(\theta)/I(0) = 1/2$. If this is calculated from Eq. (13) for optimum ω_0 , we obtain

$$\theta_{FWHP} \approx 1.18 \theta_2 \approx 0.842 \frac{\lambda}{D_T}$$

However, Eq. (13) is modified somewhat when we use the exact expression for the intensity and becomes

$$I(\theta) = I(0) e^{-2\theta^2 / \theta_2^2} T^2(\theta) \quad (15)$$

where

$$T = \left[1 - e^{(\rho_2^2 / \omega_2^2 - a^2 / \omega_0^2)} \sum_{m=0}^{\infty} (-1)^m S_m J_m(ka) \right] / \left(1 - e^{-a^2 / \omega_0^2} \right) \quad (16)$$

On the basis of these expressions, the full width half-power angle can be found by iteration, with the result that

$$\theta_{FWHP} = 1.61 \theta_2 = 1.13 \frac{\lambda}{D_T} \quad (17)$$

For a diameter of 30 cm and a wavelength of 0.53 μ , $\theta_{FWHP} = 2.00 \mu\text{rad}$.

The beam intensity or power per steradian is given by

$$J = \frac{2\pi\omega^2}{\lambda^2} P_T = 1.24 \frac{D_T^2}{\lambda^2} P_T \quad (18)$$

and the average radiance of the source N , in watts per steradian per square meter is

$$N = \frac{8\omega^2}{\lambda^2 D_T^2} P_T = 1.59 \frac{P_T}{\lambda^2} \quad (19)$$

for optimum conditions.

Another quantity of interest is the off-axis gain. This is directly related to the intensity as a function of angle θ . Equation (15) gives this relationship, which is plotted in Fig. 2 with $I(\theta/\theta_2)/I(0)$ shown as a function of θ/θ_2 . Note that when $\theta = 0.8 \theta_2$, the intensity is down by 3 dB, in agreement with Eq. (17). The first side lobe maximum for an "optimally" truncated Gaussian is down 25.2 dB, and occurs at $\theta \sim 2.6 \theta_2 \sim 1.6 \theta_{FWHP}$.

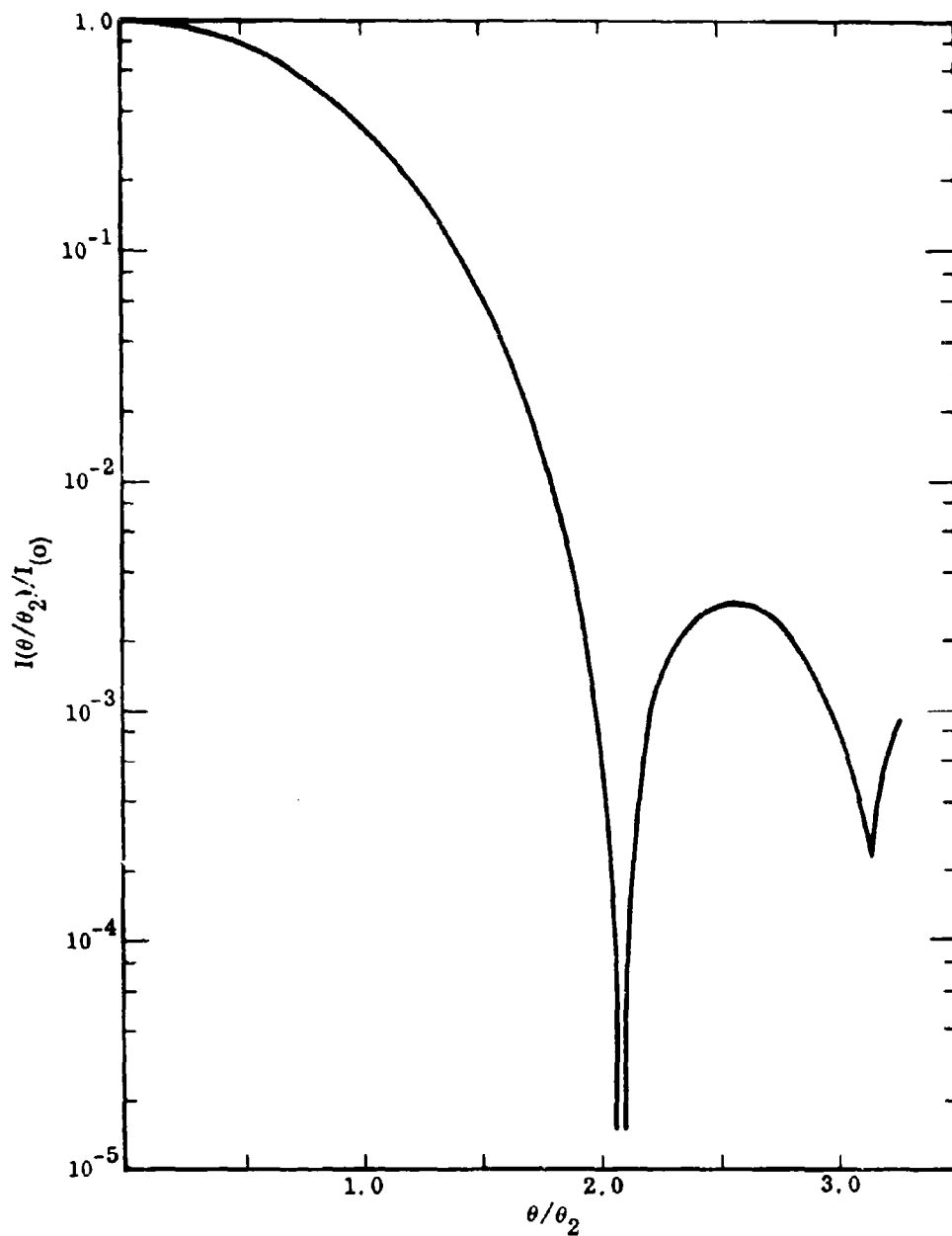


Fig. 2 Angular Antenna Pattern for a Gaussian Illuminated Antenna With Truncation for Maximum Antenna Gain

F-9

LOCKHEED PALO ALTO RESEARCH LABORATORY
LOCKHEED MISSILES & SPACE COMPANY
A GROUP DIVISION OF LOCKHEED AIRCRAFT CORPORATION

Appendix G

OPTICAL BACKGROUNDS

by

Mr. W. G. Uplinger

(Revision of Technical Memorandum No. 16)

LOCKHEED PALO ALTO RESEARCH LABORATORY
LOCKHEED MISSILES & SPACE COMPANY
A GROUP DIVISION OF LOCKHEED AIRCRAFT CORPORATION

Section 1

INTRODUCTION

Background sources of possible importance include the sun, moon, planets, stars, and various sources associated with the earth. The last of these include sunlit clouds, atmospheric aerosols, and the earth's surface. The most intense of these earth-related sources, sun reflection from the ocean, is analyzed in Appendix H. Accordingly, this report will deal only with the other sources. Backgrounds due to atmospheric and cloud scattering will be considered first, and in the greatest detail, as these are the ones most likely to be encountered in practice. Then data representative of the nonterrestrial sources will be presented.

G-1

LOCKHEED PALO ALTO RESEARCH LABORATORY
LOCKHEED MISSILES & SPACE COMPANY
A GROUP DIVISION OF LOCKHEED AIRCRAFT CORPORATION

Section 2

SKY BACKGROUND SOURCES

There are four cases to be considered in which sky or cloud backgrounds may affect operation of the links. The first is that of a receiver on the ground, with the laser transmitter in a satellite. The background is clear sky or thin clouds through which communications can be received. In the second case, the transmitter and receiver are interchanged; and the third case is that of a low-altitude satellite transmitting to a high-altitude satellite. In the last two cases, sunlight reflected by clouds is the background of interest. Important variables to be considered are the laser wavelength, cloud types, and whether the receiver is looking at transmitted or reflected background radiation. The laser systems studied operated in the visible or near-infrared.

2.1 RADIATION OF THE CLEAR SKY - THEORETICAL DATA

The radiance of a cloudless sky as seen from the ground is determined by scattering from molecules and aerosols in the atmosphere. It is also influenced by the reflection properties of the ground because radiation reflected from the ground can be scattered back into the field of view of the receiver by the atmosphere.

Scattering by molecules is described by Rayleigh's law. A discussion of the scattering properties of molecules and aerosols is given in Bullrich (Ref. 1). Rayleigh scattering is the dominant mechanism only on extremely clear days; thus, it sets a lower limit on the radiance of a clear atmosphere. The scattering properties of aerosols depend largely on the number and size distribution of the aerosol at each altitude. Theoretical analyses integrate the complicated Mie scattering functions over analytical size distributions. Figure 1 shows the scattering functions for molecular (Rayleigh) and aerosol (Mie) scattering (Ref. 2). The aerosol scattering function is for a typical aerosol size distribution. The curves are normalized so that the integral over 4π sr is unity. The

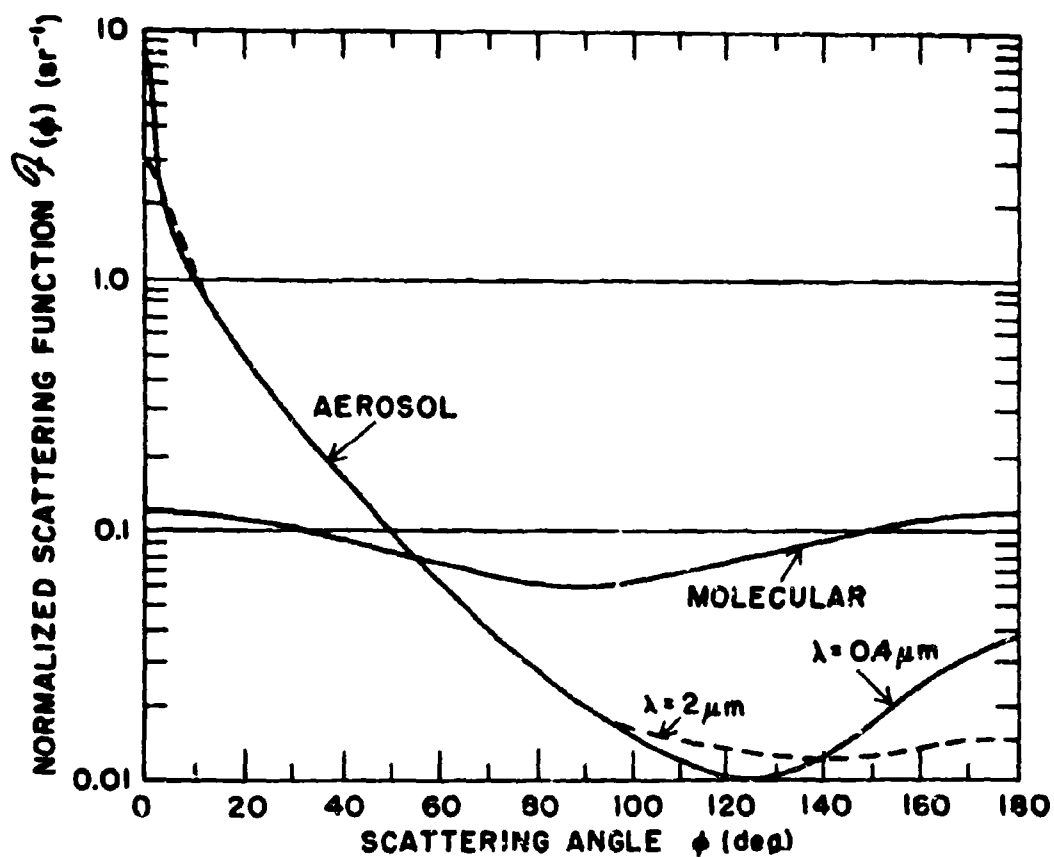


Fig. 1 Normalized Scattering Function of Aerosol and Air

G-3

LOCKHEED PALO ALTO RESEARCH LABORATORY
 LOCKHEED MISSILES & SPACE COMPANY
 A GROUP DIVISION OF LOCKHEED AIRCRAFT CORPORATION

strong forward scattering by the aerosols is typical of aerosol and cloud scattering. Only for small scattering angles is the scattering function strongly dependent on wavelength.

Figure 2, from Ref. 2, presents the results of theoretical calculations of reflected and transmitted radiance for a cloudless sky. The data on which Fig. 2 is based were taken from Ref. 3, and Monte Carlo techniques were used to include the effects of multiple scattering. The calculations used the aerosol scattering function in Fig. 1. The incident solar flux is normalized to a value of unity at each wavelength. This permits evaluation of relative effects at each wavelength, and also simplifies interpolation between the wavelengths given. Notice that the difference between 0.4 and 0.7 μm is considerable but that there is little difference between 0.7 and 1.67 μm . The circles with the dot in the center indicate the position of the sun. The effect of the ground albedo is seen to be sizable. The largest value (0.8) is representative of fresh snow while the lower values correspond to forest.

The spectral solar constant is required to calculate absolute values from Fig. 2. The latest revised values (Ref. 4) are plotted as a function of wavelength in Fig. 3. The value of the solar constant at the laser wavelengths of interest can be determined from this figure.

2.2 RADIANCE OF THE CLEAR SKY - EXPERIMENTAL DATA

Clear sky radiance has been measured at several locations. The most relevant of these appears to be a series of measurements at Haleakala, Hawaii, by Bullrich and Eiden (Ref. 5). The measurements were made on the summit of the crater of the extinct volcano, Haleakala, on the island of Maui. The latitude is 23°43'N, and the altitude is 3400 m above sea level. Figures 4, 5, and 6 show the distribution of sky irradiance at three different wavelengths. The values at $\lambda = 1.06 \mu\text{m}$ were scaled from those at $\lambda = 0.848 \mu\text{m}$, using spectral solar constants from Fig. 3. This procedure was based on Fig. 2, which indicates that the only difference would be that due

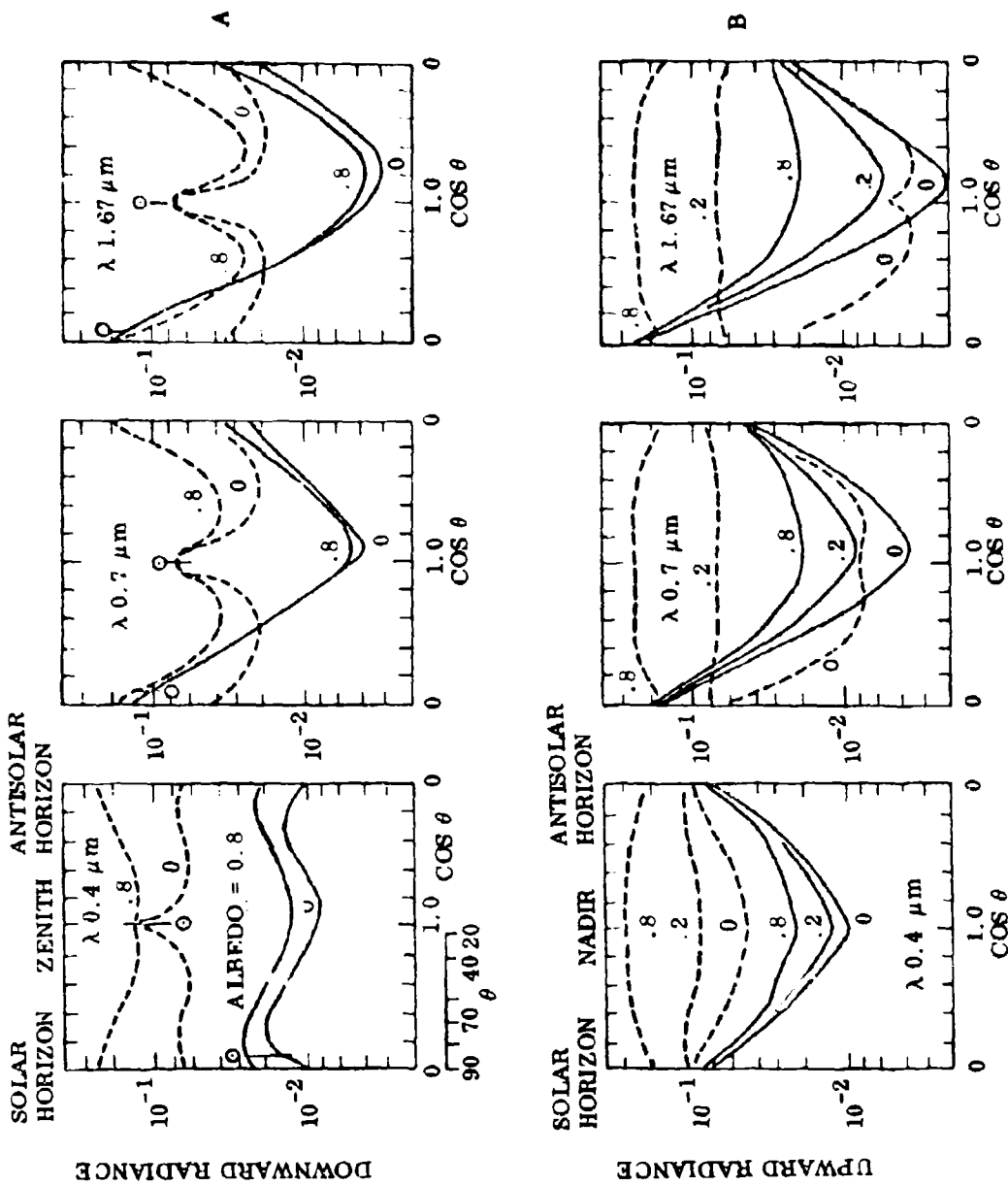


Fig. 2 Downward and Upward Radiance Computed by Monte Carlo Techniques. Dashed curves are for the sun in the zenith; solid curves are for the sun at $\theta = 86.3^\circ$. The indicated parameter is the surface albedo

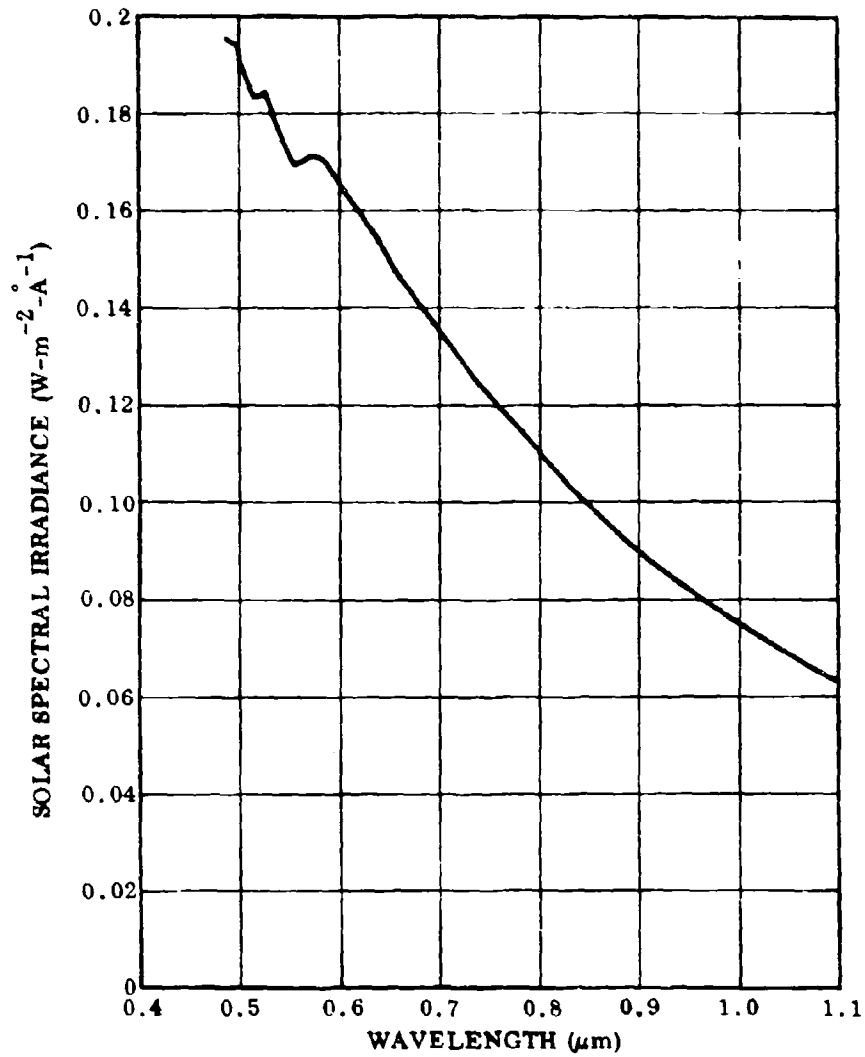


Fig. 3 Solar Spectral Irradiance

G-6

LOCKHEED PALO ALTO RESEARCH LABORATORY
 LOCKHEED MISSILES & SPACE COMPANY
 A GROUP DIVISION OF LOCKHEED AIRCRAFT CORPORATION

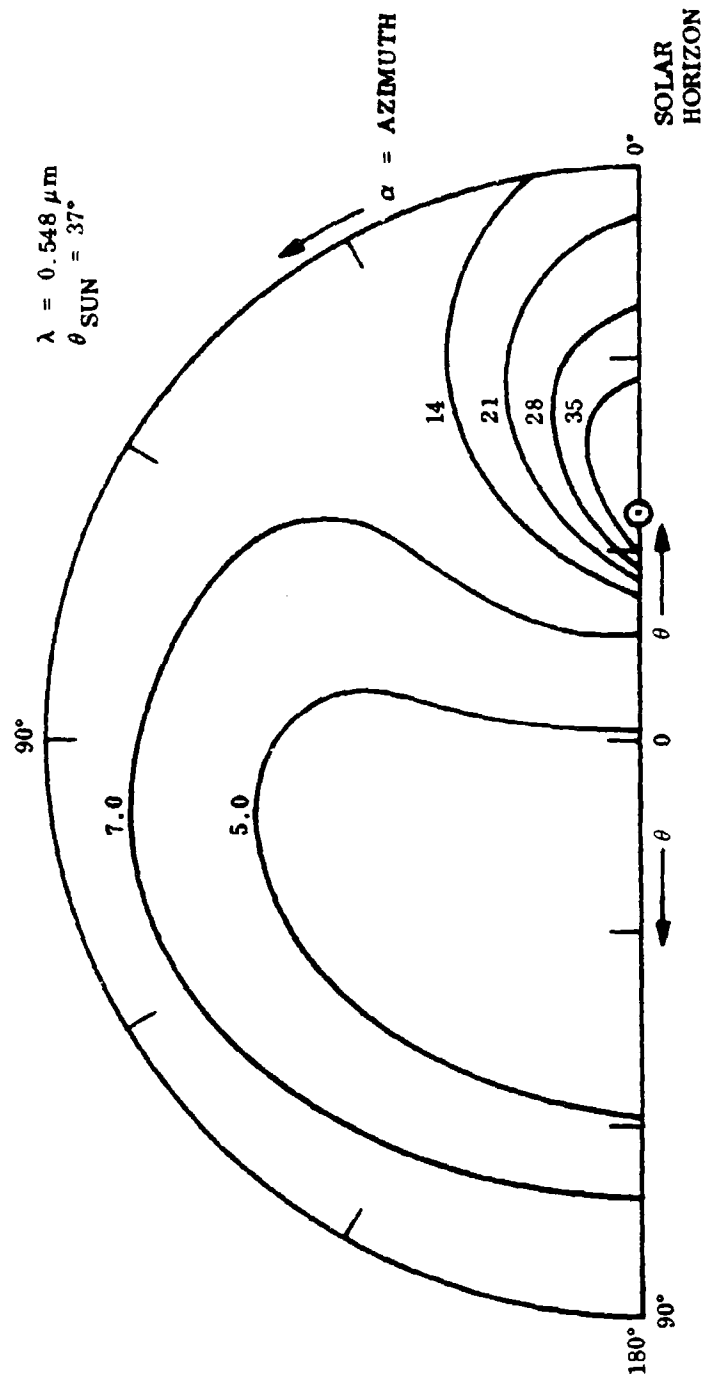


Fig. 4 Sky Background Irradiance at Haleakala Summit (in $\text{W} \cdot \text{m}^{-2} \cdot \text{sr}^{-1} \cdot \text{A}^{-1}$)

G-7

LOCKHEED PALO ALTO RESEARCH LABORATORY
 LOCKHEED MISSILES & SPACE COMPANY
 A GROUP DIVISION OF LOCKHEED AIRCRAFT CORPORATION

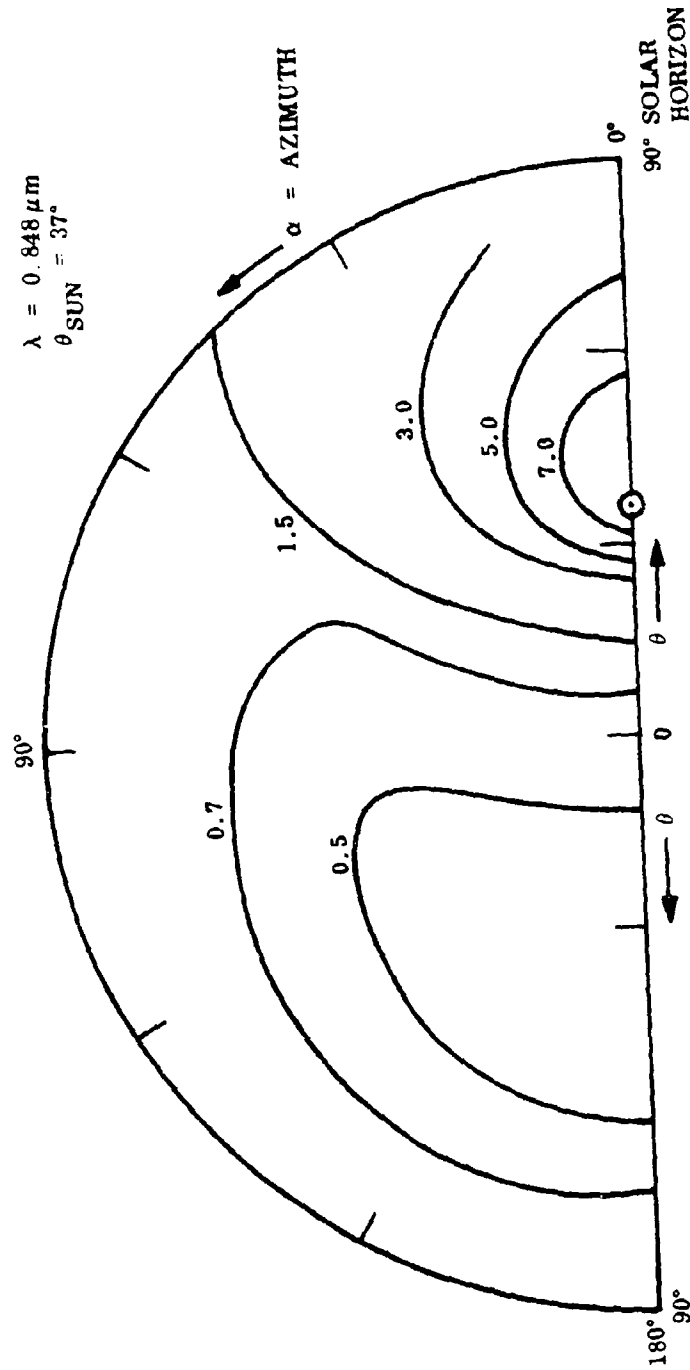


Fig. 5 Sky Background Irradiance at Haleakala Summit (in $\text{W}\cdot\text{m}^{-2}\cdot\text{sr}^{-1}\cdot\text{Å}^{-1}$)

G-8

LOCKHEED PALO ALTO RESEARCH LABORATORY
 LOCKHEED MISSILES & SPACE COMPANY
 A GROUP DIVISION OF LOCKHEED AIRCRAFT CORPORATION

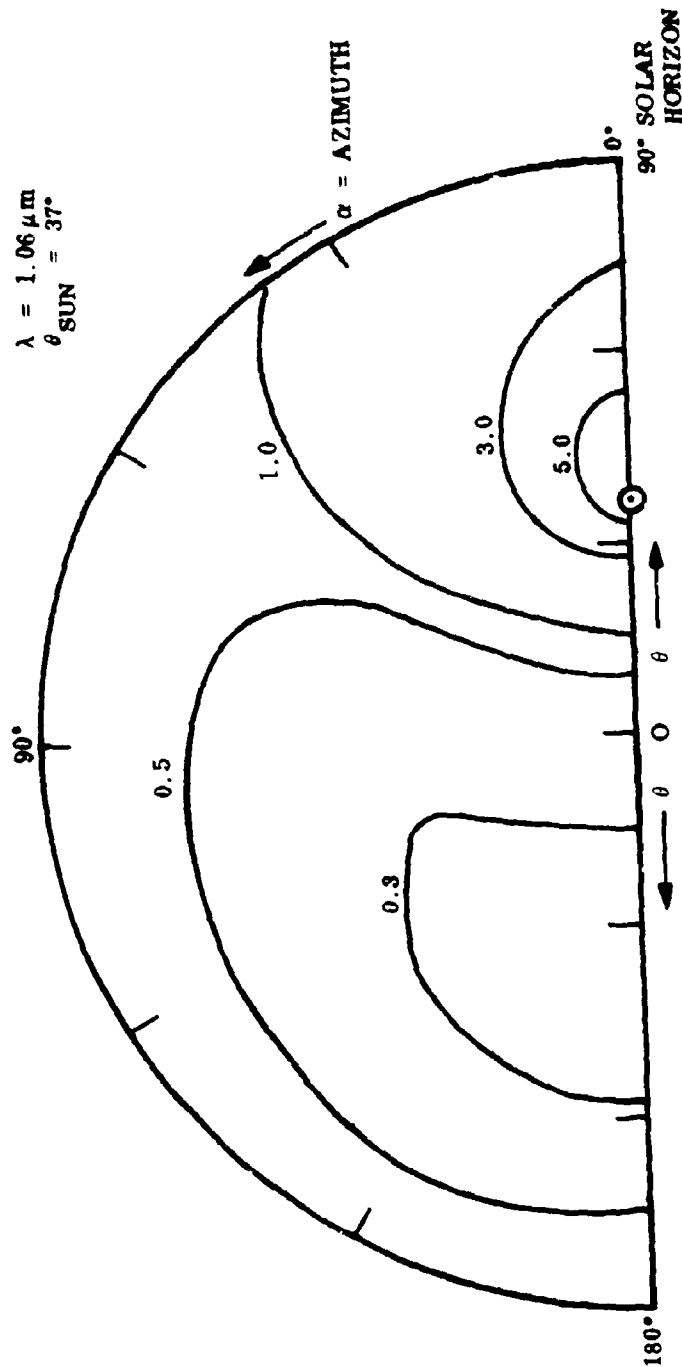


Fig. 6 Sky Background Irradiance at Haleakala Summit (in $\text{W} \cdot \text{m}^{-2} \cdot \text{sr}^{-1} \cdot \text{Å}^{-1}$)

G-9

LOCKHEED PALO ALTO RESEARCH LABORATORY
LOCKHEED MISSILES & SPACE COMPANY
A GROUP DIVISION OF LOCKHEED AIRCRAFT CORPORATION

to the difference in solar radiation. At the time of the measurements, the sky underneath the observation site was covered with clouds. In a trade wind situation, clouds typically develop below a temperature inversion. The clouds increase the overall brightness of the sky, as indicated in Fig. 2. A direct comparison of these measurements with Fig. 2 is not possible because of the difference in solar angles. The minima shown in Fig. 2 also are found in the measured values. Other measurements indicate that when more aerosols are present, the intensity is higher but distribution is more uniform (Ref. 6).

2.3 RADIANCE TRANSMITTED THROUGH CLOUDS

Radiation from clouds is more difficult to characterize due to the great variability of size distribution and thickness of clouds. The geographical location affects both the amount of cloud cover and the type of cloud present. Some of the relevant physical properties of clouds will be discussed, and a few examples of the radiative properties of clouds will be given.

Laser communication through clouds with the restrictions on size and power imposed by satellites requires a relatively small attenuation of the laser beam. A cloud with an optical thickness τ attenuates the incident radiation by $e^{-\tau}$. For a cloud through which one can just see the disk of the sun, τ is less than 10. Most of the radiation reaching the ground through clouds thicker than this is scattered radiation. The optical thickness of thicker clouds can be estimated by the following:

$$\tau = 8 \times \frac{\text{light from sun reaching ground without cloud}}{\text{light from sun with cloud}}$$

The optical thickness of clouds is usually less than 100 (Ref. 7). More information can be obtained from Ref. 8. Optically thick clouds are relevant to this study for their reflective properties.

Optical communications may be feasible through thin cirrus and noctilucent clouds. Therefore, the backgrounds presented by these clouds are important. Cirrus and probably noctilucent clouds are composed of ice crystals instead of water drops. Noctilucent clouds usually are observed in the summer between the latitudes of 45° and 80° N. Nearly always they form waves and resemble high, thin, cirrus clouds in appearance. These clouds are so thin optically that bright stars shine through them. Noctilucent clouds form at an altitude of about 80 km and are probably not more than a few kilometers thick (Ref. 9).

There are significant differences in the scattering of infrared radiation by ice and water droplet clouds. These differences are due to the larger size of the ice crystals and to the different real and imaginary parts of the index of refraction for ice and water. A difficulty in making theoretical calculations is that the ice particles are flat, so that the Mie theory (for spherical particles) is of questionable applicability. This difficulty is somewhat mitigated if it can be assumed that the ice particles are randomly oriented, so that the average scattering function is that of a spherical particle; the validity of this assumption is uncertain, however. A theoretical discussion of the differences between ice and water clouds is given in Ref. 10.

Plass and Kattawar (Ref. 11) used Monte Carlo techniques to study optically thin water and ice clouds. Figures 7 and 8 present the transmitted radiance at several different wavelengths for optical thicknesses of 1 and 10. An incident solar flux of unity is assumed. Values at wavelengths of interest can be found by interpolating between the wavelengths given and using the solar flux given in Fig. 3.

2.4 RADIANCE REFLECTED BY CLOUDS

The background seen by a high-altitude satellite is the earth's surface or clouds. The albedo of the ground is important in determining the reflected radiance for optically thin clouds. Figures 9 and 10 present the results of theoretical calculations of reflected radiance for water and ice clouds (Ref. 12). Figure 11 shows the reflected radiance

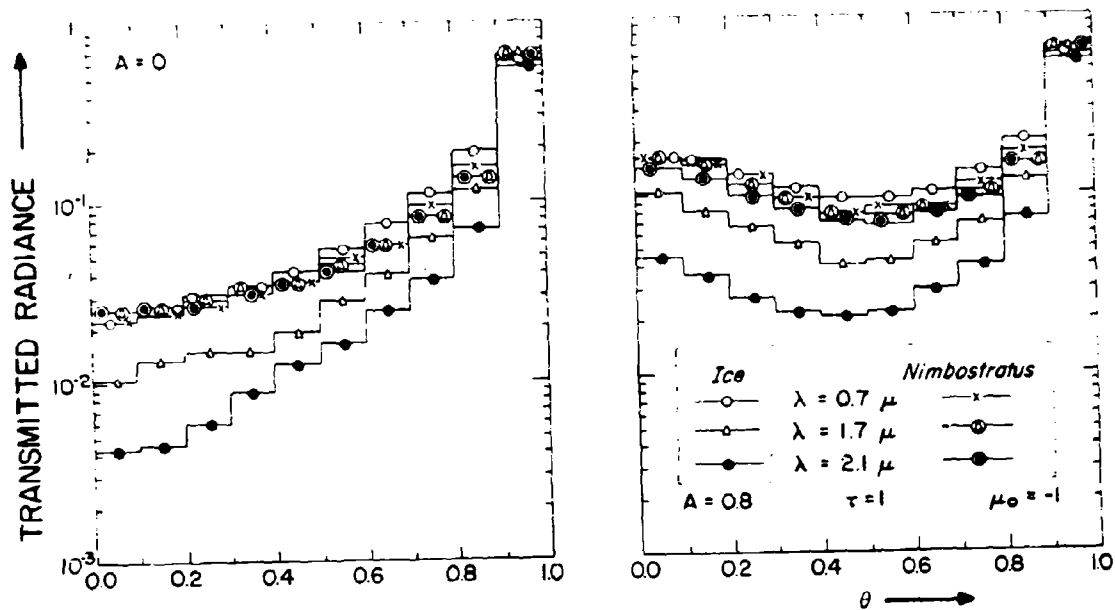


Fig. 7 Transmitted Radiance as a Function of θ for Ice and Nimbostratus Cloud Models With Sun at Zenith; $A = 0$ and 0.8 ; $\tau = 1$; $\lambda = 0.7 \mu$, 1.7μ , and 2.1μ

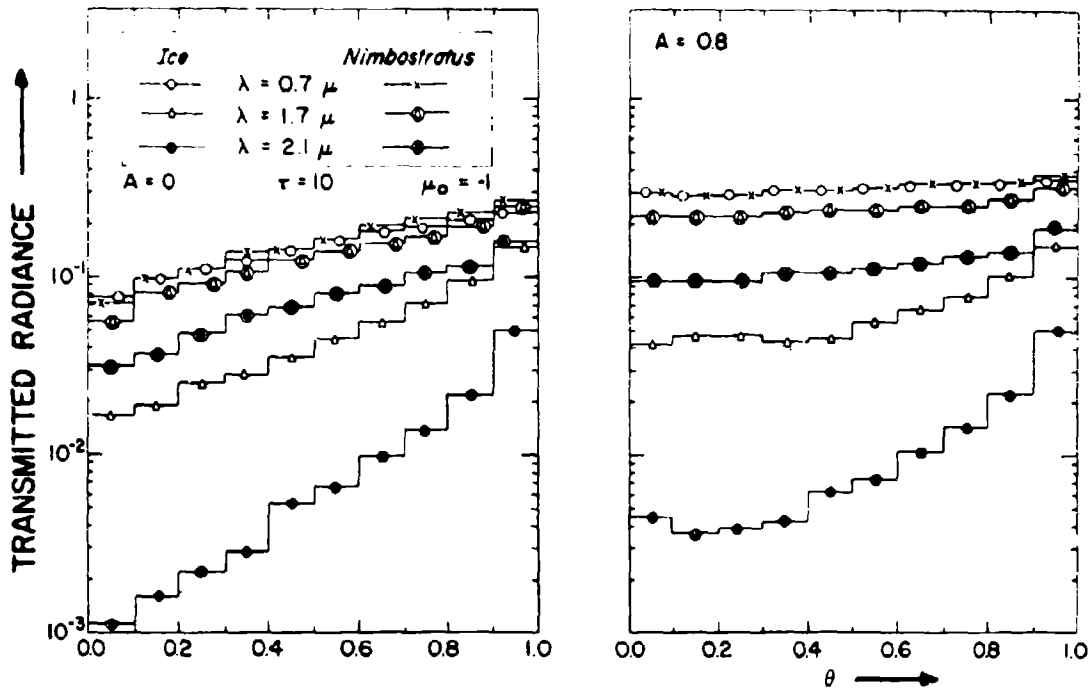


Fig. 8 Transmitted Radiance as a Function of θ for Ice and Nimbostratus Cloud Models With Sun at Zenith; $A = 0$ and 0.8 ; $\tau = 10$; $\lambda = 0.7 \mu$, 1.7μ , and 2.1μ

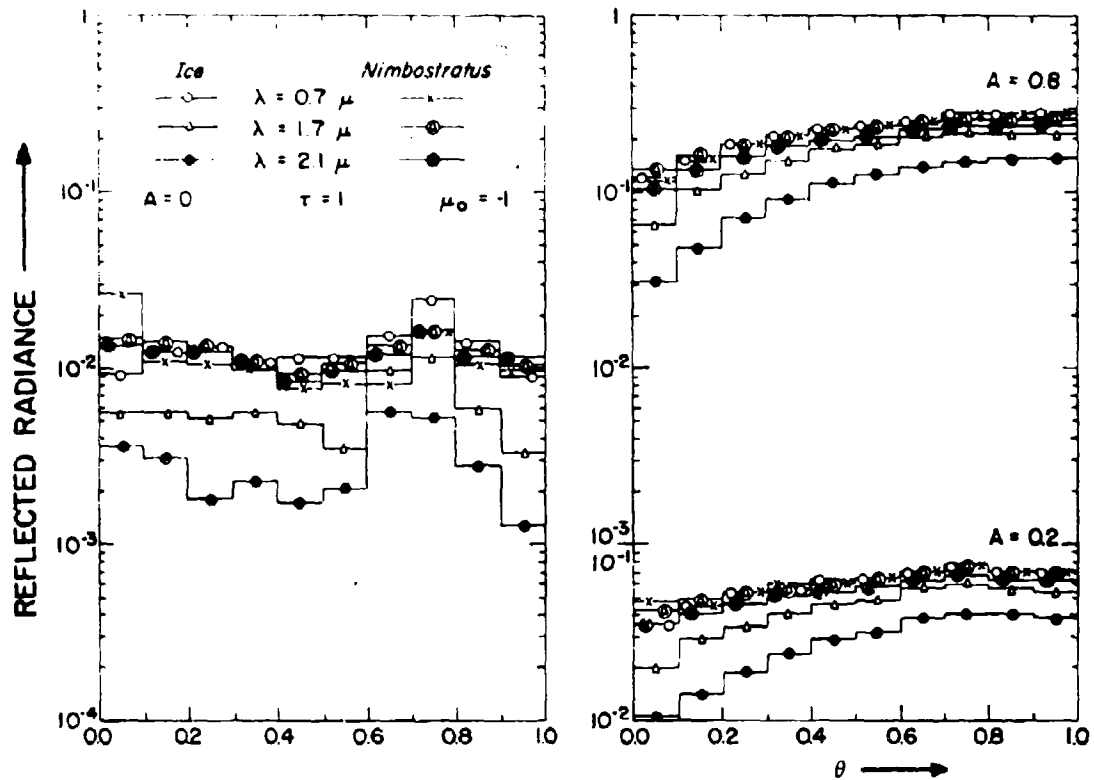


Fig. 9 Reflected Radiance as a Function of θ for Ice and Nimbostratus Cloud Models With Sun at Zenith; $A = 0, 0.2, 0.8$; $\tau = 1$; $\lambda = 0.7 \mu, 1.7 \mu$, and 2.1μ

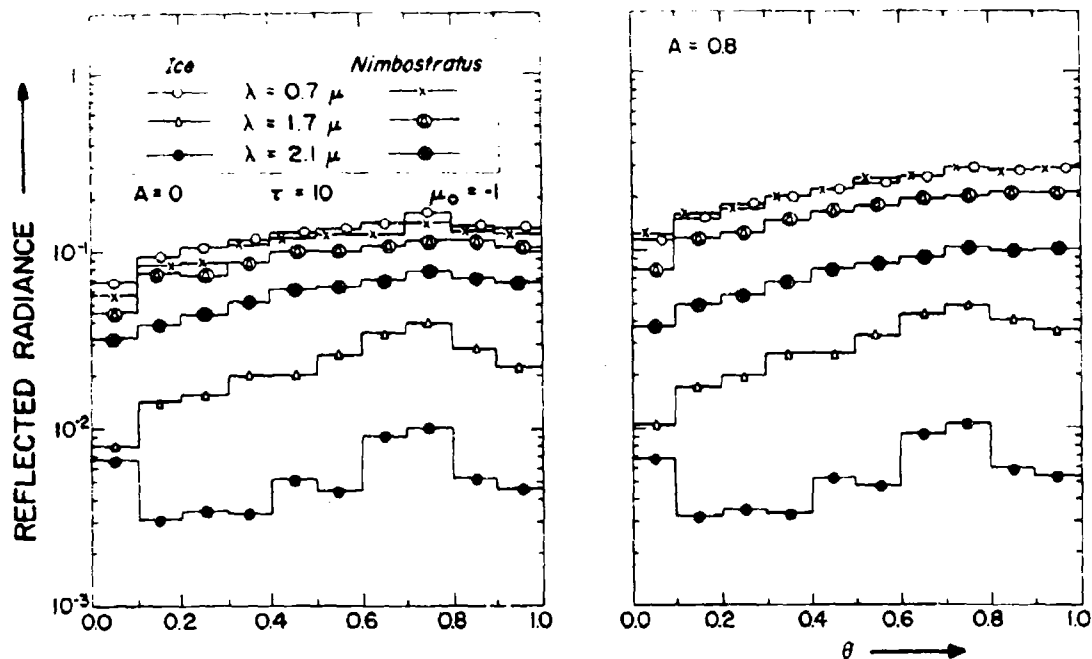


Fig. 10 Reflected Radiance as a Function of θ for Ice and Nimbostratus Cloud Models With Sun at Zenith; $A = 0$ and 0.8 ; $\tau = 10$; $\lambda = 0.7 \mu$, 1.7μ , and 2.1μ

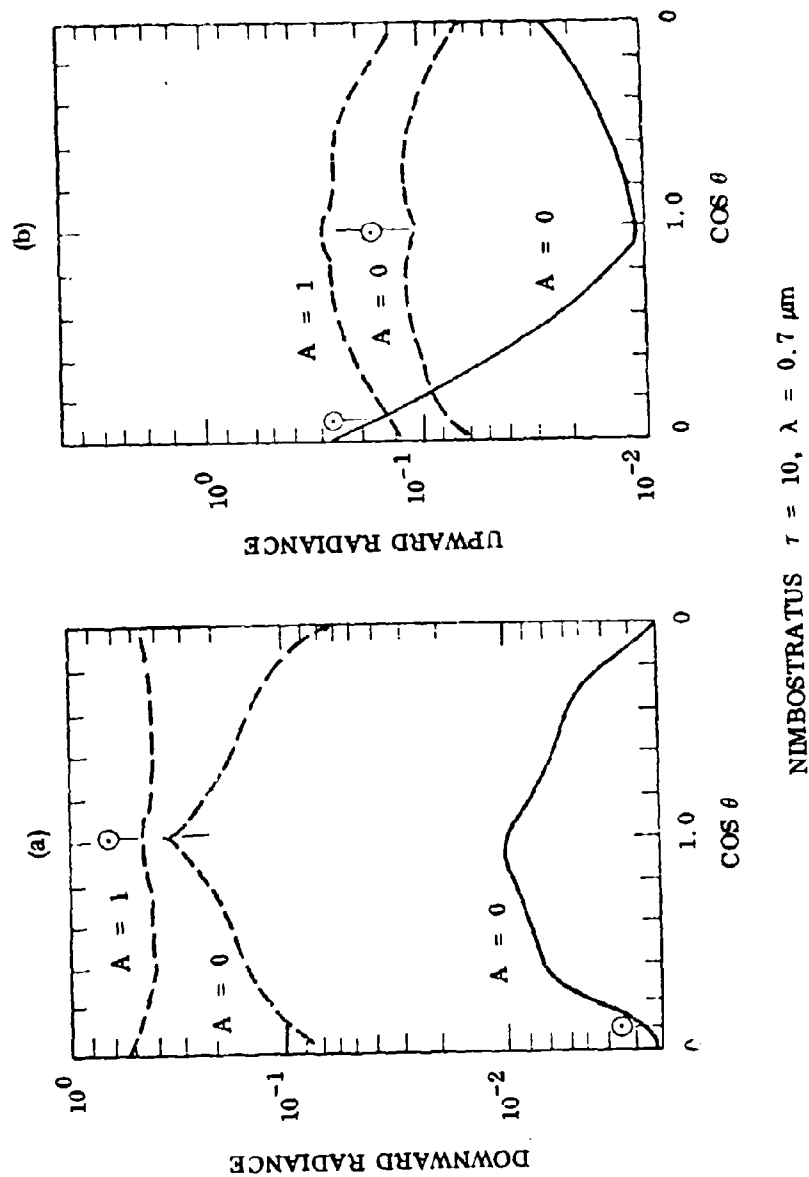


Fig. 11 Downward and Upward Radiance Computed for a Dense Nimbostratus Cloud. Dashed curves are for the sun in the zenith; solid curves are for the sun at $\theta = 86.3^\circ$

at $\lambda = 0.7 \mu\text{m}$ for two different sun angles (Ref. 2). These figures are normalized to a solar flux of unity. Figure 3 can be used to determine the absolute value of the radiance at a desired wavelength. If the clouds were ideal diffuse radiators, the plots in Figs. 9 through 11 would be horizontal straight lines. Strong forward scattering produces the variations from a straight line in these plots.

The backscattering and attenuation coefficients, per unit length, are given for eight water cloud models in Ref. 12. Also, variations in these optical properties are discussed. The backscattering coefficients given there can be used to calculate the reflected radiance for the sun at the zenith if the albedo of the ground is ignored.

Measurements of the reflected radiance from clouds were made in an airplane flying at 13.1-km altitude (Ref. 13). Figures 12 and 13 show the reflected radiance as a function of wavelength for a cirrus and cirrostratus cloud. These measured values can be compared with the theoretical values of Fig. 10 at $\lambda = 0.7 \mu\text{m}$. Using the solar irradiance in Fig. 3 yields values of 0.04 and 0.02 $\text{W}\cdot\text{m}^{-2}\cdot\text{sr}^{-1}\cdot\text{\AA}^{-1}$ for albedos of 0.8 and 0.0, respectively. Assuming an atmospheric transmission of 70% gives values of 0.028 and 0.014 $\text{W}\cdot\text{m}^{-2}\cdot\text{sr}^{-1}\cdot\text{\AA}^{-1}$, which bracket the range of experimental values. A more exact comparison is not possible because neither the optical thickness of the clouds nor the ground albedo was measured in the experiment that provided the values shown in Figs. 12 and 13.

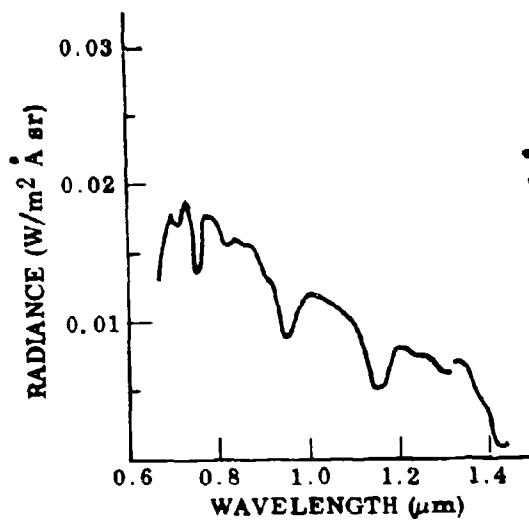


Fig. 12 Reflectance of a Cirrus Deck at 12.80 km

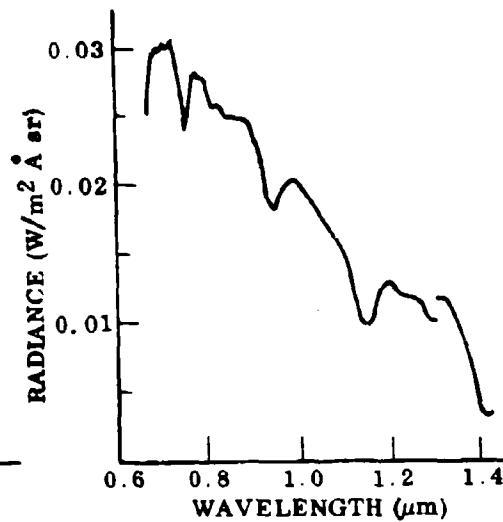


Fig. 13 Reflectance of a Cirrostratus Deck at 8.20 km

Section 3

EXTRATERRESTRIAL BACKGROUND SOURCES

The spectral radiance of sources such as the sun, the planets, and the moon can be derived readily from data available in the literature (Refs. 14, 15). Values for the radiance of direct sunlight were calculated by assuming the sun to be a 5900°K blackbody. The irradiance of a 2nd-magnitude star also assumed a 5900°K blackbody. An 11,000°K blackbody was used for Sirius.

The radiances of the moon and sunlit cloud were obtained from the solar irradiance in Fig. 3 and the assumption of a Lambertian (diffuse) scattering. In accordance with this assumption, the solar irradiance was multiplied by the albedo and then divided by π to convert to radiance. Results of these rough calculations of cloud radiance are given in Table 1. They are in reasonable agreement with the measured values given in Figs. 12 and 13.

Solar irradiance incident on Venus was calculated by multiplying the values in Fig. 3 by the square of the ratio of the radius of the earth's orbit to the radius of Venus' orbit. Multiplication by albedo/ π gives the radiance values in Table 1. The values given for Venus must be used with caution, since they apply only if the disk of the planet fills the field-of-view of the receiver. Since the angular size of Venus as seen from the earth varies from 9.9 to 64.5 arcsec, the values given are generally applicable only for systems having angular fields appreciably less than 9 arcsec. The difference in units between the point sources and the extended sources should be noted and appropriate allowance made in using these values to calculate received background power.

Table 1

BACKGROUND RADIANCE OF EXTENDED SOURCES (IN $\text{W-m}^{-2}\text{-sr}^{-1}\text{-\AA}^{-1}$)
AND IRRADIANCE OF STARS (IN $\text{W-m}^{-2}\text{-\AA}^{-1}$)

Background Source	Wavelength (μm)			
	0.53	0.633	0.86	1.06
<u>Extended Sources</u>				
Direct Sunlight	2.90×10^3	2.55×10^3	1.58×10^3	0.99×10^3
Sunlit Cloud (Albedo = 0.7)	4.1×10^{-2}	3.5×10^{-2}	2.2×10^{-2}	1.5×10^{-2}
Moon (Albedo = 0.073)	4.3×10^{-3}	3.7×10^{-3}	2.3×10^{-3}	1.6×10^{-3}
Venus (Albedo = 0.76)	8.5×10^{-2}	7.3×10^{-2}	4.5×10^{-2}	3.1×10^{-2}
<u>Point Sources</u>				
Sirius	1.8×10^{-11}	1.16×10^{-11}	0.5×10^{-11}	0.25×10^{-11}
2nd-Magnitude Star	6.4×10^{-13}	5.6×10^{-13}	3.5×10^{-13}	2.2×10^{-13}

Section 4
REFERENCES

1. K. Bullrich, "Scattered Radiation in the Atmosphere and the Natural Aerosol," Adv. in Geophys., Vol. X, 1964
2. R. A. McClatchey, R. W. Fenn, J. E. A. Selby, F. E. Volz, and J. S. Garing, Optical Properties of the Atmosphere (Revised), AFCRL-71-0279, 10 May 1971
3. G. N. Plass and G. W. Kattawar, "Calculations of Reflected and Transmitted Radiance for Earth's Atmosphere," Appl. Opt., Vol. 7, 1968, pp. 1129-1135
4. M. P. Thekaekara and A. J. Drummond, "Standard Values for the Solar Constant and Its Spectral Components," Nature, Phys. Sci., Vol. 229, 4 Jan 1971, pp. 6-9
5. K. Bullrich and R. Eiden, Optical Transmission of the Atmosphere in Hawaii, Final Technical Report, Contract DA-91-591-Euc-2964, Johannes Gutenberg Universitat, Mainz, Germany, 30 Sep 1964
6. K. Bullrich, E. DeBary, K. Danzer, R. Eiden, and K. Heger, Research on Atmospheric Optical Radiation Transmission, AFCRL-65-0109, 1965
7. R. M. Lerner and A. E. Holland, "The Optical Scatter Channel," Proc. IEEE, Vol. 58, 1970, pp. 1547-1563
8. R. E. Danielson, D. R. Moore, and H. C. van de Hulst, "The Transfer of Visible Radiation Through Clouds," J. Atmo. Sci., Vol. 26, 1969, pp. 1078-1087
9. A. E. Cole, R. J. Donaldson, R. Dyer, A. J. Kantor, and R. A. Skrivaneck, Precipitation and Clouds: A Revision of Chapter 5, Handbook of Geophysics and Space Environments, AFCRL-69-0487, 1969
10. J. E. Hansen and J. B. Pollack, "Near-Infrared Light Scattering by Terrestrial Clouds," J. Atmo. Sci., Vol. 27, 1970, pp. 265-281

11. G. N. Plass and G. W. Kattawar, "Radiative Transfer in Water and Ice Clouds in the Visible and Infrared Region," Appl. Opt., Vol. 10, 1971, pp. 738-748
12. L. W. Carrier, G. A. Cato, and K. J. von Essen, "The Backscattering and Extinction of Visible and Infrared Radiation by Selected Major Cloud Models," Appl. Opt., Vol. 6, 1967, pp. 1209-1216
13. W. A. Hovis, Jr., L. R. Blaine, and M. L. Norman, "Infrared Reflectance of High Altitude Clouds," Appl. Opt., Vol. 9, 1970, pp. 561-563
14. R. C. Ramsey, "Spectral Irradiance From Stars and Planets, Above the Atmosphere From 0.1 to 100.0 Microns," Appl. Opt., Vol. 1, Jul 1962, pp. 465-471
15. C. W. Allen, Astrophysical Quantities, 2nd Ed., The Athlone Press, London, 1963

Appendix H

**BRIGHTNESS OF THE IMAGE OF
THE SUN REFLECTED IN
THE OCEAN SURFACE**

by

Dr. D. L. Fried

Consultant to LMSC

(Previously distributed as Technical Memorandum No. 12)

LOCKHEED PALO ALTO RESEARCH LABORATORY
LOCKHEED MISSILES & SPACE COMPANY
A GROUP DIVISION OF LOCKHEED AIRCRAFT CORPORATION

We wish to calculate the apparent brightness of the image of the sun as seen reflected from the ocean surface. The brightness is reduced by two factors - first the low reflectivity $\rho(\theta)$, and second, the fact that the ocean surface is rough so that only a fraction of the surface viewed will provide a specular reflection. We use θ to denote the zenith angle of the sun at the reflection point.

In our calculations, we make use of the fact that if the ocean surface were perfectly flat and had unity reflectivity, we would see the solar image at full brightness, which is

$$L_o = \begin{cases} 2.4 \times 10^3 \text{ W/cm}^2\text{-}\mu\text{-ster @ } \lambda = 0.53 \mu \\ 9.5 \times 10^2 \text{ W/cm}^2\text{-}\mu\text{-ster @ } \lambda = 1.06 \mu \end{cases}$$

We also shall make use of the fact that the solar disk subtends an angle of about $1/2$ degree, so that its radius is

$$\theta_o = 4.3 \times 10^{-3} \text{ rad}$$

and its solid angle is

$$\Omega = 1.5 \times 10^{-5} \text{ ster}$$

We shall make use of the data given by Cox and Monk for the ocean surface.* They give the ocean surface reflectivity as

* Cox and Monk, J. Opt. Soc. Am., 44, 785 (1954)

$$\begin{aligned}\rho &= 0.02 \quad \text{for } \theta = 0^\circ \\ &= 0.021 \quad \text{for } \theta = 30^\circ \\ &= 0.060 \quad \text{for } \theta = 60^\circ \\ &= 1.00 \quad \text{for } \theta = 90^\circ\end{aligned}$$

They also give the distribution of surface slope as gaussian (with a minor skewness correction, which we shall ignore), with rms slopes of

$$\begin{aligned}\sigma_x &= 3.16 \times 10^{-3} W \\ \sigma_y &= 0.003 + 1.92 \times 10^{-3} W\end{aligned}$$

where W is the surface wind speed (in m/sec) and the x -axis is taken parallel to the wind. The probability that a surface sample will have slopes u_x to $u_x + du_x$ and u_y to $u_y + du_y$ is

$$\frac{1}{2\pi\sigma_x\sigma_y} \exp \left\{ -\frac{1}{2} \left[\left(\frac{u_x}{\sigma_x} \right)^2 + \left(\frac{u_y}{\sigma_y} \right)^2 \right] \right\} du_x du_y$$

Therefore, when looking at a point on the ocean such that, if the surface were flat, the center of the sun would be seen, the fraction of the surface that will reflect a part of the solar disk into the field of view will be

$$A = \iint_{\substack{\text{disk of} \\ \text{radius } \theta_0/2}} du_x du_y \frac{1}{2\pi\sigma_x\sigma_y} \exp \left\{ -\frac{1}{2} \left[\left(\frac{u_x}{\sigma_x} \right)^2 + \left(\frac{u_y}{\sigma_y} \right)^2 \right] \right\}$$

For wind speeds as low as 2 m/sec, u_x/σ_x and u_y/σ_y are significantly less than unity, so that we may set the exponential in the double

integral approximately equal to one. Then we get

$$A = \frac{1}{8} \left(\frac{\theta_0}{\sigma_x} \right) \left(\frac{\theta_0}{\sigma_y} \right) \\ = 1/8 (0.73 W) (0.70 + 0.95 W) .$$

The apparent brightness of the sun will then be

$$L = L_0 \rho A .$$

In Table 1, we tabulate some sample values of L.

TABLE I

Apparent Brightness of the Reflected Solar Image
 L (W/cm^2 -ster- μ)

	$\lambda = 0.53$			$\lambda = 1.06$		
	$W = 2$	$W = 5$	$W = 10$	$W = 2$	$W = 5$	$W = 10$
$\theta = 0^\circ$	2.6	.56	.16	1.0	.22	.062
$\theta = 30^\circ$	2.7	.59	.17	1.1	.23	.065
$\theta = 60^\circ$	7.8	1.7	.47	3.1	.66	.19
$\theta = 90^\circ$	130	28	7.9	51	11.	3.1

Appendix I

ATMOSPHERIC EFFECTS ON
AN OPTICAL DATA LINK;
SPACE-TO-GROUND

by

Dr. D. L. Fried
Consultant to LMSC

(Previously distributed as Technical Memorandum No. 11)

LOCKHEED PALO ALTO RESEARCH LABORATORY
LOCKHEED MISSILES & SPACE COMPANY
A GROUP DIVISION OF LOCKHEED AIRCRAFT CORPORATION

An optical communications link utilizing a photon counting receiver, with some portion of the propagation path in the atmosphere, will have its performance influenced by atmospheric turbulence. The effects will be of two forms -- 1) possible transmitter average antenna gain limitations; and 2) received carrier strength variations.* Other effects, such as carrier polarization variation and spreading of the width of picosecond pulses, have not been observed, although the latter should be observable when the state of the art is able to accommodate short enough pulses. The significance to an optical data link of average antenna gain limitations is apparent. Less transmitter antenna gain means that more total laser power has to be transmitted to get the same received power. The significance of carrier strength fluctuations is more subtle. While at first it might appear that the fluctuations would appear as spurious modulation, i.e., as multiplicative noise showing up in the demodulated signal unless special coding schemes were being used, actually this is not generally the case. Carrier strength fluctuations have a spectrum confined to the range of d.c. to a few kilohertz or less. We almost never consider wide band optical communications with the bandwidth extending down to d.c. or even down to a few kilohertz. As a consequence, spurious atmospheric turbulence induced modulation is always easily distinguishable from intended signal modulation of the carrier, pretty much independent of what modulation technique is used. The choice of modulation scheme is almost entirely a matter of component technology

*If heterodyne detection is used for the receiver, then other effects, such as optical frequency spreading and wavefront distortion, which are not normally observable with a photon counting receiver, will manifest themselves.

and such "practical" considerations.

However, atmospheric turbulence induced carrier strength fluctuations can have a serious effect on the link's performance in terms of reducing the quality of the received signal producing, for example, an increased error rate during carrier fades associated with the fluctuation. To compensate for these fades, it is necessary to transmit all the time a higher average power than would otherwise be required. The extra required power is, in a sense, a propagation loss factor for the link.* This fluctuating carrier loss factor, as well as transmitter antenna gain limitations, can be calculated from the available theory of optical propagation in the turbulent atmosphere^{1-6**} and from information about the vertical distribution of turbulence in the atmosphere⁷⁻¹¹. For our purposes, the effects of the atmosphere on the laser beam can be measured in terms of two quantities, r_0 , the coherence distance, and $C_k(0)$, the log-amplitude variance. r_0 , which is a measure of the distance across the wavefront over which a wave remains coherent, is most easily defined operationally in terms of the antenna gain of a heterodyne receiver accepting a laser beam with a distorted wavefront. Normalized antenna gain Ψ as a function of antenna diameter is shown in Fig. DLF-1, clearly indicating the operational significance of r_0 . The significance of $C_k(0)$, the log-amplitude variance, is most clearly seen by considering a dB meter

*This loss factor could be avoided if long, highly redundant modulation codes were used. This would provide averaging over the fades. However, since the duration of the fades is typically a few to a few hundred milliseconds, generation of a suitable length code would require a code generator with a few hundred megabits of memory to accommodate a gigabit per second data rate.

**The available theory is apparently not applicable for propagation paths for which the theory predicts strong scintillation.

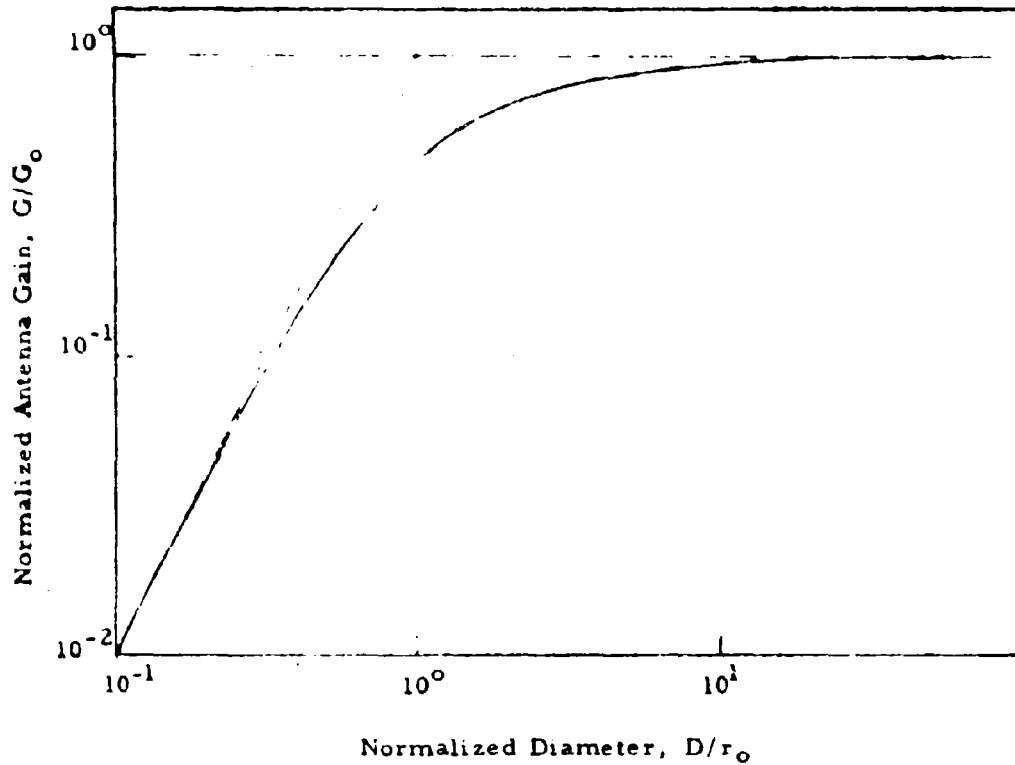


Fig. DLF-1 Dependence of Antenna Gain of an Atmospheric Turbulence Limited Optical Transmitter on Antenna Diameter. D is the diameter of the transmitter and r_0 is a length which characterizes the optical strength of turbulence along the propagation path for this effect. G is the antenna gain and is directly proportional to the average power density achieved in the center of the far-field pattern. G_0 is the corresponding free-space antenna gain for an antenna of diameter r_0 .

measuring the fluctuating received carrier power for a simple optical propagation experiment. The dB reading will fluctuate with a variance of

$$\sigma_{dB}^2 = 75.3 C_k(0). \quad (\text{DLF-1})$$

Measurement of the fluctuation in terms of dB or log-amplitude variance is particularly appropriate since theory predicts, and all available experimental data appears to confirm, that these quantities have a normal distribution for their fluctuations.

The calculation of r_0 and $C_k(0)$ is based upon knowledge of the refractive-index structure constant C_N^2 along the path of propagation. Without becoming involved in a detailed examination of the mechanical and optical properties of turbulence, it is sufficient to note that C_N^2 is a quantity which, by itself, completely characterizes the local optical strength of turbulence adequately for all of our purposes.

The only published estimates of the vertical distribution of C_N^2 are due to Hufnagel and Stanley⁷, and more recently by Hufnagel⁸. The former is now acknowledged to be incorrect, and the latter is presented without back-up material and in a form too imprecise to be really meaningful. We have, therefore, recently undertaken to develop a model for the vertical distribution of turbulence based on relevant although indirect measurements⁹⁻¹¹. The results of this analysis are shown in Fig. DLF-2.

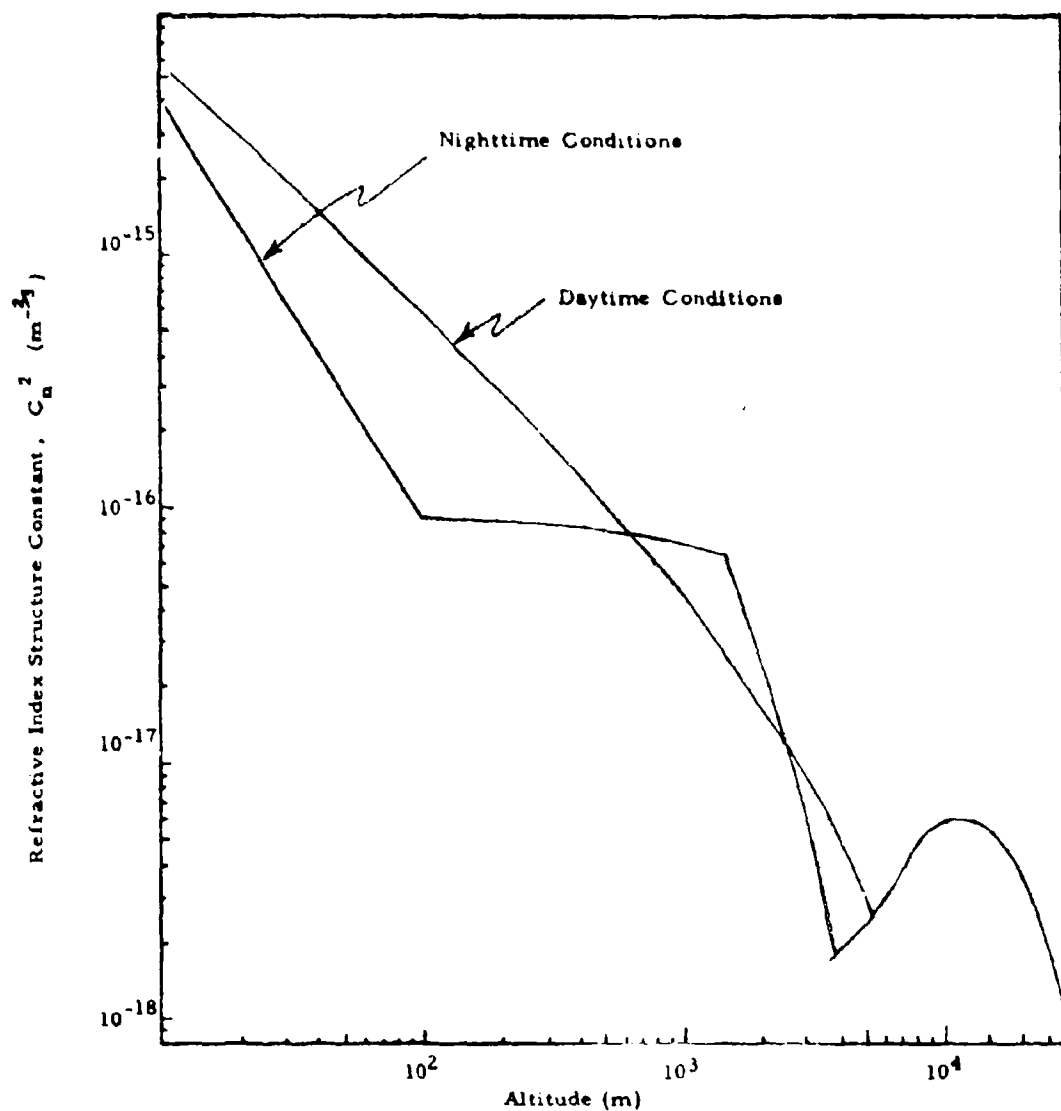


Fig. DLF-2 Suggested Model For The Vertical Distribution Of The Refractive Index Structure Constant, C_n^2 . This model is based on the temperature probe data of Koprov and Tsyang¹⁴, on near the ground laser scintillation measurements¹⁵ of C_n^2 , and on stellar scintillation measurements.

Based on this model for C_N^2 , and using the equations

$$C_k(0) = 0.567 \left(\frac{2\pi}{\lambda} \right)^{7/6} \int_{\text{path}} ds C_N^2 \left[\frac{s(z-s)}{z} \right]^{5/6} \quad (\text{DLF-2})$$

where z is the total path length and λ is the wavelength of interest, we obtain the result that

$$C_k(0) = 2.55 \times 10^{-2} (\lambda/10^{-6})^{7/6} \sec^{11/6} \theta \quad (\text{DLF-3})$$

or

$$\sigma_{\text{dB}}^2 = 1.92 (\lambda/10^{-6})^{7/6} \sec^{11/6} \theta \quad (\text{dB})^2 \quad (\text{DLF-3'})$$

which is applicable equally well for a propagation path from space to the ground or from the ground to space. Here θ is the zenith angle associated with the propagation path.

Using the equation

$$r_0 = \left[0.423 \left(\frac{2\pi}{\lambda} \right)^2 \int_{\text{path}} ds C_N^2 (s/z)^{5/3} \right]^{-3/5}, \quad (\text{DLF-4})$$

where it is to be understood that the propagation path is taken from the source toward the receiver, i.e., $s = 0$ at the source, we obtain the result that

$$r_0 = 0.155 (\lambda/10^{-6})^{5/3} \cos^{3/5} \theta, \quad (\text{downward radiation}) \quad (\text{DLF-5a})$$

for a point source in space and the receiver on the ground, with r_0

characterizing the coherence at the receiver. For the inverse case of the point source on the ground and the receiver in space, the coherence at the receiver is given by

$$r_0 = 0.900 \times 10^{-5} (\lambda/10^{-6})^{8/5} H \sec^{2/5} \theta \quad (\text{Upward radiation}) \quad (\text{DLF-5b})$$

where H is the height of the source and $H \sec \theta$ is the total path length. (In the above, all units are MKS.)

For a set of sample cases of interest, we obtain the data given in Table DLF-1.

From the value of r_0 associated with the downward radiation, we can determine the atmospheric limit on the achievable antenna gain for a ground based transmitter. The argument is based on the principles of reciprocity for electromagnetic propagation in a non-dissipative medium, with the heterodyne receiver, for which r_0 applies, replaced by an ideal transmitter, for which we argue that r_0 applies equally well. The transmitter beam spread then should be of the order of λ/r_0 . Identical arguments apply for the limitations on the antenna gain of the space-based receiver. However, in this case, as we can see from Table DLF-1, the values of r_0 (for upward radiation to a heterodyne receiver in space) are significantly larger than the practical physical limitations on diameter. Hence, atmospheric effects will not impose any limitation in this case.

For the ground based transmitter, we would set the beam spread at λ/r_0 , except that from reference 5 we see that if the physical diameter

TABLE DLF-1

Representative Values of $C(0)$ and r_0

λ (Microns)	$C^2(0)$ (Nepers)	σ_{ds}	r_0 (Downward Radiation)	r_0 @ H (Upward Radiation)
0.53	$5.35 \times 10^{-2} \text{ sec}^{1/6} \theta$	$2.01 \text{ sec}^{1/12} \theta$ dB	$7.25 \times 10^{-2} \cos^{3/5} \theta, \text{ m}$	$.421 \text{ sec}^{2/5} \theta, \text{ m @ } 10^2 \text{ km}$ $4.21 \text{ sec}^{2/5} \theta, \text{ m @ } 10^3 \text{ km}$ $1.69 \times 10^2 \text{ sec}^{2/5} \theta, \text{ m @ } 4 \times 10^4 \text{ km}$
1.06	$2.38 \times 10^{-2} \text{ sec}^{1/6} \theta$	$1.34 \text{ sec}^{1/6} \theta$ dB	$1.661 \times 10^{-1} \cos^{3/5} \theta, \text{ m}$	$.965 \text{ sec}^{2/5} \theta, \text{ m @ } 10^2 \text{ km}$ $9.65 \text{ sec}^{2/5} \theta, \text{ m @ } 10^3 \text{ km}$ $3.86 \times 10^2 \text{ sec}^{2/5} \theta, \text{ m @ } 4 \times 10^4 \text{ km}$

is equal to r_0 , then there will be substantial modulation noise associated with fluctuations in the transmitter* efficiency. For $D = r_0$, we expect a variance of 0.5, i.e., an rms fluctuation of intensity transmitted in the forward direction of 70.7%, a very substantial and unacceptable fluctuation. It appears likely (although there are no serious analyses or experimental results available to confirm this) that fluctuations of this sort have a log-normal distribution. If this is so, then we may expect that this corresponds to a normal distribution, for the fluctuation of antenna gain measured in dB, with a variance of $\sigma_{dB}^2 = 7.6 = (2.8 \text{ dB})^2$. Because of the problems associated with carrier fading, we can not accept a fluctuation of this magnitude and must, therefore, plan to use a transmitter diameter significantly less than r_0 . It would appear, from reference 5, that this problem can be avoided by using a transmitter diameter of about $r_0/3$. This means that for the up-link we are limited to a transmitter diameter of

$$D_{\text{trans}} = 2.42 \times 10^{-2} \cos^{3/5} \theta, \text{ m} \quad (\lambda = 0.53 \mu, \text{ ground transmitter})$$

$$D_{\text{trans}} = 5.54 \times 10^{-2} \cos^{3/5} \theta, \text{ m} \quad (\lambda = 1.06 \mu, \text{ ground transmitter})$$

It can be shown that at the satellite receiver altitude, the receiver diameter will be so small compared to the scintillation pattern correlation length (which is of the order of $\sqrt{\lambda H}$), that the receiver will be equivalent to a point-aperture receiver as far as aperture averaging of

* Actually, reference 5 refers to heterodyne receiver modulation noise, but, by reciprocity, this applies equally to transmitter antenna gain fluctuations.

scintillation is concerned.¹² This means that the rms fluctuations on the up-link will be $2.01 \sec^{1/2} \theta$ dB if $\lambda = 0.53$ microns, or $1.34 \sec^{1/2} \theta$ dB if $\lambda = 1.06$ microns. (If we had allowed the transmitter diameter to equal r_0 , instead of $r_0/3$, the corresponding values of rms fluctuation would be about 4.81 dB and 4.14 dB, respectively, for the case $\theta = 0^\circ$.)

For the down-link, we have no limitation on the transmitter size other than the purely practical one. There will be no scintillation associated with fluctuations in transmitter antenna gain.

For a 0.30 (0.60) meter diameter receiver, we expect aperture averaging¹² to reduce the intensity scintillation by a factor \oplus . Typical values of \oplus are shown in Table DLF-2

TABLE DLF-2

Aperture Averaging

D = 0.30 (0.60) m		
λ	θ	\oplus
0.53	0°	1.5×10^{-2} , (3.8×10^{-3})
0.53	80°	1.0×10^{-1} , (2.5×10^{-2})
1.06	0°	2.5×10^{-2} , (6.3×10^{-3})
1.06	80°	1.7×10^{-1} , (4.3×10^{-2})

Utilizing Mitchell's results¹³, we expect that the aperture average scintillation will also be log-normally distributed, with a log-amplitude variance $\tilde{\sigma}_l^2$. We can calculate $\tilde{\sigma}_l^2$ from the equation

$$\exp(4\tilde{\sigma}_l^2) - 1 = 8 [\exp(4\sigma_l^2) - 1] \quad \text{DLF-6}$$

From this, it is a straightforward matter to determine $\tilde{\sigma}_{dB}$, the rms fluctuation of the aperture averaged signal measured in dB. Table DLF-3 summarizes these results, along with useful aperture diameter results.

TABLE DLF-3
Atmospheric Effects Parameters

Link	$\lambda (\mu)$	θ (deg)	Useful Transmitter Diameter (m)	Received Signal Scintillation (dB)
Up	0.53	0	0.024	2.0
Up	0.53	80	0.0084	10.0*
Up	1.06	0	0.055	1.3
Up	1.06	80	0.019	6.4
Down	0.53	0	Practical limits only	0.2 (0.13)
Down	0.53	80		7.7*, (5.8*)
Down	1.06	0		0.4 (0.11)
Down	1.06	80		4.0 (2.3)

* The magnitude of the scintillation predicted for this case is so large that it appears likely that the theory is not accurate -- smaller values will probably be encountered.

REFERENCES

1. V. I. Tatarski, "Wave Propagation in a Turbulent Medium," McGraw-Hill, New York 1961.
2. J. I. Davis, Appl. Opt. 5, 139 (1966).
3. D. L. Fried, Appl. Opt. 6, 1729 (1967).
4. D. L. Fried, Proc. IEEE, 55 (1967).
5. D. L. Fried, J. Quant. Elec., 3, 213 (1967).
6. D. L. Fried, J. Opt. Soc. Am., 57, 175 (1967).
7. R. E. Hufnagel and N. R. Stanley, J. Opt. Soc. Am. 54, 52 (1964).
8. R. E. Hufnagel, in the report of the Woods Hole Summary Study, July 1966, on the "Restoration of Atmospherically Degraded Images, July 1966," National Research Council, National Academy of Science, Vol. 2, Appendix 3.
9. V. M. Koprov and L. R. Tsvang, Izv. Atmos. and Ocean Phys. 2, 1142 (1966), translated on p. 705.
10. J. J. Burke, J. Opt. Soc. Am. 60, 1262 (1970).
11. A. A. Hoag, Bulletin Astronomique, XXIV, Part 2, 269 (1964).
12. D. L. Fried, J. Opt. Soc. Am. 57, 169 (1967).
13. R. L. Mitchel, J. Opt. Soc. Am. 58, 1267 (1968).

Appendix J

ANTENNA GAIN RECIPROCITY
FOR PROPAGATION IN A TURBULENT MEDIUM

by

Dr. D. L. Fried
Consultant to LMSC

(Prepared in consultation with H. A. Yura, Aerospace Corporation)

LOCKHEED PALO ALTO RESEARCH LABORATORY
LOCKHEED MISSILES & SPACE COMPANY
A GROUP DIVISION OF LOCKHEED AIRCRAFT CORPORATION

In the microwave region, the term "antenna gain" is used to indicate the relative performance of an antenna compared to a simple dipole. For a transmitter, antenna gain is measured in terms of the peak power density achieved in the far field; while for a receiver, it is measured in terms of the maximum achievable signal-to-noise power ratio. High gain is considered synonymous with a narrow angular sensitivity or radiation pattern, and implies high angular resolution. In fact, the width or resolution of the antenna pattern can be used as a measure of antenna gain. The microwave community knows that reciprocity exists between transmitter and receiver antenna gain; i.e., if transmission and reception are at the same wavelength, an antenna used as part of a receiver system will have the same gain as when it is used as part of a transmitter system.

The term "antenna gain" is equally applicable if used with reference to the telescope (i.e., recollimating optics) of a laser transmitter, or to the telescope (i.e., collecting optics) of an optical heterodyne receiver. Here, as in the microwave case, we may assume reciprocity of antenna gain between transmitter and receiver use of a telescope - at least for free space propagation. However, unlike the microwave case, the effects of the atmosphere, in particular of atmospheric turbulence, upon optical system antenna gain can be substantial (Refs. 1,2,3,4).

Although in the past it has been conjectured to be the case, it is by no means clear that an optical antenna operating through the atmosphere will have the same antenna gain regardless of whether it functions as part of a laser transmitter or as part of an optical heterodyne receiver. (The same wavelength of operation is assumed in both cases.) To allow a discussion of the effects of one antenna at a time, rather than simultaneously considering them for both ends of the link, we study the case where the other end of the link is a point-source or a point-detector. The problem in establishing this reciprocity has appeared complicated, involving as it does the comparison, in the vicinity of the plane of the antenna, of a finite diameter beam from a laser transmitter, with a space filling radiation pattern from a distant point source, only part of which is going into the optical heterodyne receiver.

The purpose of this communication is to call attention to the fact that all of the necessary formulations have appeared in the published literature (Refs. 1,2,4) and to allow us to conclude with no additional analysis that, including the effects of atmospheric turbulence, reciprocity exists between the performance of a telescope (i.e., an antenna) functioning as part of an optical heterodyne receiver and its performance when functioning as part of a laser transmitter. We base this conclusion on the formal equivalence of previously proven representations for the antenna gain in these two cases. (The critical feature is the point-to-point wave propagation reciprocity proven in Ref. 4.) To demonstrate the formal equivalence, we repeat here the pertinent results.

It has been shown by Lutomirski and Yura (Ref. 4) that $I(P)$, the intensity at some point P a distance away from a laser transmitter, due to the laser transmitter, is given by the expression

$$I(P) = A \iint \vec{dr}_1 \vec{dr}_2 \exp [ik (s_1 - s_2)] \exp [\psi(\vec{r}_1) + \psi^*(\vec{r}_2)] \times U(\vec{r}_1) U^*(\vec{r}_2) \quad (1)$$

Here A is a constant of proportionality subsuming various minor dependencies of no concern to us here, the \vec{r}_1 - and \vec{r}_2 -integrations are over the plane of the antenna aperture, and $U(\vec{r})$ is the electromagnetic wave function at \vec{r} , associated with the operation of the laser. The quantity $\psi(\vec{r})$ is the complex phase* perturbation associated with the presence of turbulence in the propagation path, and corresponds to the perturbation observed at P for a wave originating from a point-source at \vec{r} .

Lutomirski and Yura have been able to show that $\psi(\vec{r})$ is identical in value to the complex phase perturbation observed at \vec{r} for a wave originating from a point-source at P , assuming, of course, that we retain for this comparison exactly the same turbulent structure over the propagation path, and of course the same wavelength.**

We shall view Eq. (1) as involving this latter definition for ψ , i.e., the one involving propagation from P to \vec{r} .

*The term "complex phase" is used to denote the combination of ordinary phase variation ϕ and log-amplitude variation ℓ ; i.e., $\psi = \ell + i\phi$.

**Attention is called to the fact that this is not a statistical equivalence. It is a statement of the exact equivalence of two random variables: their correlation is perfect.

It has been shown by Fried (Ref. 1), and in a slightly more general form by Moreland and Collins (Ref. 2), that the signal-to-noise ratio achievable by an optical heterodyne receiver can be written in the form

$$S/N = B \iint d\vec{r}_1 d\vec{r}_2 \exp [ik (s_1' - s_2')] \exp [\chi(\vec{r}_1) + \chi(\vec{r}_2)] \times V(\vec{r}_1) V^*(\vec{r}_2) \quad (2)$$

where B is a constant of proportionality subsuming all the factors of no particular relevance here, the \vec{r}_1 - and the \vec{r}_2 -integrations are over the plane of the antenna aperture, and $V(\vec{r})$ is, in this case, the electromagnetic wave function associated with the local oscillator, as projected forward in the system as though the local oscillator were mixed with the incoming wave by a beam splitter located just in front of the antenna aperture. (In this regard, attention is called to Appendix A of Ref. 1.) The term $\chi(\vec{r})$ in Eq. (2) denotes the complex phase perturbations due to atmospheric turbulence in the path, as observed at \vec{r} for a wave originating at some distant source which we denote by P' . [It may be noted that Eq. (2) includes allowance for a non-uniform local oscillator pattern following Moreland and Collins (Ref. 2) rather than Fried (Ref. 1), who assumes a uniform oscillator. In addition, the path length factor $\exp [ik (s_1' - s_2')]$ has been introduced to allow the results to apply to a point-source which may be in the near-field of the antenna, rather than assuming a nominal incident plane wave from a collimated transmitter or a point-source at infinity, as in both Fried (Ref. 1) and Moreland and Collins (Ref. 2).]

With P' chosen identical to P , so that $s_1(s_2)$ and $s_1'(s_2')$ are identical, and recalling that the point-to-point propagation reciprocity proven by Lutomirski and Yura now allows us to equate $\psi(\vec{r})$ and $\chi(\vec{r})$, then it is immediately apparent that Eqs. (1) and (2) have exactly the same form of dependence on turbulence. If we let the antenna aperture and the laser pattern for the local oscillator and for transmissions be the same for the unit functioning as a laser transmitter and functioning as an optical heterodyne receiver, so that $U(\vec{r})$ and $V(\vec{r})$ are identical, then the antenna gains manifestly have the same dependence on the turbulence pattern in the propagation path. Note that this equivalence is exact in the sense that the two antenna gains, viewed as random variables, have a perfect correlation. In this sense, there is a perfect reciprocity between laser transmitter and optical heterodyne antenna gain for propagation in a turbulent medium.

This means, for example, that the strength of the received optical heterodyne signal can be used as a cue for triggering burst transmission for a shared aperture system. The equivalence is so complete in its inner structure, i.e., within the integrals, that to the extent that wavefront distortion can be considered to be to a large extent just random tilting (Ref. 5), and to the extent that the antenna gain of the optical heterodyne receiver can be improved by tracking this tilt by local oscillator alignment adjustment (Ref. 6), to exactly this same extent the antenna gain of the laser transmitter can be improved by tracking this tilt by adjusting the pointing of the antenna. This equivalence follows from the fact that tracking of the tilt corresponds to replacing $\psi(\vec{r})$ in Eq. (1), or $\chi(\vec{r})$ in Eq. (2) with $\psi(\vec{r}) - i\vec{a} \cdot \vec{r}$, or $\chi(\vec{r}) - i\vec{a} \cdot \vec{r}$, respectively, where \vec{a} is the estimated wavefront tilt being tracked. A given value of \vec{a} has the same effect in both expressions, and obviously the same value of \vec{a} maximizes both the expressions. Moreover, since the same value of \vec{a} maximizes the laser transmitter's and the optical heterodyne receiver's antenna gains, the signal to drive the tracking servo-mechanism of the transmitter can be obtained from an optical heterodyne receiver sharing the antenna with the transmitter, and tracking a beacon source located at the other end of the link.

As a practical matter, it is, in addition, worthwhile to note that, from Ref. 7, a very slightly modified version of Eq. (2) applies equally well to the intensity of the image of the beacon, for intensity measured at the center of the focal plane associated with the use of the antenna (i.e., telescope) as a high-resolution imaging device. Tracking of wavefront tilt corresponds to a displacement of the point at which intensity is measured a distance proportional to \vec{a} . The effect of this displacement is incorporated into the modified version of Eq. (2) that applies to imagery by replacing $\chi(\vec{r})$ by $\chi(\vec{r}) - i\vec{a} \cdot \vec{r}$. This means that rather than having to use an optical heterodyne receiver to obtain the signals to drive a wavefront-tilt tracking laser transmitter, a simple imaging type tracker can be used.

If we allow the term "antenna gain" to apply also to the intensity at some measurement point in the focal plane of an antenna used as an image forming device viewing a point-source, then we may draw this general conclusion:

For a given optical antenna operating through atmospheric turbulence to some distant point, the effect of atmospheric turbulence upon antenna gain will be the same whether the antenna is used as part of a laser transmitter, an optical heterodyne receiver, or an image forming device.

From this we may state the following corollaries:

- Calculations of the statistics for one form of use of the antenna may be applied to the other forms of use.
- Measurements at some site, made with one type of unit, may be applied to predict expected performance for either of the other two types of units at that site.
- If the same antenna is used in two or more ways simultaneously, such as as a transmitter and as an imaging device, measurements made on the performance in one role may be used to gauge the concurrent performance in the other role.

References

1. D. L. Fried, Proc. IEEE, Vol. 55, 1967, p. 57
2. J. P. Moreland and S. A. Collins, Jr., J. Opt. Soc. Am., Vol. 59, 1969, p. 10
3. D. L. Fried, J. Quant. Elec., Vol. QE-3, 1967, p. 213
4. R. F. Lutomirski and H. T. Yura, Appl. Opt., Vol. 10, 1971, p. 1652
5. D. L. Fried, J. Opt. Soc. Am., Vol. 55, 1965, p. 1427
6. D. M. Chase, J. Opt. Soc. Am., Vol. 56, 1966, p. 33
7. D. L. Fried, J. Opt. Soc. Am., Vol. 56, 1966, p. 1372

Appendix K

ATMOSPHERIC TURBULENCE EFFECTS
ON A GROUND-BASED OPTICAL TRANSMITTER
IN A GROUND-TO-SPACECRAFT LINK

by

Dr. D. L. Fried
Consultant to LMSC

(Previously distributed as Technical Memorandum No. 5)

LOCKHEED PALO ALTO RESEARCH LABORATORY
LOCKHEED MISSILES & SPACE COMPANY
A GROUP DIVISION OF LOCKHEED AIRCRAFT CORPORATION

Introduction

We are concerned here with the matter of the effects of atmospheric turbulence on the performance of a diffraction-limited optical transmitter, when the transmitter is on the ground, immersed in the atmosphere, in a ground-to-space link. We expect two distinct effects to control the performance of the transmitter. The first of these we refer to as antenna gain saturation, and the second we denote as antenna gain modulation. It is through these two effects that atmospheric turbulence limits the optical transmitter's performance.

Antenna gain saturation refers to the fact that for a given wavelength and propagation path, with some particular distribution of the optical strength of atmospheric turbulence along the path, there is a length r_0 which represents a limit on achievable antenna gain over that path.^{1,2} For antenna diameters much smaller than r_0 , atmospheric turbulence will not affect antenna performance and the achieved antenna gain will be very close to the free space value. For antenna diameters much larger than r_0 , the antenna gain measured over an ensemble of turbulence conditions will be far below the free space value we would associate with the antenna's actual diameter, and will, in fact, be quite close to the free space antenna gain of an antenna whose diameter was only r_0 . For large diameter antennas, this can be quite a bit below the free space ideal value.

Antenna gain modulation refers to the fact that for antenna diameters large enough for their average gain to be significantly less than the expected

free space value, i.e., for antenna diameters of the order of r_0 or greater, the instantaneous antenna gain is a random variable fluctuating from instant to instant as the pattern of atmospheric turbulence fluctuations continuously changes. For antenna diameters much less than r_0 , there is little atmospherically induced variation in antenna gain just as there is little atmospherically induced reduction of average antenna gain. As the ratio of antenna diameter to r_0 approaches unity and goes to larger values, the magnitude of the scintillation, as measured by a modulation factor, goes from nearly zero to very large values.

We are motivated in the development of this paper by the consideration that the performance of a data channel is strongly affected by fluctuations in channel strength, such as would be coupled with transmitter antenna gain variations. Because of the much poorer than average performance to be expected during a deep fade, it is necessary to run a channel that is subject to fading at an average channel strength significantly above the level we would require if there were no fading, which means that we need to transmit with more power, or somehow obtain a larger or higher efficiency receiver. In short, fluctuations in transmitter antenna gain make us design the rest of the channel as though the effective transmitter antenna gain were less than the average antenna gain. As a consequence, we shall find that we optimize performance when we set the transmitter antenna diameter to be significantly below r_0 , emphasizing minimization of antenna gain modulation as much as maximization of average antenna gain.

Antenna Gain Theory

A well-developed theory for the performance of a coherent optical receiver, i.e., an optical heterodyne receiver, is presently available in terms of references 1, 2, and 3. No such comparable theory for the diffraction-limited transmitter exists. However, it can be argued on the grounds of reciprocity, and has been analytically established first in a moderately rigorous manner in reference 4, and more recently in a fully rigorous manner⁵, that the antenna gain results developed for a coherent receiver are equally applicable to a coherent (i.e., diffraction-limited) transmitter. We shall base all of our further discussion on this argument.

It can be shown^{1,2} that atmospheric turbulence limits the average transmitter antenna gain in the manner indicated in Fig. 1. This effect is more precisely quantified in Table 1. The quantities G and G_0 are measures of the average optical power density at the center of the far-field antenna pattern, with unit power transmission in all cases. G_0 refers to the far-field power density to be expected in the absence of atmospheric turbulence effects if the transmitter diameter is r_0 . G is given as a function of transmitter diameter, D . Quite obviously, from the point of view of atmospheric turbulence effects on average antenna gain, r_0 serves as an entirely adequate and complete measure of the effect of turbulence over the propagation path.

In reference 3, it is shown that antenna gain will fluctuate in such a way that the instantaneous far-field intensity at the nominal (i.e., static

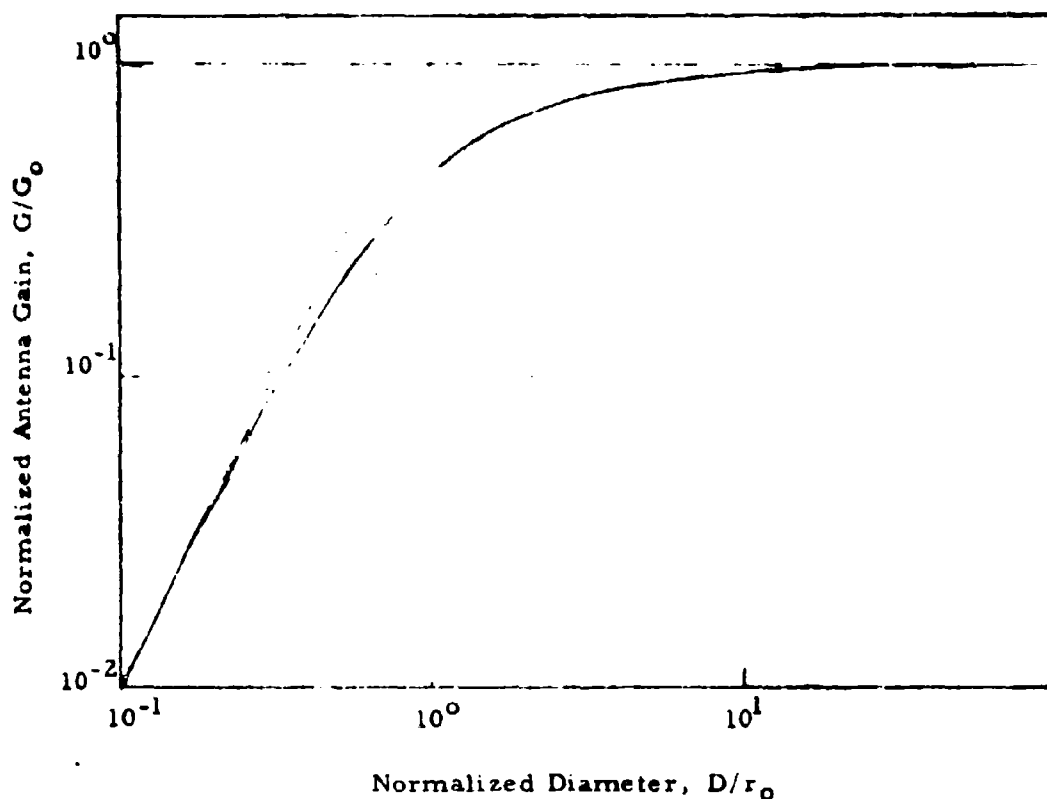


Fig. 1 Dependence of Antenna Gain of an Atmospheric Turbulence Limited Optical Transmitter on Antenna Diameter. D is the diameter of the transmitter and r_0 is a length which characterizes the optical strength of turbulence along the propagation path for this effect. G is the antenna gain and is directly proportional to the average power density achieved in the center of the far-field pattern. G_0 is the corresponding free-space antenna gain for an antenna of diameter r_0 .

and non-fluctuating) center of the pattern has a variance, σ_G^2 , where σ_G^2 is as shown in Fig. 2, and more exactly in Table 2. σ_G^2 is the normalized antenna gain variance. If P is the instantaneous far-field power density, and $\langle \rangle$ denote an ensemble average, then

$$\sigma_G^2 = \frac{\langle (P - \langle P \rangle)^2 \rangle}{\langle P \rangle^2} \quad (1)$$

Here again it is quite clear that r_0 completely characterizes the dependence of the effect, in this case antenna gain variance, upon the optical strength of turbulence over the propagation path.

It has not been shown in any rigorous manner, but we argue on the basis of a generalization of Mitchell's work⁴ from the log-normal to the complex-phase-normal, that the instantaneous signal power in a heterodyne receiver, and correspondingly in the power density in the far-field of a diffraction-limited transmitter, should be log-normally distributed due to atmospheric turbulence effects. If this is the case, which we shall assume, then the logarithm of the antenna gain, i.e., the logarithm of the power density in the far-field, will be normally distributed. This leads us to the log-amplitude variance, σ_L^2 , and perhaps more usefully to σ_{dB}^2 , the variance of the power density measured in dB. Since the distribution is log-normal, it can be shown that

$$\sigma_L^2 = \frac{1}{4} \ln(\sigma_G^2 + 1) \quad (2)$$

$$\begin{aligned} \sigma_{dB}^2 &= 75.3 \sigma_L^2 \\ &= 18.8 \ln(\sigma_G^2 + 1) \end{aligned} \quad (3)$$

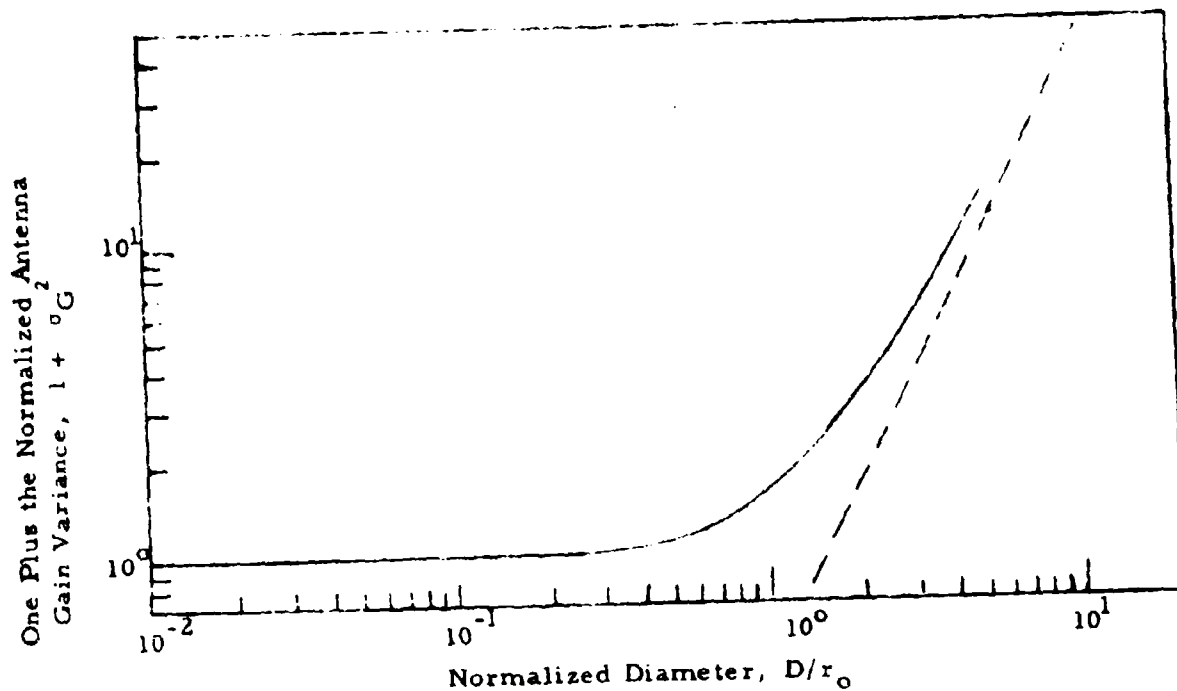


Fig. 2 Dependence of Transmitter Antenna Gain Variance Due to Atmospheric Turbulence Effects on Transmitter Antenna Diameter. D is the diameter of the transmitter and r_0 is a length which characterizes the optical strength of turbulence along the propagation path, and is the same factor as used in Fig. 1. The normalized antenna gain variance is the variance of the power density in the center of the far-field pattern divided by the average far-field power density.

Table 1

Average Transmitter Antenna Gain
As A Function Of
Transmitter Diameter

D/r_0	G/G_0
0.1	0.0098
0.5	0.1852
1.0	0.445
2.0	0.699

Table 2

Transmitter Antenna Gain Variance
As A Function Of
Transmitter Diameter

D/r_0	σ_G^2
0.1	0
0.5	0.11
1.0	0.51
2.0	2.18

In Table 3, we show the transmitter antenna diameter dependence of both average antenna gain and gain variance, both measured in dB, the former denoted by G_{dB} and the latter by σ_{dB}^2 , where

$$G_{dB} = 10 \log_{10} (G/G_0) \quad (4)$$

In Fig. 3, we show an estimate of the extra power that has to be transmitted to insure a bit error rate of 10^{-6} in binary communications to allow for the difference in performance in the absence of antenna gain modulation (i.e., in the absence of fading) and in its presence'. This is expressed as a loss factor in dB, L_{dB} denoting the extra power that has to be transmitted, and is taken as 10 times the log of the power ratio which should be contrasted with the factor of 20 in Eq. (42) of reference 7.

This is based on a fixed gaussian noise in the receiver, and gaussian rather than Poisson statistics. As such, the result should be considered to be only weakly relevant to the more interesting optical communications links, where Poisson statistics are relevant and quite distinct from gaussian statistics. In Table 4, we have shown the dependence of both average antenna gain G_{dB} and the loss factor L_{dB} on the ratio D/r_0 . It is clear from this table that optimum performance in the sense of least required transmitter power is obtained with a transmitter antenna diameter of the order of $0.5 r_0$ to $0.7 r_0$.

The problem before us at this point, then, is the calculation of r_0 . This matter we take up in the next section.

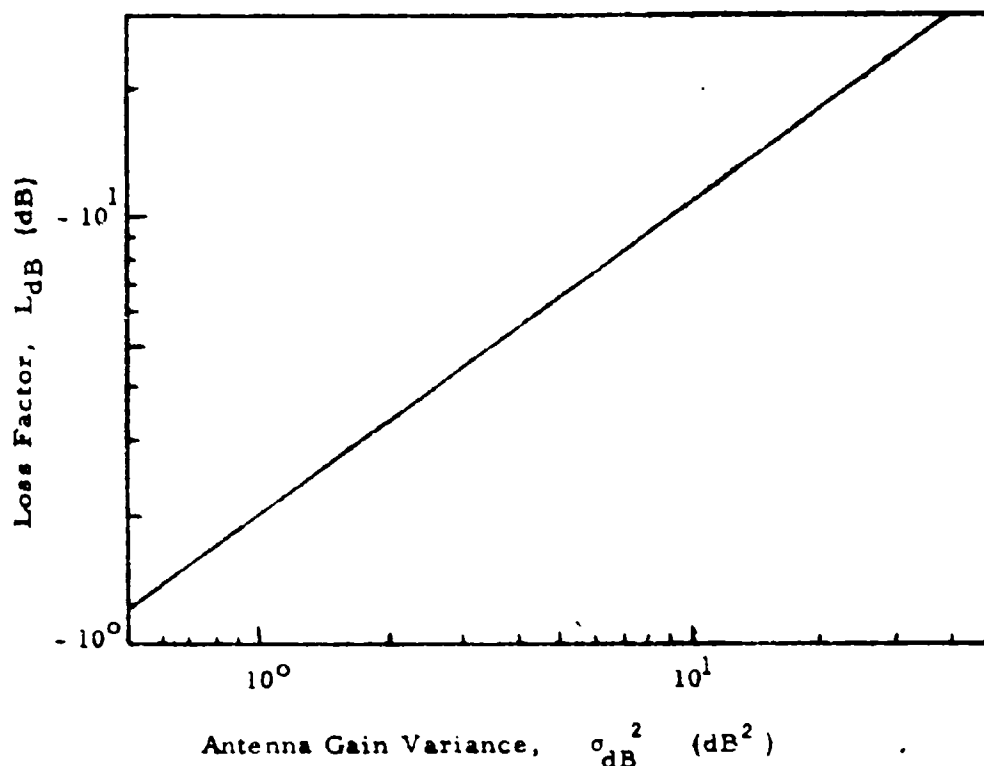


Fig. 3 Dependence Of The Nominal Channel Fluctuation Loss Factor On Antenna Gain Variance. The loss factor, L_{dB} , is a measure in dB of the extra optical power that has to be transmitted to compensate for the effect of channel strength fluctuations. Channel strength fluctuations are measured by σ_{dB}^2 , the variance of the instantaneous channel strength on transmitter antenna gain expressed in dB. The results are for a binary channel with a bit error rate of 10^{-6} , and assumes that fading measured in dB has a normal distribution. The results are based on the assumption that receiver noise is gaussian with a variance that is independent of the occurrence of fades in the channel. The results are therefore only of order-of-magnitude type relevance to an optical communications link for which Poisson statistics, as distinct from gaussian statistics, are applicable.

Table 3

Average Transmitter Antenna Gain and Transmitter Variance
Both in dB As A Function Of Transmitter Diameter

D/r_o	G_{dB} (dB)	σ_{dB}^2 (dB ²)	σ_l^2 (nepers ²)
0.1	-20.1	0	0
0.5	- 7.3	1.96	0.026
1.0	- 3.5	7.75	0.103
2.0	- 1.6	21.8	0.290

Table 4

Transmitter Average Antenna Gain and
Gain Modulation Loss Factor
As A Function Of
Transmitter Diameter

D/r_o	G_{dB} (dB)	L_{dB} (dB)	$G_{dB} + L_{dB}$
0.1	- 20.1	0	- 20.1
0.5	- 7.3	- 3.4	- 10.7
1.0	- 3.5	- 9.0	- 12.5
2.0	- 1.6	-18.0	-19.6

Evaluation of r_0

The basic expression for r_0 is⁸

$$r_0 = \left\{ 0.423 k^2 \int_{\text{path}} ds C_n^2 \right\}^{-3/5} \quad (5)$$

Here k is the optical wave number, $2\pi/\lambda$, and C_n^2 is a quantity called the refractive index structure constant. C_n^2 is a measure of the local optical strength of turbulence. If we know C_n^2 , we can calculate r_0 directly. Unfortunately, however, our knowledge of the vertical distribution of C_n^2 is very imprecise and is not really sufficient to support by itself a calculation of r_0 . Rather, we shall obtain r_0 rather directly from astronomical observations. We shall use what knowledge we have of C_n^2 to argue the rather general applicability of the astronomical data, and therefore, for the moment, consider the state of our knowledge regarding C_n^2 .

The earliest published model for the vertical distribution of C_n^2 is due to Hufnagel and Stanley.⁹ Fried approximated this curve by

$$C_n^2 = A h^{-1/3} \exp(-h/h_0), \quad A = 4.2 \times 10^{-14} \text{ m}^{-1/3} \\ h_0 = 3200 \text{ m} \quad (6)$$

where h is the altitude, in meters, at which C_n^2 is being measured, and used this expression for stellar scintillation calculations.¹⁰ It has since been recognized that the basic model is inadequate and Hufnagel¹¹ has suggested an alternate distribution, but with enough vagueness in the

model that exact calculations can not be performed. Hullett¹², recognizing the fact that the original model gave much too large a prediction for stellar scintillation, suggested that A in Eq. (6) be reduced by about a factor of 30. Titterton¹³ used the same sort of facts (only based on measurements involving a laser and a satellite) to argue that h_0 in Eq. (6) should be revised down by a factor of 20, to about 150 m. It is not clear that any simple correction to the model in Eq. (6) is really adequate.

Recently Koprov and Tsvang¹⁴ have flown a high speed temperature probe in an airplane and obtained data directly proportional to C_n^2 . From their results in conjunction with close to the ground optical measurements¹⁵ of C_n^2 , we have formulated the model for the vertical distribution of C_n^2 shown in Fig. 4. The peak in C_n^2 at high altitudes is probably the only uncertain portion of the curve, and depends on the value for the magnitude of stellar scintillation that we use in developing the model. Fortunately, however, in terms of calculating r_0 , this high altitude peak is irrelevant. The value of the integral in Eq. (5) is determined almost entirely by the values of C_n^2 in the first few tens of meters. There is, quite apparently, about a factor of two difference between the value of the integral in Eq. (5) according to whether we use the daytime or the nighttime values for C_n^2 , with the daytime value being the larger. This means that r_0 for daytime should be $2^{-\frac{3}{5}} = 0.64$ times the value at night. We shall develop our exact value for r_0 from nighttime astronomical observations and will use this factor of 0.64 to put the results in a form applicable to daytime.

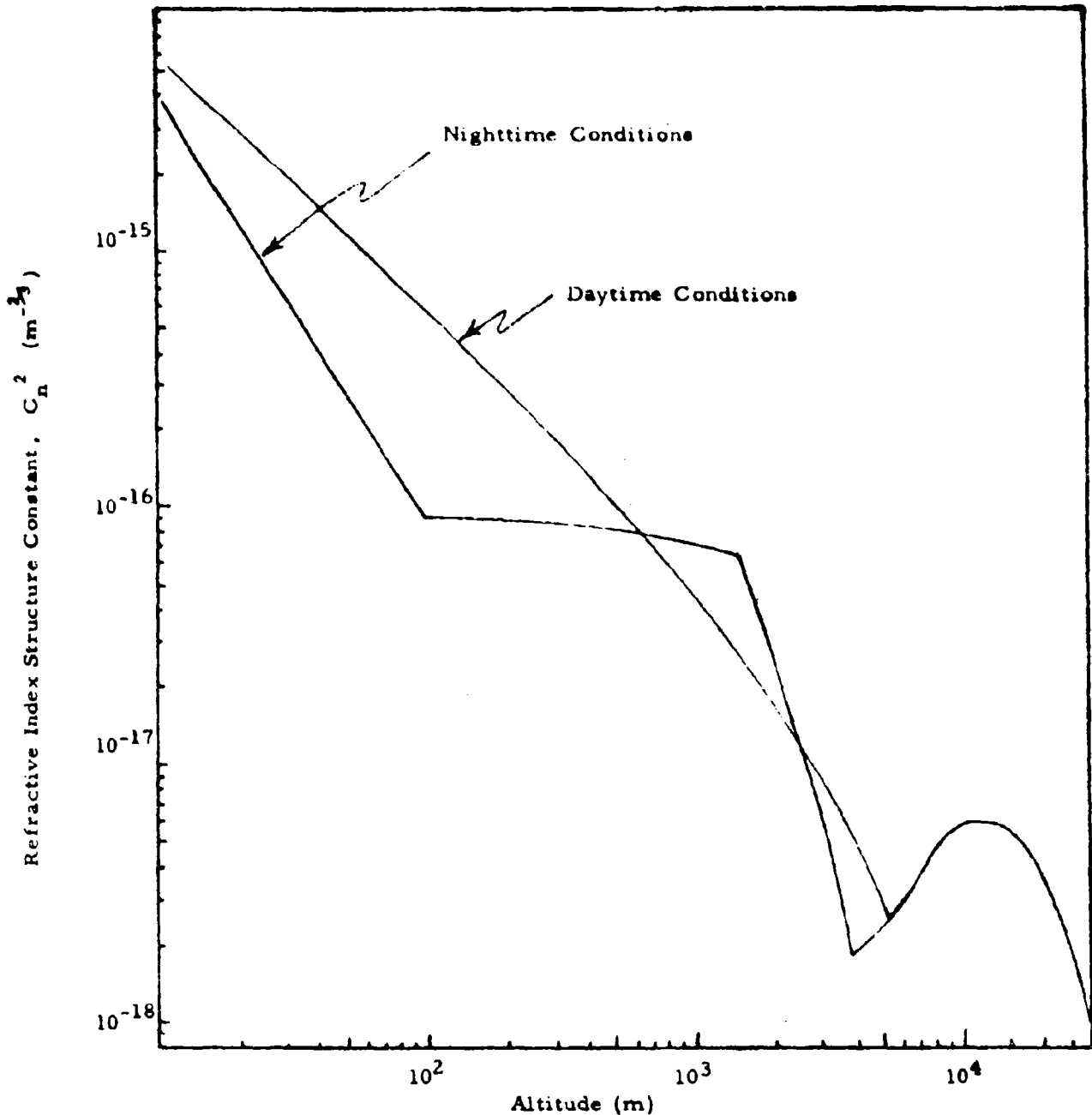


Fig. 4 Suggested Model For The Vertical Distribution Of The Refractive Index Structure Constant, C_n^2 . This model is based on the temperature probe data of Koprov and Tsyang¹⁴, on near the ground laser scintillation measurements¹⁵ of C_n^2 , and on stellar scintillation measurements.

A key point that should be noted about the distribution of C_n^2 is that it is such that evaluation of r_0 is dominated by conditions very near the ground. This suggests that altitude per se of the transmitter location will have no significant effect on r_0 (unless the altitude is so high that the local atmospheric density is reduced), and that data taken at an observatory on a mountain is applicable to almost any reasonable transmitter site.*

We shall base our evaluation of r_0 on the data taken by Hoag¹⁶, and shown in Fig. 5. (Equivalent data by Meinel¹⁷ is available and is in good agreement with Hoag's results.) These measurements are for a nominal center frequency of 5500 Å at near zenith. The slit width can be directly related to r_0 for a wavelength of 0.53 microns and of 1.06 microns. If the slit width is w (radians), then

$$r_{0,0.53} = 2.52 \times 10^{-7} / w, \quad (7a)$$

$$r_{0,1.06} = 5.71 \times 10^{-7} / w. \quad (7b)$$

From the data in Fig. 5, we see that the median value of w is about

$$w_{50\%} = 3.4 \times 10^{-6} \text{ rad.} \quad (8a)$$

However, half the time it is larger than that and results based on $w_{50\%}$

* Nothing said here should be taken to apply to the case of a transmitter located in a high altitude aircraft. There it is probable that boundary layer effects are dominant, and we currently have no sound data applicable to this situation.

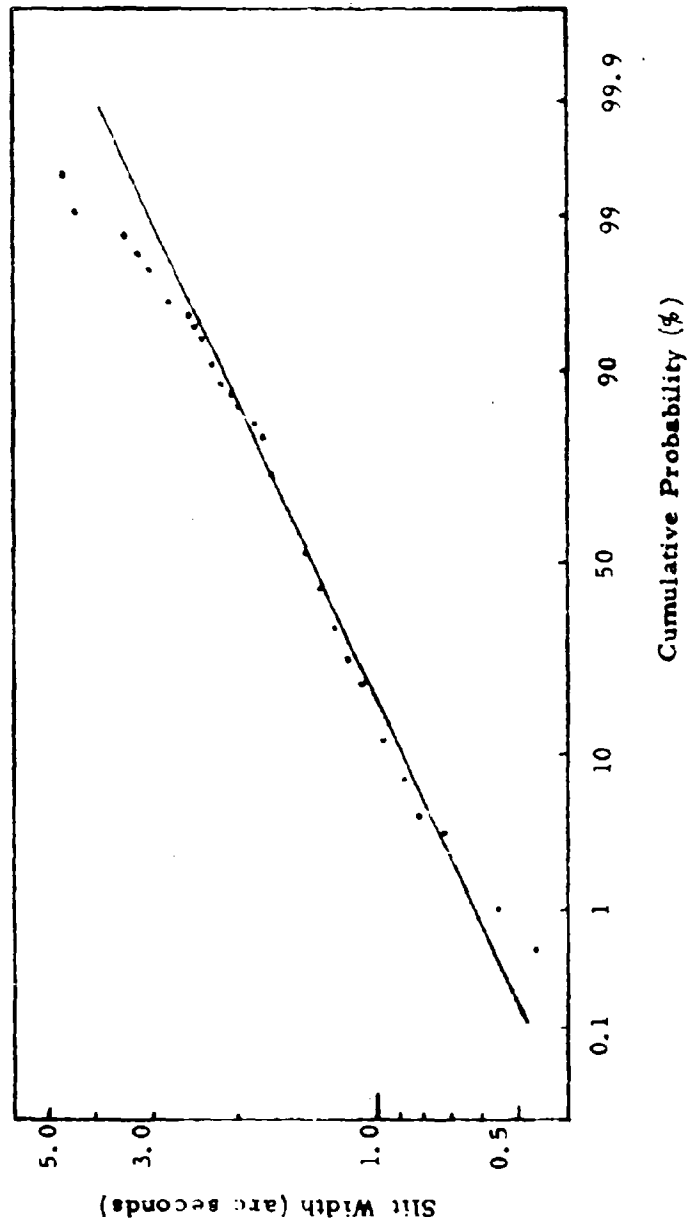


Fig. 5 Slit Width Required to Pass 68% of the Energy in a Stellar Image vs the Cumulative Probability of Occurrence, from Hoag's Data, Reference 16.

are, in a sense, optimistic. To introduce a more conservative note, we utilize the value of w that goes with 90%, so that we are sure that nine out of ten times w will be smaller and r_0 larger than our predictions. We get

$$w_{90\%} = 10.0 \times 10^{-6} \text{ rad.} \quad (8b)$$

We could substitute this value of w into Eq.'s (7a) and (7b), but first we wish to make allowance for the fact that we are interested in both day and night time operation, and that we will be operating at a zenith angle of about 40 degrees.* There is a correction factor of 0.64 for the night to day conversion, and of $\sec^{-\frac{3}{5}}(40^\circ) = 0.85$ for the zenith angle. Using these factors and the data in Eq.'s (7a and b) and (8a and b), we get the results shown in Table 5.**

Conclusions and Comments

The results shown in Table 5 for r_0 , coupled with the fact that Table 4 seems to indicate that we can not profitably use a transmitter diameter much larger than $0.5 r_0$, would certainly seem to be quite serious. The allowable diameters are disturbingly small. For the moment, we must consider these results to represent a true limit.

* This zenith angle corresponds to viewing an equatorial stationary satellite from a mid-latitude ground position.

** It is interesting to note that these values of r_0 fall into the general region of values presented by Kerr et al.¹⁸, in his Table V, although because of the way he developed his starting data, i.e., his expression for C_n^2 , we do not attach too much significance to this agreement.

Table 5
Estimated Values of r_0 (Meters)

		0.53 Microns	1.06 Microns
50%	Day	0.040	0.092
	Night	0.063	0.143
90%	Day	0.014	0.031
	Night	0.021	0.049

There is, however, an important but still quite unverified possibility that by utilizing a transmitter that was capable of following the high frequency (probably below 100 Hz) jitter in the apparent direction to the receiver, * thus compensating for a major portion of the effect of atmospheric turbulence, it will be possible to allow use of a transmitter diameter of perhaps 2 or 3 times r_0 without suffering serious modulation noise. We know from theoretical analysis¹⁹ that the average antenna gain will follow the increase in diameter, but we have no analysis of the effect on modulation noise of using high speed tracking. On the simplest basis for looking at the situation, namely the ratio of average antenna gain to free space antenna gain, we would expect about a factor of three in useful antenna diameter -- i.e., we should be able to go from $0.5 r_0$ to $1.5 r_0$, a factor of almost 10 dB, by using high speed tracking. There is reason to believe, however, that in correcting for wavefront tilt, we will be taking out the most severe aspect of atmospheric turbulence antenna gain modulation so that we will be able to use diameters as large as $2.5 r_0$ or $3.0 r_0$ without undue modulation loss.

* By tracking a beacon from the receiver, the transmitter can always tell what bending of the path the atmosphere is, at any instant, introducing between the transmitter and the receiver -- providing that the atmospheric turbulence isoplanatism patch covers the point ahead angle. Since the dominant turbulence is so near the ground, it is almost certain that the isoplanatism patch will be large enough.

References

1. D. L. Fried, Proc. IEEE 55, 57 (1967).
2. I. Goldstein, P. A. Miles, and A. Chabot, Proc. IEEE 53, 1172 (1965).
3. D. L. Fried, J. Q. E. 3, 213 (1967).
4. D. L. Fried, Appendix G, NASA SP-217, "Optical Space Communications," Proceedings of an MIT-NASA Workshop held at Williams College, Williamstown, Massachusetts, August 4-17, 1968.
5. Yura and Ludimerski, Rand Corporation, private communications.
6. R. L. Mitchel, J. Opt. Soc. Am. 58, 1267 (1968).
7. D. L. Fried and R. A. Schmeltzer, App. Opt. 6, 1729 (1967).
8. This can be easily obtained from Eq. 's (2.25) and (4.3) of D. L. Fried, J. Opt. Soc. Am. 56, 1380 (1966).
9. R. E. Hufnagel and N. R. Stanley, J. Opt. Soc. Am. 54, 52 (1964).
10. D. L. Fried and J. D. Cloud, J. Opt. Soc. Am. 56, 1667 (1966).
11. R. E. Hufnagel, in the report of the Woods Hole Summer Study, July 1966, on the "Restoration of Atmospherically Degraded Images, July 1966," National Research Council, National Academy of Science, Vol. 2, Appendix 3.
12. H. R. Hullett, J. Opt. Soc. Am. 57, 1335 (1967).
13. P. J. Titterton, J. Opt. Soc. Am. 60, 417 (1970)
14. V. M. Koprov and L. R. Tsvang, Izv. Atmos. and Ocean Phys. 2, 1142 (1966), translated on p. 705.
15. D. L. Fried, G. E. Mevers, and M. P. Keister, Jr., J. Opt. Soc. Am. 57, 787 (1967).
16. A. A. Hoag, Bulletin Astronomique, XXIV, Part 2, 269 (1964):
17. A. B. Meinel, "Final Report on the Site Selection Survey for the National Astronomical Observatory," Contributions from the Kitt Peak National Observatory, No. 45 (Oct. 1963).

References (Continued)

18. J. R. Kerr, P. J. Titterton, A. R. Kraemer, and C. R. Cooke,
Proc. IEEE 58, 1691 (1970).
19. D. L. Fried, J. Opt. Soc. Am. 56, 1372 (1966).

Appendix L

EFFECTS OF ATMOSPHERIC TURBULENCE
ON STATIC AND TRACKING OPTICAL HETERODYNE
RECEIVERS/AVERAGE ANTENNA GAIN
AND ANTENNA GAIN VARIATION

by

Dr. D. L. Fried
Consultant to LMSC

(Previously distributed as Technical Memorandum No. 14)

LOCKHEED PALO ALTO RESEARCH LABORATORY
LOCKHEED MISSILES & SPACE COMPANY
A GROUP DIVISION OF LOCKHEED AIRCRAFT CORPORATION

INTRODUCTION

It is well known that atmospheric turbulence will affect the performance of an optical heterodyne receiver. The effects have been explored experimentally and theoretically by a number of workers.¹⁻⁵ The single most prominent aspect effect of atmospheric turbulence on optical heterodyne detection is the fact that there is an upper limit on the average antenna gain achievable for any particular wavelength and set of propagation conditions. It has been shown^{2, 3} that for each wavelength and propagation path, there is an associated length r_0 which represents a measure of the atmospheric turbulence limit on an optical heterodyne receiver antenna gain. No matter how large we make the actual receiver diameter, D , the average antenna gain $\langle G \rangle$ achieved will not be larger than G_0 , the free space antenna gain associated with a receiver diameter r_0 . For an optical heterodyne receiver whose diameter is smaller than r_0 , the average antenna gain $\langle G \rangle$ follows the expected free space value for an antenna of that diameter; but for antennas larger than r_0 , the average antenna gain $\langle G \rangle$ asymptotically (and monotonically) approaches G_0 .^{*}

The use of the term "average" in describing $\langle G \rangle$, the average achieved antenna gain, is significant. Its use is indicative of the fact that atmospheric turbulence and its effects are random processes, characterizable only in terms of statistical parameters such as mean, variance, covariance, etc. The antenna gain achieved at any instant of time $G(t)$, is a randomly varying quantity whose mean value is $\langle G \rangle$. The variance σ_G^2 associated with $G(t)$ is generally a non-zero quantity. Its magnitude has been evaluated in previous work⁴, and it is found that for optical heterodyne receiver

^{*}This result needs to be qualified by the stated assumption that $r_0 \ll L_0$, where L_0 is the outer scale of turbulence. ($L_0 \sim 1$ meter or larger almost always so that for visible and near infrared radiation, in most cases $r_0 \ll L_0$.) In this regard, see A. F. Lutomirski and H. T. Yura, J. Opt. Soc. Am., 61, 482 (1971).

diameters D of the order of r_0 or larger, the value of σ_G^2 is comparable to or much larger than $\langle G \rangle^2$. This means that the heterodyne receiver signal strength carries substantial atmospheric modulation. In the parlance of communications engineering, we would say that a channel based on optical heterodyne reception with atmospheric turbulence effects is subject to fading, and that if the receiver diameter is of the order of r_0 or larger, then the fades will be quite deep. This, in turn, carries the implication that the channel performance will be significantly degraded below the expected free-space value. Available results^{5,7} show that for the type of fading statistics we expect due to the effect of atmospheric turbulence on an optical heterodyne receiver's antenna gain, namely a log-normal fading distribution, the degradation in channel performance can only be made up in a straightforward manner by transmitting considerably more optical power, which can be a rather severe penalty. The effect of fading is, in a sense, like a loss in the effective average antenna gain.

Since antenna gain variance, σ_G^2 , goes up with increasing antenna diameter, D , without bounds while the average antenna gain $\langle G \rangle$ does not increase significantly when the antenna diameter is increased beyond r_0 , it is apparent that the optimum performance condition, considering both effects of $\langle G \rangle$ and σ_G^2 is achieved with an optical heterodyne receiver diameter of the order of r_0 or less. Rudimentary calculations utilizing the results of references 4 and 6 indicate that best performance is to be expected with an antenna diameter about equal to $\frac{1}{2} r_0$. It is not our intention to pursue in this paper the subject of the implications of atmospheric turbulence induced antenna gain variance for an optical communications link utilizing heterodyne reception. Rather, we shall be concerned here with evaluation of a technique for minimizing the variance of the antenna gain, based on the use of tracking heterodyne reception.

TRACKING HETERODYNE RECEPTION

Some early and rather picturesque thinking regarding the nature of the optical effect of atmospheric turbulence depicted the atmosphere as acting like a random collection of wedges and lenses, resulting in "dancing" and defocus blurring of the image seen in a telescope. It was even suggested that a telescope capable of following this tilt and defocus by rapid adjustment of optical elements in the telescope might be able to achieve an image with sharpness much superior to what atmospheric turbulence normally allows. This subject was first investigated in a quantitative analytic manner by the present author in a paper titled "Statistics of a Geometric Interpretation of Wavefront Distortion."⁶ In this investigation, the statistics of the distortion of a wavefront after passing through a turbulent atmospheric path was quantified in terms of the accuracy of the fit of simple geometric shapes (tilted planes, spherical surfaces, and hyperbolic surfaces) to the wavefront. In this analysis, it was found that much of the distortion could be represented as wavefront tilt, but that allowing matching to include higher order shapes yielded results that indicated no particular relevance should be attached to the particular nature of these higher order shapes.* It was shown that while the distorted wavefront in a circle (aperture) of diameter r_0 had an rms (complex) phase variation of one radian (neper), if we subtracted the best fit tilted plane match to the distorted wave, then the rms variation was one radian (neper) for a circle of diameter $3.4 r_0$. Based on this, it was suggested in that paper⁶ that short exposure imagery, which is possibly distorted

* Quantitatively, this means that while each shape type that we allowed in trying to match the wavefront represented an additional degree of freedom and therefore would improve the fit to some extent, the tilt adjustments gave more improvement than one would expect for the number of degrees of freedom involved, while the other higher order shapes gave no more improvement than one would expect simply because they represented additional degrees of freedom, i.e., tilt seemed to have a special ability to fit the distorted wavefront, which other shapes lacked.

by random wavefront tilt, but not blurred by such tilt, should have a resolution of the order of 3.4 times better than long exposure imagery, for which randomly varying tilt does result in blurring of the image. This suggestion was investigated analytically⁸ and it was found that an improvement like this, although not quite as large as first suggested, could be achieved.

It was also suggested in the paper on the geometric interpretation of wavefront distortion⁸ that the good match to the distorted wavefront achieved by an optimally tilted plane meant that for optical heterodyne reception, while an ordinary (or what we shall call a static) optical heterodyne receiver had an average antenna gain limitation associated with an aperture diameter r_0 , a tracking optical heterodyne receiver, i.e., a receiver which at the necessary rate tracked the apparent tilt of the received wavefront, would have an atmospheric turbulence limit on the average antenna gain that would be associated with an aperture diameter of $3.4 r_0$. This would suggest an increase of 11.4 in the average antenna gain.* The tracking heterodyne receiver per se was first analyzed by Chase⁹. He was able to show that the maximum average antenna gain was achieved with a receiver diameter of about $3.4 r_0$ (in agreement with previous suggestions), although because of a problem in evaluating integrals, Chase did not give detailed numerical results for the expected average antenna gain as a function of receiver diameter.

Because of the problems associated with atmospheric turbulence induced modulation noise, i.e., antenna gain variance, σ_G^2 , in an ordinary static optical heterodyne receiver, we are now motivated to reexamine the

* Based on the more exact analysis for short exposure resolution in reference 9, which is nearly equivalent to the analysis for a tracking heterodyne receiver, this factor of 11.4 was later revised downward to only 4.3.

performance of the tracking optical heterodyne receiver -- in particular, to evaluate its antenna gain variance. (We shall also develop quantitative results for the average antenna gain.) Our motivation is based on the fact that a tracking receiver will be subject to less apparent wavefront distortion than a static receiver of the same aperture diameter, and therefore should manifest less variability in its antenna gain.

In the next section, we address ourselves to the problem of the formulation of expressions for the instantaneous antenna gain, the average antenna gain, and the antenna gain variance for both the static and tracking optical heterodyne receivers. In the section after that, we concern ourselves with the reduction of these expressions to calculable form. Finally, we carry out the numerical evaluations, present the results, and discuss their interpretation and significance.

FORMULATION

The basic expression for G , the instantaneous signal-to-noise ratio, or antenna gain of an optical heterodyne receiver operating with an optical signal whose wavefront has been distorted by atmospheric turbulence can be obtained from reference 3. Assuming a receiver with a circular aperture of diameter D , the expression is

$$G = \alpha D^{-2} \iint d\vec{x}_1 d\vec{x}_2 W_0(\vec{x}_1; D) W_0(\vec{x}_2; D) \exp [i(\vec{x}_1) + i(\vec{x}_2)] \times \cos [\varphi(\vec{x}_1) - \varphi(\vec{x}_2)] . \quad (1)$$

In this expression, α is a constant of proportionality and the function $W_0(\vec{x}; D)$ defines a circle of diameter D on the \vec{x} -plane. (Here and in the balance of this paper \vec{x} is a two-dimensional vector defined in the receiver aperture plane.) $W_0(\vec{x}; D)$ is defined by the expression

$$W_0(\vec{x}; D) = \begin{cases} 1 & \text{if } x \leq D/2 \\ 0 & \text{if } x > D/2 \end{cases} \quad (2)$$

The integrations over \vec{x}_1 and \vec{x}_2 are to be taken over the infinite plane, but the presence of the W_0 -functions in the integrand, in effect, limits the range of the integrations. $L(\vec{x})$ and $\varphi(\vec{x})$, called the log-amplitude fluctuation and the phase fluctuation, respectively, represent the perturbations imposed on the received wavefront by atmospheric turbulence. The log-amplitude variation, $L(\vec{x})$, is, as its name implies, the logarithm of the local wave amplitude variation at \vec{x} caused by atmospheric turbulence. The reference amplitude for definition purposes is the rms of the varying amplitude. The phase variation, $\varphi(\vec{x})$, is just the variation in the ordinary phase at \vec{x} induced by atmospheric turbulence. It is often convenient to combine phase and log-amplitude variation into a single complex quantity, the complex-phase variation, denoted by $\psi(\vec{x})$, where

$$\psi(\vec{x}) = \varphi(\vec{x}) - i L(\vec{x}). \quad (3)$$

For many purposes, there is no need to distinguish between the real and the imaginary parts of $\psi(\vec{x})$.

There is fairly good evidence available that the statistics of phase and log-amplitude fluctuations are each normally distributed¹¹⁻¹⁴. This means that the statistics of each of these quantities are completely defined by their first and second moments. Moreover, since the statistics are apparently locally homogeneous and isotropic¹⁵, and since we shall only be interested in the statistics of the difference of phase fluctuations measured at two points, \vec{x}_1 and \vec{x}_2 , we shall not need to consider the first moment of phase fluctuation.

i.e., the mean value of phase fluctuation*. The following are the statistical quantities we shall make use of in this paper: the mean value of log-amplitude \bar{L} , where

$$\bar{L} = \langle L(\vec{x}) \rangle, \quad (4a)$$

the log-amplitude covariance, $C_L(\rho)$, where

$$C_L(\rho) = \langle [L(\vec{x}_1) - \bar{L}] [L(\vec{x}_0) - \bar{L}] \rangle, \quad (4b)$$

the log-amplitude variance, σ_L^2 , where

$$\sigma_L^2 = C_L(0), \quad (4c)$$

the log-amplitude-structure function, $D_L(\rho)$, where

$$D_L(\rho) = \langle [L(\vec{x}_1) - L(\vec{x}_0)]^2 \rangle, \quad (4d)$$

the phase-structure function,

$$D_\varphi(\rho) = \langle [\varphi(\vec{x}_1) - \varphi(\vec{x}_0)]^2 \rangle, \quad (4e)$$

and the wave-structure function, $D_\psi(\rho)$, where

$$D_\psi(\rho) = \langle [\psi(\vec{x}_1) - \psi(\vec{x}_0)]^* [\psi(\vec{x}_1) - \psi(\vec{x}_0)] \rangle. \quad (4f)$$

In the above, the angle brackets, i.e., $\langle \cdot \rangle$ denote an ensemble average, and in Eq. (4f), the asterisk, $*$, denotes complex conjugation. ρ is the magnitude of the distance between \vec{x}_1 and \vec{x}_0 , and is defined by the expression

$$\rho = |\vec{x}_1 - \vec{x}_0|. \quad (5)$$

* It is fortunate that we do not need to consider the mean value of phase fluctuation (or even the variance of phase fluctuation) since the presently available theory does not treat the low spatial frequency portion of the atmospheric turbulence spectrum in proper detail, and, as a consequence, if the presently available theory is used to calculate these quantities, divergent results are obtained.

It is obvious from Eq.'s (3) and (4d, e, and f) that the wave-structure function is simply the sum of the log-amplitude and phase-structure functions, i.e.,

$$D_{\psi}(\rho) = D_L(\rho) + D_{\phi}(\rho). \quad (6)$$

It can be shown¹⁸ that under normal circumstances*, the wave structure function is given by the expression

$$D_{\psi}(\rho) = 6.88 (\rho/r_0)^{5/3}, \quad (7)$$

where r_0 is the quantity introduced in the previous section in terms of the limits on performance of a heterodyne receiver. r_0 is a function of the wavelength and of the length of the propagation path and the distribution of the strength of turbulence along that path.

We shall have occasion to make use of the fact that

$$D_L(\rho) = 2[\sigma_L^2 - C_L(\rho)], \quad (8)$$

which relationship can be derived quite easily from Eq.'s (4b, c, and d). An interesting feature regarding the statistics of log-amplitude variance is that in order for energy to be conserved, it can be shown that⁹

$$\overline{L} = -\sigma^2, \quad (9)$$

which follows from the fact that log-amplitude variance is normally distributed, and that the reference value for L is taken as the rms value.

* The term "normal conditions" refers to the absence of strong intensity scintillation and the absence of the phenomena known as saturation of scintillation. The variety of distinct derivations available for Eq. (7) makes it likely that it is valid even under conditions of saturation of scintillation--although we have no assurance of this. For this reason, we restrict our attention in this paper to "normal circumstances", that is conditions of relatively weak intensity scintillation, values of σ_L^2 about 0.5 or less.

We shall also make use of the fact that if α and β are two independent gaussian random variables with mean values $\bar{\alpha}$ and $\bar{\beta}$, and if a and b are two arbitrary constants, then³

$$\langle \exp (a \alpha + b \beta) \rangle = \exp \left\{ \frac{1}{2} [a^2 \langle (\alpha - \bar{\alpha})^2 \rangle + b^2 \langle (\beta - \bar{\beta})^2 \rangle + (a \bar{\alpha} + b \bar{\beta})] \right\}. \quad (10)$$

The concept of a tracking optical heterodyne receiver is based on the fact that for any particular random sample of wavefront distortion over an aperture, there is a corresponding random vector \vec{a} which, in a minimum mean square deviation sense, most accurately provides a match through the function $\vec{a} \cdot \vec{x}$ to the distorted wavefront phase $\varphi(\vec{x})$.^{*} The tracking optical heterodyne receiver is continuously adjusting its operation to correct for this tilt, so that it sees a distorted wavefront with log-amplitude and phase fluctuation which appear to be $l(\vec{x})$ and $\varphi(\vec{x}) - \vec{a} \cdot \vec{x}$. This means that the instantaneous antenna gain for tracking optical heterodyne detection, which we denote by \hat{G} , is, in analogy with Eq. (1), given by the expression

$$\hat{G} = \alpha D^{-2} \iint d\vec{x}_1 d\vec{x}_2 W_0(\vec{x}_1; D) W_0(\vec{x}_2; D) \exp [l(\vec{x}_1) + l(\vec{x}_2)] \times \cos \{ [\varphi(\vec{x}_1) - \vec{a} \cdot \vec{x}_1] - [\varphi(\vec{x}_2) - \vec{a} \cdot \vec{x}_2] \}. \quad (11)$$

In our calculations, we shall only be concerned with the statistics of \vec{a} in terms of $\langle \vec{a} \cdot \vec{a} \rangle$, and shall use the fact that \vec{a} , being derived by a linear process from $\varphi(\vec{x})$, must, like $\varphi(\vec{x})$, have a normal distribution. In reference 8, it is shown that

* We restrict the allowed values of \vec{a} , the tilt, to real values, although if we had allowed complex values, we could have matched $\vec{a} \cdot \vec{x}$ to the complex phase $\psi(\vec{x})$ rather than just the real part, $\varphi(\vec{x})$. Tracking of complex values of \vec{a} could be accomplished in a tracking optical heterodyne receiver by varying the local oscillator intensity across the aperture, although this will be quite a bit more involved than simply tracking a real \vec{a} . Because we are restricting our attention to weak intensity scintillation (cf. the previous note), the restriction of \vec{a} to real values and tracking only $\varphi(\vec{x})$ and not the entire $\psi(\vec{x})$ should impose no very great limitation on system performance. (For strong scintillation and saturation of scintillation, the situation is, of course, much more complex and some aspects appear to be beyond the capability of presently available theory.)

$$\langle \vec{a} \cdot \vec{a} \rangle = \frac{64}{\pi D^3} \int_0^1 u du [(12u - 8u^3)(1 - u^2)^{1/2} - 4 \cos^{-1} u] D_\varphi(Du), \quad (12)$$

where D is the diameter of the circular aperture over which we sample the wavefront and match \vec{a} . Substitution of Eq. (7) into this expression yields the result that

$$\langle \vec{a} \cdot \vec{a} \rangle = 2 \times 6.88 r_0^{-5/3} D^{-3/2} \quad (12')$$

The quantity we are ultimately interested in evaluating is the normalized antenna gain variance for the tracking heterodyne receiver, $\sigma_{\hat{G}}^2$. We define this quantity by the expression

$$\sigma_{\hat{G}}^2 = \frac{\langle (\hat{G} - \langle \hat{G} \rangle)^2 \rangle}{\langle \hat{G} \rangle^2}, \quad (13a)$$

although for completeness, we shall provide a parallel evaluation of the normalized antenna gain variance for the static optical heterodyne receiver, σ_G^2 , where

$$\sigma_G^2 = \frac{\langle (G - \langle G \rangle)^2 \rangle}{\langle G \rangle^2}, \quad (13b)$$

as well as, of course, calculating the average antenna gain for the tracking and the static systems, $\langle \hat{G} \rangle$ and $\langle G \rangle$, respectively. Making use of the commutivity of integration and ensemble averaging, and recognizing that a product of two integrals can be rewritten as a double integral, it is quite easy to see from Eq.'s (1), (11), and (13a and b) that

$$\langle G \rangle = \alpha D^{-2} \iint d\vec{x}_1 d\vec{x}_2 W_0(\vec{x}_1; D) W_0(\vec{x}_2; D) \langle 1 \rangle, \quad (14a)$$

$$\langle \hat{G} \rangle = \alpha D^{-2} \iint d\vec{x}_1 d\vec{x}_2 W_0(\vec{x}_1; D) W_0(\vec{x}_2; D) \langle 2 \rangle, \quad (14b)$$

$$\sigma_G^2 = [\langle G \rangle^{-2} \alpha^2 D^{-4} \iiint d\vec{x}_1 d\vec{x}_2 d\vec{x}_3 d\vec{x}_4 W_0(\vec{x}_1; D) W_0(\vec{x}_2; D) \times W_0(\vec{x}_3; D) W_0(\vec{x}_4; D) \langle 3 \rangle] - 1, \quad (14c)$$

* The value given as 2 in Eq. (12') is apparently more precisely given as 2.05, but for convenience, we approximate it as 2.

$$\sigma_{\hat{G}}^2 = [\langle \hat{G} \rangle^2 \alpha^2 D^{-4} \int \int \int \int d\vec{x}_1 d\vec{x}_2 d\vec{x}_3 d\vec{x}_4 W_0(\vec{x}_1; D) W_0(\vec{x}_2; D) \\ \times W_0(\vec{x}_3; D) W_0(\vec{x}_4; D) \langle 4 \rangle]^{-1}, \quad (14d)$$

where

$$\langle 1 \rangle = \langle \exp [L(\vec{x}_1) + L(\vec{x}_2)] \cos [\varphi(\vec{x}_1) - \varphi(\vec{x}_2)] \rangle, \quad (15a)$$

$$\langle 2 \rangle = \langle \exp [L(\vec{x}_1) + L(\vec{x}_2)] \cos [[\varphi(\vec{x}_1) - \vec{a} \cdot \vec{x}_1] - [\varphi(\vec{x}_2) - \vec{a} \cdot \vec{x}_2]] \rangle, \quad (15b)$$

$$\langle 3 \rangle = \langle \exp [L(\vec{x}_1) + L(\vec{x}_2) + L(\vec{x}_3) + L(\vec{x}_4)] \cos [\varphi(\vec{x}_1) - \varphi(\vec{x}_2)] \\ \times \cos [\varphi(\vec{x}_3) - \varphi(\vec{x}_4)] \rangle, \quad (15c)$$

$$\langle 4 \rangle = \langle \exp [L(\vec{x}_1) + L(\vec{x}_2) + L(\vec{x}_3) + L(\vec{x}_4)] \cos [[\varphi(\vec{x}_1) - \vec{a} \cdot \vec{x}_1] \\ - [\varphi(\vec{x}_2) - \vec{a} \cdot \vec{x}_2]] \cos [[\varphi(\vec{x}_3) - \vec{a} \cdot \vec{x}_3] - [\varphi(\vec{x}_4) - \vec{a} \cdot \vec{x}_4]] \rangle. \quad (15d)$$

SIMPLIFICATION AND REDUCTION

In order to present the simplifications and reductions in the most easy to follow manner, we shall adopt an orderly approach of subtasks of incrementally increasing complexity, each drawing as much as possible on the preceding. We shall first consider the evaluation of $\langle G \rangle$, then of $\langle \hat{G} \rangle$, and then of σ_G^2 , and only finally as the most complex of the tasks, of $\sigma_{\hat{G}}^2$.

The treatment of $\langle G \rangle$ follows that presented in reference 3. We start by noting that because of the isotropy of propagation statistics $[L(\vec{x}_1) + L(\vec{x}_2)]$ is independent of $[\varphi(\vec{x}_1) - \varphi(\vec{x}_2)]$ since

$$\langle [L(\vec{x}_1) + L(\vec{x}_2)] [\varphi(\vec{x}_1) - \varphi(\vec{x}_2)] \rangle = 0, \quad (16)$$

and since the two are gaussian, which means that if their lowest non-trivial joint moment has zero value, then so do all of their joint moments. The validity of Eq. (16) follows from the fact that interchange of \vec{x}_1 and \vec{x}_2 does nothing more than introduce a 180° rotation so that consideration of isotropy leads to the conclusion that the l. h. s. of Eq. (16) must be unchanged, but

manifestly the interchange of \vec{x}_1 and \vec{x}_2 reverses the sign of the contents of the angle brackets. The only way both considerations can be satisfied is for the l.h.s. of Eq. (16) to vanish, hence the validity of Eq. (16). From this it follows that we can rewrite (1) as

$$\langle 1 \rangle = \langle \exp [l(\vec{x}_1) + l(\vec{x}_2)] \rangle \langle \cos [\varphi(\vec{x}_1) - \varphi(\vec{x}_2)] \rangle, \quad (17)$$

Now, by making use of Eq.'s (4a, b, and c), (8), (9), and (10), we can show that

$$\langle \exp [l(\vec{x}_1) + l(\vec{x}_2)] \rangle = \exp [-\frac{1}{2} D_\rho(\rho)], \quad (18a)$$

and that

$$\langle \cos [\varphi(\vec{x}_1) - \varphi(\vec{x}_2)] \rangle = \exp [-\frac{1}{2} D_\varphi(\rho)], \quad (18b)$$

so that in accordance with Eq. (6),

$$\langle 1 \rangle = \exp [-\frac{1}{2} D_\rho(\rho)]. \quad (19)$$

(To obtain Eq. (18b), we had to decompose the cosine into its exponential form.)

If we now combine Eq.'s (14a) and (19), we see that

$$\langle G \rangle = \alpha D^{-2} \int \int d\vec{x}_1 d\vec{x}_2 W_0(\vec{x}_1; D) W_0(\vec{x}_2; D) \exp [-\frac{1}{2} D_\rho(\rho)]. \quad (20)$$

If we transform the variables of integration from \vec{x}_1, \vec{x}_2 to $\vec{\rho}, \vec{\sigma}$ where

$$\vec{\rho} = \vec{x}_1 - \vec{x}_2 \quad (21a)$$

$$\vec{\sigma} = \frac{1}{2} (\vec{x}_1 + \vec{x}_2), \quad (21b)$$

and define the function $W_1(\rho; D)$ by the equation

$$W_1(\vec{\rho}; D) = \int d\vec{\sigma} W_0(\vec{\sigma} + \frac{1}{2}\vec{\rho}; D) W_0(\vec{\sigma} - \frac{1}{2}\vec{\rho}; D), \quad (22)$$

then we see that Eq. (20) can be rewritten as

$$\langle G \rangle = 2\pi \alpha D^{-3} \int_0^D \rho d\rho W_1(\bar{\rho}; D) \exp \left[-\frac{1}{2} D_1(\rho) \right]. \quad (23)$$

[Here we have viewed the ρ -integration as being over polar-coordinates and have made use of the fact that $W_1(\bar{\rho}; D)$ is dependent only on the magnitude and not the orientation of $\bar{\rho}$, to allow us to perform the angular part of the integration, thereby developing the factor of 2π .] Consideration of the nature of the integrand in Eq. (22) makes it clear that it is a function equal to unity in a region in $\vec{\sigma}$ -space corresponding to the overlap of two circles of diameter D and a distance $\bar{\rho}$ apart (center-to-center), and equal to zero elsewhere. This makes $W_1(\bar{\rho}; D)$ equal to the area of overlap of the two circles. From simple trigonometric analysis, it can be shown that

$$W_1(\bar{\rho}; D) = \begin{cases} \frac{1}{2} D^2 \{ \cos^{-1}(\rho/D) - (\rho/D) [1 - (\rho/D)^2]^{\frac{1}{2}} \} & \text{if } \rho \leq D \\ 0 & \text{if } \rho > D, \end{cases} \quad (24)$$

so that quite obviously the limits on the integration in Eq. (23) are somewhat redundant. If we substitute Eq.'s (7) and (24) into Eq. (23), and choose α to be equal to $(4/\pi r_0)^3$, we get

$$\langle G \rangle = \frac{16}{\pi} \left(\frac{D}{r_0} \right)^3 \int_0^1 u du [\cos^{-1} u - u(1 - u^2)^{\frac{1}{2}}] \exp \left[-3.44 (D/r_0)^3 \frac{u^6}{u^3} \right]. \quad (25)$$

This particular choice of value for α insures that the asymptotic value of $\langle G \rangle$ for very large values of (D/r_0) is unity. This completes the reduction and simplification for $\langle G \rangle$, since the u -integration can be quite easily carried out on a digital computer.

Our treatment of $\langle \hat{G} \rangle$ follows essentially the same procedure, except that we need to call attention to three lemmas, first presented in reference 9. These are that (1) the distribution of \bar{a} , like that of φ and l

is gaussian; (II) the distribution of $[\varphi(\vec{x}) - \vec{a} \cdot \vec{x}]$ is independent of the distribution of \vec{a} ; and (III) the distribution of $\{[\varphi(\vec{x}_1) - \vec{a} \cdot \vec{x}_1] - [\varphi(\vec{x}_0) - \vec{a} \cdot \vec{x}_0]\}$ is independent of the distribution of $[\varphi(\vec{x}_1) + \varphi(\vec{x}_0)]$. Lemma I follows from the fact that \vec{a} is determined as a linear function of φ . Lemma II follows from a plausability argument regarding the independence of the sign of \vec{a} (i.e., \vec{a} and $-\vec{a}$ should be equally likely), quite separate from the nature of the higher order distortions of the wavefront. Lemma III follows from an isotropy argument, equivalent to that leading to Eq. (16), together with Lemma I.

Lemma (III) allows us to rewrite Eq. (15b) as

$$\langle 2 \rangle = \langle \exp [l(\vec{x}_1) + l(\vec{x}_0)] \rangle \langle \cos \{[\varphi(\vec{x}_1) - \vec{a} \cdot \vec{x}_1] - [\varphi(\vec{x}_0) - \vec{a} \cdot \vec{x}_0]\} \rangle. \quad (26)$$

From Lemma (I), it follows that the argument of the cosine in Eq. (26) has a gaussian distribution, so that with the cosine written in its exponential form, and recalling Eq. (18a), we get

$$\langle 2 \rangle = \exp \left[-\frac{1}{2} D_f(\rho) \right] \exp \left(-\frac{1}{2} \langle \{[\varphi(\vec{x}_1) - \vec{a} \cdot \vec{x}_1] - [\varphi(\vec{x}_0) - \vec{a} \cdot \vec{x}_0]\}^2 \rangle \right). \quad (27)$$

With a little manipulation, we can show that

$$\begin{aligned} \langle \{[\varphi(\vec{x}_1) - \vec{a} \cdot \vec{x}_1] - [\varphi(\vec{x}_0) - \vec{a} \cdot \vec{x}_0]\}^2 \rangle &= \langle [\varphi(\vec{x}_1) - \varphi(\vec{x}_0)]^2 \rangle \\ &- \langle [\vec{a} \cdot (\vec{x}_1 - \vec{x}_0)]^2 \rangle + 2 \langle \{[\varphi(\vec{x}_1) - \vec{a} \cdot \vec{x}_1] - [\varphi(\vec{x}_0) - \vec{a} \cdot \vec{x}_0]\} \\ &\times \vec{a} \cdot (\vec{x}_1 - \vec{x}_0) \rangle \end{aligned} \quad (28)$$

Lemma II implies that the last term on the r.h.s. of Eq. (28) equals zero. Since \vec{a} is an isotropically distributed random variable, while $(\vec{x}_1 - \vec{x}_0)$ is a non-random quantity, then it follows that

$$\begin{aligned} \langle [\vec{a} \cdot (\vec{x}_1 - \vec{x}_0)]^2 \rangle &= \frac{1}{2} \langle \vec{a} \cdot \vec{a} \rangle |\vec{x}_1 - \vec{x}_0|^2 \\ &= \frac{1}{2} \langle \vec{a} \cdot \vec{a} \rangle \rho^2. \end{aligned} \quad (29)$$

Now, also recalling Eq. (4e), we see that we can write

$$\langle [\varphi(\vec{x}_1) - \vec{a} \cdot \vec{x}_1] - [\varphi(\vec{x}_2) - \vec{a} \cdot \vec{x}_2] \rangle^2 = D_\varphi(\rho) - \frac{1}{2} \langle \vec{a} \cdot \vec{a} \rangle \rho^2, \quad (30)$$

so that, with Eq.'s (6), (7), and (12'), we get

$$\langle 2 \rangle = \exp \left\{ -\frac{1}{2} D_\varphi(\rho) [1 - (\rho/D)^{\frac{1}{2}}] \right\}. \quad (31)$$

Now, with exactly the same simplifications in treating the double vector-integration in Eq. (14b), that we previously applied in evaluating $\langle G \rangle$, we get for $\langle \hat{G} \rangle$,

$$\langle \hat{G} \rangle = \frac{16}{\pi} \left(\frac{D}{r_0} \right)^3 \int_0^1 u \, du [\cos^{-1} u - u(1-u^2)^{\frac{1}{2}}] \exp [-3.44(D/r_0)^{\frac{5}{2}} u^{\frac{5}{2}}(1-u^{\frac{1}{2}})]. \quad (32)$$

In this form, we can now carry out our evaluation of $\langle \hat{G} \rangle$ by simple numerical integration, and may, therefore, consider our treatment of $\langle \hat{G} \rangle$ complete to the extent intended in this section. We now proceed to the treatment of σ_G^2 .

We start our simplification of σ_G^2 by substituting Eq. (15c) into Eq. (14c), making use of the fact that $2 \cos A \cos B = \cos(A+B) + \cos(A-B)$ to get the product of cosines into a single cosine function, and then using our ability to simply interchange the two variables of integration labeled \vec{x}_2 and \vec{x}_4 so as to get the terms corresponding to $\cos(A+B)$ and to $\cos(A-B)$ into the same form. Thus we get

$$\sigma_G^2 = \left[\langle G \rangle^{-2} \left(\frac{4}{\pi r_0} \right)^4 D^{-4} \iiint \int d\vec{x}_1 d\vec{x}_2 d\vec{x}_3 d\vec{x}_4 W_0(\vec{x}_1; D) W_0(\vec{x}_2; D) W_0(\vec{x}_3; D) \right. \\ \left. \times W_0(\vec{x}_4; D) \langle 3' \rangle \right] - 1 \quad (33)$$

where

$$\langle 3' \rangle = \langle \exp [l(\vec{x}_1) + l(\vec{x}_2) + l(\vec{x}_3) + l(\vec{x}_4)] \cos [\varphi(\vec{x}_1) - \varphi(\vec{x}_2) + \varphi(\vec{x}_3) - \varphi(\vec{x}_4)] \rangle. \quad (34)$$

We now invoke arguments regarding isotropy of the statistics to allow us to separate the averages over l and φ in Eq. (34), and thus can rewrite $\langle 3' \rangle$ as

$$\langle 3' \rangle = \langle \exp [l(\vec{x}_1) + l(\vec{x}_2) + l(\vec{x}_3) + l(\vec{x}_4)] \rangle \langle \cos [\varphi(\vec{x}_1) - \varphi(\vec{x}_2) + \varphi(\vec{x}_3) - \varphi(\vec{x}_4)] \rangle. \quad (35)$$

Now by making use of Eq. 's (4a, b, and d) and (10), we can, after some manipulation of terms, write

$$\begin{aligned} \langle \exp [l(\vec{x}_1) + l(\vec{x}_2) + l(\vec{x}_3) + l(\vec{x}_4)] \rangle = & \exp \left\{ -\frac{1}{2} [D_l(|\vec{x}_1 - \vec{x}_2|) - D_l(|\vec{x}_1 - \vec{x}_3|) \right. \\ & + D_l(|\vec{x}_1 - \vec{x}_4|) + D_l(|\vec{x}_2 - \vec{x}_3|) - D_l(|\vec{x}_2 - \vec{x}_4|) + D_l(|\vec{x}_3 - \vec{x}_4|) \\ & \left. + C_l(|\vec{x}_1 - \vec{x}_3|) + C_l(|\vec{x}_2 - \vec{x}_4|)] \right\}. \end{aligned} \quad (36)$$

The fact that for any values of a , b , c , and d

$$\begin{aligned} (a - b + c - d)^\eta = & (a - b)^\eta - (a - c)^\eta + (a - d)^\eta + (b - c)^\eta - (b - d)^\eta \\ & + (c - d)^\eta; \quad \text{for } \eta = 1 \text{ or } 2. \end{aligned} \quad (37)$$

allows us, upon consideration of Eq. 's (4c) and (10), to write down by inspection

$$\begin{aligned} \langle \cos [\varphi(\vec{x}_1) - \varphi(\vec{x}_2) + \varphi(\vec{x}_3) - \varphi(\vec{x}_4)] \rangle = & \exp \left\{ -\frac{1}{2} [D_\varphi(|\vec{x}_1 - \vec{x}_2|) - D_\varphi(|\vec{x}_1 - \vec{x}_3|) \right. \\ & + D_\varphi(|\vec{x}_1 - \vec{x}_4|) + D_\varphi(|\vec{x}_2 - \vec{x}_3|) - D_\varphi(|\vec{x}_2 - \vec{x}_4|) + D_\varphi(|\vec{x}_3 - \vec{x}_4|)] \left. \right\} \end{aligned} \quad (38)$$

where in applying Eq. (10), we have considered the cosine function to be replaced by its exponential representation.

Now, by taking note of Eq. (6), we see that

$$\begin{aligned} \langle 3' \rangle = & \exp \left\{ -\frac{1}{2} [D_\varphi(|\vec{x}_1 - \vec{x}_2|) - D_\varphi(|\vec{x}_1 - \vec{x}_3|) + D_\varphi(|\vec{x}_1 - \vec{x}_4|) + D_\varphi(|\vec{x}_2 - \vec{x}_3|) \right. \\ & \left. - D_\varphi(|\vec{x}_2 - \vec{x}_4|) + D_\varphi(|\vec{x}_3 - \vec{x}_4|)] + 2 [C_l(|\vec{x}_1 - \vec{x}_3|) + C_l(|\vec{x}_2 - \vec{x}_4|)] \right\}. \end{aligned} \quad (39)$$

We now make use of Eq. (7) and argue that inasmuch as Eq. (37) is valid for $\eta = 1$ and for $\eta = 2$, it should be approximately valid for $\eta = 5/3$. (Certain minor deficiencies in this approximation will become apparent later in our analysis, and we shall introduce appropriate corrections at that time.) This permits us to write

$$\langle 3' \rangle = \exp \left\{ -\frac{1}{2} D_{\downarrow} (|\vec{x}_1 - \vec{x}_2 + \vec{x}_3 - \vec{x}_4|) + 2[C_L(|\vec{x}_1 - \vec{x}_3|) + C_L(|\vec{x}_2 - \vec{x}_4|)] \right\}. \quad (40)$$

We now substitute the expression back into Eq. (33) and argue that except in cases of very severe intensity scintillation, which lie outside the bounds of our treatment, the dominant effect governing the performance of the optical heterodyne receiver is due to phase distortion and is contained in the D_{\downarrow} -term. As far as receiver gain variations are concerned, the C_L -terms in Eq. (40) can be thought of as contributing basically in terms of the variation in total signal power incident on the heterodyne receiver aperture. The fact that the terms have an \vec{x} -dependence rather than being simply of the form of $C_L(0)$ can be considered to represent the fact that the variation in total power onto the aperture is less than $C_L(0)$ because of aperture averaging. Aperture averaging is treated in reference 14, where it is shown that the signal power collected in an aperture of diameter D has a variance given by $\Theta[\exp(4\sigma_L^2) - 1]$, where σ_L^2 is, of course, just the log-amplitude variance and Θ is a quantity called the aperture averaging factor. Θ is a function of (D/ρ_0) , where ρ_0 is the correlation distance for log-amplitude variations. ρ_0 is of the order of $(L\lambda)^{1/2}$ where λ is the optical wavelength and L is the propagation path length, or for a non-uniform path such as one vertically through the atmosphere, the distance to the dominant turbulence region. For D/ρ_0 smaller than unity, Θ is of the order of unity, while for values of D/ρ_0 much larger than unity, Θ approaches a value of zero. For our purposes, rather than use the expression $\Theta[\exp(4\sigma_L^2) - 1]$ to

express aperture averaging, it is more convenient to work in terms of an aperture averaging factor, Θ' which has the same general characteristics as Θ as far as its (D/ρ_0) -dependence is concerned, but with somewhat different values incorporating a σ_L^2 -dependence so that the collected power variance can be written as $[\exp(4\Theta' \sigma_L^2) - 1]$.

The form of the Θ' -dependence, as well as the preceding argument concerning the significance of the C_L -dependence for Eq. (40) substituted into Eq. (33), leads us to the conclusion that it is reasonably accurate to write

$$\sigma_G^2 = \left\{ \langle G \rangle^{-2} \left(\frac{4}{\pi r_0} \right)^4 D^{-4} \exp(4\Theta' \sigma_L^2) \iiint d\vec{x}_1 d\vec{x}_2 d\vec{x}_3 d\vec{x}_4 W_0(\vec{x}; D) \times W_0(\vec{x}_1; D) W_0(\vec{x}_2; D) W_0(\vec{x}_3; D) \exp \left[-\frac{1}{2} D_\phi (|\vec{x}_1 - \vec{x}_2 + \vec{x}_3 - \vec{x}_4|) \right] \right\} - 1. \quad (41)$$

In order to simplify this quadruple vector integration, we first make the coordinate transformations that

$$\vec{\rho}_1 = \vec{x}_1 - \vec{x}_2; \quad \vec{\rho}_1' = \frac{1}{2}(\vec{x}_1 + \vec{x}_2), \quad (42a)$$

$$\vec{\rho}_2 = \vec{x}_3 - \vec{x}_4; \quad \vec{\rho}_2' = \frac{1}{2}(\vec{x}_3 + \vec{x}_4), \quad (42b)$$

so that we can write

$$\sigma_G^2 = \left\{ \langle G \rangle^{-2} \left(\frac{4}{\pi r_0} \right)^4 D^{-4} \exp(4\Theta' \sigma_L^2) \iint d\vec{\rho}_1 d\vec{\rho}_2 W_1(\vec{\rho}_1; D) W_1(\vec{\rho}_2; D) \times \exp \left[-\frac{1}{2} D_\phi (|\vec{\rho}_1 - \vec{\rho}_2|) \right] \right\} - 1, \quad (43)$$

where we have made use of Eq. (22) to allow us to perform the $\vec{\rho}_1'$ - and the $\vec{\rho}_2'$ -integrations. Now if we made the further transformation of variables that

$$\vec{\sigma} = \vec{\rho}_1 - \vec{\rho}_2; \quad \vec{\sigma}' = \frac{1}{2}(\vec{\rho}_1 + \vec{\rho}_2), \quad (44)$$

and define $W_2(\vec{\sigma}; D)$ as

$$W_2'(\vec{\sigma}; D) = \int d\vec{\sigma}' W_1(\vec{\sigma}' + \frac{1}{2}\vec{\sigma}; D) W_1(\vec{\sigma}' - \frac{1}{2}\vec{\sigma}; D), \quad (45)$$

then we can write σ_G^2 as

$$\sigma_G^2 = [\langle G \rangle^{-2} (512/\pi^3 r_0^4 D^4) \exp(4\theta^2 \sigma_A^2) \int d\sigma d\sigma' W_2'(\vec{\sigma}; D) \exp[-\frac{1}{2} D_\phi(\sigma)]]^{-1}. \quad (46)$$

In this form, we can consider the evaluation of σ_G^2 to be a straightforward matter involving a one-dimensional numerical integration, except that first we need a useable expression for W_2 . We have found that because of the nature of the boundary conditions involved in the integral in Eq. (45), we can not reduce this expression to less than a two-dimensional integral. With a little manipulation of terms, and recognizing that the integrand is such that we can divide the region of integration into four equivalent quadrants, and so need only carry out the integration over one of those four quadrants, we get the result that

$$W_2'(\vec{\sigma}; D) = D^2 \int_0^{P'} dp \int_0^{Q'} dq f(p + \frac{1}{2} \frac{\sigma}{D}, q) f(p - \frac{1}{2} \frac{\sigma}{D}, q), \quad (47a)$$

where

$$P' = 1 - \frac{1}{2} \frac{\sigma}{D}; \quad Q' = [1 - (p + \frac{1}{2} \frac{\sigma}{D})^2]^{\frac{1}{2}}, \quad (47b)$$

$$f(x, y) = \begin{cases} \cos^{-1}[(x^2 + y^2)^{\frac{1}{2}}] - (x^2 + y^2)^{\frac{1}{2}} [1 - (x^2 + y^2)]^{\frac{1}{2}} & \text{for } x^2 + y^2 < 1 \\ 0 & \text{for } x^2 + y^2 > 1. \end{cases}$$

This representation for W_2 is entirely adequate for numerical computation, so that we may consider our simplification of the expression complete, and will now proceed to the simplification of the expression for σ_G^2 . [However, before closing this section, we shall return to the form of the expression for σ_G^2 as given in Eq. (46) to introduce the corrections for the approximate

nature of Eq. (37) when used, as we have done, with $\eta = 5/3$, for the derivation of Eq. (40).]

We start our treatment of σ_G^2 by noting that the same arguments that allowed us to recast (3) as given by Eq. (15c) in the form of (3') as given by Eq. (35) are equally applicable to (4). For the purposes of evaluating σ_G^2 in Eq. (14d), we can replace (4) by (4'), where (4') is given by the expression

$$\begin{aligned} \langle 4' \rangle = & \langle \exp [l(\vec{x}_1) + l(\vec{x}_2) + l(\vec{x}_3) + l(\vec{x}_4)] \rangle \langle \cos \{ [\varphi(\vec{x}_1) - \vec{a} \cdot \vec{x}_1] \\ & - [\varphi(\vec{x}_2) - \vec{a} \cdot \vec{x}_2] + [\varphi(\vec{x}_3) - \vec{a} \cdot \vec{x}_3] - [\varphi(\vec{x}_4) - \vec{a} \cdot \vec{x}_4] \} \rangle. \end{aligned} \quad (48)$$

The ensemble average for the log-amplitude expression is given by Eq. (36). With the cosine function replaced by its exponential form, Eq. (10) allows us to write

$$\begin{aligned} & \langle \cos \{ [\varphi(\vec{x}_1) - \vec{a} \cdot \vec{x}_1] - [\varphi(\vec{x}_2) - \vec{a} \cdot \vec{x}_2] + [\varphi(\vec{x}_3) - \vec{a} \cdot \vec{x}_3] - [\varphi(\vec{x}_4) - \vec{a} \cdot \vec{x}_4] \} \rangle \\ & = \exp \left(-\frac{1}{2} \langle \{ [\varphi(\vec{x}_1) - \vec{a} \cdot \vec{x}_1] - [\varphi(\vec{x}_2) - \vec{a} \cdot \vec{x}_2] + [\varphi(\vec{x}_3) - \vec{a} \cdot \vec{x}_3] \right. \\ & \quad \left. - [\varphi(\vec{x}_4) - \vec{a} \cdot \vec{x}_4] \}^2 \rangle \right) \end{aligned} \quad (49)$$

By making use of Lemma II, as presented before to argue the independence of \vec{a} and $[\varphi(\vec{x}_i) - \vec{a} \cdot \vec{x}_i]$, and after extensive algebraic manipulations, we can obtain the result that

$$\begin{aligned} & \langle \{ [\varphi(\vec{x}_1) - \vec{a} \cdot \vec{x}_1] - [\varphi(\vec{x}_2) - \vec{a} \cdot \vec{x}_2] + [\varphi(\vec{x}_3) - \vec{a} \cdot \vec{x}_3] - [\varphi(\vec{x}_4) - \vec{a} \cdot \vec{x}_4] \}^2 \rangle \\ & = D_\varphi(|\vec{x}_1 - \vec{x}_2|) - D_\varphi(|\vec{x}_1 - \vec{x}_3|) + D_\varphi(|\vec{x}_1 - \vec{x}_4|) + D_\varphi(|\vec{x}_2 - \vec{x}_3|) \\ & \quad - D_\varphi(|\vec{x}_2 - \vec{x}_4|) + D_\varphi(|\vec{x}_3 - \vec{x}_4|) - \langle [\vec{a} \cdot (\vec{x}_1 - \vec{x}_2)]^2 \rangle + \langle [\vec{a} \cdot (\vec{x}_1 - \vec{x}_3)]^2 \rangle \\ & \quad - \langle [\vec{a} \cdot (\vec{x}_1 - \vec{x}_4)]^2 \rangle + \langle [\vec{a} \cdot (\vec{x}_2 - \vec{x}_3)]^2 \rangle - \langle [\vec{a} \cdot (\vec{x}_2 - \vec{x}_4)]^2 \rangle \\ & \quad - \langle [\vec{a} \cdot (\vec{x}_3 - \vec{x}_4)]^2 \rangle. \end{aligned} \quad (50)$$

With this equation substituted into Eq. (49) and that into Eq. (48), with Eq. (36) also substituted into Eq. (48), and taking note of Eq. (6), we can write

$$\begin{aligned} \langle 4' \rangle = \exp \left\{ - \frac{1}{2} \left[D_{\psi}(|\vec{x}_1 - \vec{x}_0|) - D_{\psi}(|\vec{x}_1 - \vec{x}_3|) + D_{\psi}(|\vec{x}_1 - \vec{x}_0|) + D_{\psi}(|\vec{x}_0 - \vec{x}_3|) \right. \right. \\ - D_{\psi}(|\vec{x}_0 - \vec{x}_4|) + D_{\psi}(|\vec{x}_3 - \vec{x}_4|) - \langle [\vec{a} \cdot (\vec{x}_1 - \vec{x}_0)]^2 \rangle + \langle [\vec{a} \cdot (\vec{x}_1 - \vec{x}_3)]^2 \rangle \\ - \langle [\vec{a} \cdot (\vec{x}_1 - \vec{x}_0)]^2 \rangle - \langle [\vec{a} \cdot (\vec{x}_0 - \vec{x}_3)]^2 \rangle + \langle [\vec{a} \cdot (\vec{x}_0 - \vec{x}_4)]^2 \rangle \\ \left. \left. - \langle [\vec{a} \cdot (\vec{x}_3 - \vec{x}_4)]^2 \rangle \right] + 2[C_L(|\vec{x}_1 - \vec{x}_3|) + C_L(|\vec{x}_0 - \vec{x}_4|)] \right\}. \end{aligned} \quad (51)$$

Now if we make use of Eq. (30) with the argument that the equation is approximately valid with $\eta = 5/3$, and take note of Eq. (9), then we can combine all of the D_{ψ} -terms in Eq. (51) into a single term equal to $D_{\psi}(|\vec{x}_1 - \vec{x}_0 + \vec{x}_3 - \vec{x}_4|)$. Similarly, we can use Eq. (30), in its exact form with $\eta = 2$ to allow us to combine all of the $\vec{a} \cdot (\vec{x}_1 - \vec{x}_j)$ -terms into a single term equal to $\{ - \langle [\vec{a} \cdot (\vec{x}_1 - \vec{x}_0 + \vec{x}_3 - \vec{x}_4)]^2 \rangle \}$. Since \vec{a} is an isotropically distributed random vector, while $(\vec{x}_1 - \vec{x}_0 + \vec{x}_3 - \vec{x}_4)$ is a non-random vector, we can write

$$- \langle [\vec{a} \cdot (\vec{x}_1 - \vec{x}_0 + \vec{x}_3 - \vec{x}_4)]^2 \rangle = - \frac{1}{2} \langle \vec{a} \cdot \vec{a} \rangle |\vec{x}_1 - \vec{x}_0 + \vec{x}_3 - \vec{x}_4|^2. \quad (52)$$

Thus we are able to write

$$\begin{aligned} \langle 4' \rangle = \exp \left\{ - \frac{1}{2} \left[D_{\psi}(|\vec{x}_1 - \vec{x}_0 + \vec{x}_3 - \vec{x}_4|) - \frac{1}{2} \langle \vec{a} \cdot \vec{a} \rangle |\vec{x}_1 - \vec{x}_0 + \vec{x}_3 - \vec{x}_4|^2 \right] \right. \\ \left. + 2[C_L(|\vec{x}_1 - \vec{x}_3|) + C_L(|\vec{x}_0 - \vec{x}_4|)] \right\}. \end{aligned} \quad (53)$$

Now if we make use of Eq. (7) and (12'), we can write

$$\begin{aligned} \langle 4' \rangle = \exp \left\{ - \frac{1}{2} D_{\psi}(|\vec{x}_1 - \vec{x}_0 + \vec{x}_3 - \vec{x}_4|) \left[1 - (|\vec{x}_1 - \vec{x}_0 + \vec{x}_3 - \vec{x}_4|/D)^{\frac{1}{2}} \right] \right. \\ \left. + 2[C_L(|\vec{x}_1 - \vec{x}_3|) + C_L(|\vec{x}_0 - \vec{x}_4|)] \right\}, \end{aligned} \quad (54)$$

in analogy with the treatment leading to Eq. (31). If we substitute this result into Eq. (14d) [with $\langle 4' \rangle$ replacing $\langle 4 \rangle$ in accordance with the discussion preceding Eq. (48)], introducing the arguments regarding aperture

averaging just as we did in going from Eq. (40) to Eq. (41), make the coordinate transformations first to $\vec{\rho}_1, \vec{\rho}_1', \vec{\rho}_2, \vec{\rho}_2'$, and then to $\vec{\sigma}$ and $\vec{\sigma}'$, and perform as many of the integrations as possible, we obtain the result that

$$\sigma_{\hat{G}}^2 = \left(\langle \hat{G} \rangle^{-2} (512/\pi^3 r_0^4 D^4) \exp(46' \sigma_1^2) \int \sigma d\sigma W_2'(\vec{\sigma}; D) \times \exp \left[-\frac{1}{2} D_{\downarrow}(\sigma) [1 - (\sigma/D)^{\frac{1}{3}}] \right] \right) - 1. \quad (55)$$

Since we have a numerically calculable expression for W_2 , as given by Eq.'s (47a, b, and c), we may consider that we have a suitably simplified form for $\sigma_{\hat{G}}^2$. However, before we can close this section, we need to call attention to an inaccuracy in our results, deriving from the approximate nature of Eq. (37) when used with $\eta = 5/3$, and attempt to correct its effect on the results for $\sigma_{\hat{G}}^2$ and $\sigma_{\hat{G}}^2$.

We call attention to the fact that $W_2(\vec{\sigma}; D)$ is non-zero for values of σ up to $2D$, which can be seen by consideration of Eq.'s (47a, b, and c). This means that the factor $[1 - (\sigma/D)^{\frac{1}{3}}]$ in the exponent in Eq. (55) goes negative for much of the range of values of σ . If we consider that this factor [and its equivalent in Eq. (32)] is supposed to represent the fact that wavefront tracking removes some of the phase variations as far as the optical heterodyne receiver is concerned, then we see that the fact that $[1 - (\sigma/D)^{\frac{1}{3}}]$ is negative indicates that in making our approximations, we have let the tracking subtract more phase variation than our approximations indicate is present with no tracking. Clearly, this inaccuracy needs to be controlled. Inasmuch as there is no inaccuracy in the $(\sigma/D)^{\frac{1}{3}}$ term, since it was calculated using the exact form of Eq. (37) (i.e., with $\eta = 2$), it is obvious that the unity value in $[1 - (\sigma/D)^{\frac{1}{3}}]$ needs to be replaced with something larger. The problem can be seen as arising for values of σ of the

order of $2D$, because for such large values to occur within the boundary constraints it is necessary for $(\vec{x}_1 - \vec{x}_2)$ and $(\vec{x}_3 - \vec{x}_4)$ to both have magnitudes of the order of D and to be nearly parallel. For smaller values of σ , of magnitude D or less, this constraint is much weaker, and almost entirely disappears for σ nearly equal to zero, where we see that the unity value is apparently valid. We thus argue that an adequate replacement for unity in the expression $[1 - (\sigma/D)^{1/2}]$ is $[1 + \frac{1}{2}(2^{1/2} - 1)(\sigma/D)]$ so that we have*

$$\sigma_{\hat{G}}^2 = \left(\langle \hat{G} \rangle^{-2} \exp(4 \theta' \sigma_{\hat{L}}^2) (512/\pi^3 r_0^4 D^4) \int \sigma d\sigma W_2'(\vec{\sigma}; D) \times \exp \left\{ -\frac{1}{2} D_{\frac{1}{2}}(\sigma) \left[1 + \frac{1}{2} (2^{1/2} - 1)(\sigma/D) - (\sigma/D)^{1/2} \right] \right\} \right) - 1. \quad (55')$$

Similarly, we make an equivalent change in the expression for σ_G^2 , and thus obtain the result that

$$\sigma_G^2 = \left(\langle G \rangle^{-2} \exp(4 \theta' \sigma_L^2) (512/\pi^3 r_0^4 D^4) \int \sigma d\sigma W_2'(\vec{\sigma}; D) \times \exp \left\{ -\frac{1}{2} D_{\frac{1}{2}}(\sigma) \left[1 + \frac{1}{2} (2^{1/2} - 1)(\sigma/D) \right] \right\} \right) - 1. \quad (46')$$

We are now ready to proceed with the numerical evaluation of the expressions for $\langle G \rangle$, $\langle \hat{G} \rangle$, σ_G^2 , and $\sigma_{\hat{G}}^2$, which we perform in the next section.

NUMERICAL EVALUATION

Eq.'s (25) and (32), which we repeat here, are entirely adequate for programming.

$$\langle G \rangle = \frac{16}{\pi} \left(\frac{D}{r_0} \right)^2 \int_0^1 u du [\cos^{-1} u - u(1-u^2)^{1/2}] \exp[-3.44 (D/r_0)^{2/3} u^{5/3}]. \quad (25)$$

$$\langle \hat{G} \rangle = \frac{16}{\pi} \left(\frac{D}{r_0} \right)^2 \int_0^1 u du [\cos^{-1} u - u(1-u^2)^{1/2}] \exp[-3.44 (D/r_0)^{2/3} u^{5/3} (1-u^{1/3})]. \quad (32')$$

* It should be recognized that this correction is not accounted for in a previous paper, i.e., reference 4.

For convenience, we introduce the function $W_2(u)$ in place of $W_2'(\vec{\sigma}; D)$, where

$$W_2(u) = W_2'(2\vec{u}; D) D^{-2} \quad (56)$$

so that

$$W_2(u) = \int_0^P dp \int_0^Q dq f(p+u, q) f(p-u) \quad (57a)$$

with

$$P = 1-u; \quad Q = [1 - (p+u)^2]^{\frac{1}{2}} \quad (57b)$$

and

$$f(x, y) = \begin{cases} \cos^{-1}[(x^2 + y^2)^{\frac{1}{2}}] - (x^2 + y^2)^{\frac{1}{2}} [1 - (x^2 + y^2)]^{\frac{1}{2}}, & \text{for } x^2 + y^2 < 1 \\ 0, & \text{for } x^2 + y^2 > 1 \end{cases} \quad (57c)$$

Now we can write

$$\sigma_G^2 = \left[\left(\exp(4\theta' \sigma_L^2) \frac{28}{\pi} \int_0^1 u du W_2(u) \exp[-3.44 \times 2^{5/3} (D/r_0)^{2/3} u^{5/3}] \times [1 + (2^{1/3} - 1)u] \right) / \left(\int_0^1 u du [\cos^{-1} u - u(1-u^2)^{\frac{1}{2}}] \times \exp[-3.44(D/r_0)^{2/3} u^{5/3}] \right)^2 \right] - 1, \quad (58)$$

and

$$\sigma_{\hat{G}}^2 = \left[\left(\exp(4\theta' \sigma_L^2) \frac{8}{\pi} \int_0^1 u du W_2(u) \exp[-3.44 \times 2^{5/3} (D/r_0)^{2/3} u^{5/3}] \times [1 + (2^{1/3} - 1)u - 2^{1/3} u^{\frac{4}{3}}] \right) / \left(\int_0^1 u du [\cos^{-1} u - u(1-u^2)^{\frac{1}{2}}] \times \exp[-3.44(D/r_0)^{2/3} (1-u^{\frac{4}{3}})] \right)^2 \right] - 1. \quad (59)$$

To limit the calculations, it is useful to separate the σ_L^2 -dependence and the wavefront distortion dependence. We do this by introducing the functions $\hat{\Phi}(D/r_0)$ and $\hat{\Phi}^*(D/r_0)$, where

$$\hat{\Phi}(D/r_0) = \frac{8}{\pi} \frac{\int_0^1 u du W_2(u) \exp[-10.92(D/r_0)^{2/3} u^{5/3} (1 + 0.26 u)]}{\left(\int_0^1 u du [\cos^{-1} u - u(1-u^2)^{\frac{1}{2}}] \exp[-3.44(D/r_0)^{2/3} u^{5/3}] \right)^2}, \quad (60)$$

and

$$\hat{\epsilon}(D/r_0) = \frac{8}{\pi} \frac{\int_0^1 u \, du \, W_2(u) \exp[-10.92 (D/r_0)^{1/2} u^{3/2} (1 + 0.26 u - 1.26 u^2)]}{\left\{ \int_0^1 u \, du [\cos^{-1} u - u(1-u^2)^{1/2}] \exp[-3.44 (D/r_0)^{1/2} u^{3/2} (1-u^2)] \right\}^2} \quad (61)$$

Then we can compute the wavefront distortion by evaluating $\hat{\epsilon}$ and/or $\hat{\epsilon}$, and combine this with the log-amplitude variance dependence, as shown in Eq.'s (62a and b),

$$\sigma_G^2 = \exp(4 \theta' \sigma_{\hat{\epsilon}}^2) \hat{\epsilon}(D/r_0) - 1 \quad (62a)$$

$$\sigma_{\hat{G}}^2 = \exp(4 \theta' \sigma_{\hat{\epsilon}}^2) \hat{\epsilon}(D/r_0) - 1 \quad (62b)$$

to obtain σ_G^2 and/or $\sigma_{\hat{G}}^2$.

We have programmed the numerical calculations of $\langle G \rangle$, $\langle \hat{G} \rangle$, $\hat{\epsilon}(D/r_0)$, and $\hat{\epsilon}(D/r_0)$ with all integrations performed by means of a Simpson's Rule approximation. For the two-dimensional integration involved in evaluating $W_2(u)$, we used 20-intervals for each dimension. For the u -integration in Eq.'s (25), (32), (60), and (61), we use a 50-interval form of Simpson's Rule. In Table I, we show the calculated values for $W_1^*(u)$, where

$$W_1^*(u) = \frac{2}{D^2} W_1(\bar{u}; D; D) \quad (63)$$

and for $W_2(u)$, for the set of values of $u = (0.0, 0.02, 1.0)$. In Table II, we show the computed values of $\langle G \rangle$, $\langle \hat{G} \rangle$, $\hat{\epsilon}(D/r_0)$, $\hat{\epsilon}(D/r_0)$ for a variety of values of D/r_0 . The fact that even for the smallest values of (D/r_0) , where the aperture is so small that we do not expect any wavefront distortion modulation of the antenna gain, the values computed for $\hat{\epsilon}$ and $\hat{\epsilon}$ are not exactly unity suggests that minor inaccuracies in our constants, because they are in

the exponent, are responsible. The effect* should be suppressed in interpreting our results, and to this objective, we have titled our columns $\hat{\epsilon}(D/r_0) + .027$ and $\hat{\epsilon}(D/r_0) + .0276$, rather than just $\hat{\epsilon}(D/r_0)$ and $\hat{\epsilon}(D/r_0)$.

In the next section, we shall discuss the significance of these results and their implications.

DISCUSSION OF RESULTS

The significance of the results are quite clear from a consideration of Table II. The basic conjecture is borne out that modulation noise will be much less severe in a tracking than in a static optical heterodyne receiver. For the same level of modulation noise, the tracking optical heterodyne receiver, compared to the static heterodyne receiver, appears to have almost ten times the average antenna gain. To see this, consider the following sample of the data. (We assume σ_L^2 is very small and can be neglected.) Serious channel fading may be expected to manifest itself when the antenna gain variance is about equal to 0.1, or $\hat{\epsilon} = 1.1$. For the static system, this would appear to occur at $D/r_0 = 0.50$, while for the tracking system, it occurs at $D/r_0 = 1.65$. The corresponding average antenna gains are about 0.18 and 1.79, for the static and tracking optical heterodyne receivers, respectively. The ratio of 10 comes close to equalling the original prediction⁸ of an improvement of about $(3.4)^2 = 11.6$ between static and tracking receivers.

As far as the effect of log-amplitude variance is concerned, the fact that θ' is smaller for larger apertures indicates that a tracking heterodyne receiver will be better than the static receiver, even when there is significant intensity variation - although in this case, the performance ratio

* It should be noted that even with $\sigma_L^2 = 0$, a value of $\hat{\epsilon} = 1.0276$ corresponds to an rms variation of the optical heterodyne receiver's antenna gain of $100(1.0276 - 1)\% = 16.6\%$, which is certainly not a negligible amount.

will probably not be so large.

Clearly, the extra servo bandwidth required to make an optical heterodyne receiver with any tracking capability fast enough so that it will perform as a tracking rather than an apparently static unit will be well worth the effort.

It is interesting to note that the reduced antenna gain variance of the tracking heterodyne receiver compared to the static receiver could have been inferred from a comparison of curves A and C of Fig. 1 in reference 9. There the resolution (which, in the sense of antenna gain, can be equated with heterodyne receiver performance) for long and for short exposure, which are equivalent to static and tracking receivers, respectively, can be seen in comparison with the straight line, free space value, as a function of D/r_0 . The nearness of the curve to the free space value implies the absence of atmospheric effects. In that figure, the same fractional deviation is seen to occur for the short exposure (i.e., the tracking receiver) case at an average resolution (i.e., antenna gain) about ten times the value for the long exposure (i.e., the static receiver) case. It was, in fact, this observation that motivated the performance of the analysis reported in this paper.

REFERENCES

1. S. Gardner, IEEE Internat'l. Conv. Rec. 12 pt. 6, 337 (1964)
2. I. Goldstein, P. A. Miles, and A. Chabot, Proc. IEEE 53, 1172 (1965)
3. D. L. Fried, Proc. IEEE 55, 57 (1967)
4. D. L. Fried, IEEE J. Q. E. 3, 213 (1967)
5. D. M. Chase, J. Opt. Soc. Am. 56, 33 (1966)
6. D. L. Fried and R. A. Schmeltzer, Appl. Opt. 6, 1729 (1967)
7. J. P. Speck, J. Opt. Soc. Am. 61, 676A (1971)
8. D. L. Fried, J. Opt. Soc. Am. 55, 1427 (1965); 56, 410E (1966)
9. D. L. Fried, J. Opt. Soc. Am. 56, 1372 (1966)
10. D. L. Fried, G. E. Mevers, and M. P. Keister, Jr., J. Opt. Soc. Am. 57, 787 (1967)
11. V. I. Tatarski, "Wave Propagation in a Turbulent Medium," New York; McGraw-Hill, 1961
12. J. Richard Kerr, Oregon Graduate Center for Study and Research, Portland, Oregon, private communications
13. R. L. Kurtz and J. L. Hayes, "Experimental Measurements of Optical Angular Deviation Caused by Atmospheric Turbulence and Refraction," NASA Tech. Note, NASA TN D-3439, May 1966
14. D. L. Fried, J. Opt. Soc. Am. 57, 169 (1967)

TABLE I

	u	$W_1^*(u)$	$W_2(u)$
0	0.00	1.5707963	.2226499
1	.02	1.5307990	.2220154
2	.04	1.4908177	.2201890
3	.06	1.4508684	.2171250
4	.08	1.4109672	.2129221
5	.10	1.3711302	.2076856
6	.12	1.3313736	.2014962
7	.14	1.2917137	.1944222
8	.16	1.2521670	.1865652
9	.18	1.2127499	.1780589
10	.20	1.1734792	.1690215
11	.22	1.1343719	.1595060
12	.24	1.0954450	.1496817
13	.26	1.0567159	.1396533
14	.28	1.0182022	.1294963
15	.30	.9799219	.1193486
16	.32	.9418932	.1092987
17	.34	.9041348	.0994395
18	.36	.8666656	.0898632
19	.38	.8295052	.0806422
20	.40	.7926734	.0718521
21	.42	.7561909	.0635488
22	.44	.7200786	.0557826
23	.46	.6843584	.0485893
24	.48	.6490527	.0419913
25	.50	.6141848	.0359987
26	.52	.5797789	.0306056
27	.54	.5458601	.0257938
28	.56	.5124547	.0215370
29	.58	.4795901	.0178037
30	.60	.4472952	.0145588
31	.62	.4156005	.0117655
32	.64	.3845381	.0093854
33	.66	.3541423	.0073799
34	.68	.3244495	.0057108
35	.70	.2954988	.0043403
36	.72	.2673327	.0032321
37	.74	.2399969	.0023513
38	.76	.2135417	.0016649
39	.78	.1880225	.0011422
40	.80	.1635011	.0007546
41	.82	.1400472	.0004764
42	.84	.1177405	.0002844
43	.86	.0966738	.0001581
44	.88	.0769573	.0000801
45	.90	.0587259	.0000357
46	.92	.0421510	.0000133
47	.94	.0274620	.0000037
48	.96	.0149941	.0000006
49	.98	.0053173	.0000000
50	1.00	0.0000000	0.0000000

TABLE II

D/r_0	$\langle G \rangle$	$\langle \hat{G} \rangle$	$\ddagger(D/r_0) \pm .0277$	$\ddagger(D/r_0) \pm .0276$
.03	.00087	.00087	1.02768	1.02755
.05	.00240	.00242	1.02799	1.02768
.07	.00468	.00473	1.02845	1.02785
.10	.00946	.00964	1.02943	1.02816
.15	.02083	.02160	1.03208	1.02885
.20	.03607	.03824	1.03636	1.02971
.30	.07603	.08507	1.05152	1.03192
.40	.12495	.14911	1.07796	1.03474
.60	.23376	.32375	1.17256	1.04215
.80	.33865	.55056	1.32772	1.05199
1.00	.42891	.81650	1.54161	1.06444
1.20	.50283	1.10814	1.80792	1.07983
1.40	.56262	1.41247	2.11960	1.09857
1.60	.61132	1.71753	2.47107	1.12119
1.80	.65150	2.01290	2.85899	1.14833
2.00	.68505	2.28993	3.28198	1.18074
2.30	.72575	2.65698	3.98227	1.24123
2.60	.75754	2.95363	4.76343	1.31928
2.90	.78256	3.17412	5.62745	1.41938
3.20	.80242	3.31991	6.57476	1.54695
3.50	.81834	3.39768	7.60399	1.70836
3.80	.83127	3.41738	8.71259	1.91084
4.10	.84189	3.39049	9.89736	2.16230
4.40	.85072	3.32863	11.15500	2.47102
4.70	.85810	3.24259	12.48224	2.84513
5.00	.86429	3.14168	13.87584	3.29205

APPENDIX

Computer Program for the Calculation of

 $W_1^*(u)$, $W_2(u)$, $\langle G \rangle$, $\langle \hat{G} \rangle$, $\hat{t}(D/r_0)$, and $\hat{\theta}(D/r_0)$

```

100 DIMENSION W1(0:50), W2(0:50)
110 WRITE(1,0) '*****'
120 DO 10 I = 0,50
125 XI = I
130 U = XI/50
140 CP = 1-U
149 IF((1-U**2).LT.0) W1(I) = 0 ; GO TO 100
150 W1(I) = (ACOS(U)-U*SQRT(1-U**2))
160 100 JC = 0
170 SJ = 0
180 DO 20 J = 0,20
190 JC = JC+1
200 IF(JC.EQ.1) JF = 2
210 IF(JC.EQ.2) JF = 4 ; JC = 0
230 IF(J.EQ.0) JF = 1
240 IF(J.EQ.20) JF = 1
250 P = J*CP/20
259 IF((1-(P+U)**2).LT.0) GO TO 20
260 CQ = SQRT(1-(P+U)**2)
270 KC = 0
280 SK = 0
290 DO 30 K = 0,20
300 KC = KC+1
310 IF(KC.EQ.1) KF = 2
320 IF(KC.EQ.2) KF = 4 ; KC = 0
340 IF(K.EQ.0) KF = 1
350 IF(K.EQ.20) KF = 1
360 Q = K*CQ/20
370 RP2 = (P+U)**2+Q**2
380 RN2 = (P-U)**2+Q**2
390 RP = SQRT(RP2)
400 RN = SQRT(RN2)
408 IF((1-RP2).LT.0) F = 0 ; GO TO 90
409 IF((1-RN2).LT.0) F = 0 ; GO TO 90
410 F = (ACOS(RP)-RP*SQRT(1-RP2))*(ACOS(RN)-RN*SQRT(1-RN2))
420 90 SK = SK+KF*F
430 30 CONTINUE
440 SK = CQ*SK/60
450 SJ = SJ +JF*SK
460 20 CONTINUE
470 W2(I) = CP*SJ/60
480 WRITE(1,40) I,U,W1(I),W2(I)
490 40 FORMAT(12,3X,F5.2,2(3X,F9.7))
500 10 CONTINUE

```

APPENDIX (Continued)

```

510 WRITE(1,0) '*****'
520 REPEAT 50, FOR D = .03,.05,.07,.1,.15,.2,.3,
530 +(.4,2.,.2),(2.3,5.,.3)
540 DP = D*(5.0/3.0)
550 IC = 0
560 S1 = 0
570 S2 = 0
580 S3 = 0
590 S4 = 0
600 D0 60 I = 0,50
605 XI = 1
610 U = XI/50
619 IF(I.EQ.0) S1 = 0 ; S2 = 0 ; S3 = 0 ; S4 = 0 ; GO TO 60
620 UP5 = U*(5.0/3.0)
630 UP1 = U*(1.0/3.0)
640 F1 = U*W2(I)*EXP(-10.92*DP*UP5*(1+.26*U-1.26*UP1))
650 F2 = U*W2(I)*EXP(-10.92*DP*UP5*(1+.26*U))
660 F3 = U*W1(I)*EXP(-3.44*DP*UP5*(1-UP1))
670 F4 = U*W1(I)*EXP(-3.44*DP*UP5)
680 IC = IC+1
690 IF(IC.EQ.1) XIF = 2.0/150.
700 IF(IC.EQ.2) XIF = 4.0/150. ; IC = 0
720 IF(I.EQ.0) XIF = 1.0/150.
730 IF(I.EQ.20) XIF = 1.0/150.
740 S1 = XIF*F1+S1
750 S2 = XIF*F2+S2
760 S3 = XIF*F3+S3
770 S4 = XIF*F4+S4
780 60 CONTINUE
790 TG = 16.*D*2*S3/3.141592658
795 XIG = 16.*D*2*S4/3.141592658
800 TMN = 8.*S1/(3.141592658*S3*2)
805 XTMN = 8.*S2/(3.141592658*S4*2)
810 WRITE(1,70) D,XIG,TG,XTMN,TMN
820 70 FORMAT(F6.2,4(X,F10.5))
830 50 CONTINUE
840 STOP

```

Appendix M

QUANTITATIVE ESTIMATES OF THE EFFECTS
OF ATMOSPHERIC TURBULENCE ON
THE PERFORMANCE OF A LASER
COMMUNICATION GROUND STATION

by

Dr. D. L. Fried

Consultant to LMSC

LOCKHEED PALO ALTO RESEARCH LABORATORY
LOCKHEED MISSILES & SPACE COMPANY
A GROUP DIVISION OF LOCKHEED AIRCRAFT CORPORATION

Introduction

We are concerned in this report with the presentation of a fairly comprehensive set of results in tabular form for the expected effects of atmospheric turbulence on ground-based laser communication systems. We deal with two types of ground-based units: a photon-bucket type laser receiver, and a laser transmitter attempting to operate in a diffraction limited mode.

There are two types of effects that concern us. First of all, for the transmitter there is a limitation on the average antenna gain that the atmosphere will allow. For all cases of interest to us here, there is a dimension r_0 which may be associated with a particular propagation path experiencing a particular level of turbulence and with a particular wavelength λ . For a transmitter diameter D much less than r_0 , the average antenna gain will be close to the free space value associated with λ/D . However, for a value of D much larger than r_0 , the average antenna gain will be about equal to the free space value associated with λ/r_0 , rather than with λ/D -- a loss associated with the quantity D/r_0 . This loss can represent a severe limitation.

The second type of effect with which we are concerned relates to the fact that a data link must perform on a continuous basis. Here, if the strength of the received signal fluctuates, our error rate, being a highly nonlinear function of the signal-to-noise ratio (and thus of the signal strength) will strongly reflect these fades. To counter the effect of these fades, it is necessary to transmit a higher average power, so that even during the fades the signal-to-noise ratio will be sufficient to keep the

error-rate at an acceptable level. The increase in power required to counteract these fluctuations can be considered a loss factor. This means signal fluctuations must be minimized, compatible with other system constraints, of course.

We expect signal fluctuations for both the ground-based photon-bucket receiver and for the ground-based laser transmitter. In the case of the photon-bucket receiver, the fluctuations are due to the same phenomenon that causes stellar scintillation. In the case of this phenomenon, the larger the aperture, the less the observed signal variation, percentage-wise. For the laser transmitter, there is a bit of the same phenomenology in effect, and just as in the case of the photon-bucket receiver, the larger the aperture, the less significant this effect is. However, the dominant cause of fluctuations in the antenna gain of a ground-based laser transmitter is due to wavefront distortion associated with refractive inhomogeneities near the aperture -- the same effect that limits resolution in astronomical imagery. The magnitude of the effect is controlled by r_0 , the same dimension that controlled average laser transmitter antenna gain. It can be shown that for an aperture diameter D much less than r_0 , wavefront distortion does not produce any significant amount of antenna gain variation. However, for values of D of the order of r_0 or larger, the amount of variation can be prohibitively large.

In quantifying the effects of atmospheric turbulence on a laser transmitter, we have considered two basic types of transmitters which we denote as the static system and the fast-tracking system. The fast-tracking system is able to follow the rapid apparent fluctuations due to atmospheric turbulence, of a beacon on the satellite receiver, and so is

• • •

able to compensate for linear variations (apparent tilt) in the wavefront. The effect on performance will be seen to be significantly better with the fast-tracking system than with the static system.

Fluctuation Loss

It is well known that scintillation observed by a point detector obeys a log-normal distribution.¹ The spread associated with the distribution is most often measured by the log-amplitude variance σ_L^2 . The fact that the distribution is log-normal means that the logarithm of the intensity (and, of course, of one-half the logarithm of the intensity, which corresponds to the logarithm of the amplitude) is normally distributed. σ_L^2 is the variance of the distribution of one-half the natural logarithm of the intensity. It has been observed that the fluctuations of the flux collected by a large aperture, for which there is averaging over the independent fluctuations in different portions of the aperture, also manifests a log-normal distribution.² A theoretical explanation of why this is so when we might ordinarily have expected the distribution to tend toward a normal rather than a log-normal form has been provided by Mitchell.³ In fact, a generalization based on what we may call the complex phase-normal rather than merely the log-(amplitude)-normal, allows us to use Mitchell's work to argue that for a heterodyne receiver, the signal strength should fluctuate in accordance with a log-normal distribution. We have shown elsewhere⁷ that for a common path the performance of an antenna operating as a transmitter is identical to what it will be when operating as a heterodyne receiver, taking into account atmospheric turbulence of the propagation path. This equivalence is an identity between random variables, so that the fact that

the heterodyne receiver's performance has a log-normal distribution means that the transmitter's performance will be log-normally distributed.

We conclude that for all cases of interest to us here, the signal fading may be considered to have a log-normal distribution. In Fig. 1, we show results generated by H. Hance (Lockheed Palo Alto Research Lab) for the relationship between the log-amplitude variance σ_L^2 and fading loss. As can readily be seen from Fig. 1, the loss varies almost linearly with σ_L^2 . A log-amplitude variance of 0.01 results in about 1 dB of loss. As a rule of thumb, we can take $\sigma_L^2 = 0.01$ as the value at which fading goes from an insignificant to a significant problem.

Incoherent Receiver Signal Fading

For a laser data link from space to the ground with reception provided by what we may term a photon bucket, the fluctuation of the collected signal is a function of two features of the problem. The first of these is the scintillation we would observe if we were using a very small diameter collector. The second feature is the degree of aperture averaging provided by the size of the actual collector.

Probably the best available data for the magnitude of point collector scintillation is that published by Burke,⁴ based on observation of stellar scintillation for observation of a star near the zenith. Measurement wavelength for Burke's results is about 0.55 μm , with the observed log-amplitude variance being about $(\sigma_L^2)_0 = 0.05 \text{ (nepers}^2\text{)}$. Theory¹ tells us that the magnitude of the scintillation for our case should depend on the wavelength λ , and zenith angle, θ , of the source according to the relationship

$$\sigma_L^2 = \sec^{1/6} \theta (0.55/\lambda)^{7/6} (\sigma_L^2)_0 \quad (1)$$

Burke's results correspond to night time measurements in one location. To allow for variations in conditions from location to location, we consider it expedient to consider a scintillation range from 0.01 to 0.1 (although we suspect that 0.07 is probably a practical upper limit). We have, therefore, based our calculations in Table 1 on $(\sigma_L^2)_0$ covering the range from 0.01 to 0.1.

In setting this range of values for $(\sigma_L^2)_0$, we have assumed that there is no difference to be expected between day time and night time conditions. We base this argument on the fact that the various measured and estimated forms for the vertical distribution of the strength of turbulence in the atmosphere makes it apparent that stellar scintillation is generated by high altitude turbulence, * i.e., turbulence above 2 km to 4 km. In this regard, Figs. 2 and 3 are quite indicative, especially when we consider that the strength of turbulence at an altitude h is to be multiplied by $h^{5/6}$ to determine the contribution to log-amplitude variance. Fig. 2 represents the only data we have for comparison of day time and night time conditions, and in this respect is based entirely on the hot wire thermometer airplane flight measurements of Koprov and Tsvang.⁵ What we see from their results is that in the altitude region where stellar scintillation is produced, there is apparently no important change between day time and night time conditions.

* We might say that the much greater amount of turbulence near the ground simply does not have the lever-arm necessary to cause intensity variations, although it can certainly produce significant amounts of wavefront distortion.

Our treatment of aperture averaging is based on reference 6, where it was shown that for a large aperture, we could consider signal variance to be reduced from the small collector value by a factor of Θ , where

$$\Theta = (\rho_0/D)^2 . \quad (2)$$

Here ρ_0 is a measure of the correlation distance for scintillation, and is given by

$$\rho_0 = 0.8 (h_0 \lambda \sec \theta)^{\frac{1}{2}} , \quad (3)$$

where h_0 is a scale height characteristic of the location of the scintillation generating turbulence. We have selected the two sample values of $h_0 = 5$ km and $h_0 = 10$ km as reasonably representative of the situation.

To accommodate a variety of aperture diameters, not all of which are larger than ρ_0 , we have generalized Eq. (2) to the form

$$\Theta = [1 + (D/\rho_0)^2]^{-1} , \quad (4)$$

which form insures reasonable results for all values of D .

The aperture averaging factor Θ refers directly to reduction in signal variance and not to log-amplitude variance. To establish this connection, we use the fact that for log-normally distributed scintillation, the signal variance σ_s^2 is related to the log-amplitude variance σ_ℓ^2 by the formula

$$\sigma_s^2 = \exp(4\sigma_\ell^2) - 1 , \quad (5)$$

so that the aperture averaged log-amplitude variance can be written as

$$\sigma_L^2, \text{ap. avg.} = \frac{1}{2} \ln \{ 1 + \Theta [\exp (4\sigma_L^2) - 1] \} . \quad (6)$$

For our calculations, we have considered values of zenith, 0.55 μm , stellar scintillation of

$$(\sigma_L^2)_0 = 0.01, 0.02, 0.04, 0.07, 0.1 ; \quad (7a)$$

values of wavelength of

$$\lambda = 0.53 \mu\text{m}, 0.633 \mu\text{m}, 1.06 \mu\text{m} ; \quad (7b)$$

zenith angles of

$$\theta = 0^\circ, 40^\circ ; \quad (7c)$$

aperture diameters of

$$D = 0.15 \text{ m}, 0.255 \text{ m}, 0.3 \text{ m}, 0.6 \text{ m} ; \quad (7d)$$

and the two scale heights of

$$h_0 = 5 \text{ km}, 10 \text{ km} . \quad (7e)$$

The results of the calculations of $\sigma_L^2, \text{ap. avg.}$ for these sets of conditions are shown in Table 1, along with the FORTRAN program for their calculation in Table 2. The values in parentheses refer to $h_0 = 10 \text{ km}$, while the ones alongside but out of the parentheses refer to $h_0 = 5 \text{ km}$.

The results are fairly self-explanatory. We only point out that for the larger apertures, i.e., $D = 0.3 \text{ m}$ and 0.6 m , there are no significant scintillation effects, while for the smaller apertures, the effects are significant only for the most severe conditions. In general, we may say that the

space-to-ground link, with an incoherent photon-bucket type receiver on the ground, would be influenced only very slightly by atmospheric turbulence.

We are now ready to turn our attention to the effects of turbulence on a ground-based transmitter. In the next section, we consider the pertinent phenomenology and the applicable theory. In the subsequent section, we introduce estimates for the governing parameters, and then cast the results in a form to facilitate a tabulation.

Laser Transmitter Effects

GENERAL FORMULATION - The key point in our treatment of atmospheric turbulence on a ground-to-space laser transmitter is recognition of the existence of a perfect reciprocity between the performance of any two of the following three types of devices: 1) a laser transmitter; 2) an optical heterodyne receiver; and 3) point intensity measurement in the focal plane of an image forming device. This reciprocity exists if the two systems share a common aperture, work at the same wavelength, and are responding to the same distant point. The perfect nature of the reciprocity means that not only are the signal strengths for the two systems going to fluctuate in synchronism (so that the normalized moments of the statistical fluctuation are equal), but also the way in which the turbulence affects the antenna phenomenology is so completely equivalent between the systems that if a slight angular reorientation of one system will improve the signal strength for that system, * then exactly the same improvement will be achieved in the other system by just this amount of angular reorientation! This very general antenna gain

* The tilting takes advantage of the fact that to a significant extent wavefront distortion due to atmospheric turbulence may be considered to be just a random wavefront tilt, so that tracking the tilt can result in suppression of a large part of the effect of turbulence on the system's performance.

reciprocity result is demonstrated in reference 7.

We shall have occasion to make use of these results in two ways. First of all, we shall utilize reciprocity in our treatment here of the expected performance of a laser transmitter by arguing that reciprocity allows us to apply the results of previous calculations for the performance of an optical heterodyne receiver to the performance of a laser transmitter. More important, however, is the hardware implication that we can utilize an imaging system tracking a beacon originating at the distant (receiver) point to generate an optimum atmospheric turbulence tilt tracking signal so that the laser transmitter can be pointed, in a sufficiently agile manner, as to compensate for the part of the atmospheric turbulence effect which can be considered to be wavefront tilt. We refer to a system utilizing this agile pointing as a "fast-tracking system" in distinction to an ordinary system, which has to track the beacon but does not attempt to track anything except the beacon's mean position, which we refer to as a "static system". To emphasize the significance of the distinction between the fast-tracking and the static systems, we shall sometimes refer to these two types of systems as "tracking" and "static", respectively. The reciprocity relationship will allow us to utilize the theoretical results for a fast-tracking optical heterodyne receiver to predict the performance to be expected from a fast-tracking laser transmitter. The necessary results for the static and the fast-tracking optical heterodyne receiver are presented in reference 8. As we shall see from examination of the tabular results developed later in this report, the use of the fast-tracking rather than the static system can result in about a 10 dB improvement in performance! For this reason, we shall explore the utilization of the fast-tracking concept rather fully in this paper.

In what follows in this section, when we discuss the performance of a static or a fast-tracking optical heterodyne receiver, it should be understood that our attention is actually directed toward the performance of the laser transmitter, which is equivalent according to reciprocity.⁷ We couch our discussion in terms of the receiver for the reasons that 1) the analysis we shall quote is given in terms of the optical heterodyne receiver, and 2) it is easier to discuss the pertinent aspects of atmospheric turbulence effects in terms of a receiver, which deals with an incident, already distorted wavefront, rather than to discuss the "going to happen" effects of atmospheric turbulence on a perfect wavefront leaving a laser transmitter.

It is convenient to separate the effects of atmospheric turbulence on an optical heterodyne receiver into the two subject areas of 1) effects on the average antenna gain, and 2) effects of the variance of the antenna gain. It is a well known result that the average antenna gain of a static optical heterodyne receiver is limited by atmospheric turbulence to some finite upper value no matter how large the antenna diameter,^{8,9,10} (providing that we are not considering a short path length/weak-turbulence product, horizontal propagation path near the ground, for long wavelength propagation, in which case there may be no upper limit to the achievable antenna gain¹¹.) Associated with any wavelength λ and propagation path-turbulence distribution there is a length r_0 which by itself fairly completely characterizes the atmospheric effects on average antenna gain. For an antenna diameter D , much less than r_0 , the average antenna gain of a static system is very nearly equal to what it would be in free space for that diameter. But for a diameter much larger than r_0 , the average antenna gain is very nearly equal to the free space value for an antenna of diameter

r_0 . The dependence of average antenna gain $\langle G \rangle$ upon diameter D , as shown by the curve labeled "Static System" in Fig. 4, manifests a well defined knee at a diameter equal to r_0 .*

The average antenna gain for the fast-tracking system is also shown in Fig. 4, by the curve labeled "Fast-Tracking System". The data for both of these curves in Fig. 4 are taken from reference 8, although equivalent data is available in terms of imaging system performance in reference 12 (which, by reciprocity⁷, we can equate with optical heterodyne performance). There, the short exposure resolution corresponds to fast-tracking.[†] The behavior of the antenna gain for the fast-tracking system calls for some comment. Although it is not apparent in Fig. 4, for very large diameters, i.e., $D \gg r_0$, the average antenna gain approaches the same asymptotic limit as does the static system -- namely, the free space value for an antenna of diameter r_0 . This is because for a large diameter, the distortion of the wave is so severe that even after tracking out any wavefront tilt, there is so much residual distortion that this remaining distortion is still the limiting factor. As the diameter increases, the residual distortion increases, but for small diameters, i.e., $D \leq 3.4 r_0$, the effect of the increase in collection area exceeds in significance the effect of the increase in distortion. For $D > 3.8 r_0$, the situation is reversed: the effect of the increase in distortion exceeds in significance the effect of

* It is sometimes the practice to utilize a somewhat different quantity denoted by ρ_0 in place of r_0 to describe atmospheric effects on an optical heterodyne receiver. Since $r_0 \approx 2.1 \rho_0$, so that there does not appear to be any fundamental difference which value is used, and since r_0 so nicely describes the operationally pertinent values, we shall restrict our discussion to one utilizing r_0 exclusively.

† It should be noted that in reference 12, the calculations are in terms of the integrated MTF versus D/r_0 . However, as O'Neill¹³ points out, the integrated MTF is equivalent to the Strehl definition, which in turn is directly proportional to the intensity in the focal plane at the center of the image point.

the increase in collection area. In Table 3, we present a set of values of average antenna gain as a function of the ratio of D/r_0 for a static system and for a fast-tracking system.

Variations in the antenna gain of an optical heterodyne receiver are caused by atmospheric turbulence in two ways. First, there is a variation caused by simple variations in the total optical power collected by the aperture. If less (more) optical energy than the average enters the aperture, then all other things being equal, the magnitude of the optical heterodyne signal will be less (more) than average. In addition to this sort of variation-producing mechanism, even if the total optical energy collected is constant, variations in the wavefront distortion and in the uniformity of the energy density will result in optical heterodyne signal strength variations.

The first of these two mechanisms, i.e., the variation in the total collected optical power, is unique to the signal strength variation problem, while the latter is closely tied to the same phenomenology that produces a limit to the average antenna gain. For the ground/space link with the optical heterodyne receiver on the ground, the variations in total collected optical energy are associated with the atmospheric turbulence at 5 km to 20 km where the stellar scintillation effects are produced (as discussed in the previous section). The wavefront distortions are produced for the most part by low level turbulence, i.e., turbulence at altitudes below a few hundred meters, since wavefront distortion is an unweighted integral over the strength of turbulence in the path, and as we can see from Figs. 2 or 3, the dominant contribution to this integral will come from the low altitudes.

Optical heterodyne signal strength variations, to the extent that they depend on variations in the total optical power collected, decrease

in magnitude as the aperture diameter is increased. The effect is essentially the same aperture averaging phenomenon discussed in the previous section. To the extent that the variations in signal strength depend on wavefront distortion and intensity non-uniformity across the aperture, the variations increase as the aperture diameter is increased. For a static system, this latter effect is minor or insignificant for diameters much less than r_0 , but becomes very large for diameters much larger than r_0 . r_0 is the critical length for this effect, while for the effect due to variations in the total optical power collected, it is ρ_0 that is the critical parameter. For a fast-tracking system, the effects are basically the same as for a static system, except that the critical length for the wavefront distortion effects is of the order of $3.4 r_0$, instead of just r_0 .

The phenomenology of optical heterodyne signal modulation is covered in reference 8. From this, we can write that the signal strength variation has the form

$$\sigma_s^2 = \exp(4 \Theta' \sigma_\ell^2) \frac{1}{2} (D/r_0) - 1 \quad (8)$$

where σ_s^2 is defined by the expression

$$\sigma_s^2 = \frac{\langle (S - \langle S \rangle)^2 \rangle}{\langle S \rangle^2} \quad (9)$$

and S is the instantaneous randomly fluctuating optical heterodyne receiver's output signal strength. σ_ℓ^2 is the log-amplitude variance of the incident wave, defined by Eq. (1). Θ' is a modified aperture averaging factor which can be related to the aperture averaging factor Θ defined in Eq. (4), by use of an equation of the general form of Eq. (6). We have

$$\exp(4\Theta'\sigma_L^2) - 1 = \Theta[\exp(4\sigma_L^2) - 1] \quad (10)$$

so that

$$\Theta' = (4\sigma_L^2)^{-1} \ln\{\Theta[\exp(4\sigma_L^2) - 1] + 1\} \quad (11)$$

The function $\Phi(D/r_0)$ governs the wavefront distortion effects. It has been calculated for both the static system and the fast-tracking system in reference 8. The results are given in Table 4, and in Fig. 5. As can be readily seen, $\Phi(D/r_0) \approx 1$ for $D/r_0 \ll 1$, but increases rapidly for $D/r_0 \gtrsim 0.5$ for a static system, and for $D/r_0 \gtrsim 1.5$ for a fast-tracking system.

Gathering together all of the pertinent relationships, we have, for propagation of a wavelength λ , coming down at a zenith angle θ , for an aperture D , the effective log-amplitude variance associated with the variations in signal strength out of an optical heterodyne receiver is

$$\begin{aligned} (\sigma_L^2)_{\text{sig}} &= \frac{1}{4} \ln\{1 + \sigma_s^2\} \\ &= \frac{1}{4} \ln\{1 + \exp(4\Theta'\sigma_L^2)\Phi(D/r_0) - 1\} \\ &= \frac{1}{4} \ln\{\exp(4\Theta'\sigma_L^2)\Phi(D/r_0)\} \\ &= \frac{1}{4} \ln\left\{\{\Theta[\exp(4\sigma_L^2) - 1] + 1\}\Phi(D/r_0)\right\} \end{aligned} \quad (12)$$

where

$$\Theta = [1 + (D/\rho_0)^2]^{-1} \quad (4)$$

$$\rho_0 = 0.8 (h_0 \lambda \sec \theta)^{\frac{1}{2}} \quad (3)$$

$$\sigma_L^2 = \sec^{1/8} \theta (0.55/\lambda)^{7/8} (\sigma_L^2)_0 \quad (1)$$

The driving consideration is, of course, the value of r_0 . Formally, this is given by the expression

$$r_0 = 0.183 \lambda^{6/5} \left[\int ds C_n^2 \right]^{-3/5} . \quad (13)$$

The integration is to be taken over the propagation path. Formally, this expression could be used to evaluate r_0 using the data in Figs. 2 or 3. and we could then proceed with the calculation of effects of atmospheric turbulence on the performance of an optical heterodyne receiver, and thus of a laser transmitter. However, evaluation of r_0 from the integral in Eq. (13) is likely to give rather unreliable results since the available data on the vertical distribution of the strength of turbulence, i.e., C_n^2 is not very precise. Rather we shall, in the next sub-section, show available optical measurements can be used to develop a reliable estimate for r_0 , which we will then use to calculate the effects of atmospheric turbulence on laser-transmitter performance.

r_0 - ESTIMATION - Rather than rely on the available data for the vertical distribution of the optical strength of turbulence, such as that of Figs. 2 and 3, about which there is some significant uncertainty, it is profitable to seek an estimate of r_0 directly from optical measurements. This spares us the difficulty of becoming involved in an attempt to develop a full profile for C_n^2 , when all we want is a single number, i.e., the value of r_0 . Moreover, we shall find that the available data on r_0 is much richer in frequency of occurrence information than what information we could presently hope to obtain from a study of the vertical distribution of turbulence. This is not to say that we shall not make any use of information

regarding the vertical distribution of the optical strength of turbulence. We shall use such data for scaling results for r_0 from one set of measurement conditions to another - in particular, from night time to day time conditions.

It is pointed out in reference 7 that a perfect equivalence exists between the effects of atmospheric turbulence on a laser transmitter, an optical heterodyne receiver, and an imaging system. The quantity r_0 and the ratio D/r_0 is equally applicable to all three types of systems. In fact, if we simply relabel the vertical axis in Fig. 4, we can consider two curves in that figure to refer to the integrated MTF for a long exposure (equivalent to a static system) and for a short exposure (equivalent to a fast-tracking system). The implication of this general relationship is that we can use data taken in observing stars with an astronomical telescope to deduce what r_0 is for a vertical path through the atmosphere. Measurement of the spread of a stellar image is directly relatable to r_0 . Based on the fact that the atmospheric turbulence modulation transfer function is nearly gaussian [it is actually of the form of $\exp(-\alpha f^{5/3})$ instead of $\exp(-\alpha' f^{6/3})$, which we would expect if it were exactly gaussian], we may expect the image spread to also be nearly gaussian. This means that the standard deviation of the image spread corresponds to one-half the angular subtense of a slit sufficiently wide to pass exactly 68% of the total energy in the stellar image.* Making allowance for the fact that the image is not exactly gaussian, it can be shown that if w is one-half the slit width, measured in radians, then

* The 68% corresponds to the fact that

$$\int_{-\sigma}^{+\sigma} dx (2\pi \sigma^2)^{-1/2} \exp(-\frac{1}{2} x^2 / \sigma^2) \approx 0.68$$

the corresponding value of r_0 is

$$r_{0, \text{meas}} \approx 2.64 \times 10^{-7} w^{-1} \quad (14)$$

Exactly the sort of data required has been obtained separately by Hoag¹⁴ and by Meinel¹⁶. These workers made repeated measurements over a large number of nights of the slit width required at various times to pass 68% of the stellar image energy. Their results have been assembled in cumulative probability distribution form, with the results as shown in Figs. 6 and 7. The straight line nature of the cumulative distributions makes it clear that the distribution of "seeing" conditions is log-normal. These sets of measurement data may be associated with a wavelength $\lambda = 0.55 \mu$ and a zenith angle $\theta = 0$ deg. It follows from Eqs. (13) and (14) that the corresponding value for a different wavelength, zenith angle, and set of measurement conditions is given by

$$\begin{aligned} r_0 &= r_{0, \text{meas}} [A (\lambda/0.55)^{8/5} \cos^{3/5} \theta] \\ &= 2.64 \times 10^{-7} w^{-1} [A (\lambda/0.55)^{8/5} \cos^{3/5} \theta] \end{aligned} \quad (15)$$

Here A is a coefficient which allows us to scale for different measurement conditions.

In order to estimate A , we first of all take note of the fact that in accordance with the general nature of the data in Figs. 2 and 3, the dominant contribution to $\int ds C_n^2$ comes from the first few hundred meters above the ground. This means that the altitude of the ground station, say between sea level and one-mile high, should make little difference as far as r_0 is concerned. It is the height above the ground, not absolute altitude that matters. The second point of significance to note from Fig. 2 is

the indicated difference between the day time and the night time values of C_n^2 . This difference reflects the difference in high speed thermometer measurements obtained by Koprov and Tsvang⁵ and in near ground laser scintillation measurements from day time to night time. While we are somewhat reluctant to place too much confidence in the absolute value of C_n^2 in this figure, we may treat the relative magnitudes with much more confidence. Consideration of the effect of the difference of the day or night curves in Fig. 2 leads to a ratio in $[\int ds C_n^2]^{-3/5}$ from night to day of 1.56, so that we estimate that

$$A = (1.56)^{-1} = 0.64 \quad (16)$$

Now we note from Figs. 6 and 7 that for the 50% probable frequency, the slit width required to pass 68% of the energy is about 1.4 arc seconds. This leads to a value of w of 3.4×10^{-6} rad. 50% of the time, the standard deviation of the stellar image is 3.4 μ rad or less. The 90% probable slit width is about 2.1 arc seconds. The corresponding value of w is 5.0×10^{-6} rad. 90% of the time, the standard deviation of the stellar image is 5.0 μ rad or less. These values are, of course, for night time conditions. We use the factor $A = 0.64$ to obtain corresponding day time values. From this information and utilizing Eqs. (14) and (15), we can write that for any wavelength and zenith angle,

$$r_0 = (r_0)_{i,j} (\lambda/0.55)^{6/5} \cos^{3/5} \theta \quad (17)$$

where $(r_0)_{i,j}$ takes the four values

$$(r_0)_{\text{day}, 50\%} = 0.049 \text{ m ,}$$

$$(r_0)_{\text{day}, 90\%} = 0.033 \text{ m ,}$$

$$\begin{aligned}(r_0)_{\text{night}, 50\%} &= 0.076 \text{ m.} \\ (r_0)_{\text{night}, 90\%} &= 0.052 \text{ m.}\end{aligned}\tag{18}$$

With the above data and formulations, we are now ready to proceed with calculations of the effects of atmospheric turbulence on a laser transmitter.

We wish to consider a wide variety of conditions, and therefore Table 5, which presents the results of our calculations, is fairly extensive. Each page in Table 5 can be separated into two parts. The upper part of the page represents the effective log-amplitude variance we expect for each parameter set of interest. Calculations are in accordance with Eq. (12) and subsidiary Eqs. (1), (3), (4), (17), and (8), and the data in Table 4. In the lower part of each page, we show the results of combining the effective log-amplitude variance results, via the signal variation loss factor information given in Fig. 1, with the average antenna gain information in Table 3, to allow us to calculate an effective antenna gain. This effective antenna gain incorporates both the fluctuation loss factor and average gain. All effective antenna gain factors are given in dB relative to the free space value for the value of r_0 given at the top of the page.

For all of the calculations in Table 5, we have allowed for two scale heights, $h_0 = 5 \text{ km}$ and $h_0 = 10 \text{ km}$. The results corresponding to the latter scale height are shown in parentheses immediately below the values for the former scale height. The six columns of data correspond to conditions of high altitude turbulence producing stellar scintillation at 0.55μ from the zenith of $\sigma_\ell^2 = 0.00, 0.01, 0.02, 0.04, 0.07, 0.10$, which we have scaled to the conditions of interest by making use of Eq. (1).

The column to the left of the basic data gives the value of D/r_0 for which the results of that row were computed. It should be noted that for the static and the fast-tracking systems, we show results covering basically different ranges of D/r_0 . The appropriateness of these ranges is demonstrated by the fact that in Table 5 we see that the ranges for each type of system span the D/r_0 value that peaks the performance. Results have been calculated not only for the two types of systems, i.e., static and fast-tracking, but also for the four conditions listed in Eq. (18), i.e., (day, 50%), (day, 90%), (night, 50%), and (night, 90%), the three wavelengths $\lambda = 0.53, 0.633, \text{ and } 1.06$, and the two zenith angles of $\theta = 0^\circ$ and 40° . In Table 6, we give the FORTRAN Program used to prepare Table 5.

Any number of detailed conclusions can be obtained from careful examination of Table 5. We wish to call attention here to the fact that the peak performance of the fast-tracking laser transmitter system is about 10 dB better than that of the static system. This peak performance is obtained with a diameter equal to about $1.8 r_0$. The performance achieved is about equal to the free space performance of an antenna of diameter r_0 . (For cases of strong stellar scintillation, the peak performance may occur at a slightly larger diameter, and the performance may be somewhat poorer.)

Additional Comments and Considerations

In this section, we wish to consider several special points concerning the laser transmitter. In the order in which we shall take them up, they concern 1) the point-ahead and wavelength dependence problem for beacon tracking in a fast-tracking laser transmitter; 2) the tracking servo bandwidth required for the fast-tracking laser system; 3) some comments concerning burst communications to get around laser transmitter fading;

4) the effect of using multiple transmitters.

POINT-AHEAD AND WAVELENGTH - Fundamental to the concept of the fast-tracking system is the assumption that the received beacon signal can be used to provide the necessary tracking signals for the laser transmitter. This, in turn, assumes that the beacon is at the same wavelength as the laser transmitter, and traverses the same path as the beam from the laser transmitter. In fact, neither of these assumptions is actually fulfilled, the first because the beacon and the laser transmitter are not, as a practical matter, at the same wavelength. The second assumption is violated because of the point-ahead requirement associated with the satellite's velocity in inertial-space. (Note: A stationary satellite is moving rapidly in inertial space.) We shall show that these discrepancies are not significant.

For a stationary satellite, the inertial velocity is about 3×10^3 m/sec so that the point-ahead angle is $2v/c = 2 \times 10^{-6}$ rad. Most of the wavefront distortion that the fast-tracking system is trying to track out is generated in the first 100 m above the ground. In this region the 20μ rad point-ahead only results in a maximum displacement between the collected part of the incoming beacon and the outgoing laser transmitter beam of $0.2 \text{ sec } \theta \text{ cm}$.

This is so much less than r_0 , which is really the distance over which the turbulence effects are well correlated, that we can be sure that correlation between the wavefront distortion in signal we get from the beacon and the wavefront distortion that the outgoing signal will experience is very good. Point-ahead should produce no significant degradation in the fast-tracking laser transmitter's performance.

In reference 16, it is shown that there is a very high degree of correlation of wavefront distortion for different wavelengths. In fact, for a factor of two difference in wavelength, there is nearly an 80% correlation between wavefront distortion at the two wavelengths. Hence we do not expect the difference between the beacon and transmitter wavelengths to significantly affect the fast-tracking system's performance.

TRACKING SERVO BANDWIDTH - The required fast-tracking system servo bandwidth may be estimated by considering that it is wind velocity that transports the wavefront distortion pattern across the antenna aperture, i.e., the distortion changes mostly by shifting rather than by actual reformation of the turbulence itself. When the pattern has moved a distance of the order of about r_0 , the change in wavefront tilt starts to become significant. In this time, the servo must have been able to sense and track out this change in tilt. Since most of the wavefront distortion is generated by turbulence in the first 100 m above the ground, we are concerned with wind speeds near the ground. A 30 mph wind, which is a substantial one near the ground, is equivalent to about 13.5 m/sec. For $r_0 = 0.05$ m, which together with the 30 mph wind represents a fairly extreme situation, the time for the servo to respond should be higher than $(270)^{-1}$ sec. This corresponds to a frequency of $270/2\pi = 43$ Hz. To be conservative, we would seek a servo bandwidth of 100 to 200 Hz, to insure that under all circumstances we will have a more than adequate servo bandwidth to make the fast-tracking laser transmitter system work as planned.

BURST COMMUNICATIONS - The concept of burst communication is that if we have an adequate data storage buffer for a fluctuating channel, we can

restrict data transmission to periods of extra good signal strength. Reciprocity of transmitter and receiver antenna gain⁷ assure us that we can use the strength of the received beacon signal to tell when to transmit data. We ask how long we may have to wait for a good transmission period. Actually, we shall simply concern ourselves here with the period for the fading to change and then assume that one out of every ten sample conditions is suitable for transmission (although this 1:10 factor actually should be studied in some detail). For a low wind speed of 1 m/sec and a large $r_0 = 0.2$ m, which combination represents a fairly pessimistic situation for the burst communications concept, the duration of a fade condition should be about 0.2 sec. This means that at least once every two seconds a suitable transmission interval will occur. To accommodate a 50k bit data rate, we would need at least 100k bits of buffer storage, times, of course, some safety factor.

MULTIPLE TRANSMITTERS - One approach to the problem of achieving better transmitter performance with a ground-based laser transmitter is to use multiple lasers and multiple transmitter apertures. Obviously, to avoid unacceptable far-field interference, the lasers must be sufficiently far apart in wavelength that their beat frequencies are outside the data modulation frequency range. There are a number of advantages in the use of multiple transmitters. First of all, we note that more power is transmitted. If two transmitters are used, there is an increase by two in total power and so a 3 dB link improvement. (For ten transmitters, there is a 10 dB improvement.) Moreover, the use of multiple transmitters suppresses fading and alleviates the fading loss. This is a second more important advantage. As a rule of thumb, to estimate the fading loss improvement,

use the data in Table 5 to obtain the effective log-amplitude variance for a single transmitter, convert this to a loss factor by multiplying by 100 (in approximate agreement with Fig. 1), and then figure that the use of n transmitters eliminates $(1 - n^{-1})$ of this loss. For example, the use of 4 transmitters when the transmitter's log-amplitude variance is 0.05 should get back about 4 dB of the fading loss, as well as, of course, providing 6 dB more power. The exact details of an optimum utilization of multiple transmitters should, in general, take account of the fact that suppressing fading will result in the individual transmitter diameter's being larger for optimum performance than they would be for a single transmitter.

References

1. V. I. Tatarski, "Wave Propagation in a Turbulent Medium," McGraw-Hill, New York (1961), Chap. 12, Fig. 25.
2. D. L. Fried, G. E. Mevers, and M. P. Keister, Jr., J. Opt. Soc. Am. 57, 787 (1967).
3. R. L. Mitchell, J. Opt. Soc. Am. 58, 1267 (1968).
4. J. J. Burke, J. Opt. Soc. Am. 60, 1262 (1970).
5. V. M. Koprov and L. R. Tsvang, Izv. Atmos. and Ocean Phys. 2, 1142 (1966).
6. D. L. Fried, J. Opt. Soc. Am. 57, 169 (1967).
7. D. L. Fried, Optical Science Consultants Report No. TR-030, "Antenna Gain Reciprocity for Propagation in a Turbulent Medium," Sept. 1971.
8. D. L. Fried, Optical Science Consultants Report No. TR-027, "Effects of Atmospheric Turbulence on Static and Tracking Optical Heterodyne Receivers/Average Antenna Gain and Antenna Gain Variation," Aug. 1971.
9. I. Goldstein, P. A. Miles, and A. Chabot, Proc. IEEE 53, 1172 (1965).
10. D. L. Fried, Proc. IEEE 55, 57 (1967).
11. R. F. Lutomirski and H. T. Yura, J. Opt. Soc. Am. 61, 482 (1971).
12. D. L. Fried, J. Opt. Soc. Am. 56, 1372 (1966).
13. E. L. O'Neill, "Introduction to Statistical Optics," Addison-Wesley, Reading, Mass. (1963), Chap. 7.
14. A. A. Hoag, Bulletin Astronomique, XXIV, Pt. 2, 269 (1964).
15. A. B. Meinel, "Final Report on the Site Selection Survey for the National Astronomical Observatory," Contributions from the Kitt Peak National Observatory, No. 45 (Oct. 1963).
16. D. L. Fried, Appl. Opt. 10, 721 (1971).

TABLE I

Aperture Averaged Log-Amplitude Variance
For A Photon-Bucket Type Receiver

(Results are presented for collection aperture diameters of 0.15 m, 0.255 m, 0.3 m, and 0.6 m and for zenith angles of 0° and 40° . Calculations are for laser wavelengths of $\lambda = 0.53 \mu$, 0.633μ , and 1.06μ , and for turbulence conditions that would produce zenith angle stellar scintillation at 0.55μ of $(\sigma_\ell^2)_0 = 0.01, 0.02, 0.04, 0.07, \text{ and } 0.10$. The quantities in parentheses are calculated for a turbulence scale height $h_0 = 10 \text{ km}$. Those without parentheses are for $h_0 = 5 \text{ km}$.)

DIAMETER = .150 (METER)

ZENITH ANGLE = 0. (DEG)

	$\lambda = 0.53 \mu$	0.633 μ	1.06 μ
$\sigma_l^2 =$			
.01	.001 (.001)	.001 (.001)	.001 (.001)
.02	.002 (.003)	.001 (.003)	.001 (.002)
.04	.003 (.006)	.003 (.005)	.003 (.004)
.07	.006 (.011)	.005 (.010)	.005 (.008)
.10	.009 (.016)	.008 (.015)	.007 (.012)

ZENITH ANGLE = 40. (DEG)

	$\lambda = 0.53 \mu$	0.633 μ	1.06 μ
$\sigma_l^2 =$			
.01	.003 (.005)	.002 (.004)	.002 (.003)
.02	.005 (.010)	.005 (.009)	.004 (.007)
.04	.012 (.021)	.011 (.019)	.009 (.014)
.07	.023 (.041)	.021 (.036)	.016 (.026)
.10	.038 (.065)	.033 (.056)	.024 (.038)

DIAMETER = .255 (METER)

ZENITH ANGLE = 0. (DEG)

	$\lambda = 0.53 \mu$	0.633 μ	1.06 μ
$\sigma_l^2 =$			
.01	.000 (.001)	.000 (.001)	.000 (.000)
.02	.001 (.001)	.001 (.001)	.000 (.001)
.04	.001 (.002)	.001 (.002)	.001 (.002)
.07	.002 (.004)	.002 (.004)	.002 (.003)
.10	.003 (.006)	.003 (.006)	.003 (.005)

ZENITH ANGLE = 40. (DEG)

	$\lambda = 0.53 \mu$	0.633 μ	1.06 μ
$\sigma_l^2 =$			
.01	.001 (.002)	.001 (.002)	.001 (.001)
.02	.002 (.004)	.002 (.004)	.002 (.003)
.04	.004 (.008)	.004 (.008)	.003 (.006)
.07	.009 (.017)	.008 (.015)	.006 (.012)
.10	.015 (.028)	.013 (.024)	.010 (.018)

DIAMETER = .600 (METER)

ZENITH ANGLE = 0. (DEG)

	$\lambda = 0.53 \mu$	0.633 μ	1.06 μ
$\sigma_L^2 =$			
.01	.0000 (.0000)	.0000 (.0000)	.0000 (.0000)
.02	.0000 (.0001)	.0000 (.0001)	.0000 (.0001)
.04	.0001 (.0002)	.0001 (.0002)	.0001 (.0001)
.07	.0003 (.0003)	.0001 (.0003)	.0001 (.0002)
.10	.0003 (.0005)	.0002 (.0004)	.0002 (.0004)

ZENITH ANGLE = 40. (DEG)

	$\lambda = 0.53 \mu$	0.633 μ	1.06 μ
$\sigma_L^2 =$			
.01	.0001 (.0001)	.0001 (.0001)	.0001 (.0001)
.02	.0001 (.0003)	.0001 (.0003)	.0001 (.0002)
.04	.0003 (.0006)	.0003 (.0006)	.0003 (.0005)
.07	.0007 (.0013)	.0006 (.0011)	.0005 (.0009)
.10	.0011 (.0021)	.0010 (.0018)	.0007 (.0013)

DIAMETER = .600 (METER)

ZENITH ANGLE = 0. (DEG)

	$\lambda = 0.53 \mu$	0.633 μ	1.06 μ
$\sigma_L^2 =$			
.01	.0000 (.0000)	.0000 (.0000)	.0000 (.0000)
.02	.0000 (.0000)	.0000 (.0000)	.0000 (.0000)
.04	.0000 (.0000)	.0000 (.0000)	.0000 (.0000)
.07	.0000 (.0001)	.0000 (.0001)	.0000 (.0001)
.10	.0001 (.0001)	.0001 (.0001)	.0000 (.0001)

ZENITH ANGLE = 40. (DEG)

	$\lambda = 0.53 \mu$	0.633 μ	1.06 μ
$\sigma_L^2 =$			
.01	.0000 (.0000)	.0000 (.0000)	.0000 (.0000)
.02	.0000 (.0001)	.0000 (.0001)	.0000 (.0001)
.04	.0001 (.0002)	.0001 (.0002)	.0001 (.0001)
.07	.0002 (.0003)	.0002 (.0003)	.0001 (.0002)
.10	.0003 (.0006)	.0002 (.0005)	.0002 (.0004)

TABLE 2

Listing of FORTRAN Program

Used to Prepare Table 1

LIST

```

100 DIMENSION H(2), WL(3), TH(2), STH(2), D(4), SL(5),
110 +SLA(2,3,2,4,5)
120 H(1)=5.E3;H(2)=1.E4
130 WL(1)=.53;WL(2)=.633;WL(3)=1.06
140 TH(1)=0.0;TH(2)=40.0
150 STH(1)=1.0;STH(2)=1.556
160 D(1)=0.15;D(2)=0.255;D(3)=0.30;D(4)=0.60
170 SL(1)=.01;SL(2)=.02;SL(3)=.04;SL(4)=.07;SL(5)=.10
180 DO 10 I=1,2
190 DO 20 J=1,3
200 DO 30 K=1,2
210 R=.9* SORT (H(I)*WL(J)*(1.E-6)* STH(K))
220 DO 40 L=1,4
230 AF=1./(1. + (D(L)/R)**2)
240 DO 50 M=1,5
245 SF=(STH(K))*(11.0/6.0)*(0.55/WL(J))*(7.0/6.0)
250 SLA(I,J,K,L,M)=.25*ALOG(AF*(EXP(4.*SF*SL(M))-1.))+1)
260 50 CONTINUE
270 40 CONTINUE
280 30 CONTINUE
290 20 CONTINUE
300 10 CONTINUE
310 DO 60 L=1,4
320 WRITE(1,70) ' ', 'DIAMETER = ', D(L), '(METER)'
330 70 FORMAT (F 6.3)
340 DO 80 K=1,2
350 WRITE (1,90)' ', 'ZENITH ANGLE = ', TH(K), ' (DEG)', ' '
360 90 FORMAT (F4.0)
370 DO 100 M=1,5
380 WRITE (1,110) SL(M), SLA(1,1,K,L,M),SLA(2,1,K,L,M),
390 +SLA(1,2,K,L,M),SLA(2,2,K,L,M),SLA(1,3,K,L,M),SLA(2,3,K,L,M)
400 110 FORMAT(6X,F4.2,3X,3(4X,F5.3,1X,"(",F5.3,")"))
410 100 CONTINUE
420 80 CONTINUE
430 60 CONTINUE
440 STOP

```

TABLE 3

Average Antenna Gain As A Function of D/r_0

(All antenna gains are normalized to a free space propagation value of unity for an antenna of diameter r_0 .)

<u>D/r_0</u>	<u>Average Antenna Gain</u>	
	(Static System)	(Fast-Tracking System)
0.1	0.0095	0.0096
0.15	0.0208	0.0216
0.2	0.0361	0.0382
0.3	0.0760	0.0851
0.4	0.125	0.149
0.6	0.234	0.324
0.8	0.339	0.551
1.0	0.429	0.817
1.2	0.503	1.108
1.4	0.563	1.412
1.6	0.611	1.717
1.8	0.652	2.01
2.0	0.685	2.29
2.3	0.726	2.66
2.6	0.757	2.95
2.9	0.782	3.17
3.2	0.802	3.32
3.5	0.818	3.40
3.8	0.831	3.42
4.1	0.842	3.39
4.4	0.851	3.33
4.7	0.858	3.24
5.0	0.864	3.14

TABLE 4

Antenna Gain Variance Factor, $\Phi(D/r_0)$

(The significance of Φ in computing antenna gain variance is presented in Eq. (12) in the text.)

D/r_0	$\Phi(D/r_0)$	
	(Static System)	(Fast-Tracking System)
0.1	1.0017	1.0005
0.15	1.0043	1.0012
0.2	1.0087	1.0021
0.3	1.0238	1.0053
0.4	1.0502	1.0071
0.6	1.145	1.0146
0.8	1.300	1.0224
1.0	1.514	1.0368
1.2	1.780	1.0522
1.4	2.09	1.0710
1.6	2.45	1.0936
1.8	2.83	1.121
2.0	3.25	1.153
2.3	3.96	1.214
2.6	4.74	1.292
2.9	5.60	1.492
3.2	6.55	1.519
3.5	7.58	1.681
3.8		1.883
4.1		2.13
4.4		2.44
4.7		2.82
5.0		3.26

TABLE 5

Atmospheric Turbulence Effects On A Laser Transmitter

(Results are shown in terms of the effective signal log-amplitude variance in the upper half of each data set, and in terms of antenna gain relative to the free space antenna gain for an antenna of diameter r_0 . The gain includes both the average gain associated with the diameter and the effective gain loss, per Fig. 1, due to signal strength variations. Results in each sub-section are arranged with columns corresponding to stellar scintillation levels of $\sigma_L^2 = 0.00, 0.01, 0.02, 0.04, 0.07, \text{ and } 0.10$. The rows, labeled at the left, correspond to different values of D/r_0 -- 0.10, 0.20, 0.30, 0.40, 0.60, 0.80, 1.00, 1.20 for the static systems, and 0.30, 0.60, 1.00, 1.40, 1.80, 2.30, 2.90, 3.50 for the tracking systems. Results in parentheses are computed for a scale height of $h_0 = 10 \text{ km}$, and appear just below the corresponding values for $h_0 = 5 \text{ km}$. The pertinent parameters for each data set appear in the upper left hand portion of the page.)

STATIC SYSTEM
 DAY/50-PERCENTILE
 WAVE LENGTH= 0.530 (MICRONS)
 ZENITH ANGLE= 0. (DEG.)
 R-ZERO= 0.047 (METER)

EMSC B200200 III

0.10	0.000 (0.000)	0.011 (0.011)	0.021 (0.021)	0.042 (0.042)	0.073 (0.073)	0.104 (0.104)
0.20	0.002 (0.002)	0.012 (0.012)	0.022 (0.023)	0.042 (0.043)	0.072 (0.074)	0.102 (0.104)
0.30	0.006 (0.006)	0.015 (0.016)	0.024 (0.025)	0.043 (0.045)	0.072 (0.075)	0.101 (0.105)
0.40	0.012 (0.012)	0.021 (0.022)	0.030 (0.031)	0.047 (0.050)	0.074 (0.079)	0.102 (0.108)
0.60	0.034 (0.034)	0.041 (0.042)	0.048 (0.051)	0.063 (0.068)	0.086 (0.095)	0.110 (0.122)
0.80	0.066 (0.066)	0.071 (0.073)	0.077 (0.081)	0.089 (0.096)	0.108 (0.119)	0.128 (0.144)
1.00	0.104 (0.104)	0.108 (0.110)	0.113 (0.117)	0.123 (0.130)	0.138 (0.151)	0.155 (0.172)
1.20	0.144 (0.144)	0.148 (0.150)	0.152 (0.155)	0.160 (0.167)	0.172 (0.185)	0.186 (0.204)
0.10	-20.2 (-20.2)	-21.4 (-21.4)	-22.4 (-22.4)	-24.3 (-24.3)	-26.6 (-26.6)	-28.7 (-28.8)
0.20	-14.6 (-14.6)	-15.8 (-15.8)	-16.8 (-16.8)	-18.5 (-18.6)	-20.8 (-20.9)	-22.9 (-23.0)
0.30	-11.8 (-11.8)	-12.8 (-12.9)	-13.8 (-13.9)	-15.4 (-15.6)	-17.6 (-17.8)	-19.6 (-19.8)
0.40	-10.3 (-10.3)	-11.2 (-11.3)	-12.1 (-12.3)	-13.5 (-13.8)	-15.5 (-15.9)	-17.4 (-17.9)
0.60	-9.7 (-9.7)	-10.3 (-10.4)	-10.9 (-11.1)	-12.0 (-12.4)	-13.6 (-14.2)	-15.2 (-15.9)
0.80	-10.6 (-10.6)	-11.0 (-11.1)	-11.4 (-11.7)	-12.3 (-12.7)	-13.5 (-14.2)	-14.7 (-15.6)
1.00	-12.2 (-12.2)	-12.5 (-12.6)	-12.8 (-13.0)	-13.4 (-13.8)	-14.3 (-15.0)	-15.2 (-16.1)
1.20	-13.9 (-13.9)	-14.1 (-14.2)	-14.3 (-14.5)	-14.8 (-15.2)	-15.5 (-16.1)	-16.2 (-17.1)

STATIC SYSTEM
 DAY/50-PERCENTILE
 WAVE LENGTH= 0.530 (MICRONS)
 ZENITH ANGLE= 60. (DEG.)
 R-ZERO= 0.036 (METER)

LMSC-B290200-III

0.10	0.000 (0.000)	0.024 (0.024)	0.047 (0.047)	0.094 (0.094)	0.164 (0.164)	0.234 (0.235)
0.20	0.002 (0.002)	0.025 (0.026)	0.048 (0.049)	0.095 (0.095)	0.164 (0.165)	0.234 (0.236)
0.30	0.006 (0.006)	0.028 (0.029)	0.051 (0.052)	0.096 (0.098)	0.165 (0.167)	0.234 (0.237)
0.40	0.012 (0.012)	0.034 (0.035)	0.056 (0.058)	0.100 (0.103)	0.168 (0.172)	0.236 (0.241)
0.60	0.034 (0.034)	0.054 (0.056)	0.074 (0.077)	0.116 (0.121)	0.180 (0.188)	0.245 (0.256)
0.80	0.066 (0.066)	0.084 (0.086)	0.102 (0.107)	0.140 (0.149)	0.199 (0.213)	0.261 (0.279)
1.00	0.104 (0.104)	0.120 (0.123)	0.136 (0.142)	0.170 (0.182)	0.225 (0.243)	0.283 (0.307)
1.20	0.144 (0.144)	0.158 (0.162)	0.173 (0.180)	0.203 (0.217)	0.253 (0.275)	0.306 (0.336)
0.10	-20.2 (-20.2)	-22.7 (-22.7)	-24.7 (-24.7)	-28.1 (-28.1)	-32.3 (-32.3)	-36.0 (-36.0)
0.20	-14.6 (-14.6)	-17.1 (-17.1)	-19.0 (-19.1)	-22.4 (-22.4)	-26.5 (-26.5)	-30.2 (-30.2)
0.30	-11.8 (-11.8)	-14.1 (-14.2)	-16.0 (-16.0)	-19.2 (-19.4)	-23.3 (-23.4)	-26.9 (-27.1)
0.40	-10.3 (-10.3)	-12.5 (-12.6)	-14.2 (-14.3)	-17.4 (-17.5)	-21.3 (-21.5)	-24.8 (-25.1)
0.60	-9.7 (-9.7)	-11.3 (-11.5)	-12.8 (-13.0)	-15.6 (-15.9)	-19.2 (-19.7)	-22.6 (-23.1)
0.80	-10.6 (-10.6)	-11.9 (-12.0)	-13.1 (-13.4)	-15.4 (-15.9)	-18.6 (-19.3)	-21.8 (-22.6)
1.00	-12.2 (-12.2)	-13.2 (-13.4)	-14.1 (-14.5)	-16.1 (-16.7)	-18.9 (-19.8)	-21.8 (-22.9)
1.20	-13.9 (-13.9)	-14.7 (-14.9)	-15.5 (-15.9)	-17.1 (-17.8)	-19.6 (-20.7)	-22.2 (-23.6)

TRACKING SYSTEM
 DAY/50-PERCENTILE
 WAVE LENGTH= 0.530 (MICRONS)
 ZENITH ANGLE= 0. (DEG.)
 R-ZERO= 0.047 (METER)

LMSC-B290200-III

0.30	0.001 (0.001)	0.010 (0.011)	0.020 (0.021)	0.039 (0.041)	0.067 (0.071)	0.096 (0.101)
0.60	0.004 (0.004)	0.011 (0.012)	0.018 (0.021)	0.033 (0.038)	0.056 (0.065)	0.079 (0.091)
1.00	0.009 (0.009)	0.014 (0.015)	0.018 (0.022)	0.028 (0.035)	0.044 (0.056)	0.060 (0.077)
1.40	0.017 (0.017)	0.020 (0.022)	0.023 (0.027)	0.030 (0.036)	0.040 (0.052)	0.051 (0.069)
1.80	0.029 (0.029)	0.031 (0.032)	0.033 (0.035)	0.037 (0.043)	0.044 (0.055)	0.052 (0.067)
2.30	0.048 (0.048)	0.050 (0.051)	0.051 (0.053)	0.054 (0.059)	0.059 (0.067)	0.064 (0.076)
2.90	0.081 (0.081)	0.082 (0.083)	0.083 (0.084)	0.085 (0.088)	0.088 (0.094)	0.092 (0.100)
3.50	0.130 (0.130)	0.130 (0.131)	0.131 (0.132)	0.133 (0.135)	0.135 (0.139)	0.137 (0.144)

0.30	-10.8 (-10.8)	-11.8 (-11.9)	-12.8 (-12.9)	-14.5 (-14.7)	-16.7 (-17.0)	-18.8 (-19.0)
0.60	-5.2 (-5.2)	-6.1 (-6.2)	-6.8 (-7.1)	-8.3 (-8.7)	-10.1 (-10.7)	-11.8 (-12.6)
1.00	-1.9 (-1.9)	-2.3 (-2.5)	-2.8 (-3.2)	-3.8 (-4.4)	-5.1 (-6.1)	-6.4 (-7.6)
1.40	-0.3 (-0.3)	-0.6 (-0.8)	-0.9 (-1.3)	-1.6 (-2.2)	-2.4 (-3.4)	-3.3 (-4.6)
1.80	0.1 (0.1)	-0.1 (-0.2)	-0.3 (-0.5)	-0.7 (-1.1)	-1.3 (-2.0)	-1.9 (-3.0)
2.30	-0.4 (-0.4)	-0.5 (-0.5)	-0.6 (-0.7)	-0.8 (-1.1)	-1.2 (-1.7)	-1.6 (-2.4)
2.90	-2.0 (-2.0)	-2.0 (-2.1)	-2.1 (-2.2)	-2.2 (-2.5)	-2.5 (-2.9)	-2.7 (-3.3)
3.50	-4.8 (-4.8)	-4.8 (-4.9)	-4.9 (-4.9)	-4.9 (-5.1)	-5.1 (-5.3)	-5.2 (-5.6)

TRACKING SYSTEM
 DAY/50-PERCENTILE
 WAVE LENGTH= 0.530 (MICRONS)
 ZENITH ANGLE= 90. (DEG.)
 R-ZERO= 0.036 (METER)

LMSC-B200200 III

0.30	0.001 (0.001)	0.024 (0.024)	0.046 (0.047)	0.092 (0.093)	0.160 (0.163)	0.229 (0.233)
0.60	0.004 (0.004)	0.024 (0.025)	0.044 (0.047)	0.086 (0.091)	0.149 (0.158)	0.215 (0.226)
1.00	0.009 (0.009)	0.025 (0.028)	0.042 (0.047)	0.076 (0.087)	0.130 (0.149)	0.188 (0.212)
1.40	0.017 (0.017)	0.029 (0.033)	0.042 (0.050)	0.069 (0.084)	0.114 (0.139)	0.163 (0.197)
1.80	0.029 (0.029)	0.038 (0.042)	0.048 (0.056)	0.069 (0.085)	0.105 (0.133)	0.146 (0.185)
2.30	0.048 (0.048)	0.055 (0.059)	0.062 (0.070)	0.078 (0.094)	0.106 (0.134)	0.139 (0.178)
2.90	0.081 (0.081)	0.086 (0.089)	0.091 (0.097)	0.102 (0.116)	0.123 (0.147)	0.147 (0.184)
3.50	0.130 (0.130)	0.133 (0.136)	0.137 (0.142)	0.146 (0.157)	0.161 (0.182)	0.180 (0.212)
0.30	-10.8 (-10.8)	-13.2 (-13.2)	-15.1 (-15.2)	-18.4 (-18.5)	-22.5 (-22.7)	-26.2 (-26.3)
0.60	-5.2 (-5.2)	-7.4 (-7.6)	-9.2 (-9.4)	-12.2 (-12.6)	-16.1 (-16.6)	-19.6 (-20.2)
1.00	-1.9 (-1.9)	-3.5 (-3.8)	-4.9 (-5.4)	-7.5 (-8.3)	-11.0 (-12.0)	-14.2 (-15.5)
1.40	-0.3 (-0.3)	-1.6 (-1.9)	-2.6 (-3.2)	-4.7 (-5.7)	-7.7 (-9.1)	-10.5 (-12.3)
1.80	0.1 (0.1)	-0.7 (-1.1)	-1.5 (-2.1)	-3.1 (-4.2)	-5.6 (-7.2)	-8.0 (-10.1)
2.30	-0.4 (-0.4)	-0.9 (-1.2)	-1.4 (-2.0)	-2.6 (-3.6)	-4.4 (-6.1)	-6.4 (-8.6)
2.90	-2.0 (-2.0)	-2.3 (-2.5)	-2.7 (-3.1)	-3.4 (-4.2)	-4.7 (-6.1)	-6.1 (-8.1)
3.50	-4.8 (-4.8)	-5.0 (-5.1)	-5.2 (-5.5)	-5.7 (-6.3)	-6.6 (-7.7)	-7.6 (-9.3)

STATIC SYSTEM
 DAY/90-PERCENTILE
 WAVE LENGTH= 0.530 (MICRONS)
 ZENITH ANGLE= 0. (DEG.)
 R-ZERO= 0.032 (METER)

LMSC-B290200-III

0.10	0.000 (0.000)	0.011 (0.011)	0.021 (0.021)	0.042 (0.042)	0.073 (0.073)	0.104 (0.104)
0.20	0.002 (0.002)	0.012 (0.013)	0.023 (0.023)	0.043 (0.044)	0.074 (0.075)	0.105 (0.106)
0.30	0.006 (0.006)	0.016 (0.016)	0.026 (0.026)	0.046 (0.046)	0.076 (0.077)	0.106 (0.108)
0.40	0.012 (0.012)	0.022 (0.022)	0.031 (0.032)	0.051 (0.052)	0.080 (0.082)	0.109 (0.113)
0.60	0.034 (0.034)	0.043 (0.043)	0.051 (0.053)	0.069 (0.072)	0.096 (0.101)	0.123 (0.130)
0.80	0.066 (0.066)	0.073 (0.074)	0.081 (0.083)	0.097 (0.101)	0.121 (0.128)	0.146 (0.156)
1.00	0.104 (0.104)	0.110 (0.112)	0.117 (0.120)	0.131 (0.137)	0.152 (0.162)	0.174 (0.188)
1.20	0.144 (0.144)	0.150 (0.152)	0.156 (0.159)	0.168 (0.174)	0.186 (0.198)	0.206 (0.222), 2
0.10	-20.2 (-20.2)	-21.4 (-21.4)	-22.4 (-22.4)	-24.3 (-24.3)	-26.6 (-26.7)	-28.8 (-28.8)
0.20	-14.6 (-14.6)	-15.8 (-15.8)	-16.8 (-16.8)	-18.6 (-18.7)	-20.9 (-21.0)	-23.0 (-23.1)
0.30	-11.8 (-11.8)	-12.9 (-12.9)	-13.9 (-13.9)	-15.6 (-15.6)	-17.8 (-17.9)	-19.8 (-20.0)
0.40	-10.3 (-10.3)	-11.3 (-11.4)	-12.3 (-12.3)	-13.8 (-13.9)	-15.9 (-16.1)	-17.9 (-18.1)
0.60	-9.7 (-9.7)	-10.4 (-10.5)	-11.1 (-11.2)	-12.4 (-12.7)	-14.3 (-14.7)	-16.0 (-16.4)
0.80	-10.6 (-10.6)	-11.1 (-11.2)	-11.7 (-11.9)	-12.8 (-13.1)	-14.3 (-14.7)	-15.7 (-16.3)
1.00	-12.2 (-12.2)	-12.6 (-12.7)	-13.0 (-13.2)	-13.8 (-14.2)	-15.0 (-15.6)	-16.3 (-17.0)
1.20	-13.9 (-13.9)	-14.2 (-14.3)	-14.6 (-14.7)	-15.2 (-15.6)	-16.2 (-16.8)	-17.3 (-18.1)

STATIC SYSTEM
 DAY/90-PERCENTILE
 WAVE LENGTH= 0.530 (MICRONS)
 ZENITH ANGLE= 40. (DEG.)
 R-ZERO= 0.024 (METER)

LMSC-B290200-III

0.10	0.000 (0.000)	0.024 (0.024)	0.047 (0.047)	0.094 (0.094)	0.164 (0.165)	0.235 (0.235)
0.20	0.002 (0.002)	0.026 (0.026)	0.049 (0.049)	0.095 (0.096)	0.166 (0.166)	0.236 (0.236)
0.30	0.006 (0.006)	0.029 (0.029)	0.052 (0.052)	0.098 (0.099)	0.168 (0.169)	0.238 (0.239)
0.40	0.012 (0.012)	0.035 (0.035)	0.058 (0.058)	0.103 (0.105)	0.172 (0.174)	0.242 (0.244)
0.60	0.034 (0.034)	0.056 (0.056)	0.078 (0.079)	0.122 (0.125)	0.189 (0.194)	0.257 (0.263)
0.80	0.066 (0.066)	0.086 (0.088)	0.107 (0.110)	0.150 (0.154)	0.215 (0.222)	0.281 (0.290)
1.00	0.104 (0.104)	0.123 (0.125)	0.143 (0.146)	0.183 (0.190)	0.245 (0.256)	0.309 (0.323)
1.20	0.144 (0.144)	0.162 (0.165)	0.181 (0.185)	0.218 (0.227)	0.278 (0.291)	0.339 (0.357)
0.10	-20.2 (-20.2)	-22.7 (-22.7)	-24.7 (-24.7)	-28.1 (-28.1)	-32.3 (-32.3)	-36.0 (-36.0)
0.20	-14.6 (-14.6)	-17.1 (-17.1)	-19.1 (-19.1)	-22.4 (-22.5)	-26.6 (-26.6)	-30.2 (-30.3)
0.30	-11.8 (-11.8)	-14.2 (-14.2)	-16.1 (-16.1)	-19.4 (-19.4)	-23.4 (-23.5)	-27.1 (-27.2)
0.40	-10.3 (-10.3)	-12.6 (-12.6)	-14.3 (-14.4)	-17.5 (-17.6)	-21.5 (-21.6)	-25.1 (-25.3)
0.60	-9.7 (-9.7)	-11.5 (-11.5)	-13.1 (-13.2)	-15.9 (-16.1)	-19.7 (-19.9)	-23.2 (-23.4)
0.80	-10.6 (-10.6)	-12.1 (-12.2)	-13.4 (-13.6)	-15.9 (-16.2)	-19.4 (-19.8)	-22.7 (-23.2)
1.00	-12.2 (-12.2)	-13.4 (-13.5)	-14.5 (-14.7)	-16.7 (-17.1)	-19.9 (-20.5)	-23.0 (-23.7)
1.20	-13.9 (-13.9)	-14.9 (-15.0)	-15.9 (-16.2)	-17.9 (-18.3)	-20.8 (-21.5)	-23.7 (-24.6)

TRACKING SYSTEM
 DAY/90-PERCENTILE
 WAVE LENGTH= 0.530 (MICRONS)
 ZENITH ANGLE= 0. (DEG.)
 R-ZERO= 0.032 (METER)

LMSC-B290200-III

0.30	0.001 (0.001)	0.011 (0.011)	0.021 (0.021)	0.041 (0.042)	0.071 (0.072)	0.101 (0.103)
0.60	0.004 (0.004)	0.012 (0.013)	0.021 (0.022)	0.039 (0.042)	0.065 (0.071)	0.093 (0.100)
1.00	0.009 (0.009)	0.016 (0.017)	0.022 (0.025)	0.036 (0.042)	0.058 (0.067)	0.080 (0.093)
1.40	0.017 (0.017)	0.022 (0.024)	0.027 (0.031)	0.037 (0.044)	0.054 (0.066)	0.071 (0.088)
1.80	0.029 (0.029)	0.032 (0.034)	0.036 (0.039)	0.044 (0.051)	0.056 (0.069)	0.070 (0.087)
2.30	0.048 (0.048)	0.051 (0.053)	0.054 (0.057)	0.059 (0.066)	0.068 (0.080)	0.078 (0.095)
2.90	0.081 (0.081)	0.083 (0.084)	0.085 (0.087)	0.088 (0.094)	0.095 (0.104)	0.102 (0.116)
3.50	0.130 (0.130)	0.131 (0.132)	0.132 (0.135)	0.135 (0.140)	0.140 (0.148)	0.145 (0.157)
0.30	-10.8 (-10.8)	-11.9 (-11.9)	-12.9 (-13.0)	-14.7 (-14.8)	-17.0 (-17.1)	-19.1 (-19.2)
0.60	-5.2 (-5.2)	-6.2 (-6.3)	-7.1 (-7.3)	-8.7 (-9.0)	-10.8 (-11.2)	-12.7 (-13.2)
1.00	-1.9 (-1.9)	-2.6 (-2.7)	-3.2 (-3.5)	-4.5 (-5.0)	-6.2 (-6.9)	-7.8 (-8.7)
1.40	-0.3 (-0.3)	-0.8 (-1.0)	-1.3 (-1.7)	-2.2 (-2.8)	-3.5 (-4.4)	-4.8 (-6.0)
1.80	0.1 (0.1)	-0.3 (-0.4)	-0.6 (-0.9)	-1.2 (-1.8)	-2.2 (-3.1)	-3.1 (-4.4)
2.30	-0.4 (-0.4)	-0.6 (-0.7)	-0.8 (-1.0)	-1.2 (-1.7)	-1.8 (-2.7)	-2.6 (-3.7)
2.90	-2.0 (-2.0)	-2.1 (-2.2)	-2.2 (-2.4)	-2.5 (-2.9)	-2.9 (-3.5)	-3.4 (-4.2)
3.50	-4.8 (-4.8)	-4.9 (-4.9)	-4.9 (-5.1)	-5.1 (-5.3)	-5.4 (-5.8)	-5.7 (-6.3)

TRACKING SYSTEM
 DAY/90-PERCENTILE
 WAVE LENGTH= 0.53 (MICRONS)
 ZENITH ANGLE=40. (DEG.)
 R-ZERO= 0.024 (METER)

LMSC-B290200-III

0.30	0.001 (0.001)	0.024 (0.024)	0.047 (0.048)	0.093 (0.094)	0.163 (0.164)	0.233 (0.234)
0.60	0.004 (0.004)	0.026 (0.026)	0.048 (0.049)	0.092 (0.095)	0.159 (0.163)	0.227 (0.233)
1.00	0.009 (0.009)	0.028 (0.030)	0.048 (0.052)	0.088 (0.095)	0.151 (0.161)	0.215 (0.228)
1.40	0.017 (0.017)	0.034 (0.037)	0.051 (0.056)	0.086 (0.097)	0.142 (0.159)	0.201 (0.223)
1.80	0.029 (0.029)	0.042 (0.046)	0.057 (0.064)	0.087 (0.101)	0.137 (0.159)	0.190 (0.219)
2.30	0.048 (0.048)	0.060 (0.064)	0.071 (0.079)	0.096 (0.112)	0.137 (0.164)	0.184 (0.219)
2.90	0.081 (0.081)	0.089 (0.093)	0.098 (0.106)	0.118 (0.134)	0.151 (0.179)	0.189 (0.229)
3.50	0.130 (0.130)	0.136 (0.140)	0.143 (0.151)	0.159 (0.174)	0.186 (0.213)	0.217 (0.257)

0.30	-10.8 (-10.8)	-13.2 (-13.3)	-15.2 (-15.2)	-18.6 (-18.6)	-22.7 (-22.7)	-26.4 (-26.4)
0.60	-5.2 (-5.2)	-7.6 (-7.6)	-9.4 (-9.5)	-12.6 (-12.8)	-16.7 (-16.9)	-20.3 (-20.5)
1.00	-1.9 (-1.9)	-3.8 (-4.0)	-5.5 (-5.7)	-8.4 (-8.8)	-12.2 (-12.8)	-15.6 (-16.3)
1.40	-0.3 (-0.3)	-1.9 (-2.2)	-3.3 (-3.7)	-5.9 (-6.6)	-9.3 (-10.3)	-12.5 (-13.7)
1.80	0.1 (0.1)	-1.1 (-1.4)	-2.2 (-2.7)	-4.4 (-5.3)	-7.5 (-8.7)	-10.4 (-11.9)
2.30	-0.4 (-0.4)	-1.2 (-1.5)	-2.1 (-2.6)	-3.8 (-4.8)	-6.3 (-7.8)	-8.8 (-10.7)
2.90	-2.0 (-2.0)	-2.6 (-2.8)	-3.2 (-3.7)	-4.4 (-5.3)	-6.3 (-7.8)	-8.4 (-10.4)
3.50	-4.8 (-4.8)	-5.2 (-5.4)	-5.6 (-6.0)	-6.4 (-7.3)	-7.9 (-9.3)	-9.5 (-11.5)

STATIC SYSTEM
 NIGHT/50-PERCENTILE
 WAVE LENGTH= 0.530 (MICRONS)
 ZFNITH ANGLE= 0. (DEC.)
 R-ZERO= 0.073 (METER)

LMSC-B290200-III

0.10	0.000 (0.000)	0.010 (0.011)	0.021 (0.021)	0.041 (0.041)	0.071 (0.072)	0.102 (0.103)
0.20	0.002 (0.002)	0.012 (0.012)	0.021 (0.022)	0.040 (0.042)	0.068 (0.072)	0.097 (0.102)
0.30	0.006 (0.006)	0.014 (0.015)	0.022 (0.024)	0.039 (0.043)	0.064 (0.071)	0.091 (0.099)
0.40	0.012 (0.012)	0.019 (0.021)	0.026 (0.029)	0.041 (0.046)	0.063 (0.072)	0.086 (0.099)
0.60	0.034 (0.034)	0.039 (0.041)	0.044 (0.047)	0.054 (0.061)	0.071 (0.083)	0.089 (0.106)
0.80	0.066 (0.066)	0.069 (0.071)	0.073 (0.076)	0.080 (0.087)	0.092 (0.105)	0.106 (0.123)
1.00	0.104 (0.104)	0.106 (0.108)	0.109 (0.112)	0.114 (0.121)	0.124 (0.135)	0.133 (0.150)
1.20	0.144 (0.144)	0.146 (0.147)	0.148 (0.151)	0.152 (0.158)	0.159 (0.169)	0.167 (0.181)

0.10	-20.2 (-20.2)	-21.4 (-21.4)	-22.4 (-22.4)	-24.2 (-24.3)	-26.5 (-26.6)	-28.7 (-28.7)
0.20	-14.6 (-14.6)	-15.7 (-15.7)	-16.6 (-16.7)	-18.4 (-18.5)	-20.5 (-20.8)	-22.5 (-22.8)
0.30	-11.8 (-11.8)	-12.7 (-12.8)	-13.5 (-13.7)	-15.0 (-15.3)	-17.0 (-17.5)	-18.9 (-19.4)
0.40	-10.3 (-10.3)	-11.1 (-11.2)	-11.8 (-12.1)	-13.0 (-13.5)	-14.8 (-15.4)	-16.4 (-17.3)
0.60	-9.7 (-9.7)	-10.2 (-10.3)	-10.6 (-10.8)	-11.4 (-11.9)	-12.6 (-13.4)	-13.8 (-15.0)
0.80	-10.6 (-10.6)	-10.8 (-11.0)	-11.1 (-11.4)	-11.6 (-12.1)	-12.5 (-13.3)	-13.3 (-14.4)
1.00	-12.2 (-12.2)	-12.4 (-12.5)	-12.5 (-12.7)	-12.9 (-13.2)	-13.4 (-14.1)	-14.0 (-14.9)
1.20	-13.9 (-13.9)	-14.0 (-14.1)	-14.1 (-14.3)	-14.4 (-14.7)	-14.7 (-15.3)	-15.2 (-16.0)

STATIC SYSTEM
 NIGHT/50-PERCENTILE
 WAVE LENGTH= 0.530 (MICRONS)
 ZENITH ANGLE=40. (DEG.)
 R-ZERO= 0.056 (METER)

LMSC-B290200-III

0.10	0.000 (0.000)	0.023 (0.024)	0.047 (0.047)	0.093 (0.094)	0.163 (0.164)	0.233 (0.234)
0.20	0.002 (0.002)	0.025 (0.025)	0.047 (0.048)	0.093 (0.094)	0.161 (0.164)	0.230 (0.234)
0.30	0.006 (0.006)	0.027 (0.028)	0.049 (0.050)	0.092 (0.096)	0.158 (0.164)	0.225 (0.233)
0.40	0.012 (0.012)	0.032 (0.034)	0.052 (0.055)	0.093 (0.099)	0.157 (0.166)	0.222 (0.234)
0.60	0.034 (0.034)	0.051 (0.053)	0.068 (0.073)	0.103 (0.114)	0.160 (0.176)	0.219 (0.241)
0.80	0.066 (0.066)	0.079 (0.083)	0.093 (0.101)	0.123 (0.137)	0.172 (0.195)	0.225 (0.255)
1.00	0.104 (0.104)	0.115 (0.119)	0.126 (0.134)	0.151 (0.167)	0.193 (0.219)	0.239 (0.275)
1.20	0.144 (0.144)	0.153 (0.157)	0.163 (0.171)	0.183 (0.199)	0.218 (0.246)	0.258 (0.297)

0.10	-20.2 (-20.2)	-22.7 (-22.7)	-24.7 (-24.7)	-28.1 (-28.1)	-32.2 (-32.3)	-35.9 (-35.9)
0.20	-14.6 (-14.6)	-17.0 (-17.1)	-19.0 (-19.0)	-22.2 (-22.4)	-26.3 (-26.5)	-30.0 (-30.1)
0.30	-11.8 (-11.8)	-14.0 (-14.1)	-15.6 (-16.0)	-18.9 (-19.2)	-22.9 (-23.2)	-26.5 (-26.8)
0.40	-10.3 (-10.3)	-12.3 (-12.5)	-13.9 (-14.2)	-16.6 (-17.3)	-20.7 (-21.2)	-24.1 (-24.7)
0.60	-9.7 (-9.7)	-11.1 (-11.3)	-12.4 (-12.8)	-14.8 (-15.4)	-18.1 (-19.0)	-21.2 (-22.3)
0.80	-10.6 (-10.6)	-11.6 (-11.8)	-12.6 (-13.0)	-14.4 (-15.2)	-17.2 (-18.4)	-19.9 (-21.4)
1.00	-12.2 (-12.2)	-12.9 (-13.1)	-13.6 (-14.0)	-15.0 (-15.9)	-17.2 (-18.6)	-19.6 (-21.4)
1.20	-13.9 (-13.9)	-14.4 (-14.6)	-14.9 (-15.4)	-16.1 (-16.9)	-17.9 (-19.3)	-19.9 (-21.8)

TRACKING SYSTEM
 NIGHT/50-PERCENTILE
 WAVE LENGTH= 0.530 (MICRONS)
 ZENITH ANGLE= 0. (DEG.)
 R-ZERO= 0.073 (METER)

1.MSC-B290200-III

0.30	0.001 (0.001)	0.009 (0.010)	0.017 (0.019)	0.034 (0.038)	0.060 (0.066)	0.086 (0.095)
0.60	0.004 (0.004)	0.009 (0.010)	0.014 (0.017)	0.024 (0.031)	0.041 (0.053)	0.058 (0.075)
1.00	0.009 (0.009)	0.012 (0.013)	0.014 (0.017)	0.020 (0.026)	0.029 (0.040)	0.039 (0.055)
1.40	0.017 (0.017)	0.019 (0.020)	0.020 (0.022)	0.023 (0.028)	0.029 (0.037)	0.035 (0.047)
1.80	0.029 (0.029)	0.030 (0.030)	0.031 (0.032)	0.033 (0.036)	0.036 (0.042)	0.040 (0.049)
2.30	0.048 (0.048)	0.049 (0.050)	0.050 (0.051)	0.051 (0.053)	0.053 (0.058)	0.056 (0.062)
2.90	0.081 (0.081)	0.081 (0.082)	0.082 (0.082)	0.083 (0.084)	0.084 (0.087)	0.086 (0.090)
3.50	0.130 (0.130)	0.130 (0.130)	0.130 (0.131)	0.131 (0.132)	0.132 (0.134)	0.133 (0.136)
0.30	-10.8 (-10.8)	-11.7 (-11.8)	-12.6 (-12.8)	-14.2 (-14.5)	-16.2 (-16.6)	-18.0 (-18.6)
0.60	-5.2 (-5.2)	-5.8 (-6.0)	-6.4 (-6.7)	-7.4 (-8.1)	-8.9 (-9.8)	-10.3 (-11.5)
1.00	-1.9 (-1.9)	-2.1 (-2.3)	-2.4 (-2.7)	-3.0 (-3.6)	-3.9 (-4.8)	-4.7 (-6.0)
1.40	-0.3 (-0.3)	-0.5 (-0.6)	-0.6 (-0.9)	-1.0 (-1.4)	-1.5 (-2.2)	-2.0 (-3.0)
1.80	0.1 (0.1)	-0.0 (-0.1)	-0.1 (-0.3)	-0.3 (-0.6)	-0.6 (-1.1)	-0.9 (-1.6)
2.30	-0.4 (-0.4)	-0.4 (-0.5)	-0.5 (-0.5)	-0.6 (-0.7)	-0.7 (-1.1)	-0.9 (-1.4)
2.90	-2.0 (-2.0)	-2.0 (-2.0)	-2.0 (-2.1)	-2.1 (-2.2)	-2.2 (-2.4)	-2.3 (-2.6)
3.50	-4.8 (-4.8)	-4.8 (-4.8)	-4.8 (-4.8)	-4.9 (-5.0)	-4.9 (-5.0)	-5.0 (-5.2)

TRACKING SYSTEM
 NIGHT/50-PERCENTILE
 WAVE LENGTH= 0.530 (MICRONS)
 ZENITH ANGLE=40. (DEG.)
 R-ZERO= 0.056 (METER)

LMSC-B290200-III

0.30	0.001 (0.001)	0.022 (0.023)	0.044 (0.046)	0.087 (0.091)	0.154 (0.159)	0.221 (0.228)
0.60	0.004 (0.004)	0.020 (0.023)	0.038 (0.043)	0.073 (0.084)	0.129 (0.146)	0.189 (0.210)
1.00	0.009 (0.009)	0.020 (0.024)	0.032 (0.040)	0.057 (0.072)	0.098 (0.124)	0.144 (0.180)
1.40	0.017 (0.017)	0.024 (0.028)	0.032 (0.040)	0.049 (0.059)	0.079 (0.107)	0.114 (0.153)
1.80	0.029 (0.029)	0.034 (0.037)	0.039 (0.046)	0.051 (0.065)	0.073 (0.098)	0.099 (0.136)
2.30	0.048 (0.048)	0.052 (0.054)	0.056 (0.061)	0.064 (0.075)	0.079 (0.099)	0.097 (0.129)
2.90	0.081 (0.081)	0.083 (0.085)	0.086 (0.089)	0.091 (0.099)	0.101 (0.117)	0.114 (0.139)
3.50	0.130 (0.130)	0.131 (0.133)	0.133 (0.136)	0.137 (0.143)	0.144 (0.157)	0.154 (0.173)

0.30	-10.8 (-10.8)	-13.1 (-13.2)	-15.0 (-15.1)	-18.1 (-18.4)	-22.2 (-22.5)	-25.7 (-26.1)
0.60	-5.2 (-5.2)	-7.1 (-7.3)	-8.6 (-9.1)	-11.3 (-12.1)	-15.0 (-15.9)	-18.3 (-19.4)
1.00	-1.9 (-1.9)	-3.0 (-3.4)	-4.1 (-4.8)	-6.1 (-7.2)	-9.0 (-10.6)	-11.8 (-13.8)
1.40	-0.3 (-0.3)	-1.1 (-1.5)	-1.8 (-2.4)	-3.2 (-4.4)	-5.4 (-7.2)	-7.6 (-9.9)
1.80	0.1 (0.1)	-0.4 (-0.7)	-0.8 (-1.4)	-1.8 (-2.8)	-3.4 (-5.1)	-5.2 (-7.4)
2.30	-0.4 (-0.4)	-0.6 (-0.8)	-0.9 (-1.3)	-1.5 (-2.3)	-2.6 (-4.0)	-3.9 (-5.8)
2.90	-2.0 (-2.0)	-2.1 (-2.3)	-2.3 (-2.6)	-2.7 (-3.2)	-3.4 (-4.3)	-4.2 (-5.6)
3.50	-4.8 (-4.8)	-4.9 (-5.0)	-5.0 (-5.1)	-5.2 (-5.6)	-5.6 (-6.3)	-6.2 (-7.2)

STATIC SYSTEM
 NIGHT/90-PERCENTILE
 WAVE LENGTH= 0.530 (MICRONS)
 ZENITH ANGLE= 0. (DEG.)
 R-ZERO= 0.050 (METER)

LMSC-B290200-III

0.10	0.000 (0.000)	0.011 (0.011)	0.021 (0.021)	0.041 (0.042)	0.072 (0.073)	0.103 (0.104)
0.20	0.002 (0.002)	0.012 (0.012)	0.022 (0.023)	0.042 (0.043)	0.072 (0.074)	0.102 (0.104)
0.30	0.006 (0.006)	0.015 (0.015)	0.024 (0.025)	0.043 (0.045)	0.071 (0.075)	0.100 (0.105)
0.40	0.012 (0.012)	0.021 (0.022)	0.029 (0.031)	0.047 (0.050)	0.073 (0.079)	0.100 (0.108)
0.60	0.034 (0.034)	0.041 (0.042)	0.048 (0.051)	0.062 (0.067)	0.084 (0.093)	0.107 (0.120)
0.80	0.066 (0.066)	0.071 (0.073)	0.077 (0.080)	0.088 (0.095)	0.106 (0.118)	0.125 (0.141)
1.00	0.104 (0.104)	0.108 (0.110)	0.112 (0.116)	0.122 (0.129)	0.136 (0.149)	0.152 (0.169)
1.20	0.144 (0.144)	0.148 (0.149)	0.151 (0.155)	0.158 (0.165)	0.170 (0.182)	0.183 (0.201)
0.10	-20.2 (-20.2)	-21.4 (-21.4)	-22.4 (-22.4)	-24.3 (-24.3)	-26.6 (-26.6)	-28.7 (-28.8)
0.20	-14.6 (-14.6)	-15.7 (-15.8)	-16.8 (-16.8)	-18.5 (-18.6)	-20.8 (-20.9)	-22.9 (-23.0)
0.30	-11.8 (-11.8)	-12.8 (-12.8)	-13.7 (-13.8)	-15.4 (-15.5)	-17.5 (-17.8)	-19.5 (-19.8)
0.40	-10.3 (-10.3)	-11.2 (-11.3)	-12.1 (-12.2)	-13.5 (-13.7)	-15.5 (-15.9)	-17.3 (-17.8)
0.60	-9.7 (-9.7)	-10.3 (-10.4)	-10.9 (-11.1)	-11.9 (-12.3)	-13.5 (-14.2)	-15.0 (-15.8)
0.80	-10.6 (-10.6)	-11.0 (-11.1)	-11.4 (-11.6)	-12.2 (-12.6)	-13.4 (-14.1)	-14.5 (-15.5)
1.00	-12.2 (-12.2)	-12.5 (-12.6)	-12.7 (-13.0)	-13.3 (-13.7)	-14.1 (-14.8)	-15.0 (-16.0)
1.20	-13.9 (-13.9)	-14.1 (-14.2)	-14.3 (-14.5)	-14.7 (-15.1)	-15.4 (-16.0)	-16.0 (-17.0)

STATIC SYSTEM
 NIGHT/90-PERCENTILE
 WAVE LENGTH= 0.530 (MICRONS)
 ZENITH ANGLE=40. (DEG.)
 R-ZERO= 0.038 (METER)

LMSC-B290200-III

0.10	0.000 (0.000)	0.024 (0.024)	0.047 (0.047)	0.094 (0.094)	0.164 (0.164)	0.234 (0.235)
0.20	0.002 (0.002)	0.025 (0.025)	0.048 (0.049)	0.094 (0.095)	0.164 (0.165)	0.234 (0.235)
0.30	0.006 (0.006)	0.028 (0.029)	0.051 (0.052)	0.096 (0.098)	0.164 (0.167)	0.233 (0.237)
0.40	0.012 (0.012)	0.034 (0.035)	0.056 (0.057)	0.100 (0.103)	0.167 (0.171)	0.234 (0.241)
0.60	0.034 (0.034)	0.054 (0.055)	0.074 (0.077)	0.114 (0.121)	0.177 (0.187)	0.242 (0.255)
0.80	0.066 (0.066)	0.083 (0.086)	0.101 (0.106)	0.138 (0.147)	0.196 (0.211)	0.257 (0.276)
1.00	0.104 (0.104)	0.119 (0.122)	0.135 (0.141)	0.168 (0.180)	0.221 (0.241)	0.278 (0.303)
1.20	0.144 (0.144)	0.158 (0.161)	0.171 (0.175)	0.201 (0.215)	0.249 (0.272)	0.300 (0.331)
0.10	-20.2 (-20.2)	-22.7 (-22.7)	-24.7 (-24.7)	-28.1 (-28.1)	-32.3 (-32.3)	-35.9 (-36.0)
0.20	-14.6 (-14.6)	-17.1 (-17.1)	-19.0 (-19.1)	-22.4 (-22.4)	-26.5 (-26.5)	-30.1 (-30.2)
0.30	-11.8 (-11.8)	-14.1 (-14.2)	-16.0 (-16.0)	-19.2 (-19.3)	-23.2 (-23.4)	-26.9 (-27.0)
0.40	-10.3 (-10.3)	-12.5 (-12.5)	-14.2 (-14.3)	-17.3 (-17.5)	-21.2 (-21.5)	-24.8 (-25.1)
0.60	-9.7 (-9.7)	-11.3 (-11.4)	-12.8 (-13.0)	-15.5 (-15.9)	-19.1 (-19.6)	-22.4 (-23.0)
0.80	-10.6 (-10.6)	-11.8 (-12.0)	-13.1 (-13.4)	-15.3 (-15.8)	-18.5 (-19.2)	-21.6 (-22.5)
1.00	-12.2 (-12.2)	-13.1 (-13.3)	-14.1 (-14.4)	-15.5 (-16.6)	-18.7 (-19.7)	-21.5 (-22.8)
1.20	-13.9 (-13.9)	-14.7 (-14.9)	-15.4 (-15.8)	-17.0 (-17.7)	-19.4 (-20.6)	-21.9 (-23.4)

TRACKING SYSTEM
 NIGHT/90-PERCENTILE
 WAVE LENGTH= 0.530 (MICRONS)
 ZENITH ANGLE= 0. (DEG.)
 R-ZERO= 0.050 (METER)

LMSC-B290200-III

0.30	0.001 (0.001)	0.010 (0.011)	0.020 (0.021)	0.038 (0.040)	0.067 (0.070)	0.095 (0.100)
0.60	0.004 (0.004)	0.011 (0.012)	0.018 (0.020)	0.032 (0.037)	0.054 (0.063)	0.077 (0.090)
1.00	0.009 (0.009)	0.013 (0.015)	0.018 (0.021)	0.027 (0.034)	0.041 (0.054)	0.057 (0.075)
1.40	0.017 (0.017)	0.020 (0.021)	0.023 (0.026)	0.029 (0.035)	0.038 (0.050)	0.049 (0.065)
1.80	0.029 (0.029)	0.030 (0.032)	0.032 (0.035)	0.036 (0.042)	0.043 (0.053)	0.050 (0.064)
2.30	0.048 (0.048)	0.050 (0.051)	0.051 (0.053)	0.054 (0.058)	0.058 (0.065)	0.063 (0.074)
2.90	0.081 (0.081)	0.082 (0.082)	0.083 (0.084)	0.084 (0.087)	0.087 (0.093)	0.090 (0.098)
3.50	0.130 (0.130)	0.130 (0.131)	0.131 (0.132)	0.132 (0.134)	0.134 (0.138)	0.137 (0.143)

0.30	-10.8 (-10.8)	-11.8 (-11.9)	-12.8 (-12.9)	-14.5 (-14.7)	-16.7 (-16.9)	-18.7 (-19.0)
0.60	-5.2 (-5.2)	-6.0 (-6.2)	-6.8 (-7.1)	-8.2 (-8.6)	-9.9 (-10.6)	-11.6 (-12.5)
1.00	-1.9 (-1.9)	-2.3 (-2.5)	-2.8 (-3.1)	-3.7 (-4.3)	-4.9 (-5.9)	-6.1 (-7.4)
1.40	-0.3 (-0.3)	-0.6 (-0.8)	-0.9 (-1.2)	-1.5 (-2.1)	-2.3 (-3.2)	-3.1 (-4.4)
1.80	0.1 (0.1)	-0.1 (-0.2)	-0.3 (-0.5)	-0.6 (-1.0)	-1.1 (-1.9)	-1.7 (-2.8)
2.30	-0.4 (-0.4)	-0.5 (-0.5)	-0.6 (-0.7)	-0.8 (-1.1)	-1.1 (-1.6)	-1.5 (-2.2)
2.90	-2.0 (-2.0)	-2.0 (-2.1)	-2.1 (-2.2)	-2.2 (-2.4)	-2.4 (-2.8)	-2.6 (-3.2)
3.50	-4.8 (-4.8)	-4.8 (-4.8)	-4.9 (-4.9)	-4.9 (-5.0)	-5.0 (-5.3)	-5.2 (-5.5)

TRACKING SYSTEM
 NIGHT/90-PERCENTILE
 WAVE LENGTH= 0.530 (MICRONS)
 ZENITH ANGLE=40. (DEG.)
 R-ZERO= 0.038 (METER)

LMSC-B290200-111

0.30	0.001 (0.001)	0.023 (0.024)	0.046 (0.047)	0.091 (0.093)	0.169 (0.162)	0.279 (0.232)
0.60	0.004 (0.004)	0.023 (0.025)	0.043 (0.047)	0.084 (0.090)	0.147 (0.157)	0.212 (0.224)
1.00	0.009 (0.009)	0.024 (0.028)	0.040 (0.047)	0.074 (0.085)	0.127 (0.146)	0.183 (0.209)
1.40	0.017 (0.017)	0.029 (0.033)	0.041 (0.045)	0.067 (0.082)	0.110 (0.135)	0.157 (0.192)
1.80	0.029 (0.029)	0.037 (0.041)	0.046 (0.054)	0.066 (0.083)	0.101 (0.128)	0.140 (0.179)
2.30	0.048 (0.048)	0.055 (0.058)	0.061 (0.069)	0.076 (0.091)	0.102 (0.129)	0.132 (0.171)
2.90	0.081 (0.081)	0.085 (0.088)	0.090 (0.096)	0.100 (0.113)	0.119 (0.143)	0.142 (0.177)
3.50	0.130 (0.130)	0.133 (0.135)	0.136 (0.141)	0.144 (0.155)	0.158 (0.178)	0.176 (0.206)

0.30	-10.8 (-10.8)	-13.2 (-13.2)	-15.1 (-15.2)	-18.4 (-18.5)	-22.5 (-22.7)	-26.1 (-26.3)
0.60	-5.2 (-5.2)	-7.4 (-7.5)	-9.1 (-9.4)	-12.1 (-12.5)	-16.0 (-16.5)	-19.5 (-20.1)
1.00	-1.9 (-1.9)	-3.4 (-3.8)	-4.8 (-5.3)	-7.3 (-8.2)	-10.8 (-11.9)	-13.9 (-15.3)
1.40	-0.3 (-0.3)	-1.5 (-1.8)	-2.5 (-3.1)	-4.5 (-5.6)	-7.4 (-8.9)	-10.1 (-12.0)
1.80	0.1 (0.1)	-0.7 (-1.0)	-1.4 (-2.0)	-2.9 (-4.1)	-5.3 (-7.0)	-7.6 (-9.8)
2.30	-0.4 (-0.4)	-0.8 (-1.1)	-1.3 (-1.9)	-2.4 (-3.4)	-4.2 (-5.8)	-6.0 (-8.2)
2.90	-2.0 (-2.0)	-2.3 (-2.5)	-2.6 (-3.0)	-3.3 (-4.1)	-4.4 (-5.8)	-5.8 (-7.7)
3.50	-4.8 (-4.8)	-5.0 (-5.1)	-5.2 (-5.5)	-5.6 (-6.2)	-6.4 (-7.5)	-7.4 (-9.0)

STATIC SYSTEM
 DAY/50-PERCENTILE
 WAVE LENGTH= 0.633 (MICRONS)
 ZENITH ANGLE= 0. (DEG.)
 R-ZERO= 0.058 (METER)

LMSC-B290200-III

0.10	0.000 (0.000)	0.009 (0.009)	0.017 (0.017)	0.034 (0.034)	0.059 (0.059)	0.084 (0.085)
0.20	0.002 (0.002)	0.010 (0.010)	0.018 (0.019)	0.034 (0.035)	0.058 (0.060)	0.083 (0.085)
0.30	0.006 (0.006)	0.013 (0.014)	0.021 (0.022)	0.035 (0.037)	0.058 (0.061)	0.081 (0.086)
0.40	0.012 (0.012)	0.019 (0.020)	0.026 (0.027)	0.039 (0.042)	0.060 (0.065)	0.081 (0.088)
0.60	0.034 (0.034)	0.039 (0.040)	0.045 (0.047)	0.056 (0.060)	0.073 (0.081)	0.090 (0.102)
0.80	0.066 (0.066)	0.070 (0.071)	0.074 (0.077)	0.083 (0.098)	0.096 (0.106)	0.110 (0.124)
1.00	0.104 (0.104)	0.107 (0.108)	0.110 (0.113)	0.117 (0.123)	0.128 (0.138)	0.139 (0.154)
1.20	0.144 (0.144)	0.147 (0.148)	0.149 (0.152)	0.155 (0.160)	0.163 (0.173)	0.172 (0.186)

0.10	-20.2 (-20.2)	-21.1 (-21.1)	-22.0 (-22.0)	-23.7 (-23.7)	-25.6 (-25.6)	-27.4 (-27.5)
0.20	-14.6 (-14.6)	-15.5 (-15.6)	-16.4 (-16.4)	-17.9 (-18.0)	-19.8 (-19.9)	-21.5 (-21.7)
0.30	-11.8 (-11.8)	-12.6 (-12.7)	-13.4 (-13.5)	-14.8 (-14.9)	-16.5 (-16.8)	-18.2 (-18.5)
0.40	-10.3 (-10.3)	-11.0 (-11.1)	-11.7 (-11.9)	-12.9 (-13.2)	-14.5 (-14.9)	-16.1 (-16.5)
0.60	-9.7 (-9.7)	-10.2 (-10.3)	-10.6 (-10.8)	-11.5 (-11.8)	-12.7 (-13.3)	-13.9 (-14.7)
0.80	-10.6 (-10.6)	-10.9 (-11.0)	-11.2 (-11.4)	-11.8 (-12.2)	-12.7 (-13.4)	-13.6 (-14.5)
1.00	-12.2 (-12.2)	-12.4 (-12.5)	-12.6 (-12.8)	-13.0 (-13.4)	-13.6 (-14.2)	-14.3 (-15.1)
1.20	-13.9 (-13.9)	-14.0 (-14.1)	-14.2 (-14.4)	-14.5 (-14.8)	-15.0 (-15.5)	-15.5 (-16.2)

STATIC SYSTEM
 DAY/50-PERCENTILE
 WAVE LENGTH= 0.633 (MICRONS)
 ZENITH ANGLE= 40. (DEG.)
 R-ZERO= 0.044 (METER)

LMSC-B290200-III

0.10	0.000 (0.000)	0.019 (0.019)	0.038 (0.038)	0.076 (0.076)	0.133 (0.134)	0.190 (0.191)
0.20	0.002 (0.002)	0.021 (0.021)	0.040 (0.040)	0.077 (0.078)	0.133 (0.135)	0.190 (0.191)
0.30	0.006 (0.006)	0.024 (0.024)	0.042 (0.043)	0.078 (0.080)	0.134 (0.136)	0.189 (0.193)
0.40	0.012 (0.012)	0.030 (0.030)	0.047 (0.049)	0.082 (0.085)	0.136 (0.141)	0.191 (0.197)
0.60	0.034 (0.034)	0.050 (0.051)	0.065 (0.068)	0.098 (0.103)	0.148 (0.157)	0.199 (0.211)
0.80	0.066 (0.066)	0.079 (0.082)	0.093 (0.098)	0.122 (0.131)	0.168 (0.181)	0.215 (0.233)
1.00	0.104 (0.104)	0.116 (0.118)	0.128 (0.133)	0.153 (0.164)	0.194 (0.211)	0.237 (0.260)
1.20	0.144 (0.144)	0.154 (0.157)	0.165 (0.171)	0.187 (0.199)	0.223 (0.243)	0.262 (0.290)

0.10	-20.2 (-20.2)	-22.3 (-22.3)	-24.0 (-24.0)	-26.9 (-26.9)	-30.5 (-30.5)	-33.7 (-33.7)
0.20	-14.6 (-14.6)	-16.6 (-16.7)	-18.3 (-18.4)	-21.1 (-21.2)	-24.7 (-24.8)	-27.9 (-28.0)
0.30	-11.8 (-11.8)	-13.7 (-13.7)	-15.3 (-15.4)	-18.0 (-18.1)	-21.5 (-21.7)	-24.6 (-24.8)
0.40	-10.3 (-10.3)	-12.1 (-12.2)	-13.5 (-13.7)	-16.1 (-16.3)	-19.5 (-19.8)	-22.5 (-22.8)
0.60	-9.7 (-9.7)	-11.0 (-11.1)	-12.2 (-12.4)	-14.5 (-14.8)	-17.4 (-17.9)	-20.2 (-20.8)
0.80	-10.6 (-10.6)	-11.6 (-11.7)	-12.6 (-12.8)	-14.4 (-14.8)	-16.9 (-17.7)	-19.4 (-20.4)
1.00	-12.2 (-12.2)	-12.9 (-13.1)	-13.7 (-14.0)	-15.1 (-15.7)	-17.3 (-18.2)	-19.5 (-20.7)
1.20	-13.9 (-13.9)	-14.5 (-14.7)	-15.1 (-15.4)	-16.3 (-16.9)	-18.1 (-19.2)	-20.1 (-21.4)

TRACKING SYSTEM
 DAY/50-PERCENTILE
 WAVE LENGTH= 0.633 (MICRONS)
 ZENITH ANGLE= 0. (DEG.)
 R-ZERO= 0.058 (METER)

LMSC-B290200-III

0.30	0.001 (0.001)	0.008 (0.009)	0.016 (0.017)	0.031 (0.033)	0.053 (0.057)	0.076 (0.081)
0.60	0.004 (0.004)	0.009 (0.010)	0.014 (0.017)	0.026 (0.030)	0.043 (0.051)	0.060 (0.071)
1.00	0.009 (0.009)	0.012 (0.014)	0.016 (0.018)	0.022 (0.028)	0.033 (0.043)	0.044 (0.059)
1.40	0.017 (0.017)	0.019 (0.020)	0.021 (0.024)	0.026 (0.031)	0.032 (0.041)	0.040 (0.053)
1.80	0.029 (0.029)	0.030 (0.031)	0.031 (0.033)	0.034 (0.038)	0.039 (0.046)	0.044 (0.055)
2.30	0.048 (0.048)	0.049 (0.050)	0.050 (0.052)	0.052 (0.055)	0.055 (0.061)	0.059 (0.067)
2.90	0.081 (0.081)	0.081 (0.082)	0.082 (0.083)	0.083 (0.085)	0.085 (0.089)	0.088 (0.093)
3.50	0.130 (0.130)	0.130 (0.131)	0.131 (0.131)	0.132 (0.133)	0.133 (0.136)	0.135 (0.139)
0.30	-10.8 (-10.8)	-11.6 (-11.7)	-12.4 (-12.5)	-13.9 (-14.1)	-15.7 (-15.9)	-17.4 (-17.7)
0.60	-5.2 (-5.2)	-5.9 (-6.0)	-6.4 (-6.7)	-7.6 (-8.0)	-9.0 (-9.7)	-10.4 (-11.2)
1.00	-1.9 (-1.9)	-2.2 (-2.4)	-2.5 (-2.8)	-3.2 (-3.8)	-4.3 (-5.1)	-5.2 (-6.3)
1.40	-0.3 (-0.3)	-0.5 (-0.7)	-0.7 (-1.0)	-1.2 (-1.7)	-1.8 (-2.6)	-2.4 (-3.5)
1.80	0.1 (0.1)	-0.1 (-0.2)	-0.2 (-0.4)	-0.4 (-0.8)	-0.8 (-1.4)	-1.2 (-2.0)
2.30	-0.4 (-0.4)	-0.4 (-0.5)	-0.5 (-0.6)	-0.6 (-0.9)	-0.9 (-1.3)	-1.1 (-1.7)
2.90	-2.0 (-2.0)	-2.0 (-2.0)	-2.1 (-2.1)	-2.1 (-2.3)	-2.3 (-2.5)	-2.4 (-2.8)
3.50	-4.8 (-4.8)	-4.8 (-4.8)	-4.8 (-4.9)	-4.9 (-5.0)	-5.0 (-5.1)	-5.1 (-5.3)

TRACKING SYSTEM
 DAY/50-PERCENTILE
 WAVE LENGTH= 0.633 (MICRONS)
 ZENITH ANGLE=40. (DEG.)
 R-ZERO= 0.044 (METER)

LMSC-B290200-III

0.30	0.001 (0.001)	0.019 (0.020)	0.037 (0.038)	0.074 (0.076)	0.129 (0.132)	0.185 (0.188)
0.60	0.004 (0.004)	0.019 (0.021)	0.035 (0.038)	0.068 (0.073)	0.117 (0.127)	0.169 (0.181)
1.00	0.009 (0.009)	0.021 (0.024)	0.033 (0.039)	0.059 (0.069)	0.099 (0.117)	0.142 (0.166)
1.40	0.017 (0.017)	0.026 (0.029)	0.035 (0.041)	0.054 (0.067)	0.086 (0.108)	0.121 (0.151)
1.80	0.029 (0.029)	0.035 (0.038)	0.042 (0.048)	0.056 (0.069)	0.081 (0.104)	0.109 (0.141)
2.30	0.048 (0.048)	0.053 (0.056)	0.058 (0.064)	0.068 (0.080)	0.086 (0.107)	0.107 (0.138)
2.90	0.081 (0.081)	0.084 (0.086)	0.087 (0.092)	0.095 (0.104)	0.108 (0.125)	0.123 (0.149)
3.50	0.130 (0.130)	0.132 (0.134)	0.135 (0.138)	0.140 (0.148)	0.149 (0.164)	0.161 (0.183)

0.30	-10.8 (-10.8)	-12.7 (-12.8)	-14.4 (-14.5)	-17.2 (-17.3)	-20.8 (-20.9)	-23.9 (-24.0)
0.60	-5.2 (-5.2)	-7.6 (-7.1)	-8.5 (-8.7)	-10.9 (-11.3)	-14.3 (-14.8)	-17.2 (-17.8)
1.00	-1.9 (-1.9)	-3.1 (-3.4)	-4.3 (-4.7)	-6.3 (-7.0)	-9.1 (-10.2)	-11.7 (-13.0)
1.40	-0.3 (-0.3)	-1.2 (-1.5)	-2.0 (-2.6)	-3.6 (-4.5)	-5.8 (-7.3)	-8.1 (-9.8)
1.80	0.1 (0.1)	-0.5 (-0.8)	-1.0 (-1.5)	-2.2 (-3.1)	-3.9 (-5.5)	-5.8 (-7.7)
2.30	-0.4 (-0.4)	-0.7 (-0.9)	-1.1 (-1.5)	-1.8 (-2.7)	-3.1 (-4.5)	-4.5 (-6.3)
2.90	-2.0 (-2.0)	-2.2 (-2.3)	-2.4 (-2.7)	-2.9 (-3.5)	-3.7 (-4.8)	-4.7 (-6.2)
3.50	-4.8 (-4.8)	-4.9 (-5.0)	-5.1 (-5.3)	-5.4 (-5.8)	-5.9 (-6.7)	-6.5 (-7.7)

STATIC SYSTEM
 DAY/90-PERCENTILE
 WAVE LENGTH= 0.633 (MICRONS)
 ZENITH ANGLE= 0. (DEG.)
 R-ZERO= 0.039 (METER)

LMSC-B290200-III

0.10	0.000 (0.000)	0.009 (0.009)	0.017 (0.017)	0.034 (0.034)	0.059 (0.059)	0.085 (0.085)
0.20	0.002 (0.002)	0.010 (0.011)	0.019 (0.019)	0.035 (0.036)	0.060 (0.061)	0.085 (0.086)
0.30	0.006 (0.006)	0.014 (0.014)	0.022 (0.022)	0.038 (0.039)	0.062 (0.063)	0.086 (0.088)
0.40	0.012 (0.012)	0.020 (0.020)	0.027 (0.028)	0.043 (0.044)	0.066 (0.069)	0.089 (0.093)
0.60	0.034 (0.034)	0.041 (0.041)	0.047 (0.049)	0.061 (0.064)	0.082 (0.087)	0.103 (0.110)
0.80	0.066 (0.066)	0.071 (0.072)	0.077 (0.075)	0.089 (0.093)	0.107 (0.115)	0.126 (0.136)
1.00	0.104 (0.104)	0.109 (0.110)	0.114 (0.116)	0.124 (0.129)	0.139 (0.148)	0.156 (0.168)
1.20	0.144 (0.144)	0.148 (0.150)	0.152 (0.155)	0.161 (0.167)	0.174 (0.184)	0.188 (0.202)

0.10	-20.2 (-20.2)	-21.1 (-21.2)	-22.0 (-22.1)	-23.7 (-23.7)	-25.6 (-25.7)	-27.5 (-27.5)
0.20	-14.6 (-14.6)	-15.6 (-15.6)	-16.4 (-16.4)	-18.0 (-18.0)	-19.9 (-20.0)	-21.7 (-21.8)
0.30	-11.8 (-11.8)	-12.7 (-12.7)	-13.5 (-13.5)	-14.9 (-15.0)	-16.8 (-16.9)	-18.5 (-18.7)
0.40	-10.3 (-10.3)	-11.1 (-11.2)	-11.9 (-12.0)	-13.2 (-13.3)	-14.9 (-15.1)	-16.6 (-16.9)
0.60	-9.7 (-9.7)	-10.3 (-10.4)	-10.6 (-10.9)	-11.9 (-12.1)	-13.4 (-13.7)	-14.8 (-15.2)
0.80	-10.6 (-10.6)	-11.0 (-11.1)	-11.4 (-11.6)	-12.2 (-12.5)	-13.4 (-13.9)	-14.6 (-15.2)
1.00	-12.2 (-12.2)	-12.5 (-12.6)	-12.8 (-13.0)	-13.4 (-13.7)	-14.3 (-14.8)	-15.2 (-15.9)
1.20	-13.9 (-13.9)	-14.1 (-14.2)	-14.4 (-14.5)	-14.6 (-15.2)	-15.6 (-16.1)	-16.3 (-17.1)

STATIC SYSTEM
 DAY/90-PERCENTILE
 WAVE LENGTH= 0.633 (MICRONS)
 ZENITH ANGLE=40. (DEG.)
 R-ZERO= 0.030 (METER)

LMSC-B290200-III

0.10	0.000 (0.000)	0.019 (0.019)	0.038 (0.038)	0.076 (0.077)	0.134 (0.134)	0.191 (0.191)
0.20	0.002 (0.002)	0.021 (0.021)	0.040 (0.040)	0.078 (0.078)	0.135 (0.135)	0.192 (0.192)
0.30	0.006 (0.006)	0.024 (0.025)	0.043 (0.043)	0.080 (0.081)	0.137 (0.138)	0.193 (0.195)
0.40	0.012 (0.012)	0.030 (0.031)	0.049 (0.050)	0.086 (0.087)	0.141 (0.144)	0.197 (0.200)
0.60	0.034 (0.034)	0.051 (0.052)	0.069 (0.070)	0.104 (0.107)	0.158 (0.162)	0.212 (0.218)
0.80	0.066 (0.066)	0.082 (0.083)	0.098 (0.101)	0.132 (0.136)	0.183 (0.190)	0.235 (0.245)
1.00	0.104 (0.104)	0.119 (0.120)	0.134 (0.137)	0.165 (0.172)	0.213 (0.224)	0.263 (0.277)
1.20	0.144 (0.144)	0.158 (0.160)	0.172 (0.176)	0.201 (0.209)	0.246 (0.260)	0.293 (0.311)
0.10	-20.2 (-20.2)	-22.3 (-22.3)	-24.0 (-24.0)	-26.9 (-26.9)	-30.5 (-30.5)	-33.7 (-33.7)
0.20	-14.6 (-14.6)	-16.7 (-16.7)	-18.4 (-18.4)	-21.2 (-21.2)	-24.8 (-24.8)	-28.0 (-28.0)
0.30	-11.8 (-11.8)	-13.7 (-13.8)	-15.4 (-15.4)	-18.1 (-18.2)	-21.7 (-21.8)	-24.8 (-24.9)
0.40	-10.3 (-10.3)	-12.2 (-12.2)	-13.7 (-13.7)	-16.4 (-16.4)	-19.8 (-19.9)	-22.8 (-23.0)
0.60	-9.7 (-9.7)	-11.1 (-11.2)	-12.4 (-12.5)	-14.9 (-15.0)	-18.0 (-18.2)	-20.9 (-21.2)
0.80	-10.6 (-10.6)	-11.7 (-11.8)	-12.9 (-13.0)	-14.9 (-15.2)	-17.7 (-18.2)	-20.5 (-21.0)
1.00	-12.2 (-12.2)	-13.1 (-13.2)	-14.0 (-14.2)	-15.8 (-16.1)	-18.3 (-18.9)	-20.8 (-21.5)
1.20	-13.9 (-13.9)	-14.7 (-14.8)	-15.4 (-15.7)	-17.0 (-17.4)	-19.3 (-20.0)	-21.6 (-22.4)

TRACKING SYSTEM
 DAY/90-PERCENTILE
 WAVE LENGTH= 0.633 (MICRONS)
 ZENITH ANGLE= 0. (DEG.)
 R-ZERO= 0.039 (METER)

LMSC-B290200-III

0.30	0.001 (0.001)	0.009 (0.009)	0.017 (0.017)	0.033 (0.034)	0.057 (0.059)	0.081 (0.084)
0.60	0.004 (0.004)	0.010 (0.011)	0.017 (0.019)	0.031 (0.034)	0.052 (0.057)	0.073 (0.080)
1.00	0.009 (0.009)	0.014 (0.015)	0.019 (0.022)	0.029 (0.034)	0.045 (0.054)	0.061 (0.073)
1.40	0.017 (0.017)	0.021 (0.022)	0.024 (0.027)	0.031 (0.037)	0.043 (0.053)	0.055 (0.069)
1.80	0.029 (0.029)	0.031 (0.032)	0.034 (0.036)	0.039 (0.044)	0.047 (0.057)	0.056 (0.070)
2.30	0.048 (0.048)	0.050 (0.051)	0.052 (0.054)	0.056 (0.060)	0.062 (0.070)	0.068 (0.080)
2.90	0.081 (0.081)	0.082 (0.083)	0.083 (0.085)	0.086 (0.089)	0.090 (0.096)	0.094 (0.104)
3.50	0.130 (0.130)	0.131 (0.131)	0.132 (0.133)	0.133 (0.136)	0.136 (0.142)	0.140 (0.147)

0.30	-10.8 (-10.8)	-11.7 (-11.7)	-12.5 (-12.6)	-14.1 (-14.2)	-16.0 (-16.1)	-17.7 (-17.9)
0.60	-5.2 (-5.2)	-6.0 (-6.1)	-6.7 (-6.9)	-8.1 (-8.3)	-9.7 (-10.1)	-11.3 (-11.8)
1.00	-1.9 (-1.9)	-2.4 (-2.5)	-2.9 (-3.1)	-3.9 (-4.3)	-5.2 (-5.9)	-6.4 (-7.3)
1.40	-0.3 (-0.3)	-0.7 (-0.8)	-1.0 (-1.3)	-1.7 (-2.2)	-2.7 (-3.5)	-3.6 (-4.7)
1.80	0.1 (0.1)	-0.2 (-0.3)	-0.4 (-0.6)	-0.8 (-1.3)	-1.5 (-2.2)	-2.2 (-3.2)
2.30	-0.4 (-0.4)	-0.5 (-0.6)	-0.6 (-0.8)	-0.9 (-1.3)	-1.4 (-2.0)	-1.8 (-2.7)
2.90	-2.0 (-2.0)	-2.1 (-2.1)	-2.1 (-2.3)	-2.3 (-2.6)	-2.6 (-3.0)	-2.9 (-3.5)
3.50	-4.8 (-4.8)	-4.8 (-4.9)	-4.9 (-5.0)	-5.0 (-5.2)	-5.2 (-5.5)	-5.3 (-5.8)

TRACKING SYSTEM
 DAY/90-PERCENTILE
 WAVE LENGTH= 0.633 (MICRONS)
 ZENITH ANGLE=40. (DEG.)
 R-2FRD= 0.030 (METER)

LMSC-B290200-III

0.30	0.001 (0.001)	0.020 (0.020)	0.038 (0.039)	0.076 (0.077)	0.132 (0.133)	0.189 (0.190)
0.60	0.004 (0.004)	0.021 (0.022)	0.039 (0.040)	0.074 (0.077)	0.128 (0.132)	0.182 (0.188)
1.00	0.009 (0.009)	0.024 (0.026)	0.039 (0.043)	0.070 (0.077)	0.119 (0.129)	0.168 (0.183)
1.40	0.017 (0.017)	0.020 (0.022)	0.042 (0.047)	0.069 (0.079)	0.111 (0.127)	0.155 (0.177)
1.80	0.029 (0.029)	0.039 (0.042)	0.049 (0.055)	0.071 (0.083)	0.107 (0.127)	0.145 (0.173)
2.30	0.048 (0.048)	0.056 (0.060)	0.064 (0.071)	0.082 (0.095)	0.111 (0.133)	0.143 (0.174)
2.90	0.081 (0.081)	0.087 (0.090)	0.092 (0.099)	0.106 (0.119)	0.128 (0.151)	0.154 (0.186)
3.50	0.130 (0.130)	0.134 (0.137)	0.139 (0.144)	0.149 (0.160)	0.166 (0.187)	0.187 (0.217)

0.30	-10.8 (-10.8)	-12.8 (-12.8)	-14.5 (-14.5)	-17.3 (-17.4)	-20.9 (-21.0)	-24.1 (-24.2)
0.60	-5.2 (-5.2)	-7.1 (-7.2)	-8.7 (-8.8)	-11.4 (-11.6)	-14.9 (-15.1)	-17.9 (-18.2)
1.00	-1.9 (-1.9)	-3.4 (-3.6)	-4.8 (-5.0)	-7.1 (-7.6)	-10.3 (-11.0)	-13.2 (-13.9)
1.40	-0.3 (-0.3)	-1.6 (-1.8)	-2.6 (-3.0)	-4.6 (-5.3)	-7.5 (-8.4)	-10.0 (-11.2)
1.80	0.1 (0.1)	-0.8 (-1.0)	-1.6 (-2.1)	-3.3 (-4.1)	-5.7 (-6.9)	-8.0 (-9.5)
2.30	-0.4 (-0.4)	-1.0 (-1.2)	-1.6 (-2.0)	-2.8 (-3.7)	-4.7 (-6.0)	-6.6 (-8.3)
2.90	-2.0 (-2.0)	-2.4 (-2.6)	-2.8 (-3.2)	-3.6 (-4.4)	-5.0 (-6.3)	-6.4 (-8.2)
3.50	-4.8 (-4.8)	-5.0 (-5.2)	-5.2 (-5.6)	-5.9 (-6.5)	-6.9 (-8.0)	-7.9 (-9.5)

STATIC SYSTEM
 NIGHT/50-PERCENTILE
 WAVE LENGTH= 0.633 (MICRONS)
 ZENITH ANGLE= 0. (DEG.)
 R-ZERO= 0.090 (METER)

LMSC-B290200-III

0.10	0.000 (0.000)	0.008 (0.009)	0.017 (0.017)	0.033 (0.034)	0.058 (0.059)	0.082 (0.084)
0.20	0.002 (0.002)	0.010 (0.010)	0.017 (0.018)	0.032 (0.034)	0.054 (0.058)	0.077 (0.082)
0.30	0.006 (0.006)	0.012 (0.013)	0.018 (0.020)	0.031 (0.035)	0.051 (0.057)	0.071 (0.079)
0.40	0.012 (0.012)	0.017 (0.019)	0.023 (0.025)	0.033 (0.038)	0.050 (0.058)	0.067 (0.079)
0.60	0.034 (0.034)	0.037 (0.039)	0.041 (0.044)	0.048 (0.054)	0.060 (0.070)	0.072 (0.087)
0.80	0.066 (0.066)	0.068 (0.069)	0.070 (0.073)	0.076 (0.081)	0.084 (0.093)	0.093 (0.106)
1.00	0.104 (0.104)	0.105 (0.107)	0.107 (0.109)	0.111 (0.116)	0.117 (0.125)	0.123 (0.135)
1.20	0.144 (0.144)	0.145 (0.146)	0.147 (0.149)	0.149 (0.153)	0.154 (0.161)	0.159 (0.169)

0.10	-20.2 (-20.2)	-21.1 (-21.1)	-22.0 (-22.0)	-23.6 (-23.6)	-25.5 (-25.6)	-27.3 (-27.4)
0.20	-14.6 (-14.6)	-15.5 (-15.5)	-16.2 (-16.4)	-17.7 (-17.9)	-19.5 (-19.7)	-21.1 (-21.5)
0.30	-11.8 (-11.8)	-12.5 (-12.6)	-13.1 (-13.3)	-14.4 (-14.7)	-16.0 (-16.4)	-17.5 (-18.1)
0.40	-10.3 (-10.3)	-10.9 (-11.0)	-11.4 (-11.7)	-12.4 (-12.8)	-13.8 (-14.4)	-15.0 (-15.9)
0.60	-9.7 (-9.7)	-10.0 (-10.2)	-10.3 (-10.6)	-10.9 (-11.4)	-11.8 (-12.5)	-12.7 (-13.7)
0.80	-10.6 (-10.6)	-10.8 (-10.9)	-10.9 (-11.1)	-11.3 (-11.7)	-11.9 (-12.6)	-12.5 (-13.4)
1.00	-12.2 (-12.2)	-12.3 (-12.4)	-12.4 (-12.6)	-12.6 (-12.9)	-13.0 (-13.5)	-13.4 (-14.1)
1.20	-13.9 (-13.9)	-14.0 (-14.0)	-14.1 (-14.2)	-14.2 (-14.4)	-14.5 (-14.8)	-14.7 (-15.3)

STATIC SYSTEM
 NIGHT/50-PERCENTILE
 WAVE LENGTH= 0.633 (MICRONS)
 ZENITH ANGLE=40. (DEG.)
 R-ZERO= 0.069 (METER)

LMSC-B290200-III

0.10	0.000 (0.000)	0.019 (0.019)	0.038 (0.038)	0.076 (0.076)	0.132 (0.133)	0.189 (0.190)
0.20	0.002 (0.002)	0.020 (0.021)	0.038 (0.039)	0.075 (0.077)	0.130 (0.133)	0.185 (0.189)
0.30	0.006 (0.006)	0.023 (0.024)	0.040 (0.042)	0.074 (0.078)	0.127 (0.133)	0.180 (0.188)
0.40	0.012 (0.012)	0.028 (0.029)	0.043 (0.047)	0.075 (0.081)	0.125 (0.134)	0.176 (0.188)
0.60	0.034 (0.034)	0.046 (0.049)	0.059 (0.064)	0.086 (0.096)	0.128 (0.144)	0.173 (0.194)
0.80	0.066 (0.066)	0.075 (0.079)	0.086 (0.092)	0.107 (0.120)	0.142 (0.163)	0.180 (0.209)
1.00	0.104 (0.104)	0.111 (0.115)	0.120 (0.126)	0.137 (0.150)	0.166 (0.188)	0.198 (0.229)
1.20	0.144 (0.144)	0.150 (0.153)	0.157 (0.163)	0.171 (0.184)	0.194 (0.217)	0.221 (0.254)
0.10	-20.2 (-20.2)	-22.2 (-22.3)	-24.0 (-24.0)	-26.8 (-26.9)	-30.5 (-30.5)	-33.6 (-33.7)
0.20	-14.6 (-14.6)	-16.6 (-16.6)	-18.2 (-18.2)	-21.0 (-21.1)	-24.5 (-24.7)	-27.6 (-27.8)
0.30	-11.8 (-11.8)	-13.6 (-13.7)	-15.1 (-15.3)	-17.7 (-18.0)	-21.1 (-21.5)	-24.1 (-24.5)
0.40	-10.3 (-10.3)	-11.9 (-12.1)	-12.2 (-12.5)	-15.6 (-16.0)	-18.8 (-19.4)	-21.7 (-22.4)
0.60	-9.7 (-9.7)	-10.8 (-11.0)	-11.7 (-12.1)	-13.6 (-14.3)	-16.3 (-17.2)	-18.8 (-20.0)
0.80	-10.6 (-10.6)	-11.3 (-11.5)	-12.0 (-12.5)	-13.4 (-14.2)	-15.5 (-16.7)	-17.6 (-19.1)
1.00	-12.2 (-12.2)	-12.7 (-12.9)	-13.2 (-13.6)	-14.2 (-14.9)	-15.8 (-17.0)	-17.5 (-19.1)
1.20	-13.9 (-13.9)	-14.3 (-14.4)	-14.6 (-15.0)	-15.4 (-16.1)	-16.7 (-17.8)	-18.0 (-19.7)

TRACKING SYSTEM
NIGHT/50-PERCENTILE
WAVE LENGTH= 0.633 (MICRONS)
ZENITH ANGLE= 0. (DEG.)
R-ZERO= 0.090 (METER)

LMSC-B290200-III

0.30	0.001 (0.001)	0.007 (0.008)	0.014 (0.015)	0.026 (0.030)	0.046 (0.052)	0.066 (0.075)
0.60	0.004 (0.004)	0.007 (0.009)	0.011 (0.014)	0.018 (0.024)	0.030 (0.040)	0.042 (0.057)
1.00	0.009 (0.009)	0.011 (0.012)	0.013 (0.015)	0.016 (0.021)	0.022 (0.031)	0.029 (0.041)
1.40	0.017 (0.017)	0.018 (0.019)	0.019 (0.021)	0.021 (0.024)	0.025 (0.030)	0.028 (0.037)
1.80	0.029 (0.029)	0.029 (0.030)	0.030 (0.031)	0.031 (0.033)	0.033 (0.037)	0.036 (0.042)
2.30	0.048 (0.048)	0.049 (0.049)	0.049 (0.050)	0.050 (0.052)	0.051 (0.054)	0.053 (0.057)
2.90	0.081 (0.081)	0.081 (0.081)	0.081 (0.082)	0.082 (0.083)	0.083 (0.085)	0.084 (0.086)
3.50	0.130 (0.130)	0.130 (0.130)	0.130 (0.131)	0.131 (0.131)	0.131 (0.132)	0.132 (0.134)
0.30	-10.8 (-10.8)	-11.5 (-11.6)	-12.2 (-12.4)	-13.5 (-13.8)	-15.1 (-15.6)	-16.6 (-17.3)
0.60	-5.2 (-5.2)	-5.6 (-5.8)	-6.1 (-6.4)	-6.8 (-7.4)	-8.0 (-8.8)	-9.0 (-10.1)
1.00	-1.9 (-1.9)	-2.1 (-2.2)	-2.2 (-2.5)	-2.6 (-3.1)	-3.2 (-4.0)	-3.9 (-4.9)
1.40	-0.3 (-0.3)	-0.4 (-0.5)	-0.5 (-0.7)	-0.7 (-1.1)	-1.1 (-1.7)	-1.5 (-2.2)
1.80	0.1 (0.1)	0.0 (-0.1)	-0.1 (-0.2)	-0.2 (-0.4)	-0.4 (-0.7)	-0.6 (-1.0)
2.30	-0.4 (-0.4)	-0.4 (-0.4)	-0.4 (-0.5)	-0.5 (-0.6)	-0.6 (-0.8)	-0.7 (-1.0)
2.90	-2.0 (-2.0)	-2.0 (-2.0)	-2.0 (-2.0)	-2.0 (-2.1)	-2.1 (-2.2)	-2.2 (-2.4)
3.50	-4.8 (-4.8)	-4.8 (-4.8)	-4.8 (-4.8)	-4.8 (-4.9)	-4.9 (-4.9)	-4.9 (-5.0)

TRACKING SYSTEM
 NIGHT/50-PERCENTILE
 WAVE LENGTH= 0.633 (MICRONS)
 ZENITH ANGLE=40. (DEG.)
 R-ZERO= 0.009 (METER)

LMSC-B290200-III

0.30	0.001 (0.001)	0.018 (0.019)	0.025 (0.037)	0.069 (0.073)	0.122 (0.128)	0.175 (0.183)
0.60	0.004 (0.004)	0.016 (0.019)	0.029 (0.034)	0.056 (0.066)	0.098 (0.114)	0.143 (0.164)
1.00	0.009 (0.009)	0.017 (0.020)	0.025 (0.022)	0.042 (0.055)	0.071 (0.094)	0.103 (0.135)
1.40	0.017 (0.017)	0.022 (0.025)	0.027 (0.033)	0.039 (0.051)	0.058 (0.080)	0.081 (0.112)
1.80	0.029 (0.029)	0.032 (0.034)	0.035 (0.040)	0.043 (0.053)	0.057 (0.075)	0.073 (0.100)
2.30	0.048 (0.048)	0.051 (0.052)	0.053 (0.057)	0.058 (0.066)	0.067 (0.082)	0.078 (0.100)
2.90	0.081 (0.081)	0.082 (0.084)	0.084 (0.086)	0.087 (0.093)	0.093 (0.104)	0.101 (0.117)
3.50	0.130 (0.130)	0.131 (0.132)	0.132 (0.134)	0.134 (0.138)	0.139 (0.147)	0.144 (0.156)

0.30	-10.8 (-10.8)	-12.6 (-12.7)	-14.2 (-14.4)	-16.9 (-17.1)	-20.3 (-20.7)	-23.4 (-23.8)
0.60	-5.2 (-5.2)	-6.6 (-6.9)	-7.9 (-8.4)	-10.1 (-10.8)	-13.1 (-14.1)	-15.7 (-16.9)
1.00	-1.9 (-1.9)	-2.7 (-3.0)	-3.5 (-4.1)	-5.0 (-6.0)	-7.2 (-8.7)	-9.4 (-11.3)
1.40	-0.3 (-0.3)	-0.8 (-1.1)	-1.4 (-1.9)	-2.3 (-3.3)	-3.8 (-5.4)	-5.5 (-7.5)
1.80	0.1 (0.1)	-0.2 (-0.4)	-0.5 (-0.9)	-1.2 (-1.9)	-2.2 (-3.5)	-3.4 (-5.3)
2.30	-0.4 (-0.4)	-0.5 (-0.7)	-0.7 (-1.0)	-1.1 (-1.7)	-1.8 (-2.8)	-2.6 (-4.1)
2.90	-2.0 (-2.0)	-2.1 (-2.2)	-2.2 (-2.4)	-2.4 (-2.8)	-2.8 (-3.5)	-3.3 (-4.3)
3.50	-4.8 (-4.8)	-4.8 (-4.9)	-4.9 (-5.0)	-5.0 (-5.3)	-5.3 (-5.7)	-5.6 (-6.3)

STATIC SYSTEM
 NIGHT/90-PERCENTILE
 WAVE LENGTH= 0.633 (MICRONS)
 ZENITH ANGLE= 0. (DEG.)
 R-ZERO= 0.062 (METER)

LMSC-B290200-III

0.10	0.000 (0.000)	0.009 (0.009)	0.017 (0.017)	0.034 (0.034)	0.059 (0.059)	0.084 (0.084)
0.20	0.002 (0.002)	0.010 (0.010)	0.018 (0.019)	0.034 (0.035)	0.058 (0.060)	0.082 (0.085)
0.30	0.006 (0.006)	0.013 (0.014)	0.020 (0.021)	0.035 (0.037)	0.057 (0.061)	0.080 (0.085)
0.40	0.012 (0.012)	0.019 (0.020)	0.025 (0.027)	0.039 (0.042)	0.059 (0.065)	0.080 (0.088)
0.60	0.034 (0.034)	0.039 (0.040)	0.044 (0.047)	0.055 (0.060)	0.071 (0.080)	0.088 (0.100)
0.80	0.066 (0.066)	0.069 (0.071)	0.073 (0.076)	0.082 (0.087)	0.094 (0.104)	0.108 (0.122)
1.00	0.104 (0.104)	0.107 (0.108)	0.110 (0.113)	0.116 (0.122)	0.126 (0.136)	0.137 (0.151)
1.20	0.144 (0.144)	0.146 (0.148)	0.149 (0.152)	0.154 (0.159)	0.162 (0.171)	0.170 (0.184)
0.10	-20.2 (-20.2)	-21.1 (-21.1)	-22.0 (-22.0)	-23.6 (-23.7)	-25.6 (-25.6)	-27.4 (-27.5)
0.20	-14.6 (-14.6)	-15.5 (-15.6)	-16.4 (-16.4)	-17.9 (-18.0)	-19.8 (-19.9)	-21.5 (-21.7)
0.30	-11.8 (-11.8)	-12.6 (-12.6)	-13.3 (-13.4)	-14.7 (-14.9)	-16.5 (-16.7)	-18.1 (-18.5)
0.40	-10.3 (-10.3)	-11.0 (-11.1)	-11.7 (-11.9)	-12.9 (-13.1)	-14.4 (-14.9)	-15.9 (-16.5)
0.60	-9.7 (-9.7)	-10.2 (-10.3)	-10.6 (-10.8)	-11.4 (-11.8)	-12.6 (-13.2)	-13.8 (-14.6)
0.80	-10.6 (-10.6)	-10.9 (-11.0)	-11.2 (-11.4)	-11.7 (-12.1)	-12.6 (-13.3)	-13.5 (-14.3)
1.00	-12.2 (-12.2)	-12.4 (-12.5)	-12.6 (-12.7)	-13.0 (-13.3)	-13.5 (-14.1)	-14.2 (-15.0)
1.20	-13.9 (-13.9)	-14.0 (-14.1)	-14.2 (-14.3)	-14.5 (-14.7)	-14.9 (-15.4)	-15.4 (-16.1)

STATIC SYSTEM
 NIGHT/90-PERCENTILE
 WAVE LENGTH= 0.633 (MICRONS)
 ZENITH ANGLE= 40. (DEG.)
 R-7CR0= 0.047 (METER)

LMSC-B290200-III

0.10	0.000 (0.000)	0.015 (0.019)	0.038 (0.038)	0.076 (0.076)	0.133 (0.134)	0.190 (0.191)
0.20	0.002 (0.002)	0.021 (0.021)	0.039 (0.040)	0.077 (0.078)	0.133 (0.134)	0.189 (0.191)
0.30	0.006 (0.006)	0.024 (0.024)	0.042 (0.043)	0.078 (0.080)	0.133 (0.136)	0.188 (0.192)
0.40	0.012 (0.012)	0.029 (0.030)	0.047 (0.048)	0.082 (0.085)	0.135 (0.140)	0.189 (0.196)
0.60	0.034 (0.034)	0.049 (0.051)	0.065 (0.068)	0.096 (0.103)	0.146 (0.156)	0.196 (0.209)
0.80	0.066 (0.066)	0.079 (0.081)	0.092 (0.097)	0.121 (0.130)	0.165 (0.179)	0.211 (0.231)
1.00	0.104 (0.104)	0.115 (0.118)	0.127 (0.132)	0.151 (0.162)	0.190 (0.209)	0.232 (0.257)
1.20	0.144 (0.144)	0.154 (0.157)	0.164 (0.170)	0.185 (0.197)	0.219 (0.240)	0.257 (0.285)

0.10	-20.2 (-20.2)	-22.3 (-22.3)	-24.0 (-24.0)	-26.9 (-26.9)	-30.5 (-30.5)	-33.7 (-33.7)
0.20	-14.6 (-14.6)	-16.6 (-16.7)	-18.3 (-18.4)	-21.1 (-21.2)	-24.7 (-24.8)	-27.8 (-27.9)
0.30	-11.8 (-11.8)	-13.7 (-13.7)	-15.3 (-15.4)	-18.0 (-18.1)	-21.5 (-21.7)	-24.5 (-24.8)
0.40	-10.3 (-10.3)	-12.1 (-12.2)	-13.5 (-13.6)	-16.1 (-16.3)	-19.4 (-19.7)	-22.4 (-22.8)
0.60	-9.7 (-9.7)	-11.0 (-11.1)	-12.1 (-12.4)	-14.4 (-14.8)	-17.3 (-17.9)	-20.1 (-20.8)
0.80	-10.6 (-10.6)	-11.5 (-11.7)	-12.5 (-12.8)	-14.2 (-14.8)	-16.8 (-17.6)	-19.2 (-20.2)
1.00	-12.2 (-12.2)	-12.9 (-13.1)	-13.6 (-13.9)	-15.0 (-15.6)	-17.1 (-18.1)	-19.3 (-20.5)
1.20	-13.9 (-13.9)	-14.4 (-14.6)	-15.0 (-15.3)	-16.1 (-16.8)	-17.9 (-19.0)	-19.8 (-21.2)

TRACKING SYSTEM
 NIGHT/90-PERCENTILE
 WAVE LENGTH= 0.633 (MICRONS)
 ZENITH ANGLE= 0. (DEG.)
 R-ZERO= 0.062 (METER)

LMSC-B290200-III

0.30	0.001 (0.001)	0.008 (0.009)	0.016 (0.017)	0.030 (0.032)	0.053 (0.056)	0.075 (0.080)
0.60	0.004 (0.004)	0.009 (0.010)	0.014 (0.017)	0.025 (0.030)	0.041 (0.049)	0.058 (0.070)
1.00	0.009 (0.009)	0.012 (0.014)	0.015 (0.018)	0.021 (0.027)	0.031 (0.042)	0.042 (0.057)
1.40	0.017 (0.017)	0.019 (0.020)	0.021 (0.023)	0.025 (0.030)	0.031 (0.040)	0.038 (0.050)
1.80	0.029 (0.029)	0.030 (0.031)	0.031 (0.033)	0.034 (0.037)	0.038 (0.045)	0.042 (0.052)
2.30	0.048 (0.048)	0.049 (0.050)	0.050 (0.051)	0.052 (0.055)	0.055 (0.060)	0.058 (0.065)
2.90	0.081 (0.081)	0.081 (0.082)	0.082 (0.083)	0.083 (0.085)	0.085 (0.088)	0.087 (0.092)
3.50	0.130 (0.130)	0.130 (0.131)	0.131 (0.131)	0.131 (0.133)	0.133 (0.135)	0.134 (0.138)

0.30	-10.8 (-10.8)	-11.6 (-11.7)	-12.4 (-12.5)	-13.9 (-14.0)	-15.6 (-15.9)	-17.3 (-17.6)
0.60	-5.2 (-5.2)	-5.8 (-6.0)	-6.4 (-6.7)	-7.5 (-8.0)	-8.9 (-9.6)	-10.2 (-11.1)
1.00	-1.9 (-1.9)	-2.2 (-2.3)	-2.5 (-2.8)	-3.1 (-3.7)	-4.1 (-4.9)	-5.0 (-6.1)
1.40	-0.3 (-0.3)	-0.5 (-0.6)	-0.7 (-0.9)	-1.1 (-1.6)	-1.7 (-2.4)	-2.3 (-3.3)
1.80	0.1 (0.1)	-0.1 (-0.1)	-0.2 (-0.3)	-0.4 (-0.7)	-0.7 (-1.3)	-1.1 (-1.9)
2.30	-0.4 (-0.4)	-0.4 (-0.5)	-0.5 (-0.6)	-0.6 (-0.8)	-0.8 (-1.2)	-1.1 (-1.6)
2.90	-2.0 (-2.0)	-2.0 (-2.0)	-2.0 (-2.1)	-2.1 (-2.3)	-2.2 (-2.5)	-2.4 (-2.7)
3.50	-4.8 (-4.8)	-4.8 (-4.8)	-4.8 (-4.9)	-4.9 (-5.0)	-4.9 (-5.1)	-5.0 (-5.2)

TRACKING SYSTEM
 RIGHT/90-PERCENTILE
 WAVE LENGTH= 0.633 (MICRONS)
 ZENITH ANGLE=40. (DEG.)
 R-ZERO= 0.047 (METER)

LMSC-B290200-III

0.30	0.001 (0.001)	0.019 (0.020)	0.037 (0.038)	0.073 (0.075)	0.128 (0.131)	0.184 (0.188)
0.60	0.004 (0.004)	0.015 (0.021)	0.035 (0.038)	0.066 (0.073)	0.115 (0.125)	0.166 (0.179)
1.00	0.009 (0.009)	0.020 (0.023)	0.032 (0.038)	0.057 (0.069)	0.096 (0.114)	0.137 (0.162)
1.40	0.017 (0.017)	0.025 (0.029)	0.034 (0.040)	0.052 (0.065)	0.082 (0.104)	0.115 (0.146)
1.80	0.029 (0.029)	0.035 (0.038)	0.041 (0.047)	0.054 (0.067)	0.077 (0.100)	0.103 (0.136)
2.30	0.048 (0.048)	0.053 (0.055)	0.057 (0.062)	0.067 (0.078)	0.083 (0.103)	0.103 (0.132)
2.90	0.081 (0.081)	0.084 (0.086)	0.087 (0.091)	0.093 (0.102)	0.105 (0.122)	0.119 (0.144)
3.50	0.130 (0.130)	0.132 (0.134)	0.134 (0.137)	0.139 (0.146)	0.147 (0.161)	0.158 (0.179)
0.30	-10.8 (-10.8)	-12.7 (-12.8)	-14.4 (-14.5)	-17.2 (-17.3)	-20.7 (-20.9)	-23.8 (-24.0)
0.60	-5.2 (-5.2)	-6.9 (-7.1)	-8.4 (-8.7)	-10.8 (-11.3)	-14.1 (-14.7)	-17.0 (-17.7)
1.00	-1.9 (-1.9)	-3.0 (-3.3)	-4.2 (-4.6)	-6.1 (-6.9)	-8.9 (-10.0)	-11.4 (-12.8)
1.40	-0.3 (-0.3)	-1.2 (-1.5)	-1.9 (-2.5)	-3.4 (-4.4)	-5.6 (-7.1)	-7.7 (-9.5)
1.80	0.1 (0.1)	-0.5 (-0.7)	-1.0 (-1.5)	-2.0 (-3.0)	-3.7 (-5.2)	-5.5 (-7.4)
2.30	-0.4 (-0.4)	-0.7 (-0.9)	-1.0 (-1.4)	-1.7 (-2.5)	-2.9 (-4.3)	-4.2 (-6.0)
2.90	-2.0 (-2.0)	-2.2 (-2.3)	-2.4 (-2.7)	-2.8 (-3.4)	-3.6 (-4.6)	-4.4 (-5.9)
3.50	-4.8 (-4.8)	-4.9 (-5.0)	-5.0 (-5.2)	-5.3 (-5.7)	-5.8 (-6.6)	-6.4 (-7.5)

STATIC SYSTEM
 DAY/50-PERCENTILE
 WAVE LENGTH= 1.060 (MICRONS)
 ZENITH ANGLE= 0. (DEG.)
 R-ZERO= 0.108 (METER)

LMSC-B290200-III

0.10	0.006 (0.006)	0.005 (0.005)	0.005 (0.005)	0.018 (0.015)	0.032 (0.032)	0.045 (0.046)
0.20	0.002 (0.002)	0.006 (0.007)	0.010 (0.011)	0.015 (0.020)	0.031 (0.033)	0.044 (0.046)
0.30	0.006 (0.006)	0.005 (0.010)	0.013 (0.014)	0.020 (0.022)	0.031 (0.034)	0.042 (0.046)
0.40	0.012 (0.012)	0.015 (0.016)	0.018 (0.020)	0.024 (0.027)	0.034 (0.038)	0.043 (0.049)
0.60	0.034 (0.034)	0.036 (0.037)	0.038 (0.040)	0.042 (0.046)	0.049 (0.055)	0.056 (0.064)
0.80	0.066 (0.066)	0.067 (0.068)	0.069 (0.070)	0.072 (0.075)	0.076 (0.082)	0.081 (0.089)
1.00	0.104 (0.104)	0.105 (0.105)	0.106 (0.107)	0.108 (0.111)	0.111 (0.116)	0.115 (0.122)
1.20	0.144 (0.144)	0.145 (0.146)	0.146 (0.147)	0.147 (0.150)	0.150 (0.154)	0.153 (0.159)

0.10	-20.2 (-20.2)	-20.7 (-20.7)	-21.2 (-21.2)	-22.2 (-22.2)	-23.5 (-23.5)	-24.6 (-24.6)
0.20	-14.6 (-14.6)	-15.1 (-15.1)	-15.6 (-15.6)	-16.4 (-16.5)	-17.6 (-17.8)	-18.7 (-18.9)
0.30	-11.8 (-11.8)	-12.2 (-12.2)	-12.6 (-12.7)	-13.3 (-13.5)	-14.4 (-14.7)	-15.3 (-15.6)
0.40	-10.3 (-10.3)	-10.7 (-10.7)	-11.0 (-11.1)	-11.6 (-11.8)	-12.5 (-12.8)	-13.2 (-13.7)
0.60	-9.7 (-9.7)	-9.9 (-10.0)	-10.1 (-10.2)	-10.4 (-10.7)	-11.0 (-11.4)	-11.5 (-12.1)
0.80	-10.6 (-10.6)	-10.7 (-10.8)	-10.8 (-10.9)	-11.0 (-11.2)	-11.4 (-11.7)	-11.7 (-12.2)
1.00	-12.2 (-12.2)	-12.3 (-12.3)	-12.3 (-12.4)	-12.5 (-12.6)	-12.7 (-13.0)	-12.9 (-13.3)
1.20	-13.9 (-13.9)	-14.0 (-14.0)	-14.0 (-14.1)	-14.1 (-14.2)	-14.2 (-14.5)	-14.4 (-14.7)

STATIC SYSTEM
 DAY/50-PERCENTILE
 WAVE LENGTH= 1.060 (MICRONS)
 ZENITH ANGLE=40. (DEG.)
 R-ZERO= 0.083 (METER)

LMSC-B290200-III

0.10	0.000 (0.000)	0.011 (0.011)	0.021 (0.021)	0.042 (0.042)	0.073 (0.073)	0.104 (0.104)
0.20	0.002 (0.002)	0.012 (0.012)	0.022 (0.022)	0.042 (0.043)	0.072 (0.074)	0.103 (0.105)
0.30	0.006 (0.006)	0.015 (0.016)	0.025 (0.026)	0.043 (0.045)	0.072 (0.075)	0.101 (0.106)
0.40	0.012 (0.012)	0.021 (0.022)	0.030 (0.031)	0.047 (0.050)	0.074 (0.079)	0.102 (0.109)
0.50	0.034 (0.034)	0.041 (0.042)	0.048 (0.051)	0.063 (0.068)	0.086 (0.095)	0.110 (0.122)
0.80	0.066 (0.066)	0.071 (0.073)	0.077 (0.081)	0.085 (0.096)	0.108 (0.120)	0.128 (0.144)
1.00	0.104 (0.104)	0.108 (0.110)	0.113 (0.117)	0.123 (0.130)	0.138 (0.151)	0.155 (0.172)
1.20	0.144 (0.144)	0.148 (0.150)	0.152 (0.155)	0.160 (0.167)	0.172 (0.185)	0.186 (0.204)
0.10	-20.2 (-20.2)	-21.4 (-21.4)	-22.4 (-22.4)	-24.3 (-24.3)	-26.6 (-26.7)	-28.8 (-28.8)
0.20	-14.6 (-14.6)	-15.8 (-15.8)	-16.8 (-16.8)	-18.6 (-18.6)	-20.8 (-20.9)	-22.9 (-23.0)
0.30	-11.8 (-11.8)	-12.8 (-12.9)	-13.8 (-13.9)	-15.4 (-15.6)	-17.6 (-17.8)	-19.6 (-19.8)
0.40	-10.3 (-10.3)	-11.2 (-11.3)	-12.1 (-12.3)	-13.6 (-13.8)	-15.6 (-15.9)	-17.4 (-17.9)
0.60	-9.7 (-9.7)	-10.3 (-10.4)	-10.9 (-11.1)	-12.0 (-12.4)	-13.7 (-14.3)	-15.2 (-15.9)
0.80	-10.6 (-10.6)	-11.0 (-11.1)	-11.4 (-11.7)	-12.3 (-12.7)	-13.5 (-14.2)	-14.7 (-15.6)
1.00	-12.2 (-12.2)	-12.5 (-12.6)	-12.8 (-13.0)	-13.4 (-13.8)	-14.3 (-15.0)	-15.2 (-16.2)
1.20	-13.9 (-13.9)	-14.1 (-14.2)	-14.3 (-14.5)	-14.8 (-15.2)	-15.5 (-16.1)	-16.2 (-17.1)

TRACKING SYSTEM
 DAY/50-PERCENTILE
 WAVE LENGTH= 1.060 (MICRONS)
 ZENITH ANGLE= 0. (DEG.)
 R-ZERO= 0.108 (METER)

LMSC-B290200-III

0.30	0.001 (0.001)	0.005 (0.005)	0.008 (0.009)	0.015 (0.017)	0.026 (0.029)	0.037 (0.042)
0.60	0.004 (0.004)	0.006 (0.007)	0.008 (0.010)	0.012 (0.015)	0.019 (0.024)	0.026 (0.034)
1.00	0.009 (0.009)	0.010 (0.011)	0.011 (0.013)	0.013 (0.016)	0.017 (0.022)	0.020 (0.027)
1.40	0.017 (0.017)	0.018 (0.018)	0.018 (0.019)	0.020 (0.022)	0.022 (0.025)	0.024 (0.029)
1.80	0.029 (0.029)	0.029 (0.029)	0.029 (0.030)	0.030 (0.031)	0.031 (0.034)	0.033 (0.036)
2.30	0.048 (0.048)	0.049 (0.049)	0.049 (0.049)	0.049 (0.050)	0.050 (0.052)	0.051 (0.054)
2.90	0.081 (0.081)	0.081 (0.081)	0.081 (0.081)	0.082 (0.082)	0.082 (0.083)	0.083 (0.084)
3.50	0.130 (0.130)	0.130 (0.130)	0.130 (0.130)	0.130 (0.131)	0.131 (0.131)	0.131 (0.132)
0.30	-10.8 (-10.8)	-11.2 (-11.2)	-11.6 (-11.7)	-12.3 (-12.5)	-13.5 (-13.8)	-14.4 (-14.8)
0.60	-5.2 (-5.2)	-5.5 (-5.6)	-5.7 (-5.9)	-6.2 (-6.5)	-6.9 (-7.5)	-7.6 (-8.3)
1.00	-1.9 (-1.9)	-2.0 (-2.1)	-2.1 (-2.2)	-2.3 (-2.6)	-2.7 (-3.2)	-3.0 (-3.7)
1.40	-0.3 (-0.3)	-0.4 (-0.4)	-0.5 (-0.5)	-0.6 (-0.8)	-0.8 (-1.1)	-1.0 (-1.5)
1.80	0.1 (0.1)	0.0 (-0.0)	-0.0 (-0.1)	-0.1 (-0.2)	-0.2 (-0.4)	-0.3 (-0.6)
2.30	-0.4 (-0.4)	-0.4 (-0.4)	-0.4 (-0.4)	-0.4 (-0.5)	-0.5 (-0.6)	-0.6 (-0.8)
2.90	-2.0 (-2.0)	-2.0 (-2.0)	-2.0 (-2.0)	-2.0 (-2.1)	-2.1 (-2.1)	-2.1 (-2.2)
3.50	-4.8 (-4.8)	-4.8 (-4.8)	-4.8 (-4.8)	-4.8 (-4.8)	-4.8 (-4.9)	-4.9 (-4.9)

TRACKING SYSTEM
 DAY/50-PERCENTILE
 WAVE LENGTH= 1.060 (MICRONS)
 ZENITH ANGLE=40. (DEG.)
 R-ZERO= 0.083 (METER)

LMSC-B290200-III

0.30	0.001 (0.001)	0.010 (0.011)	0.020 (0.021)	0.039 (0.041)	0.068 (0.071)	0.097 (0.101)
0.60	0.004 (0.004)	0.011 (0.012)	0.018 (0.021)	0.033 (0.038)	0.056 (0.065)	0.080 (0.092)
1.00	0.009 (0.009)	0.014 (0.015)	0.018 (0.022)	0.028 (0.035)	0.044 (0.056)	0.060 (0.078)
1.40	0.017 (0.017)	0.020 (0.022)	0.023 (0.027)	0.030 (0.036)	0.040 (0.052)	0.051 (0.069)
1.80	0.029 (0.029)	0.031 (0.032)	0.033 (0.036)	0.037 (0.043)	0.044 (0.055)	0.052 (0.067)
2.30	0.048 (0.048)	0.050 (0.051)	0.051 (0.053)	0.054 (0.059)	0.059 (0.067)	0.065 (0.076)
2.90	0.081 (0.081)	0.082 (0.083)	0.083 (0.084)	0.085 (0.088)	0.088 (0.094)	0.092 (0.100)
3.50	0.130 (0.130)	0.130 (0.131)	0.131 (0.132)	0.133 (0.135)	0.135 (0.139)	0.137 (0.144)

0.30	-10.8 (-10.8)	-11.8 (-11.9)	-12.8 (-12.9)	-14.6 (-14.7)	-16.7 (-17.0)	-18.8 (-19.1)
0.60	-5.2 (-5.2)	-6.1 (-6.2)	-6.8 (-7.1)	-8.3 (-8.7)	-10.1 (-10.7)	-11.8 (-12.6)
1.00	-1.9 (-1.9)	-2.4 (-2.5)	-2.8 (-3.2)	-3.8 (-4.4)	-5.1 (-6.1)	-6.4 (-7.6)
1.40	-0.3 (-0.3)	-0.6 (-0.8)	-0.9 (-1.3)	-1.6 (-2.2)	-2.5 (-3.4)	-3.3 (-4.6)
1.80	0.1 (0.1)	-0.1 (-0.2)	-0.3 (-0.5)	-0.7 (-1.1)	-1.3 (-2.0)	-1.9 (-3.0)
2.30	-0.4 (-0.4)	-0.5 (-0.5)	-0.6 (-0.7)	-0.8 (-1.1)	-1.2 (-1.8)	-1.6 (-2.4)
2.90	-2.0 (-2.0)	-2.0 (-2.1)	-2.1 (-2.2)	-2.2 (-2.5)	-2.5 (-2.9)	-2.7 (-3.3)
3.50	-4.8 (-4.8)	-4.8 (-4.9)	-4.9 (-4.9)	-4.9 (-5.1)	-5.1 (-5.3)	-5.2 (-5.6)

STATIC SYSTEM
 DAY/90-PERCENTILE
 WAVE LENGTH= 1.060 (MICRONS)
 ZENITH ANGLE= 0. (DEG.)
 R-ZERO= 0.073 (METER)

LMSC-B290200-III

0.10	0.000 (0.000)	0.005 (0.005)	0.009 (0.009)	0.019 (0.019)	0.032 (0.033)	0.046 (0.046)
0.20	0.007 (0.007)	0.007 (0.007)	0.011 (0.011)	0.020 (0.020)	0.033 (0.034)	0.046 (0.047)
0.30	0.006 (0.006)	0.010 (0.010)	0.014 (0.014)	0.022 (0.023)	0.034 (0.036)	0.047 (0.049)
0.40	0.012 (0.012)	0.016 (0.016)	0.020 (0.020)	0.027 (0.029)	0.039 (0.041)	0.050 (0.054)
0.60	0.034 (0.034)	0.037 (0.037)	0.040 (0.041)	0.046 (0.049)	0.055 (0.060)	0.065 (0.071)
0.80	0.066 (0.066)	0.068 (0.069)	0.070 (0.072)	0.075 (0.078)	0.082 (0.088)	0.090 (0.098)
1.00	0.104 (0.104)	0.106 (0.106)	0.107 (0.109)	0.111 (0.114)	0.117 (0.123)	0.123 (0.131)
1.20	0.144 (0.144)	0.146 (0.146)	0.147 (0.149)	0.150 (0.153)	0.155 (0.160)	0.159 (0.167)
0.10	-20.2 (-20.2)	-20.7 (-20.7)	-21.2 (-21.2)	-22.2 (-22.2)	-23.5 (-23.6)	-24.6 (-24.7)
0.20	-14.6 (-14.6)	-15.1 (-15.1)	-15.6 (-15.7)	-16.5 (-16.6)	-17.8 (-17.9)	-18.9 (-19.0)
0.30	-11.8 (-11.8)	-12.3 (-12.3)	-12.7 (-12.7)	-13.5 (-13.6)	-14.7 (-14.8)	-15.7 (-15.9)
0.40	-10.3 (-10.3)	-10.7 (-10.8)	-11.1 (-11.2)	-11.9 (-12.0)	-12.9 (-13.1)	-13.8 (-14.1)
0.60	-9.7 (-9.7)	-10.0 (-10.0)	-10.2 (-10.3)	-10.7 (-10.9)	-11.4 (-11.8)	-12.1 (-12.6)
0.80	-10.6 (-10.6)	-10.8 (-10.8)	-10.9 (-11.0)	-11.3 (-11.5)	-11.8 (-12.2)	-12.3 (-12.8)
1.00	-12.2 (-12.2)	-12.3 (-12.4)	-12.4 (-12.5)	-12.7 (-12.9)	-13.0 (-13.3)	-13.4 (-13.8)
1.20	-13.9 (-13.9)	-14.0 (-14.0)	-14.1 (-14.2)	-14.2 (-14.4)	-14.5 (-14.8)	-14.8 (-15.2)

STATIC SYSTEM
 DAY/90-PERCENTILE
 WAVE LENGTH= 1.60 (MICRONS)
 ZENITH ANGLE=40. (DEG.)
 R-ZERO= 0.056 (METER)

LMSC-B290200-III

1

0.10	0.000 (0.000)	0.011 (0.011)	0.021 (0.021)	0.042 (0.042)	0.073 (0.073)	0.104 (0.105)
0.20	0.002 (0.002)	0.012 (0.013)	0.023 (0.023)	0.043 (0.044)	0.074 (0.075)	0.105 (0.106)
0.30	0.006 (0.006)	0.016 (0.016)	0.026 (0.026)	0.046 (0.047)	0.076 (0.077)	0.106 (0.108)
0.40	0.012 (0.012)	0.022 (0.022)	0.031 (0.032)	0.051 (0.052)	0.080 (0.083)	0.109 (0.113)
0.60	0.034 (0.034)	0.042 (0.043)	0.051 (0.052)	0.069 (0.072)	0.096 (0.101)	0.123 (0.130)
0.80	0.066 (0.066)	0.073 (0.074)	0.081 (0.083)	0.097 (0.101)	0.121 (0.129)	0.146 (0.155)
1.00	0.104 (0.104)	0.110 (0.112)	0.117 (0.120)	0.131 (0.137)	0.152 (0.162)	0.175 (0.188)
1.20	0.144 (0.144)	0.150 (0.152)	0.156 (0.159)	0.168 (0.174)	0.186 (0.198)	0.206 (0.222)
0.10	-20.2 (-20.2)	-21.4 (-21.4)	-22.4 (-22.5)	-24.3 (-24.3)	-26.7 (-26.7)	-28.8 (-28.8)
0.20	-14.6 (-14.6)	-15.8 (-15.8)	-16.8 (-16.8)	-18.6 (-18.7)	-20.9 (-21.0)	-23.0 (-23.1)
0.30	-11.8 (-11.8)	-12.9 (-12.9)	-12.9 (-12.9)	-15.6 (-15.6)	-17.8 (-17.9)	-19.9 (-20.0)
0.40	-10.3 (-10.3)	-11.3 (-11.4)	-12.3 (-12.3)	-13.9 (-13.9)	-15.9 (-16.1)	-17.9 (-18.1)
0.60	-9.7 (-9.7)	-10.5 (-10.5)	-11.1 (-11.3)	-12.4 (-12.7)	-14.3 (-14.7)	-16.0 (-16.4)
0.80	-10.6 (-10.6)	-11.1 (-11.2)	-11.7 (-11.9)	-12.8 (-13.1)	-14.3 (-14.7)	-15.7 (-16.3)
1.00	-12.2 (-12.2)	-12.6 (-12.7)	-13.0 (-13.2)	-13.9 (-14.2)	-15.1 (-15.6)	-16.3 (-17.0)
1.20	-13.9 (-13.9)	-14.2 (-14.3)	-14.6 (-14.7)	-15.2 (-15.6)	-16.2 (-16.8)	-17.3 (-18.1)

TRACKING SYSTEM
 DAY/90-PERCENTILE
 WAVE LENGTH= 1.060 (MICRONS)
 ZENITH ANGLE= 0. (DEG.)
 R-ZERO= 0.073 (METER)

LMSC-B290200-III

0.30	0.001 (0.001)	0.005 (0.005)	0.009 (0.010)	0.017 (0.018)	0.030 (0.032)	0.042 (0.045)
0.60	0.004 (0.004)	0.007 (0.007)	0.010 (0.011)	0.016 (0.018)	0.025 (0.030)	0.035 (0.041)
1.00	0.009 (0.009)	0.011 (0.012)	0.013 (0.014)	0.017 (0.020)	0.022 (0.028)	0.028 (0.036)
1.40	0.017 (0.017)	0.018 (0.019)	0.019 (0.021)	0.022 (0.025)	0.026 (0.031)	0.029 (0.037)
1.80	0.029 (0.029)	0.029 (0.030)	0.030 (0.031)	0.032 (0.034)	0.034 (0.038)	0.037 (0.043)
2.30	0.048 (0.048)	0.049 (0.049)	0.050 (0.050)	0.051 (0.052)	0.052 (0.055)	0.054 (0.058)
2.90	0.081 (0.081)	0.081 (0.082)	0.082 (0.082)	0.082 (0.083)	0.083 (0.085)	0.084 (0.088)
3.50	0.130 (0.130)	0.130 (0.130)	0.130 (0.131)	0.131 (0.132)	0.132 (0.133)	0.132 (0.135)
0.30	-10.8 (-10.8)	-11.2 (-11.2)	-11.7 (-11.8)	-12.6 (-12.7)	-13.8 (-14.0)	-14.8 (-15.0)
0.60	-5.2 (-5.2)	-5.6 (-5.7)	-6.0 (-6.1)	-6.6 (-6.8)	-7.5 (-8.0)	-8.4 (-8.9)
1.00	-1.9 (-1.9)	-2.1 (-2.1)	-2.3 (-2.4)	-2.6 (-3.0)	-3.2 (-3.8)	-3.8 (-4.5)
1.40	-0.3 (-0.3)	-0.4 (-0.5)	-0.6 (-0.7)	-0.8 (-1.1)	-1.2 (-1.7)	-1.6 (-2.2)
1.80	0.1 (0.1)	-0.0 (-0.1)	-0.1 (-0.2)	-0.2 (-0.4)	-0.4 (-0.8)	-0.7 (-1.1)
2.30	-0.4 (-0.4)	-0.4 (-0.4)	-0.4 (-0.5)	-0.5 (-0.7)	-0.7 (-0.9)	-0.8 (-1.1)
2.90	-2.0 (-2.0)	-2.0 (-2.0)	-2.0 (-2.1)	-2.1 (-2.1)	-2.1 (-2.3)	-2.2 (-2.4)
3.50	-4.8 (-4.8)	-4.8 (-4.8)	-4.8 (-4.8)	-4.8 (-4.9)	-4.9 (-5.0)	-4.9 (-5.1)

TRACKING SYSTEM
 DAY/90-PERCENTILE
 WAVE LENGTH= 1.060 (MICRONS)
 ZENITH ANGLE=40. (DEG.)
 R-ZERO= 0.056 (METER)

LMSC-B290200-III

0.30	0.001 (0.001)	0.011 (0.011)	0.021 (0.021)	0.041 (0.042)	0.071 (0.073)	0.101 (0.103)
0.60	0.004 (0.004)	0.012 (0.013)	0.021 (0.023)	0.039 (0.042)	0.066 (0.071)	0.093 (0.100)
1.00	0.009 (0.009)	0.016 (0.017)	0.022 (0.025)	0.036 (0.042)	0.058 (0.067)	0.080 (0.094)
1.40	0.017 (0.017)	0.022 (0.024)	0.027 (0.031)	0.037 (0.045)	0.054 (0.066)	0.071 (0.088)
1.80	0.029 (0.029)	0.032 (0.034)	0.035 (0.040)	0.044 (0.051)	0.056 (0.069)	0.070 (0.088)
2.30	0.048 (0.048)	0.051 (0.053)	0.054 (0.057)	0.059 (0.066)	0.068 (0.080)	0.078 (0.095)
2.90	0.081 (0.081)	0.083 (0.084)	0.085 (0.087)	0.088 (0.094)	0.095 (0.104)	0.102 (0.116)
3.50	0.130 (0.130)	0.131 (0.132)	0.133 (0.135)	0.135 (0.140)	0.140 (0.148)	0.145 (0.157)

0.30	-10.8 (-10.8)	-11.9 (-11.9)	-12.9 (-13.0)	-14.7 (-14.8)	-17.0 (-17.1)	-19.1 (-19.2)
0.60	-5.2 (-5.2)	-6.2 (-6.3)	-7.1 (-7.3)	-8.7 (-9.0)	-10.8 (-11.2)	-12.7 (-13.2)
1.00	-1.9 (-1.9)	-2.6 (-2.7)	-3.2 (-3.5)	-4.5 (-5.0)	-6.2 (-6.9)	-7.8 (-8.7)
1.40	-0.3 (-0.3)	-0.8 (-1.0)	-1.3 (-1.7)	-2.2 (-2.8)	-3.5 (-4.4)	-4.8 (-6.0)
1.80	0.1 (0.1)	-0.3 (-0.4)	-0.6 (-0.9)	-1.2 (-1.8)	-2.2 (-3.1)	-3.2 (-4.4)
2.30	-0.4 (-0.4)	-0.6 (-0.7)	-0.8 (-1.0)	-1.2 (-1.7)	-1.9 (-2.7)	-2.6 (-3.7)
2.90	-2.0 (-2.0)	-2.1 (-2.2)	-2.2 (-2.4)	-2.5 (-2.9)	-2.9 (-3.6)	-3.4 (-4.3)
3.50	-4.8 (-4.8)	-4.9 (-4.9)	-4.9 (-5.1)	-5.1 (-5.3)	-5.4 (-5.8)	-5.7 (-6.3)

STATIC SYSTEM
 NIGHT/50-PERCENTILE
 WAVE LENGTH= 1.060 (MICRONS)
 ZENITH ANGLE= 0. (DEG.)
 R-ZERO= 0.167 (METER)

LMSC-B290200-III

0.10	0.000 (0.000)	0.005 (0.005)	0.009 (0.009)	0.017 (0.018)	0.030 (0.032)	0.044 (0.045)
0.20	0.002 (0.002)	0.006 (0.006)	0.009 (0.010)	0.016 (0.018)	0.027 (0.030)	0.038 (0.043)
0.30	0.006 (0.006)	0.008 (0.009)	0.011 (0.013)	0.017 (0.019)	0.025 (0.030)	0.033 (0.040)
0.40	0.012 (0.012)	0.014 (0.015)	0.016 (0.018)	0.020 (0.024)	0.027 (0.032)	0.033 (0.041)
0.60	0.034 (0.034)	0.035 (0.036)	0.036 (0.038)	0.039 (0.042)	0.042 (0.047)	0.046 (0.054)
0.80	0.066 (0.066)	0.066 (0.067)	0.067 (0.068)	0.069 (0.071)	0.071 (0.075)	0.074 (0.079)
1.00	0.104 (0.104)	0.104 (0.105)	0.105 (0.106)	0.106 (0.107)	0.107 (0.110)	0.109 (0.113)
1.20	0.144 (0.144)	0.145 (0.145)	0.145 (0.146)	0.146 (0.147)	0.147 (0.149)	0.148 (0.151)
0.10	-20.2 (-20.2)	-20.7 (-20.7)	-21.2 (-21.2)	-22.1 (-22.2)	-23.4 (-23.5)	-24.4 (-24.6)
0.20	-14.6 (-14.6)	-15.0 (-15.1)	-15.4 (-15.6)	-16.2 (-16.4)	-17.3 (-17.6)	-18.2 (-18.6)
0.30	-11.8 (-11.8)	-12.1 (-12.2)	-12.4 (-12.5)	-13.0 (-13.2)	-13.8 (-14.3)	-14.6 (-15.2)
0.40	-10.3 (-10.3)	-10.6 (-10.6)	-10.8 (-10.9)	-11.2 (-11.5)	-11.8 (-12.3)	-12.4 (-13.1)
0.60	-9.7 (-9.7)	-9.8 (-9.9)	-9.9 (-10.1)	-10.1 (-10.4)	-10.4 (-10.8)	-10.8 (-11.3)
0.80	-10.6 (-10.6)	-10.6 (-10.7)	-10.7 (-10.8)	-10.8 (-11.0)	-11.0 (-11.3)	-11.2 (-11.6)
1.00	-12.2 (-12.2)	-12.2 (-12.3)	-12.3 (-12.3)	-12.3 (-12.4)	-12.4 (-12.6)	-12.5 (-12.8)
1.20	-13.9 (-13.9)	-13.9 (-13.9)	-13.9 (-14.0)	-14.0 (-14.1)	-14.1 (-14.2)	-14.1 (-14.3)

STATIC SYSTEM
 NIGHT/50-PERCENTILE
 WAVE LENGTH= 1.060 (MICRONS)
 ZENITH ANGLE=40. (DEG.)
 R-ZERO= 0.128 (METER)

LMSC-B290200-III

0.10	0.000 (0.000)	0.010 (0.011)	0.021 (0.021)	0.041 (0.042)	0.072 (0.073)	0.102 (0.104)
0.20	0.002 (0.002)	0.012 (0.012)	0.021 (0.022)	0.040 (0.042)	0.068 (0.072)	0.097 (0.102)
0.30	0.006 (0.006)	0.014 (0.015)	0.022 (0.024)	0.039 (0.043)	0.065 (0.071)	0.091 (0.100)
0.40	0.012 (0.012)	0.019 (0.021)	0.026 (0.029)	0.041 (0.046)	0.063 (0.072)	0.087 (0.099)
0.60	0.034 (0.034)	0.039 (0.041)	0.044 (0.047)	0.054 (0.061)	0.071 (0.083)	0.089 (0.106)
0.80	0.066 (0.066)	0.069 (0.071)	0.073 (0.076)	0.080 (0.087)	0.093 (0.105)	0.106 (0.123)
1.00	0.104 (0.104)	0.106 (0.108)	0.109 (0.112)	0.115 (0.121)	0.124 (0.135)	0.133 (0.150)
1.20	0.144 (0.144)	0.146 (0.147)	0.148 (0.151)	0.152 (0.158)	0.159 (0.169)	0.167 (0.181)

0.10	-20.2 (-20.2)	-21.4 (-21.4)	-22.4 (-22.4)	-24.2 (-24.3)	-26.5 (-26.6)	-28.7 (-28.7)
0.20	-14.6 (-14.6)	-15.7 (-15.7)	-16.6 (-16.8)	-18.4 (-18.5)	-20.5 (-20.8)	-22.5 (-22.8)
0.30	-11.8 (-11.8)	-12.7 (-12.8)	-13.5 (-13.7)	-15.1 (-15.4)	-17.0 (-17.5)	-18.9 (-19.5)
0.40	-10.3 (-10.3)	-11.1 (-11.2)	-11.8 (-12.1)	-13.0 (-13.5)	-14.8 (-15.4)	-16.4 (-17.3)
0.60	-9.7 (-9.7)	-10.2 (-10.3)	-10.6 (-10.8)	-11.4 (-11.9)	-12.6 (-13.5)	-13.8 (-15.0)
0.80	-10.6 (-10.6)	-10.8 (-11.0)	-11.1 (-11.4)	-11.6 (-12.1)	-12.5 (-13.3)	-13.3 (-14.4)
1.00	-12.2 (-12.2)	-12.4 (-12.5)	-12.5 (-12.7)	-12.9 (-13.2)	-13.4 (-14.1)	-14.0 (-14.9)
1.20	-13.9 (-13.9)	-14.0 (-14.1)	-14.1 (-14.3)	-14.4 (-14.7)	-14.8 (-15.3)	-15.2 (-16.0)

TRACKING SYSTEM
 NIGHT/50-PERCENTILE
 WAVE LENGTH= 1.060 (MICRONS)
 ZENITH ANGLE= 0. (DEG.)
 R-ZERO= 0.167 (METER)

LMSC-B290200-III

0.30	0.001 (0.001)	0.004 (0.004)	0.006 (0.008)	0.017 (0.015)	0.020 (0.025)	0.029 (0.036)
0.60	0.004 (0.004)	0.005 (0.006)	0.006 (0.008)	0.009 (0.011)	0.012 (0.017)	0.016 (0.024)
1.00	0.009 (0.009)	0.010 (0.010)	0.010 (0.011)	0.011 (0.013)	0.013 (0.016)	0.015 (0.019)
1.40	0.017 (0.017)	0.017 (0.018)	0.018 (0.018)	0.018 (0.019)	0.019 (0.021)	0.020 (0.023)
1.80	0.029 (0.029)	0.025 (0.029)	0.029 (0.029)	0.029 (0.030)	0.030 (0.031)	0.030 (0.032)
2.30	0.048 (0.048)	0.049 (0.049)	0.049 (0.049)	0.049 (0.049)	0.049 (0.050)	0.050 (0.051)
2.90	0.081 (0.081)	0.081 (0.081)	0.081 (0.081)	0.081 (0.081)	0.081 (0.082)	0.082 (0.082)
3.50	0.130 (0.130)	0.130 (0.130)	0.130 (0.130)	0.130 (0.130)	0.130 (0.131)	0.130 (0.131)

0.30	-10.8 (-10.8)	-11.1 (-11.1)	-11.4 (-11.5)	-12.0 (-12.3)	-12.8 (-13.3)	-13.7 (-14.3)
0.60	-5.2 (-5.2)	-5.4 (-5.5)	-5.5 (-5.7)	-5.8 (-6.1)	-6.2 (-6.7)	-6.6 (-7.4)
1.00	-1.9 (-1.9)	-1.9 (-2.0)	-2.0 (-2.1)	-2.1 (-2.3)	-2.3 (-2.6)	-2.4 (-2.9)
1.40	-0.3 (-0.3)	-0.4 (-0.4)	-0.4 (-0.4)	-0.4 (-0.5)	-0.5 (-0.7)	-0.6 (-0.9)
1.80	0.1 (0.1)	0.0 (0.0)	0.0 (-0.0)	-0.0 (-0.1)	-0.1 (-0.2)	-0.1 (-0.3)
2.30	-0.4 (-0.4)	-0.4 (-0.4)	-0.4 (-0.4)	-0.4 (-0.4)	-0.4 (-0.5)	-0.5 (-0.5)
2.90	-2.0 (-2.0)	-2.0 (-2.0)	-2.0 (-2.0)	-2.0 (-2.0)	-2.0 (-2.0)	-2.0 (-2.1)
3.50	-4.8 (-4.8)	-4.8 (-4.8)	-4.8 (-4.8)	-4.8 (-4.8)	-4.8 (-4.8)	-4.8 (-4.8)

TRACKING SYSTEM
 NIGHT/50-PERCENTILE
 WAVE LENGTH= 1.060 (MICRONS)
 ZENITH ANGLE=40. (DEG.)
 R-ZERO= 0.128 (METER)

LMSC-B290200-III

0.30	0.001 (0.001)	0.009 (0.010)	0.017 (0.019)	0.034 (0.038)	0.060 (0.066)	0.086 (0.095)
0.60	0.004 (0.004)	0.009 (0.010)	0.014 (0.017)	0.024 (0.031)	0.041 (0.053)	0.059 (0.076)
1.00	0.009 (0.009)	0.012 (0.013)	0.014 (0.017)	0.020 (0.026)	0.029 (0.040)	0.039 (0.055)
1.40	0.017 (0.017)	0.019 (0.020)	0.020 (0.022)	0.023 (0.028)	0.029 (0.037)	0.035 (0.047)
1.80	0.029 (0.029)	0.030 (0.030)	0.031 (0.032)	0.033 (0.036)	0.036 (0.042)	0.040 (0.049)
2.30	0.048 (0.048)	0.049 (0.050)	0.050 (0.051)	0.051 (0.053)	0.053 (0.058)	0.056 (0.062)
2.90	0.081 (0.081)	0.081 (0.082)	0.082 (0.082)	0.083 (0.084)	0.084 (0.087)	0.086 (0.090)
3.50	0.130 (0.130)	0.130 (0.130)	0.130 (0.131)	0.131 (0.132)	0.132 (0.134)	0.133 (0.136)
0.30	-10.8 (-10.8)	-11.7 (-11.8)	-12.6 (-12.8)	-14.2 (-14.5)	-16.2 (-16.6)	-18.1 (-18.7)
0.60	-5.2 (-5.2)	-5.8 (-6.0)	-6.4 (-6.7)	-7.4 (-8.1)	-8.9 (-9.9)	-10.3 (-11.5)
1.00	-1.9 (-1.9)	-2.1 (-2.3)	-2.4 (-2.7)	-3.0 (-3.6)	-3.9 (-4.8)	-4.7 (-6.0)
1.40	-0.3 (-0.3)	-0.5 (-0.6)	-0.6 (-0.9)	-1.0 (-1.4)	-1.5 (-2.2)	-2.0 (-3.0)
1.80	0.1 (0.1)	-0.0 (-0.1)	-0.1 (-0.3)	-0.3 (-0.6)	-0.6 (-1.1)	-0.9 (-1.6)
2.30	-0.4 (-0.4)	-0.4 (-0.5)	-0.5 (-0.5)	-0.6 (-0.7)	-0.7 (-1.1)	-0.9 (-1.4)
2.90	-2.0 (-2.0)	-2.0 (-2.0)	-2.0 (-2.1)	-2.1 (-2.2)	-2.2 (-2.4)	-2.3 (-2.6)
3.50	-4.8 (-4.8)	-4.8 (-4.8)	-4.8 (-4.8)	-4.9 (-4.9)	-4.9 (-5.0)	-5.0 (-5.2)

STATIC SYSTEM
 NIGHT/90-PERCENTILE
 WAVE LENGTH= 1.060 (MICRONS)
 ZENITH ANGLE= 0. (DEG.)
 R-ZERO= 0.114 (METER)

LMSC-B290200-III

0.10	0.000 (0.000)	0.005 (0.005)	0.009 (0.009)	0.018 (0.015)	0.032 (0.032)	0.045 (0.046)
0.20	0.002 (0.002)	0.006 (0.007)	0.010 (0.011)	0.018 (0.020)	0.031 (0.033)	0.043 (0.046)
0.30	0.006 (0.006)	0.009 (0.010)	0.013 (0.014)	0.020 (0.022)	0.030 (0.034)	0.041 (0.046)
0.40	0.012 (0.012)	0.015 (0.016)	0.018 (0.019)	0.024 (0.027)	0.033 (0.037)	0.042 (0.049)
0.60	0.034 (0.034)	0.036 (0.037)	0.038 (0.039)	0.042 (0.045)	0.048 (0.054)	0.054 (0.062)
0.80	0.066 (0.066)	0.067 (0.068)	0.068 (0.070)	0.071 (0.074)	0.075 (0.081)	0.080 (0.088)
1.00	0.104 (0.104)	0.105 (0.105)	0.106 (0.107)	0.108 (0.110)	0.111 (0.115)	0.114 (0.121)
1.20	0.144 (0.144)	0.145 (0.145)	0.146 (0.147)	0.147 (0.149)	0.149 (0.153)	0.152 (0.157)

0.10	-20.2 (-20.2)	-20.7 (-20.7)	-21.2 (-21.2)	-22.2 (-22.2)	-23.5 (-23.5)	-24.6 (-24.6)
0.20	-14.6 (-14.6)	-15.1 (-15.1)	-15.6 (-15.6)	-16.4 (-16.5)	-17.6 (-17.8)	-18.6 (-18.8)
0.30	-11.8 (-11.8)	-12.2 (-12.2)	-12.6 (-12.7)	-13.3 (-13.5)	-14.3 (-14.6)	-15.2 (-15.6)
0.40	-10.3 (-10.3)	-10.6 (-10.7)	-10.9 (-11.1)	-11.5 (-11.8)	-12.4 (-12.8)	-13.1 (-13.6)
0.60	-9.7 (-9.7)	-9.9 (-10.0)	-10.1 (-10.2)	-10.4 (-10.6)	-10.9 (-11.3)	-11.4 (-12.0)
0.80	-10.6 (-10.6)	-10.7 (-10.7)	-10.8 (-10.9)	-11.0 (-11.2)	-11.3 (-11.7)	-11.6 (-12.1)
1.00	-12.2 (-12.2)	-12.3 (-12.3)	-12.3 (-12.4)	-12.4 (-12.6)	-12.6 (-12.9)	-12.8 (-13.2)
1.20	-13.9 (-13.9)	-13.9 (-14.0)	-14.0 (-14.0)	-14.1 (-14.2)	-14.2 (-14.4)	-14.3 (-14.6)

STATIC SYSTEM
 NIGHT/90-PERCENTILE
 WAVE LENGTH= 1.060 (MICRONS)
 ZENITH ANGLE=40. (DEG.)
 R-ZERO= 0.088 (METER)

LMSC-B290200-III

0.10	0.000 (0.000)	0.011 (0.011)	0.021 (0.021)	0.042 (0.042)	0.073 (0.073)	0.104 (0.104)
0.20	0.002 (0.002)	0.012 (0.012)	0.022 (0.023)	0.042 (0.043)	0.072 (0.074)	0.102 (0.104)
0.30	0.006 (0.006)	0.015 (0.016)	0.024 (0.025)	0.043 (0.045)	0.071 (0.075)	0.100 (0.105)
0.40	0.012 (0.012)	0.021 (0.022)	0.029 (0.031)	0.047 (0.050)	0.073 (0.079)	0.100 (0.108)
0.60	0.034 (0.034)	0.041 (0.042)	0.048 (0.051)	0.062 (0.068)	0.084 (0.094)	0.107 (0.120)
0.80	0.066 (0.066)	0.071 (0.073)	0.077 (0.080)	0.088 (0.095)	0.106 (0.118)	0.125 (0.141)
1.00	0.104 (0.104)	0.108 (0.110)	0.112 (0.116)	0.122 (0.129)	0.136 (0.149)	0.152 (0.169)
1.20	0.144 (0.144)	0.148 (0.149)	0.151 (0.155)	0.158 (0.165)	0.170 (0.183)	0.183 (0.201)

0.10	-20.2 (-20.2)	-21.4 (-21.4)	-22.4 (-22.4)	-24.3 (-24.3)	-26.6 (-26.7)	-28.7 (-28.8)
0.20	-14.6 (-14.6)	-15.7 (-15.8)	-16.8 (-16.8)	-18.5 (-18.6)	-20.8 (-20.9)	-22.9 (-23.0)
0.30	-11.8 (-11.8)	-12.8 (-12.9)	-13.7 (-13.8)	-15.4 (-15.5)	-17.5 (-17.8)	-19.5 (-19.8)
0.40	-10.3 (-10.3)	-11.2 (-11.3)	-12.1 (-12.2)	-13.5 (-13.8)	-15.5 (-15.9)	-17.3 (-17.8)
0.60	-9.7 (-9.7)	-10.3 (-10.4)	-10.9 (-11.1)	-11.9 (-12.3)	-13.5 (-14.2)	-15.1 (-15.8)
0.80	-10.6 (-10.6)	-11.0 (-11.1)	-11.4 (-11.6)	-12.2 (-12.7)	-13.4 (-14.1)	-14.5 (-15.5)
1.00	-12.2 (-12.2)	-12.5 (-12.6)	-12.7 (-13.0)	-13.3 (-13.7)	-14.1 (-14.9)	-15.0 (-16.0)
1.20	-13.9 (-13.9)	-14.1 (-14.2)	-14.3 (-14.5)	-14.7 (-15.1)	-15.4 (-16.0)	-16.0 (-17.0)

TRACKING SYSTEM
NIGHT/90-PERCENTILE
WAVE LENGTH= 1.060 (MICRONS)
ZENITH ANGLE= 0. (DEG.)
R-ZERO= 0.114 (METER)

LMSC-B290200-III

0.30	0.001 (0.001)	0.004 (0.005)	0.008 (0.009)	0.015 (0.017)	0.026 (0.029)	0.036 (0.041)
0.60	0.004 (0.004)	0.006 (0.006)	0.008 (0.009)	0.012 (0.015)	0.018 (0.023)	0.024 (0.032)
1.00	0.009 (0.009)	0.010 (0.011)	0.011 (0.012)	0.013 (0.016)	0.016 (0.021)	0.019 (0.026)
1.40	0.017 (0.017)	0.018 (0.018)	0.018 (0.019)	0.019 (0.021)	0.021 (0.024)	0.023 (0.028)
1.80	0.029 (0.029)	0.029 (0.029)	0.029 (0.030)	0.030 (0.031)	0.031 (0.033)	0.032 (0.036)
2.30	0.048 (0.048)	0.049 (0.049)	0.049 (0.049)	0.049 (0.050)	0.050 (0.052)	0.051 (0.053)
2.90	0.081 (0.081)	0.081 (0.081)	0.081 (0.081)	0.081 (0.082)	0.082 (0.083)	0.082 (0.084)
3.50	0.130 (0.130)	0.130 (0.130)	0.130 (0.130)	0.130 (0.131)	0.131 (0.131)	0.131 (0.132)

0.30	-10.8 (-10.8)	-11.1 (-11.2)	-11.5 (-11.7)	-12.3 (-12.5)	-13.4 (-13.7)	-14.4 (-14.7)
0.60	-5.2 (-5.2)	-5.5 (-5.6)	-5.7 (-5.9)	-6.2 (-6.5)	-6.8 (-7.4)	-7.4 (-8.2)
1.00	-1.9 (-1.9)	-2.0 (-2.0)	-2.1 (-2.2)	-2.3 (-2.5)	-2.6 (-3.1)	-2.9 (-3.6)
1.40	-0.3 (-0.3)	-0.4 (-0.4)	-0.4 (-0.5)	-0.6 (-0.7)	-0.7 (-1.1)	-0.9 (-1.4)
1.80	0.1 (0.1)	0.0 (-0.0)	-0.0 (-0.1)	-0.1 (-0.2)	-0.2 (-0.4)	-0.3 (-0.5)
2.30	-0.4 (-0.4)	-0.4 (-0.4)	-0.4 (-0.4)	-0.4 (-0.5)	-0.5 (-0.6)	-0.5 (-0.7)
2.90	-2.0 (-2.0)	-2.0 (-2.0)	-2.0 (-2.0)	-2.0 (-2.0)	-2.0 (-2.1)	-2.1 (-2.2)
3.50	-4.8 (-4.8)	-4.8 (-4.8)	-4.8 (-4.8)	-4.8 (-4.8)	-4.8 (-4.9)	-4.8 (-4.9)

TRACKING SYSTEM
 NIGHT/90-PERCENTILE
 WAVE LENGTH= 1.060 (MICRONS)
 ZENITH ANGLE=40. (DEG.)
 R-ZEPC= 0.088 (METER)

LMSC-B290200-III

0.30	0.001 (0.001)	0.010 (0.011)	0.020 (0.021)	0.038 (0.040)	0.067 (0.070)	0.096 (0.100)
0.60	0.004 (0.004)	0.011 (0.012)	0.018 (0.020)	0.032 (0.037)	0.054 (0.063)	0.077 (0.090)
1.00	0.009 (0.009)	0.012 (0.015)	0.018 (0.021)	0.027 (0.034)	0.042 (0.054)	0.057 (0.075)
1.40	0.017 (0.017)	0.020 (0.022)	0.023 (0.026)	0.029 (0.035)	0.038 (0.050)	0.049 (0.066)
1.80	0.029 (0.029)	0.030 (0.032)	0.032 (0.035)	0.036 (0.042)	0.043 (0.053)	0.050 (0.065)
2.30	0.048 (0.048)	0.050 (0.051)	0.051 (0.053)	0.054 (0.058)	0.058 (0.065)	0.063 (0.074)
2.90	0.081 (0.081)	0.082 (0.082)	0.083 (0.084)	0.084 (0.087)	0.087 (0.093)	0.091 (0.098)
3.50	0.130 (0.130)	0.130 (0.131)	0.131 (0.132)	0.132 (0.134)	0.134 (0.138)	0.137 (0.143)

0.30	-10.8 (-10.8)	-11.8 (-11.9)	-12.8 (-12.9)	-14.5 (-14.7)	-16.7 (-16.9)	-18.7 (-19.0)
0.60	-5.2 (-5.2)	-6.1 (-6.2)	-6.8 (-7.1)	-8.2 (-8.6)	-9.9 (-10.6)	-11.6 (-12.5)
1.00	-1.9 (-1.9)	-2.3 (-2.5)	-2.8 (-3.1)	-3.7 (-4.3)	-4.9 (-5.9)	-6.1 (-7.4)
1.40	-0.3 (-0.3)	-0.6 (-0.8)	-0.9 (-1.2)	-1.5 (-2.1)	-2.3 (-3.2)	-3.1 (-4.4)
1.80	0.1 (0.1)	-0.1 (-0.2)	-0.3 (-0.5)	-0.6 (-1.0)	-1.1 (-1.9)	-1.7 (-2.8)
2.30	-0.4 (-0.4)	-0.5 (-0.5)	-0.6 (-0.7)	-0.8 (-1.1)	-1.1 (-1.6)	-1.5 (-2.2)
2.90	-2.0 (-2.0)	-2.0 (-2.1)	-2.1 (-2.2)	-2.2 (-2.4)	-2.4 (-2.8)	-2.6 (-3.2)
3.50	-4.8 (-4.8)	-4.8 (-4.8)	-4.9 (-4.9)	-4.9 (-5.0)	-5.0 (-5.3)	-5.2 (-5.5)

TABLE 6

Listing of FORTRAN Program Used
to Prepare Table 5

```

DIMENSION X(5),Y(5),A(4),B(4),WL(3),TH(2),STH(2),
1H(2),RZR(4),SL(6),D(2,8),PHI(2,8),G(2,8),
2SLE(2,6,8),EAC(2,6,8)
X(1) = 0.003
Y(1) = 0.276
X(2) = 0.01
Y(2) = 1.09
X(3) = 0.03
Y(3) = 3.12
X(4) = 0.1
Y(4) = 8.30
X(5) = 0.3
Y(5) = 18.93
DO 10 I = 1,4
XL = ALOG(X(I)/X(I+1))
YL = ALOG(Y(I)/Y(I+1))
XXL = ALOG(X(I))
B(I) = YL/XL
A(I) = Y(I)*EXP(-YL*XXL/XL)
10 CONTINUE
WL(1) = 0.53
WL(2) = 0.633
WL(3) = 1.06
TH(1) = 0.0
TH(2) = 40.0
STH(1) = 1.0
STH(2) = 1.556
SL(1) = 0.0
SL(2) = 0.01
SL(3) = 0.02
SL(4) = 0.04
SL(5) = 0.07
SL(6) = 0.10
D(1,1) = 0.1
D(1,2) = 0.2
D(1,3) = 0.3
D(1,4) = 0.4
D(1,5) = 0.6
D(1,6) = 0.8
D(1,7) = 1.0
D(1,8) = 1.2
D(2,1) = 0.3
D(2,2) = 0.6
D(2,3) = 1.0
D(2,4) = 1.4
D(2,5) = 1.8
D(2,6) = 2.3
D(2,7) = 2.9
D(2,8) = 3.5
PHI(1,1) = 1.001
PHI(1,2) = 1.009
PHI(1,3) = 1.023
PHI(1,4) = 1.050
PHI(1,5) = 1.145
PHI(1,6) = 1.300

```

```

PHI(1,7) = 1.514
PHI(1,8) = 1.780
PHI(2,1) = 1.004
PHI(2,2) = 1.015
PHI(2,3) = 1.037
PHI(2,4) = 1.071
PHI(2,5) = 1.121
PHI(2,6) = 1.214
PHI(2,7) = 1.382
PHI(2,8) = 1.681
G(1,1) = 0.0095
G(1,2) = 0.036
G(1,3) = 0.076
G(1,4) = 0.125
G(1,5) = 0.234
G(1,6) = 0.339
G(1,7) = 0.429
G(1,8) = 0.503
G(2,1) = 0.085
G(2,2) = 0.324
G(2,3) = 0.817
G(2,4) = 1.412
G(2,5) = 2.013
G(2,6) = 2.657
G(2,7) = 3.174
G(2,8) = 3.398
H(1)=5000.
H(2)=10000.
RZR(1)=0.049
RZR(2)=0.033
RZR(3)=0.076
RZR(4)=0.052
DO 100 K=1,3
DO 110 J=1,4
DO 120 I=1,2
DO 130 L=1,2
DO 140 M=1,2
RHO=0.8*SQRT(H(M)*WL(K)*(1.E-06)*STH(L))
RZ=RZR(J)*(WL(K)/0.55)**(1.2)*(STH(L))**(-.6)
SF=(0.55/WL(K))**(7./6.)*(STH(L))**(11./6.)
DO 150 N=1,6
DO 160 NN=1,8
AF=1./(1.+(D(I,NN)*RZ/RHO)**2)
SI=(AF*(EXP(4*SF*SL(N))-1.)+1.)*PHI(I,NN)-1.
SLE(M,N,NN)=0.25*ALOG(SI+1.)
ST=SLE(M,N,NN)
IF(ST.GE.0.1) GO TO 170
IF(ST.GE.0.03) GO TO 180
IF(ST.GE.0.01) GO TO 190
YL=A(1)*(ST**B(1))
GO TO 200
190 YL=A(2)*(ST**B(2))
GO TO 200
180 YL=A(3)*(ST**B(3))
GO TO 200

```

```

170  YL=A(4)*(ST**B(4))
200  CONTINUE
    AG=10.*ALOG10(G(I,NN))
    EAG(M,N,NN)=AG-YL
160  CONTINUE
150  CONTINUE
140  CONTINUE
    IF(I.EQ.1) WRITE(8,9)
9     FORMAT(1H1,9X,'STATIC SYSTEM')
    IF(I.EQ.2) WRITE(8,11)
11    FORMAT(1H1,9X,'TRACKING SYSTEM')
    IF(J.EQ.1) WRITE(8,12)
12    FORMAT(10X,'DAY/50-PERCENTILE')
    IF(J.EQ.2) WRITE(8,13)
13    FORMAT(10X,'DAY/90-PERCENTILE')
    IF(J.EQ.3) WRITE(8,14)
14    FORMAT(10X,'NIGHT/50-PERCENTILE')
    IF(J.EQ.4) WRITE(8,15)
15    FORMAT(10X,'NIGHT/90-PERCENTILE')
    WRITE(8,210) WL(K)
210   FORMAT(10X,'WAVE LENGTH= ',F5.3,1X,'(MICRONS)')
    WRITE(8,220) TH(L)
220   FORMAT(10X,'ZENITH ANGLE= ',F3.0,1X,'(DEG.)')
    WRITE(8,230) RZ
230   FORMAT(10X,'R-ZERO= ',F5.3,1X,'(METER)')
    WRITE(8,16)
16    FORMAT(10X,///)
    DO 231 NN=1,8
        WRITE(8,240) D(I,NN),SLE(1,1,NN),SLE(1,2,NN),SLE(1,3,NN),
1SLE(1,4,NN),SLE(1,5,NN),SLE(1,6,NN),SLE(2,1,NN),SLE(2,2,NN),
2SLE(2,3,NN),SLE(2,4,NN),SLE(2,5,NN),SLE(2,6,NN)
240   FORMAT(11X,F4.2,3X,6(3X,F5.3,1X),/,18X,6(2X,'( ',F5.3,') '),/)
231   CONTINUE
        WRITE(8,17)
17    FORMAT(10X,/)
    DO 250 NN=1,8
        WRITE(8,260) D(I,NN),EAG(1,1,NN),EAG(1,2,NN),EAG(1,3,NN),
1EAG(1,4,NN),EAG(1,5,NN),EAG(1,6,NN),EAG(2,1,NN),EAG(2,2,NN),
2EAG(2,3,NN),EAG(2,4,NN),EAG(2,5,NN),EAG(2,6,NN)
260   FORMAT(11X,F4.2,3X,6(3X,F5.1,1X),/,18X,6(2X,'( ',F5.1,') '),/)
250   CONTINUE
130   CONTINUE
120   CONTINUE
110   CONTINUE
100   CONTINUE
    STOP
    END

```

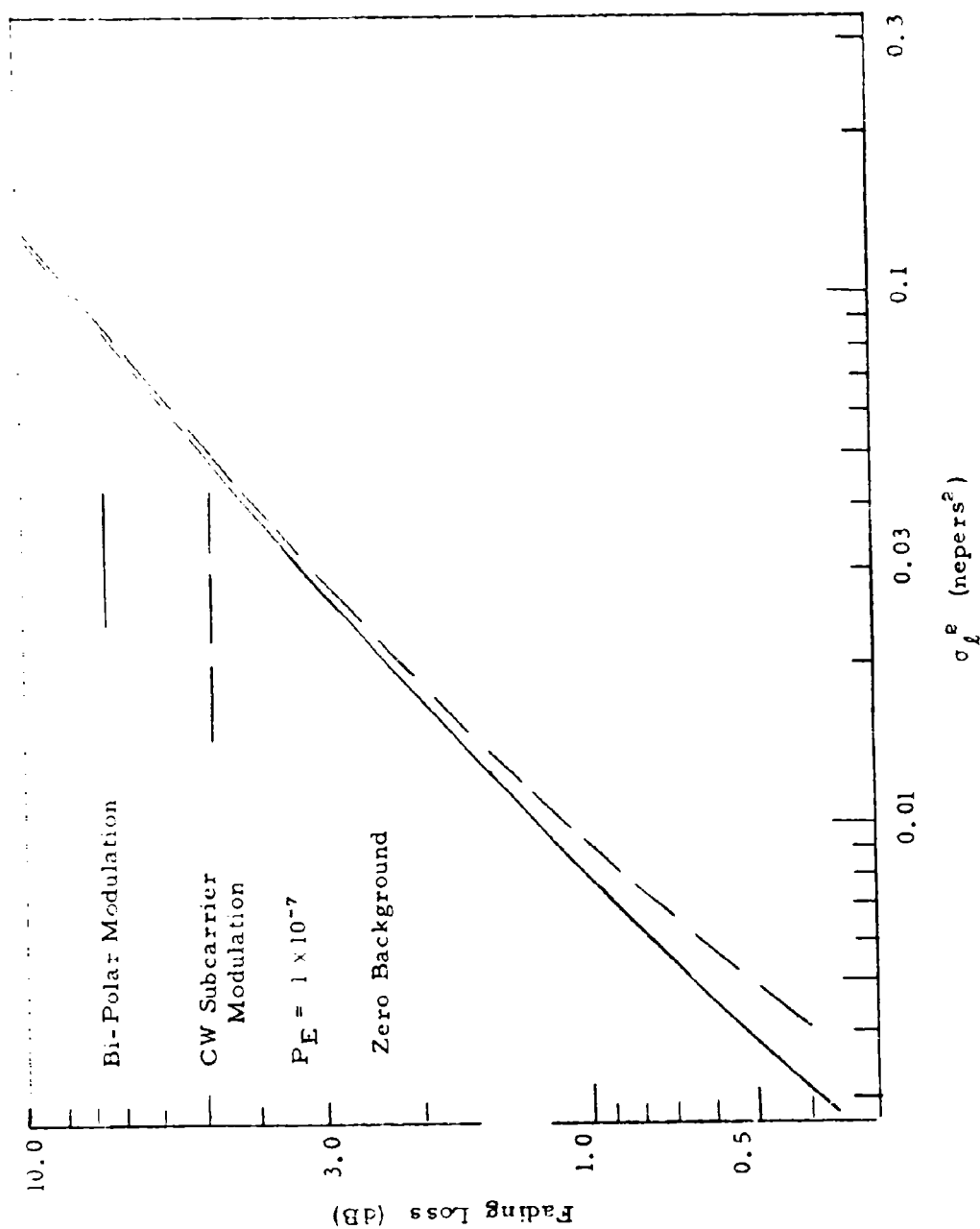


Figure 1. Fading Loss As A Function Of Log-Amplitude Variance. Results are shown for a zero background case, for both bi-polar and cw subcarrier modulation. The loss is calculated on the basis of a required error probability of 10^{-7} .

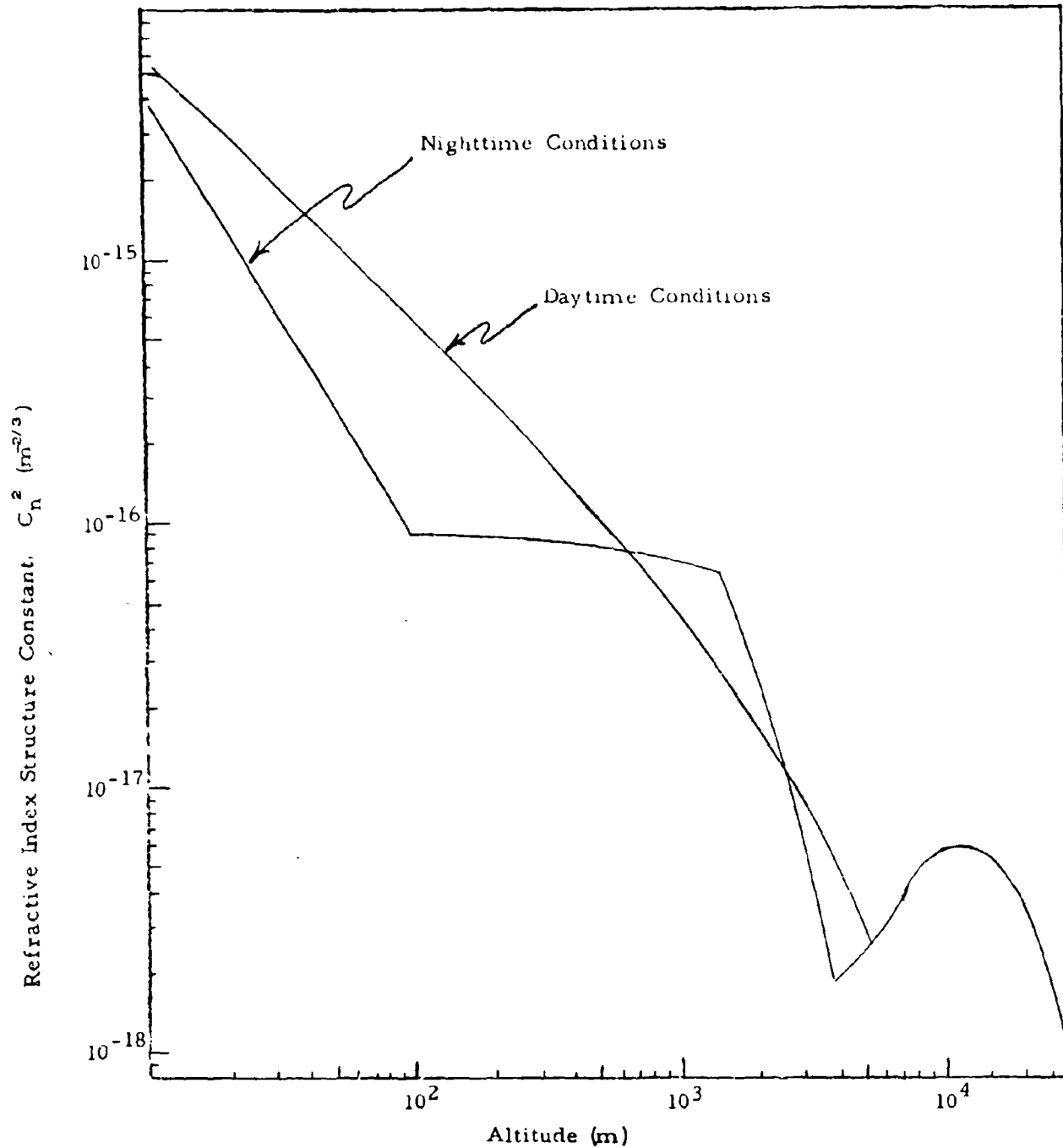


Fig. 2 Suggested Model For The Vertical Distribution Of The Refractive Index Structure Constant, C_n^2 . This model is based on the temperature probe data of Koprov and Tsvang⁵, on near the ground laser scintillation measurements of C_n^2 , and on stellar scintillation measurements.⁴

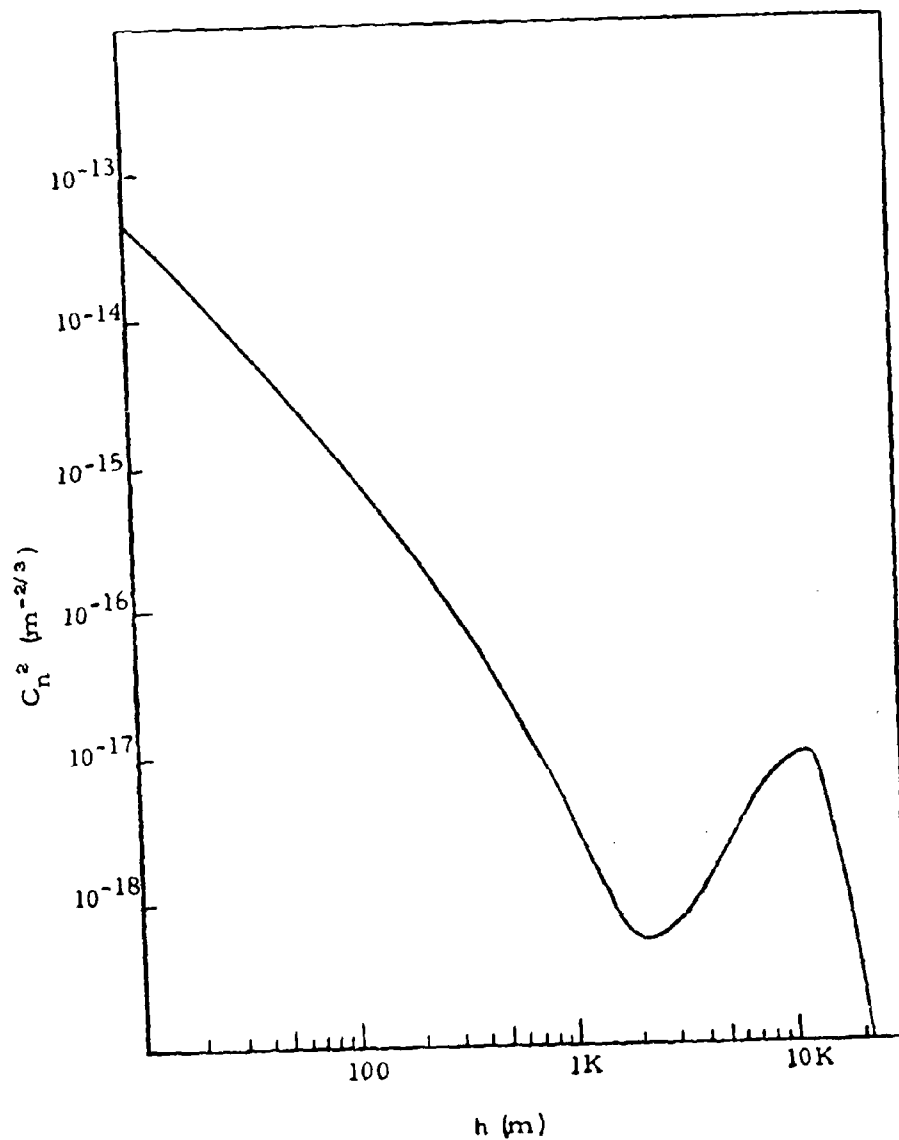


Fig. 3 Typical Nighttime Vertical Distribution of the Optical Strength of Turbulence. (From J. L. Bafton. "An Investigation of Atmospheric Turbulence by Stellar Observations." Master's Thesis, Univ. of Maryland, 1970.)

Fig. 4 Average Antenna Gain. Average antenna gain is shown as a function of D/r_0 for a static and for a fast-tracking optical heterodyne receiver or laser transmitter. $\langle G \rangle$ is the average gain and G_0 is the free space gain for a diameter r_0 .

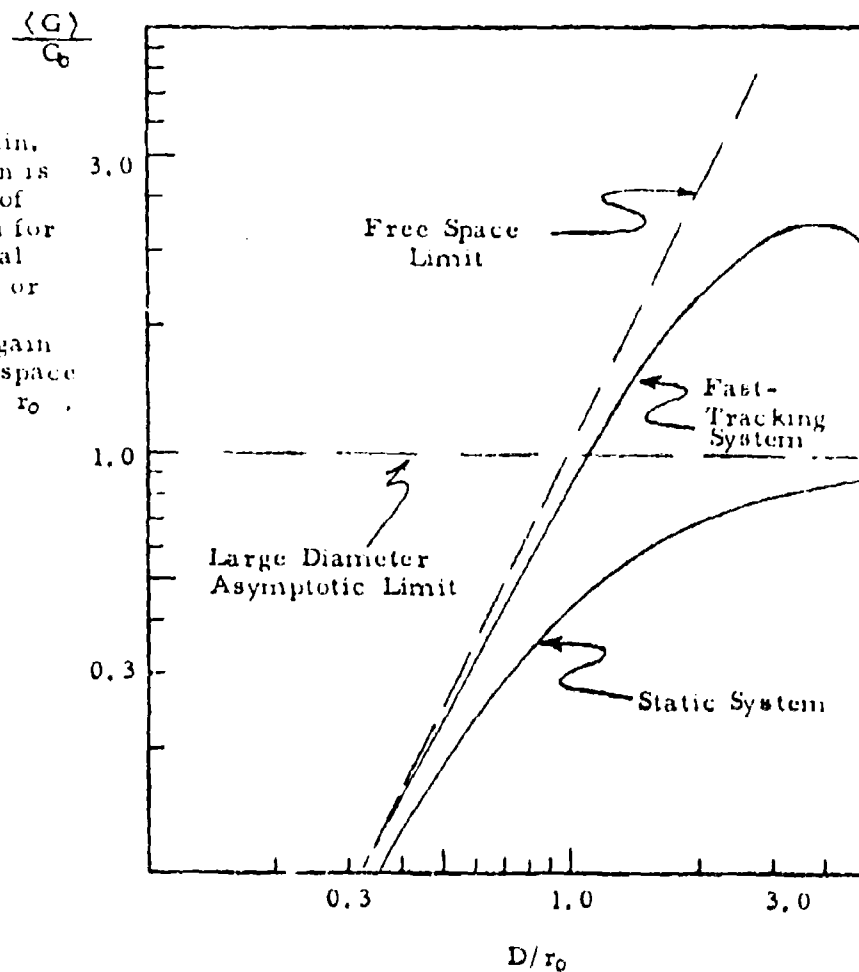
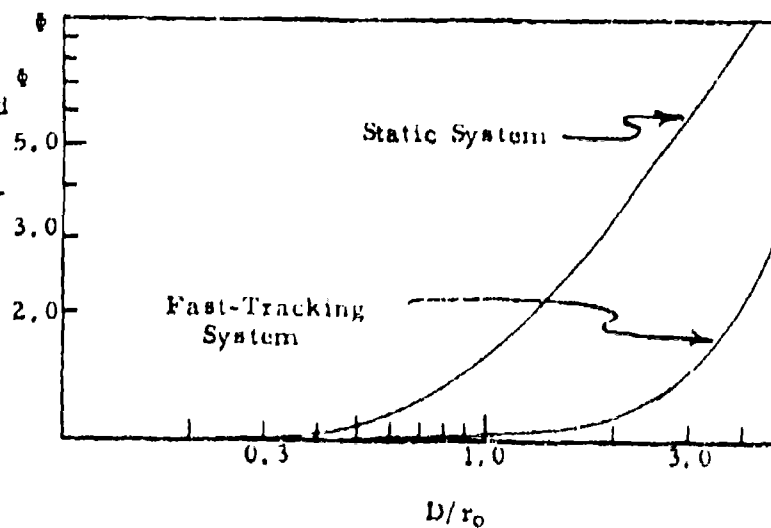


Fig. 5 Noise Modulation Factor ϕ . ϕ is operationally defined in the text by Eq. (8). Results are shown for both static and fast-tracking systems.



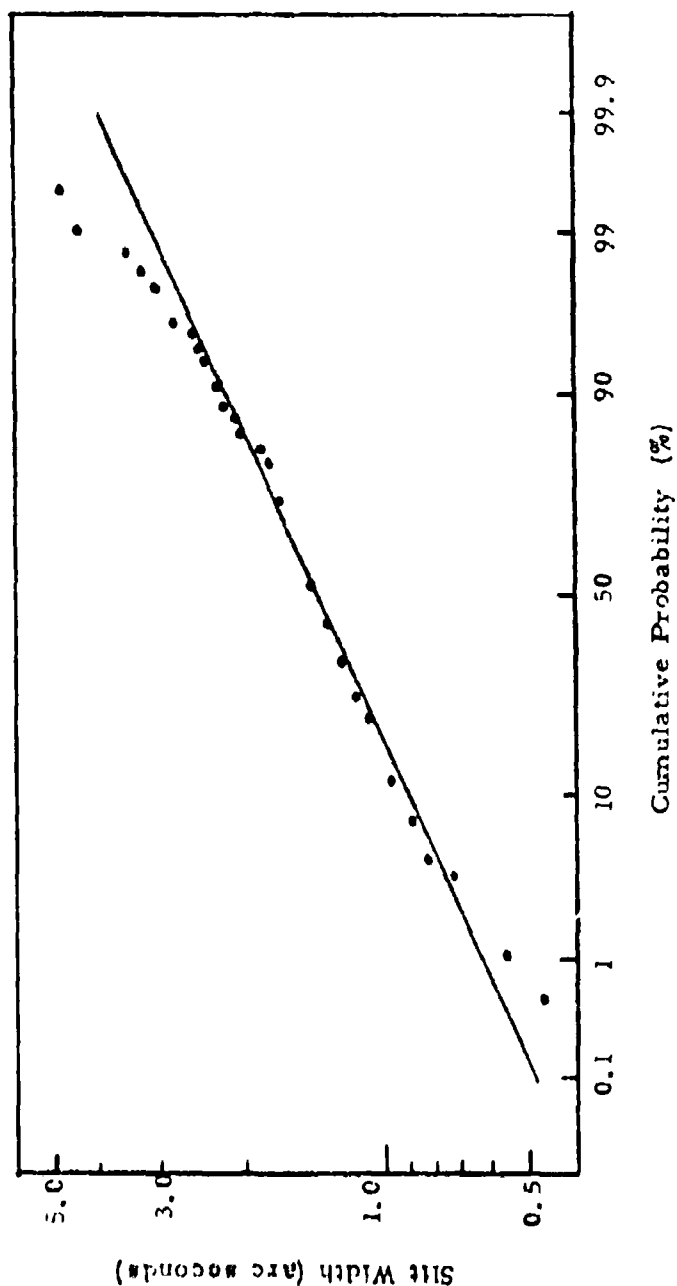


Fig. 6 Slit Width Required to Pass 68% of the Energy in a Stellar Image¹⁴ vs. Cumulative Probability of Occurrence; From the Data of Hoag

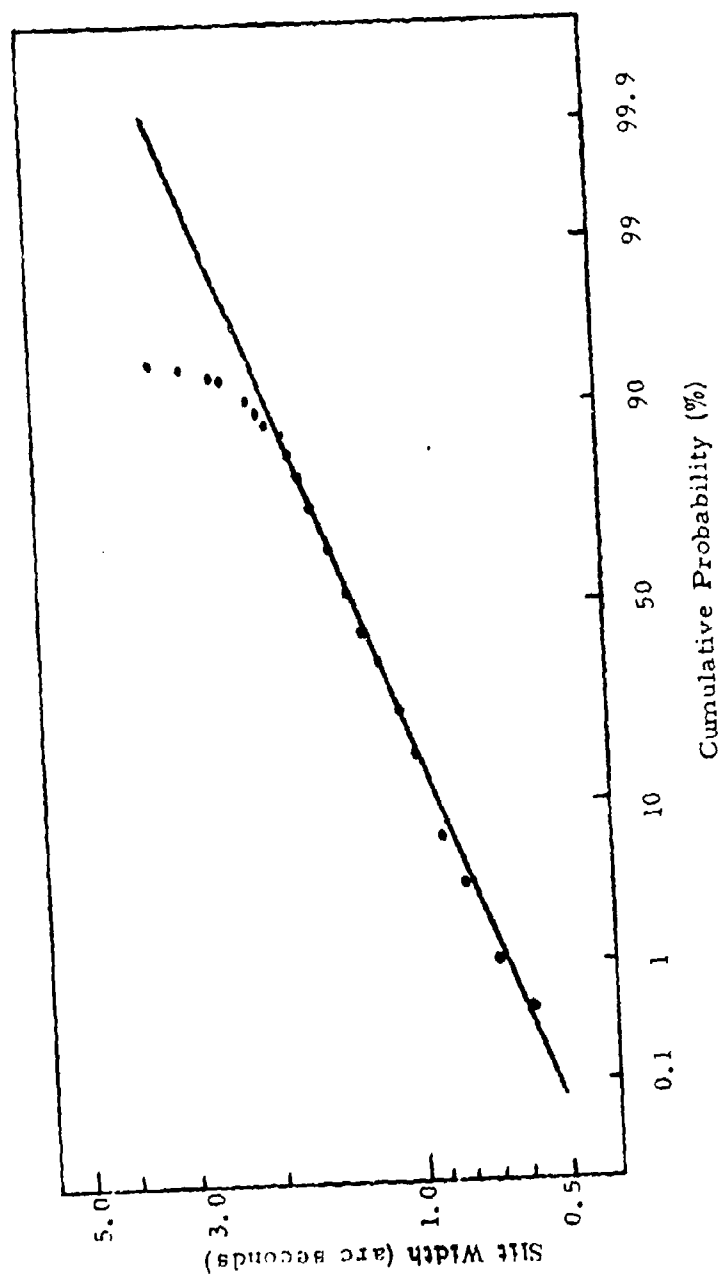


Fig. 7. Slit Width Required to Pass 68% of the Energy in a Stellar Image¹⁵
vs. Cumulative Probability of Occurrence; From the Data of Meinel¹⁵

Appendix N

COMPUTER PROGRAMS

by

Dr. A. D. MacDonald

LOCKHEED PALO ALTO RESEARCH LABORATORY
LOCKHEED MISSILES & SPACE COMPANY
A GROUP DIVISION OF LOCKHEED AIRCRAFT CORPORATION

Computer programs have been prepared and used for four applications in the laser communication system:

- I. Link analysis calculations for the high-data-rate system
- II. Link calculations for the acquisition and tracking systems
- III. Calculation of fading effects caused by atmospheric scintillation
- IV. Link analysis calculations for the low-data-rate system

PROGRAM I

This program is designed to calculate link margins for either high or low data rates for any of the six links considered in this study. It can also be used to calculate the laser power required to close the link with any desired link margin.

The bit error rate used in these calculations is 10^{-7} , and the use of three types of modulation is available in the program. For low data rates, binary polarization is used with an explicit expression for the signal required to produce the desired error rate. For the high-data-rate system, calculations can be made for both the quadriphase-shift-keyed system and the mode locked on-off system. The expression for the required signal in the quadriphase system is based on the Herrmann expression, using the Chernoff upper bound described in detail in Appendix B. (The program also has available the option of using the Gaussian expression, but all data presented in this report are based on the Chernoff bound.) The expression used for the mode-locked system is that of Bucher, based on a Chernoff bound. This expression does not lend itself readily to obtaining an explicit expression for the signal required and so a search technique was used with an expression for the error rate as a function of background and signal counts as a basis.

The listing of the Fortran program included at the end of this appendix contains sufficient comments at the beginning to enable the reader to follow the logic, but a number of features should be emphasized.

The first part of the output lists all input parameters, including laser and antenna properties, optical properties of transmitting and receiving elements, and receiving properties such as integration time and detector quantum efficiency, as well as all the elements that result in degradation of the received information (i.e., excess noise factor and bit detection efficiency loss). The second part of the output is the power budget calculation in logarithmic units with the resultant calculations for either link margin for a given laser power, or the laser power required for a specified link margin.

Included among the input quantities are estimates of the range of uncertainty to which many of the quantities are known. These are converted to decibel units and are shown as uncertainties in the various elements in the power budget calculation, leading to an overall uncertainty in the estimate of power required or link margin.

Detailed descriptions of the terms used in both the input section and the power budget section are contained in the link analysis chapter, which also includes all equations used for the links and for the statistics.

PROGRAM II

The acquisition and tracking computer program is a modified version of the link analysis program in which the signal and background photoelectron counts for appropriate links are calculated. The same link equations are used but the calculation procedure for required signals is different for the different phases and is done separately from the computer program in phases 1, 2, 3, and 4.

The comments at the beginning of the listing describe the input parameters in detail.

PROGRAM III

The atmospheric scintillation program is designed to calculate the effects of atmospheric turbulence on the fading of laser link signals. The comments at the beginning of the

program describe the method of use and the meaning of the input and output parameters. This program has been designed as a module that can become part of the link analysis program for calculating the laser power required or the link margin for laser links that have a path through the atmosphere. As it now stands, it is used to calculate the photoelectron signal count which is required to produce a bit error rate of 10^{-7} for given atmospheric conditions. The program can be used for either binary polarization or quadriphase modulations. The probability of error is calculated by integration of the appropriate probability density function multiplied by the log-normal distribution function as described in Section 1. A starting value of required signal is used, the probability of error is calculated, and the values of required signal are successively adjusted until the probability of error is 10^{-7} within about 2%.

The input parameters are modulation index, modulation type, background count, and log amplitude variance of signal fluctuations. The probability density functions used are the Herrmann expressions for the Chernoff upper bound for the quadriphase case and the Bucher modified expression in the binary polarization case.

PROGRAM IV

The Low-Data-Rate Laser Link Analysis Program computes link margins for a 20-kbit/sec command and range determination link using the following five candidate system approaches:

<u>System Type</u>	<u>Wavelength (μm)</u>	<u>Laser</u>	<u>Modulations</u>
1	0.89	Semiconductor	M-ary PPM
2	0.63	HeNe	CW, Bipolarization, PN
3	1.06	Nd:YAG	Bipolarization, Pulse
4	1.06	Nd:YAG	Bipolarization, Pulse
5	1.06	Nd:YAG	CW, Bipolarization, PN

Early system tradeoff analysis determined that System Type 2 was the most desirable; consequently, all published low-data-rate link calculations are for the HeNe laser.

To facilitate computation and the updating of the program with new values when required, a time-sharing computer system was used. This permitted many parameters to be entered from the terminal, with results immediately available. The programming language used is TYMSHARE SUPERBASIC.

The program computes link margins (defined as the received photoelectrons per bit minus the required photoelectrons per bit for a 10^{-7} bit error rate, both in decibel notation) for specific link configurations (ground terminal to synchronous relay satellite, synchronous relay satellite to low orbit satellite, etc.). The detection statistics used to compute required photoelectrons per bit for 10^{-7} BER are based on Bucher's formula. In cases where the link passes through the atmosphere, a turbulent air loss factor based on Fried's work (Appendix C) is included. The Bucher formulas (Vol. II, section 1.4.3.2) used for each system type are shown below. The symbols are defined below.

- P_E = bit error probability
- τ_T = transmitted pulse width (bit period for cw laser case)
- τ_R = receiver gate width (when applicable)
- f_R = laser repetition rate
- f_D = data rate (bits/sec)
- M = M-ary constant
- k = data words per range pulse opportunity
- B = mean background photoevent rate of an ungated polarization-insensitive receiver with the same aperture and efficiency as the actual receiver
- S = same as above but for signal photoevents

System Type	Bucher Equation	Ancillary Formulas Used With Bucher's Equation
1	$P_E = \frac{1}{4}(M-1) \exp \{-S \tau_T E_C\}$	$E_C = \frac{\sqrt{1 + \frac{S \tau_T}{B \tau_R}} - 1}{\sqrt{1 + \frac{S \tau_T}{B \tau_R}} + 1}$ $f_d = 2 \times 10^4 \text{ bits/sec}$ $f_R = f_d \frac{(k + \frac{1}{2})}{k \log_2 M}$ $\tau_T = \frac{3 \times 10^{-4}}{f_R}$ $\tau_R = 2 \tau_T$
2	$P_E = \frac{1}{2} \exp \{-S \tau_T E_C\}$	$E_C = \frac{\sqrt{1 + 2 \frac{S}{B}} - 1}{\sqrt{1 + 2 \frac{S}{B}} + 1}$ $\tau_T = \frac{1}{f_d} = 5 \times 10^{-5} \text{ sec}$
3	$P_E = \frac{1}{2} \exp \{-SN \tau_T E_C\}$	$E_C = \frac{\sqrt{1 + 2 \frac{SN \tau_T}{BN \tau_R}} - 1}{\sqrt{1 + 2 \frac{SN \tau_T}{BN \tau_R}} + 1}$ $\tau_R = 2 \tau_T$ <p>N = number of data pulses per bit period</p>
4	$P_E = \frac{1}{2} \exp \{-2S \tau_T E_C\}$	$E_C = \frac{\sqrt{1 + \frac{S}{B}} - 1}{\sqrt{1 + \frac{S}{B}} + 1}$
5	Same as System Type 2	

N-5

N-6

LOCKHEED PALO ALTO RESEARCH LABORATORY
LOCKHEED MISSILES & SPACE COMPANY
 A GROUP DIVISION OF LOCKHEED AIRCRAFT CORPORATION

IV 360N-FO-477 3-5

MAINPOM

DATE 10/03/71

TIME 14.26.48

```

140 FORMAT('C',20X,'SS TO AU, LOW DATA RATE')
150 FORMAT('C',20X,'AT TO SS, LOW DATA RATE')
200 FORMAT('D',10X,'BACKGROUND',1,544,'MODULATION',1,544)
210 FORMAT('C',2X,'LASER WAVELENGTH',1,F8.4,' MICRONS
    ')
220 FORMAT('3X',1, 'OUTPUT POWER -AVERAGE',1,F8.4,' WATTS')
230 FORMAT('3X',1, 'PULSE WIDTH',1,F12.4,' NANOSEC')
240 FORMAT('3X',1, 'REPETITION RATE',1,F8.4,' KPCS')
250 FORMAT('3X',1, 'PEAK POWER',1,F8.4,' WATTS')
260 FORMAT('3X',1,'BIT ERROR RATE BY 10 TO -7',1,F8.4)
270 FORMAT('3X',1,'DATA RATE',1,F9.4,' MBPS')
280 FORMAT('3X',1,'MODULATION INDEX',1,F8.4)
281 FORMAT('3X',1,'EXTINCTION RATIO',1,F8.4,' DB')
290 FORMAT('3X',1,'XMTX ANTENNA DIAMETER',1,F8.4,' METERS')
291 FORMAT('3X',1,'XMTX ANTENNA BEAMWIDTH',1,F10.4,' MICRORAD')
292 FORMAT('3X',1, 'EFFECTIVE ANTENNA DIAMETER',1,F8.4,' METERS')
293 FORMAT('3X',1, 'FWHP BEAMWIDTH',1,F8.4,' MICRORAD')
300 FORMAT('3X',1, 'ANTENNA EFFICIENCY',1,F8.4)
301 FORMAT('3X',1, 'ILLUMINATION FACTOR',1,F8.4)
310 FORMAT('3X',1, 'OPTICAL TRANSMITTANCE',1,F8.4)
312 FORMAT('3X',1, 'POINTING ERROR FACTOR',1,F8.4)
314 FORMAT('3X',1,'RCVR ANTENNA DIAMETER',1,F8.4,' METERS')
316 FORMAT('3X',1, 'ANTENNA EFFICIENCY',1,F8.4)
318 FORMAT('3X',1, 'OPTICAL TRANSMITTANCE',1,F8.4)
320 FORMAT('3X',1, 'FILTER BANDWIDTH',1,F8.4,' ANGSTROMS')
322 FORMAT('3X',1, 'FIELD OF VIEW',1,F10.4,' MICRORAD')
324 FORMAT('3X',1, 'DET QUANTUM EFFICIENCY',1,F8.4)
326 FORMAT('3X',1, 'EXCESS NOISE FACTOR',1,F8.4)
327 FORMAT('3X',1, 'BIT DETECTION EFFICIENCY',1,F8.4)
327 FORMAT('3X',1, 'THRESHOLD LOSS FACTOR',1,F8.4)
328 FORMAT('3X',1, 'INTEGRATION TIME',1,F12.4,' NANOSEC')
328 FORMAT('3X',1, 'INTEGRATION TIME',1,F12.4,' MICROSEC')
329 FORMAT('3X',1, 'GATE TIME',1,F12.4,' NANOSEC')
330 FORMAT('3X',1,'BACKGROUND RADIANCE',1,F8.4,' W/STER-A-SQ
    (M*)')
332 FORMAT('3X',1,'BACKGROUND PE/INTEGRATION TIME',1,F12.4)
333 FORMAT('3X',1,'BACKGROUND PE/INT TIME-EFF',1,F12.4)
334 FORMAT('3X',1,'REQUIRED SGNL PE/INT TIME',1,F12.4)
335 FORMAT('3X',1,'RECEIVED SIGNAL PE/INT TIME',1,F12.4)
336 FORMAT('3X',1,'RANGE',1,F12.4,' KILOMETERS')
339 FORMAT('3X',1,'RECEIVED PE/INT TIME EFF',1,F12.4)
350 FORMAT('3X',1,'ATMOSPHERIC ABSORPTION FACTOR',1,F8.4)
352 FORMAT('3X',1,'ATMOSPHERIC VARIANCE CL',1,F8.4)
354 FORMAT('3X',1,'COHERENCE DISTANCE',1,F8.4)
356 FORMAT('3X',1,'ATMOSPHERIC TRANSMITTANCE',1,F8.4)
360 FORMAT('D',25X,'LINK MARGIN CALCULATION')
362 FORMAT('C',25X,'POWER BUDGET CALCULATION')
390 FORMAT('C',47X,'19H DB UNCERTAINTY')
400 FORMAT('34H LASER POWER',1,F6.1,' DBW',8X,F5.1)
405 FORMAT('34H TRANSMITTER LOSS',1,F6.1,' DB',8X,F5.1)
410 FORMAT('34H TRANSMITTER ANTENNA GAIN',1,F6.1,' DB',8X,F5.1)
415 FORMAT('34H POINTING LOSS',1,F6.1,' DB',8X,F5.1)
420 FORMAT('34H SPACE LOSS',1,F6.1,' DB',8X,F5.1)
425 FORMAT('34H ATMOSPHERIC LOSS',1,F6.1,' DB',8X,F5.1)

```

```

CAN IV 360N-FO-77 3-5      MAINPGM      DATE 10/C1/71      TIME 14.26.48

430 FORMAT(34H RECEIVER ANTENNA GAIN      ,F6.1, ' DB ',AX,F5.1)
435 FORMAT(34H RECEIVER LOSS              ,F6.1, ' DB ',BX,F5.1)
440 FORMAT(34H RECEIVED POWER             ,F6.1, ' DBW ',BX,F5.1)
445 FORMAT(34H BIT PERIOD                  ,F6.1, ' DBS ',BX,F5.1)
450 FORMAT(34H RECEIVED ENERGY/INT TIME  ,F6.1, ' DBJ ',BX,F5.1)
455 FORMAT(34H ENERGY/PHOTON             ,F6.1, ' LEJ ',BX,F5.1)
460 FORMAT(34H RECEIVED PHOTONS/INT TIME  ,F6.1, ' DBI ',BX,F5.1)
465 FORMAT(34H QUANTUM EFFICIENCY          ,F6.1, ' DBI ',BX,F5.1)
466 FORMAT(34H EXCESS NOISE FACTOR LOSS   ,F6.1, ' DBI ',BX,F5.1)
467 FORMAT(34H BIT DETECTION EFFICIENCY LOSS ,F6.1, ' DBI ',BX,F5.1)
468 FORMAT(34H THRESHOLD SETTING LOSS     ,F6.1, ' DBI ',BX,F5.1)
469 FORMAT(34H ATMOSPHERIC TURBULENCE LOSS ,F6.1, ' DB ',BX,F5.1)
470 FORMAT(34H RECEIVED PE/INT TIME       ,F6.1, ' DBI ',BX,F5.1)
475 FORMAT(34H REQUIRED PE/INT TIME         ,F6.1, ' DBI ',BX,F5.1)
490 FORMAT(34H MARGIN                      ,F6.1, ' DB ',BX,F5.1)
479 FORMAT(34HOMARGIN                     ,F6.1,12X,F5.1)
492 FORMAT(34HCSIGNAL REQD -MILLIMICROWATTS ,F10.4)
493 FORMAT(34H SIGNAL REQUIRED -DBW        ,F6.1,12X,F5.1)
494 FORMAT(3X,'CSIGN MARGIN                ',F5.1,' DB')
495 FORMAT(34H LASER POWER REQUIRED -WATTS  ,F8.3)
496 FORMAT(34HCLASER POWER REQUIRED -DBW   ,F6.1,12X,F5.1)
497 FORMAT(34HOLASER POWER AVAILABLE WATTS ,F8.4)
498 FORMAT(34H LASER POWER AVAILABLE -DBW ,F6.1,12X,F5.1)
540 FORMAT(4X,F10.4,2X,F6.2,F10.2,4X,F6.2,4X,F10.6)
541 FORMAT(13,13,13,13)
545 FORMAT(5A4)
546 FORMAT(5A4,5X,F6.2)
550 FORMAT(4X,F10.4,2X,F6.2, F10.2,4X,F6.2,F12.4)
560 FORMAT( F14.4,2X,F8.4,2X, F8.4,2X,F8.4,F10.4)
561 FORMAT(6X,F6.2,4X,F6.2,4X,F6.2,4X,F6.2)
570 FORMAT(8X,F6.4,2X,F8.4,2X,F6.2)
580 FORMAT(7X,F6.3,4X,F6.3,3X,F10.6, F6.2,2X,F8.2)
590 READ(1,545)AZ,AY,AX,AY,AV
591 READ(1,546)BZ,BY,BX,BW,BV,PRBRK
592 READ(1,541)I,J,K,KPLS
600 READ(1,540)PLA,DM,RNGK,PTF,AB
601 READ(1,561) PTFER,ABER
610 READ(1,550)CRATE,ALYBDA,TAU,AMOD,TAUT
620 READ(1,560)ALP,AIB,CL,RO,TXBMM
621 READ(1,561)ALBER,AIBER
631 READ(1,570)EFFD,FD ,RBOWTH
632 READ(1,561)EFFDER,FDER
640 READ(1,580)DTR,DRE,EFFT,EFFR,THTFM
641 READ(1,561)EFFTER,CFFRER,THTFR
650 READ(1,561)TTR,TREC,BCEF,ATMFAD
651 READ(1,561) TTRK,TKER,BDEFR,ATMFDR
650 IF(I-6) 665,665,662
662 READ(1,560) PLSWTH,REPTR,PKPWR1
665 CONTINUE
666 IF(K-7) 668,667,668
667 READ(1,560) TCATE,ISLF
668 CONTINUE
700 PKPWR=PKPWR1
701 RNG=1000.*RNGK

```

AN IV 160N-FO-47, 3 5

MAINPGM

DATE 10/03/71

TIME 14.26.48

```

702 THIF=THIF/1000000.
703 ALMDM=ALMDM/1000000.
710 WLPTR=ALMDM/(12.5664*HNG)
711 SPL=WLPTR*WLPTR
720 SPLDB=10.*ALOG10(SPL)
741 EFFRDB=10.*ALOG10(EFFR)
742 EFFCDB=10.*ALOG10(EFFC)
751 TTRERD=10.*ALOG10(TTR)
760 TTRERD=10.*ALOG10(TTRER)
770 TRECRD=10.*ALOG10(TREC)
780 TRECRD=10.*ALOG10(TREER)
781 RCLSRD=EFFRDB+TRECRD
782 RCLSRD=EFFRDB+TRECRD
    IF(K-7) 785,783,785
783 TSLFDB=10.*ALOG10(TSLF)
785 EXTR=2./(1.000001-AMOD)
786 EXRDB=10.*ALOG10(EXTR)
792 THIF=(AMMW/1000000.
797 IF(I-6) 800,800,810
800 GANT=C.82*1.1416*3.1415*(DTR*TR)/(ALMDM*ALMDM)
801 GO TO 811
810 GANT=10.3/(THIF*THIF)
811 GANTCE=10.*ALOG10(GANT)
816 GFAC=0.82
812 GANTI=GANT/GFAC
813 GNTIDB=10.*ALOG10(GANTI)
817 GFACDB=10.*ALOG10(GFAC)
821 EFFTDB=10.*ALOG10(EFFT)
823 EFFTDB=10.*ALOG10(EFFTER)
824 TXLSDB=EFFTDB+TTRDB+GFACDB
825 TXLSDB=EFFTDB+TTRERD
830 XDR=(C.7854*THIF*DRE)*(C.7854*THIF*DRE)
831 XDR=(C.7854*DRE)*(C.7854*DRE)
832 IF(K-7) 840,833,840
833 HNTB=1.9875/(ALMDM*TAU*RBOWTH)
835 GO TO 851
840 HNTB=1.9875/(ALMDM*TAU*RBOWTH)
851 FDBB=10.*ALOG10(1./FD)
852 BDEFDB=10.*ALOG10(BDEF)
853 BDEFDB=10.*ALOG10(BDEF)
861 FDBRDB=10.*ALOG10(FDBR)
C   AKB AND AIB GIVEN FOR BANDWIDTH IN ANGSTROMS NOT METERS, SO
C   FACTOR OF 10 TO 10 IS REQUIRED
863 ATT=1.CF*10
870 AKJ=ALH*ATT*XDR*TREC*EFFR*EFFD/(HNTB*FD)
880 AKJER=ALBER*EFFDER*THIFER*THIFER*FDER
891 AKJ=AKB
901 CONTINUE
903 IF(K.FI,7) GO TO 5922
C   K=4 MEANS GE HERRMANN EXPRESSION FOR AKS
905 IF(K.EG,4) GO TO 919
906 IF(I-6) 910,910,915
910 AKS=(54.22/(AMOD*AMOD))*(1.+SQRT(1.+AMOD*AMOD*AKB/27.1))
911 AKSX=(54.22/(AMOD*AMOD))*(1.+SQRT(1.+AMOD*AMOD*AKBER/27.1))

```

IN TV 160N-10-479 3-9

MAINPGM

DATE 10/03/71

TIME

14.26.48

```

514 GO TO 918
515 AKS = (15.44/(AMOD*AMOD)) * (1. + SQRT(1. - AMOD*AMOD*AKB / 7.72))
516 AKSX = (15.44/(AMOD*AMOD)) * (1. + SQRT(1. - AMOD*AMOD*AKB / 7.72))
518 CONTINUE
519 GO TO 925
519 AMGFH = AMOD*AMOD * (1. + AMOD*AMOD/6.)
520 AKS = 64.48 * (1. + SQRT(1. + AKB * AMGFH/32.24)) / AMGFH
521 AKSX = 64.48 * (1. + SQRT(1. + AKB * AMGFH/32.24)) / AMGFH
522 GO TO 925
C THIS MODULE (5931 TO 6150) CALCULATES KS REQUIRED FOR MODE
C LOCKED LASER FOR 10 TO -7 BIT ERROR RATE USING CHERNOFF BOUND
C FOR ON OFF MODULATION AS DESCRIBED BY BUCHER.
C PROBABILITY OF ERROR IS CALCULATED FOR A STARTING VALUE OF KS AND
C CALCULATED VALUE OF KB AND VALUE OF KS IS SUCCESSIVELY MODIFIED UNTIL
C CALCULATED VALUE OF PROBABILITY OF ERROR IS BETWEEN 10 TO -7 AND 10 TO -7.5
C AND THEN LOGARITHMIC EXTRAPOLATION IS USED TO FIND VALUE OF KS REQUIRED.
5922 L=0
5923 AKS1=AKB+ 16.3
5924 L=L+1
5931 GO TO 5940
5935 AKS1=AKS1*1.5
5936 GO TO 5940
5937 AKS1=AKS1*1.1
5938 GO TO 5940
5939 AKS1=C.75*AKS1
5940 ALPHA1=(1.+AKB/AKS1)*ALOG(1.+AKS1/AKB)
5950 BETA1=1.-(ALOG(ALPHA1))/ALPHA1-1./ALPHA1
5960 PELM1=EXP(-(AKS1+AKB)*BETA1)
5970 PELM1L=ALOG10(PELM1)
5980 PQ=-PELM1L
5981 IF(PQ.GT.7.5) GO TO 5939
5982 IF(PQ.LT.6.) GO TO 5935
5983 IF(PQ.LT.7.) GO TO 5937
5984 IF(PQ.EQ.7.) GO TO 6140
5985 IF(PQ.GT.7.) GO TO 6000
6000 AKS2=C.9*AKS1
6040 ALPHA2=(1.+AKB/AKS2)*ALOG(1.+AKS2/AKB)
6050 BETA2=1.-(ALOG(ALPHA2))/ALPHA2-1./ALPHA2
6060 PELM2=EXP(-(AKS2+AKB)*BETA2)
6070 PELM2L=ALOG10(PELM2)
6080 CONTINUE
6100 SLOPE=(PELM1L-PELM2L)/(AKS1-AKS2)
6110 AKS3=AKS2-(PELM1L+7.)/SLOPE
6120 AKS=AKS3
6121 AKSX=AKS*1.05
6130 GO TO 6150
6140 AKS=AKS1
6141 AKSX=AKS*1.05
6150 CONTINUE
6151 IF(L.EQ.2) GO TO 6160
6152 AKB= AKB + AKS/EXTR
6160 IF(L.EQ.1) GO TO 5923
925 AKSXQ=AKS/3DEF
927 AKSER=AKSX/AKS

```

IV 3604-FD-479 3-5

MAINPGM

DATE 10/03/71

TIME

14.26.48

```

930 TATM=AU
940 TATMD=10.*ALOG10(A)
950 TATM1=10.*ALOG10(ABER)
960 PTFDB=10.*ALOG10(PTF)
970 PTFER=10.*ALOG10(PTFER)
970 FWHMTH=0.95*ALMBDA/OTR
2005 AMW=1.0E-09
C H-NU/TAU IS .19875, SO USING .19875 GIVES POWER IN MILLIMICROWATTS
2006 IF(X.EQ.7) GO TO 2015
2010 PREQ=ANS*C.19875*FD/LEFFD*HDEF*ALMBDA*TAU
2011 GO TO 2018
2015 PREQ=ANS*O.19875*FD/(LEFFD*HDEF*ALMBDA*TAU*TSLE)
2018 PRQDPW=10.*ALOG10(PREQ*AMW)
2020 PREQER=ANS*HDEF*HDEF*HDEF
2025 RANT=3.1416*3.1416*ORE*ORE/(ALMDH*ALMDH)
2030 ETAL=GANT*SPL*OTR*TRER*TATM*EFFR*PTF*EFFE*RANT
2040 PLRQD=AMW*PREQ*DM/ETAL
2041 PLRQD=10.*ALOG10(PLRQ)
2042 ETALER=EFFER*OTRER*TRER*ABER*EFFER
2043 PLRER=PREQER*ETALER*HDEF
2044 PLRERD=10.*ALOG10(PLRER)
2050 AMAR=PLA*ETAL/(PREQ*AMW)
2051 PLARD=10.*ALOG10(PLA)
2052 AMARER=10.*ALOG10(AMAR)
2053 AMARER=PREQER*ETALER
2054 AMARERD=10.*ALOG10(AMARER)
2060 BMDTH=314159C./SQRT(GANT)
2062 CMDB=10.*ALOG10(DM)
2064 PLAPLS=PKPWR*TAUT/TAU
2066 IF(1-6) 2091,2091,2088
2068 RECPWR=PLAPLS*ETAL/DM
2069 GO TO 2092
2091 RECPWR=PLA*ETAL/DM
2092 RECPER=RECPWR*EFFD*ALMBDA*TAU/(O.19875*FD*AMW)
2095 RECPER=RECPER*HDEF
2100 CONTINUE
2200 CALL DATE(DATE1)
2300 TAUDB=10.*ALOG10(TAU*AMW)
2310 IF(1-5) 2340,2340,2320
2320 EOTR=1.021*ALMBDA/IXDMW
2330 GO TO 2341
2340 EOTR=OTR
2341 CONTINUE
2401 RGNTDB=10.*ALOG10(RANT)
2405 IF(IJ.EQ.1) GO TO 2410
2406 GO TO 2420
2410 PRECDB=PLRQD*IXLSDB*GNTIDB*PTFDB*SPLDB*TATMD*RGNTDB*RCLSD
2415 GO TO 2421
2420 PRECDB=PLRER*IXLSDB*GNTIDB*PTFDB*SPLDB*TATMD*RGNTDB*RCLSD
2421 PRECDB=IXLSDB*PTFER*GNTIDB*TATMD*RCLSD
2430 REBCB=PRECDB*TAUDB
2432 REBCB=PRECDB
2440 HNU=198.75*AMW*AMW*AMW/ALMDH
2441 EPPDB=10.*ALOG10(HNU)

```

14 IV 0004-11-019 3-5 MAINPGM DATE 10/03/71 TIME 14.26.48

```

2460 RPFECB=RESCB+RPPDB
2461 RPFECB=RESCB+RPPDB
2462 IF(1-7) 2470,2464,2473
2464 RPFECB=RESCB+RPPDB+RPFDB+RPFDB
2465 GO TO 2471
2470 RPFECB=RESCB+RPPDB+RPFDB+RPFDB
2471 RPFECB=RESCB+RPPDB+RPFDB
2472 RPFECB=RESCB+RPPDB
2473 IF(1-3) 2515,2491,2497
2491 RPFECB=RESCB+RPPDB
2493 RPFECB=RESCB+RPPDB
2515 CONTINUE
498 IF(J-1)1000,1010,1000
1000 WRITE(3,10)DATE1
GO TO 1011
1010 WRITE(3,70)DATE1
1011 GO TO 11040,1050,1060,1070,1080,1090,1100,1110,1120,1130,1140,
1150,1
1040 WRITE(3,40)
GO TO 1271
1050 WRITE(3,50)
GO TO 1271
1060 WRITE(3,60)
GO TO 1271
1070 WRITE(3,70)
GO TO 1271
1080 WRITE(3,80)
GO TO 1271
1090 WRITE(3,90)
GO TO 1271
1100 WRITE(3,100)
GO TO 1271
1110 WRITE(3,110)
GO TO 1271
1120 WRITE(3,120)
GO TO 1271
1130 WRITE(3,130)
GO TO 1271
1140 WRITE(3,140)
GO TO 1271
1150 WRITE(3,150)
1271 CONTINUE
1272 WRITE(3,200) AZ,AY,AX,AW,AV,BZ,BY,BX,BW,BV
1310 WRITE(3,210) AL*30A
1315 IF(J.EQ.1) GO TO 1321
1320 WRITE(3,220) PLA
GO TO 1322
1321 WRITE(3,494) DMD8
1322 IF(1-4) 1352,1352,1330
1330 WRITE(3,230) PLS*TH

```

PN	IV	360N-FD-479	1-5	MAINPGM	DATE	10/03/71	TIME	14.26.48
1340	WRITE(3,240)	REPRT						
1350	WRITE(3,250)	PKPWRI						
1352	CONTINUE							
1360	WRITE(3,260)	PRBERR						
1370	WRITE(3,270)	PRATE						
1380	WRITE(3,280)	AMJD						
1381	IF(K-7)	1383,1382,1393						
1382	WRITE(3,281)	EXTRDB						
1393	CONTINUE							
1385	IF(I-6)	1390,139C,1391						
1390	WRITE(3,290)	DIR						
	GO TO	1400						
1391	WRITE(3,291)	TXBMM						
1392	WRITE(3,292)	EDTR						
1400	WRITE(3,293)	FMMPTM						
1405	WRITE(3,300)	EFFI						
1410	WRITE(3,310)	TR						
1412	WRITE(3,312)	PTF						
1414	WRITE(3,314)	DRF						
1416	WRITE(3,316)	EFFR						
1418	WRITE(3,318)	TRFC						
1420	WRITE(3,320)	RHDWTH						
1422	WRITE(3,322)	THTFM						
1425	WRITE(3,324)	EFFD						
1426	WRITE(3,326)	FO						
1427	WRITE(3,327)	RDEF						
	IF(K-7)	1428,1427,1428						
7427	WRITE(3,7327)	ISLF						AFTR1427
1428	WRITE(3,328)	TAU						
	IF(K-7)	1430,1429,1430						
1429	WRITE(3,329)	IGATE						
1430	WRITE(3,330)	ALB						
	IF(K-7)	1432,7432,1432						
7432	WRITE(3,332)	AKBO						
7433	WRITE(3,333)	AKB						
7434	GO TO	1434						
1432	WRITE(3,332)	AKB						
1434	WRITE(3,334)	AKS						
	IF(J.EQ.1)	GO TO 1436						
1435	WRITE(3,335)	RECPE						
	WRITE(3,339)	RECPEF						1435
1436	WRITE(3,336)	RNGK						
1437	IF(I-3)	1456,1438,1438						
1438	IF(I-5)	1450,1450,1439						
1439	IF(I-9)	1450,1456,1456						
1450	WRITE(3,350)	AO						
1456	WRITE(3,356)	TATM						
1457	IF(J.EQ.2)	GO TO 1460						
1458	WRITE(3,382)							
1459	GO TO	1461						
1460	WRITE(3,380)							
1461	WRITE(3,390)							
	IF(J.EQ.1)	GO TO 1463						
1462	WRITE(3,400)	PLADB						

LMSC-B290200-III

CAN IV 360N-FU-479 3-5 MAINPGM DATE 10/03/71 TIME 14.26.48

1463 WRITE(3,410) CONTIN

1464 WRITE(3,415) TXLSOR, TXLSOR

1465 WRITE(3,415) PTEOR, PTEOR

1466 WRITE(3,420) SPLOR

1467 WRITE(3,425) TAIMOB, TAIMOB

1468 WRITE(3,430) RNTOR

1469 WRITE(3,435) ACLSOR, ACLSOR

1470 WRITE(3,440) PRECOR, PRECOR

1471 WRITE(3,445) TADOB

1472 WRITE(3,450) REBEL, REBEL

1473 WRITE(3,455) EPPOR

1474 WRITE(3,460) ERPOR

1475 WRITE(3,465) EEFOR, EEFOR

1475 WRITE(3,466) EFOR, EFOR

1476 WRITE(3,467) HDEFOR, HDEFOR

IF (C77) GO TO 1477

1476 WRITE(3,468) ISFOR

1477 IF (J.EQ.1) GO TO 1477

IF (I-3) 1476, 1477, 1477

1477 WRITE(3,469) ATMEOR, ATMEOR

1478 WRITE(3,470) KPEBOR, KPEBOR

1477 WRITE(3,475) KQPEOR

1478 IF (J.EQ.1) GO TO 1484

1480 WRITE(3,480) PMREOR, PMREOR

1482 GO TO 1488

1484 WRITE(3,490) PLKOR, PLKOR

1485 WRITE(3,495) PLRC

1499 CONTINUE

1600 CONTINUE

STOP

END

1475

AFTER 077

PROGRAM II

AN IV 360N-ED-479 3-4 MAINPGM DATE 10/03/71 TIME 16.02.21

```

C THIS PROGRAM CALCULATES THE PHOTOELECTRON COUNT RECEIVED IN EACH OF
C THE ACQUISITION AND TRACKING LINKS FOR EACH PHASE. THE METHOD OF
C CALCULATION IS SIMILAR TO THAT OF THE HIGH DATA RATE LINK PROGRAM.
C EIGHT DATA CARDS ARE USED FOR THE CW LINKS AND NINE DATA CARDS FOR
C THE PULSED LINK. CARD 1 IS AN ALPHANUMERIC CARD FOR COMMENT. I AND
C J IN CARD 2 DESIGNATE THE LINK AND PHASE RESPECTIVELY. THE
C ABBREVIATIONS USED IN THE OTHER DATA CARDS ARE AS FOLLOWS
C PKPWR-PEAK POWER OF LASER, PLA AVERAGE POWER, RNGK- RANGE IN
C KILOMETERS, PTF- POINTING LOSS FACTOR, AB ATMOSPHERIC ABSORPTION.
C DRATE-NOT USED, ALMD00- WAVELENGTH IN MICRONS, TAU- RECEIVER
C INTEGRATING TIME, AMOD-MODULATION INDEX, TAUT- IN PHASE1, THE XMTR
C PULSE LENGTH, IN PHASE 5 AND 6, TRACKING ERROR ANGLE
C ALB-BACKGROUND RADIANCE, FALARM-FALSE ALARM PROBABILITY, PMISS-
C MISS PROBABILITY IN PHASES 1 THRU 4, REQUIRED SIGNAL TO NOISE IN
C DB IN PHASES 5 AND 6, TXBW- TRANSMITTER BEAM WIDTH IN MICRORADIANS
C EFFD-DETECTOR QUANTUM EFFICIENCY, F0- EXCESS NOISE FACTOR,
C RBWTH- RECEIVER BANDWIDTH IN ANGSTROMS
C DTR AND DRE- TRANSMITTER AND RECEIVER DIAMETERS METERS, EFFT AND
C EFFR- EFFICIENCIES IF XMTR AND RCVR ANTENNAS, THFM- RECEIVER
C FIELD OF VIEW IN MICRORADIANS
C TTR AND TREC- TRANSMITTER AND RECEIVER OPTICAL TRANSMITTANCES
C NDEF-SCINTILLATION LOSS IN DB, RIFOV- RECEIVER INSTANTANEOUS FIELD
C OF VIEW IN MICRORADIANS.
C PLSWTH-XMTR PULSE WIDTH, REPR- REPETITION RATE IN PPS.
C DIMENSION DATE1(2)
10 FORMAT('1',20X,'ACQUISITION AND TRACKING ANALYSIS',5X,2A4)
18 FORMAT(20A4)
20 FORMAT('0',10X,20A4)
210 FORMAT('0',2X,'LASER WAVELENGTH',F8.4,' MICRONS
1')
220 FORMAT(3X,' OUTPUT POWER -AVERAGE',F9.3,' WATTS')
230 FORMAT(3X,' PULSE WIDTH',F9.3,' NANOSEC')
240 FORMAT(3X,' REPETITION RATE',F9.3,' PPS')
250 FORMAT(3X,' PEAK POWER',F9.3,' WATTS')
260 FORMAT(3X,' MODULATION INDEX',F8.4)
281 FORMAT(3X,'EXTINCTION RATIO',F8.4,' DB')
290 FORMAT(3X,'XMTR ANTENNA DIAMETER',F8.4,' METERS')
291 FORMAT(3X,'XMTR ANTENNA BEAMWIDTH',F10.4,' MICRORAD')
292 FORMAT(3X,' EFFECTIVE ANTENNA DIAMETER',F8.4,' METERS')
293 FORMAT(3X,' FWHP BEAMWIDTH',F8.4,' MICRORAD')
300 FORMAT(3X,' ANTENNA EFFICIENCY',F8.4)
301 FORMAT(3X,' ILLUMINATION FACTOR',F8.4)
310 FORMAT(3X,' OPTICAL TRANSMITTANCE',F8.4)
312 FORMAT(3X,' POINTING ERROR FACTOR',F8.4)
314 FORMAT(3X,'RCVR ANTENNA DIAMETER',F8.4,' METERS')
316 FORMAT(3X,' ANTENNA EFFICIENCY',F8.4)
318 FORMAT(3X,' OPTICAL TRANSMITTANCE',F8.4)
320 FORMAT(3X,' FILTER BANDWIDTH',F8.4,' ANGSTROMS')
322 FORMAT(3X,' FIELD OF VIEW',F10.4,' MICRORAD')
323 FORMAT(3X,' INSTANTANEOUS FOV',F10.4,' MICRORAD')
324 FORMAT(3X,' DET QUANTUM EFFICIENCY',F8.4)
326 FORMAT(3X,' EXCESS NOISE FACTOR',F8.4)
327 FORMAT(3X,'ATMOSPHERIC TURBULENCE LOSS',F8.4)
328 FORMAT(3X,' INTEGRATION TIME',F9.3,' NANOSEC')

```

IN IV 360N-FU-479 3-4

MAINPGM

DATE 10/03/71

TIME

16.02.21

```

330 FORMAT(3X,'BACKGROUND RADIANCE',E9.3,' W/STER-A-SO
    IM')
332 FORMAT(10I,2X,'BACKGROUND PE/INT TIME',E9.3)
333 FORMAT(10I,2X,'BACKGROUND PL/PULSE',E9.3)
334 FORMAT(3X,'RECEIVED SIGNAL PL/PULSE',E9.3)
335 FORMAT(3X,'RECEIVED SIGNAL PL/INT TIME',E9.3)
336 FORMAT(3X,'RANGE',F12.4,' KILOMETERS')
350 FORMAT(3X,'ATMOSPHERIC ABSORPTION FACTOR',F8.4)
356 FORMAT(3X,'ATMOSPHERIC TRANSMITTANCE',F8.4)
357 FORMAT(3X,'TRACKING ERROR ANGLE',F6.2,' MICRORAD')
370 FORMAT(3X,'FALSE ALARM/INT TIME',E9.3)
371 FORMAT(3X,'FALSE ALARM/PULSE',E9.3)
372 FORMAT(3X,'MISS PROBABILITY/INT TIME',E9.3)
373 FORMAT(3X,'MISS PROBABILITY/PULSE',E9.3)
374 FORMAT(3X,'SIGNAL/NOISE REQUIRED',F6.1,' DB')
375 FORMAT(3X,'SIGNAL/NOISE RECEIVED',F6.1,' DB')
376 FORMAT(3X,'THRESHOLD PE',E9.3)
382 FORMAT(10I,25X,'POWER BUDGET CALCULATION')
400 FORMAT(34H,LASER POWER AVERAGE,F6.1,' DBW',8X,F5.1)
402 FORMAT(34H,LASER POWER PEAK,F6.1,' DBW',8X,F5.1)
405 FORMAT(34H, TRANSMITTER LOSS,F6.1,' DB ',8X,F5.1)
410 FORMAT(34H, TRANSMITTER ANTENNA GAIN,F6.1,' DB ',8X,F5.1)
415 FORMAT(34H, POINTING LOSS,F6.1,' DB ',8X,F5.1)
420 FORMAT(34H, SPACE LOSS,F6.1,' DB ',8X,F5.1)
425 FORMAT(34H, ATMOSPHERIC LOSS,F6.1,' DB ',8X,F5.1)
430 FORMAT(34H, RECEIVER ANTENNA GAIN,F6.1,' DB ',8X,F5.1)
435 FORMAT(34H, RECEIVER LOSS,F6.1,' DB ',8X,F5.1)
440 FORMAT(34H, RECEIVED POWER,F6.1,' DBW',8X,F5.1)
445 FORMAT(34H, INTEGRATION TIME,F6.1,' DGS',8X,F5.1)
446 FORMAT(34H, PULSE WIDTH,F6.1,' DHS',8X,F5.1)
450 FORMAT(34H, RECEIVED ENERGY/INT TIME,F6.1,' DBJ',8X,F5.1)
451 FORMAT(34H, RECEIVED ENERGY/PULSE,F6.1,' DBJ',8X,F5.1)
455 FORMAT(34H, ENERGY/PHOTON,F6.1,' DBJ',8X,F5.1)
460 FORMAT(34H, RECEIVED PHOTONS/INT TIME,F6.1,' DBI',8X,F5.1)
461 FORMAT(34H, RECEIVED PHOTONS/PULSE,F6.1,' DBI',8X,F5.1)
465 FORMAT(34H, QUANTUM EFFICIENCY,F6.1,' DBI',8X,F5.1)
466 FORMAT(34H, EXCESS NOISE FACTOR LOSS,F6.1,' DBI',8X,F5.1)
467 FORMAT(34H, DET COLLECTION EFFICIENCY LOSS,F6.1,' DBI',8X,F5.1)
468 FORMAT(34H, ATMOSPHERIC FLUCTUATION LOSS,F6.1)
470 FORMAT(34H, SIGNAL PE RECD/INT TIME,F6.1,' DBI',8X,F5.1)
471 FORMAT(34H, SIGNAL PE RECD/PULSE,F6.1,' DBI',8X,F5.1)
475 FORMAT(34H, REQUIRED PE/INT TIME,F6.1,' DBI',8X,F5.1)
480 FORMAT(34H, LINK MARGIN,F6.1,' DB ',8X,F5.1)
492 FORMAT(34H, SIGNAL/NOISE,F10.4)
494 FORMAT(1X,'SIGNAL/NOISE REQUIRED',F5.1,' DB')
540 FORMAT( F14.4,2X,F8.4, F8.2,4X,F6.2,4X,F10.6)
541 FORMAT(13,13,13,13)
550 FORMAT(4X,F10.4,2X,F6.2, F10.2,4X,F6.2,F12.4)
560 FORMAT( F14.4,6X, F10.2,F10.2,2X, F10.4)
561 FORMAT(6X,F6.2,4X,F7.3,3X,F6.2,F10.4)
570 FORMAT(8X,F6.4,2X,F8.4,2X,F6.2)
580 FORMAT(7X,F6.3,4X,F6.3,3X,F10.6, F6.2,7X,F8.2)
590 READ(1,18)A,U,C,O,E,W,V,X,Y,Z,AW,BV,CX,DY,EZ,WA,VB,XC,YD,ZE
592 READ(1,541)I,J,K,XPLS

```

AN IV 360N-FU-479 3-4 MAINPGM DATE 10/03/71 TIME 16.02.21

```

600 READ(1,540)PKPWR,PLA,ANCK,PTF,AB
610 READ(1,550)DHATE,ALMBDA,TAU,AMOD,TAUT
620 READ(1,560)ALB, FALARM,PHISS,YXUMW
631 READ(1,570)EFFD,FO,XBOWTH
640 READ(1,580)DTN,DRE,EFFT,EFEN,THTFM
650 READ(1,590)ITR,TREC,BDEF,RIFDV
652 IF(J-1) 665,662,665
662 READ(1,560) PLSWTH,KEPRT
665 CONTINUE
670 TAU=TAU*1000.
    IF(J-5) 671,672,672
671 TAUT=TAUT*1000.
672 PAVRG=PLA
680 IF(J-1) 701,690,701
690 PLA=PKPWR*TAUT/TAU
701 ANG=1000.*RNGK
702 THTF=THTFM/1000000.
703 ALMOD=ALMBDA/1000000.
710 WLP1R=ALMOD/(12.5664*RNG)
711 SPL=WLP1R*WLP1R
720 SPLDB=10.*ALOG10(SPL)
741 EFFRDB=10.*ALOG10(EFFR)
750 TTRDB=10.*ALOG10(ITR)
770 TRECCB=10.*ALOG10(TREC)
781 RCLSDH=EFFTDB+TRECCB
792 THTT=TXBOW/1000000.
810 GANT= 9.5/(THTT*THTT)
811 GANTDB=10.*ALOG10(GANT)
815 GFAC=0.82
812 GANTI=GANT/GFAC
813 GNTIDS=10.*ALOG10(GANTI)
817 GFACDB=10.*ALOG10(GFAC)
821 EFFTDB=10.*ALOG10(EFFT)
824 TXLSCB=EFFTDB+TTRDB+GFACDB
825 RIFQVR=RIFCV/1000000.
830 XDR=(0.7854*RIFQVR*DRE)*(0.7854*RIFQVR*DRE)
831 XDR1=(0.7854*DRE)*(0.7854*DRE)
840 HNTR=1.9875/(ALMOD*TAU*RBOWTH)
851 FIDDB=10.*ALOG10(1./FO)
852 BDEFDB=10.*ALOG10(BDEF)
C   ALB AND AIB GIVEN FOR BANDWIDTH IN ANGSTROMS NOT METERS, SO
C   FACTOR OF 10 TO 10 IS REQUIRED
863 ATT=1.0E+10
870 AKB=ALB*ATT*XDR*TREC*EFFR*EFFD/(HNTR*FO)
930 TATM=AB*BDEF
940 TATMDB=10.*ALOG10(TATM)
901 CONTINUE
960 PTFDB=10.*ALOG10(PTF)
970 FWHPTH=C.95*ALMBDA/OTR
2005 AMWK=1.0E-09
C   HNU/TAU IS .19875, SO USING .19875 GIVES POWER IN MILLIMICROWATTS
2025 HANT=3.1416*3.1416*DRE*DRE/(ALMOD*ALMOD)
2030 ETAL=GANT*SPL*TTR*TREC*TATM*EFFR*PIF *EFFT*HANT
2051 PLADB=10.*ALOG10(PLA)

```

IN IV 360N-FD-479 3-4

MAINPGM

DATE 10/03/71

TIME

16.02.21

```

2052 PKPWR=10.*ALOG10(PKPWR)
2080 BMWDT=3141590./3JKT(GANT)
2091 RECPWR=PLA*ETAL
2092 RECPWR=RECPWR*EFFD*ALM8DA*TAU/(0.19875*FD*AMMW)
2100 SN=0.5*AMOD*AMOD*RECPWR*RCPE/(RECPWR*2.*AKB)
2101 SNRC=10.*ALOG10(SN)
2120 CONTINUE
2250 CALL DATE(DATE1)
2300 TAU=10.*ALOG10(TAU*AMMW)
2401 GNTC=10.*ALOG10(GANT)
2420 PRECDH=PLA*TXLS*GNTC*PTFDB+SPLDB*TATMDB*RCNTC*RCLSDB
2440 RECDH=PRECDH*TAUDB
2452 RECDH=PRECDH
2460 HNU=198./5*AMMW*AMMW*AMMW/ALMOM
2441 EPPDB=10.*ALOG10(HNU)
2450 ERPDB=RECDH-EPPDB
2460 EFFDB=10.*ALOG10(EFFD)
2470 RPEDB=EFFDB*ERPDB+EDDB
2490 PMRDB=RPEDB*RECDH
2495 PMRDB=RPEDB*RECDH
2515 CONTINUE
1000 WRITE(3,10)DATE1
1010 WRITE(3,20)A,B,C,D,E,W,V,X,Y,Z,AW,BV,CX,CY,EZ,WA,VB,XC,YD,ZF
1310 WRITE(3,210) ALM8DA
1320 WRITE(3,220) PAVRG
1321 IF(J-1) 1350,1350,1380
1350 WRITE(3,250) PKPWR
1350 WRITE(3,230) PLSWTH
1340 WRITE(3,240) REPT
1340 WRITE(3,280) AMJO
1385 IF(J-6) 1391,1390,1391
1390 WRITE(3,290) DTR
1391 WRITE(3,291) TXOMW
1405 WRITE(3,300) EFFD
1410 WRITE(3,310) TTR
1412 WRITE(3,312) PTF
1414 WRITE(3,314) DRE
1416 WRITE(3,316) EFFR
1418 WRITE(3,318) TREC
1420 WRITE(3,320) RBDWTH
1422 WRITE(3,322) THFM
1423 WRITE(3,323) RIFOV
1425 WRITE(3,324) EFFD
1426 WRITE(3,326) FD
1428 WRITE(3,328) TAU
1430 WRITE(3,330) ALB
1436 WRITE(3,336) HMOX
    IF(J-5) 1451,4456,4456
1451 WRITE(3,370) FALARM
1452 WRITE(3,372) PMISS
4456 IF(1.EQ.1) GO TO 1456
    IF(1.EQ.6) GO TO 1456
1453 WRITE(3,350) AB
1454 WRITE(3,327) HDEF

```

AFTR1452

LMSC-B290200-III

IN IV 360N-FU-479 3-4

MAINPGM

DATE 10/03/71

TIME 16.02.21

1456 WRITE(3,356) TAIN
 1432 WRITE(3,332) AKO
 1435 WRITE(3,335) RECPE
 2436 IF(J-5) 1458,1437,1437
 1437 WRITE(3,374) PAISS
 2437 WRITE(3,357) TAJT
 1433 WRITE(3,375) SNHEC
 1458 WRITE(3,382)
 1460 IF(J-1) 1462,1461,1462
 1461 WRITE(3,402) PKPWOB
 GO TO 1463
 1462 WRITE(3,400) PLADB
 1463 WRITE(3,410) GNTIDB
 1464 WRITE(3,405) TXLSOB
 1465 WRITE(3,415) PTFDB
 1466 WRITE(3,420) SPLDB
 1467 WRITE(3,425) TATMOB
 1468 WRITE(3,430) RGNTDB
 1469 WRITE(3,435) RCLSOB
 1470 WRITE(3,440) PRECOB
 IF(J.EQ.1) GO TO 3471
 1471 WRITE(3,445) TAUDB
 1472 WRITE(3,450) RFBDDB
 1473 WRITE(3,455) EPPDB
 1474 WRITE(3,460) ERPROB
 1475 WRITE(3,465) EFFDDB
 075 WRITE(3,466) FDDDB
 IF(J-5) 1476,076,076
 076 WRITE(3,467) RDEFDB
 1476 WRITE(3,470) RPEBDB
 GO TO 1477
 3471 WRITE(3,446) TAUDB
 3472 WRITE(3,451) REBDB
 3473 WRITE(3,455) EPPDB
 3474 WRITE(3,461) ERPROB
 3475 WRITE(3,465) EFFDDB
 3075 WRITE(3,466) FDDDB
 3476 WRITE(3,471) RPEBDB
 1477 WRITE(3,475)
 IF(I.FQ.5) GO TO 1478
 IF(I.CO.6) GO TO 1478
 GO TO 1480
 1478 IF(J.EQ.2) GO TO 1479
 IF(J.EQ.4) GO TO 1479
 IF(J.EQ.6) GO TO 1479
 GO TO 1480
 1479 WRITE(3,468)
 1480 WRITE(3,490)
 1600 CONTINUE
 STOP
 END

AFTR1435

AFTR1477
 BFR 1478

PROGRAM III

AN IV 360N-F0-479 3-4

MAINPGM

DATE 10/03/71

TIME

16.09.54

```

C THE LASER LINK ATMOSPHERIC EFFECTS PROGRAM CALCULATES PHOTOELECTRON
C COUNTS REQUIRED TO MAINTAIN BIT ERROR PROBABILITY AT 10 TO -7 FOR
C GIVEN TURBULENCE CONDITIONS. CALCULATIONS ARE MADE FOR CW SUBCARRIER
C OR BINARY POLARIZATION MODULATION. THE REQUIRED SIGNAL IS CALCULATED BY
C CALCULATING ERROR PROBABILITY
C CALCULATING ERROR PROBABILITY USING A GRAND AVERAGE OVER THE
C APPROPRIATE PROBABILITY DISTRIBUTION AND THE DISTRIBUTION OF
C ATMOSPHERIC AMPLITUDE FLUCTUATIONS, WITH CL THE VARIANCE OF THE
C LOG AMPLITUDE FLUCTUATION AS PARAMETER. THE INTEGRAL INVOLVED IS
C CALCULATED BY USING THE RIEMANN SUM AND THE FIRST DATA CARD GIVES THE
C NUMBER OF ELEMENTS IN THE SUM. THE MAIN DATA CARD USES AMOD FOR
C MODULATION INDEX, AK8 FOR BACKGROUND COUNT, CL FOR LOG AMPLITUDE
C VARIANCE, ND TO INDICATE LAST DATA CARD, NS FOR NUMBER OF STEPS,
C TYPMOD AND T1 TO T5 FOR TYPE OF MODULATION, AND K INDICATES
C CW SUBCARRIER BY 1 AND BINARY POLARIZATION BY 2.
3900 FORMAT(49HNUMBER OF STEPS KB CL MODULATION)
3910 FC44AT(5X,16,5X,F8.4,2X,F8.4,5X,5A4)
3920 FORMAT(6F12.4)
3930 FORMAT(3F8.4,6X,13,15,1X,5A4,13)
3931 FORMAT(13)
3940 FORMAT( AKSHQ PEBRLA PEBRL AKSBR AKSB
1RA AMOD*)
49 READ(1,3931)NJ
3030 DO 3480 JJ=1,NJ
50 READ(1,3930)AMOD,AK8,CL,ND,NS,TYPMOD,T2,T3,T4,T5,K
3050 IF(K.EQ.1) GO TO 3100
3052 IF(K.EQ.2) GO TO 3300
3100 AKSHR=(54.2/(AMOD*AMOD))*(1.+SQRT(1.+AMOD*AMOD*AK8/27.1))
3101 GO TO 3110
3105 AKSBR=AKSHR*1.5
3106 GO TO 3110
3107 AKSBR=AKSHR*1.1
3108 GO TO 3110
3109 AKSBR=0.75*AKSHR
3110 X=0.
3111 PEHAR=0.
3120 DO 3180 MX=1,1000
3130 X=X+1.
3140 AMXB=AMOD*AMOD*X/X/((X+AK8)*(X+AK8))
3150 CLX=0.5*ALOG(X/AKSBR) + CL
3151 VBL1=(X+AK8)*AMXB*.167*(0.75+AMOD*AMOD/8.)
3152 IF(VBL1.GT.80.C) GO TO 3180
3153 VBL2=CLX*CLX/(2.*CL)
3154 IF(VBL2.GT.80.C) GO TO 3180
3160 PE=EXP(-VBL1)
3170 PEHAR=PEHAR+PE*EXP(-VBL2/(5.02*X*SQRT(CL)))
3180 CONTINUE
3190 PEBRL = ALOG10(PEHAR)
3191 PQ=-PEBRL
3192 IF(PJ.GT.7.5) GO TO 3109
3193 IF(PJ.LT.6.) GO TO 3105
3194 IF(PJ.LT.7.) GO TO 3107
3195 IF(PJ.EQ.7.) GO TO 3940
3196 IF(PJ.GT.7.) GO TO 3210

```

TRAN IV 36JN-FU-479 3-4

MAINPGM

DATE 10/03/71

TIME

16.09.54

```

3210 AKSBR = 0.9*AKSBR
3211 PEBARA=0.
3212 X=0.
3220 DO 3280 MX=1,1000
3230 X=X+1.
3240 AMXB=AMOD*AMOD*X*Y/((X*AKB)*(X*AKB))
3250 CLX=0.5*ALOG(X/AKSBR) + CL
3251 VBL1=(X*AKB)*AMXB*.167*(0.75+AMOD*AMOD/8.)
3252 IF(VBL1.GT.80.0) GO TO 3280
3253 VBL2= CLX*CLX/(2.*CL)
3254 IF(VBL2.GT.80.0) GO TO 3280
3260 PE=EXP(-VBL1)
3270 PEBAR=PEBAR+PE*EXP(-VBL2)/(5.02*X*SQRT(CL))
3280 CONTINUE
3290 PEHRLA=ALOG10(PEBAR)
3291 GO TO 3320
3300 AKSBR=(15.44/(AMOD*AMOD))*((1.+SQRT(1.-AMOD*AMOD+AKB/7.72))
3301 GO TO 3310
3305 AKSBR=AKSBR*1.5
3306 GO TO 3310
3307 AKSBR=AKSBR*1.1
3308 GO TO 3310
3309 AKSBR=0.75*AKSBR
3310 X=0.
3311 PEBAR=0.
3320 DO 3380 MX=1,1000
3330 X=X+1.
3340 AMXB=SQRT(1.+2.*AMOD*X/(AKB+(1.-AMOD)*X))
3350 CLX=0.5*ALOG(X/AKSBR) + CL
3351 VBL1= AMOD*X*(AMXB-1.)/(AMXB+1.)
3352 IF(VBL1.GT.80.0) GO TO 3380
3353 VBL2= CLX*CLX/(2.*CL)
3354 IF(VBL2.GT.80.0) GO TO 3380
3355 PE=0.5*EXP(-VBL1)
3370 PEHRLA=PEBAR+PE*EXP(-VBL2)/(5.02*X*SQRT(CL))
3380 CONTINUE
3390 PEHRLA=ALOG10(PEBAR)
3391 PQ=-PEHRLA
3392 IF(PQ.GT.7.5) GO TO 3309
3393 IF(PQ.LT.6.) GO TO 3305
3394 IF(PQ.LT.7.) GO TO 3307
3395 IF(PQ.EQ.7.) GO TO 3340
3396 IF(PQ.GT.7.) GO TO 3410
3410 AKSBR = 0.9*AKSBR
3411 PEBARA=0.
3412 X=0.
3420 DO 3480 MX=1,1000
3430 X=X+1.
3440 AMXB=SQRT(1.+2.*AMOD*X/(AKB+(1.-AMOD)*X))
3450 CLX=0.5*ALOG(X/AKSBR) + CL
3451 VBL1= AMOD*X*(AMXB-1.)/(AMXB+1.)
3452 IF(VBL1.GT.80.0) GO TO 3480
3453 VBL2= CLX*CLX/(2.*CL)
3454 IF(VBL2.GT.80.0) GO TO 3480

```

IV 300N-FD-479 3-4

MAINPOM

DATE 10/03/71

TIME 16.09.54

```

3460 PE=C.5*EXPI-VBL1)
3470 PEHAKA=PEHAKA+PE*EXPI-VBL2)/(5.02*X*SQRT(CL))
3480 CONTINUE
3490 PEHRLA=ALOG10(PEHARA)
3520 SLIPI=(PEHRL-PEHRLA)/(AKSBK-AKSHRA)
3530 AKSRQ=AKSBK-(PEHRL+7.0)/SLOPE
3539 GO TO 3841
3840 AKSRQ=AKSBR
3841 CONTINUE
      WRITE(3,3900)
      WRITE(3,3910)NS,AKB,CL,IYPMOD,T2,T3,T4,T5
      WRITE(3,3940)
      WRITE(3,3920) AKSRQ,PEBRLA,PEHRL,AKSBK,AKSHRA,AMCD
3980 CONTINUE
      STOP
      END

```

PROGRAM IV

```

10 VAR=ZERO
15 PRINTINFORM"8/20B 'LASER LINK ANALYSIS'2/'ENTER THE FOLLOWING: '/"
20 PRINT"SYSTEM TYPE (1 TO 5)":
25 INPUT Q1
30 IF Q1=1 THEN L=.89,N1="DIODE,PPM" ELSE IF Q1=2 THEN L=.63,
N1="HE-NE,BIPOL PN" ELSE IF Q1=3 THEN L=1.06,N1="CAV DUMPED YAG"
ELSE IF Q1=4 THEN L=1.06,N1="Q-SWITCHED YAG" ELSE IF Q1=5 THEN
L=1.06,N1="CW YAG,BIPOL PN"
35 PRINT"BACKGROUND IRRADIANCE (W/M^2) AND NOMENCLATURE":
40 INPUT W,N
45 H=6.625E-34,C=2.998E8,F2=1.00,F=C/(L*1E-6),D2=.15,E1=.9,
M5=2E-5,D=20E3
50 IF L=1.06 THEN B5=5,F1=.03,L2=1.3,R0=.031,E2=.4
55 IF L=.89 THEN B5=20,F1=.20,L2=1.6,R0=.031*(.89/1.06)+1.1,E2=.6
60 IF L=.63 THEN B5=5,F1=.37,L2=1.8,R0=.031*(.63/1.06)+1.1,E2=.4
65 Q=W*(PI*M5*D2)/(2*B5*E1*E2*F1/(16*F2)),B=Q/(H*F)
70 DEF FNE(X)=(SQR(1+K*X*T1/(B*T2))-1)/(SQR(1+K*X*T1/(B*T2))+1)
75 ON Q1 GOSUB 100,200,300,400,500
80 GOTO 2000
100 PRINT"DATA WORDS/RANGE PULSE OPPORTUNITY":
105 INPUT A
110 PRINT"M-ARY CONSTANT":
115 INPUT M
120 A1=D*(A+.5)/(A*LOG2(M)),T1=3E-4/A1,T2=2*T1,K=1,Y=1
125 DEF FNP(X)=.25*(M-1)*EXP(-X*T1*FNE(X))
130 GOSUB 1000
135 RETURN
200 T2,T1=5E-5,K=2,M=2,Y=1
205 DEF FNP(X)=.5*EXP(-X*T1*FNE(X))
210 GOSUB 1000
215 RETURN
300 PRINT"TAU SUB T IN SECONDS":
305 INPUT T1
310 PRINT"DATA PULSES/DATA PERIOD":
315 INPUT U
320 T2=2*T1,K=2,M=2,Y=U
325 DEF FNP(X)=.5*EXP(-X*U*T1*FNE(X))
330 GOSUB 1000
335 RETURN
400 PRINT"TAU SUB T IN SECONDS":
405 INPUT T1
410 T2=2*T1,K=2,U=.05,M=2,Y=1
415 DEF FNP(X)=.5*EXP(-X*T1*FNE(X))
420 GOSUB 1000
425 RETURN
500 GOTO 200
1000 IF Q1=3 THEN V=2/(T1*U) ELSE V=2/T1
1005 FOR S1=V TO 1000*V BY V
1010 IF FNP(S1)<=1.02E-7 THEN 1100
1015 NEXT S1
1100 FOR S2=.9*S1 TO 1.1*S1 BY .01*S1
1105 IF FNP(S2)<=1.02E-7 THEN 1200
1110 NEXT S2
1200 FOR S=.9*S2 TO 1.1*S2 BY .001*S2
1205 IF FNP(S)<=1.02E-7 THEN 1215
1210 NEXT S

```

```

1215 P=FNP(S)
1220 RETURN
2000 DIM D(50)
2005 STRING T(50),U(50)
2010 T(1)="WAVELENGTH",T(2)="XMTR ANTENNA BEAMWIDTH",T(3)="XMTR
ANTENNA EFFICIENCY",T(4)="XMTR OPTICS TRANSMITTANCE",T(5)="RCVR
ANTENNA APERTURE",T(6)="RCVR ANTENNA EFFICIENCY"
2015 T(7)="RCVR OPTICS TRANSMITTANCE",T(8)="RCVR FIELD OF VIEW",
T(9)="RCVR OPTICAL PASSBAND",T(10)="XMTR EFFECTIVE ANTENNA DIAMETER",
T(11)="RCVR PM QUANTUM EFFICIENCY",T(12)="BACKGROUND IRRADIANCE"
2020 T(13)="BACKGROUND PE RATE",T(14)="BACKGROUND PE COUNT/DECISION TIME",
T(15)="REQUIRED PE SIGNAL RATE",T(16)="SIGNAL PE COUNT/DECISION TIME",
T(17)="TAU SUB T",T(18)="TAU SUB R"
2025 T(19)="BUCHER ERROR PROBABILITY",T(20)="SLANT RANGE",T(21)="
DATA RATE",T(22)="POINTING LOSS FACTOR",T(24)="TOTAL LASER OUTPUT
POWER (PEAK)",T(23)="TOTAL LASER OUTPUT POWER (AVG)",T(50)="LASER
OUTPUT POWER"
2030 T(27)="M-ARY CONSTANT",T(28)="DATA WORDS/RANGING OPPORTUNITY",
T(29)="DATA PULSES/DATA PERIOD",T(25)="ATMOSPHERIC COHERENCE DISTANCE",
U(25)="CM"
2035 T(31)="XMTR OPTICS LOSS",T(32)="XMTR ANTENNA GAIN",T(33)="
POINTING LOSS",T(34)="SPACE LOSS",T(35)="ATMOSPHERIC ABSORPTION LOSS",T(
"RCVR OPTICS LOSS"
2040 T(37)="RCVR ANTENNA GAIN",T(38)="RECEIVED POWER",T(39)="INTEGRATED
SIGNAL PERIOD",T(40)="RECEIVED ENERGY/BIT",T(41)="ENERGY/PHOTON",T(42)="
RECEIVED PHOTONS/BIT"
2045 T(43)="QUANTUM EFFICIENCY",T(44)="RECEIVED PHOTOELECTRONS/BIT",
T(45)="REQUIRED PHOTOELECTRONS/BIT",T(46)="TURBULENT AIR LOSS
FACTOR",T(47)="MARGIN"
2050 U(1)="MICRONS",U(2),U(8)="MICRORADIANS",U(5),U(10)="CM",U(9)="
ANGSTROMS",U(12)="MW/SQM-ST-ANG",U(13),U(15)="COUNTS/SEC",
U(17),U(18)="NANOSECONDS",U(20)="KM",U(21)="KBPS",U(23),U(24)="MW"
2055 U(30),U(38)="DBW",U(39)="DB-SEC",U(40),U(41)="DBJ",U(1)="DB"
FOR I=31 TO 37,42 TO 47
2060 Z1="6BD.DD",Z2="3B3Z,3Z",Z3="7Z.ZZ",Z4="6Z.3Z",Z5="2BD.DDESDD",
Z6="7SD.D",Z7="2B38X 8S.S B20X/",Z8="2B38X 10Z B20X/",Z9="7ZD.D"
2065 W1=20E-6,X1=.75,X2=.8,X3=.95
2070 PRINT"TOTAL AVG XMTR POWER IN MW AND NUMBER OF XMTRS":
2075 INPUT P$,N$
2080 PRINT"SLANT RANGE IN KM":
2085 INPUT R
2090 N9=STR(N$)
2095 IF R>45E3 THEN L2=0
2100 DEF FND(X)=10*LGT(X)
2105 L1=82.2-2*FND(R*.5396)-2*FND(F),L3=FND(X3),D1=1.125*(L+1E-6)/W1
2110 G1=FND(X1*(PI*D1/(L+1E-6)):.2),G2=FND(E1*(PI*D2/
(L+1E-6)):.2),G0=FND(X1*(PI*R0/(L+1E-6)):.2)
2115 D(1)=L,D(2)=W1*1E6,D(3)=X1,D(4)=X2,D(5)=100*D2,D(6)=E1,D(7)=E2,
D(8)=M5*1E6
2120 D(9)=B$,D(10)=100*D1,D(11)=F1,D(12)=W*1E3,D(13)=B,D(14)=B*Y*T2,
D(15)=S,D(16)=S*Y*T1
2125 D(17)=T1*1E9,D(18)=T2*1E9,D(19)=P,D(20)=R,D(21)=D*1E-3,
D(22)=X3,D(23)=P$,D(25)=100*R0
2130 IF Q1=1 THEN D(24)=P$/3E-4
2135 IF Q1=2 OR Q1=5 THEN D(24)=D(23)
2140 IF Q1=3 OR Q1=4 THEN D(24)=P$/(T1+D*(U+1))

```

```

2145 D(27)=M,D(28)=A,D(29)=U,D(30)=FND(D(24)/1E3),D(31)=FND(X2)
2150 IF R<45E3 AND N#"SUN GLINT"
THEN D(32)=G0+(1/((2.5323E-3)-.30766*D1/R0)),T(32)=
T(32)+(" (TURBULENT AIR)"ELSE D(32)=G1,T(32)=T(32)+
" (FREE SPACE)"
2155 L3=G2+FND(F2)+L1-L2+L3+FND(X2)+D(32)
2160 D(33)=FND(X5),D(34)=L1,D(35)=-L2,D(36)=FND(E2),D(37)=G2,
D(38)=D(30)+L5
2165 D(39)=FND(T1*Y/LOG2(M)),D(40)=D(38)+D(39),D(41)=FND(H*F),
D(42)=D(40)-D(41),D(43)=FND(F1/F2),D(44)=D(42)+D(43)
2170 D(45)=FND(S*T1*Y/LOG2(M))
2175 IF D(23)=D(24) THEN T(30)=T(50)+(" (AVG)" ELSE T(30)=T(50)+
" (PEAK)"
2180 IF R<45E3 AND N#"SUN GLINT" THEN GOSUB 2500
2185 D(47)=D(44)-D(45)+D(46)
2190 IF R<45E3 THEN N8="(GT TO SS)" ELSE IF R>45E3 THEN N8=
"(SS TO SS)" ELSE IF R<45E3 AND N#"SUN GLINT" THEN N8="(AT TO SS)"
2195 PRINTINFORM"9/11B'LOW DATA RATE LASER LINK ANALYSIS'4B10X3/
3B'BACKGROUND:'B15X 3B40X3/'LINK PARAMETERS:'2/":N8,N,N1+
" SYSTEM -"+N9+" LASER"
2200 FOR I=1 TO 25
2205 IF I=25 AND R>45E3 OR I=25 AND N#"SUN GLINT" THEN 2255
2210 PRINTINFORM"2B38X":T(1)
2215 PRINTINFORM Z1:D(1) IF I=1
2220 PRINTINFORM Z2:D(1) IF I=2 OR I=8 OR I=9 OR I=17 OR I=
18 OR I=20 OR I=21 OR I=24
2225 PRINTINFORM Z3:D(1) IF I>2 AND I<8 OR I=10 OR I=22 OR I=
16 OR I=25
2230 PRINTINFORM Z4:D(1) IF I=11
2235 PRINTINFORM Z5:D(1) IF I=13 OR I=14 OR I=15 OR I=19
2240 PRINTINFORM Z9:D(1) IF I=12 OR I=23
2245 PRINTINFORM "B20X/":U(1)
2250 NEXT I
2255 IF Q1#1 THEN 2275
2260 FOR I=27 TO 28
2265 PRINTINFORM Z8:T(1),D(1),U(1)
2270 NEXT I
2275 PRINTINFORM Z8:T(29),D(29),U(29) IF Q1=3
2280 PRINTINFORM"/'LINK CALCULATION:'2/"
2285 FOR I=30 TO 47
2290 IF I=46 AND R>45E3 THEN 2310
2295 PRINTINFORM Z7:T(1),D(1),U(1)
2300 PRINT IF I=46
2305 NEXT I
2310 PRINTINFORM"/'PREPARED ON'BY5X10/":DATE
2315 QUIT
2500 CS=-.04+.158*(D1/R0)
2505 IF NS>1 THEN CS=.25*LOG((1/NS)*(EXP(4*CS)-1)+1)
2510 KS=21*EXP(14.45*CS) IF D(14)<1
2515 KS=40*EXP(15*CS) IF D(14)>=1 AND D(14)<50
2520 KS=104*EXP(21.7*CS) IF D(14)>=50
2525 D(46)=FND(D(16)/KS)
2530 RETURN

```

Appendix O

ACQUISITION AND TRACKING ANALYSIS

by

Dr. R. C. Ohlmann

LOCKHEED PALO ALTO RESEARCH LABORATORY
LOCKHEED MISSILES & SPACE COMPANY
A GROUP DIVISION OF LOCKHEED AIRCRAFT CORPORATION

INTRODUCTION

The conceptual and mathematical analysis of the acquisition and tracking system required for a satellite data relay system is presented here. The subject is divided according to the acquisition and tracking phases or sequences, since different detection and tracking strategies apply to the different phases. Two terminals of the satellite data relay system are required to acquire and track each other. One terminal carries a Package A transceiver designed to transmit high-rate data; the other terminal carries a Package B transceiver designed to receive high-rate data and transmit a beacon carrying low-rate data. A separate acquisition beacon also may be carried on Package B.

The acquisition and tracking phases may be described as follows:

- I - Package A receiver acquires Package B beacon.
- II - Package B receiver acquires Package A signal.
- III - Package A receiver tracks Package B beacon.
- IV - Package B receiver tracks Package A signal.
- V - Packages A and B fine-track each other.

Several stages are assumed since the signal-to-noise ratio improvement at each stage must be sufficient to permit further improvement in the tracking and pointing accuracy in the succeeding stage.

The analysis is dependent upon an understanding of quadrant and image dissector photodetectors, so their characteristics are briefly described. The beacon lasers available are also listed. Detection strategies are considered, and an analysis of detection statistics is presented.

O-1

LOCKHEED PALO ALTO RESEARCH LABORATORY
LOCKHEED MISSILES & SPACE COMPANY
A GROUP DIVISION OF LOCKHEED AIRCRAFT CORPORATION

Section 1

INITIAL ACQUISITION - PHASE I

1.1 DEFINITION

Package A will always acquire the beacon on Package B in the first phase, since Package B will carry a beacon laser especially suitable for this phase. Phase I includes the following:

- (1) The alignment of the telescope on each terminal to point in the direction of the other within the altitude and ephemeris uncertainties present
- (2) The transmission of a beacon signal from one terminal to the other
- (3) The reception of the beacon signal and verification that the received signal was not due to noise
- (4) The improvement in pointing of the receiver until a predetermined pointing accuracy is achieved and the receiver can transmit its own laser beam to permit Phase II to begin

The time it takes to perform the initial alignment of the two terminals will depend on the amount of misalignment present and the rate at which the telescopes can be driven. In the case of two terminals that are idle before the initial acquisition begins, this initial alignment time is of no system consequence since it can be accomplished during the idle time. For example, a low-orbit satellite just coming over the horizon into view of a synchronous satellite relay can be performing initial alignment before it comes into view. However, if one terminal is transferring transmission from one distant terminal to another, the initial alignment time is very significant and must be included in the acquisition time. This case occurs when a low-orbit satellite user switches from using one relay to another, or when a relay satellite finishes relaying the message of one user and switches to relay or receive from another user.

A complete discussion of the initial alignment time is presented in Vol. II, Task 3. It involves a detailed discussion of the inertia of the telescopes, the torques of the drives, and the reaction on the platform. For the purpose of the present analysis, both the alignment time and the propagation time for the beacon signal to travel between the terminals (about 0.25 sec at most) are treated as system parameters which must be added to the receiver acquisition time.

The receiver acquisition time is thus defined as the time required for the receiver terminal to:

- (1) Search its uncertainty field of view
- (2) Receive and verify the detection of a beacon signal
- (3) Improve its pointing accuracy to the required degree for returning its own beacon to the distant terminal. The receiver acquisition time is a random variable, since system noise and initial pointing uncertainty will cause the time to vary. In general, the acquisition time is $T_A(P)$ with a probability P that the acquisition will take place in time $T_A(P)$ or shorter.

It is relevant to define the 99% probable receiver acquisition time such that 99% of the initial acquisitions will take place in that time or less. The selection of 99% as the probability criterion is arbitrary, and must be examined in terms of the system effect of a longer time for 1% of the acquisitions, and also how much longer a time is expected for these exceptional cases. A detailed requirements analysis is beyond the scope of this program, since it is a function of the mission that the relay subsystem is supporting. Some cases have been considered in "Acquisition and Tracking - Subsystem Requirements Analysis," Technical Memorandum No. 13, and summarized in Appendix V, where it is concluded that an acquisition time defined for 99% of the acquisitions is adequate if 99.99% of the acquisitions occur within twice this time.

1.2 INITIAL ACQUISITION BEACON ALTERNATIVES

Several types of beacons are considered for the subsystem. Since the beacon must also act as the carrier for the low-data-rate channel, the most desirable beacons

are those that can perform all functions and require low development risk and cost, and have low weight and prime power requirements. A complete exposition of available beacon characteristics is presented in Vol. II under Task 5. These have been selected with attention given to the constraints on weight and prime power of Package B. In particular, the prime power goal of 50 W for Package B has limited consideration to a semiconductor laser diode, a semiconductor-diode-pumped, Q-switched Nd:YAG laser and a flash-lamp pumped Nd:YAG laser for the initial acquisition (Phase I). For later phases (III and V), a HeNe space-qualified laser is also considered.

1.3 PHOTODETECTORS

Two types of photodetectors can provide pointing information: a quadrant detector and an image dissector detector.

1.3.1 Quadrant Detector Characteristics

With a quadrant detector used for initial acquisition, the receiver field of view is divided into four quadrants, each of which is imaged onto a separate photodetector surface. For maximum acquisition efficiency, each quadrant is sensitive at all times and each has its own electronic receiving and decision circuits. The image of the received signal, focused to a size much smaller than a quadrant detector diameter, is incident on one of the quadrants. When the receiver decides that one quadrant contains the signal, using the logic described below, tracking information has been obtained. Receiver pointing may be improved by commanding the tracking mirrors to move so that the image moves toward the center of the field. The first verified signal pulse may move the image one-half a quadrant diagonal (one-fourth of the field of view). The second signal pulse then moves the image one-quarter of the diagonal, etc., so that after N_q signal pulses the receiver tracking and pointing uncertainty has improved by a factor R_q , where

$$R_q = 2^{N_q}, \quad \text{or} \quad N_q = \log_2 R_q \quad (1.1)$$

The final pointing uncertainty is $(1/R_q)$ of the initial field of view.

O-4

1.3.2 Image Dissector Detector Characteristics

For the image dissector detector, the instantaneous field of view (IFOV) is smaller than the total uncertainty field because the detector is designed to collect photoelectrons over only a portion of its total sensitive area. This portion is electrically scanned over the entire cathode or uncertainty field. When a verified signal is received in one time slot during a receiver scan, the knowledge of the scan position at that time reduces the pointing uncertainty from its initial value to that corresponding to the instantaneous field-of-view angle.

An improvement in acquisition time can result if the image dissector has several masks to provide several different instantaneous fields-of-view. The largest IFOV is scanned first; after it receives a verified signal, and the receiver corrects its pointing, control is switched to the next smaller IFOV which scans the uncertainty field of the larger mask, etc. Let the ratio of the total uncertainty field-of-view to the desired final pointing uncertainty be $R_m \gg 1$. If the pointing improvement of each IFOV mask over the previous one is R_i , and each of g masks results in the same improvement factor over the previous mask, then

$$R_m = R_i^2 \quad (1.2)$$

Since the receiver scan elements must overlap slightly, the number of elements in a scan line is R_i/f , where f is an overlap factor (less than one representing the fraction not overlapped). At least $(R_i/f)^2$ pulses must be received to scan one mask over its field. The total number of receiver pulses N_m to reduce the pointing uncertainty to R_m , assuming the whole field must be scanned, is thus

$$N_m = g \left(\frac{R_i}{f} \right)^2 = g R_m^{2/g} f^{-2} \quad (1.3)$$

1.3.3 Detector Comparisons

The advantage of the image dissector detector over a quadrant detector is that the background signal can be made significantly smaller because the IFOV of the image dissector is much smaller than a one-quadrant field-of-view. Also, a single verified signal reduces the receiver tracking uncertainty to the IFOV angle in an image dissector system, while several signal pulses are required by a quadrant detector system.

The image dissector has a disadvantage for an acquisition search in that it makes inefficient use of the incoming signal. For most of the search time, the signal image is not detected since the IFOV is not aimed at the transmitter. Thus, signal photons hitting the cathode are wasted during most of the search. It can be shown that the loss of incoming signal causes the image dissector to take considerably longer to acquire than a quadrant detector when background is low. However, with high background, an image dissector may be the only feasible type of detector to find the signal.

The relative inefficiency of the image dissector for acquisition is made clearer by the following example. Assume that a receiver pointing improvement factor of 64 is desired, so that $R = R_m = R_q = 64$. Compare the quadrant detector with two different image dissectors, one having $g = 1$ (one IFOV mask) and the other having $g = 4$ (four IFOV masks), and assume no overlap ($f = 1$). By Eqs. (1.1) and (1.3), one finds that the required number of signal pulses are $N_q = 6$ for the quadrant detector, $N_m = 4096$ for the $g = 1$ image dissector, and $N_m = 32$ for the $g = 4$ image dissector. Thus, the quadrant detector requires by far the fewest received signal pulses. It has been implicitly assumed that a complete field scan by the image detector is required to detect with greater than 99% probability.

The quadrant detector is not necessarily the fastest acquisition receiver if background is present and the pulse repetition rate is variable. With background present, the smaller IFOV of the image dissector results in a lower background so that signal detection requires less pulse energy. Thus, for a constant average laser power a higher pulse repetition rate is feasible using the image dissector than with the quadrant detector. With low background, the quadrant detector is clearly preferred.

1.4 DETECTION STRATEGY FOR PULSE ACQUISITION

The simplest detection rule is that for a monopulse threshold detection system in which the receiver decides that a signal is present if a preset (but adaptive) threshold is exceeded. In one type of system, no advantage is taken of the known repetition period of the laser. This type of simple monopulse detection is adequate only if the signal is very strong, permitting the threshold to be set high enough so that background will not cause a high probability of false detections.

A more optimum and easily implemented system is one which takes advantage of the regular pulse interval out of the beacon laser. The first pulse received over threshold starts a clock and sets a receiver detection gate to again open at the expected arrival time of the second signal pulse. The receiver decides that a signal pulse has been received only if the signal in the second period is also over threshold. This type of detection circuitry can be used with either quadrant detectors or image dissectors.

With a quadrant detector, it is assumed that each quadrant has its own two-pulse verification circuitry. If an initial pulse arrives at any quadrant, that quadrant is deactivated for a time that is a little less than the expected pulse interval t_D . The gate opens with a width Δt (to account for Doppler shifts and other uncertainties) and the decision circuit determines if a second pulse over threshold is received. As soon as any quadrant has made a verified acquisition, the gate timing becomes common for all quadrants. If a second signal pulse is not received, the initial search condition restarts. Figure 1 shows the electrical signals at the receiver during this process.

With an image dissector, a single two-pulse verification circuit is used. As the IFOV is scanned, a pulse over threshold will be received at some detector element in the scanned field. The scan is stopped and a return is made to that element to wait for the verification pulse. A gate is opened at the expected time of arrival of the second pulse. If no pulse is observed, scan continues. Depending on the background conditions, gating may or may not be necessary.

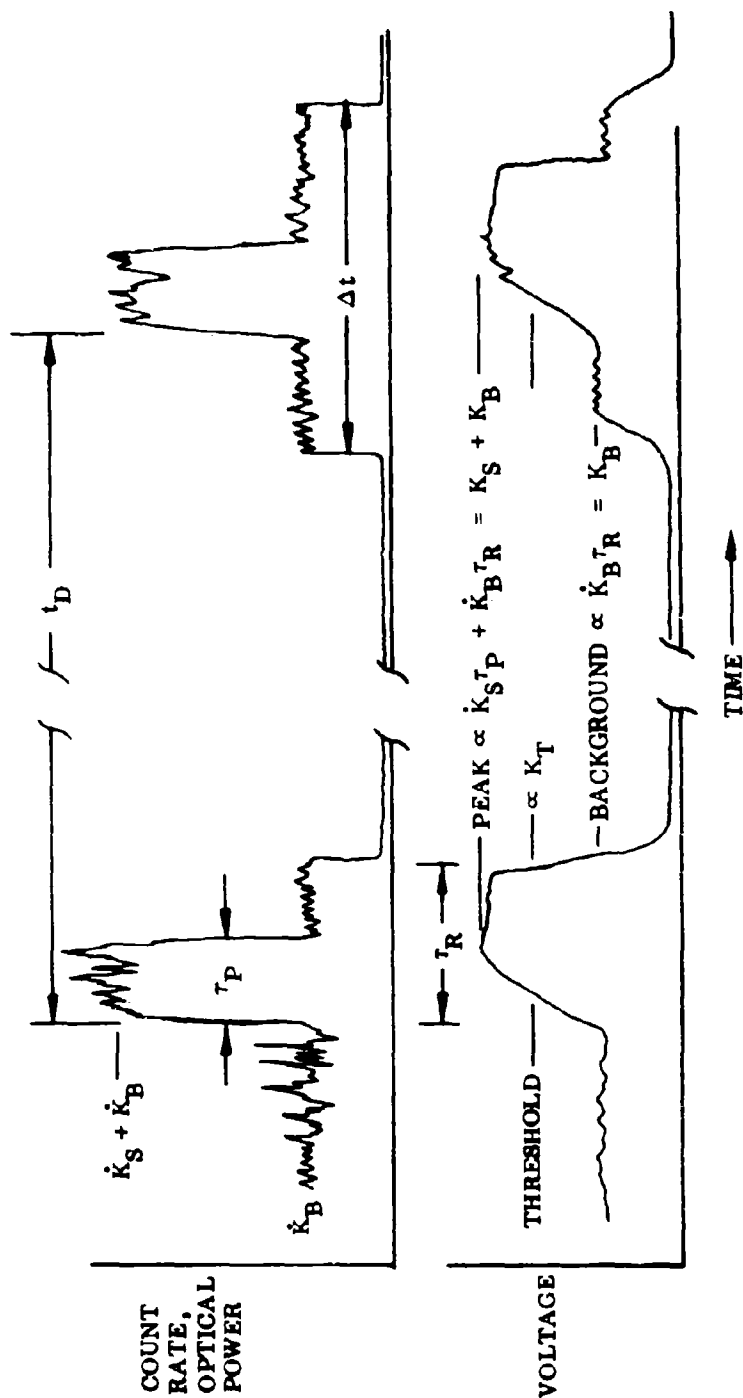


Fig. 1 Signals Observed at the Acquisition Receiver During Acquisition and Verification of a Received Signal Pulse

1.5 MONOPULSE DETECTION STATISTICS

A receiver which is to optimally detect a pulse of optical energy in the presence of background power is a quantum detector which effectively counts photoelectrons in each integration period and compares the number to an optimally selected threshold value. In practice, this can be achieved with a photomultiplier having sufficient gain that photocathode shot noise predominates over amplifier Johnson noise. However, if the quantum efficiency of the photomultiplier is very low, a better detector may be one that has a higher quantum efficiency but little or no gain, even if Johnson noise becomes significant. The detection statistics are analyzed on the basis of a detector circuit shown in Fig. 2.

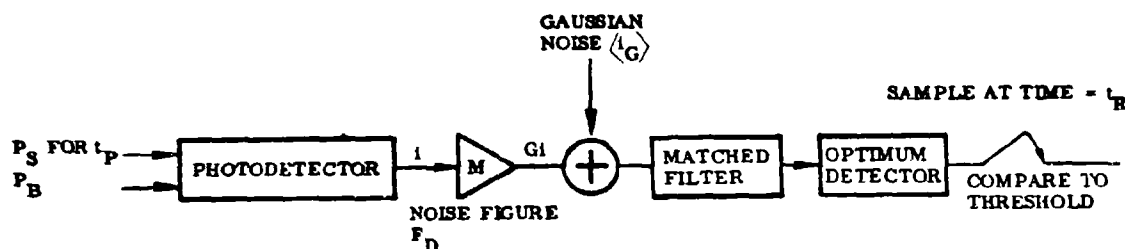


Fig. 2 Receiver for Pulse Detection

The analysis is first performed for the case of negligible Gaussian noise. In each integration time t_R , background photoelectrons equal to K_B on the average are released from the detector. If P_B is the background power incident on the IFOV of the detector with quantum efficiency η_D and noise figure F_D , then

$$K_B = \frac{\eta_D P_B t_R}{F_D h \nu} \quad (1.4)$$

where h is Planck's constant and ν is the optical frequency. The receiver noise factor is assumed to effectively reduce the quantum efficiency. When a signal pulse arrives with peak power P_S and duration t_P , additional photoelectrons are released, where the mean additional number released is

$$K_S = \frac{\eta_D P_S t_P}{F_D h \nu} \quad (1.5)$$

The total mean number of photoelectrons released during t_R when a signal pulse is present is thus

$$K = K_S + K_B \quad (1.6)$$

It is well known that the actual number of photoelectrons emitted from the photocathode closely follows a Poisson distribution. The output of the optimum detector in Fig. 2 will be proportional to the number of photoelectrons emitted during each interval t_R . If a threshold is set that is proportional to a definite number of emitted photoelectrons K_T , then the receiver decides a signal has been received if the threshold is equaled or exceeded, and decides that no signal has been sent if the threshold is not exceeded. The selection of the optimum threshold is a subject reserved for later discussion.

The false detection probability during a time t_R is the probability P_f that the threshold is exceeded when only background is present, and is given by

$$P_f = \sum_{n=K_T}^{\infty} \frac{(K_B)^n e^{-K_B}}{n!} \approx \frac{(K_B)^{K_T} e^{-K_B}}{K_T! [1 - (K_B/K_T)]} \quad (1.7)$$

where the approximation is useful when $K_B/K_T < 0.8$ and when $K_T > 10$. A plot of K_T versus K_B for a several values of P_f is given in Fig. 3. When K_B is large (> 100), a Gaussian approximation is useful,

$$P_f \approx \frac{1}{(2\pi)^{1/2}} \int_X^\infty \exp\left(-\frac{X^2}{2}\right) dX \approx \left[\frac{1}{(2\pi)^{1/2}} \frac{\exp(-X^2/2)}{X} \quad \text{for } X > 3 \right] \quad (1.8)$$

where

$$X = \frac{K_T - K_B}{(K_B)^{1/2}} \quad (1.9)$$

Tables of functions of Eqs. (1.7) and (1.8) are given in a number of places (Ref. 1) and have been extended by LMSC to very low values of P_f (10^{-34}) for selected values of $K_B < 200$.

The probability of missing a signal pulse incident on the receiver is the probability that the threshold is not exceeded. This miss probability, P_m , is given by

$$P_m = \sum_{n=0}^{K_T-1} \frac{K^n e^{-K}}{n!} \approx \frac{K^{K_T} e^{-K}}{K_T! [(K/K_T) - 1]} \quad (1.10)$$

where the approximation is useful for $K_T/K < 0.8$ and $K_T > 10$. The exact expression for P_m was used to plot Fig. 4 relating K and K_T for several values of P_m . When K is large (> 100), the Gaussian approximation for P_m is

$$P_m \approx \frac{1}{(2\pi)^{1/2}} \int_Y^\infty \exp\left(-\frac{Y^2}{2}\right) dY \approx \left[\frac{1}{(2\pi)^{1/2}} \frac{\exp(-Y^2/2)}{Y} \quad \text{for } Y > 3 \right] \quad (1.11)$$

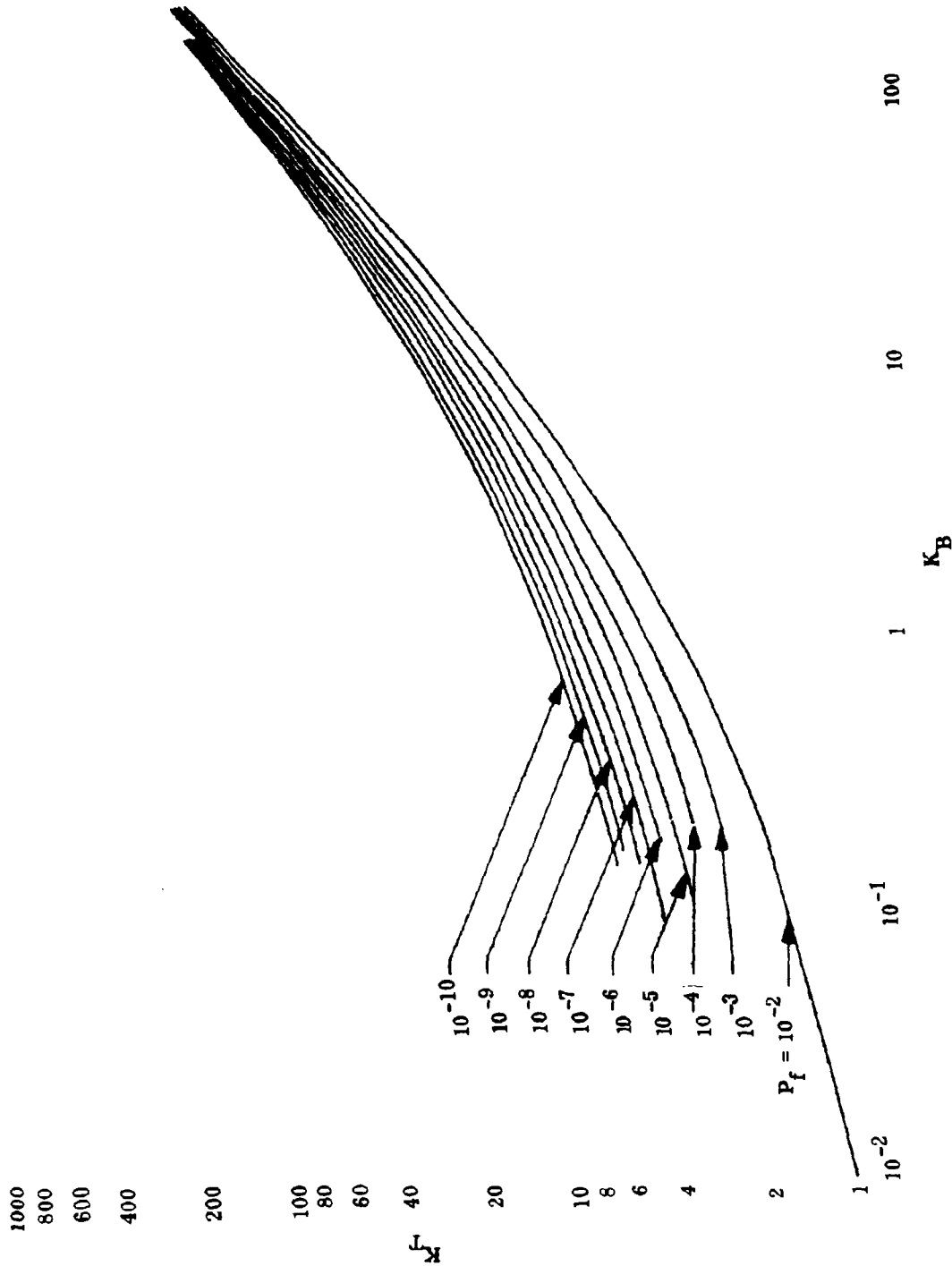


Fig. 3 Plots Relating Threshold Count K_T to Background Count K_B and False Alarm Probability

$$P_f = \sum_{n=K_T}^{\infty} (K_B)^n e^{-K_B/n!}$$

O-12

LOCKHEED PALO ALTO RESEARCH LABORATORY
LOCKHEED MISSILES & SPACE COMPANY
A GROUP DIVISION OF LOCKHEED AIRCRAFT CORPORATION

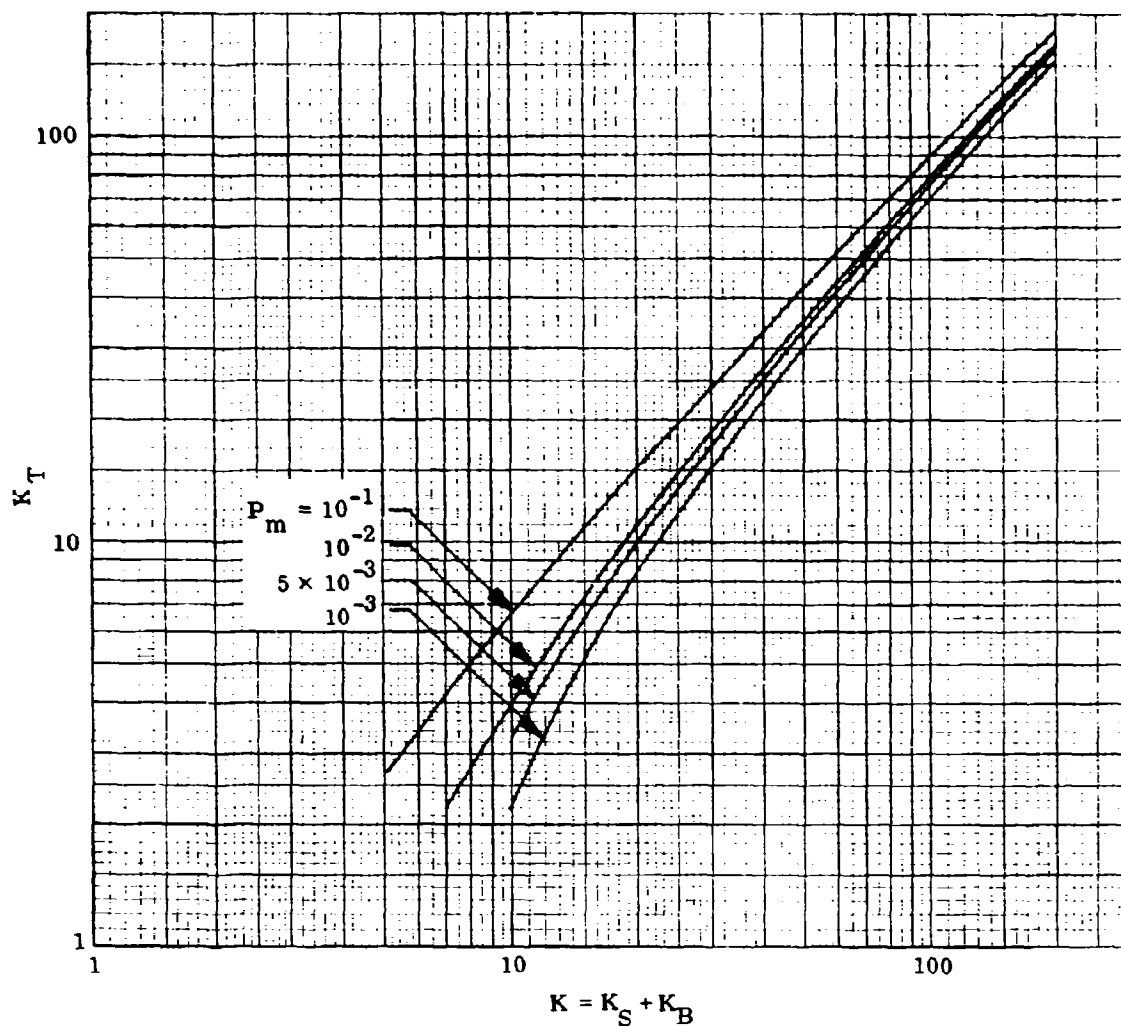


Fig. 4 Plots Relating Threshold Count K_T to Signal Plus Background Count $K = K_B + K_S$ and False Alarm Probability $P_m = \sum_{n=0}^{K_T-1} \frac{K^n}{n!} e^{-K}$

where

$$Y = \frac{K - K_T}{(K)^{1/2}} \quad (1.12)$$

For ease in writing, an effective background K_B' will be assumed to include dark current counts; i.e., $K_B' = K_B + (I_{DR}/e)$. Whenever K_B is written, this substitution shall be understood.

For ease in performing calculations, a plot of Eq. (1.8) [and Eq. (1.11), which is identical in form] is given in Fig. 5. With P_f and P_m selected, this curve can be used to obtain X and Y by entering the curve at $P_e = P_f$ and $P_e = P_m$. When K_B is known, K_T can be determined by using Eq. (1.9). Equations (1.6) and (1.12) can then be used to find the required K_S . When $K_B \gg K_S > 100$, a further simplification can be made by eliminating an intermediate calculation of X , Y , and K_T . It can be shown that the voltage signal-to-noise ratio $(S/N)_V$ in a baseband system from a pure Poisson process is

$$\left(\frac{S}{N}\right)_V = \frac{K_S}{(K_S + K_B)^{1/2}} \approx \frac{K_S}{(K_B)^{1/2}} = X + Y \quad (1.13)$$

Thus, given P_f and P_m , only one value of $(S/N)_V$ is found that satisfies Eqs. (1.8), (1.9), (1.11), (1.12), and (1.14). The results are plotted in Fig. 6. However, when K_B is not much greater than K_S , it is more accurate to use Fig. 5 and the relationship

$$K_S = XK_B^{1/2} + Y \left[K_B + XK_B^{1/2} + \left(\frac{Y^2}{4} \right) \right]^{1/2} + \left(\frac{Y^2}{2} \right) \quad (1.14)$$

The calculation of P_f and P_m when additive Gaussian noise is present is much more complex, since both Poisson and Gaussian processes are present. However, when K and K_B are large enough so that the Poisson distribution can be approximated by a

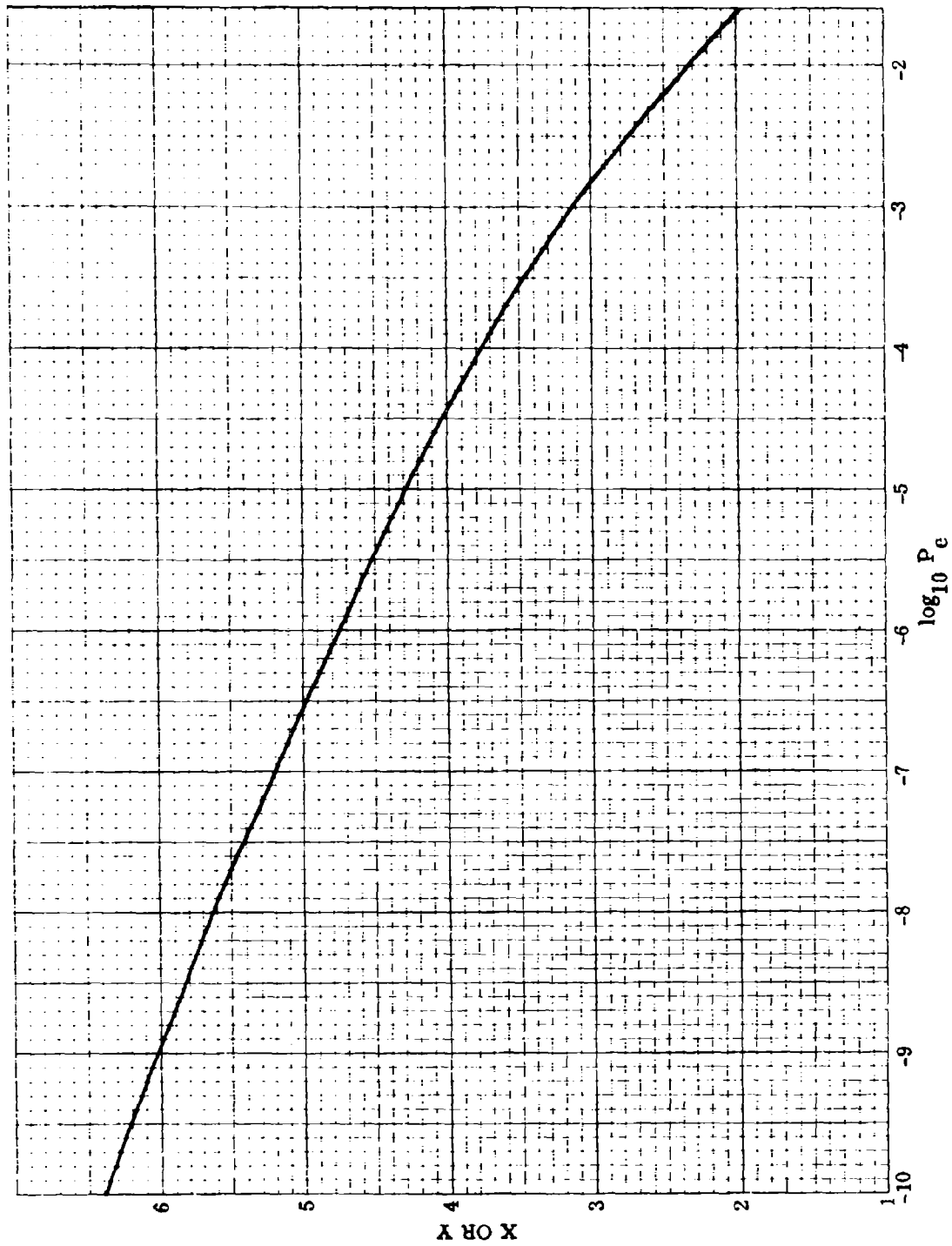


Fig. 5 Gaussian Approximation for P_m and P_f . For $P_e = P_f$, $X = (K_T - K_B)/\sqrt{K_B}$; for $P_e = P_m$, $Y = (K - K_T)/\sqrt{K}$

O-15

LOCKHEED PALO ALTO RESEARCH LABORATORY
LOCKHEED MISSILES & SPACE COMPANY
A GROUP DIVISION OF LOCKHEED AIRCRAFT CORPORATION

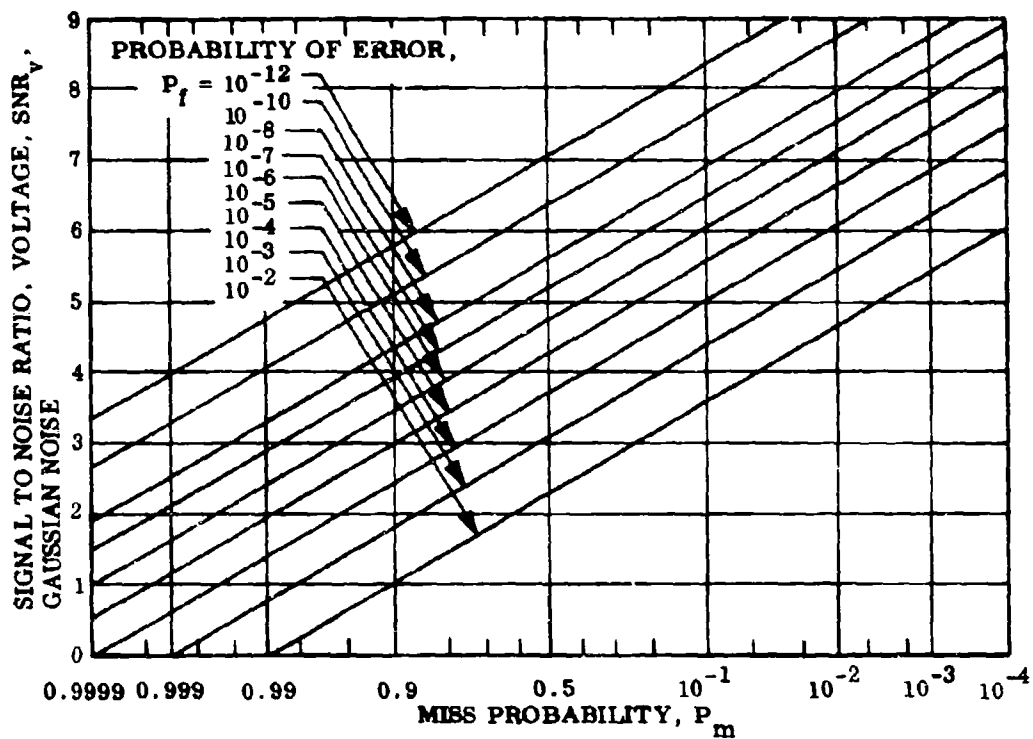


Fig. 6 Plot of the Required Signal-to-Noise Ratio Versus Miss and Error Probability for the Case of Gaussian Noise

Gaussian distribution, the solution is available. Let I_B be the cathode current due to background which has an associated Gaussian noise current [shot noise with $t_R = (2B)^{-1}$] of

$$\langle I_{Bn} \rangle^2 = \frac{eI_B}{t_R} \quad (1.15)$$

where e is the charge on an electron. Note that, if dark current I_D adds to the current, then

$$I_B = \left(\frac{\eta_D e P_B}{F_D h \nu} \right) + I_D = \left(\frac{K_B e}{t_R} \right) + I_D \quad (1.16)$$

Similarly, the total photocurrent present when a signal is present is

$$I_{SB} = \frac{\eta_D e (P_S + P_B)}{F_D h \nu} \quad (1.17)$$

which has a noise current

$$\langle I_{SBn} \rangle^2 = \frac{eI_{SB}}{t_R} \quad (1.18)$$

The amplifier is assumed to amplify noise and cathode current equally by M , so the output current is MI_B with noise $\langle MI_{Bn} \rangle^2 = eI_B M^2 / t_R$ when no signal is present, and MI_{SB} with noise $\langle MI_{SBn} \rangle^2 = eI_{SB} M^2 / t_R$ when the signal is present. The resultant current, including additive Gaussian noise current I_G , is therefore

$$\begin{aligned} I_0 &= MI_B + MI_{Bn} + I_G \quad (\text{no signal}) \\ I_1 &= MI_{SB} + MI_{SBn} + I_G \quad (\text{signal}) \end{aligned} \quad (1.19)$$

The values of P_f and P_m can be determined by Eqs. (1.8) and (1.11), with a threshold current I_T and

$$X = \frac{(I_T - MI_B)}{(MI_{Bn} + I_G)} \quad (1.20)$$

and

$$Y = \frac{(MI_{SB} - I_T)}{(MI_{SBn} + I_G)} \quad (1.21)$$

Note that these reduce to Eqs. (1.9) and (1.12) when $I_G = 0$ and $I_T = MeK_T/t_R$. For a thermal noise source of equivalent resistance R_S at a temperature T , having a noise figure F_R , the noise current is

$$I_G = \left(\frac{2kTF_R}{R_S t_R} \right)^{1/2} \quad (1.22)$$

where k is the Boltzmann constant.

The application of these equations to the practical problem of the design and performance analysis of the acquisition phase is approached by first determining the desired values of P_f and P_m and calculating P_B for a given system. The desired probabilities are discussed in the next section. Once they are determined, K_T or I_T can be calculated for a given system assuming values for t_R , η_D , F_D , and for M and I_G if necessary. Then, with P_m and K_T (or I_T) known, a calculation of the required K_S or $P_S t_P$ is performed. Comparing this with the actual signal energy or K_S received provides the design margin.

1.6 OPTIMIZATION OF DETECTION

The acquisition detection technique used determines the optimum values of P_f and P_m . These probabilities are selected by an implicit Bayesian criterion, which means that

relative weights are given to the effects of false alarms and misses. However, the determination of the relative weights to assign to minimize acquisition time becomes sufficiently complex that an approximate approach is used. Since the approach for the quadrant detector and that for the image dissector detector are different, they are treated separately.

1.6.1 Acquisition Using a Quadrant Detector

In this detection technique, it is assumed that receiver gating for the expected repetition rate takes place whenever a quadrant receiver detects a pulse over threshold. If the first pulse is verified by a second pulse about t_D later, pointing improves by one-half the field-of-view and time gating is operative. If no verification takes place, further pulses are examined without gating.

After the first verification takes place, it is assumed that gating reduces the total false alarm probability in a gate width to such a degree that only signal misses have to be considered. The problem is to determine and then optimize the acquisition time T expected with 99% probability using probabilities P_m and P_f in each time interval t_R . The acquisition time is that required to improve the pointing by a factor R . It has already been shown that at least $N_q = \log_2 R$ detected and verified signal pulses are required to obtain R improvement.

The total acquisition time T is

$$T = Nt_D \quad (1.23)$$

where N is the total number of possible pulses the receiver must have incident to ensure 99%, and t_D is the time between received signal pulses. The number of pulses required is equal to

$$N = (N_q + 1) + N_f + N_{m1} + 2N_{m2} + N_{m3} \quad (1.24)$$

where

N_q = detected signal pulses

N_f = number of false alarms in the signal quadrant before a signal is received

- N_{m1} = number of signal misses of the first of a verification pair
 N_{m2} = number of verification pulses missed after a signal pulse is received and detected
 N_{m3} = number of signal misses after verification

The reason that N_{m2} is multiplied by 2 in Eq. (1.24) is that a missed detection of a verification pulse wastes both its own pulse and the first signal pulse calling for verification.

The probability $P(N)$ of acquiring in N pulses is determined by the product of the probabilities, $P(N_f)P(N_{m1})P(N_{m2})P(N_{m3})$, with summation over all combinations which give N . Detailed analysis is extremely tedious, and only some of the results are indicated here.

$$P(N_f) \approx \frac{(\bar{N}_f)^{N_f} e^{-\bar{N}_f}}{N_f!} \quad (1.25)$$

where

$$\bar{N}_f = \frac{P_f(N_{m1} + 2N_{m2} + 0.5)t_D}{t_R} \quad (1.26)$$

$$P(N_{m1}) = (1 - P_m)^{N_{m1}} \quad (1.27)$$

$$P(N_{m2}) = (1 - P_m)^{N_{m2}+1} P_m^{N_{m2}} \quad (1.28)$$

$$P(N_{m3}) = \binom{N_q + N_{m3} - 2}{N_{m3}} (1 - P_m)^{N_q-1} P_m^{N_{m3}} \quad (1.29)$$

Only the situation with $N_f = 0$, $N_{m1} + 2N_{m2} + N_{m3} \leq 2$, and $N_q = 6$ will be considered ($R = 64$). The cumulative acquisition probability is then

$$\sum_{i=1}^4 P(N = N_q + i)$$

which can be calculated and set equal to 0.99. Expanding to second order, one finds

$$\sum_{N=7}^9 P(N) = 1 - \frac{(0.5 + 3P_m) P_f t_D}{t_R} - 8P_m^2 \quad (1.30)$$

The miss probability P_m has canceled out in first order because the terms in $P(N = 8)$ and $P(N = 9)$ cancel the term in $P(N = 7)$. A range of values of P_m and P_f will allow $P(N \leq 9) \approx 0.99$. Three possible values are (1) $P_f t_D / t_R = 0.02$, $P_m < 0.001$; (2) $P_f t_D / t_R = 0.01$, $P_m = 0.02$; and (3) $P_f t_D / t_R \leq 0.001$, $P_m = 0.1$. The set of values in possibility (2) has been arbitrarily selected for link analysis calculations.

1.6.2 Acquisition Using an Image Dissector Detector

In a receiver using an image dissector, it is assumed as before that a verification must take in each IFOV element that shows a current exceeding threshold. Since the detector is electronically scanned, the only delay in verification is t_D , with no significant time required for the sweep to stop and start. Since an acquisition time probability of 99% is of interest, at least one complete scan of the field is assumed to be required. The time required for one complete scan will be approximately

$$T_1 = (N + N_f + 1)t_D \quad (1.31)$$

where N is the number of elements in the scan, N_f is the number of false alarms, and the dwell time per scan element is made equal to t_D . The probability of acquiring in time T_1 is

$$P(T_1) = (1 - P_m)^2 P(N_f) \quad (1.32)$$

The probability of obtaining exactly N_f false alarms with $N_f \ll N$ is given by Eq. (1.25), with

$$\bar{N}_f = \frac{P_f(N + N_f)t_D}{t_R} \quad (1.33)$$

If either the first signal pulse or its verification pulse is missed, the acquisition time becomes $2T_2$ with a probability $P(2T_1) = 2(1 - P_m)^2 P_m P(2N_f)$. Since two full scans significantly increase the acquisition time, the system should be designed so $P_m \leq 0.005$, giving $P(2T_1) < 0.01$. The probability of having N'_f or less false alarms,

$$\sum_0^{N'_f} P(N_f)$$

is set at less than 0.98 so it has negligible effect on the acquisition time probability. For example, when $\bar{N}_f = 5$,

$$\sum_0^{N'_f} P(N_f) = 0.98$$

when $N'_f = 10$; other typical numbers are $N'_f = 30$ when $\bar{N}_f = 20$ and $N'_f = 121$ when $\bar{N}_f = 100$. Selecting N'_f to be about 10% of N , Eq. (1.33) is used to choose the desired value of P_f . For example, when N is 100, $N'_f = 10$, $\bar{N}_f = 5$, and $P_f t_D / t_R \approx 0.05$; when N is large (> 1000), $N'_f \approx \bar{N}_f$, and $P_f t_D / t_R = 0.1$. For link calculations, the values $P_f t_D / t_R = 0.05$ and $P_m = 0.005$ are chosen.

In order to relate these concepts to a tracking improvement ratio R , reference must be made to the concepts in section 1.3. The number of scan elements N for a single mask detector is related to R by

$$N = \left(\frac{R}{f} \right)^2 \quad (1.34)$$

where f is the overlap factor. For a detector with g masks, Eq. (1.3) applies, but the value of K_B and thus N_f^1 must be considered separately for the scanning operation of each mask.

1.7 ALTERNATIVE TRANSMITTER AND RECEIVER SCAN PATTERNS

Four alternate approaches to the initial acquisition phase can be considered:

- (1) A broad-beam transmitter illuminating a wide field of view receiver
- (2) A scanned transmitter beam illuminating a wide field of view receiver
- (3) A broad-beam transmitter illuminating a scanning receiver
- (4) A scanning transmitter beam illuminating a scanning receiver

1.7.1 Broad-Beam Transmitter and Wide Field of View Receiver

This approach uses a quadrant detector receiver strategy. Transmitter pulses reach the receiver separated by the laser pulse interval $t_L = t_D$. All the receiver concepts developed in section 1.6.1 apply to this case. The only feasible laser beacon for the initial acquisition can be shown to be a Q-switched Nd:YAG by link analysis because the broad transmitter beamwidth results in a small number of photons reaching the receiver from each laser pulse. Strategies could be developed to sum many pulses, but they quickly lose efficiency and become too complex.

Since the Q-switched laser typically has pulse widths of 10 to 50 nsec, a value for t_R of 100 nsec or less is feasible. The selection of the laser pulse repetition rate or pulse period, $t_L = t_D$, is determined primarily by the energy per pulse required to provide satisfactory link margin. The previous analysis provides the value of $P_S t_P$ or K_S required at the receiver for each background power assumed. For a given average laser output power, the received energy is directly proportional to t_L . A value of $t_L = 0.1$ sec (10 pps) has been chosen initially since link calculations indicate that a satisfactory margin is then achieved. Higher repetition rates are feasible and would have the advantage that smaller receiver vehicle motion would take place

between pulses. This motion limits R to a value such that the vehicle motion between pulses is less than the final receiver uncertainty angle.

1.7.2 Scanning Transmitter Beam and Wide Field of View Receiver

When the laser average power is low and the pulse repetition rate is or must be relatively high, as for a cw-pumped Q-switched Nd:YAG or a diode laser beacon, this technique is recommended for cases of low background. In this technique the transmitter beam is made narrower than the transmitter pointing uncertainty, and the uncertainty field is scanned by the beam. The advantage of this approach is that the high transmitter antenna gain permits more signal photons to reach the receiver. However, it has the disadvantage that transmitted signal is wasted whenever the transmitter is not pointed at the receiver. Thus, the acquisition time will be longer than for a broad-beam transmitter having enough pulse energy to be acquired. The transmitter scan technique also has the limitation that the beamwidth cannot be made so narrow that transmitter motion during the scan prevents overlap of the scan pattern.

The analysis for the scanning transmitter assumes a beamwidth θ_B , a transmitter uncertainty angle of θ_{TU} , and an overlap factor f . The number of scan elements m is therefore

$$m = \left(\frac{\theta_{TU}}{f\theta_B} \right)^2 \quad (1.35)$$

The laser repetition rate ($1/t_L$) is selected so that either one or two pulses occur during each transmitter scan element. If one pulse per element is used, then

$$t_D = mt_L = \left(\frac{\theta_{TU}}{f\theta_B} \right)^2 t_L \quad (1.36)$$

is the time for a complete scan. Using a quadrant detector, all the analysis in section 1.6.1 is applicable, using t_D as the time between received pulses.

Although more laser power is required, there is an advantage to using two laser pulses per scan element if either receiver or transmitter terminals have significant angular motion during acquisition. The signal verification is then made only $t_D - t_L$ later, which can be a significantly shorter time than mt_L . Initial false alarm probability must still be calculated using mt_L for t_D , and the overall acquisition time is still given by Eq. (1.28) with $t_D - mt_L$. The receiver circuitry becomes more complex since it is required to close and open a gate t_L later, as well as t_D later after verification is made.

1.7.3 Broad-Beam Transmitter and Scanning Receiver

This technique uses an image dissector detector to reduce background. The analysis follows the lines given in section 1.6.2. The number of elements to be scanned is given by Eq. (1.34) ($N = R^2/r^2$) with

$$R = \left(\frac{\theta_{RU}}{\theta_{Rf}} \right) \quad (1.37)$$

where θ_{RU} is the initial receiver angular uncertainty and θ_{Rf} is the final uncertainty (the final IFOV mask size). The transmitter laser is designed to have a pulse period $t_L = t_D$, the receiver dwell time. The limitation in R or θ_{Rf} achievable is determined by the condition that receiver terminal motion does not prevent overlap of the scans, i. e., move an acquired signal outside of θ_{Rf} in a time t_D .

1.7.4 Scanning Transmitter and Scanning Receiver

A scan-on-scan approach is feasible only if one scan completes a raster before the other scan moves to its next field element. Since the image dissector can scan most rapidly, it is selected to scan the receiver field-of-view while the transmitter is holding on one element of the transmitter field. If there are m transmitter field elements and N receiver field elements, the acquisition time is given by

$$T = m(N + N_f + 1)t_D \quad (1.38)$$

where N_f^1 is the false alarms per scan and t_D is the image dissector dwell time per element of its field. The laser pulse period is chosen to be equal to the dwell time of the image dissector on each element of its field, and the transmitter must dwell for at least $(N + N_f^1 + 1)t_L$ on each element of the transmitter field.

It is clear that the acquisition time can become very long in this technique unless t_L is short; however, short values of t_L reduce the pulse energy. Therefore, this technique is considered to be a last resort for acquiring a laser limited in energy per pulse output in the presence of background.

Section 2

SECOND ACQUISITION - PHASE II

2.1 DEFINITION

This phase includes the acquisition of the laser signal from Package A by the receiver on Package B, the improvement in pointing of Package B, and the return of a narrower beam beacon back to A.

The distinguishing feature of the analysis compared with Phase I is that a cw laser is assumed on Package A, not a pulsed laser, and it is assumed that the laser cannot be pulsed with peak power enhancement. Thus, either a constant-intensity or a modulated-intensity laser beam must be acquired by Package B. The analysis below examines receiver statistics for both modulated and unmodulated beams. It is shown that although an unmodulated beam has appreciable signal-to-noise advantage over a modulated beam, it is much more sensitive to background variations or intentional jamming, since no signature is available to separate signal from background, at least in the case of a broad beam transmitter. With a scanning transmitter, the total scan time between transmitter rasters does provide a signature on the signal. However, transmitter motion makes this type of signature unreliable because of its timing uncertainties.

2.2 PHASE II DETECTION ANALYSIS

2.2.1 Detection Considerations

All the considerations of Section 1 concerning quadrant and image dissector detectors are relevant in Phase II except that receiver optimization for a cw signal must be analyzed. When the laser beam is not modulated, the optimum detector utilizes an integrate and dump circuit which effectively counts photoelectrons during each receiver integration time t_R . Poisson statistics still apply and K_S and K_B are calculated

as for a pulse input, with K_S being the signal count in the period t_R . With a broad beam transmitter, t_R is equal to t_D , the decision time, but with a scanning transmitter beam, t_D is the time for a full scan of the receiver field and t_R , the receiver integration time, is equal to dwell time per element of the field.

For a receiver which is to acquire a light beam that is sinusoidally modulated in intensity but whose modulation phase is unknown, an analysis of the optimum detector and its statistics must be made. The optimum detector strategy is one that explicitly accounts for the Poisson noise statistics. The probabilities for false alarms and misses should be calculated on this basis.

Unfortunately, such an exact analysis has not yet been performed. The difficulty of the problem may be likened to that of determining the statistics of a biphase modulated sub-carrier with Poisson noise, as presented in the document Poisson Noise and Error Probabilities in Optical Communications Using Biphase Modulated Subcarriers, by G. F. Herrman (Ref. 2). By analogy to the case of Gaussian noise, the optimum receiver should be one which correlates with a peaked sine and cosine reference signal at the modulation frequency. The resultant should be squared, added, and compared to the threshold setting. This procedure is described for Gaussian noise by A. D. Whalen in Detection of Signals in Noise (Ref. 3). Figure 7 shows the quadrature receiver form and its matched filter equivalent for additive Gaussian noise.

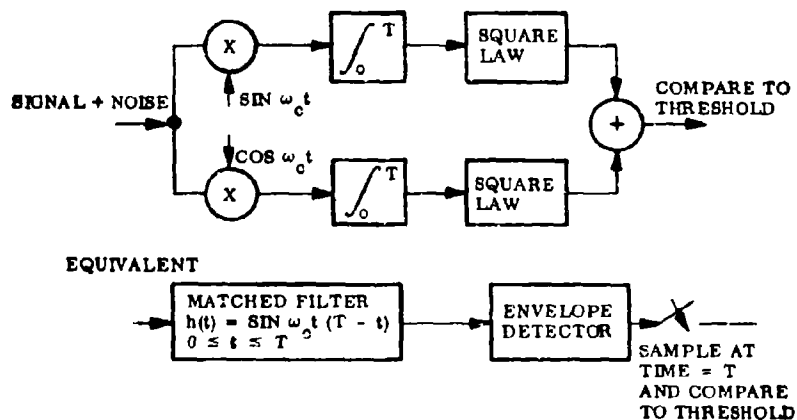


Fig. 7 A Quadrature Receiver and Its Incoherent Matched Filter Equivalent

It has been assumed (and confirmed by link calculations) that the number of background photoelectrons received in an integration time is very large. Therefore, Gaussian statistics are approximately valid using the additive noise caused by the fluctuations of the background and possibly detector or receiver noise. In section 2.2.3, an analysis of the signal-to-noise ratio is presented. The results will be applied to the appropriate statistics derived in section 2.2.2, for the envelope of the signal to be compared to the threshold.

2.2.2 Detection Statistics

Using the density distribution for the envelope of a sine wave plus narrowband Gaussian noise, the false alarm and miss probabilities are given by (Ref. 3)

$$P_f = \int_{\beta}^{\infty} Z e^{-Z^2/2} dZ = e^{-\beta^2/2} \quad (2.1)$$

and

$$(1 - P_m) = \int_{\beta}^{\infty} Z e^{-(Z^2 + \alpha^2)/2} I_0(\alpha Z) dZ \quad (2.2)$$

where

$I_0(\alpha Z)$ = the modified Bessel function of zero order

β = η/σ_T = the normalized threshold

σ_T^2 = $N_o t_R/4$ = variance of the noise

N_o = noise spectral density

α^2 = $2E/N_o$

E = signal energy in $t_R = A^2 t_R/2$

A = signal amplitude at threshold detector

The probabilities given above are directly related to each other for a given value of E/N_0 . This relation has been plotted in Ref. 4 and reproduced in Fig. 8.

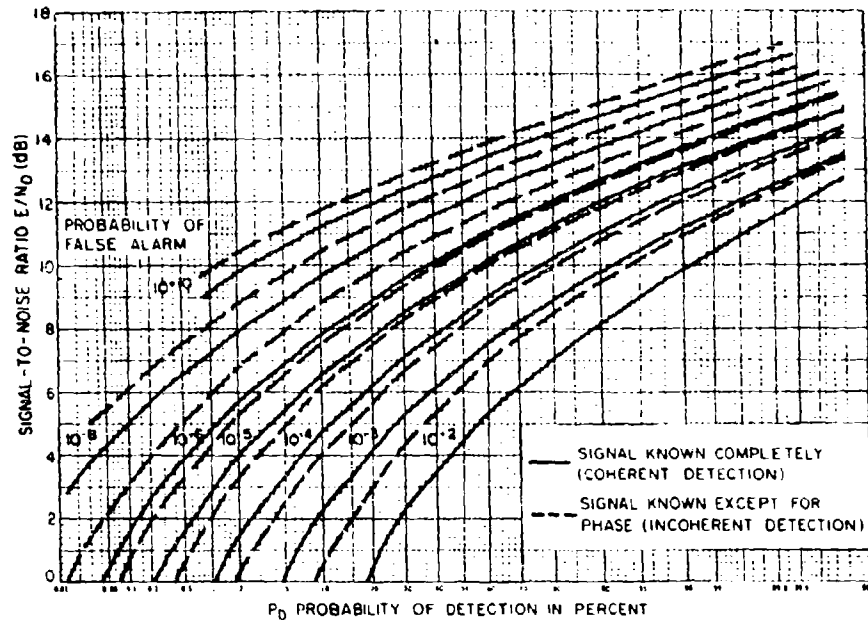


Fig. 8 Detection Statistics for Envelope Detection in the Presence of Gaussian Noise. The miss probability $P_m = 1 - P_D$. The dashed curves are used for acquisition analysis. (From Detection of Signals in Noise, A. D. Whalen, 1971; printed with permission of Academic Press)

2.2.3 Signal-to-Noise Ratio for a Modulated Light Beam

In order to use the analysis in section 2.1, the signal energy per integration time per noise power per unit bandwidth for an intensity-modulated signal in the presence of background and detector noise must be calculated. The symbol for this ratio is E/N_0 . The expression for S/N given in Section 1 is not valid for a modulated wave.

Let P_S be the maximum instantaneous received power or intensity when modulation is present. If the optical intensity is sinusoidally modulated with 100% modulation depth, the rms signal current after amplification by a factor M is given by

$$I_S = M \eta_D e P_R / 2\sqrt{2} h \nu F_D \quad (2.3)$$

where

η_D = detector quantum efficiency

F_D = detector noise figure

The numerical factor, $2\sqrt{2}$, arises from the conversion of peak-to-peak current to rms current. The rms noise current after photodetector multiplication is

$$I_n = \left[2M^2 e I_{av} B_o + (4kT B_o / R) \right]^{1/2} \quad (2.4)$$

Here

$$I_{av} = \frac{\eta_D e}{h \nu F_D} \left[\frac{P_R}{2} + P_B \right] + I_D \quad (2.5)$$

is the average detector current before amplification with background power P_B reaching the detector, and I_D is the photosurface dark current. The amplifier has an equivalent input resistance R , and a noise bandwidth B_o . The noise power per unit bandwidth for incoherent detection is

$$N_o = \frac{I_n^2 R}{B_o} = 2M^2 I_{av} R + 4kT \quad (2.6)$$

The signal energy collected in time t_R is

$$E = I_S^2 R t_R = (M \eta_D e P_R / 2\sqrt{2} h \nu F_D)^2 R t_R \quad (2.7)$$

Therefore

$$\frac{E}{N_o} = \frac{(M\eta_D e/h\nu F_D)^2 P_R^2 t_R}{16M^2 e \left[(\eta_D e/h\nu F_D) \left[(P_R/2) + P_B \right] + I_D \right] + (32 kT/R)} \quad (2.8)$$

Equation (2.8) reduces to the formulation by Pratt (Ref. 5) when $t_R = (1/B_{sc}) = (1/2 B_o)$, where B_{sc} is the subcarrier bandwidth and B_o is the post-detection bandwidth.

The acquisition bandwidth in Phase II acquisition can be made low enough so that for most detectors the Johnson noise is negligible compared to the other noise sources. This is true when

$$2 kT F_A / R \ll M^2 e I_{av} \quad (2.9)$$

For typical values $F_A = 2$ at $T = 300^\circ K$,

$$R \gg 4 \times 10^{-4} / M^2 I_{av} \quad (2.10)$$

For a photomultiplier, $M I_{av}$ is the dc average anode current that can be from 1 to 100 μA . Thus, for a 1 μA anode current, if $R \gg 400/M$, Johnson noise is negligible; $M > 100$ would normally be used. For diode detectors, $M = 1$ and $I_{av} \approx I_D \sim 0.1 - 1 \mu A$ at room temperature. Therefore, for $I_D = 1 \mu A$, $R \gg 400 \Omega$ is required. In a conjugate tuned circuit, $R \approx R_S Q^2$, so for $Q = 10^2$ and $R_S = 10 \Omega$, $R \approx 10^5 \Omega$, showing that Johnson noise can be neglected. If bandwidths of about 100 Hz are required, the modulation frequency should be greater than 10 kHz for reasonable values of Q and R .

Equation (2.8) can be rewritten, neglecting Johnson noise, as

$$\begin{aligned} K_S &= (\eta_D e/h\nu F_D) P_R t_R \\ K_B' &= (\eta_D e/h\nu F_D) P_B t_R + I_D t_R / e \end{aligned} \quad (2.11)$$

O-32

LOCKHEED PALO ALTO RESEARCH LABORATORY
LOCKHEED MISSILES & SPACE COMPANY
A GROUP DIVISION OF LOCKHEED AIRCRAFT CORPORATION

so

$$\frac{E}{N_o} = \frac{K_S^2}{8 K_S + 16 K_B'} \quad (2.12)$$

Usually the modulation is received as circular polarization modulation and is then converted to intensity modulation using a quarter-wave plate and polarizer in front of the photodetector. It must be noted that the background power is usually unpolarized, so P_B is half of that received without a polarizer.

A further detection improvement is possible by modulating with a square wave rather than a sine wave. The detected energy when correlated with a square wave is then doubled, because I_S is given by

$$I_S = M \eta_D e P_R / 2 h \nu F_D \quad (2.13)$$

Thus, E/N_o is twice that given by Eqs. (2.8) and (2.12):

$$\frac{E}{N_o} = \frac{K_S^2}{4 K_S + 8 K_B'} \quad (\text{square wave}) \quad (2.14)$$

The implementation of the receiver would then be of the form shown in Fig. 9. Since the modulation can take place at relatively low frequencies (~ 100 kHz), the correlator is easily implemented with digital logic.

In the calculations performed for Phase II, values of P_f and P_m are set by the same considerations as given in Section 1. Then, given P_B and K_B' , the required K_S or P_R is determined by using Fig. 8 and Eq. (2.14) or (2.9). This required value is compared to that received signal power to determine the link margin.

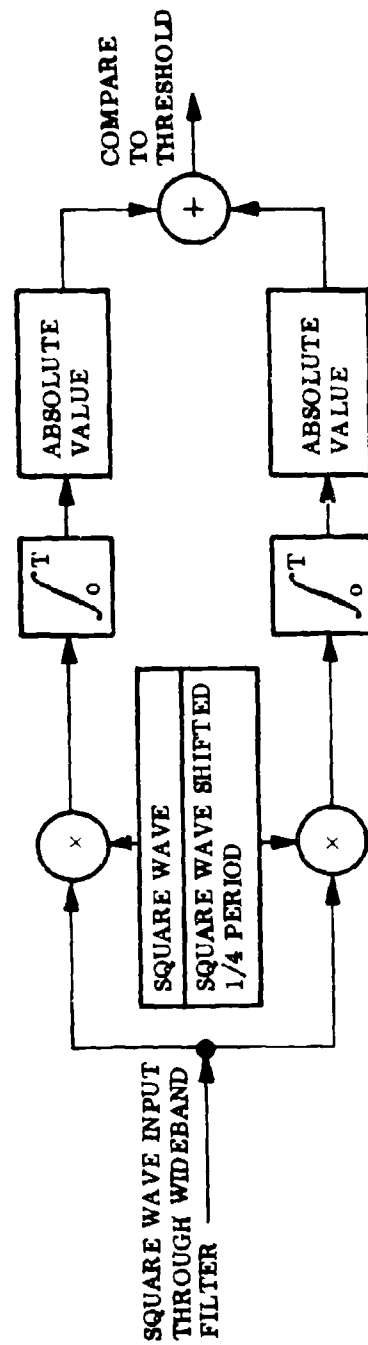


Fig. 9 Detector for Square Wave Input of Known Frequency but Unknown Phase

Section 3
PHASES III AND IV - IMPROVED TRACKING

Receiver tracking is further improved in both Phases III and IV by a transition to a fine tracking detection system. The reasons for performing the acquisition and tracking in two steps at each terminal when a 10^4 improvement in pointing accuracy is required are:

- (1) The initial broad field of view requires that the coarse tracking detector be at the telescope prime focus in order to reduce the size of the optic element needed to accommodate off-axis rays.
- (2) The fine tracking detector must be in the secondary optics after the fast beam steerer.
- (3) The angular magnification of the optics must be different for coarse and fine tracking.
- (4) The detection method of Package A must change from detection of a low-rate pulse input to detection of either a modulated cw laser beam or a very high repetition rate laser, since the incoming signal must be at least semicontinuous for fast tracking during vehicle motion and gimbal friction effects.
- (5) The receiver of both Packages A and B must be able to convert from an acquisition mode to a track mode.

The improved pointing and tracking knowledge of each terminal permits narrower beamwidths, thus increasing the signal power at the receiver, and also permits narrower receiver fields of view, thus reducing the background power. These improvements are partially offset by the greater bandwidth necessary for the fast tracking capability.

To perform the transition between the coarse tracking detector and the fine tracking detector, the latter must perform an acquisition sequence within its narrower field of view. For a signal from a 100% modulated cw laser, the acquisition analysis is exactly as described in Section 2. The verification that a detection is due to signal and not noise will still be required except when the link margin is so high that P_f becomes negligible. The verification can be done by integrating for two or three receiver time constants and comparing with a second threshold.

Both the quadrant detector and an image dissector detector are candidates for the fine tracking detector. The selection of one over the other is primarily determined by the tracking function rather than the acquisition function performed after transition from coarse acquisition. A comparison of the detectors for tracking is given in the following section.

Section 4

PHASE V - HIGH PRECISION TRACKING

4.1 SYSTEM CONSIDERATIONS

The tracking system must be able to continue to function in a considerably higher background radiance environment than the acquisition system. It has been assumed that acquisition may be delayed for a few minutes to avoid the most severe background situations: sun glint off the ocean surface as viewed from the synchronous satellite, a bright planet or sun scatter by the optics as viewed by the synchronous or low-orbit satellite, and forward scatter of sunlight by the atmosphere when an aircraft or ground station views within 1° of the sun.* Experimental data on the actual worst background power expected is not very reliable for most of these cases, although estimates on the order of 0.1% of that received looking directly into the sun have been made, i.e., about $1-3 \text{ W/m}^2 \text{ sr}^\circ$.

It is desirable to be able to continue tracking; even in these severe background situations so that the link is not broken; otherwise, reacquisition is required. Since the expected backgrounds are not well known, the link calculations have been done as a function of the background power.

A complete analysis of the tracking capabilities of the system must include the feedback loop analysis, including complex loop response, amplifier gains, gimbal and mirror response, mechanical noise, etc. This analysis has been developed elsewhere. In this section, inputs to that analysis, the angle error signal and the detector electrical noise, are derived. This derivation is done separately for the quadrant detector and the image dissector detector, and is followed by a comparison of these tracking detectors.

*Section 5 contains a derivation of the frequency of occurrence of direct sunlight in the field of view.

4.2 QUADRANT DETECTOR TRACKING

4.2.1 Tracking System

A typical dual-channel tracking system using a quadrant detector has the incident light beam focused on the apex of a four-faceted pyramid. If the focal point is centered on the apex, the light is then divided equally to four detectors; if the focal point is slightly shifted from the apex, the detectors receive different signals. An error signal is developed, proportional to the angle error for small error, by taking the difference between the amplified detector signals from detectors sensing opposing quadrants. The detector gains used before differences are taken must be almost equal or a bias error results.

The received signal into the quadrant detector may be either a continuous light beam or a modulated light beam. The choice depends on whether spoofing or jamming vulnerability is a significant factor in the system, and whether background that is unequally distributed among the quadrants is significant compared with the signal. A modulated signal will protect against both conditions but at the expense of lowering the detector signal-to-noise ratio. A sufficiently small receiver field of view also protects against both conditions and may be adequate protection.

Tracking must take place using incoming signals that also carry data modulation. Package B receives the high-rate data; the incoming signal from Package A has a frequency spectrum above the range of existing tracking detectors. Therefore, additional low-frequency modulation of intensity may be desired for tracking purposes. However, the modulation depth must be quite low ($< 5\%$) in order not to interfere with the high-rate data system. Similarly, Package A is receiving low-rate data, and if it becomes excessively difficult to use the low-data-rate format for tracking, an additional low depth modulation for tracking may be placed on the Package B beacon.

4.2.2 Tracking Sensitivity

4.2.2.1 Tracking on Baseband Signals

The analysis in this section uses many of the results of Lopez (Ref. 6). Figure 10 shows the focal image slightly off-track from the apex of the four quadrants of the dissecting prism. Each quadrant detector puts out a dc current of $M_1 I_1$, where I_1 is the photocurrent and M_1 is the amplification of quadrant current. These currents have associated noise, discussed in the next section. The total field of view is θ_{FOV} , and a tracking error along one axis of $\delta\theta$ is assumed. It is convenient to refer to input angle space, which can easily be related to image space by multiplying by the effective focal length.

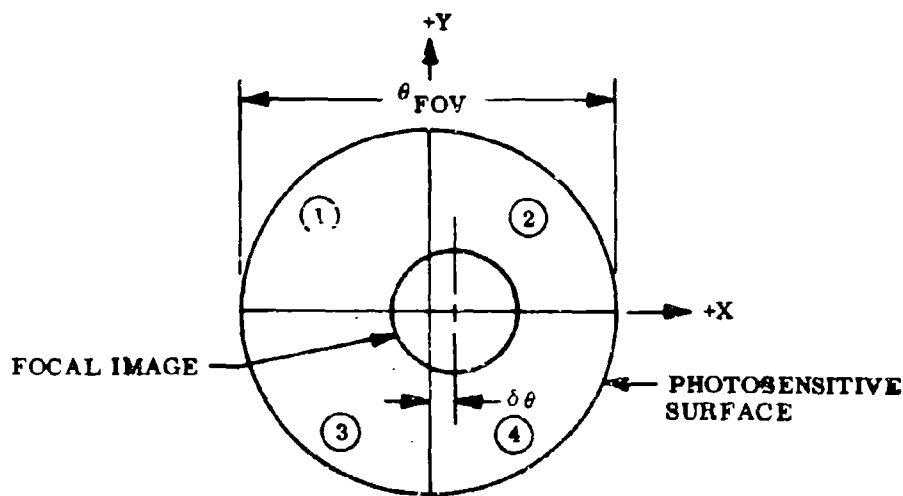


Fig. 10 Quadrant Detector Tracking Technique

The dc error current signals, I_X and I_Y , in the X and Y directions, are generated by

$$\left. \begin{aligned} I_X &= M_2 I_2 + M_4 I_4 - M_1 I_1 - M_3 I_3 \\ I_Y &= M_1 I_1 + M_3 I_3 - M_2 I_2 - M_4 I_4 \end{aligned} \right\} \quad (4.1)$$

During the boresighting operation before acquisition, automatic gain control circuits make $M_1 = M_2 = M_3 = M_4 = M$ by flood illuminating the quadrant detectors. Since the X and Y axes are orthogonal, a one-axis analysis is given to relate I_X to $\delta\theta$.

The focal image of a diffraction-limited optical system has an angle dependence of intensity that is symmetric about the center of the pattern and follows the Airy function at an angle θ from the center:

$$\varphi(\theta) = \left[\frac{2J_1(\theta/\theta_0)}{(\theta/\theta_0)} \right]^2, \quad \text{and} \quad \theta_0 = \frac{\lambda}{\pi D} \quad (4.2)$$

where J_1 is the first-order Bessel function, λ is the wavelength of light, and D is the aperture diameter. Letting $\theta/\theta_0 = (x^2 + y^2)^{1/2}$, Eq. (4.2) can be written in Cartesian coordinates. If the θ_{FOV} is much larger than $2.4\lambda/D$, Eq. (4.2) is already normalized to unit area. Then I_X/MI_0 , the fractional error signal, is the fractional difference in the area of the Airy pattern on each side of the centerline, or

$$\frac{I_X}{MI_0} = \int_{-\delta\theta}^{\infty} L(x) dx - \int_{-\infty}^{-\delta\theta} L(x) dx \quad (4.3)$$

where

$$L(x) = \int_{-\infty}^{\infty} \varphi(x, y) dy \quad (4.4)$$

O-40

and

$$I_o = I_{1S} + I_{2S} + I_{3S} + I_{4S} \quad (4.5)$$

where I_{1S} is the total photocurrent due to signal (not including background or dark current).

The integrals in Eq. (4.3) have been expressed as a series expansion referred to by Lopez (Ref. 6). Only the first term is required for small errors, which gives

$$\frac{I_X}{MI_o} \approx \frac{16}{3\pi^2} \frac{\delta\theta}{\theta_o} \quad (4.6)$$

When the signal current contains an additive noise current having an rms value, I_n , then an rms equivalent noise angle ϵ_X due to noise in the X channels is present,

$$\frac{I_X + I_n}{MI_o} \approx \frac{16}{3\pi^2} \cdot \frac{\delta\theta + \epsilon_X}{\theta_o} \quad (4.7)$$

For uncorrelated noise on the X and Y channels, the total noise angle $\epsilon = (\epsilon_X^2 + \epsilon_Y^2)^{1/2} = \sqrt{2} \epsilon_X$, so that

$$\epsilon \approx \frac{3\sqrt{2}\pi^2}{16} \frac{\theta_o I_n}{MI_o} = 0.83 \frac{\lambda}{D} \frac{I_n}{MI_o} = 0.83 \frac{\lambda}{D} \left(\frac{S}{N}\right)_p^{-1/2} \quad (4.8)$$

Here $(S/N)_p$ is an equivalent signal-to-noise power ratio defined as $(MI_o/I_n)^2$. This can be determined from the total dc signal power, S_p , where

$$S_p = (MI_o)^2 R \quad (4.9)$$

which is the average dc signal power due to radiation signal power P_R incident on all four quadrants. Note that if data modulation is already impressed on the incoming radiation via polarization modulation, and a polarizer is in front of the tracking detector, then P_R is only one-half of that P_R present without modulation. However, for unpolarized background radiation, P_B is also one-half of that without the polarizer. Note that S_p can be written in terms of P_R or K_S ,

$$S_p = M^2 \left(\frac{e\eta_D}{h\nu F_D} \right)^2 P_R^2 = \frac{M^2 e^2 K_S^2 R}{t_R^2} \quad (4.10)$$

where the symbols are as previously defined.

The noise power is the sum of shot noise and Johnson noise from all four quadrants. Neglecting Johnson noise,

$$\begin{aligned} N_p &= I_n^2 R = 2eM^2 I_{av} B_o R = 2eM^2 (I_o + I_B + I_D) B_o R \\ &= 2M^2 e \left[\left(\frac{e\eta_D}{h\nu F_D} \right) (P_R + P_B) + I_D \right] B_o R = 2M^2 e \left[\frac{e(K_S + K_B)}{t_R} + I_D \right] B_o R \end{aligned} \quad (4.11)$$

For $t_R = 1/(2B_o)$ and I_D included in an equivalent P'_B and K'_B ,

$$\left(\frac{S}{N} \right)_p = \frac{(\eta_D/h\nu F_D) P_R^2}{2(P_R + P'_B) B_o} = \frac{K_S^2}{K_S + K'_B} \quad (4.12)$$

4.2 2.2 Tracking on a Modulated Signal

Design of the system to track on a modulated incoming signal reduces the chance of successful jamming. During fine tracking, there is already a modulation on the signal

due to either the high- or the low-data-rate communication system. Since the modulation rate or format is not always suitable for the tracking system, an additional intensity modulation of about 5% modulation depth may be used for tracking. The frequency of the modulation must be much higher than the tracking loop bandwidth. The receiver then amplifies and detects the modulated signal to obtain an error signal.

If the peak-to-peak depth of sinusoidal intensity modulation is mP_R , where P_R is the peak power received, then the error signal amplitude before detection is $(m/2)I_X$, where I_X is the equivalent unmodulated error signal. The rms equivalent angle error is that due to rms noise on the output of the synchronous detector, and is given by Eq. (4.8), with MI_0 interpreted as the synchronous detector dc output with all the signal in one hemisphere. The $(S/N)_p$ in Eq. (4.8) is the output signal-to-noise ratio in bandwidth B_0 . For synchronous detection, or high S/N , this equals the input S/N , or

$$\left(\frac{S}{N}\right)_p = \frac{m^2(\eta_D/h\nu F_D)P_R^2}{16[(P_R/2) + P_B]B_{SC}} = \frac{m^2K_S^2}{8(K_S + 2K'_B)} \quad (4.13)$$

In this equation, P_R is the peak input power on the detector and B_{SC} is the bandpass filter bandwidth, with $K_S = (\eta_D/h\nu F_D)P_R t_R$, where $t_R = 1/B_{SC}$.

4.3 IMAGE DISSECTOR DETECTOR TRACKING

4.3.1 Tracking Error Signal Generation

At the end of the acquisition sequence using an image dissector detector, the focal spot on the cathode generates photoelectrons which are directed by the electromagnetic deflection fields through the small mask in the detector. The fields immediately start a small cyclic variation so as to dither the electron stream through the mask, which then generates a tracking signal. In addition, the dc value of the field moves to its boresight plus point-ahead position. The fast tracking mirrors receive the error

signal and maintain the received radiation signal on the sensitive position on the photocathode, i.e., at the projection of the mask on the cathode.

The error signal can be generated by either a cruciform or circular dither motion of the projection of the electron mask on the cathode. Maximum tracking sensitivity is obtained with a circular motion that is shown in Fig. 11. Such motion is obtained with quadrature signals of frequency f_t driving the orthogonal deflection plates. Frequencies above 10 kHz are easily achieved. Figure 11 shows the situation when a small tracking error $\delta\theta$ exists.

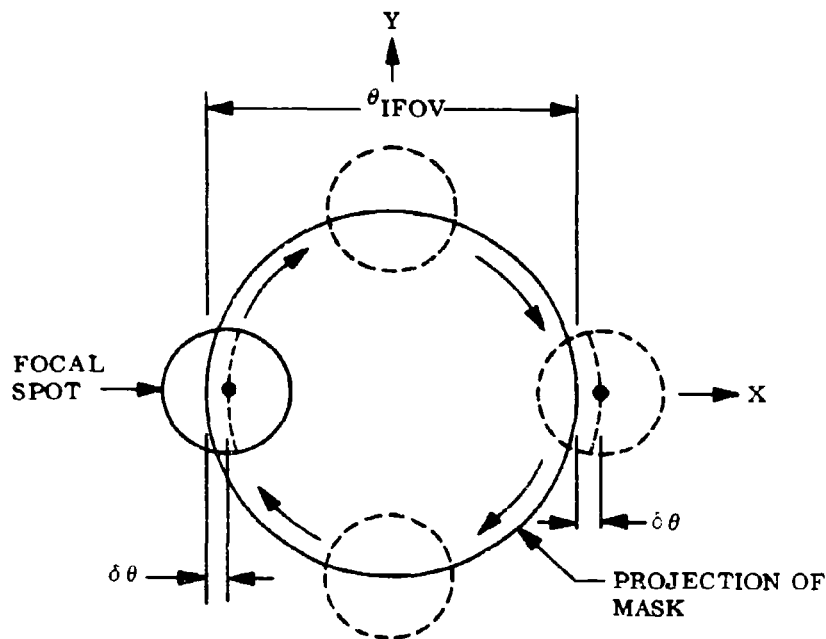


Fig. 11 Image Dissector Tracking Motion. The deflection fields actually rotate the projection of the mask about the focal spot, but that is equivalent in relative motion to the focal spot moving

An angular tracking error causes an error signal at frequency f_t to be generated. That signal is coherently detected by cross-correlation with the deflection dither drive voltage. Correlation is performed in two parallel channels using each of the quadrature driving signals in order to obtain both X and Y axis error signals. Tracking loop gain must be sufficient to keep $\delta\theta$ to a small fraction of the focal spot size, since not only is high tracking accuracy desired but also the incoming signal may be used to carry low-data-rate signals.

The incoming signals may be either modulated for tracking or effectively unmodulated as far as the tracking system is concerned. If a modulated tracking signal is used to reduce the possibility of jamming or false tracking, its modulation frequency must be considerably higher than the dither frequency. Note, however, that the instantaneous field of view may be kept sufficiently small (≤ 4 arcsec) so that jamming of the tracking signals becomes extremely difficult, even without using beacon coding or modulation.

4.3.2 Tracking Sensitivity and Signal-to-Noise Calculation

The amplitude of the sinusoidal error signal, I_X , is determined in the same manner as it was for the quadrant detector if the curvature of the field mask is neglected. However, quadrant signal differences are not being taken, so the amplitude is half that given by Eq. (4.6):

$$\begin{aligned} I_X(t) &\approx \left(\frac{8}{3\pi} \cdot MI_0 \cdot \frac{\delta\theta}{\theta_0} \right) \sin 2\pi f_t t \\ &= I_{X0} \sin \omega_t t \end{aligned} \quad (4.14)$$

where MI_0 is the dc current present if the spot was centered on a large hole and $\theta_0 = \lambda/\pi D$ as before.

The error signal, $L_X(t)$, is synchronously detected, i.e., cross-correlated with a sine wave and averaged over many cycles, to provide the tracking loop error current, I_e :

$$I_e = \frac{1}{t_R} \int_0^{t_R} I_{X0} \sin^2 \omega_1 t dt = \frac{1}{2} I_{X0} = \frac{4}{3\pi^2} (MI_0) \frac{\delta \theta}{\theta_0} \quad (4.15)$$

for a unit amplitude correlation function. The rms angular error, ϵ , arising from the noise on I_e on both axes is

$$\epsilon = \frac{3\pi^2}{4} \sqrt{2} \left(\frac{I_{ne}}{MI_0} \right) \theta_0 \quad (4.16)$$

when I_{ne} is the rms noise on I_e .

In correlation detection, it can be shown that the output noise power is one-half of the input noise power for a unit correlation function and white Gaussian noise input. Therefore,

$$I_{ne} = 2^{-1/2} I_{n(input)} = 2^{-1/2} M(2eI_{av} B_{SC})^{1/2} \quad (4.17)$$

neglecting Johnson noise. Here

$$I_{av} = M \left(\frac{I_0}{2} + I_B + I_D \right) \quad (4.18)$$

Defining the signal-to-noise power ratio at the input as the dc power if the input light was centered to the rms noise power during tracking, or

$$\left(\frac{S}{N} \right)_p = \left(\frac{MI_0}{I_n} \right)^2 \quad (4.19)$$

then ϵ can be written in terms of $(S/N)_p$:

$$\epsilon = \frac{3\pi^2}{4} \theta_o \left(\frac{S}{N} \right)_p^{-1/2} = 2.36 \left(\frac{\lambda}{D} \right) \left(\frac{S}{N} \right)_p^{-1/2} \quad (4.20)$$

The calculation of $(S/N)_p$ can be performed in terms of (P_R, P_B) or (K_S, K_B) using Eqs. (4.17), (4.18), and (4.19):

$$\left(\frac{S}{N} \right)_p = \frac{(\eta_D/h\nu F_D) P_R^2}{(P_R + 2P'_B) B_{SC}} = \frac{K_S^2}{K_S + 2K'_B} \quad (4.21)$$

where P_R is the received power with the focal spot in the center of the aperture,

$K_S = (\eta_D/h\nu F_D) P_R t_R$, $K'_B = (\eta_D/h\nu F_D) P'_B t_R$, and $\tau_R = 1/B_{SC}$.

If the incoming signal is modulated for tracking purposes at a frequency much higher than the dither frequency, the signal-to-noise is degraded. For a modulation depth m resulting in a peak-to-peak intensity variation of mP_R , the signal power is reduced by $m^2/8$ and the average signal power is $P_R/2$. Thus,

$$\left(\frac{S}{N} \right)_{p_{\text{input mod}}} = \frac{m^2 (\eta_D/h\nu F_D) P_R^2}{8[(P_R/2) + 2P'_B] B_{SC}} = \frac{m^2 K_S^2}{4K_S + 16P'_B} \quad (4.22)$$

4.3.3 Comparison of Tracking Detectors

The comparison of the quadrant detectors and the image dissector detectors may be expressed by defining:

- ϵ_q = rms noise angle for a quadrant detector
- ϵ_i = rms noise angle for the image dissector
- K_{Bq} = background counts in t_R for a quadrant detector
- K_{Bi} = background counts in t_R for an image dissector

Then for the same K_S received,

$$\frac{\epsilon_i}{\epsilon_q} = 2\sqrt{2} \left(\frac{K_S + 2K_{Bi}}{K_S + K_{Bq}} \right)^{1/2} \quad (4.23)$$

In the system situation where background is negligible, $(\epsilon_i/\epsilon_q)_1 \approx 2\sqrt{2}$, whereas if background is most important, $(\epsilon_i/\epsilon_q)_2 \approx 4(K_{Bi}/K_{Bq})^{1/2}$. This basis of comparison shows the quadrant detector to be better by $2\sqrt{2}$ in rms error angle when no background is present. However, when background is important, the comparison depends on the relative fields of view of the quadrant detector versus the image dissector. If an aperture can easily be used with the quadrant detector so its FOV matches the image dissector, an advantage of 4 exists. However, if the FOV of the quadrant detector is more than a factor of 4 greater in angular diameter than the IFOV of the image dissector, the tracking advantage will swing to the image dissector in the high background case.

The image dissector photomultiplier has possible advantages in size over the combination of a prism beam splitter, lenses, and a four-quadrant photomultiplier. The physical sizes of the tubes themselves are roughly comparable when four dynode structures are used in the quadrant detector.

Another important consideration is the case of implementing a point-ahead angle from the boresight position. This can be done by setting an electrical bias on the deflection plates of the image dissector but will require an extra steering optical element for the quadrant detector. Since electronic controls are usually preferred over electro-mechanical controls, this factor favors the image dissector.

Considering all factors, if the system can be designed to have sufficient link margin for the desired rms noise angle, an image dissector appears to be preferable.

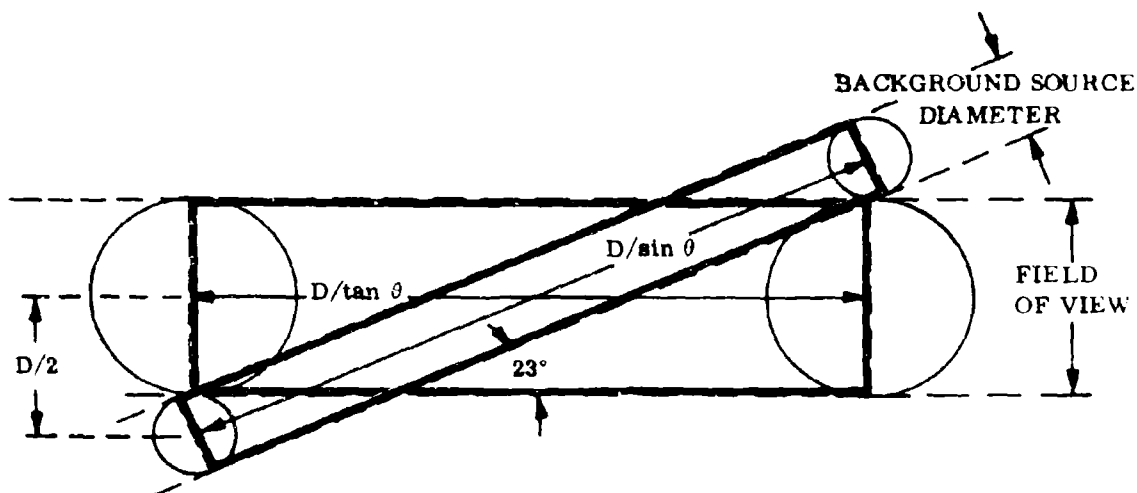
Section 5
PROBABILITY OF THE SUN OR MOON IN THE BACKGROUND
DURING ACQUISITION

Acquisition with a solar background is acknowledged to be impossible within the present state-of-the-art and acquisition with a lunar background may also be quite a problem. A pertinent question is whether these two backgrounds appear with sufficient probability to be significant in delaying acquisition.

In geocentric coordinates, the sun and the moon sweep a swath $1/2^\circ$ wide around the celestial sphere in the plane of the ecliptic. The sun does this in a year and the moon in a lunar month. A synchronous satellite, viewed directly overhead from earth, traces a complete path around the celestial sphere in the equatorial plane once each day. It is desired to determine the probability that the sun or the moon will be in the field of view of a low-altitude user pointing at the synchronous satellite in an attempt to acquire.

The low-orbiting satellite, in its orbits around the earth, can be anywhere up to about 12° from the nadir of the synchronous satellite. Its field of view, therefore, will see the sun or moon only when they are within 12° of the equatorial plane. Since 12° is scarcely more than half of the 23° angle between the ecliptic and equatorial planes, this determines that the sun or moon will be visible only during the time when they are within 30° ($30^\circ = \sin^{-1} 0.5$) in their apparent orbits of the two points where their orbits go through the equatorial plane, or a total of 120° , which is one-third of the total time.

The 1° field of view of the receiver, if pointing at the synchronous satellite, sweeps a swath 1° wide crossing the ecliptic of the sun or moon twice a day. Their relationship is shown in Fig. 12. Swaths for the sun or moon and for the receiver field of view are shown. The sun and moon can be considered to move so slowly in the celestial coordinates



$$D = \text{FOV} + \text{BACKGROUND SOURCE DIAMETER}$$

$$\theta = 23^\circ$$

	Background Source Swath Length $D/\sin \theta$	Receiver Swath Length $D/\tan \theta$
FOV $\approx 1^\circ$		
BSD $\approx 1/2^\circ$	3.84°	3.53°
D $\approx 1-1/2^\circ$		
FOV $\approx 1^\circ$		
BSD $\approx 2-1/2^\circ$	8.95°	8.23°
D $\approx 3-1/2^\circ$		
FOV $\approx 0^\circ$		
BSD $\approx 2-1/2^\circ$	6.4°	6.9°
D $\approx 2-1/2^\circ$		
FOV $\approx .4^\circ$		
BSD $\approx .5^\circ$	2.2°	2.22°
D $\approx .9^\circ$		

Fig. 12 Intersection of Field of View With Sun and Moon as Background Sources

that for a given crossing their position is fixed. The receiver field of view, however, sweeps across at a much faster rate.

For this approximate analysis, it is considered that the pointing direction and the ecliptic cross at an angle of 23° . If either the sun or the moon is anywhere in the 3.84° segment shown, it will be seen by the field of view during a 3.53° long segment of the field-of-view swath. These considerations lead to the following factors:

- The sun and moon are possibly visible only one-third of the time (120° of its 360° revolution).
- They must be within a particular 3.84° segment of their 360° swath (3.8 days twice a year for the sun and 7 hr twice a month for the moon).
- The field of view must be centered within a particular 3.53° segment of its 360° swath (possibly 14.6 min/day).
- The two swaths intersect twice.

$$P = (3.84/360) \times (3.53/360) \times 2 = 2.1 \times 10^{-4}$$

When the field of view sees the moon in the background, it will stay in the background for a maximum of $(1^\circ + 0.5^\circ) (4 \text{ min/deg}) = 6 \text{ min}$, and only about 4 min on the average. Thus, if the system will not acquire with moon background, it will not be able to acquire about $(4 \text{ min}/1440 \text{ min}) \times 3.84/360 \times 2 = 0.59 \times 10^{-4}$ of the time. During 14 hr/month it will not acquire $(4/1440) = 2.7 \times 10^{-3}$ of the time.

The sun is a greater problem due to flare in the optical system. If the optics is designed to point within 1° of the sun, the apparent diameter of the sun becomes 2.5° . The apparent sun diameter results in a sun intersection range of 8.95° , and a field-of-view intersection range of 8.23° . Thus, the probability of intersection is $2(8.95/360) (8.23/360) = 1.14 \times 10^{-3}$. It will stay in the background for 3.5° or 14 min maximum and about 10 min average. Thus, for 8.95 days twice a year the sun can be in the background, and for 10 min per day during those days no acquisition can take place. Thus, acquisition will be stopped by the sun 3.4×10^{-4} of the time.

For the very narrow field of view present during communications, a 2.5° apparent sun diameter can be in the background for 6.4° of each satellite orbit, and this can happen for 5.9° in the sun's orbit, or 5.8 days twice a year. On those days the communications will be down for $2.5^\circ \times 4 \text{ min}/^\circ = 10 \text{ min}$ on each orbit. The fractional down time is thus $2 (2.5/360) (5.9/360) = 2.2 \times 10^{-4}$ average over a year, but is $2.5/360 = 7 \times 10^{-3}$ on 11 days per year. These statements are true for all links looking toward space.

The problem is very similar for a synchronous satellite acquiring another synchronous satellite with 0.4° field of view and moon background. In this case, the smaller field of view means that the intersection length of the swath swept by the field of view and the 0.5° band of the ecliptic is 2.22° for the synchronous satellite and 2.20° for the moon. Therefore, the probability of the moon being in the intersection region, which occurs twice for each orbit, is $2 \times (2.20/360) (2.22/360) = 0.75 \times 10^{-4}$. However, it stays in the background for only $0.9^\circ \times 4 \text{ min}/^\circ = 3.6 \text{ min}$. Therefore, the fractional down time is only $2 (0.9/360) (2.22/360) = 3.1 \times 10^{-5}$.

After the preparation of this analysis, attention was called to a more thorough analysis of the solar proximity problem which was performed by D. Martin of the Aerospace Corporation (Ref. 7). His analysis was performed by computer and covered a greater variety of configurations over a considerable range of angular separations between the lines-of-sight to the transmitter and to the sun. The LMSC data, prepared only for very small off-axis angles, are in close agreement with Martin's results, lying either within the range of his values or being slightly more pessimistic.

Section 6
REFERENCES

1. M. Abramowitz and I. A. Stegun, eds., Handbook of Mathematical Functions, National Bureau of Standards Applied Math. Series No. 55, Nov 1967
2. G. F. Herrmann, Poisson Noise and Error Probability in Optical Communications Using Biphase Modulated Subcarriers, LMSC-D179095, Jun 1971
3. A. D. Whalen, Detection of Signals in Noise, Academic Press, New York, 1971, pp. 196-205
4. Ibid., Fig. 7-5, p. 205
5. W. K. Pratt, Laser Communication Systems, John Wiley & Sons, New York, 1969, p. 180
6. J. M. Lopez, Deep Space Laser Communication Study - Acquisition and Tracking Subsystem Evaluation, Aerospace Corporation Report TOR-0059(6312-02)-2, Jan 1971
7. D. Martin, "Solar Proximity to the LSCS Receiver Optical Axis," Interoffice Correspondence 71.1830.5-18, The Aerospace Corporation, 29 Apr 1971

O-53

LOCKHEED PALO ALTO RESEARCH LABORATORY
LOCKHEED MISSILES & SPACE COMPANY
A GROUP DIVISION OF LOCKHEED AIRCRAFT CORPORATION

Appendix P

SATELLITE ATTITUDE UNCERTAINTY
USING HORIZON SENSORS

by

Mr. G. R. Chippendale

Mr. W. G. Uplinger

(Revision of Technical Memorandum No. 6)

LOCKHEED PALO ALTO RESEARCH LABORATORY
LOCKHEED MISSILES & SPACE COMPANY
A GROUP DIVISION OF LOCKHEED AIRCRAFT CORPORATION

Part I

ATTITUDE DETERMINATION FOR LASER LINK ACQUISITION

Determination of the attitude of a satellite generally entails the use of horizon sensors. Inasmuch as this uncertainty regarding attitude plays a major role in the initial pointing problem for an optical communication system, it is important to plan for the best possible accuracy that can economically be obtained. This has led to a review of the available horizon sensor systems.

The results indicate that a slight improvement over the guideline values might be expected for the relay satellite, and probably none initially for the low-orbiting user. However, there is the possibility that tracking information after the first acquisition, which might be a special case, can be used to improve the uncertainty in the LOS attitude by correcting bias errors, and thus make subsequent acquisitions in a shorter time. It has been noted, but not analyzed in this memorandum, that there are favorable positions, at zenith and nadir, where yaw uncertainty is of little consequence; initial acquisition in a minimum time would be favored in these positions.

Synchronous Spacecraft

The attitude determination of the synchronous spacecraft for earth-pointing purposes is simplified by the fact that the line-of-sight to a low-altitude spacecraft is less than 12° from the spacecraft nadir. Only 30° from nadir is required to see an equally spaced far-relay satellite. These small angles reduce the importance of yaw accuracy and allow a pitch and roll earth horizon sensor to provide the primary attitude information for attitude sensing.

Earth horizon sensors with a 3σ accuracy of 0.05° about the pitch and roll axes are available for synchronous-altitude satellites. (See Part II.) Assuming that the

misalignment errors can be less than 0.05° , 3σ and that there is a source of azimuth information with an accuracy of $\pm 0.2^\circ$, 3σ (as stated in the guidelines), line-of-sight attitude knowledge shown in Table 1 can be achieved for a synchronous spacecraft.

Table 1
LINE-OF-SIGHT ERROR FOR A SYNCHRONOUS SPACECRAFT

Source	Pointing to Low-Altitude Spacecraft	Pointing to Other Synchronous Spacecraft
Horizon Sensor	$\sqrt{2} \times 0.05$	$\sqrt{2} \times 0.05$
Misalignment Errors	$\sqrt{2} \times 0.05$	$\sqrt{2} \times 0.05$
Azimuth Uncertainty	$0.2 \times \sin 12^\circ$	$0.2 \times \sin 30^\circ$
Total RSS (3σ)	$\pm 0.11^\circ$	$\pm 0.14^\circ$

The beamwidth or scan pattern for the transmitter should provide this coverage, plus an additional amount to account for the contribution of satellite position uncertainty.

In the case of a spin-stabilized spacecraft, the frequency of the inevitable nutation from bearing runout may be higher than the bandwidth of the horizon sensor, which approximates 1 Hz. The amplitude of this nutation is on the order of 0.01° .*

Low-Altitude Spacecraft

The accurate determination of attitude is more difficult for a low-altitude spacecraft because of the shorter distance to the earth horizon and because azimuth position, which is generally determined by gyrocompassing, plays a more important part in the pointing.

*A. W. Merrill and D. H. Martin, Laser Space Communication System Conceptual Design, TOR-0059(6312)-3, The Aerospace Corporation, p. 3-3.

An approach to the attitude determination problem is to estimate the vehicle attitude using the normally available gyro and horizon sensor outputs. The gyros provide short-term incremental attitude information with relatively high precision (≈ 1 arc-min), and with a low rate of change of average attitude error (less than $2^\circ/\text{hr}$).

The onboard computer solves for the attitude using the conventional gyrocompass approach with an accuracy given approximately by

$$\begin{aligned} \text{azimuth error} &= \sqrt{\left[U(\dot{\phi}_g)\right]^2 + \left[U\left(\frac{\omega_{g_x}}{\omega_o}\right)\right]^2 + \left[U(\phi_{H/S})\left(\frac{S_r}{S_y}\right)\right]^2 + \left[U\left(\frac{\omega_{g_z}}{\omega_o}\right)\frac{S_r}{S_y}\right]^2} \\ \text{roll error} &\cong \sqrt{\left[U(\phi_{H/S}) \times \left(\frac{S_y/\omega_o}{1 + S_y/\omega_o}\right)\right]^2 + \left[U(\phi_g)\right]^2} \quad \begin{array}{l} \text{if measurement is} \\ \text{required during gas} \\ \text{jet transient} \end{array} \\ &\cong U(\phi_{H/S}) \quad \text{if no gas jet transients are present} \\ \text{pitch error} &\cong \sqrt{\left[U(\theta_{H/S})\right]^2 + \left[U(\theta_g)\right]^2} \quad \begin{array}{l} \text{if measurement is} \\ \text{required during gas} \\ \text{jet transient} \end{array} \\ &\cong U(\theta_{H/S}) \quad \text{if no gas jet transients are present} \end{aligned}$$

where

$$\begin{aligned} U\left(\omega_{g_x}\right) &= \text{roll gyro drift - includes component of orbit rate due to gyro misalignment} \\ U\left(\omega_{g_z}\right) &= \text{yaw gyro drift - includes component of orbit rate due to gyro misalignment} \\ \omega_o &= \text{orbit rate} \\ U(\phi_{H/S}) &= \text{roll horizon sensor error - includes misalignment} \\ U(\theta_{H/S}) &= \text{pitch horizon sensor error - includes misalignment} \\ S_r &= \text{roll gyrocompass gain} \end{aligned}$$

- S_y = yaw gyrocompass gain
 $U(\psi_g)$ = gyro yaw incremental angle accuracy
 $U(\phi_g)$ = gyro roll incremental angle accuracy
 $U(\theta_g)$ = gyro pitch incremental angle accuracy

Using the following typical values, including estimates of the 3σ uncertainties and systematic errors for current low-altitude vehicles, the advantage of solving for the systematic errors is evident.

<u>Gyro Drift</u>	$U(\omega_{g_x})$, $U(\omega_{g_z})$
Bias Drift:	1.5°/hr
Orbit Rate Component (0.25 rad misalignment \times 240°/hr):	0.6°/hr
Random Drift (Drift Stability):	0.3°/hr
$U(\omega_{g_x})$, $U(\omega_{g_z})$ =	1.62°/hr systematic + 0.3°/hr random

Horizon Sensor Error

Misalignment:	0.10°
Random Horizon Uncertainty:	0.15°
Systematic Horizon Error:	0.2°
Horizon Sensor Random Error:	0.1°
$U(\phi_{H/S})$ = $U(\theta_{H/S})$ =	0.224° systematic + 0.18° random

Incremental Angle Readout From Gyro

$$U(\theta_g) = U(\phi_g) = U(\psi_g) \cong 1 \text{ arcmin}$$

$$S_r = 0.3^\circ/\text{min}/\text{deg} = 17.2^\circ/\text{min}/\text{rad}$$

$$S_y = 1^\circ/\text{min}/\text{deg} = 57.3^\circ/\text{min}/\text{rad}$$

$$\omega_o = 4^\circ/\text{min}$$

One can solve for the azimuth, roll, and pitch errors before and after bias correction.
(See Table 2.)

Table 2
SUMMARY OF ATTITUDE ACCURACY DETERMINATION CAPABILITY
FOR LOW-ALTITUDE SPACECRAFT
(3 σ Values)

<u>Before First Acquisition</u>		
Knowledge of Attitude (deg)		Knowledge of Change in Attitude (arcmin) for Up to 10 sec of Time
Azimuth	0.50	≈ 1
Roll	0.40	≈ 1
Pitch	0.40	≈ 1
<u>After Determination of Systematic Errors</u>		
Azimuth	0.10	≈ 1
Roll	0.20	≈ 1
Pitch	0.20	≈ 1

Attitude rate knowledge is needed to aid acquisition if the vehicle residual rates are higher than 25°/hr. The vehicle rate is estimated using the vehicle gyros. Both the torquer inputs to and the outputs from the gyros are processed. A 3- σ accuracy of 25°/hr should be obtainable with a 2-sec time constant filter.

The gas jet system is shut off after the initial open-loop antenna alignment is completed and remains off until each transmitter has acquired the narrow, high-power beam. The total off time could be as much as 15 sec. An additional 1° of beam deflection by the outer loop gimbals would take care of the extra vehicle motion, assuming a very high vehicle rate of 240°/hr.

The time interval over which the systematic errors are predictable after loss of acquisition is not established. The earth horizon systematic error is a function of orbit position and would not be predictable for more than $\sim 40^\circ$ of orbit without special curve-fitting approaches. Acquisitions that are less than 10 min apart could make use of the reduced attitude uncertainty due to knowledge of systematic errors.

Part II
HORIZON SENSOR PERFORMANCE

Introduction

Earth horizon sensors have been used on most orbiting spacecraft because they provide a convenient means for obtaining the local vertical. In many applications horizon sensors are part of an active attitude-control system. The output signals of the horizon sensors give the spacecraft attitude with respect to the local vertical in terms of pitch and roll angles. Vehicle altitude can also be obtained from the subtended angle of the earth. No yaw information is obtained. The latitude or longitude over which the spacecraft is flying also cannot be ascertained. Early horizon sensors did not perform as expected because of various problems resulting from a lack of knowledge of the radiation emitted by the Earth. Interference from the sun and moon was also a problem. Improvements in signal processing and the choice of a better spectral region have resulted in operational horizon sensors that are not subject to the gross errors of the earliest horizon sensors. Introductory material on horizon sensors is contained in references (1) and (2).

Present day horizon sensors can be divided into two classes. Horizon scanners scan a large volume of object space with a fixed scan pattern. Examples are conical scanners and horizon crossing indicators on spinning vehicles. Signals are generated when the field of view crosses the horizon. Horizon trackers drive the field of view to the horizon. In one form the field of view is dithered across the horizon. Alternatively, a static array of detectors is driven to produce a desired output.

A brief description of some current horizon sensors and a summary of their technical specifications will be presented here. Both low altitude and synchronous orbit horizon sensors will be discussed.

LAHS

A technical comparison of five horizon sensors for low altitude use is given in Table 1. The LMSC Low Altitude Horizon Sensor (LAHS) is based on the synchronous orbit Dual Scan Horizon Sensor (DSHS). The LAHS is designed in a single sensor head per axis (pitch or roll) configuration. The sensor heads for both axes will be identical, self-contained, and independent. Each head contains a scanning double-faced mirror and two optical systems, one for each face of the mirror. The optical system has a 1.1 degree square field of view and, like all the other horizon sensors discussed, operates in the 15 micron CO_2 absorption band. The mirror scans opposite horizons simultaneously with a torsion bar suspension. An optical shaft encoder on the mirror measures the angles to the two horizons. The difference is proportional to the vehicle attitude. A horizon signal is generated only on the space-to-earth portion of the scan to minimize errors due to variations in shape of the horizon profile near the peak. Signal processing is based on a percentage of peak threshold. The accuracy is estimated from analysis since no unit has been built.

TRW A-OGO

The TRW A-OGO is a horizon tracker developed for use in highly eccentric orbits. The system consists of two dual-tracker heads and a central electronic unit. The four trackers generate analog signals representing the elevation angle of the horizon from the yaw axis of the spacecraft.

Pitch and roll information can be obtained from only three of the four trackers, which improves reliability and allows operation with the sun on the horizon. The tracker field of view (1.2 degrees) is caused to oscillate at 19 hertz with an amplitude of 2.5 degrees peak-to-peak in the tracker plane. A servo loop drives the tracker until the horizon is at the center of the dither. The heart of the tracker is a device called a Positor which rotates or dithers a mirror and provides an accurate readout of the mirror position. The Positor consists of a rotor assembly suspended on flexure pivots. Precision readout is provided by drive coils on the rotor and field coils on the stator. A flight model has been delivered but not flown.

Quantic Mod IV

The Quantic Mod IV horizon sensor is a horizon tracker with no dithering parts. A system usually consists of four independent trackers and one electronics unit. The fourth tracker allows operation with the sun on the horizon and improves reliability. The tracking mirror is mounted on a base plate with crossed bimetal springs. The crossed-spring arrangement allows the mirror to rotate about the crossover point. The springs are heated electrically to drive the mirror. An optical encoder reads the angle of the mirror without reference to the current being supplied to the springs. The optical system images the horizon on a four-segment infrared light-pipe assembly. The light pipe divides the field of view into four rectangular portions and channels the radiation into four separate detector arrays. The electrical signal from the two outside arrays is subtracted from the signal from the two inside arrays to drive the tracking

mirror. A flight model with three trackers has been flown. A report on this flight has not been issued, but preliminary results indicate an accuracy near that predicted by the analysis, except for an unexplained variation that may be due to a meteorological anomaly.

Barnes Conical Scan

The Barnes model 13-156 is a conical scanning system with two 20-degree half-angle scanners looking out in opposite directions. A signal is generated when the instantaneous field of view is over the Earth. A pitch signal is found from either head by comparing the center of the Earth pulse with a reference signal indicating the yaw axis. A roll signal is generated by comparing the lengths of the two Earth pulses.

The optical system has an off-axis primary mirror. The field of view is conically scanned by mounting the primary mirror on the rotor of a motor. The detector remains stationary on the stator. Each head is pressurized to assure long life for the moving parts. This horizon sensor is operational and flight data have been obtained.

Type 8

The LMSC Type 8 Earth Sensor is a horizon crossing indicator for a spinning spacecraft. The output provides a pulse proportional to the width of the Earth. The bandwidth of the electronics results in the pulse being delayed from the true Earth location. This delay is nearly constant over a wide range of input signal rise times. The variation in rise times is due to variations in the spin rate and changes in the horizon crossing angle as the spacecraft moves in orbit. The first unit has been delivered but no flight tests have been made.

The three synchronous orbit horizon sensors discussed here are similar but not exactly like their low altitude counterparts discussed previously. The Type 8 sensor can be used for spinning vehicles at synchronous orbit also.

Characteristics of the three horizon sensor systems are described in Table 2.

LMSC Dual Scan Horizon

The LMSC DSHS has been fully flight qualified. It is a scanning-type Earth sensor in which the field of view is scanned across the Earth in a straight line. Attitude is determined by comparing the angle between the first horizon crossing. To achieve the required off-axis performance, three detectors are scanned in each axis. There is one resonant oscillating mirror per axis; it scans the fields of view of three detectors simultaneously. Only one field of view scan is used to determine attitude, and the choice of the scan used is made by a field of view scan-selector circuit. The scan selection is dependent upon attitude and sun presence. Sun presence is detected by measuring target width and rejecting narrow targets. The system uses an optical encoder that is attached to the mirror to measure target widths. The output of the encoder is applied to an up-down counter that is gated by the horizon crossings and scan center. The residual count at the end of one complete scan is proportional to the attitude error. The Lockheed sensor has some design complexity because of the multiple detectors and preamplifiers; however, this also provides backup operational capability. For this, the LMSC system has a cross-axis attitude capability; i.e., the scans used for pitch attitude information can be used to provide roll attitude information, and vice versa. Incorporation of this capability provides attitude redundancy with minimum increased complexity. The error

analysis and testing that has been performed on the LMSC horizon sensor indicates an accuracy of ± 0.050 deg (3 sigma), including the effect of Earth radiance gradients if a calibration scheme for correcting or compensating for the radiance gradients is utilized. To extend the range an additional detector can be added to each axis. This sensor is called the DSHS-2.

Quantic Earth Sensor

The Earth sensor system (ESS) is a combination of a Quantic Industries static IR-horizon sensor system and dual-axis tracking-mirror assembly. These two components in combination establish a system capable of providing continuous off-null attitude measurement over the region of ± 12 deg of pitch and/or roll at synchronous altitude. The static sensor contains a ring of eight detectors which provide a null output when they are centered on the Earth. Due to radiance variations it is susceptible to errors at other than the design altitude. In the primary operating mode, the output of the basic static sensor is used to servo-control the angle of the dual-axis mirror so as to keep the earth image centered when the vehicle is off null. Vehicle attitude is then measured by sensing the mirror angles. The mirror position is readjusted by the output from the static sensor whenever the vehicle pitch or roll attitude changes; at all other times, the mirror is stationary. The static sensor contains separate sun sensors which switch in the proper set of detectors to avoid the sun.

The static sensor is a fully flight-qualified unit. One flight-configuration dual-axis mirror assembly has been fabricated and checked out and is currently being evaluated. Basically, this assembly consists of a front-

surfaced aluminum mirror mounted to a base structure via the unique two-axis cross-spring (flexure suspension) gimbal assembly.

The ESS is contained in two separate packages. One comprises the static sensor IR and sun telescopes and the dual-axis mirror assembly, thus permitting proper alignment of each subsystem with the other. This optical package also contains the preamplifiers. The second package comprises the signal processing, mirror drive/readout, and power supply circuits. A primary disadvantage is the requirement for a stable thermal sink. The present design is susceptible to thermal transients greater than 3 deg/hr. Quantic is investigating a new thermal housing design that is based on its low-altitude Mod IV sensor.

TRW Earth Sensor

In terms of general approach, the sensor is a "scan through" infrared scanner; i.e., a narrow optical field of view in the infrared spectrum is established and scanned through the earth in each axis. Attitude measurements are determined in each axis independently by comparing the angles at which the scan crosses the earth edges with the reference axis angle. A simple offset mechanism is provided to permit movement of the scan plane. This feature allows the earth sensor to provide precise angle measurement at spacecraft offset pointing angles of 10 or more degrees from the center of the earth. It also provides for automatic sun avoidance.

The complete earth sensor used to generate pitch and roll information consists of two sensor head units and a third package containing the processing electronics. Each sensor head unit is identical, and is mounted at right angles to allow scanning in orthogonal planes.

The scan rate is five scans per second over a total scan amplitude of 26 deg peak to peak. This amplitude allows a complete scan through the earth disc from synchronous orbit with adequate margin for scan turn-around and the establishment of a cold space reference level.

The center of the 26-deg scan can also be offset with a DC control bias voltage to allow scanning of the earth when it is offset from the vertical. The maximum amplitude of this offset is ± 11.25 deg.

When scanning, the mirror mechanism provides two sinusoidal readouts, which are used to develop a pulse output for each 0.044 deg of rotation of the sensor field of view. It also provides a reference pulse output each time the scan passes through a reference position.

As discussed above, both the scanning mirror and the offset mirror can be positioned by a DC bias voltage. Each of the two digital output signals representing the earth position with respect to the null reference planes is converted to an analog voltage in D/A converters. The analog output of the D/A converters is fed back to the offset mechanism as a bias voltage. This feedback keeps the scan pattern centered upon the earth disc, even though the spacecraft is offset from the local vertical. The voltage which is fed back to the scanning mirror to offset the scan center is also fed to the offset mirror mechanism of the other axis head to provide a deflection of the scan plane in that unit. Sun avoidance is provided by sensing the sun with a separate detector and shifting the scan with the offset mirror until the sun is out of the scan field of view.

Table 1

LOW ALTITUDE HORIZON SENSOR CHARACTERISTICS

<u>Parameter</u>	<u>LARS</u>	<u>Quantic</u>	<u>Barnes</u>	<u>TRW</u>	<u>Type 8</u>
Size (each head box)	5 x 5 x 8 in.	1340 W total	5 in long x 6 in dia 3 x 8 $\frac{1}{4}$ x 3 $\frac{3}{4}$ in. 935 W total	500 W total	3.1 x 4.3 x 5.5 in
Weight	10 lbs	18 lbs	25 lbs	19 lbs	1.4 lbs
Power	10 watts	20 watts	25 watts	19 watts	1.2 watts
Attitude Range	± 8 deg	± 10 deg	± 5 deg	± 30 deg	--
Altitude Range	80 - 2000 nm	80 - 25000 nm	80 - 1000 nm	120 - 80,000 nm	--
Scan	10 deg pk-pk sine 8 hz	Semi-static	40 deg cone 12.5 hz	2.5 deg Dither pk-pk 19 hz	Spin stabilized spacecraft
Development Status	Design 80% complete	One unit flowm	Operational	One unit de- livered but never flown	One unit deliv- ered but not yet flown

Table 2

SYNCHRONOUS ORBIT HORIZON SENSOR CHARACTERISTICS

<u>DSHS-2</u>		<u>Quantic</u>	<u>TRW Earth Sensor</u>
Size	4. 4.0 x 9.25 x 9.5 in.	Sensor 6 x 6 x 10 in. Electronics 4 x 5 x 7.5 in.	Head (two each) 6.55 x 6.75 x 4.2 in. Electronics 4.0 x 9.5 x 7.725 in.
Weight	10.0 lb	9.0 lb	13.4 lb
Power	12.0 W max	3 W	11.6 W max
Attitude Range	11.5 deg (8.0 deg DSHS-1)	12.0 deg	12.0 deg
Accuracy	± 0.05 deg	± 0.05 deg	± 0.05 deg
Altitude Range	± 5000 nm	± 300 nm	± 3000 nm
Scan	50° @ 4 Hz	12° DC	26° @ 5 Hz + 12° DC
Output	Series digital 0.01 deg/digit to 15 deg	Analog. Can provide A/D converter	16-bit binary word parallel output. 0.05°/bit
Temp Range	0° to 140°F	0° to 140° with temp rate 3°F/hr (temp sink required)	32° to 100°F
Redundancy	Yes 8×10^{-8} per hr plus redundancy	No	No
Development Status	DSHS-1 qualified	Static Sensor qualified. Mirror design fabricated and tested.	Developed and partial qual.

References

- (1) "Infrared Horizon Sensors" by Duncan, Wolfe, Oppel and Funn.
Institute of Science and Technology, University of Michigan,
April, 1965. (NAVSO P-2481).
- (2) "Spacecraft Earth Horizon Sensors" by J. H. Thomas et al. December,
1969. (NASA-SP-8033).

Appendix Q

SATELLITE STABILIZATION RECOMMENDATION
FOR LASER COMMUNICATION
PRELIMINARY SUBSYSTEM DESIGN

by
Mr. J. J. Rodden

(Previously distributed as Technical Memorandum No. 1)

LOCKHEED PALO ALTO RESEARCH LABORATORY
LOCKHEED MISSILES & SPACE COMPANY
A DIVISION OF LOCKHEED AIRCRAFT CORPORATION

SUMMARY

This appendix reviews the relative merits of three-axis stabilization and dual-spin stabilization systems for future synchronous communication satellites. It concludes that for many reasons the three-axis, or wheel-stabilized, satellite is the prime candidate over the dual-spin or body-spin stabilized satellite.

This analysis was made for a general synchronous communication satellite and not specifically for one to carry a laser communication subsystem. However, the arguments for the three-axis stabilization technique apply with even greater force to the specific case. For example, the improved attitude control and pointing alignment of three-axis stabilized satellites has a greater impact on laser acquisition and tracking than for relatively broad beam microwave communication links. Also, two Package A transmitters and three or four Package B receivers can readily be located physically on a three-axis wheel-stabilized satellite in such a way that the requirements on their viewing angles can easily be met without mutual or satellite body blockage of the field of view. Furthermore, they can be located relatively close to the heat radiators.

The physical configurations of possible locations and arrangements of the laser communication subsystem on both three-axis and dual-spin stabilized satellites are the subject of another report. However, based on preliminary designs and the conclusions of this appendix, LMSC suggests that a three-axis wheel-stabilized satellite is preferable for the synchronous relay satellite.

It is noted that NASA has chosen a three-axis stabilized design for its ATS-G satellite, which will carry a laser communication experiment.

Q-1

LOCKHEED PALO ALTO RESEARCH LABORATORY
LOCKHEED MISSILES & SPACE COMPANY
A GROUP DIVISION OF LOCKHEED AIRCRAFT CORPORATION

INTRODUCTION

Future communication missions will require increased rf channel capacity along with extended operational life and multipurpose applications. Two competing satellite design philosophies lead to systems with despun earth-pointing antennas and three-axis earth-pointing systems. Current communication satellites are spin stabilized. Considering the electrical power requirements to sustain increased communications capacity and the physical limitation on the number of solar cells that can be mounted on a spinning body drum, coupled with the physical complexity of multipurpose antennas, it is expected that three-axis wheel-stabilized satellites with sun-tracking solar arrays will be a prime candidate for future missions.

The three-axis stabilization systems using momentum and reaction wheels as control torque sources are considered to be the best choice on the basis of proven ability to meet life and accuracy requirements. A comparison of dual-spin and wheel-stabilized configurations involves consideration of each spacecraft subsystem. This appendix summarizes the findings of a tradeoff study performed at Lockheed Missiles & Space Company on these two satellite configurations.

ELECTRICAL POWER

The wheel-stabilized satellite has significant flexibility in array sizing to accommodate varying loads and features, either hardwiring of all power to the load or through slip-rings across a slow array drive system. The body-spin satellite has a solar array area limited in diameter and length with a separate battery-charging section, and requires a high-speed slip-ring/brush assembly between the array and the despun load.

Q-2

LOCKHEED PALO ALTO RESEARCH LABORATORY
LOCKHEED MISSILES & SPACE COMPANY
A GROUP DIVISION OF LOCKHEED AIRCRAFT CORPORATION

Flexibility of power requirements is inherent in the wheel-stabilized satellite. The extendible array can be designed to provide extra area per extension without further spacecraft modification except for matching the battery ampere-hours to the load. This arrangement enables easy adjustment of solar power to accommodate design changes. The body-spin satellite is severely limited in solar power flexibility, especially to increases in drum length. Since the drum and the enclosed equipment constitute the fly-wheel of a momentum device, any change in mass distribution severely affects the dynamic balance, center-of-gravity location, and bearing loads; therefore, redesign would be necessary to regain antenna pointing accuracy.

Power source weights for solar array and NiCd batteries as a function of the power requirement are shown in Fig. 1. For multikilowatt systems, the weight advantage of sun-tracking flexible substrate solar arrays is more than 10 to 1 over a cylindrical spin-stabilized system giving the same power. The brush and slip ring problem is significantly more severe for spinner systems. For a typical rotation of 60 rpm, more than 86,000 slip-ring rotations are required against one revolution of a sun-tracking system. Qualification testing has shown that slip-ring wear and resulting debris can be a major problem. Redundancy is more readily applied to the slower rotation system. A hard-wire recycling system can be used to eliminate slip-rings altogether if desired.

ATTITUDE STABILIZATION

The wheel-stabilization approach to attitude control features simple onboard equipment and onboard data processing, and gives accurate pointing without reliance on continuous ground station corrections. The wheel-stabilized satellite can be completely fail-safe through redundancy and backup systems, whereas the body-spin system has bearing failure modes leading to interruptions in communications and even permanent outage.

Both the wheel-stabilized and body-spin satellites maintain antenna beam pointing by means of gyroscopic stiffness and a nonspinning communication assembly. In the wheel-stabilized system, the entire spacecraft is despun with hermetically sealed single or multiple flywheels rather than an exposed despin joint. With the possible

Q-3

LOCKHEED PALO ALTO RESEARCH LABORATORY
LOCKHEED MISSILES & SPACE COMPANY
A GROUP DIVISION OF LOCKHEED AIRCRAFT CORPORATION

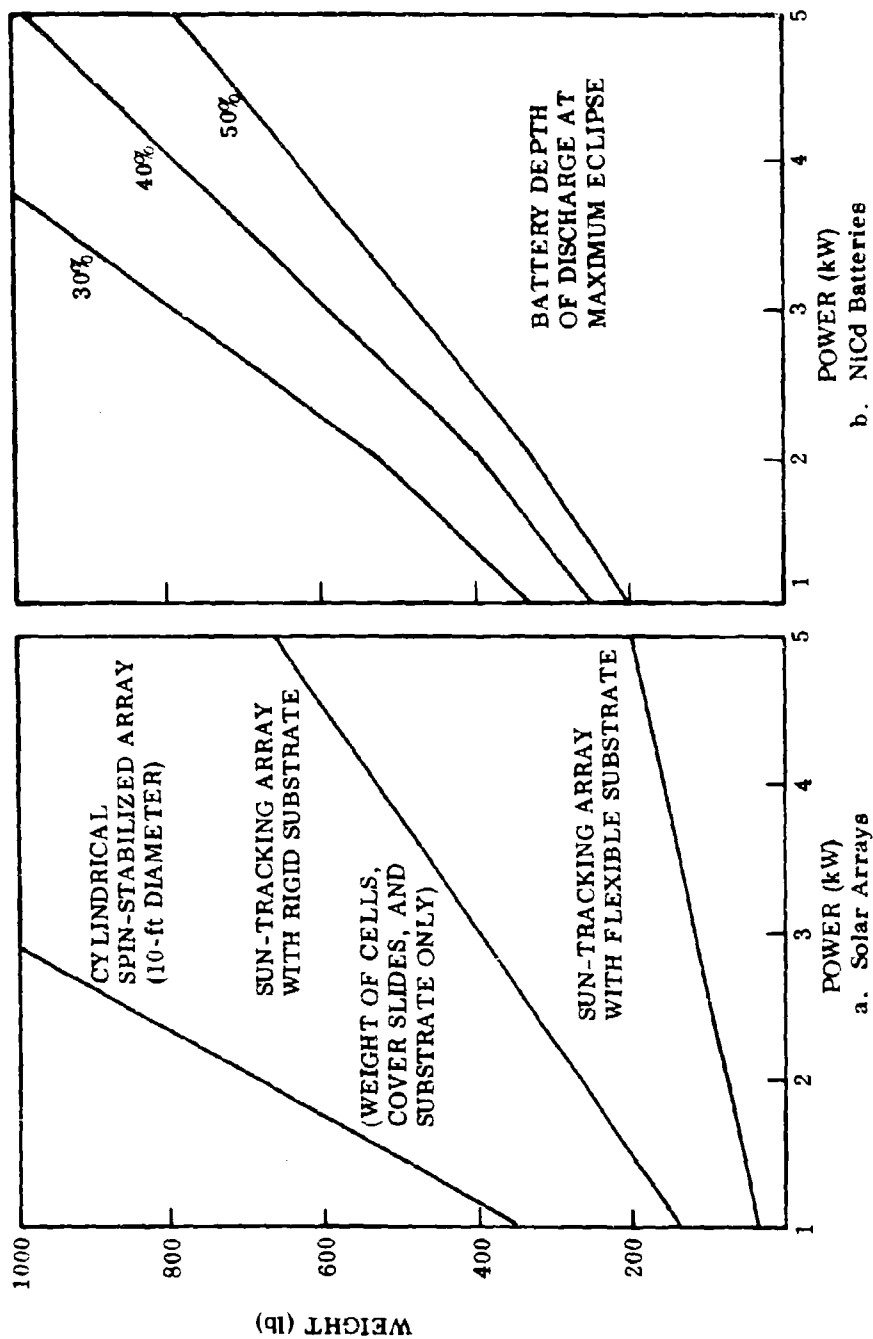


Fig. 1 Synchronous Satellite Electrical Power System Requirements

Q-4

exception of any horizon sensor's scanning mirrors, the wheel-stabilized attitude system can be, part-for-part, less complex than the body-spin system, in terms of both the equipment required and the electronic parts count.

The wheel-stabilized systems are controlled by wheel speed changes. A reaction wheel control loop commands wheel speed to change in proportion to the attitude error signal. Knowledge of wheel speed and position is not required. In the body-spin system, both the speed and position of the despun antenna must be continuously and precisely controlled with respect to the attitude reference horizon pippers located on the spinning drum. In addition, the servo system in the body-spin system requires onboard electronic data processing to capture, synchronize, and precisely orient the stationary section relative to its spinning section.

Pointing accuracy is inherent in the wheel-satellite. Alignment accuracies can be directly measured and controlled; and correction, if required, is direct. Contrasted with this simplicity is the spin system's requirement for stringent control of the dynamic balance and alignment of the rotating drum. Since the momentum stored in this drum provides the attitude orientation stiffness, any unbalance or misalignment produces a wobble in the despun antenna. Furthermore, accuracy degrades with bearing wear, thermal and load distortion of the structure, and spin rate variation.

Two considerations are important in bearing operation - preventing temporary outages and preventing catastrophic failure. In both systems, spurious thrusting from leakage of the mass expulsion system can be avoided by the use of series valves. In the wheel-stabilized system an inactive standby thruster control system can ensure antenna orientation in the event of failure of the wheel servo until control is switched to a redundant wheel. With wheel redundancy, no single failure can lead to communications outage. Any failure of the despun joint of the body-spin system, with its critical bearing design, is catastrophic.

Q-5

LOCKHEED PALO ALTO RESEARCH LABORATORY
LOCKHEED MISSILES & SPACE COMPANY
A GROUP DIVISION OF LOCKHEED AIRCRAFT CORPORATION

POSITIONING AND ORIENTATION

The wheel-stabilized and body-spin satellites can both feature multiple redundancy of hardware and meet the communication system specification with one thruster out. By employing sufficient thrusters, the wheel-stabilized satellite provides multiple redundancy in the required functions of despin, reorientation, roll, pitch stationkeeping, and wheel desaturation. Such a system performs normally with any thruster failed closed, and in some cases with two thrusters failed closed.

Propellant management of the wheel-stabilized satellite in the zero-gravity environment may be obtained by use of an aluminum perforated sheet ball, installed inside the propellant tank 0.1 in. from the tank wall. Liquid surface tension entraps propellant between the ball and the tank wall. This method ensures that liquid will fill the tank outlet under any orientation and at externally applied forces up to 1 g. The forces imposed on the propellant by the thrusters do not exceed 0.01 g. This tank system requires only two tanks for complete redundancy and affords the further advantages of having no pressure balance lines and having all metal surfaces wetted with propellant. In addition, it does not require precise installation location. Tank design in the wheel-stabilized vehicle is simplified by the absence of strict mass distribution requirements during propellant utilization.

The body-spin satellite generates an artificial gravity by spinning the tanks. This establishes the pressurant gas on the inner hemispheres of the four tanks and in the two tank pressure balance lines. These gas-to-metal surface contacts increase the possibility of pressurant leaks and resultant propellant unavailability.

STRUCTURES

The wheel-stabilized satellite structure can be more efficient and lighter than that of the body-spin system. The wheel-stabilized satellite has a central load path with compactly stowed solar arrays. This simple, lightweight structure can fit within a flight-qualified shroud. The body-spin stabilized satellite also has a central load path, but with this satellite it must support the despin assembly and the cantilevered

equipment rack and the solar-array drum. In addition, the despin bearings must support a cantilevered despun platform through the ascent environment.

TELEMETRY, COMMAND, COMMUNICATIONS, AND ANTENNAS

The telemetry and command subsystems are more complicated in the body-spin satellite because of the slip-rings between the spacecraft and the transmitter and receiver. The communications packages are the same, and the antennas are equivalent in complexity on the body-spin satellite.

In the wheel-stabilized satellites, all telemetry and command signals are hardwired to the redundant telemetry encoders. In the body-spin satellite, a method of transferring information across the despin joint is to multiplex it on each side of the joint, cross the joint on two lines per telemetry system, and combine the multiplexed signals on the transponder side. The command link similarly transmits the coded command message across the interface and decodes the proper commands on each side, requiring four slip-rings. The body-spin satellite is thus burdened by the complexity of an extra synchronized multiplexer, an extra signal conditioning box, and an extra coder over that needed for the wheel-stabilized satellite, in addition to the reliability degradation from the eight slip-rings.

THERMAL CONTROL

Passive thermal control of the wheel satellite equipment rack is provided by multilayer insulation and thermal control surfaces. Thermal control of the equipment in the solar array cylinder of the body-spin satellite is maintained by cyclic exposure to solar heating during sunlight operation. During eclipse, insulation and heaters are required in the spinning vehicle.

The insulated equipment compartment with north-south facing radiating surfaces used in the wheel-stabilized satellite isolates all spacecraft equipment from solar radiation flux to keep a uniform ambient temperature. A mosaic of optical solar reflector surfaces on the ends controls heat outflow to space. This heat rejection system is unaffected by eclipse.

Q-7

LOCKHEED PALO ALTO RESEARCH LABORATORY
LOCKHEED MISSILES & SPACE COMPANY
A GROUP DIVISION OF LOCKHEED AIRCRAFT CORPORATION

The solar-array drum of the body-spin system radiates an even temperature to all spacecraft equipment during sunlight operation, typically about 75°F. In eclipse, however, the solar array becomes an efficient radiator to space, rapidly drawing heat away from the spacecraft equipment. Temperature-sensitive equipment, such as batteries and the hydrazine tanks and thrusters, must be insulated, making the thermal design problems of the two systems the same. The wheel satellite's solar-oriented array arms experience no diurnal temperature variations but operate at about 130°F except during eclipse periods. The result is that the wheel-stabilized satellite solar arrays experience the same temperature cycles as those of the body-spin system but operate at a higher temperature.

The hydrazine thrusters of the wheel-stabilized satellite are mounted inside the insulated equipment compartment, and probably require no heaters. For the body-spin satellite, insulation and heaters are needed during eclipse, since the thrusters are tied to the solar array drum. The wheel satellite apogee motor is exposed to sunlight during transfer orbit, so it receives adequate solar energy to exceed a 40°F temperature. The body-spin apogee motor is shielded from the sun by the solar-array drum, so it requires insulation blankets and a heater. Larger view factors on the wheel-stabilized communications electronic assemblies make the thermal control problems and solutions more tractable due to the larger radiation areas available. The communications package on the spinning vehicle must be thermally decoupled in order to protect the despin bearing assembly from high temperatures.

ORBIT OPERATIONS

Attitude and orbit control of both wheel- and spin-stabilized satellites are conducted in almost identical fashion in final orbit. In both satellites, east-west antenna pointing is normally controlled continuously by onboard equipment. North-south pointing drift, due to solar pressure torque, is corrected by ground command about once every 2 or 3 weeks. Orbit correction maneuvers in both systems are commanded from the ground about once every 2 weeks. A pair of jets is used for north-south stationkeeping to keep the satellite within the antenna pointing specification.

Q-8

LOCKHEED PALO ALTO RESEARCH LABORATORY
LOCKHEED MISSILES & SPACE COMPANY
A GROUP DIVISION OF LOCKHEED AIRCRAFT CORPORATION

GROUND HANDLING COMPARISONS

The wheel-stabilized satellite offers the advantages of service access to equipment without removal of fragile solar-array panels, elimination of high-precision dynamic balancing, static system testing instead of an active spinning operation, transportability in smaller aircraft, and simplified spacecraft storage.

The complete integrated systems run on the wheel-stabilized satellite can be accomplished with no spinning motion except for the stabilization wheels running inside hermetically sealed cases, no spin tables with test table slip-rings, no windage or nutation damper test uncertainties, no fragile exposed solar cells during system tests, and no dynamic balancing in the orbit condition. The stabilization wheels are permanently balanced separately at the vendor's factory. The spacecraft is balanced in a single-step process at the launch base to the ascent requirements. These requirements are based on the accuracy of the final orbit injection, which is less stringent than the requirements for stabilizing a satellite to an accurate pointing reference in final orbit.

The body-spin satellite must be balanced in a two-step process -- for the transfer orbit and for the final orbit configurations. The latter balancing has to be conducted repeatedly throughout the manufacture and test cycle whenever the configuration changes because of test instrumentation or component replacement. Test facilities for the body-spin satellite must include an accurate spin table for dynamic operation during system test. This facility must also contain highly accurate despin platform alignment equipment to monitor the operation of the despin servo. None of this equipment is necessary for system testing of the wheel-stabilized satellite.

CONCLUSIONS

Simplicity. The wheel-stabilized satellite is at least as simple as the body-spin system in spacecraft design and operations and much simpler to assemble, test, and transport.

Q-9

LOCKHEED PALO ALTO RESEARCH LABORATORY
LOCKHEED MISSILES & SPACE COMPANY
A GROUP DIVISION OF LOCKHEED AIRCRAFT CORPORATION

Confidence in Design. Both the wheel-stabilized satellite and the dual-spin designs are based on qualified hardware and approaches that have been applied successfully in major military and NASA programs.

Reliability. Of utmost importance, the wheel-stabilized satellite can be immune to any single catastrophic bearing failure mode that could cause telecommunications outage. Reliability of the body-spin system is compromised by the vulnerable slip-rings and brushes, and binding of the despin bearings could paralyze the satellite and cut off communications. There is no practical backup for these bearings.

Flexibility/Growth. In addition to its greater dependability, the wheel-stabilized satellite has inherent growth potential. Simply adding or subtracting solar-array area equips it for different missions, and updating it for longer life requires only a larger hydrazine propellant capacity. By contrast, the body-spin system is limited in growth potential. Any changes in the length of the drum or even the hydrazine capacity disrupts mass properties control and consequently the dynamic balance crucial for pointing accuracy. Therefore, adaptation to a different mission could require major redesign.

In summary, the wheel-stabilized satellite is comparable to the body-spin system in simplicity and in design experience, it can eliminate single path failure modes, and it affords mission flexibility and growth potential.

Appendix R

EFFECTS OF USING
A TELESCOPE SECONDARY MIRROR
AS A SCANNING ELEMENT

by

Mr. C. M. Klug

(Previously distributed as Technical Memorandum No. 3)

LOCKHEED PALO ALTO RESEARCH LABORATORY
LOCKHEED MISSILES & SPACE COMPANY
A GROUP DIVISION OF LOCKHEED AIRCRAFT CORPORATION

1. BACKGROUND

Recent developments in optical design have made possible the use of Cassegrain-type telescopes at angles much farther off axis than previously by tilting the secondary mirror. This led to the consideration of an agile secondary mirror for pointing and steering of the optical communication subsystem. Further investigation shows that factors other than resolution have an impact that makes this approach impractical. This memorandum provides a brief review of these factors.

2. DISCUSSION

Using the secondary mirror of a two-mirror telescope system as a scanning element directly affects the primary mirror of the system in two important parameters, both of which are a function of the scan angle:

- Primary mirror size
- Primary image size

It is easy to develop a geometric expression that equates the primary mirror diameter and the scan angle. Analyses by Perkin-Elmer, Consultants to the Electrooptical Sciences Laboratory, and by LMSC have developed equivalent expressions for the primary mirror diameter as a function of scan angle. The expression developed by Perkin-Elmer is the simplest and is presented here.

$$D_p = A \left[1 + 2 N_p \frac{1-r}{r} \tan U_f \right]$$

where

- D_p = primary mirror diameter
- A = required collecting aperture
- N_p = nominal f number of collecting aperture
- r = obscuration ratio of the secondary mirror to the collecting aperture
- U_f = half scan angle

Using an obscuration ratio of one-third, the primary mirror size as a function of N_p for a collecting aperture of 24 in. and a half scan angle of 11° is

$$D_p = 24 (1 + 0.8 N_p)$$

N_p	Focal Length	D_p
1.0	24.0	43.2
1.5	36.0	52.8
2.0	48.0	62.4

These primary mirrors would require the following f numbers to satisfy the nominal f number required for the collecting aperture:

N_p	f Number
1.0	0.55
1.5	0.68
2.0	0.77

Not only does the primary mirror diameter become excessively large, but its f-number becomes so fast that the mirror becomes difficult to fabricate.

Figure 1 shows a primary mirror with a nominal collecting aperture f-number of 1, a collecting aperture of 24 in., an obscuration ratio of one-third, and a half scan angle of 11° .

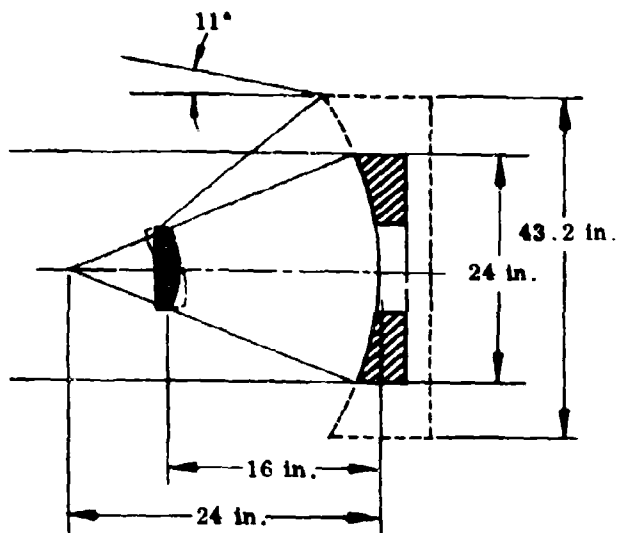


Fig. 1 Effects of Tilting Secondary Mirror

The third-order aberrations of an image formed by a mirror are readily calculated from the following standard formulas, given in the Handbook of Military Infrared Techniques:

- Paraboloidal Mirror (simplest case with stop at focal plane)

$$CC^* = \frac{y^2 U_p}{4 f}$$

where

- CC* = coma
- y = height of ray from axis
- U_p = angle of ray to optical axis
- f = focal length of mirror

- Spherical Mirror (simplest case with stop at center of curvature)

$$SC = \frac{y^2}{4 r}$$

R-3

LOCKHEED PALO ALTO RESEARCH LABORATORY
LOCKHEED MISSILES & SPACE COMPANY
A GROUP DIVISION OF LOCKHEED AIRCRAFT CORPORATION

where

SC = spherical aberration
 y = height of ray from axis
 r = radius of curvature of mirror

The angular sizes of the image of a point source from the mirror for the various focal lengths and diameters are

$\frac{N}{p}$	<u>Paraboloidal Mirror</u>	<u>Spherical Mirror</u>
1.0	0.041 rad (2.32°)	0.101 rad (5.78°)
1.5	.027 (1.55°)	.067 (3.85°)
2.0	.021 (1.21°)	.053 (3.04°)

The aberrations are seen to increase for the faster, smaller diameter mirrors, which indicates that except for relatively long focal length mirrors the image size is excessive; however, longer focal length mirrors are too large to be usable.

Appendix S

FAR FIELD PATTERN
OF
DEFOCUSED TELESCOPE

by

Dr. C. McIntyre

Perkin-Elmer

LOCKHEED PALO ALTO RESEARCH LABORATORY
LOCKHEED MISSILES & SPACE COMPANY
A GROUP DIVISION OF LOCKHEED AIRCRAFT CORPORATION

SECTION I

INTRODUCTION

Optical communications offers several advantages over the more conventional microwave or radio frequency means of communications. One of the principal advantages is the tremendous available antenna gains, allowing communications over long ranges (e.g., synchronous satellite to earth). In order to utilize this property, extremely precise pointing is required - on the order of $1/10$ to $1/100$ of an arc-second. This precision pointing is achievable with the use of a cooperative beacon. That is, one station, say "A", sends a laser beacon to its companion terminal, "B". Station "B" then locates the beacon and "acquires" and tracks the beacon with fractional arc-second precision. At this point, a laser beam is pointed back toward "A". When "A" acquires the laser from "B", the communication link is established and communications can begin. At the beginning of this acquisition sequence, the angular location of the companion terminal is not known with the precision required for pointing the acquisition beacon. Therefore, special procedures are required for acquisition.

One method is to intentionally diverge the beacon to floodlight the uncertainty area of the companion terminal. This technique creates a problem when the antenna has an obscured aperture (e.g., a Cassegrain or Gregorian type telescope). In this defocused condition, the central obscuration is projected into the far field so that a dark hole appears exactly where the companion terminal is most likely to be located. This will, in the best case, increase the acquisition time, and, in the worst case, prevent acquisition altogether. The purpose of this paper is to examine how this "hole" develops as the telescope is defocused. At the end of the analysis, alternative acquisition schemes are described that may be used to avoid this problem.

The following analysis is based upon classical diffraction theory (Rayleigh-Sommerfield) and results in description of the intensity distribution in the far field of a centrally obscured telescope illuminated by a point source at or near the telescope focus. The location of the point source is a parameter of the analysis allowing the far field intensity distribution to be computed for various amounts of defocus (including the focussed condition). The telescope (consisting of two or more mirrors) is represented by its equivalent lens, the central obscuration appearing as an opaque region in the center of the lens (Figure 1). This computation shows how the "hole" develops as the telescope is defocussed. Minor modifications to this analysis when the source is a laser operating in the TEM_{00} mode are shown.

SECTION II

ANALYSIS

Figure 1 shows the geometry assumed for the calculation. In the figure, f is the focal length of the equivalent telescope lens, r_0 is the distance from the point source to the lens, a is the radius of the telescope aperture, and b is the radius of the central obscuration. The image of the point source is also shown located at a distance r_1 from the lens. Then β is one half the geometric divergence angle of the defocused beam.

Figure 2 defines the coordinate system and notation used in the analysis. A point in the aperture plane (the plane containing the equivalent telescope lens) has coordinates (x,y) or in cylindrical coordinates $\rho = (x^2 + y^2)^{1/2}$, $\theta = \tan^{-1} \frac{y}{x}$. Similarly, a point in the observation plane, located a distance z_0 from the aperture plane, has coordinates (x',y') and $\rho' = [(x')^2 + (y')^2]^{1/2}$, $\theta' = \tan^{-1} \frac{y'}{x'}$.

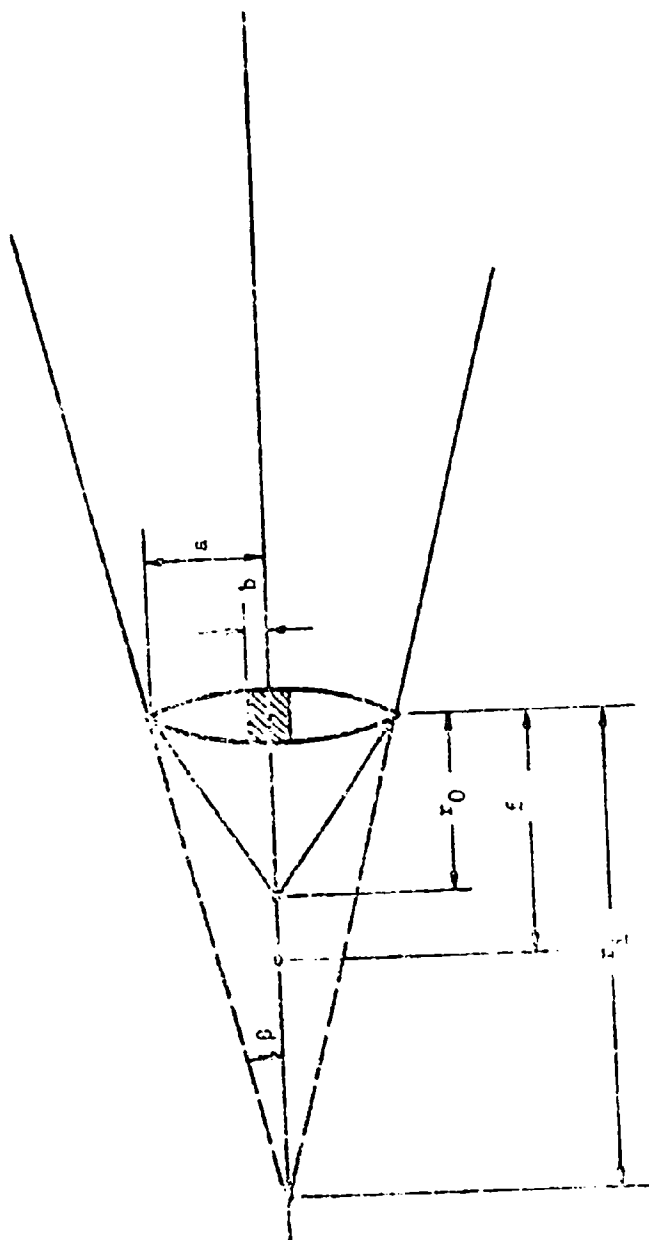
The analysis assumes a point source at r_0 . A spherical wave emanating from r_0 is then incident on the equivalent telescope lens. The amplitude and phase of this wave in the plane of the aperture, but before encountering the lens, is

$$\frac{e^{ikr_1}}{r_1}$$

where r_1 is the distance from r_0 to $P(x,y)$ (see Figure 2). The lens is represented as a pure phase transformation,*

$$e^{-i \frac{k}{2f} (x^2 + y^2)} \quad (1)$$

* Goodman, J., Introduction to Fourier Optics, McGraw-Hill, 1968.



f = distance from equivalent telescope lens to the focus = telescope effective focal length
 r_0 = distance from the equivalent telescope lens to a point source ($r_0 \neq f$ in general). ($r_0 = f$ focused condition)
 r_i = distance from equivalent telescope lens to the virtual image of the point source at r_0

Note: $\frac{1}{r_0} + \frac{1}{r_i} = \frac{1}{f}$ (1)

Figure 1- Geometry for Defocused, Obscured Aperture Telescope

NOT REPRODUCIBLE

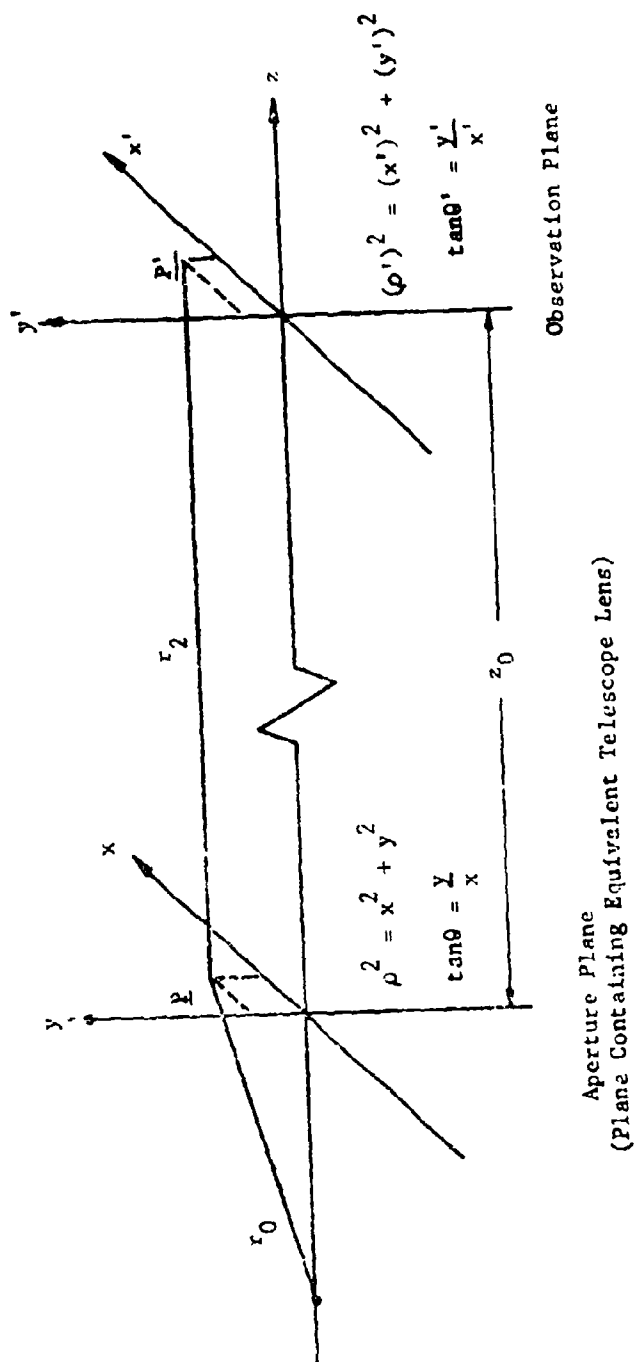


Figure 2- Coordinate System and Notation

Then using Rayleigh-Sommerfeld diffraction theory, each point of the emerging wavefront is considered to be the source of a new wave with an amplitude $1/\lambda$ times the amplitude of the emerging wave at that point, a phase equal to the phase of the emerging wave at that point minus 90° , and a directional characteristic given by $\cos(\hat{n}, \hat{r}_2)$.

(\hat{n}, \hat{r}_2) = the angle between a normal to the plane of the aperture, \hat{n} , and the direction of r_2 , \hat{r}_2

\hat{n} = unit vector perpendicular to the aperture plane and pointing toward the observation plane

\hat{r}_2 = unit vector in the direction from the point in the aperture plane (x, y) to the point in the observation plane (x', y')
(See Figure 2.)

Then the electric field amplitude at $E'(x', y')$ due to a point source at a distance r_0 from the lens is given by:

$$E = \int_A \left[\frac{e^{ikr_1}}{r_1} \right] \left[e^{-i \frac{k}{2f}(x^2 + y^2)} \right] \left[\frac{1}{i\lambda} \frac{e^{ikr_2}}{r_2} \cos(\hat{n}, \hat{r}_2) \right] dA \quad (2)$$

where

$$\left[\frac{e^{ikr_1}}{r_1} \right]$$

represents a spherical wave emanating from the point r_0 behind the lens

$$\left[e^{-i \frac{k}{2f}(x^2 + y^2)} \right]$$

is a phase transformation of the equivalent telescope lens

$$\left[\frac{1}{i\lambda} \frac{e^{ikr_2}}{r_2} \cos(\hat{n}, \hat{r}_2) \right]$$

represents a spherical wave emanating from $P(x, y)$ (Huygen's wavelets) with the amplitude factor, $\frac{1}{i\lambda}$, and obliquity factor, $\cos(\hat{n}, \hat{r}_2)$, derived in Rayleigh-Sommerfeld diffraction theory

$$k = \frac{2\pi}{\lambda}$$

λ = wavelength

A = aperture

In order to simplify the evaluation of the integral in (2), the exponential arguments may be expanded in terms of x, y and x', y' and then approximated by neglecting higher order terms:

$$\begin{aligned} r_1 &= \sqrt{r_0^2 + (x^2 + y^2)} = r_0 \sqrt{1 + \frac{(x^2 + y^2)}{r_0^2}} \\ &= r_0 \left[1 + \frac{(x^2 + y^2)}{2r_0^2} + \dots \right] = r_0 + \frac{(x^2 + y^2)}{2r_0} + \dots \\ &\approx r_0 + \frac{(x^2 + y^2)}{2r_0} \end{aligned} \quad (3)$$

This ignores terms of higher order and is the Fresnel approximation.

$$\begin{aligned} r_2 &= \sqrt{z_0^2 + (x-x')^2 + (y-y')^2} \\ &= z_0 \sqrt{1 + \frac{(x-x')^2}{z_0^2} + \frac{(y-y')^2}{z_0^2}} \\ &= z_0 \left[1 + \frac{(x-x')^2 + (y-y')^2}{2z_0^2} + \dots \right] \\ &\approx z_0 + \frac{(x-x')^2 + (y-y')^2}{2z_0} \quad \{\text{Fresnel approximation again}\} \\ &= z_0 + \frac{(x^2 + y^2) + [(x')^2 + (y')^2] - 2(xx' + yy')}{2z_0} \\ &= z_0 + \frac{(x')^2 + (y')^2}{2z_0} + \frac{x^2 + y^2}{2z_0} - \frac{xx' + yy'}{z_0} \end{aligned} \quad (4)$$

This assumes z_0 is large compared to the dimensions of interest at the aperture plane and the observation plane (true for "small" angles $< 1^\circ$). For this geometry, $\cos(\theta, r_2) \approx 1$. Also, since the major contribution to the integral comes from the oscillating exponential terms, the amplitude factors in the denominator may be approximated by

$r_1 \approx r_0$ and $r_2 \approx z_0$, respectively (the first terms in the above expansions). Then the expression for the electric field amplitude becomes:

$$E_0 = \int_A \left[\frac{1}{r_0} e^{ikr_0} e^{ik(x^2 + y^2)/2r_0} \right] \left[e^{-ik(x^2 + y^2)/2f} \right] \left[\frac{1}{i\lambda z_0} e^{ikz_0} e^{ik[(x')^2 + (y')^2]/2z_0} e^{ik(x^2 + y^2)/2z_0} e^{-ik(xx' + yy')/z_0} \right] dA$$

$$= \frac{1}{i\lambda r_0 z_0} e^{ik(r_0 + z_0)} e^{ik[(x')^2 + (y')^2]/2z_0} \int_A e^{ik\left(\frac{1}{r_0} - \frac{1}{f} + \frac{1}{z_0}\right)(x^2 + y^2)/2} e^{-ik(xx' + yy')/2z_0} dA \quad (5)$$

At this point, it is a simplification to note that the result of this calculation is the intensity in a plane at a distance z_0 from the aperture. The phase factors in front of the integral above have a magnitude of unity and will not contribute to the intensity. In addition, the amplitude factor is simply a constant scale factor and may be ignored for the purposes of this discussion. Then, in cylindrical coordinates (see Figures 1 and 2),

$$E = \int_0^a \int_0^{2\pi} e^{i\frac{k}{2}\left[\frac{1}{r_0} - \frac{1}{f} + \frac{1}{z_0}\right]\rho^2} e^{-i\frac{k}{2z_0}\rho\rho'\cos(\theta - \theta')} \rho d\rho d\theta$$

$$= 2\pi \int_0^a e^{i\frac{k}{2}\left[\frac{1}{r_0} - \frac{1}{f} + \frac{1}{z_0}\right]\rho^2} J_0\left(\frac{k\rho\rho'}{z_0}\right) \rho d\rho \quad (6)$$

Again, the 2π can be ignored as it is a constant scale factor. Now let $\frac{\rho'}{z_0} = \alpha$, the angle from the center of the aperture to the observation point. Eq. 6 describes the electric field amplitude in a plane at a distance z_0 from the aperture, under the condition that the approximations in (3) and (4) are satisfied. This

approximation is commonly referred to as Fresnel diffraction. If, in addition, the distance to the observation plane, z_0 , is large enough, the terms $\frac{x^2}{2z_0}$ and $\frac{y^2}{2z_0}$ in equation (4) can be neglected with respect to $\frac{x}{z_0} x'$ and $\frac{y}{z_0} y'$. This case is known as Fraunhofer diffraction. The appropriate expression for each case is given below.

$$E_1 = \int_b^a e^{i \frac{k}{2} \left[\frac{1}{r_0} - \frac{1}{f} + \frac{1}{z_0} \right] \rho^2} J_0(k \rho \omega) \rho d\rho \quad \{\text{Fresnel}\} \quad (7)$$

$$E_2 = \int_b^a e^{i \frac{k}{2} \left[\frac{1}{r_0} - \frac{1}{f} \right] \rho^2} J_0(k \rho \omega) \rho d\rho \quad \{\text{Fraunhofer}\} \quad (8)$$

Note that these two expressions have exactly the same form. If we define

$\Delta_1 = k \left[\frac{1}{r_0} - \frac{1}{f} + \frac{1}{z_0} \right]$, $\Delta_2 = k \left[\frac{1}{r_0} - \frac{1}{f} \right]$, and $\omega = k \rho$, then both expressions have the form

$$E = \int_b^a e^{i \Delta \rho^2 / 2} J_0(\omega \rho) \rho d\rho \quad (9)$$

where $\Delta = \Delta_1$ for Fresnel diffraction, and $\Delta = \Delta_2$ for Fraunhofer diffraction.

Eq. (9) can be evaluated in terms of the Lommel functions:*

$$U_n(u, v) = \sum_{s=0}^{\infty} (-1)^s \left(\frac{u}{v} \right)^{n+2s} J_{n+2s}(v) \quad (10)$$

$$V_n(u, v) = \sum_{s=0}^{\infty} (-1)^s \left(\frac{v}{u} \right)^{n+2s} J_{n+2s}(v) \quad (11)$$

* See, for example, Born & Wolf, Principles of Optics, p. 438, 2nd. revised edition, Macmillan, 1964.

The solution is

$$E = \frac{1}{\Delta} \left\{ e^{i \frac{\Delta}{2} a^2} [U_1(\Delta a^2, wa) - i U_2(\Delta a^2, wa)] \right. \\ \left. - e^{i \frac{\Delta}{2} a^2 p^2} [U_1(\Delta a^2 p^2, wap) - i U_2(\Delta a^2 p^2, wap)] \right\} \quad (12)$$

or

$$E = -\frac{1}{\Delta} \left\{ e^{i \Delta a^2 / 2} [V_0(\Delta a^2, wa) - i V_1(\Delta a^2, wa)] \right. \\ \left. - e^{i \frac{\Delta}{2} a^2 p^2} [V_0(\Delta a^2 p^2, wap) - i V_1(\Delta a^2 p^2, wap)] \right\} \quad (13)$$

where b has been replaced by ap . Both Equations (12) and (13) are valid. However, for the purposes of calculation, the expression utilizing the U_n is more convenient when $\left(\frac{u}{v}\right)$ is less than 1, while the expression utilizing the V_n is more convenient when $\left(\frac{u}{v}\right)$ is greater than 1 $\left[\frac{v}{u} < 1 \text{ in (11)}\right]$.

There are several interesting features to Equation (8). First note that when $b=0$ (unobscured aperture), if $r_0 = f$ (collimated telescope), then Equation (8) becomes:

$$E = \int_0^a J_0(wp) p dp = a^2 \frac{J_1(wa)}{wa}, \text{ the familiar Airy pattern.}$$

Second, Equation (8) may be simply evaluated to find the intensity in the center of the far field pattern, i.e., for $w=k \alpha=0$.

For this case:

$$E_{w=0} = \int_b^a e^{i \Delta a^2 / 2} p dp = \frac{a^2}{2} \left\{ e^{i \Delta a^2 / 4} \frac{\sin(\Delta a^2 / 4)}{\Delta a^2 / 4} \right. \\ \left. - p^2 e^{i \Delta a^2 p^2 / 4} \frac{\sin(\Delta a^2 p^2 / 4)}{\Delta a^2 p^2 / 4} \right\}$$

Then the intensity at $w = 0$ is

$$I_{(w=0)} = \frac{a^4}{4} \left\{ \left[\frac{\sin(\Delta a^2/4)}{\Delta a^2/4} \right]^2 + \left[\frac{\sin(\Delta a^2 p^2/4)}{\Delta a^2 p^2/4} \right]^2 \right. \\ \left. - 2 \cos \left[\frac{\Delta a^2 (1-p^2)/4}{(\Delta a^2/4)^2} \right] \frac{\sin(\Delta a^2/4) \sin(\Delta a^2 p^2/4)}{(\Delta a^2/4)^2} \right\} \quad (14)$$

it is particularly interesting to note that when $p = 0$, an unobscured aperture,

$$I_{(w,p=0)} = \frac{a^4}{4} \left[\frac{\sin(\Delta a^2/4)}{\Delta a^2/4} \right]^2$$

has the form $\left(\frac{\sin x}{x} \right)^2$. Note that this means that for an unobscured aperture, the central intensity can be zero for certain values of the defocus parameter $\Delta = k \left(\frac{1}{r_0} - \frac{1}{f} \right)$. This is not the case for a Gaussian beam (TEM_{00} mode laser) as shown later.

Note that for the collimated condition ($r_0 = f$), the diffraction limited beam spread, the angle between the central direction and the direction of the first dark ring of the Airy pattern, is

$$\alpha_{d.L.} = 1.22 \frac{\lambda}{D} \quad \text{where } D = 2a$$

Then

$$w_{d.L.} = k \alpha_{d.L.} = \frac{(2\pi)}{\lambda} \frac{(1.22\lambda)}{2a} = \frac{1.22\pi}{a}$$

In order to interpret

$$\Delta = k \left(\frac{1}{r_0} - \frac{1}{f} \right), \text{ note that}$$

NOT REPRODUCIBLE

$$\frac{\Delta}{k} = \frac{1}{r_0} - \frac{1}{f} = \frac{f-r_0}{r_0 f} = \frac{f-r_0}{f^2} = \frac{\sigma}{f^2} \text{ for } r_0 \approx f$$

where σ = the defocus, or displacement between r_0 and f .

Then

$$\Delta \approx \frac{2\pi}{\lambda f^2} \sigma$$

This allows us to interpret Δ in terms of the defocus.

The following figures (3 through 7) give the results of a computer evaluation of Equation 13 for five different values of Δ , the defocus parameter. The figures range from the focussed condition (Figure 3) to a defocus such that the beam spread is approximately 10 times the diffraction limit (Figure 7). At this point, the projected obscuration is clearly evident. The computer results are included as Appendix B.

These figures can readily be interpreted in terms of a specific example. Consider a 6" aperture transmitter operating at $\lambda = 0.53\mu\text{m}$. The diffraction limited beam divergence ($1.22 \frac{\lambda}{D}$ half angle) is approximately 1 arc-sec. Then, for this case, Figure 7 corresponds to a defocus such that the geometric beam divergence is 10 arc-seconds. This defocus is therefore quite small compared with that required for typical acquisition measurements.

NOT REPRODUCIBLE

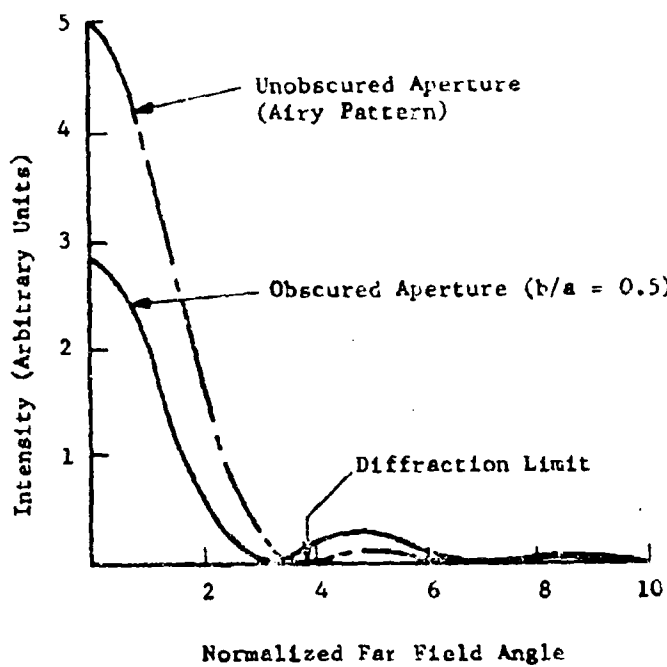


Figure 3. Intensity vs. Field Angle, for No Defocus (Diffraction Limit - Angle to First Dark Ring)

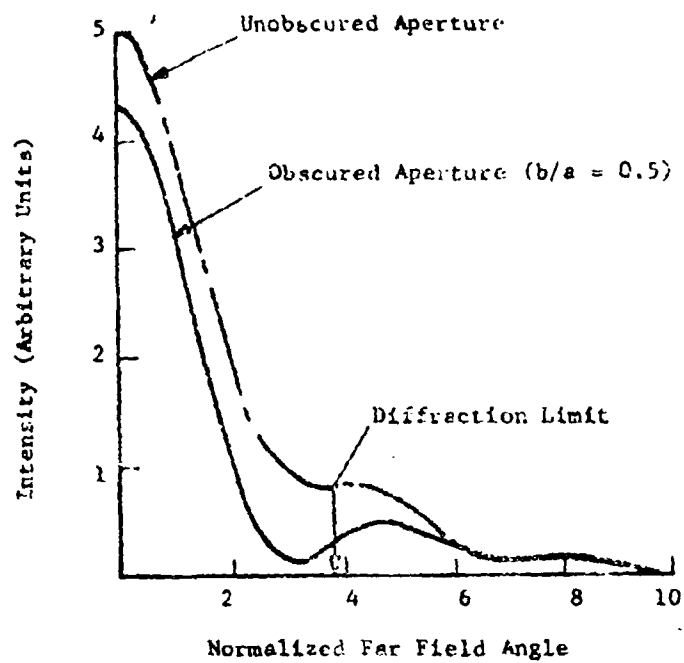


Figure 4. Intensity vs Field Angle for Small Defocus ($\Delta = 2\pi$)

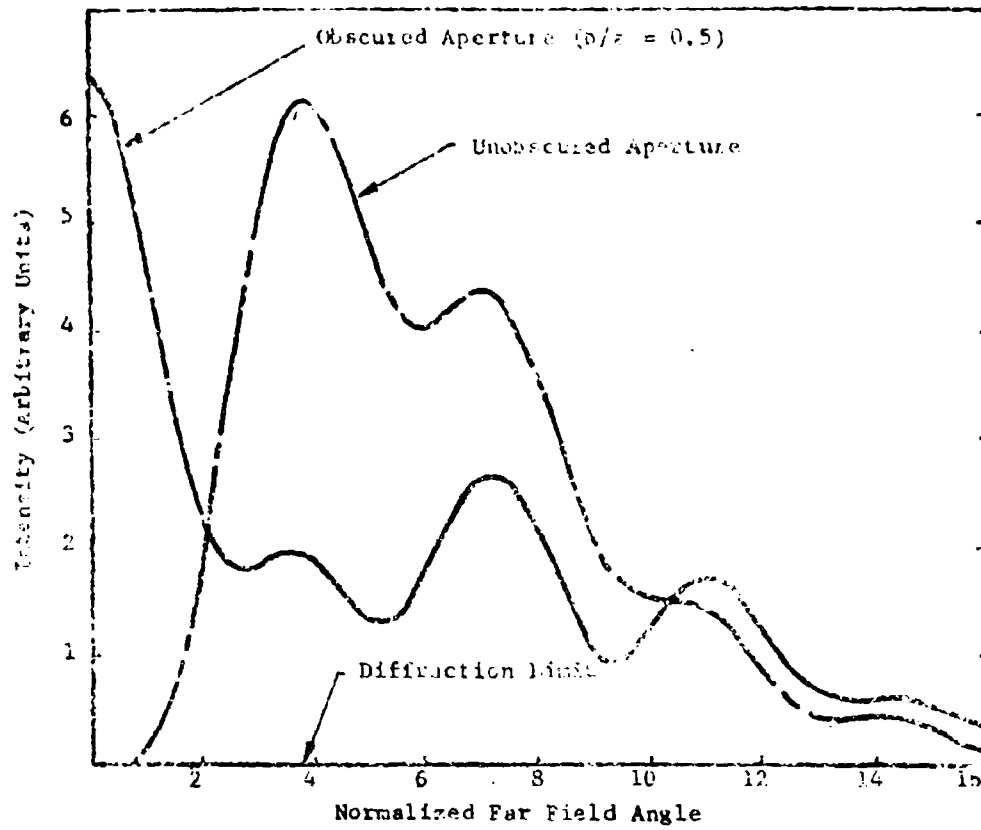


Figure 5. Intensity vs Field Angle for $\Delta=4\pi$

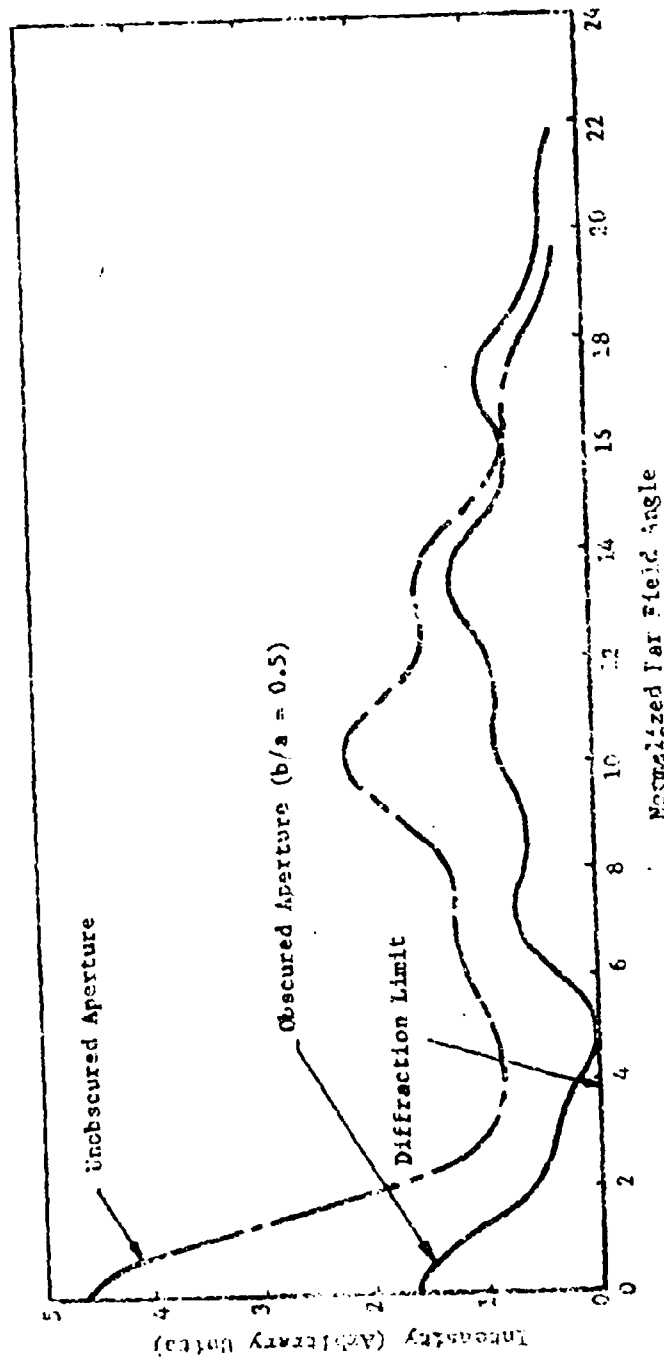


Figure 6. Intensity vs Field Angle for $\Delta=20$

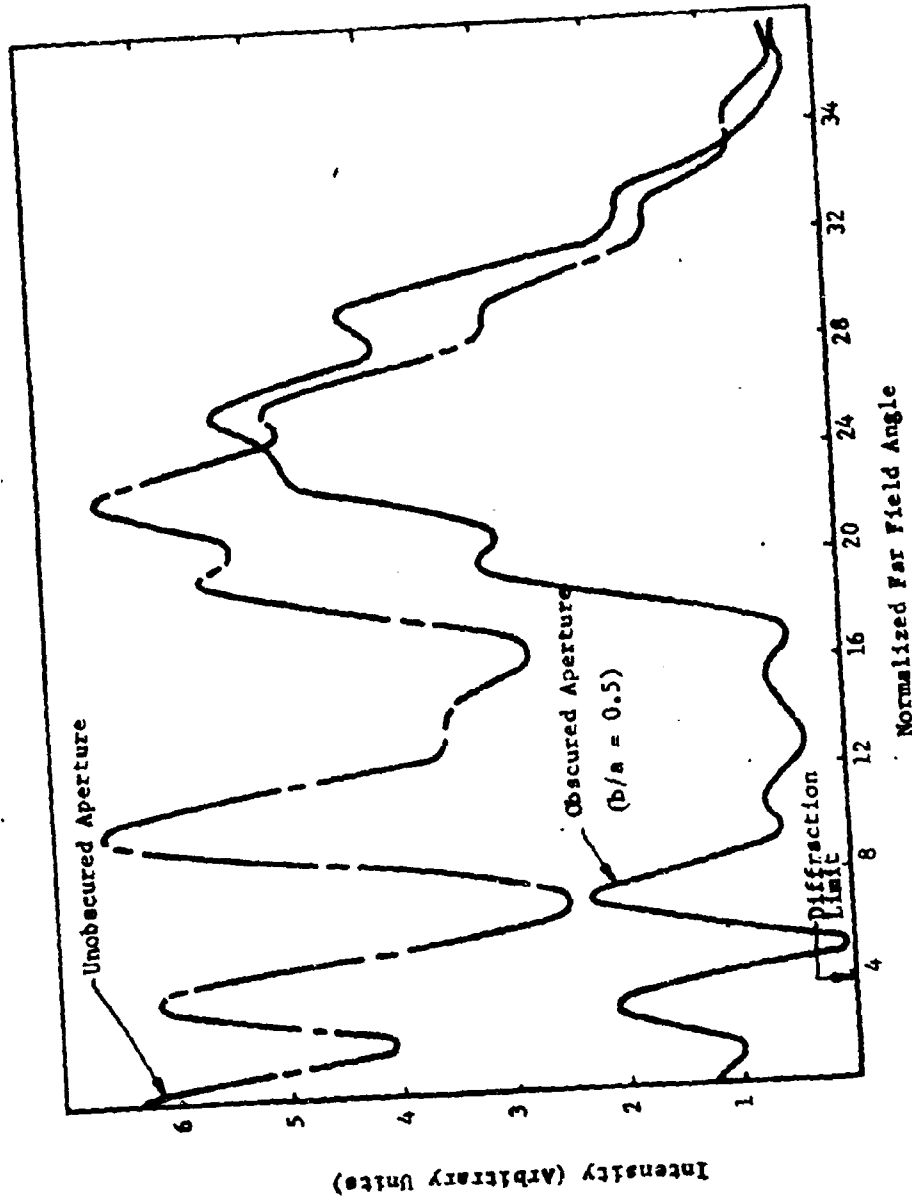


Figure 7. Intensity vs. Field Angle for $\delta=35$. For this case, the geometric beam divergence is approximately 10 times the diffraction limited divergence.

In a practical optical communication system the beacon source is most probably a laser operating in the TEM₀₀ Mode. This mode has a Gaussian transverse intensity distribution and the point source assumed in the analysis of Section II is modified so that the expanding wave incident on the telescope is of the form

$$e^{-\frac{\rho^2}{w^2}} e^{ik/2R} \quad (15)$$

where

w = beam radius measured at the 1/e point

$$w = w_0^2 \left[1 + \left(\frac{\lambda r_0}{\pi w_0^2} \right)^2 \right]$$

w_0 = beam waist (minimum beam radius)

λ = wavelength

r_0 = distance from beam waist

and

R = the radius of curvature of the expanding wavefront

$$R = r_0 \left[1 + \left(\frac{\pi w_0^2}{\lambda r_0} \right)^2 \right]$$

Note that for typical numbers, $w_0 = 10^{-4}$ meters, $\lambda = 10^{-6}$ meters, $r_0 = 3$ meters:

$R = r_0 [1 + 10^{-4}] \approx r_0$. Thus, the primary modification to the analysis of

Section II is the addition of the multiplicative factor $e^{-\frac{\rho^2}{w^2}}$. Then Equation (8) of Section II becomes

$$E_2 = \int_b^a e^{-\frac{\rho^2}{w^2}} e^{\frac{1}{2}k \left[\frac{1}{R} - \frac{1}{f} \right]} \rho^2 J_0(k\rho) \rho d\rho \quad (16)$$

$$= a^2 \int_0^1 e^{-\left(\frac{1}{w^2} - \frac{1}{2}\Delta\right)r^2} J_0(\omega r) r dr$$

$$= b^2 \int_0^1 e^{-\left(\frac{1}{w^2} - \frac{1}{2}\Delta\right)b^2 r^2} J_0(\omega r) r dr \quad (17)$$

Where

$$\Delta = \frac{k}{2} \left[\frac{1}{R} - \frac{1}{f} \right] \text{ and } \omega = kx$$

Both integrals have the form:

$$I(x) = \int_0^1 e^{-Mx^2 r^2} J_0(\omega r) r dr$$

Then in terms of I ,

$$E_2 = a^2 I(a) - b^2 I(b) = a^2 \{I(a) - p^2 I(ap)\} \quad (18)$$

where

$$p = \frac{b}{a}$$

To evaluate $I(x)$,* the Bessel function expansion

$$J_0(y) = \sum_{m=0}^{\infty} \frac{(-1)^m}{(m!)^2} \left(\frac{y}{2}\right)^{2m} \quad (19)$$

gives

$$\begin{aligned} I(x) &= \int_0^1 e^{-Mx^2 r^2} \sum_{m=0}^{\infty} \frac{(-1)^m}{(m!)^2} \left(\frac{uxr}{2}\right)^{2m} r dr \\ &= \sum_{m=0}^{\infty} \frac{(-1)^m}{(m!)^2} \left(\frac{ux}{2}\right)^{2m} \left(\frac{1}{2}\right) \int_0^1 e^{-Mx^2 u} u^m du \end{aligned} \quad (20)$$

This integral, of the form $Q(m) = \int_0^1 e^{-zs} s^m ds$, can be evaluated by repeated integration by parts to give

$$Q(m) = \left[-\frac{e^{-z}}{z} \sum_{n=0}^m \frac{m!}{(m-n)! z^n} \right] + \frac{m!}{z^{m+1}} \quad (21)$$

Using (21) with $z = Mx^2$ in (20),

$$\begin{aligned} I(x) &= \sum_{m=0}^{\infty} \frac{(-1)^m}{(m!)^2} \left(\frac{ux}{2}\right)^{2m} \left(\frac{1}{2}\right) \left\{ -\frac{e^{-Mx^2}}{Mx^2} \sum_{n=0}^m \frac{m!}{(m-n)! (Mx^2)^n} \right. \\ &\quad \left. + \frac{m!}{(Mx^2)^{m+1}} \right\} \\ &= \frac{1}{2Mx^2} \left\{ e^{-\frac{u^2}{4M}} - e^{-Mx^2} \sum_{m=0}^{\infty} \sum_{n=0}^m \frac{(-1)^m}{m!} \left(\frac{ux}{2}\right)^{2m} \frac{1}{n! (Mx^2)^{m-n}} \right\} \end{aligned} \quad (22)$$

*L.D. Dickson "Characteristics of a Propagating Gaussian Beam," Applied Optics, Vol. 9, No. 8, August, 1970

Finally, substituting (22) into (18) gives

$$E_2 = \frac{1}{2M} \left\{ e^{-Ma^2 p^2} \sum_{m=0}^{\infty} \sum_{n=0}^m \frac{(-1)^m}{m!} \left(\frac{w^2}{4} \right)^m \frac{(a^2 p^2)^n}{n! (M)^{m-n}} \right. \\ \left. - e^{-Ma^2} \sum_{m=0}^{\infty} \sum_{n=0}^m \frac{(-1)^m}{m!} \left(\frac{w^2}{4} \right)^m \frac{(a^2)^n}{n! (M)^{m-n}} \right\} \quad (23)$$

Note that this result is valid for a point source $\left(M = -1 \frac{\Delta}{2} \right)$ as well as a Gaussian $\left(M = \frac{1}{2} - i \frac{\Delta}{2} \right)$. Substituting $\left(M = -1 \frac{\Delta}{2} \right)$ into (23) gives

$$E_2 = \frac{1}{\Delta} \left\{ e^{i\Delta a^2 p^2/2} \left[v_c(\Delta a^2 p^2, w_{ap}) - i v_l(\Delta a^2 p^2, w_{ap}) \right] \right. \\ \left. - e^{i\Delta a^2/2} \left[v_c(\Delta a^2, w_a) - i v_l(\Delta a^2, w_a) \right] \right\} \quad (24)$$

This is identical to Equation (13), as expected.

In order to compute the intensity in the center of the far field for an unobscured Gaussian transmitted beam, w and p are set equal to zero in (23), giving

$$E = \frac{1}{2M} \left\{ 1 - e^{-a^2/w^2} e^{i\Delta a^2/2} \right\}$$

Then

$$I_2 = \frac{1}{4MM^*} \left\{ \left[1 + e^{-2a^2/w^2} \right] - 2e^{-a^2/w^2} \cos(\Delta a^2/2) \right\}$$

The minimum value of the factor in brackets occurs when $\frac{\Delta a^2}{2} = 0, 2\pi, \dots$

$$I_{\min} \propto \left\{ 1 + e^{-2a^2/w^2} - 2e^{-a^2/w^2} \right\}$$

$$\propto \left(1 - e^{-a^2/w^2} \right)^2 \neq 0 \text{ for } w \text{ finite and } a > 0$$

This verifies the statement that there is never a null in the center of the far field pattern for a Gaussian transmitted beam.

SECTION III

ALTERNATE ACQUISITION TECHNIQUES

There are a number of techniques for avoiding this problem:

- (a) Use an unobscured aperture.
- (b) Use collimated light (do not defocus).
- (c) Use spatially incoherent light.

Each of these alternatives has advantages and disadvantages according to the particular mission.

One way to avoid the problem is to use an unobscured telescope as the optical antenna. This method is, in concept, the simplest of the three and is attractive from another point of view. That is, when a TEM₀₀ mode laser beam (Gaussian field amplitude in the transverse plane) is transmitted through an obscured telescope, the obscuration occurs at the peak of the Gaussian field distribution and therefore obstructs a large proportion of the transmitted energy. This can be avoided by using an energy redistribution element* which has critical alignment tolerances. With an unobscured aperture, this problem is completely avoided.

An unobscured system might be either a refractive telescope or an off-axis reflective telescope. The refractive system would be useful for a 2 - 3-inch aperture, while the off-axis system is useful for a system with an aperture \geq 6 inches, with some tradeoff between the two for a system with an aperture diameter between 3 and 6 inches.

* W.M. Patern, A.M. Ledger, "Techniques for Matching a Laser TEM₀₀ Mode to Obscured Circular Aperture," Appl. Optics, Vol. 9, p. 1435, June 1970.

A second technique to avoid the far field obscuration is to scan the collimated beacon over the uncertainty area rather than diverging the beam for acquisition. This is compatible with scanning the receiver field-of-view (scan-on-scan). This technique still requires an energy redistribution element, with its associated alignment tolerances.

The above solutions are operations on the coherent wavefront which retain the coherence of the beam (defocus, phase plates, etc.). This technique suggests that the spatial coherence of the transmitted wavefront be degraded in a controlled, but random, manner to increase the divergence of the beacon during acquisition. An accurate estimate of the divergence is obtained by the following relationship:

$$\alpha = (2.4\lambda/D) \cdot D/\delta = 2.4\lambda/\delta$$

where

α = divergence in object space

D = diameter of primary

δ = spatial coherence scale as viewed at primary

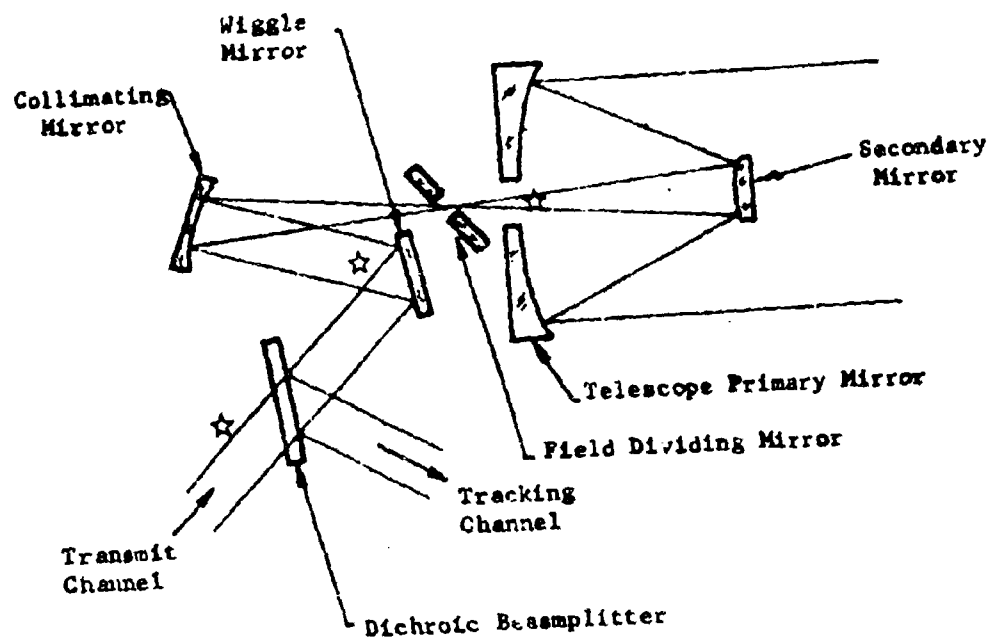
Thus, we note that for $\alpha = 0.25^\circ = .007$ radian, $\delta = 1.7 \times 10^{-4}$ meter = 170 μ at $\lambda = 0.5\mu$. The coherence scale is reduced in proportion to the angular magnification, M, of the "behind the mirror optics." Thus, if the primary aperture is ~ 6.0 in., with a ~ 1.0 in. collimated beam behind the mirror to give a value of $M = 6$, the coherence scale is $\delta' = 170./6 = 28\mu$.

An experiment which readily demonstrates the above physics is to place a sheet of Scotchlite at the focus of a convergent beam. The light reflected from the Scotchlite forms a perfect Airy pattern whose size is directly deduced from the 50 μ diameter of the individual balls of the Scotchlite (i.e., the coherence scale).

Another device that could easily be developed will probably be more efficient and more easily implemented. As suggested by T. Facey, a

decoherencer may be made by photographing a large number of randomly placed dots of various tones but the same scaled diameter δ . By bleaching the negative (as in a phase hologram), we can generate the transmission equivalent of the reflective Scotchlite. This will permit the decoherencer to be placed in the beam by a solenoid operated rotating arm.

Two potential problem areas exist. The instantaneous diverged far field pattern will have nulls. However these nulls may be temporally averaged out if a small dither of the magnitude δ is placed on the decoherencer. The second problem concerns the compatibility of the proposed concept with existing optical designs. As pointed out by C. McIntyre, the clear aperture of the relay optics may have to be increased to accommodate the diverged beam. Further study is required to determine the optimum location for the decoherence assembly. Some alternatives are noted in Figure 8.



☆ Indicates Possible Location of Transmission Decoherence

Figure 8. Decoherence Technique

SECTION IV**SUMMARY**

In optical communications systems, a laser beam is transmitted through an optical antenna or telescope. When the telescope has an obscuration, as in a Cassegrain or Gregorian design, this obscuration is projected into the far field when the transmitted beam is defocused for acquisition. Section II contains the results of the diffraction analysis presented there, showing how the far field pattern develops a hole (intensity minimum) in the center as the transmitted beam is defocused.

Section III contains a brief description of alternative acquisition concepts that avoid the problem with the obscuration. At present, it is felt that the off-axis reflective telescope design is the most desirable approach to an efficient optical communications transceiver antenna.

Appendix T

RAY TRACE COMPUTER RUN

by

Mr. F. Briscoe

Dr. C. McIntyre

Perkin-Elmer

LOCKHEED PALO ALTO RESEARCH LABORATORY
LOCKHEED MISSILES & SPACE COMPANY
A GROUP DIVISION OF LOCKHEED AIRCRAFT CORPORATION

Appendix T

RAY TRACE COMPUTER RUN

This Appendix contains the first order, thin lens, computer ray trace for Package A-1 with an $f/2.2$, 6" diameter primary mirror. Note that the principal ray and the aperture ray are paraxial rays and thus heights and angles for other rays may be scaled directly from the heights and angles. The computed heights give the heights above the base rays. The first order ray trace is summarized in Figure T-1.

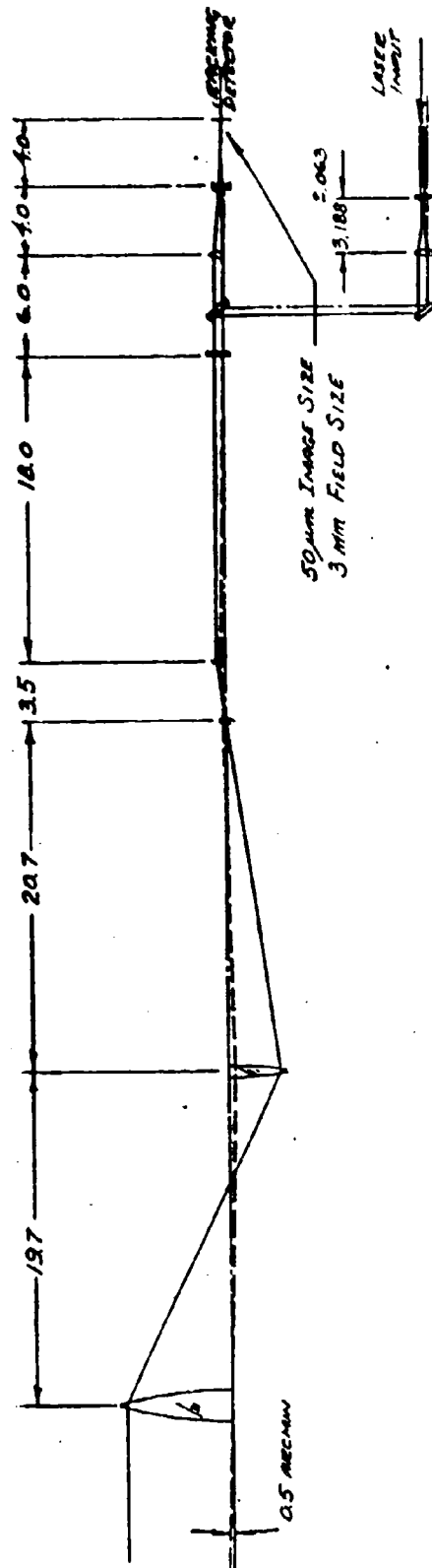
The format for the computer printout is given below. Three computations are given:

(a) Ray Trace for Image Dissector Path. This traces the rays from the telescope to the image dissector. The elements included are:

1. Primary Mirror
2. Secondary Mirror
3. Field Lens
4. Off-Axis Parabolic Collimator
5. Wiggle Mirror
6. Telephoto Lens #1 (on polacube)
7. Telephoto Lens #2

(b) Ray Trace for Beam Decollimation Path (Focussed). This traces the rays from the Beam Expander through the telescope when the beam is collimated. The elements included are:

NOT REPRODUCIBLE



T-2

ELEMENT	PRIMARY	SCATTERY	FIELD LENS	OPT. AXIS	TEMPERATURE	IN. LENS	IN. LENS
FOCAL LENGTH	132	4.95	-0.899	3.50	00	3.92	1.87
CLEAR APERTURE	6.0	2.966	0.012	0.564	0.5	3.0	0.25
HEIGHT OF SPECIFIC RAY	6.0	-2.97	0	0.50	0.5	0.572	0.14
HEIGHT OF PRINCIPAL RAY, 0.5°	0	-0.029	0.006	0.032	0	0.5	0.12
						0.01	-0.07

NOTE: ALL DIMENSIONS IN INCHES

Figure T-1. First Order Ray Trace

1. Beam Expander Lens #1
2. Beam Expander Lens #2
3. ~~Beam Expander~~ Parabolic Collimator
4. Field Lens
5. Secondary Mirror
6. Primary Mirror
7. Stop (primary mirror aperture)

(c) Ray Trace for beam Decollimation Path (Defocused) This traces the rays from the Beam Expander through the telescope when the beam is defocused to 1 arc-minute. The elements are the same as in (b).

COMPUTER PRINTOUT FORMAT

<u>Element</u>	<u>Power</u>	<u>Distance Between Elements</u>	<u>Height of Ray</u>	<u>Angle of Ray</u>
0				
1				
2				
3				
4				
5				
6				
7				

System

EFL - Effective Focal Length

BFL - Back Focal Length

YCP - Height in the Gaussian Image Plane

Enter - Distance from Entrance Pupil to First Surface

Exit - Distance from Last Surface to Exit Pupil

Barrel - Barrel Length

Lens No. 1

FL - Focal Length

D - Distance to Next Element

SO - Object Distance

SI - Image Distance

MAG - Magnification

YAR - Height of Aperture Ray

YPM - Height of Principal Ray (Meridional Plane)

Lens No. 2

-

-

-

-

-

CPA715-0116 DEMOLA

08/17/71

17.46.23

```

-4, 1, 0, 0,
0 0.0 0.0 2.083330-02 0.0
1 2.200000-01 4.000000-00 2.083330-02 -3.333330-02
2 3.375000-01 3.333330-01 -2.666170-01 3.472220-03
3 2.400000-01 2.571400-01 -1.770130-01 5.404750-02
4 3.375000-01 -1.112710-00 1.215000-02 6.750000-02
5 2.071020-01 2.015000-01 1.411960-00 -2.175410-01
6 -1.970510-01 7.675760-02 -2.875350-00 2.895150-04
7 0.0 0.0 -2.875350-00 2.895150-04
8 0.0 -9.337360-05 -2.875350-00 2.083330-02
9 0.0 0.0 0.0 4.166670-02
1 2.202590-01 4.000000-00 0.510730-03 3.623550-03
2 3.375000-00 3.333330-01 -2.174030-02 -3.623200-03
3 2.400000-01 2.571400-01 -5.521660-02 1.501010-02
4 5.500000-00 -1.112710-00 -1.268120-02 -9.956060-04
5 2.071020-01 2.015000-01 5.649780-03 -3.010950-04
6 1.970510-01 7.675760-02 3.556180-15 -3.010950-04
7 0.0 0.0 3.556180-15 -3.010950-04
8 0.0 -9.337360-05 3.556180-16 -3.010950-04

```

Y-YBAR THIS LENS TYPE

ZOOM POSITION NO

1

```

SYSTEM
EFL 1.00000 03
BFL 1.30020 05
YGP -6.15670 01
ENTER 2.20260-01
EXIT 0.0
BARREL 7.92960 01
LENS NO. 1
FL 2.50000-01
D 3.37500 00
SQ 0.0
SI 2.50000-01
TAG 0.0
YAP 2.083330-02
YPR 5.51000-02
LENS NO. 2
FL 3.00000 00
D 2.40000 01
SQ -3.12500 00
SI 7.50000 01
TAG -2.40000 01
YAP -2.50020-01
YPR 2.17400-02
LENS NO. 3
FL 3.50000 00
D 3.50000 00
SQ 5.10000 01
SI 1.27500 00
TAG 6.62200-02
YAP -1.75000-01
YPR -5.52170-02
LENS NO. 4
FL -1.07100-01
D 2.07100 01
SQ -2.27100-01

```

NOT REPRODUCIBLE

SI -1.79100-01
 MAG 7.99030-01
 YAR 1.21530-02
 YPI -1.26010-02

40386 THIS LAYOUT (BEAM-EXPANDER OUTWARDS), PUPIL AT WIGGLE-MIRROR
 Y-YBAR THIRD LENS TRACE PAGE 2

ZOOM POSITION NO

LENS NO. 5
 FL 4.95200 00
 D 1.97050 01
 SO -2.08900 01
 SI 6.49050 00
 MAG -3.10700-01
 YAR 1.41200 00
 YPI 5.94000-03
 LENS NO. 6
 FL 1.32000 01
 D 0.0
 SO -1.32100 01
 SI 9.93850 03
 MAG -7.51910 02
 YAR -2.87540 00
 YPI 3.55620-16
 LENS NO. 7
 FL 0.0
 D 0.0
 SO 9.93850 03
 SI 9.93850 03
 MAG 1.00000 00
 YAR -2.87540 00
 YPI 3.55620-16
 LENS NO. 8
 FL -1.07100 04
 D 0.0
 SO 9.93850 03
 SI 1.35020 05
 MAG 1.36570 01
 YAR -2.87540 00
 YPI 3.55620-16

NOT REPRODUCIBLE

SE 1.16870-11
 YAP 1.16870-11
 YAP 1.16870-11
 YP 1.16870-11

ADDS THIS LENS LAYOUT

Y-YEAR THIS LENS TRACE PAGE 2

LENS POSITION TO

LENS NO. 5
 FL 4.65200 00
 D 1.67010 01
 SO -2.07100 01
 SI 4.50710 00
 MAG -5.14210-01
 YAP 1.16870 00
 YP 5.70110-03

LENS NO. 6
 FL 1.32000 01
 D 0.0
 SO -1.32000 01
 SI 1.32000 00
 MAG -5.03000 00
 YAP -2.00000 00
 YP 6.03300-17

LENS NO. 7
 FL 0.0
 D 0.0
 SO 7.84070 00
 SI 7.84070 00
 MAG 1.00000 00
 YAP -3.00000 00
 YP 6.93300-17

LENS NO. 8
 FL 1.44020 05
 D 0.0
 SO 7.84070 00
 SI 1.44020 05
 MAG 1.03400-03
 YAP -3.00000 00
 YP 6.03300-17

NOT REPRODUCIBLE

REPULSE ID 000000 07/17/71 17.27.31

1	0.0	0.0	2.013330-02	0.0
0	0.0	0.0	2.013330-02	-0.333330-02
1	2.251000-01	4.000000 00	2.013330-02	-1.357700-17
2	3.250000 00	3.333330-01	-2.400000-01	7.142860-02
3	2.500000 00	2.013330-01	-0.326670-17	7.142860-02
4	3.500000 00	-1.112710 00	1.479300 00	-2.273020-01
5	2.071000 01	2.013330-01	-3.000300 00	3.226600-10
6	1.970000 01	7.575760-02	-3.000300 00	3.226600-10
7	0.0	0.0	-3.000300 00	2.013330-05
8	0.0	6.943430-06	0.0	4.166670-02
9	0.0	0.0	0.0	3.472560-03
1	2.251450-01	4.000000 00	2.013330-02	-3.472220-03
2	3.250000 00	3.333330-01	-6.266000-02	1.433440-02
3	2.400000 01	2.857140-01	-1.215200-02	0.621160-04
4	3.500000 00	-1.112710 00	5.701050-03	-2.893150-04
5	2.071000 01	2.013330-01	0.953830-17	-2.893150-04
6	1.970000 01	7.575760-02	0.953830-17	-2.893150-04
7	0.0	0.0	0.953830-17	-2.893150-04
8	0.0	6.943430-06	0.953830-17	-2.893150-04

Y-YEAR TIME LENS TYRAN

ZOOM POSITION ID

1

SYSTEM

REFL 1.00000 03
REFL 1.44020 05
YOP -6.16670 01
ENTER 2.29160-01
EXIT 0.0
MODEL 7.91650 01
LENS NO. 1
FL 2.50000-01
D 3.25000 00
SO 0.0
SI 2.50000-01
TAG 0.0
YAR 2.01333-02
YOP 0.54750-03

LENS NO. 2

FL 3.00000 00
D 2.40000 01
SO -3.00000 00
SI -1.80140 16
TAG 6.00000 15
YAR -2.50000-01
YOP 2.07270-02

LENS NO. 3

FL 3.50000 00
D 3.50000 00
SO -1.80140 16
SI 3.50000 00
TAG -1.84290-15
YAR -2.50000-01
YOP -6.26600-02

LENS NO. 4

FL -2.06710-01
D 2.07100 01
SO 1.14270-15

NOT REPRODUCIBLE

SI 5.44350-07
 DAG -1.55520-07
 YAR 2.49970-01
 YPR -6.30200-02

40326 TRIP LAYOUT (INCL. DISS. PATH), PUPIL AT BIGGLE MIRROR 710817

Y-YEAR TRIP LENS TRACE PAGE 2

ZOOM POSITION NO

LENS NO. 5
 FL 0.0
 D 6.00000-00
 SD 5.44350-07
 SI 5.44350-07
 DAG 1.00000-00
 YAR 2.49970-01
 YPR 8.65050-07

LENS NO. 6
 FL 5.32170-00
 D 4.04440-00
 SD 5.44350-07
 SI 5.32170-00
 DAG 9.77620-02
 YAR 2.49970-01
 YPR 2.10000-02

LENS NO. 7
 FL -1.06600-00
 D 4.04440-00
 SD 1.27720-00
 SI 4.04450-00
 DAG 3.16440-00
 YAR 5.99980-02
 YPR 1.92020-02

LENS NO. 8
 FL -3.97950-11
 D 0.0
 SD 6.99070-05
 SI 6.99070-05
 DAG 1.00000-00
 YAR 1.03950-05
 YPR 5.09990-02

NOT REPRODUCIBLE

CPA70S, 110 000000 00/17/71 17.06.00

-4.	1.	0.	0.	0.	3.000000-00	0.0
	0	0.0	0.0	0.0	3.000000-00	-7.212700-01
	1	1.000000-00	7.575750-02	0.0	3.000000-00	7.142000-02
	2	1.070010-01	2.010000-01	0.0	3.000000-00	7.142000-02
	3	2.071020-01	-1.112710-01	0.0	3.000000-00	-4.502050-04
	4	3.500000-00	2.357140-01	0.0	3.000000-00	-4.502050-04
	5	1.000000-01	0.0	0.0	3.000000-00	-4.502050-04
	6	6.000000-00	1.701000-01	0.0	3.000000-00	-4.502050-04
	7	4.000000-00	-2.512000-12	0.0	3.000000-00	-4.502050-04
	8	6.000000-00	-2.512000-12	0.0	3.000000-00	-4.502050-04
	0	0.0	0.0	0.0	3.000000-00	-4.502050-04
	1	1.000000-00	7.575750-02	0.0	3.000000-00	-4.502050-04
	2	1.070010-01	2.010000-01	0.0	3.000000-00	-4.502050-04
	3	2.071020-01	-1.112710-01	0.0	3.000000-00	-4.502050-04
	4	3.500000-00	2.357140-01	0.0	3.000000-00	-4.502050-04
	5	1.000000-01	0.0	0.0	3.000000-00	-4.502050-04
	6	6.000000-00	1.701000-01	0.0	3.000000-00	-4.502050-04
	7	4.000000-00	-2.512000-12	0.0	3.000000-00	-4.502050-04
	8	6.000000-00	-2.512000-12	0.0	3.000000-00	-4.502050-04

Y-YEAR 1-11 LEPS TYPE

2000 POSITION 100

SYSTEM	2.022400-02
REL	6.980070-05
REL	5.900000-02
YOP	1.000000-00
EXIT	-5.980000-00
PARREL	6.400000-01
LEPS 10.	1
FL	1.320000-01
Q	1.070010-01
SO	0.0
SI	1.320000-01
LAG	0.0
YAR	3.000000-00
YOP	2.017300-07
LEPS 10.	2
FL	6.000000-00
Q	2.071020-01
SO	-8.000000-00
SI	2.071020-01
LAG	-2.112000-00
YAR	-1.470000-00
YOP	5.700000-03
LEPS 10.	3
FL	-0.000000-00
Q	2.000000-00
SO	-2.250000-07
SI	-2.250000-07
LAG	1.000000-00
YAR	1.000000-00
YOP	-1.220000-02
LEPS 10.	4
FL	3.000000-00
Q	1.000000-00
SO	-2.500000-00

NOT REPRODUCIBLE

Appendix U

TRACKING REQUIREMENTS AND RESULTING
ACCURACIES FOR POSITION DETERMINATION
OF SATELLITES IN A SPACE DATA RELAY SYSTEM

by

Mr. L. R. Jacobs

(Previously distributed as Technical Memorandum No. 7)

LOCKHEED PALO ALTO RESEARCH LABORATORY
LOCKHEED MISSILES & SPACE COMPANY
A GROUP DIVISION OF LOCKHEED AIRCRAFT CORPORATION

SUMMARY

This memorandum presents the results of a study of position determination requirements of a space data relay system.* LMSC has a computer program which simulates the computation of an ephemeris and shows the position errors that result from various input errors. This program was used to investigate the requirements of a single link, i.e., ground to synchronous satellite, and a double link, i.e., ground through a synchronous satellite relay to a low-orbit satellite or to a second synchronous satellite. The program considers all the major error sources in ephemeris prediction, including random and bias tracking errors, ground station location and timing, radiation pressure, atmospheric drag, and gravitational model errors.

The major results and conclusions are:

- When angle, range rate, and range data were used to simulate ephemeris prediction of the synchronous satellite, only range data contributed significantly to the result.
- When range and range rate data were used to simulate ephemeris prediction of the low-orbit satellite through the synchronous satellite, only range data contributed significantly to the result.**
- The optimum fitting interval for the low-orbit satellite is 6 to 7 revolutions.
- After completion of fitting, in-track errors build up approximately linearly from 50 to 1000 m in about 10 hr.

*At the time this report was written, 50-ft range errors were being considered. Later efforts implemented a 10-ft ranging scheme. The general analysis shown here can be directly carried over to the latter scheme.

**These conclusions were based on 2 readings/min for both range and range rate. If the frequency of range rate readings were much higher than the frequency of range readings (20 to 50 times were frequent), range rate could contribute significantly; however, if there were no limitation on reading frequency, it would be preferable to increase range reading frequency instead of adding range rate.

U-1

LOCKHEED PALO ALTO RESEARCH LABORATORY
LOCKHEED MISSILES & SPACE COMPANY
A GROUP DIVISION OF LOCKHEED AIRCRAFT CORPORATION

- Drag, range, and gravity model errors were the primary causes of error in the orbit of the low-altitude satellite.
- Simultaneous 50-ft errors, both bias and random, in range measurement have approximately the same total error effect as all other sources in low-orbit ephemeris.
- One-sigma errors in relay satellite orbit were 88 ft in range, 165 ft in cross-track, and 1760 ft in in-track for 50-ft bias and random range errors.
- Errors in the second synchronous satellite orbit after 3 days of fitting were 2280 ft in cross-track and 1070 ft in in-track for 50-ft bias and random range errors.

U-2

LOCKHEED PALO ALTO RESEARCH LABORATORY
LOCKHEED MISSILES & SPACE COMPANY
A GROUP DIVISION OF LOCKHEED AIRCRAFT CORPORATION

Section 1 INTRODUCTION

A satellite is usually tracked over only a small portion of its orbit; however, knowledge of the satellite's position and velocity between observations and at future times is usually required. Conventionally, this problem of interpolation and extrapolation is solved by fitting a set of orbital equations of motion to the observed data points using standard weighted least squares techniques. Errors in calculation of this orbit determination will result from errors in the tracking data and mathematical model. The observed data will have random errors and will usually be biased due to a variety of causes such as equipment calibration and alignment errors. The tracking station locations and station time may be imperfectly known. Moreover, a solution to the orbital equations of motion cannot represent reality because of the imperfect knowledge of the geophysical model of the earth, such as the earth's gravity potential and the structure of its atmosphere.

In this report, equations are derived for determining the effect of these error sources on a weighted least squares fit for satellite position. Specific application of these equations to the Laser Communication Preliminary Subsystem design is then discussed.

U-3

LOCKHEED PALO ALTO RESEARCH LABORATORY
LOCKHEED MISSILES & SPACE COMPANY
A GROUP DIVISION OF LOCKHEED AIRCRAFT CORPORATION

Section 2 ERROR ANALYSIS

It is the purpose of an orbit determination program to give an estimate $\hat{X}(t)$ of the satellite ephemeris. This estimate is usually obtained by means of a weighted least squares fit of a set of dynamic equations to tracking data. In general, any estimate $\hat{X}(t)$ of $X(t)$ will be in error by an unknown amount $\delta X(t)$, with

$$\delta X(t) = X(t) - \hat{X}(t)$$

Error sources that are responsible for the existence of δX can be classified roughly as errors in tracking equipment, lack of knowledge of geophysical parameters, and inaccuracies in the equations of motion. In the following sections, equations are developed which describe the statistical properties of δX as a function of the statistics of a variety of error sources.

2.1 THEORETICAL AND ACTUAL OBSERVATIONS

In general, the state vector $X(t)$ cannot be observed directly. Rather, quantities such as slant range, azimuth, elevation, and Doppler frequency are observable with respect to a given coordinate system at a given point in space and time. One is thus led to define an observable q at time t_i as a function

$$q_i = q(X(t_i), \nu, t_i)$$

where $\nu = \text{col}(\nu_1, \nu_2, \dots, \nu_r)$, a vector defining the initial position of the station, the coordinate frame, and the motion of the earth. No errors have yet been assumed to exist. That is, $X(t)$ is the true state vector and ν is assumed to be an r -vector which represents reality. The fact that the value of ν is known only as an estimate will be considered later in the error analysis.

It is assumed that differential equations of motion exist which are known and solved without error. The solution to the differential equations defines the theoretical state vector $\bar{X} = \bar{X}(\lambda', t)$. The p-vector $\lambda' = \text{col}(\lambda'_1, \dots, \lambda'_p)$ consists of parameters of the equations of motion such as six initial conditions of the satellite at some specified time and constant parameters defining the geophysical model such as gravitational coefficients or the atmospheric density model. In the definition of $\bar{X} = \bar{X}(\lambda', t)$, the vector λ' is assumed to be known without error.

It should be recognized that any mathematical model that is assumed to represent satellite motion is purely deterministic. In reality, however, the motion of a satellite is influenced by random, unpredictable forces, such as meteorite impacts, unpredictable fluctuations in atmospheric drag or radiation pressure, or even random venting or leaking of fuel. It is assumed that $X(t)$ and $\bar{X}(\lambda', t)$ are related by the equation

$$X(t) = \bar{X}(\lambda', t) + \Delta X(t)$$

Given $\bar{X} = \bar{X}(\lambda', t)$, one can now define a theoretical observable by

$$\bar{q}_i = q(\bar{X}(\lambda', t_i), \nu, t_i)$$

From the assumptions given previously, it follows that

$$q(X(t_i), \nu, t_i) = \bar{q}(\bar{X}(\lambda', t_i), \nu, t_i) + \Delta q(t_i)$$

In reality, the vectors λ' and ν are not known; rather, estimates $\hat{\lambda}'$ and $\hat{\nu}$ are known which differ from the true values by small residual errors $\Delta\lambda' = \lambda' - \hat{\lambda}'$, $\Delta\nu = \nu - \hat{\nu}$. The estimated state vector $\hat{X}(t)$ is thus given by

$$\hat{X}(t) = \bar{X}(\hat{\lambda}', t)$$

and the estimated observable \hat{q} follows as

$$\hat{q}_i = \hat{q}(\bar{X}(\hat{\lambda}', t_i), \hat{\nu}, t_i)$$

U-5

The observed value of q_i , denoted by \tilde{q}_i , is that quantity actually observed and recorded at a given tracking station; \tilde{q}_i will differ from the estimate \hat{q}_i because of data biases, random data errors, and errors in the vectors λ^i and ν . That is

$$\tilde{q}_i = \hat{q}(\bar{\lambda}^i, t_i, \nu, t_i) + \frac{\partial \hat{q}_i}{\partial \lambda^i} \Delta \lambda^i + \frac{\partial \hat{q}_i}{\partial \nu} \Delta \nu + \Delta q(t_i) + \Sigma(t_i) \quad (1)$$

where $\Sigma(t_i)$ and $\Delta q(t_i)$ are the random data errors and the data biases, respectively.

In the process of determining an orbit from tracking data, a set of $K \leq P$ parameters (the fitting parameters thus comprise the K vector λ) is selected from the vector λ^i and fit to the tracking data by differentially correcting an estimate $\hat{\lambda}$ of λ using a weighted least squares fit. The $P-K$ parameters of the vector λ^i that do not appear in λ are used to define the vector $\bar{\lambda}$, together with its estimate $\hat{\bar{\lambda}}$. The second term of Eq. (1) can be expanded, causing Eq. (1) to become

$$\tilde{q}_i = \hat{q}_i + \frac{\partial \hat{q}_i}{\partial \lambda} \Delta \lambda + \frac{\partial \hat{q}_i}{\partial \bar{\lambda}} \Delta \bar{\lambda} + \frac{\partial \hat{q}_i}{\partial \nu} \Delta \nu + \Delta q(t_i) + \Sigma(t_i) \quad (2)$$

Given n observations, a system of n equations is defined by Eq. (2). This system can be written rather compactly after defining the following matrices:

$$\begin{aligned} \tilde{q} &= (\tilde{q}_i) \quad i = 1 \dots n \quad (\tilde{q} = \text{observed data}) \\ \hat{q} &= (\hat{q}_i) \quad i = 1 \dots n \quad (\hat{q} = \text{estimated data}) \\ Q &= (Q_{ij}) = \frac{\partial \hat{q}_i}{\partial \lambda_j} \quad i = 1 \dots n \\ &\quad j = 1 \dots K \end{aligned}$$

where λ_j are the fitting parameters

$$B = (B_{ij}) = \left(\frac{\partial \hat{q}_i}{\partial \bar{\lambda}_j} \right) \quad \begin{matrix} i = 1 \dots n \\ j = K+1, \dots, P \end{matrix}$$

where $\bar{\lambda}_j$ are dynamic parameters that affect the equations-of-motion but are not fitting parameters

$$N = (N_{ij}) \quad \frac{\partial \hat{q}_i}{\partial \nu_j} \quad \begin{matrix} i = 1, \dots, n \\ j = 1, \dots, r \end{matrix}$$

$$\Delta q = (\Delta q(t_i)) \quad i = 1, \dots, n$$

$$\epsilon = (\epsilon(t_i)) \quad i = 1, \dots, n$$

Then

$$\tilde{q} = \hat{q} + Q\Delta\lambda + B\Delta\bar{\lambda} + N\Delta\nu + \Delta q + \epsilon \quad (2)$$

2.2 STATISTICAL ASSUMPTIONS

In general, the quantities $\tilde{\lambda}$ and $\tilde{\nu}$ are obtained from observations subject to random errors; for example, the error in station latitude obtained from survey data is the result of random observational errors and biases. Since $\bar{\lambda}$ and ν are constant vectors, the errors in $\tilde{\lambda}$ and $\tilde{\nu}$ are constant in time; i.e., they are perfectly correlated in time. Hence, it is assumed that $\Delta\bar{\lambda}$ and $\Delta\nu$ are random variables with zero means and known covariance matrices. The same assumption is used for Δq and ϵ ; moreover, it is assumed that covariances between $\Delta\bar{\lambda}$, $\Delta\nu$, Δq , and ϵ are all zero. Under these assumptions, we define as follows:

$$\begin{aligned} \mathcal{E}(\Sigma\Sigma^t) &= W \\ \mathcal{E}(\Delta q\Delta q^t) &= \Lambda_D \\ \mathcal{E}(\Delta\nu\Delta\nu^t) &= \Lambda_\nu \\ \mathcal{E}(\Delta\bar{\lambda}\Delta\bar{\lambda}^t) &= \Lambda_B \end{aligned}$$

2.3 LEAST SQUARES EQUATIONS

The problem of estimating an orbit reduces to the obtaining of an estimate $\hat{\lambda}$ of the parameter vector λ from the observations \tilde{q}_j ; equivalently, one may obtain an estimate

$\Delta\hat{\lambda}$ of $\Delta\lambda$. In practice, the technique usually employed is that of grouping all error terms involving $\Delta\lambda$, $\Delta\nu$, Δq , and ϵ so that Eq. (3) becomes

$$\tilde{q} = \hat{q} + Q\Delta\lambda + \epsilon$$

The vector ϵ is then assumed to be normally distributed with zero mean and with diagonal covariance matrix ω (data weighted as σ^2 , with no correlation between observations). Standard techniques for minimizing $\sum(\hat{q} - \tilde{q})^2$ lead to

$$\Delta\hat{\lambda} = (Q^t \omega^{-1} Q)^{-1} Q^t \omega^{-1} (\tilde{q} - \hat{q}) \quad (4)$$

Equation (4) does not necessarily represent an optimal or maximum likelihood estimate of $\Delta\lambda$. Moreover, as can be seen from Eq. (3), $\tilde{\Sigma}$ is not a vector of independent errors, so that the covariance matrix of $\tilde{\Sigma}$ cannot be diagonal. In practice, Eq. (4) is taken to represent no more than a weighted least squares fit. In either case, it is of interest to compute the covariance matrix of the error $\delta X(t)$ in the estimated state vector $\hat{X}(t)$, given that $\hat{X}(t)$ was obtained from a least squares fit with diagonal weighting matrix ω .

2.4 VARIANCE EQUATIONS

It is assumed that a weighted least squares fit of data q has converged to a residual $\Delta\hat{\lambda}$ with

$$\Delta\hat{\lambda} = (Q^t \omega^{-1} Q)^{-1} Q^t \omega^{-1} (\tilde{q} - \hat{q})$$

Inserting $\tilde{q} - \hat{q}$ from Eq. (3) gives the following residual error in the estimate $\Delta\hat{\lambda}$:

$$-\delta\lambda = \Delta\tilde{\lambda} - \Delta\lambda = (Q^t \omega^{-1} Q)^{-1} Q^t \omega^{-1} [B\Delta\lambda + N\Delta\nu + \Delta q + \Sigma] \quad (5)$$

The covariance matrix of $\delta\lambda$ is given by

$$\text{cov}(\delta\lambda) = (Q^T \omega^{-1} Q)^{-1} + (Q^T \omega^{-1} Q)^{-1} Q^T \omega^{-1} [B \Lambda_B B^T + N \Lambda_N N^T + \Lambda_D] \omega^{-1} Q (Q^T \omega^{-1} Q)^{-1} \quad (6)$$

Let $X = X(t)$ be the state vector at time t . It follows that

$$X(t) = \bar{X}(\lambda^*, t) + \Delta X(t)$$

or

$$X(t) = \hat{X}(t) + \frac{\partial \hat{X}}{\partial \lambda} \Delta \lambda + \frac{\partial \hat{X}}{\partial \bar{\lambda}} \Delta \bar{\lambda} + \Delta X(t)$$

Thus,

$$\delta X(t) = \hat{X}(t) - \bar{X}(t) = \frac{\partial \hat{X}}{\partial \lambda} \Delta \lambda + \frac{\partial \hat{X}}{\partial \bar{\lambda}} \Delta \bar{\lambda} + \Delta X(t) \quad (7)$$

If we define

$$P(t) = (P_{ij}(t)) = \frac{\partial \hat{X}_i(t)}{\partial \lambda_j} \quad \begin{matrix} i = 1 \dots 1 \\ j = 1 \dots K \end{matrix}$$

$$R(t) = (R_{ij}(t)) = \frac{\partial \hat{X}_i(t)}{\partial \bar{\lambda}_j} \quad \begin{matrix} i = 1 \dots 1 \\ j = K+1, \dots, P \end{matrix}$$

and combine Eqs. (7) and (5), we obtain

$$\delta \mathbf{X}(t) = \left(\mathbf{R}(t) - \mathbf{P}(t) \left(\mathbf{Q}^t \omega^{-1} \mathbf{Q} \right)^{-1} \mathbf{Q}^t \omega^{-1} \mathbf{B} \right) \Delta \tilde{\lambda} + \Delta \mathbf{X}(t) - \mathbf{P}(t) \left(\mathbf{Q}^t \omega^{-1} \mathbf{Q} \right)^{-1} \mathbf{Q}^t \omega^{-1} \Delta \mathbf{q} \\ + \mathbf{M}(t) \mathbf{N} \mathbf{A}_p \mathbf{N}^T \mathbf{M}^T(t) - \mathbf{P}(t) \left(\mathbf{Q}^t \omega^{-1} \mathbf{Q} \right)^{-1} \mathbf{Q}^t \omega^{-1} (\mathbf{N} \Delta \nu + \epsilon)$$

The covariance matrix of $\delta \mathbf{X}(t)$ thus becomes

$$\text{cov}[\delta \mathbf{X}(t)] = \mathbf{P}(t) \left(\mathbf{Q}^t \omega^{-1} \mathbf{Q} \right)^{-1} \mathbf{P}^T(t) + \mathbf{M}(t) \mathbf{N} \mathbf{A}_p \mathbf{N}^T \mathbf{M}^T(t) \\ + \left(\mathbf{R}(t) - \mathbf{M}(t) \mathbf{B} \mathbf{A}_p \mathbf{B}^T \left(\mathbf{R}(t) - \mathbf{M}(t) \mathbf{B} \right)^T \right) + \mathcal{E}[\Delta \mathbf{X}(t) - \mathbf{M}(t) \Delta \mathbf{q}][\Delta \mathbf{X}(t) - \mathbf{M}(t) \Delta \mathbf{q}]^T \quad (8)$$

where $\mathbf{M}(t) = \mathbf{P}(t) \left(\mathbf{Q}^t \omega^{-1} \mathbf{Q} \right)^{-1} \mathbf{Q}^t \omega^{-1}$.

Equation (8) represents the basic error analysis equation. The first term of Eq. (8) gives the contribution to the covariance matrix of the random data errors. The positive diagonal roots of $\mathbf{P}(t) \left(\mathbf{Q}^t \omega^{-1} \mathbf{Q} \right)^{-1} \mathbf{P}^T(t)$ are the standard deviations of the components of the state vector due to random data errors. The positive diagonal roots of the remaining terms give the standard deviations of the state vector due to other groups of error sources.

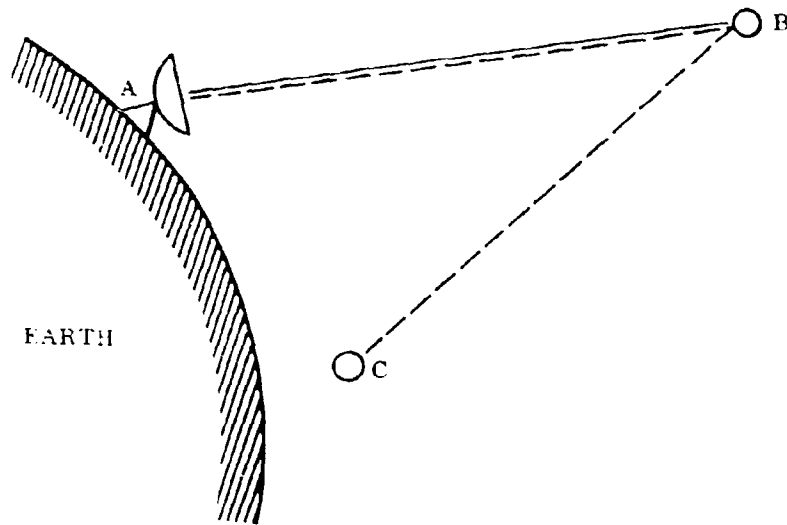
An error analysis program which simulates the least squares fit for a set of orbital parameters and generates the covariance matrix of satellite position [Eq. (8)] has been assembled at LMSC. A large number of error parameters are included, and a wide range of satellite tracking systems can be studied. The remainder of this report will discuss a specific application of the error analysis program to the Laser Communication Subsystem design.

Section 3

APPLICATION OF ERROR ANALYSIS TO LASER COMMUNICATION SYSTEM

3.1 APPROACH

The specific orbit determination problem considered here is exclusively the two-link case illustrated below.



A ground station (A) located at an arbitrary point on the earth's surface is in communication with a synchronous satellite (B). At the same time, the ground station is in communication with another satellite (C) using a data link through the synchronous relay. It is assumed that for link A-B the possible observations are range, range rate, azimuth, and elevation. For the combined link A-B-C, the possible observations are assumed to be range and range rate (the total range and range rate from the ground station to C). A number of simulated orbit fits were performed (using the computer

U-11

LOCKHEED PALO ALTO RESEARCH LABORATORY
 LOCKHEED MISSILES & SPACE COMPANY
 A GROUP DIVISION OF LOCKHEED AIRCRAFT CORPORATION

program described in the Summary) to evaluate the orbit determination accuracies, both over the fitting interval and predicted, of the above tracking system. Forces included in the equations of satellite motion were zonal and tesseral harmonics of the earth's gravitational field, lunar-solar gravity, radiation pressure, and atmospheric drag. Fitting parameters were the orbital parameters of satellites B and C.

3.2 ERROR SOURCES

The following error sources were considered:

- Random data errors
- Data bias
- Station clock
- Station locations
- Radiation pressure model
- Atmospheric drag model
- Earth's gravitation model

Random Data Errors. The following random data errors were assumed for both tracking links:

<u>Link A-B</u>	<u>Link A-B-C</u>
σ Azimuth = 10^{-3} rad	σ Range = 50 ft
σ Elevation = 10^{-3} rad	σ Range Rate = 0.3 ft/sec
σ Range = 50 ft	
σ Range Rate = 0.2 ft/sec	

Data Bias. The following data bias errors were assumed for both tracking links:

<u>Link A-B</u>	<u>Link A-B-C</u>
σ Azimuth = 10^{-3} rad	σ Range = 50 ft
σ Elevation = 10^{-3} rad	σ Range Rate = 0.2 ft/sec
σ Range = 50 ft	
σ Range Rate = 0.2 ft/sec	

Station Clock. The error in the station clock was assumed to have a standard deviation of 10^{-3} sec.

Station Locations. The following station location errors were assumed:

σ Latitude	50 ft
σ Longitude	50 ft
σ Height	50 ft

Radiation Pressure Model. It was assumed that the standard deviation of the product of the solar constant, satellite area to mass ratio, and surface reflectivity was 15% for both direct and reflected radiation pressure. (This is equivalent to assuming that the radiation pressure force has a standard deviation of 15%.)

Atmospheric Drag Model. When satellite C is in a low-altitude orbit, atmospheric density model errors are an important source of error in the orbit determination process. A dynamic density model is used in which the atmospheric density is a function of the solar flux and variations of the earth's magnetic field. The density variations with geomagnetic activity are of primary importance for the short data spans (several days or less) considered in this study. The density has been shown to be proportional to the index of geomagnetic activity (K_p or A_p) and to lag by several hours behind changes in the geomagnetic indexes. For error analysis purposes, a typical geomagnetic variation was assumed. The amplitude and time lag of this variation were then assumed to have a standard deviation of 25%. The errors in the density model produce errors in the equations-of-motion that are only partially compensated for by fitting the ballistic parameter of the low-altitude satellite.

Earth's Gravitation Model. Standard deviations for the earth's gravitation model were based on the latest determinations of the earth's gravitational field from the combined use of satellite data and surface gravity measurements. The standard deviations are

$$\sigma u/u = 2 \times 10^{-7} \text{ (gravitational constant)}$$

$$\sigma J_N = 1 \times 10^{-8} \text{ (zonal harmonics)}$$

For fully normalized tesseral coefficients \bar{C}_{NM} , \bar{S}_{NM} , the following standard deviations were used:

<u>N</u>	<u>M</u>	<u>σC_{NM}</u>	<u>σS_{NM}</u>
2	2	3.5×10^{-8}	1.5×10^{-8}
3	1	1×10^{-7}	1×10^{-8}
3	2	1.2×10^{-7}	1.8×10^{-7}
3	3	1×10^{-8}	1×10^{-9}
4	1	4×10^{-8}	5×10^{-8}
4	2	2×10^{-8}	5×10^{-9}
4	3	1.4×10^{-7}	3×10^{-8}
4	4	1.8×10^{-7}	5×10^{-8}

3.3 RESULTS

All results of the error analysis program will be presented in the orbital coordinate system. The error components are ΔR (radial) in the direction of the satellite radius vector, ΔIT (in-track) in the direction of satellite motion, and ΔCT (cross-track) perpendicular to the orbit plane. A rigorous definition of this coordinate system in terms of unit vectors is

$$\hat{e}_R = \frac{\vec{R}}{|\vec{R}|}$$

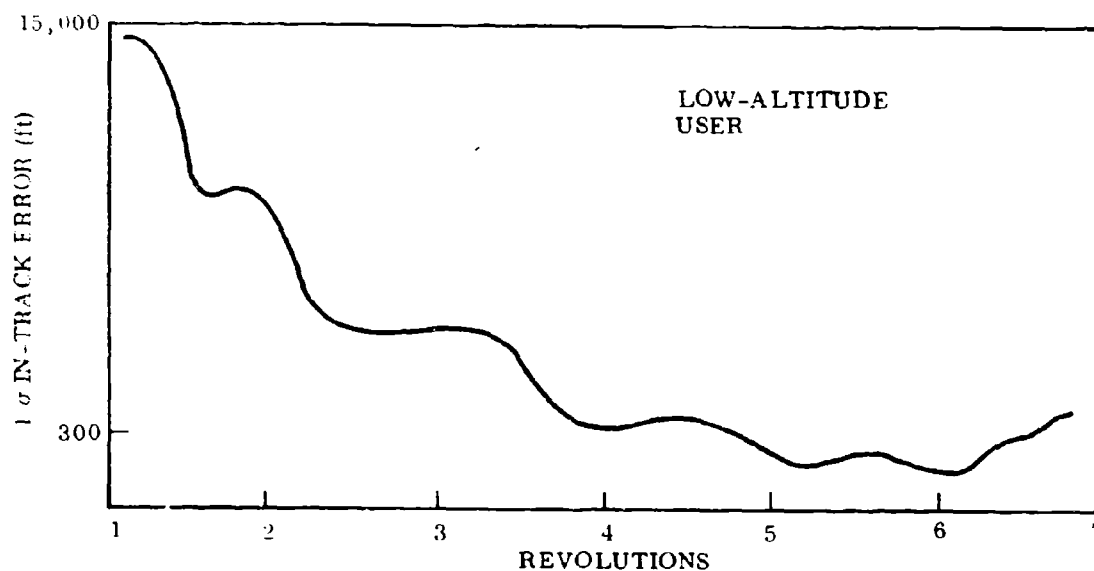
$$\hat{e}_{CT} = \frac{\vec{R} \times \vec{V}}{|\vec{R} \times \vec{V}|}$$

$$\hat{e}_{IT} = \hat{e}_{CT} \times \hat{e}_R$$

Section 4 SYNCHRONOUS RELAY AND LOW-ALTITUDE USER

Fitting parameters are the inertial position and velocity of both satellites at some epoch and the ballistic parameter of the low-altitude (200-nmi perigee height) user. It was found that the angles and range-rate data for link A-B and the range-rate data for link A-B-C did not contribute significantly to the fit. Only the range data were used in the results presented below.

The first problem investigated was the time span of data to be fit. The sketch below illustrates the reduction in the in-track error as more data are included in the orbit fit. The optimum fitting interval is approximately 7 revolutions. Fitting more data will cause the errors to increase again, mainly because of a buildup of air drag and radiation pressure errors.

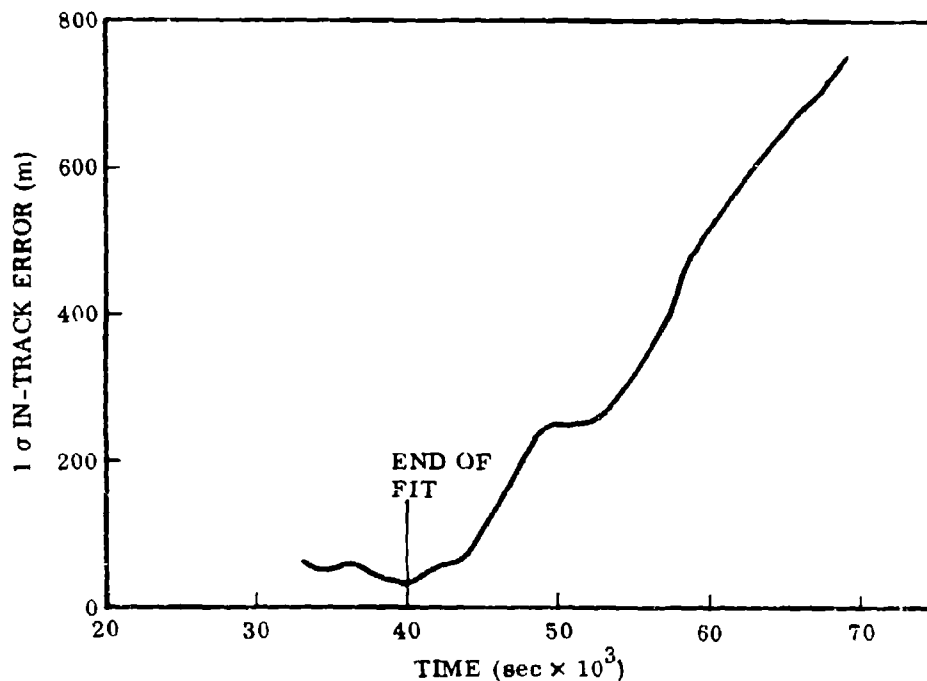


U-15

LOCKHEED PALO ALTO RESEARCH LABORATORY
LOCKHEED MISSILES & SPACE COMPANY
A GROUP DIVISION OF LOCKHEED AIRCRAFT CORPORATION

In the results that follow, a 7-revolution fitting interval was used. It was assumed that data points were processed at the rate of 1 point every 2 min. This primarily affects the contribution of random data errors, and the use of more observations would have had little effect on the final results. The errors were extrapolated beyond the fitting interval to provide an estimate of real-time prediction accuracy. Only results for the last revolution of the fitting interval are given because they are representative of the error pattern over the entire fitting interval.

The total 1σ extrapolation error for a 200-nmi orbit is shown in the graph below. It is seen that the error grows secularly during the extrapolation interval, due primarily to an error in the fitted period and errors in the atmospheric drag model. The drag errors, range errors, and gravity model errors are the primary sources of error in the orbit of the low-altitude user. The standard deviations and biases assumed for the range data cause these error sources to have an effect of the same order of magnitude as the other error sources.



U-16

LOCKHEED PALO ALTO RESEARCH LABORATORY
 LOCKHEED MISSILES & SPACE COMPANY
 A GROUP DIVISION OF LOCKHEED AIRCRAFT CORPORATION

One-sigma errors in the relay satellite orbit over the fitting interval are listed below.

$$\begin{aligned}1\sigma \Delta R &= 88 \text{ ft} \\1\sigma \Delta CT &= 165 \text{ ft} \\1\sigma \Delta IT &= 1760 \text{ ft}\end{aligned}$$

The relay errors are primarily due to the slant range data biases. It would probably be desirable to fit for these data biases in the orbit determination program in order to reduce the relay errors and the cross-track error of the low-altitude satellite.

For fitting two relay orbits, the low-altitude satellite (C) was replaced by a synchronous satellite having zero eccentricity, a longitude of 120° E of the first relay, and an inclination of 3°. The second relay cross-track and in-track errors stabilize after approximately 3 days of data are included in the fit, at which time the cross-track error is 2280 ft and the in-track error is 1070 ft. The errors due to random data errors are quite large, especially cross-track, where they are the dominant error. This indicates ill-conditioning of the normal equation, which is not surprising when one considers that the data are nearly constant and that small changes in the orbit inclinations do not produce significant changes in the data. The range rate observations for both data links and the angle data for link A-B did not contribute significantly to the orbit determination process. The results presented are based on only the range data from both links. As the inclination of the second relay approaches zero, the normal equation ill-conditioning gets worse and the cross-track errors increase significantly. Fitting the second relay in combination with a low-altitude user may be necessary to alleviate the ill-conditioning of the normal equation.

Section 5
CONCLUSIONS

Range data from links A-B and A-B-C only is sufficient to provide an accurate orbit determination capability for the Laser Communication Satellite Program. If random data and bias errors are held within the limits listed above, their contribution to orbital inaccuracies will be no greater than other significant error sources (geopotential, drag, etc.).

U-18

LOCKHEED PALO ALTO RESEARCH LABORATORY
LOCKHEED MISSILES & SPACE COMPANY
A GROUP DIVISION OF LOCKHEED AIRCRAFT CORPORATION

Appendix V

ACQUISITION AND TRACKING
SUBSYSTEM REQUIREMENTS

by

Dr. R. C. Ohlmann
Mr. C. E. McClellan

LOCKHEED PALO ALTO RESEARCH LABORATORY
LOCKHEED MISSILES & SPACE COMPANY
A GROUP DIVISION OF LOCKHEED AIRCRAFT CORPORATION

1. INTRODUCTION

The function of the acquisition and tracking subsystem is to close the pointing link between any two terminals so that communication is possible in both directions. A number of fundamental steps must be taken for the communication links to be established. Prior to any optical communication, each package is provided with ephemerides, vehicle attitude, vehicle angular rates, precision clock time, and a command (programed or transmitted) advising which other vehicle is to be acquired at what time. With this information at hand, the following basic steps are performed by each package:

- (1) Computes the pointing direction toward the other vehicle and points toward it, open loop
- (2) Transmits a beacon signal toward the other in a prearranged sequence
- (3) Identifies the received signal and points toward it more accurately
- (4) Transmits a narrow beam and tracks the received beam accurately
- (5) Maintains pointing of its transmitter with sufficient accuracy to maintain reliable communication

Two important system constraints are the conditions under which this function must be performed and the maximum time permitted to accomplish the function. These constraints have been treated as system requirements and are treated here for a baseline operational data relay subsystem.

For the operational system, mission users include aircraft, low-orbiting satellites, and synchronous satellites. These units relay their data through an equatorial synchronous satellite to either a ground or aircraft terminal. Each high-data-rate sending terminal uses a Package A, whose signal is received by a Package B on the receiving terminal. Each Package B contains a beacon that performs two functions: (1) transmitting an acquisition and tracking signal to Package A, and (2) carrying low-data-rate transmission to Package A (including ranging data).

The acquisition and tracking function occurs at both ends of each link. Initial acquisition is always performed by the Package A terminal acquiring the beacon from Package B.

The overall acquisition and tracking function between any two terminals is divided into the following phases:

- Phase I - Initial acquisition of B by A occurs at the end of this phase. A then improves pointing and sends signal toward B.
- Phase II - Acquisition of A by B occurs at the end of this phase. B then improves pointing and increases its effective power toward A.
- Phase III - Fine-pointing of A toward B occurs at the end of this phase. A sends its narrowest beam toward B.
- Phase IV - Fine-pointing of B toward A occurs in this phase. B sends its narrowest beam toward A at the end of this phase if that has not been accomplished in Phase II.
- Phase V - Closed-loop tracking occurs in this phase. Final adjustment of A and B tracking takes place before communication begins.

The designation of the links to be closed is performed in terms of Phase I, the initial acquisition. The link closures that must be performed are given in Table 1. The operational acquisition and tracking requirements for each of these links differ and are treated separately. In each case certain requirements are given for the permissible acquisition and tracking time before communication can begin.

Table 1
ACQUISITION LINKS

Initial Acquisition Receiver Package A	Beacon Direction	Acquisition Beacon Package B
Aircraft User	←	Synchronous Satellite
Low-Orbit Satellite	←	Synchronous Satellite
Synchronous Satellite	←	Synchronous Satellite
Synchronous Satellite	←	Aircraft Terminal
Synchronous Satellite	←	Ground Terminal
Ground Terminal	←	Synchronous Satellite

2. ACQUISITION AND TRACKING TIME CONSTRAINTS

The acquisition and tracking time is defined as the total time required to perform all phases. This starts when an initial command to begin the acquisition sequence is received or is initiated by an onboard computer. Thus, it is the time between the start of initial orientation of the packages toward each other until the high-data-rate communication can begin. The total acquisition and tracking time, in practice, is a random variable whose variation depends on the system noise and operating conditions. Thus, the requirements, to be exact, must specify an acquisition time with some cumulative probability -- for example, a time such that 99% of all acquisitions will occur in less than T_{99} , and 99.99% in less than $T_{99.99}$.

The mission constraints set the appropriate acquisition time requirements. These requirements depend on the effect of a longer acquisition time on successful mission performance. For example, if a user satellite is tracking enemy missiles that can perform evasive maneuvers during the period when communications are in operation, there must be continuous data flow and duplicate systems must be operating so that acquisition time will have no effect. However, even in this extreme case the mission reliability may be considered as sufficient if the probability is less than 10^{-6} that the acquisition time will be longer than a few minutes, and is less than 10^{-4} that it will be more than 20 sec. This would mean that one acquisition in 10,000 would take more than 20 sec, one in a million would take more than several minutes. In the absence of a specific mission to analyze, postulates such as these appear rational. For surveillance missions, the 20-sec time may more reasonably be chosen at the 1% level, if the system can be designed so the overall time is more than 40 sec with a probability of 0.01%.

2.1 OPERATIONAL LINK REQUIREMENTS

The operational links shown in Table 1 are considered separately, for each has unique constraints on the acquisition-time requirements and the conditions under which closing must occur.

2.1.1 Aircraft User Closing With Synchronous Relay Satellite

A high-flying aircraft collecting high-rate data is assumed to relay these data via a synchronous relay satellite. In this case, the aircraft user can establish the link some time in advance of its data-collecting operation, so that an acquisition time of several minutes is not likely to be excessive. On the other hand, if the aircraft user is moving to a location where it must switch between synchronous relay satellites, a 20-sec switching time with 99% probability will be desirable. However, the aircraft user presumably can select the time the switch will be accomplished to effect the most desirable or least unfavorable conditions for a short acquisition time.

The aircraft user's acquisition receiver views the synchronous satellite with a background that may be either the sun, the moon, scattered sunlight, or starlight. The starting time will be selected to avoid both the sun and the moon. This can be done easily since the earth's rotation moves the apparent angular position of the sun and moon $0.25^\circ/\text{min}$. Each subtends 0.5° ; in 2 min they will move off the acquisition line. Even with a 1° field of view, in 6 min these bodies will be out of the field of view. Furthermore, the probability that the sun or moon is in the field of view at all is only about 10^{-4} , as calculated in Appendix O. Thus, the background that is significant to the aircraft user is sky-scattered sunlight within a few degrees of the sun.

The attitude and position uncertainty of such an aircraft user is not specified in the guidelines. However, any user collecting high-rate data is likely to have aboard guidance equipment that will determine its position within 1 mile and its attitude to $\pm 0.1^\circ$. Because of possible structural bending between the attitude sensors and the communication subsystem, an uncertainty in subsystem attitude of $\pm 0.2^\circ$ is chosen as the guideline, although this value can be improved if the subsystem design calculations show it to be necessary.

2.1.2 Low-Orbit Satellite Closing With Synchronous Satellite

The low-orbit satellite user may acquire the synchronous satellite relay as it rises over the earth's horizon. If the low-orbit satellite already is communicating with one

relay and must switch to the next relay, mission considerations indicate that the switching time must be kept as short as feasible. The selected guideline is a requirement for less than 20 sec of the total acquisition time for 99% of the acquisitions, and 40 sec or less for 99.99% of acquisitions.

It is shown in Appendix O that the probability of the sun or moon being in the background for a 1° field of view of the low-orbit satellite is also about 10^{-4} . When either one is in the field of view, the low-orbit satellite can delay switching relays for 6 min until these background sources move from the field of view. If switching is not occurring, but only one relay is being acquired, the low-orbit satellite selects the starting time to avoid these background sources. Thus, the only significant background source for the low-orbit satellite receiver during acquisition is starlight. Noise from cathode dark current is more significant than appropriately filtered background light.

The attitude and position uncertainty of the low-orbit satellite is postulated to be $\pm 0.5^\circ$ and 10 miles cross-track after the initial burn before any tracking has been performed. The attitude uncertainty is based on very simple horizon and sun sensors, and in any operational system a user satellite collecting high-rate data is expected to have information more precise by an order of magnitude. However, to avoid undue constraints on the user satellite, $\pm 0.5^\circ$ uncertainty has been selected as a guideline. Only the cross-track position uncertainty is of importance for initial acquisition at the horizon after one orbit. Booster inertial guidance and burn controls will prevent cross-track uncertainty from exceeding 10 miles. With respect to pointing to a synchronous satellite, this uncertainty corresponds to less than $\pm 0.03^\circ$ and thus is negligible compared with the attitude uncertainty.

2.1.3 Synchronous Satellite Closing With Synchronous Satellite

The acquisition time for the synchronous satellite user or relay is significant only when switching between relays occurs. Otherwise, since the relays are in place for a long time, as much as several hours could be used for acquisition. However, the subsystem is designed so the switching acquisition time will take place in 20 sec or less 99% of the time. Almost surely, the moment of switching can be selected to avoid both sun and moon background.

V-5

LOCKHEED PALO ALTO RESEARCH LABORATORY
LOCKHEED MISSILES & SPACE COMPANY
A GROUP DIVISION OF LOCKHEED AIRCRAFT CORPORATION

Appendix O shows that the probability of having the sun or moon in the background is less than 10^{-4} , and they move out of the background in 3.6 min if the satellite field of view is $\pm 0.2^\circ$. Thus, even on a random basis, a system that cannot acquire with these backgrounds can still meet the requirement of 40 sec 99.99% of the time if it can acquire against star backgrounds. Thus, the background present during acquisition will be assumed to be starlight plus any cathode dark current present.

The attitude uncertainty of the synchronous satellite is given in the guidelines as $\pm 0.2^\circ$. Although it is possible to improve this value by an order of magnitude with improved horizon and sun sensors, the system will be designed for an uncertainty of $\pm 0.2^\circ$ to avoid increasing hardware requirements in addition to the laser communication subsystem.

2.1.4 Synchronous Satellite Closing With Aircraft Terminal

In this case, the aircraft terminal presumably has very accurate attitude knowledge as well as knowledge of the location of the synchronous satellite. The synchronous satellite receives a high-power beacon from the aircraft terminal. The acquisition time is not critical, since the aircraft cannot pass quickly from the view of one satellite to that of another.

This situation is unique in that a more powerful beacon is used at the aircraft terminal because ample prime power is available. However, the synchronous satellite's Package A receiver is the same one that at other times acquires another synchronous satellite. Therefore, the requirement is placed on the system that the same acquisition technique be used for each link so that a single space-hardware package is sufficient.

When the synchronous satellite acquisition receiver views the aircraft terminal, it is faced with a background that may consist of sunglint off the ocean, sunlight reflected from clouds, or earth albedo. The sunglint is especially severe in the unusual case of glancing incidence of sunlight off quiet water, a situation that the aircraft terminal can

avoid during acquisition by choosing an appropriate location or waiting until the condition passes. Therefore, the worst background condition occurring significantly often is assumed to be sunlit clouds filling the receiver field of view of 0.4° .

The attitude uncertainty of the beacon transmitter on the aircraft terminal is not given in the guidelines. To calculate the acquisition, it is necessary to assume the attitude knowledge available to the aircraft terminal. Preliminary design analysis assumed $\pm 0.1^\circ$ for knowledge of the aircraft attitude as the baseline; variations from the baseline are discussed.

2.1.5 Synchronous Satellite Closing With Ground Terminal

The considerations in this case are very much like those for the aircraft terminal. The ground terminal telescope has very precise pointing, with the uncertainty lying primarily with the ephemeris of the synchronous satellite. If rf links are in operation to the synchronous satellite, its position can be determined very accurately before laser communication begins, with negligible angular uncertainty for beacon pointing. Otherwise, several miles of in-track uncertainty may exist when laser communication is first attempted, resulting in an angular uncertainty of about $\pm 0.02^\circ$. The acquisition time with $\pm 0.02^\circ$ uncertainty of the ground beacon pointing is determined.

Table 2 summarizes these system requirements on the acquisition and tracking links. A review of this table shows that, in terms of range and required acquisition time, the synchronous-to-synchronous relay link is most difficult. Next in difficulty, because of the background, is the aircraft-user link that must close in 20 sec. Finally, the aircraft terminal link may be difficult because of the high background, even though the permitted acquisition time may be long.

For the acquisition and tracking subsystem design, each of these critical factors has been examined separately to find a system that will satisfy all of the requirements with the least cost and risk.

Table 2

ACQUISITION CONDITIONS

Acquiring Terminal (Receiver)	Beacon Terminal (Transmitter)	Range (km)	Angular Uncertainty	Transmitter Receiver Angular Uncertainty	Background Conditions	Required Acquisition Time (99%)
Aircraft User	Synchronous Satellite	41,700	$\pm 0.2^\circ$	$\pm 0.1^\circ$	Scattered Sunlight	20 sec
Low-Orbit Satellite	Synchronous Satellite	43,000	$\pm 0.2^\circ$	$\pm 0.5^\circ$	Starlight	20 sec
Synchronous Satellite	Synchronous Satellite	73,000	$\pm 0.2^\circ$	$\pm 0.2^\circ$	Starlight	20 sec
Synchronous Satellite	Aircraft Terminal	38,500	$\pm 0.1^\circ$	$\pm 0.2^\circ$	Sunlit Clouds	2 min
Synchronous Satellite	Ground Terminal	38,500	$\pm 0.02^\circ$	$\pm 0.2^\circ$	Sunlit Clouds	10 min
Ground Terminal	Synchronous Satellite	38,500	$\pm 0.2^\circ$	$\pm 0.02^\circ$	Scattered Sunlight	10 min

V-18

3. GUIDELINES AND CONSTRAINTS FROM WORK STATEMENT

For completeness, the guidelines and constraints given in the Contract Statement of Work that particularly affect the acquisition and tracking design are briefly tabulated below.

	Package A	Package B
Maximum Weight (lb)	100	100
Volume Without Antenna (ft ³)	1	1
Antenna Maximum Diameter (ft)	1	2
Power (W)	140	50
Design Life (yr)	7	7
Minimum Life (yr)	5	5
Acquisition Time (sec)	20	20
Pointing Optimization Time	10	10
Beamwidth (arcsec)	1 to 2	1 to 2
Pointing Accuracy	$\pm 1/10$ th Beamwidth	
Maximum Tracking Rate	$\sim 1500 \mu\text{rad/sec}$	
Maximum Point-Ahead	$70 \mu\text{rad}$	
Synchronous Satellite Uncertainty	$\pm 0.2^\circ \ 3\sigma$	
Low-Orbit Satellite Uncertainty	$\pm 0.5^\circ \ 3\sigma$	
Environmental Characteristics	Operate in ground, air-craft, and space environ-ment; withstand Titan IIC launch environment; compatible with MIL-STD-461A and space radiation environment of SAMSO Exhibit 69-13	

3.1 SPECIFIC OPERATIONAL CONDITIONS

Many operational conditions are implicit in the previously discussed constraints, even though not specifically referenced. These requirements and limits are summarized

in this section to provide a background for the discussions and analyses that follow. Factors that are implied include: orbit parameters, system coverage, initial pointing uncertainties, attitude, ephemeris, attitude rates, gimbal rates, Doppler effect, and point-ahead angle.

3.2 ORBIT PARAMETERS

Orbit conditions for the synchronous relay satellite and two typical orbits for the low-orbit user satellite are shown in Table 3.

Table 3
ORBIT PARAMETERS
(Earth Radius, 3,444 nm; Earth Rotation Rate, 15°/hr)

Parameter	Package A		Package B
Type of Orbit	Circular	Eccentric	Synchronous equatorial
Perigee/Apogee Attitude (nm)	100/100	100/1,000	19,351/19,351
Eccentricity	0	0.1128	0
Inclination (deg)	0 to 115	0 to 115	10
Inertial Velocity (ft/sec)	25,580	28,600 at perigee	10,078
Period	88.2 min	105.5 min	24 hr

3.3 ANGULAR COVERAGE

The angular coverage required at each relay terminal and user relative to all other elements of the laser communication system is shown in Table 4. The coverage is described in terms of commonly used local coordinate frames. The reflection of this coverage on the angular range of gimbals is shown in Figs. 1 and 2.

3.4 SATELLITE POINTING UNCERTAINTIES

The pointing uncertainties of user and relay satellites are dependent upon the knowledge of their own attitude and position in space as well as the position of their target.

Table 4
SYSTEM COVERAGE

View From	To	Near Relay	Far Relay	Low-Orbit User	Ground Terminal/User	Aircraft Terminal/User	Synchronous Satellite User
Near Relay ^(a)		-	$\pm 45^\circ$ IP, $\pm 10^\circ$ CP	$\pm 12^\circ$ IP/CP	$\pm 12^\circ$ IP/CP	$\pm 12^\circ$ IP/CP	$\pm 90^\circ$ IP, $\pm 12^\circ$ CP
Far Relay ^(a)		$\pm 45^\circ$ IP, $\pm 10^\circ$ CP	-	$\pm 12^\circ$ IP/CP	$\pm 12^\circ$ IP/CP (user only) ^(b)	$\pm 12^\circ$ IP/CP (user only) ^(b)	$\pm 90^\circ$ IP, $\pm 12^\circ$ CP
Low Orbit User ^(c)		$\pm 110^\circ$ IP/CP, $\pm 12^\circ$ CP/IP	$\pm 110^\circ$ IP/CP, $\pm 12^\circ$ CP/IP	-	-	-	-
Ground Terminal User ^(d)		$0 - 90^\circ$ El., $\pm 100^\circ$ Az.	$0 - 90^\circ$ El., (user only) ^(b)	-	-	-	-
Aircraft Terminal/User ^(e)		$\pm 10^\circ$ Yaw/ Pitch, $\pm 45^\circ$ Roll	$\pm 10^\circ$ Y/P (user only) ^(b) $\pm 65^\circ$ Roll	-	-	-	-
Synchronous Satellite User ^(a)		$\pm 90^\circ$ IP, $\pm 12^\circ$ CP	$\pm 90^\circ$ IP, $\pm 12^\circ$ CP	-	-	-	-

(a) View angles in-plane (IP) and cross-plane (CP) referenced to the orbit plane and geocentric radius (Nadir line).
(b) Far relay not visible from ground terminal.

(c) View angles IP and CP referenced to orbit plane and negative geocentric radius (zenith line).

(d) View angles azimuth (Az.) referenced to local North, and elevation (El.) referenced to local tangent plane at the surface.

(e) View angles roll and yaw referenced to negative geocentric radius (zenith line) and a normal to the zenith in the direction of flight.

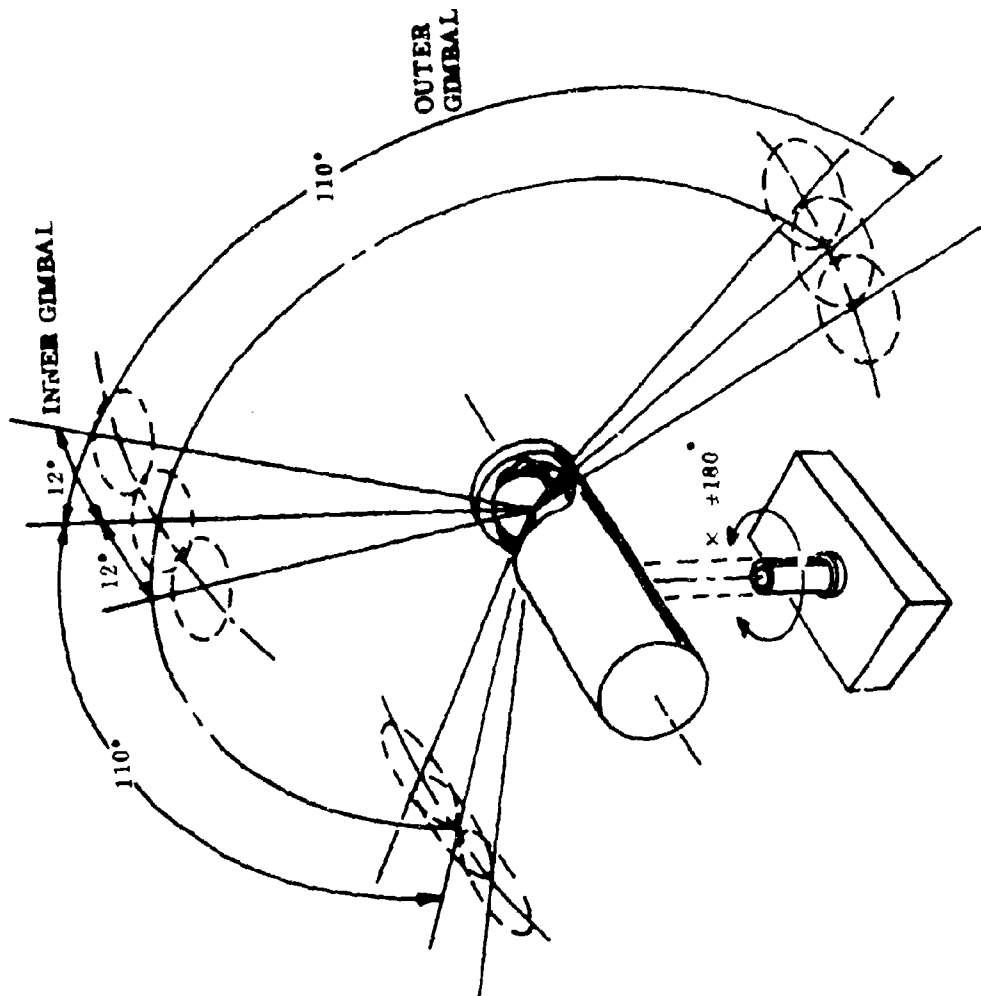


Fig. 1 Package A1 Pointing Coverage. Package A2 is similar except there is no yaw gimbal and the outer gimbal operates $\pm 90^\circ$.

V-12

LOCKHEED PALO ALTO RESEARCH LABORATORY
 LOCKHEED MISSILES & SPACE COMPANY
 A GROUP DIVISION OF LOCKHEED AIRCRAFT CORPORATION

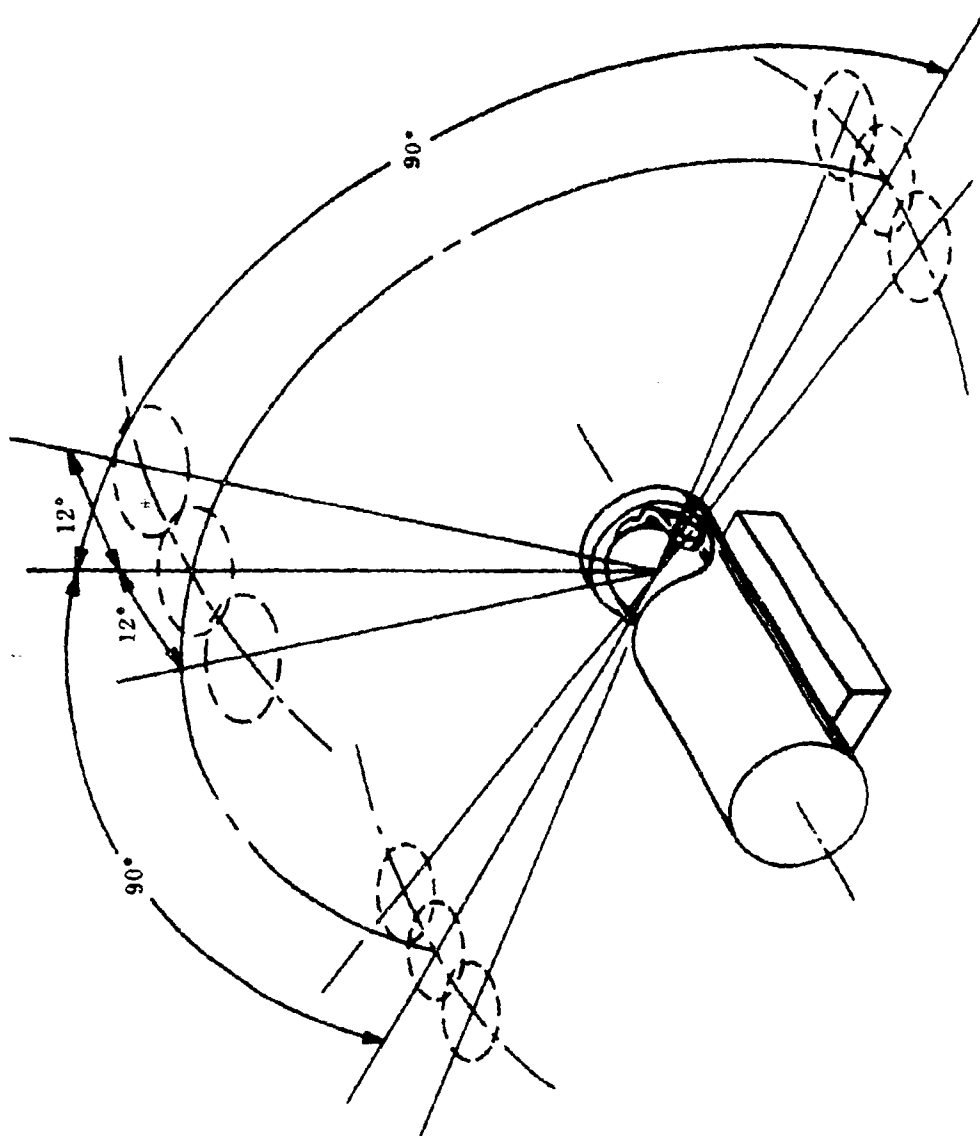


Fig. 2 Package B Pointing Coverage

V-13

LOCKHEED PALO ALTO RESEARCH LABORATORY
 LOCKHEED MISSILES & SPACE COMPANY
 A GROUP DIVISION OF LOCKHEED AIRCRAFT CORPORATION

This dependence was discussed generally in section 2.1; a more detailed analysis is presented here. The estimated accuracy of this knowledge is shown in Table 5. The initial 3σ attitude uncertainty, the reduced uncertainty after bias removal, and the uncertainty in the attitude change over an interval of time contribute directly to pointing uncertainties. The contribution of the ephemeris errors or uncertainties of both seeking and target vehicles is dependent upon the relative distance between them. These ephemeris errors are shown to make only small contributions to the total initial pointing errors.

The largest source of error, except for attitude uncertainties, is the predicted ephemeris of the low-altitude satellite. This prediction is a function of the quality and quantity of the tracking performed and the length of time ahead the ephemeris must be predicted. Assuming that the Satellite Control Facility (SCF) tracking network is used to establish the orbital characteristics of the satellite, the ephemeris of a satellite in an orbit near 100 nm over the tracking interval can be determined to an in-track accuracy of approximately 1000 ft (Ref. 1). The accuracy in the knowledge of ephemeris deteriorates rapidly as it is predicted farther into the future due to the unpredictable nature of the fluctuations in the atmospheric density. The ephemeris error for a 6-hr or approximately 4-revolution prediction using a ground computer complex grows to approximately 10,000 ft, or 1.65 nm, as shown in Fig. 3. The rapidity with which the ephemeris uncertainty is growing after a 6-hr prediction indicates that a prediction significantly beyond that time will produce large uncertainties.

The position of the synchronous satellite is known to an extremely high degree of accuracy, as it can be tracked continuously from a ground tracking station and its motion in a rotating-earth, fixed-coordinate frame can be predicted. Use of an earth-to-inertial transformation will result in an accurate synchronous satellite position prediction.

The analysis presented under Task 9 shows that the utilization of angle, range, and range rate tracking data results in 1σ position errors of 88 ft in range, 165 ft in the cross-track direction, and 1760 ft in the in-track direction, assuming the presence

Table 5

INITIAL POINTING UNCERTAINTIES OF SATELLITES^(a)

Parameter	LOS	SS	SS Despun
Attitude Uncertainty			
Knowledge of Attitude (3σ); Two-Axis Line-of-Sight Error (deg)	± 0.5	± 0.2	± 0.2
Improved Attitude Uncertainty			
Estimated Knowledge of Attitude After Bias Removal—After First Acquisition (deg)			
• Roll	0.15	0.05	0.06
• Pitch	0.15	0.05	0.06
• Yaw	0.15	0.2	0.2
Estimated Knowledge of Change in Atti- tude Over a 10-sec Period (arcmin)			
• Roll	1	1.5	1.5
• Pitch	1	1.5	2.0
• Yaw	1	1.5	2.0
Ephemeris Effects			
Own Ephemeris Error (ft)	10,000	1,760	1,760
Effect on Pointing (deg) ^(b)	0.0049	0.0009	0.0009
Target Ephemeris Error (ft)	1,760	1,000	1,000
Effect on Pointing (deg) ^(b)	0.0009	0.0005	0.0005

(a) Negligible subsystem factors, which are small.

(b) Negligible in widebeam or wide-FOV cases.

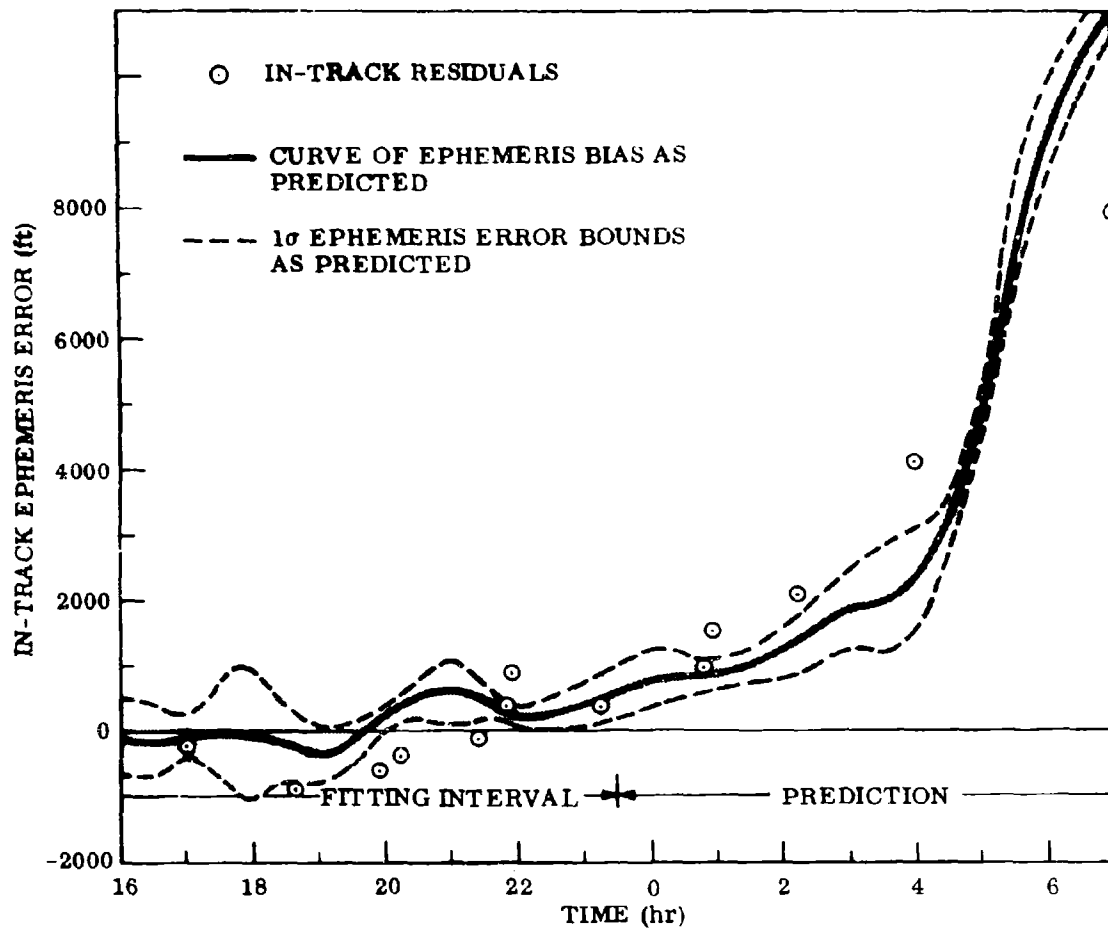


Fig. 3 Ephemeris Accuracy

of 50-ft range bias and random range rate errors. Such an error is equivalent to an angular uncertainty of 3.1 arcsec from the earth or low-orbit satellite.

3.5 SATELLITE ATTITUDE RATES

The magnitudes of the nutation rates in the scanning transmitter of a despun synchronous satellite and the attitude control system limit-cycle rates for the actively controlled low-orbit user and stabilized synchronous relay satellites are shown in Table 6. The much higher nutation rate (4000 μ rad/sec) expected for a despun satellite is one of the many reasons that this type of satellite stabilization method is not recommended for the SDRS. Other reasons are given in Appendix Q. For three-axis stabilized satellites, considerably lower rates are usually expected (Table 6). The 20- μ rad/sec attitude change rates of the stabilized synchronous satellite were determined from LMSC experience with well-stabilized spacecraft during quiescent periods. When thrusters are fired during stationkeeping rates, up to 2000 μ rad/sec can be reached. Tracking can continue when thrusters are firing, but it may be advisable to perform acquisition when they are not firing.

The rates for the LOS are for a relatively poorly stabilized Agena spacecraft. Much lower rates have been achieved on some Agena missions, but the SDRS is designed to handle the worst case.

3.6 MAXIMUM SATELLITE GIMBAL RATES

The maximum gimbal rate that will be required on the low-orbit satellite (LOS) when stationkeeping is not taking place is 1940 μ rad/sec on the pitch axis and 1290 μ rad/sec on the roll axis. These rates could be encountered at the same time in the worst-case condition. This condition occurs during a perigee passage of the LOS, which is assumed to be in a 100/1000-nmi eccentric polar orbit whose perigee is located directly below the synchronous equatorial satellite. A 25° retrograde orbit for the LOS adds up to 32 μ rad/sec on the pitch axis and 68 μ rad/sec for roll. Slightly inclined synchronous satellite orbits have effects more than an order of magnitude smaller and thus are negligible.

Table 6

SATELLITE VEHICLE ATTITUDE ANGULAR MOTION

	Limit – Cycle, 3-Axis Stabilized		Nutting, Despun SS
	LOS	SS	
Limit Cycle			
Amplitude (μrad)			
● Roll	3,500	1,750	600
● Pitch	3,500	—	20
● Yaw	3,500	1,750	600
Rates ^(a) (μrad/sec)			
● Roll	1,200	20	4,000
● Pitch	360	20	20
● Yaw	360	20	4,000
Gimbal Rates ^(b) (μrad/sec)			
● Roll	1,290 ^(c)	270	4,250
● Pitch	1,940 ^(c)	110	110
● Yaw	360	—	—
Maximum Acceleration – During Thruster Firing (μrad/sec ²)			
	5,000	250	—

(a) During stationkeeping, the three-axis stabilized satellite's rates increase up to 2,000 $\mu\text{rad}/\text{sec}$ maximum.

(b) During stationkeeping, the three-axis stabilized satellite's gimbal rates increase by the increase in their attitude rates.

(c) Slightly more for a retrograde orbit, as noted on page V-17.

The pitch gimbal rate under worst-case conditions is composed of the angular rate of the LOS in its orbit ($1330 \mu\text{rad/sec}$), the angular rate due to the LOS rising out of the plane of the synchronous ($250 \mu\text{rad/sec}$), and the pitch rate of the LOS attitude-control system limit cycle ($360 \mu\text{rad/sec}$), for a total of about $1940 \mu\text{rad/sec}$. The roll gimbal rate is composed of the synchronous satellite angular motion as seen by the LOS, which is a maximum when the LOS apogee is below the SS ($90 \mu\text{rad/sec}$), and the roll limit cycle rate of $1200 \mu\text{rad/sec}$ —or $1290 \mu\text{rad/sec}$. The roll and pitch axes are interchanged for a low-inclination-angle LOS and have slightly lower rate requirements.

The synchronous satellite's gimbals must rotate at a maximum of about $260 \mu\text{rad/sec}$ about the roll axis when tracking a polar-orbit LOS, and slightly less about the pitch axis when tracking an equatorial LOS. The pitch axis of the SS must rotate $110 \mu\text{rad/sec}$ when tracking a 1,000-nm LOS in polar orbit.

In the LMSC baseline system, these rates, as well as the higher rates and accelerations during thruster firing, have negligible perturbation on the tracking accuracy. During acquisition, it is assumed, the rates of the LOS are measurable and computable so that they are fed into the gimbal control system with about $200\text{-}\mu\text{rad/sec}$ accuracy.

3.7 AIRCRAFT ATTITUDE KNOWLEDGE AND RATES

The aircraft that may be used in conjunction with the SDRS are discussed thoroughly under Task 13, Demonstration Plan. For completeness, a summary of the data on aircraft attitude knowledge and rates is included here in Table 7.

3.8 DOPPLER EFFECT

The rate of change of the distance between two terminals of a space optical communication link is not, in general, negligible compared with the speed of light. Consequently, it is necessary to investigate the effect that this change rate may have on the acquisition and tracking.

Table 7
POTENTIAL AIRCRAFT CHARACTERISTICS

Aircraft Type	Volume	Attitude Knowledge 3σ			Attitude Rates		
		P	R	Y	P	R	Y
C-141	Large		Poor			Poor	
C-5A	Large	$\pm 0.10^\circ$	$\pm 0.10^\circ$	$\pm 0.10^\circ$		Low	
P-3	Large	$\pm 0.15^\circ$	$\pm 0.15^\circ$	$\pm 0.20^\circ$	$0.2^\circ/\text{sec}$	$1.0^\circ/\text{sec}$	$0.2^\circ/\text{sec}$
U-2(a)	Acceptable	$\pm 0.02^\circ$	$\pm 0.02^\circ$	$\pm 0.02^\circ$	$0.023^\circ/\text{sec}$	$0.006^\circ/\text{sec}$ (0.25-25 cps)	$0.028^\circ/\text{sec}$
SR-71	Tight	$\pm 0.02^\circ$	$\pm 0.02^\circ$	$\pm 0.02^\circ$	$0.086^\circ/\text{sec}$	$0.116^\circ/\text{sec}$ (0.01-30 cps)	$0.075^\circ/\text{sec}$
RB57	Large	$\pm 0.20^\circ$	$\pm 0.20^\circ$	$\pm 0.20^\circ$	$< 0.01^\circ/\text{sec}$ typical (at 60 kft-smooth air)		
KC135	Large	Not available on standard model			$0.08^\circ/\text{sec}$	$0.088^\circ/\text{sec}$	$0.06^\circ/\text{sec}$ rms
					1 ft/sec rms gust - 35 kft		
B-52	Probably would be acceptable if available						

(a) With platform from SR-71 added as a modification to the basic aircraft.

The low-orbit satellite has the greatest velocity of any of the vehicles, 28,600 ft/sec when at the perigee of a 100/1000-nmi eccentric orbit. The greatest rate of change of range will be for LOS motion directly along the line of sight to the synchronous satellite. This speed of 28,600 ft/sec is 2.85×10^{-5} of the velocity of light - so that all frequencies and time intervals transmitted from one vehicle to the other will be changed by this percentage or by a lesser percentage corresponding to a lesser relative velocity.

The explicit expression for Doppler effect for electromagnetic radiation is (Ref. 2):

$$f_r = f_t \left(1 \pm \frac{v}{c} + \frac{1}{2} \frac{v^2}{c^2} \pm \frac{1}{2} \frac{v^3}{c^3} + \dots \right)$$

where

- f_r = received frequency
- f_t = transmitted frequency
- v = relative velocity
- c = velocity of light

The relative velocity v is so much less than c that the higher order terms can be ignored.

Expressed in simple reference values, the maximum Doppler shift will be:

- 28.5 cycles shift/Mc
- 2.85×10^{-5} sec of time/sec

These scale factors are utilized in determining the maximum effect of Doppler shift on the various signal frequencies.

The effect of the Doppler shift on the time of arrival of the next pulse of a transmission is a function of the relative velocities of the transmitting and receiving satellites, and thus is a function of the two state vectors. The change in the nominal pulse interval can be calculated in real time to be effective over a to-be-determined interval of time by

$$\Delta t_p = \frac{v_{L_I}}{c} T$$

where

- C = speed of light = 9.83×10^8 ft/sec
- T = nominal pulse transmission interval
- v_{L_I} = velocity component along the relative position vector
- $$= \frac{\bar{v}_I \cdot \bar{L}_I}{|\bar{L}_I|}$$

$$\bar{V}_I = \bar{V}_{SS} - \bar{V}_{LOS}$$

$$\bar{L}_I = \bar{R}_{SS} - \bar{R}_{LOS}$$

$(\bar{R}_{SS}, \bar{V}_{SS})$ = position and velocity state vectors for the synchronous satellite

$(\bar{R}_{LOS}, \bar{V}_{LOS})$ = position and velocity state vectors for the low-orbit satellite

The variation of the change in the pulse interval is shown in Fig. 4 for sample orbital cases including the worst case of the LOS in a 100/1,000-nm eccentric orbit. The assumed nominal pulse interval was 0.1 sec. The deviation for any other pulse interval can be determined by multiplying the plotted values by the ratio of the desired to the reference interval.

The peak deviation in pulse separation is shown to be approximately 3 μ sec/interval for the case of \bar{R}_{SS} lying in the plane of an LOS eccentric orbit for which perigee occurs at the ascending mode (argument of perigee = 0°). The occurrence of perigee at an argument of 270° results in the peak deviation with opposite polarity. The figure shows that, as the LOS moves from directly below the SS, the pulse interval deviation climbs rapidly to peak at the point where the LOS velocity vector is colinear with the line of sight between the two satellites. The LOS then disappears over the horizon to reappear again at a central angle of 270° from the ascending mode. The negative maximum deviation occurs where the velocity vector is again colinear with the line of sight. The peak deviation for the LOS 100-nm circular orbit is 2.85 μ sec, occurring at a central angle of approximately 81° from the ascending node.

The variation of the pulse deviation when the SS position vector \bar{R}_{SS} lies normal to the LOS orbit plane is shown to have a low-amplitude oscillation as the LOS moves around its orbit because of the small relative velocity component in the direction of the line of sight.

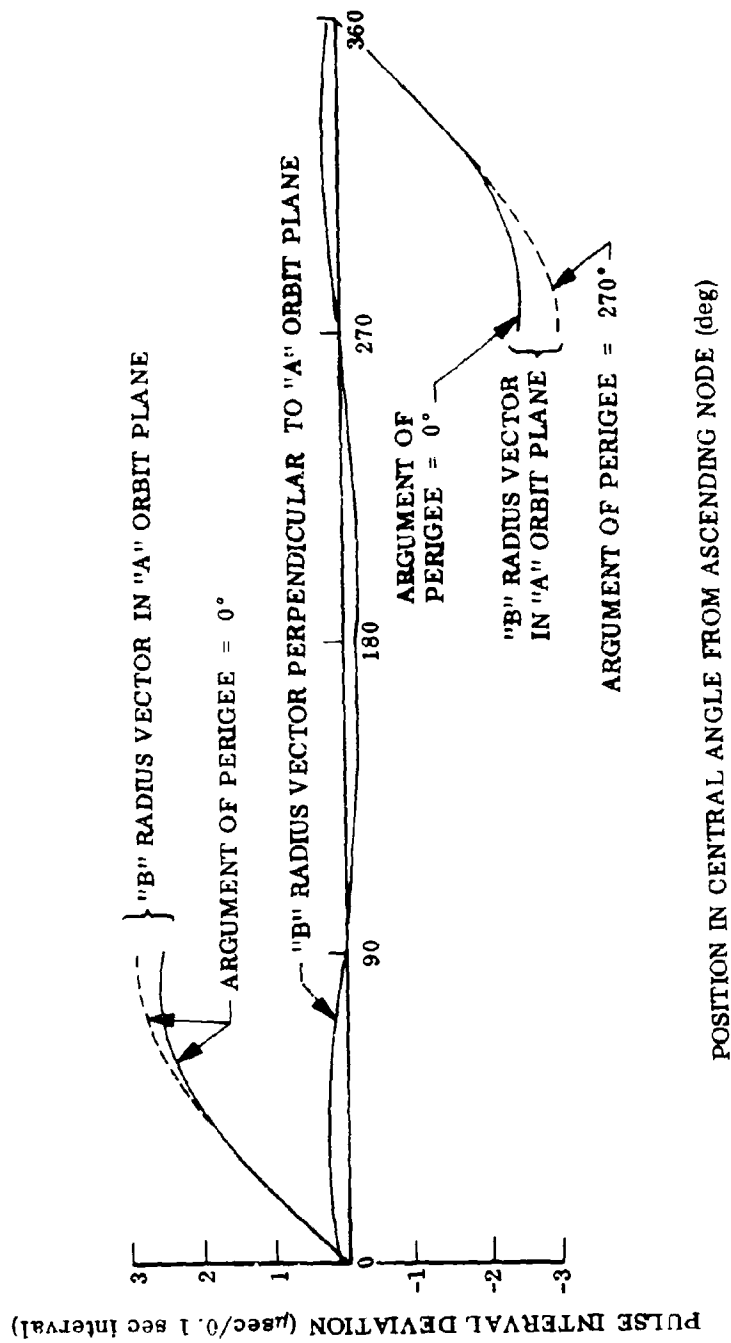


Fig. 4 Pulse Spacing Shift Due to Doppler Effect

V-23

3.9 POINT-AHEAD ANGLE

The problem of pointing receivers and transmitters from a moving platform A at another distant moving platform B in order to receive and to transmit optical signals is complicated by the relative motion of the two platforms. The apparent position of B at some instantaneous time based on the orientation of the received signal is "behind" the actual position, whereas the anticipated position to which the transmission must be directed is "ahead" of the actual position at that time. The relative angle from the optical line of sight of the receiver to that of the transmitter is referred to as the point-ahead angle, α .

This angle is a function of the relative position vector \bar{L}_I , the relative velocity vector \bar{V}_I , and the velocity of light c :

$$\begin{aligned}\bar{L}_I &= \bar{R}_B - \bar{R}_A \\ \bar{V}_I &= \bar{V}_B - \bar{V}_A\end{aligned}$$

where \bar{R}_A , \bar{V}_A and \bar{R}_B , \bar{V}_B denote the inertial position and velocity vectors of the A and B platforms, respectively. The component of the relative velocity vector normal to the relative position vector is

$$\Delta \bar{V}_N = \frac{\bar{V}_I \times \bar{L}_I}{|\bar{L}_I|}$$

The magnitude of the point-ahead angle is then

$$\alpha = 2 \left| \frac{\Delta \bar{V}_N}{c} \right|$$

where

$$c = \text{velocity of light} = 9.83 \times 10^8 \text{ ft/sec}$$

V-24

LOCKHEED PALO ALTO RESEARCH LABORATORY
LOCKHEED MISSILES & SPACE COMPANY
A GROUP DIVISION OF LOCKHEED AIRCRAFT CORPORATION

The rate of change of α is

$$\dot{\alpha} = \frac{2}{c} \left| \Delta \dot{\bar{V}}_N \right|$$

$$\text{or} \quad \dot{\alpha} = \frac{2}{c |\bar{L}_1|} \left| \dot{\bar{V}}_A \times \bar{R}_B + \bar{V}_B \times \bar{R}_A + \Delta \bar{V}_N (|\bar{V}_B - \bar{V}_A|) \right|$$

The magnitude of the point-ahead angle and its variation with time are shown in Fig. 5 for two sample Package A orbits. The Package B satellite is assumed to be in a synchronous equatorial orbit. Package A is considered to be either in a 100-nm circular or in a 100/1000-nm perigee/apogee polar orbit. Two orbit plane orientations are examined. One condition is that in which the Package B inertial position vector is normal to the plane of the Package A orbit, which results in the largest point-ahead angle. The other condition is where the B inertial position vector lies within the plane of the A orbit, which results in the highest rate of change of the point-ahead angle. The argument of perigee of the eccentric orbit was varied to examine the extreme point-ahead conditions. For the eccentric A orbit, it is assumed that coverage is desired over the low-altitude region 90° on either side of perigee. The extreme situations are brought about by argument of perigee angles of 90° and 270° (Figs. 6a and 6b, respectively), corresponding to the placement of perigee at latitudes 90°N. and 90°S. , respectively, when \bar{R}_B is normal to the A orbit plane and an 0° argument of perigee when \bar{R}_B lies in the orbit plane.

The maximum point-ahead angle of 16.2 arcsec ($81 \mu\text{rad}$) occurs when Package A is at perigee of the Fig. 6b orientation. The maximum point-ahead rate of 0.64 arcsec/min occurs in the eccentric orbit orientation of Fig. 6c at a central angle from the ascending node of approximately 315° .

Also shown in Fig. 5 is the constant point-ahead angle from Package B to the ground terminal lying along the earth longitude of the synchronous equatorial satellite as a function of the latitude of the ground terminal location.

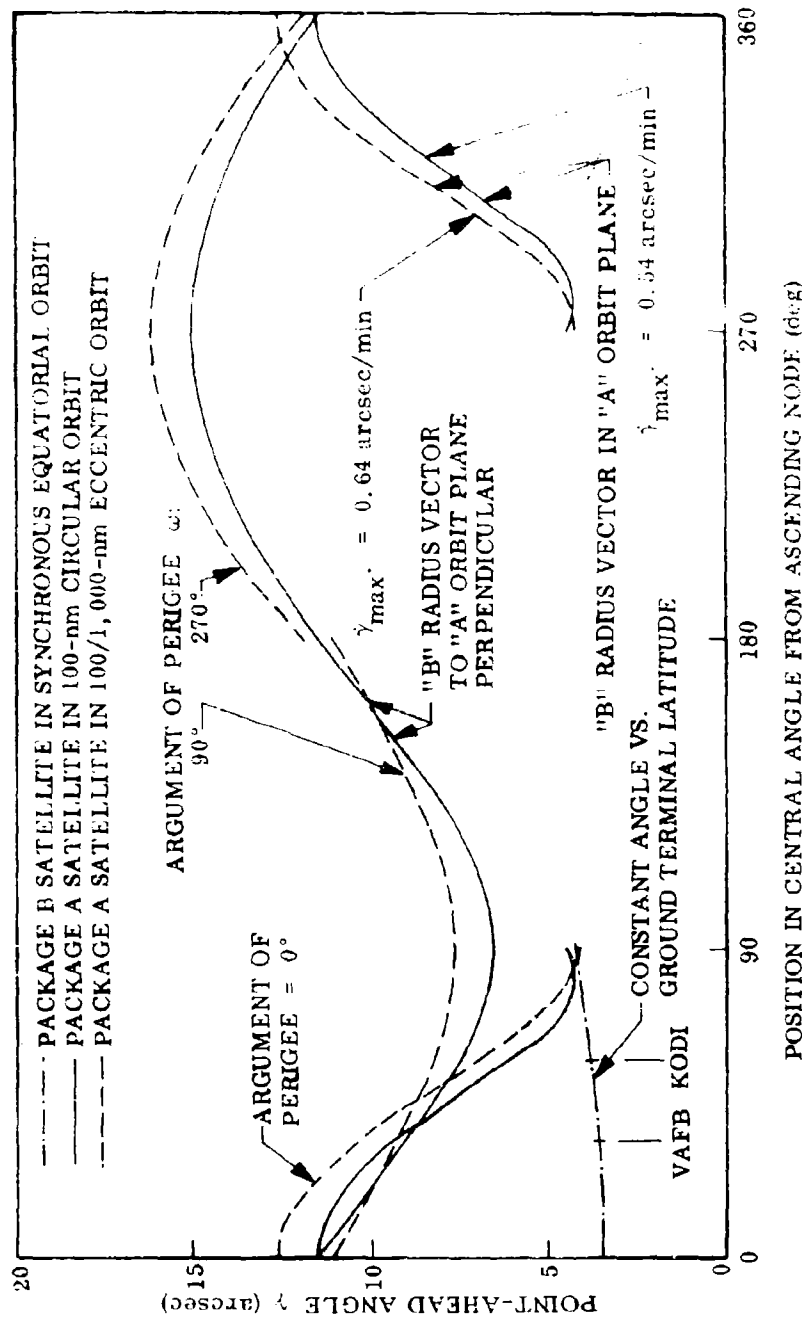


Fig. 5 Point-Ahead Angle as a Function of Orbital Position

V-26

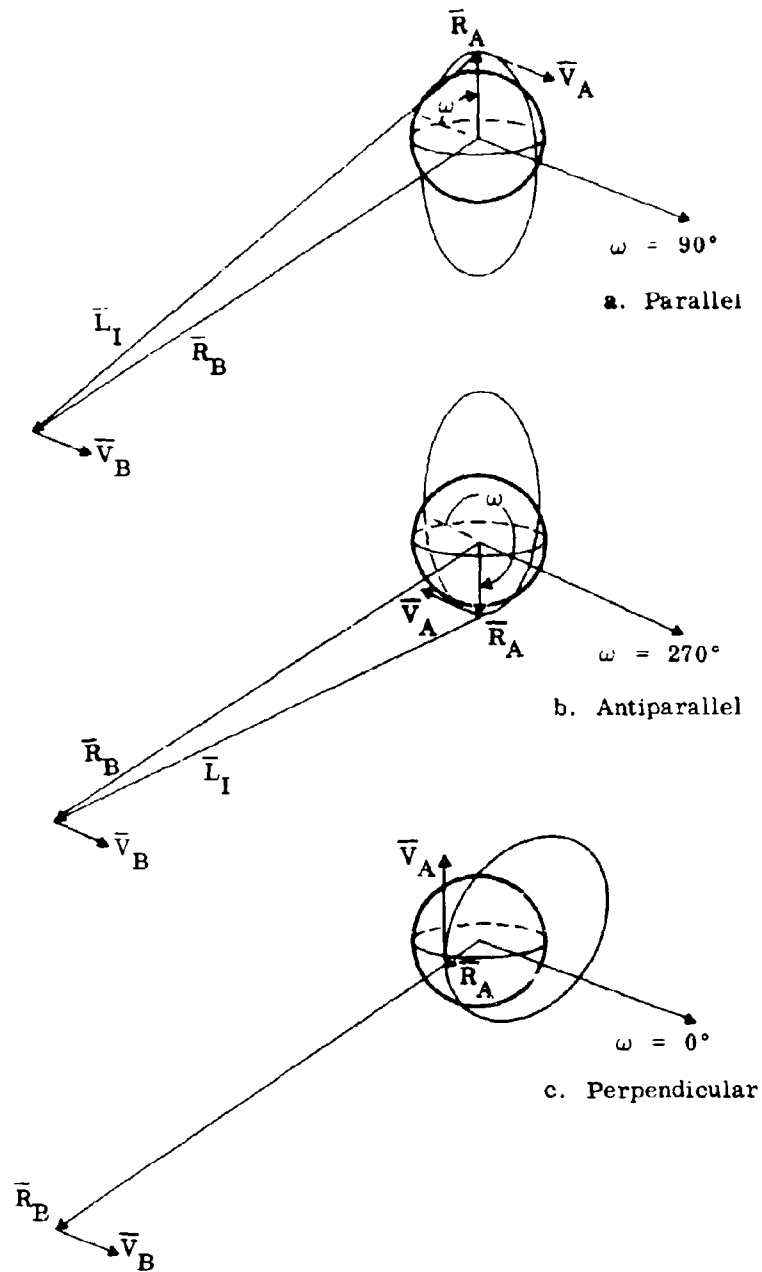


Fig. 6 Point-Ahead Velocity Vectors for Various Orbit Configurations

V-27

LOCKHEED PALO ALTO RESEARCH LABORATORY
 LOCKHEED MISSILES & SPACE COMPANY
 A GROUP DIVISION OF LOCKHEED AIRCRAFT CORPORATION

4. REFERENCES

1. M. L. Vajta, The Accuracy of Satellite Orbit Determination in the Presence of Systematic Air Drag Errors: A Comparison of Theoretical and Observed Orbit Errors (U), LMSC-D000119, LMSC TM 55-31-0M-005, Lockheed Missiles & Space Company, Sunnyvale, Calif. (C), Aug 1967
2. Jenkins and White, Fundamentals of Physical Optics, New York, McGraw-Hill Book Co., 1937

Appendix W

ANALYSIS OF COULOMB
FRICTION AND STICTION

by

Mr. G. R. Chippendale

LOCKHEED PALO ALTO RESEARCH LABORATORY
LOCKHEED MISSILES & SPACE COMPANY
A GROUP DIVISION OF LOCKHEED AIRCRAFT CORPORATION

This appendix is a review of an analysis by W. E. Nelson. * The results of the analysis show that, for a second-order system with coulomb friction torque C and stiction torque S (depending on the input), there can be (1) steady-state position errors as large as S/K , where K is the loop position gain and (2) steps of torque of magnitude $S+C$ applied to the inertia when the stiction breaks loose. The nonlinearities involved in the friction forces make linear analysis practically impossible. However, a phase-plane analysis is ideally suited to nonlinearities of this type. Since the pointing command in pitch α_c involves rates, a ramp input is ideal to test the control system. Three assumptions lead to a second-order system: (1) The time constants associated with the dc motor may be neglected; (2) the lead-lag network is replaced by a pure lead; and (3) there is no compliance in either the controlled members or the gimbals. Even when these assumptions do not hold exactly, the system may be so designed that a good separation exists between the dominant second-order poles and the remaining poles, so that it behaves as a second-order system.

A block diagram of the system based on the foregoing assumptions is given in Fig. 1. The nonlinear feedback of $\dot{\alpha}$ is caused by stiction S and coulomb friction C . For $\dot{\alpha} = 0$, the stiction torque controls the motion of the system, and for $\dot{\alpha} \neq 0$, the coulomb torque governs the response.

Since a ramp input is used to test the system, $\dot{\alpha}_c = \omega_1$ is defined as the velocity input. Then the error E is given by

$$E = \alpha_c - \alpha$$

$$\dot{E} = \dot{\alpha}_c - \dot{\alpha} = \omega_1 - \dot{\alpha}$$

and

$$\ddot{E} = \dot{\omega}_1 - \ddot{\alpha} = -\ddot{\alpha}$$

*W. E. Nelson, "Effects of Stiction and Coulomb Friction on the Response of a Position Control System Following a Ramp Input," LMSC Interdepartmental Communication 55-31-351, 30 Jan 1968.

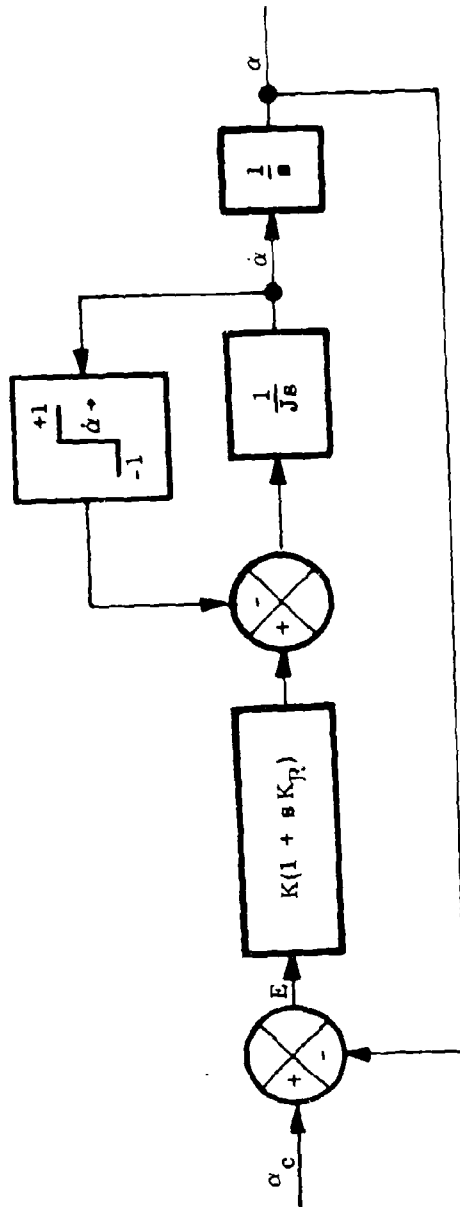


Fig. 1 Block Diagram of Second-Order Servo With Coulomb Friction and Sticktion

W-2

The equations of motion that govern the system response to a ramp input ω_i are given by

$$JE + K_R \dot{E} + KE = S \operatorname{sgn} (\omega_i - \dot{E}) \quad (1)$$

for $\dot{\alpha} = 0$, and

$$JE + K_R \dot{E} + KE = C \operatorname{sgn} (\omega_i - \dot{E}) \quad (2)$$

for $\dot{\alpha} \neq 0$. The function sgn is defined as

$$\operatorname{sgn} x = \phi$$

where $-1 \leq \phi \leq 1$ for $x = 0$, $+1$ for $x > 0$, and -1 for $x < 0$.

Equations (1) and (2) can be written in a form that is suitable for phase-plane analysis which is the plot of the transient response of E versus \dot{E} :

$$\frac{d(\dot{E})}{d(E)} = \frac{-KE - K_R \dot{E} + S \operatorname{sgn} (\omega_i - \dot{E})}{J\dot{E}} \quad (3)$$

for $\dot{E} = \omega_i$ and

$$\frac{d(\dot{E})}{d(E)} = \frac{-KE - K_R \dot{E} + C \operatorname{sgn} (\omega_i - \dot{E})}{J\dot{E}} \quad (4)$$

for $\dot{E} \neq \omega_i$. Equation (3) holds when the velocity input is first applied. The stick-torque tends to resist motion ($\dot{\alpha} = 0$) and the error rate is held constant at $\dot{E} = \omega_i$, while the error builds up to

$$E_{\text{start}} = (S/K) - K_R \omega_i$$

W-3

LOCKHEED PALO ALTO RESEARCH LABORATORY
LOCKHEED MISSILES & SPACE COMPANY
A GROUP DIVISION OF LOCKHEED AIRCRAFT CORPORATION

This corresponds to the trajectory from point 1 to point 2 of Fig. 2. At point 2 the motor torque just equals stiction, and the system breaks loose ($\dot{e} = 0$). After the transient (from 2 to 3), the system follows the ramp input with no rate error but a steady-state position error of

$$E_{\text{steady state}} = \frac{C}{K}$$

For general inputs (other than ramps), the steady-state error could be as high as S/K .

Figure 2 shows a number of important parametric effects that must be considered in the servo design. Starting and steady-state positional errors may be reduced either by reducing stiction and coulomb torques or by increasing amplifier gain K . The condition for the system to stick ($\dot{e} = 0$ or $\omega_i = \dot{E}$) is given graphically by the dividing line. If the system is lightly damped or the value of ramp input is very low, the trajectory may, after breaking loose at point 2, come around and contact the dividing line again. Under this condition, the error rate \dot{E} will remain constant at ω_i , and the position error must again build up to point 2 before breaking loose. The process will then be repeated and the system will be in a limit cycle. Since the limit cycle is caused by either very low ramp inputs or insufficient damping, it is desirable to design the system with high damping so that it will not limit the cycle at the lowest expected ramp input. Since the motion about the equilibrium point C/K is described by a linear second-order differential equation (after breaking loose of the stiction), it is possible to define the damping ratio and natural frequency of oscillation in terms of the system parameters

$$\omega_n = \frac{K}{J}$$

$$\zeta = \frac{1}{2} \sqrt{\frac{C}{J}}$$

If ζ is made greater than 1.0, the possibility of a limit cycle can be eliminated. Figure 3 shows an actual trajectory based on the values indicated.

This second-order analysis has indicated the type of behavior caused by nonlinear friction in a system that is basically second-order.

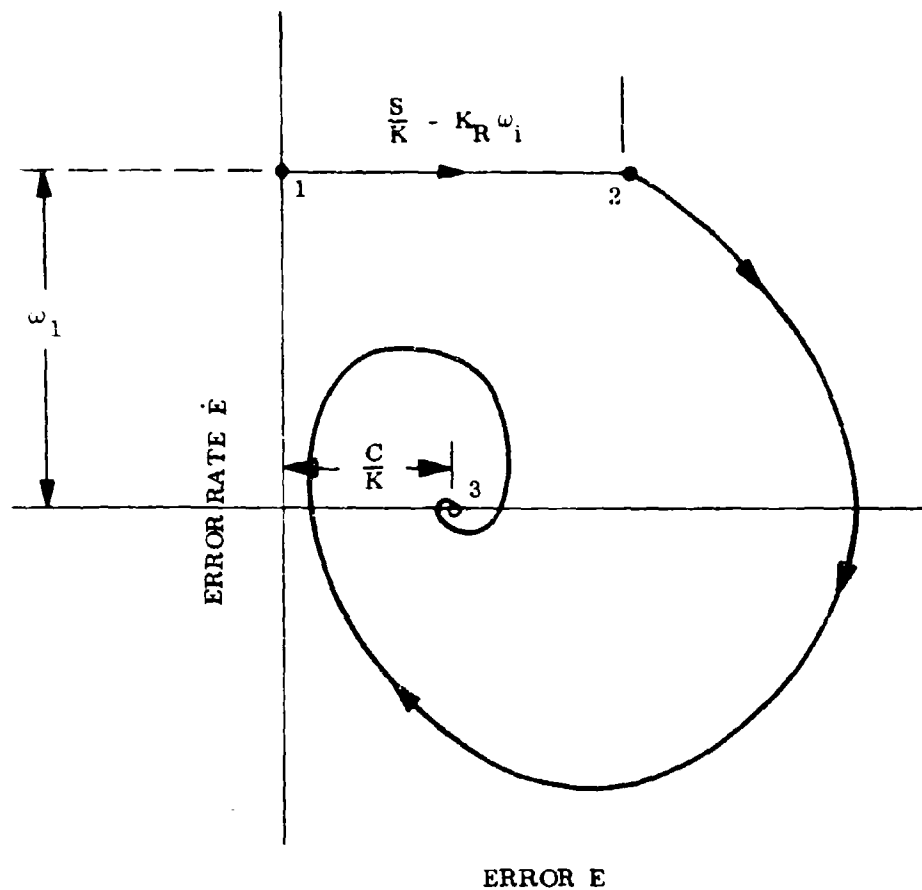


Fig. 2 Phase Portrait of Servo Showing Parametric Effects of Stiction S , Coulomb Friction C , Amplifier Gain K , and Lead Compensation K_R for a Ramp Input of ω_i

W-5

LOCKHEED PALO ALTO RESEARCH LABORATORY
LOCKHEED MISSILES & SPACE COMPANY
A GROUP DIVISION OF LOCKHEED AIRCRAFT CORPORATION

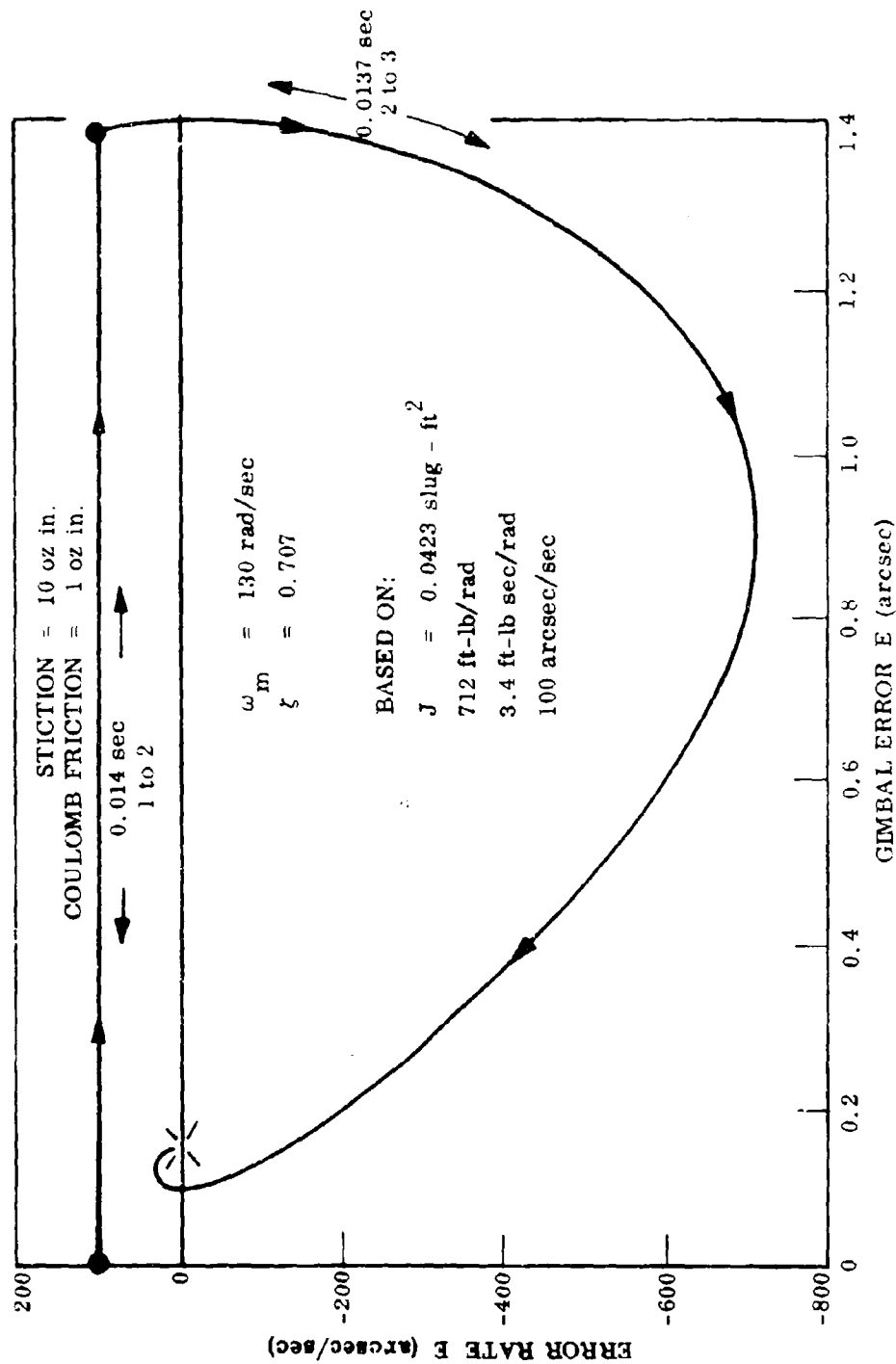


Fig. 3 Phase Plane Diagram of Servo in Response to Ramp Input. (The values are examples from Ref. 1 and do not represent the design of this report.)

Appendix X

COORDINATE TRANSFORMATIONS

by

Mr. F. Horiuchi

LOCKHEED PALO ALTO RESEARCH LABORATORY
LOCKHEED MISSILES & SPACE COMPANY
A GROUP DIVISION OF LOCKHEED AIRCRAFT CORPORATION

INERTIAL SPACE TO VEHICLE COORDINATE FRAME TRANSFORMATION

To establish an optical communication link between a spacecraft and another spacecraft or a ground terminal, it is necessary initially to point the optical systems in a coarse open-loop mode. Once the beams are locked on, a fine acquisition and tracking closed-loop mode is initiated to achieve high-resolution pointing. In the tracking mode, the error signals from two-axis detectors are utilized to provide gimbal correction signals to null the errors.

The initial nominal pointing commands for the gimbal systems are dependent on the relative position vector between the Package A and Package B terminals. Since the gimbal coordinate frames are constantly rotating relative to inertial space, it is necessary to transform the relative position vector from the inertial frame to the platform frame.

Figure 1 shows the position and velocity vectors of the two terminals and the relative position vector in the inertial coordinate frame. The relative position vector in inertial space is defined in terms of the respective position vectors, \bar{R}_a and \bar{R}_b , which are calculated from ephemeris data stored within the computers:

$$\bar{L}_I = \bar{R}_b - \bar{R}_a$$

The unit relative position vector is

$$\hat{L}_I = \frac{\bar{L}_I}{|\bar{L}_I|}$$

For Package A, the transformation T_{I2O} relates the rotating orbital coordinate frame to the fixed inertial frame (Fig. 2). Define the parameters:

X-1

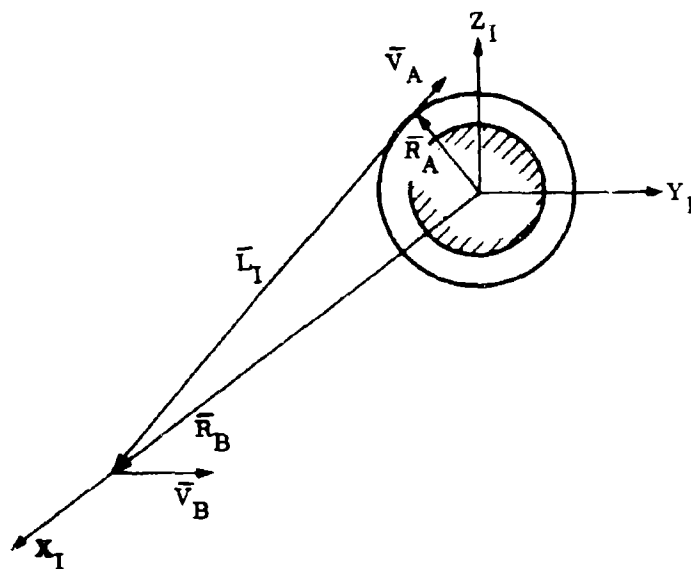


Fig. 1 Inertial Relative Position Vector

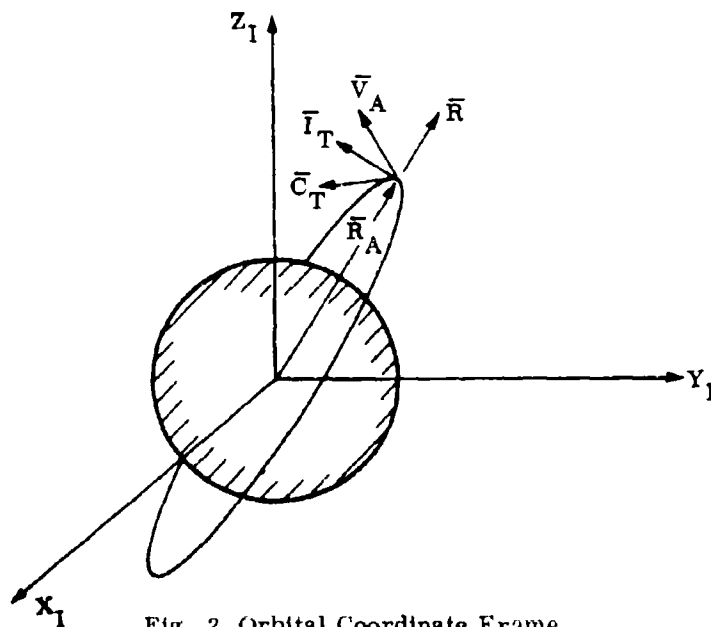


Fig. 2 Orbital Coordinate Frame

X-2

LOCKHEED PALO ALTO RESEARCH LABORATORY
 LOCKHEED MISSILES & SPACE COMPANY
 A GROUP DIVISION OF LOCKHEED AIRCRAFT CORPORATION

$$\begin{aligned}\bar{R} &= \text{direction of } \bar{R}_A & (\text{radial}) \\ \bar{IT} &= \text{direction of } (\bar{R}_A \times \bar{V}_A) \times \bar{R}_A & (\text{in-track}) \\ \bar{CT} &= \text{direction of } \bar{R}_A \times \bar{V}_A & (\text{cross-track})\end{aligned}$$

where

$$\bar{R}_A = \begin{bmatrix} x \\ y \\ z \end{bmatrix}, \quad \bar{V}_A = \begin{bmatrix} \dot{x} \\ \dot{y} \\ \dot{z} \end{bmatrix}$$

The transformation T_{120} is

$$T_{120} = \begin{bmatrix} \frac{x}{R_A} & \frac{y}{R_A} & \frac{z}{R_A} \\ \frac{R_A^2 \dot{x} - (\bar{R}_A \cdot \bar{V}_A) x}{h_A R_A} & \frac{R_A^2 \dot{y} - (\bar{R}_A \cdot \bar{V}_A) y}{h_A R_A} & \frac{R_A^2 \dot{z} - (\bar{R}_A \cdot \bar{V}_A) z}{h_A R_A} \\ \frac{y\dot{z} - z\dot{y}}{h_A} & \frac{z\dot{x} - x\dot{z}}{h_A} & \frac{x\dot{y} - y\dot{x}}{h_A} \end{bmatrix}$$

where

$$R_A = |\bar{R}_A|$$

$$h_A = |\bar{R}_A \times \bar{V}_A| = \text{angular momentum}$$

The unit relative position vector in the orbital coordinate frame is then

$$\hat{L}_O = \begin{bmatrix} \hat{R} \\ \hat{IT} \\ \hat{CT} \end{bmatrix} = T_{120} \hat{L}_I$$

X-3

LOCKHEED PALO ALTO RESEARCH LABORATORY
LOCKHEED MISSILES & SPACE COMPANY
A GROUP DIVISION OF LOCKHEED AIRCRAFT CORPORATION

The body motion within the bounds of the altitude control system requires the transformation T_{O2B} , which relates the vehicle frame to the orbital frame utilizing the body attitude measurements (ϕ , θ , ψ) monitored onboard. The orientation of the vehicle coordinate frame to the orbital frame is shown in Fig. 3. The transformation from the orbital frame to the vehicle frame is then

$$T_{O2B} = \begin{bmatrix} -s\theta c\phi c\psi + s\phi s\psi & c\theta s\psi & s\theta c\phi c\psi + c\phi s\psi \\ s\theta c\phi s\psi + s\phi c\psi & -c\theta s\psi & -s\theta s\phi s\psi + c\phi c\psi \\ c\theta c\phi & s\theta & -c\theta s\phi \end{bmatrix}$$

The unit relative position vector in the body coordinate frame is then

$$\hat{L}_{B'} = \begin{bmatrix} \hat{L}_{B'X} \\ \hat{L}_{B'Y} \\ \hat{L}_{B'Z} \end{bmatrix} = T_{O2B} T_{I2O} \hat{L}_I$$

The determination of the relative position vector in the terminal coordinate frame is valid for all terminals. The differences between Packages A1 and A2 stem from the requirement on the former to sweep approximately a hemispherical sector of the celestial sphere above it whereas the latter is required to sweep only a sector about 12° from its own radius vector to the earth center to maintain the low-altitude satellite and/or ground or aircraft terminals in its field of view. The Package A roll gimbal coverage is restricted to a movement of $\pm 12^\circ$; thus, Package A1 is required to rotate in yaw to cover its celestial hemisphere whereas Package A2 can operate satisfactorily with only pitch and roll control.

Figure 4 illustrates the relationships of the A1 and A2 gimbal frames and their detectors to the body frame. The Package A1 gimbal frame rotates about the yaw axis

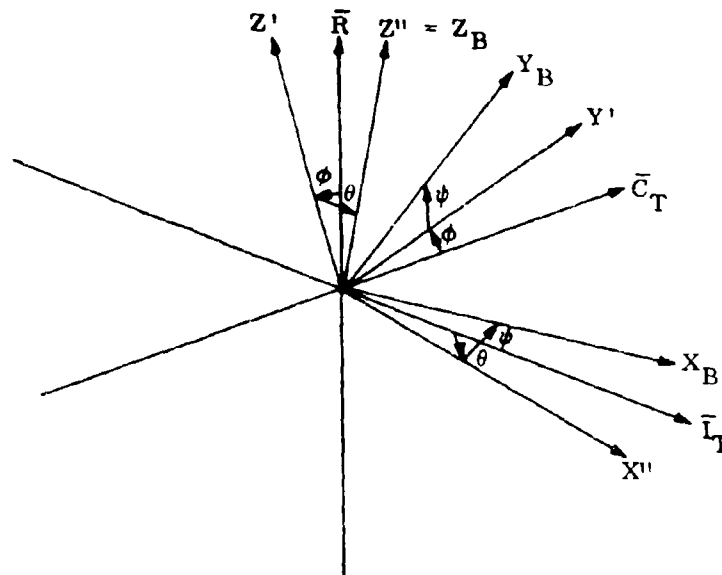


Fig. 3 Body Fixed Coordinate Frame

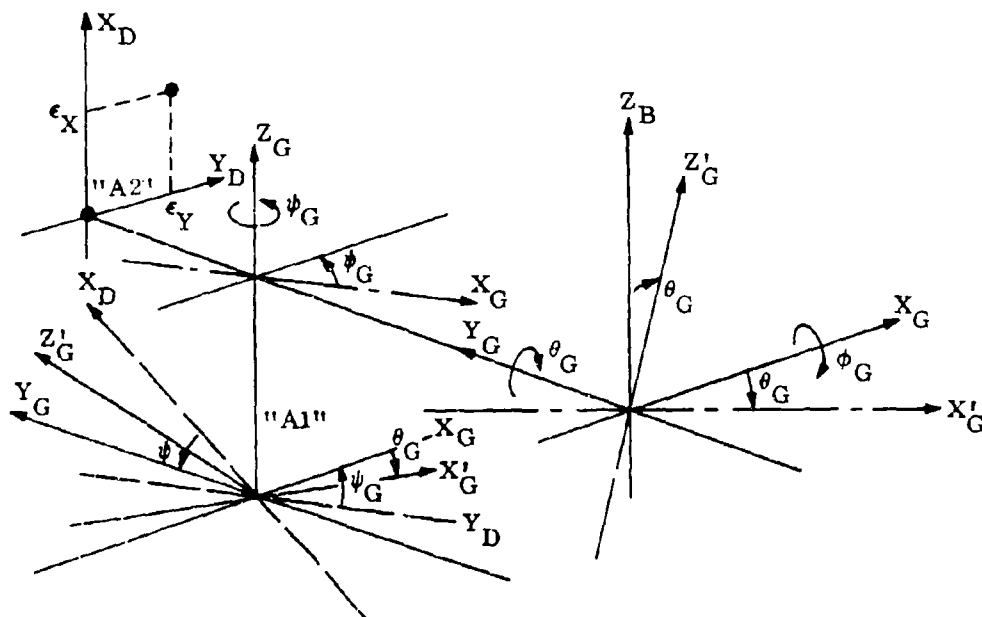


Fig. 4 Package A Gimbal and Detector Coordinate Frames

X-5

LOCKHEED PALO ALTO RESEARCH LABORATORY
LOCKHEED MISSILES & SPACE COMPANY
A GROUP DIVISION OF LOCKHEED AIRCRAFT CORPORATION

relative to the two-axis detector, which is stationary with respect to the body-axis coordinates. The Package A2 gimbal frame is fixed in yaw relative to the A1 detector and the body-axis coordinates.

PACKAGE A2 GIMBAL TRANSFORMATION

The Package A1 gimbal frame, which is nominally aligned with the body, is rotated by yaw ψ_G .

$$\psi_G = \tan^{-1} \left[\frac{\hat{L}_{Y_{B'}}}{\hat{L}_{X_{B'}}} \right]$$

and in the outer gimbal (pitch) θ_G ,

$$\theta_G = \cos^{-1} \hat{L}_{Z_B}$$

so that the Package A1 Z-axis is aligned with the relative position vector when the inner gimbal (roll) ϕ_G is set at zero:

$$\phi_G = 0^\circ$$

The Package A mirror is positioned at its fixed inner-gimbal offset of 45° .

Any error in the calculation or positioning of the nominal gimbal settings will result in generation of an error signal on the two-axis A2 detector fixed relative to the vehicle coordinate frame.

ERROR SIGNAL TO GIMBAL CORRECTION TRANSFORMATIONS

A transformation is then required to convert the error signals ϵ_X and ϵ_Y into corrections to the inner and outer gimbals of Package A2. The angular deviation of light rays from null in the inner and outer gimbal axis is indicated by the components of the ϵ_X and ϵ_Y along the Z_G and X_G axes, respectively, as shown in Fig. 5a.

The roll plane error then is

$$\phi_\epsilon = \epsilon_X \cos (\psi_G - \theta_G) - \epsilon_Y \sin (\psi_G - \theta_G)$$

and the pitch plane error is

$$\theta_\epsilon = \epsilon_X \sin (\psi_G - \theta_G) + \epsilon_Y \cos (\psi_G - \theta_G)$$

The gimbal corrections to drive these errors to null are

$$\Delta\phi_G = -\frac{1}{2} \phi_\epsilon$$

$$\Delta\theta_G = -\theta_\epsilon$$

The resolution of indicated error from the A1 detector into pitch and roll gimbal corrections is only a function of nominal pitch gimbal attitude, as shown in Fig. 5b, since the package is fixed in the yaw axis relative to the vehicle coordinate frame. The pitch and roll plane errors are thus

$$\theta_\epsilon = -\epsilon_X \sin \theta_G + \epsilon_Y \cos \theta_G$$

$$\phi_\epsilon = \epsilon_X \cos \theta_G + \epsilon_Y \sin \theta_G$$

which are identical to the relationships for Package A2 when

$$\psi_G = 0$$

X-7

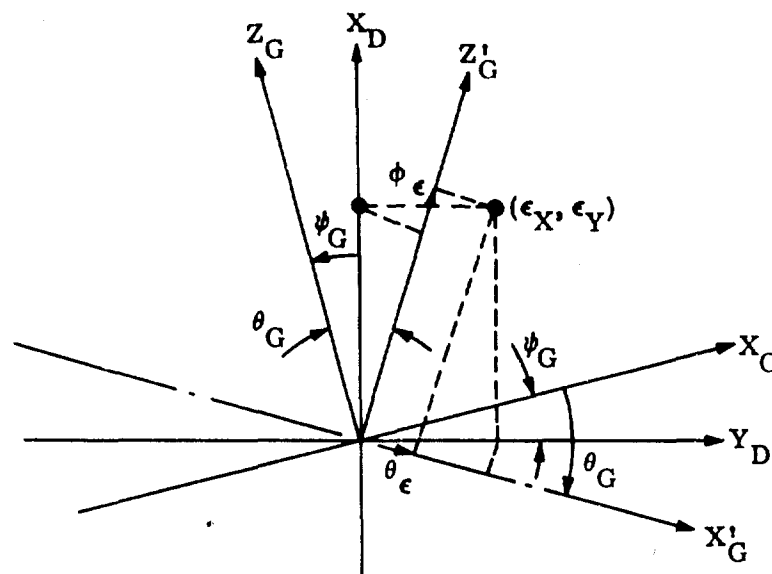


Fig. 5a A2 Detector Error Signal Resolution

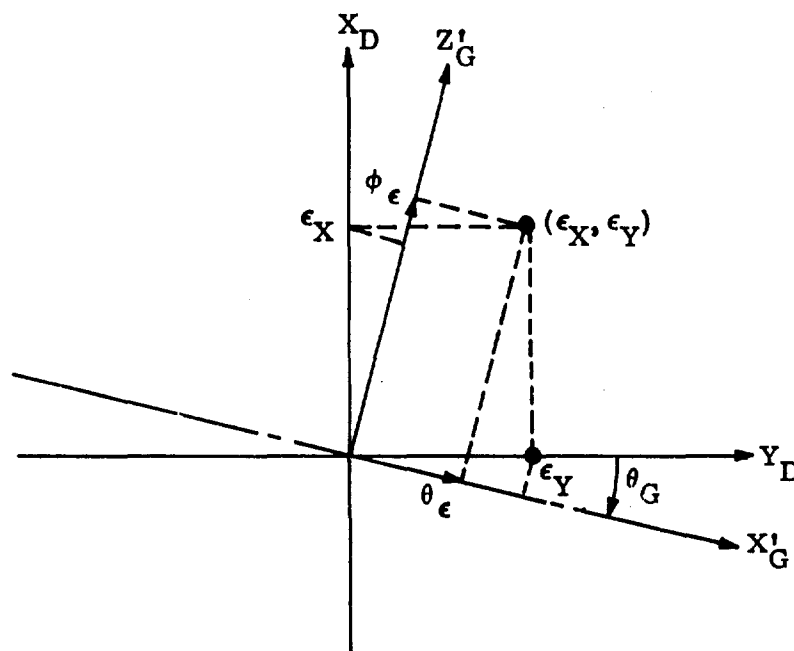


Fig. 5b A1 Detector Error Signal Resolution

X-8

UNCLASSIFIED

LOCKHEED PALO ALTO RESEARCH LABORATORY
LOCKHEED MISSILES & SPACE COMPANY
A GROUP DIVISION OF LOCKHEED AIRCRAFT CORPORATION

The gimbal corrections to drive the detector errors to null are, again,

$$\Delta\phi = -\frac{1}{2} \phi_{\epsilon}$$

$$\Delta\theta_G = -\theta_{\epsilon}$$

A high degree of accuracy in determination of the sine and cosine of the nominal outer gimbal angle is not required to maintain adequate resolution of the correction angle, since the detected errors and the resulting gimbal corrections required are on the order of seconds of arc. A simple table of 15 settings for the pitch gimbal angle (Table 1) will be stored, such that the error used in the sine and cosine will not exceed 0.05.

Table 1

SINE AND COSINE TO NEAREST 0.1

θ_G or $\psi_G - \theta_G$	<u>Sine</u>	<u>Cosine</u>
0	0	1.0
5.75	0.10	0.995
11.55	0.20	0.98
17.47	0.30	0.954
23.58	0.40	0.916
30.0	0.50	0.866
36.87	0.60	0.80
44.43	0.70	0.714
53.13	0.80	0.60
60.0	0.866	0.50
66.42	0.916	0.40
72.53	0.954	0.30
78.45	0.98	0.20
84.25	0.995	0.10
90.0	1.0	0

X-9

LOCKHEED PALO ALTO RESEARCH LABORATORY
 LOCKHEED MISSILES & SPACE COMPANY
 A GROUP DIVISION OF LOCKHEED AIRCRAFT CORPORATION

Appendix Y

CROSS-TALK IN A FREQUENCY-
MULTIPLEXED QUADRI-PHASE SYSTEM

by

Dr. G. F. Herrmann

LOCKHEED PALO ALTO RESEARCH LABORATORY
LOCKHEED MISSILES & SPACE COMPANY
A GROUP DIVISION OF LOCKHEED AIRCRAFT CORPORATION

INTRODUCTION AND SUMMARY

We consider the behavior of a communications system with a nonlinear characteristic of the form

$$v(t) = \sin u(t)$$

where $u(t)$ represents an input, or transmitted signal, and $v(t)$ the output, or received signal, both appropriately normalized. A characteristic of this form is often associated with light carriers and arises from a combination of sinusoidal intensity modulation and square-law detection. Appreciable distortion can be expected in the output when the argument $u(t)$ of the sine function approaches or exceeds unity.

The transmitted signal is assumed to be composed of a set of channels that are frequency multiplexed. There are two channels in quadrature per subcarrier frequency, and each is operated in a biphase mode. Since these channels are operated independently of each other, the peak value assumed by $u(t)$ equals the sum of the peak amplitudes of each channel. The mean (or, rather, rms) value of $u(t)$ would be smaller than this peak by roughly a factor of $1/\sqrt{n}$. Thus, if peak amplitudes were to be kept at or below $u(t) = 1$, the system would on the average be operating at a low index of modulation and therefore at low efficiency. In practice, we wish to operate in a regime where the average of $u(t)$ is close to unity. A certain amount of distortion and cross-talk is then inevitable. The purpose of the following analysis is to obtain estimates for these effects. The results can be summarized as follows. Suppose that a_k represents the amplitude in the k th channel in the absence of nonlinearity. Then the nonlinearity results in a reduction of a_k by an amount given by

$$\frac{\Delta a_k}{a_k} = -\frac{1}{4} \frac{P_{\text{tot}}}{P_c}$$

Y-1

LOCKHEED PALO ALTO RESEARCH LABORATORY
LOCKHEED MISSILES & SPACE COMPANY
A GROUP DIVISION OF LOCKHEED AIRCRAFT CORPORATION

where P_{tot} is the total input power from all channels combined and P_c is a characteristic power equivalent to an rms value of $u(t)$ equal to 1.

In addition to this systematic distortion, there is a noiselike random contribution P_n due to cross-talk among the channels, which relates to the received power P_r in any one channel according to the equation

$$\frac{P_n}{P_r} = \frac{\alpha}{64} \frac{P_{\text{tot}}^2}{P_c^2} \left(1 - \frac{1}{4} \frac{P_{\text{tot}}}{P_c} \right)^2$$

where α is a coefficient that varies between 1/2 and 3/4, depending on the particular channel.

It appears that even for $P_{\text{tot}} = P_c$ (~83% modulation) the cross-talk "noise" is within acceptable limits. At first glance, this is surprising. Clearly, peak amplitudes under these conditions will be clipped severely by the nonlinear transducer. However, it can be seen that these peaks are of very short duration relative to the bandwidth of the received channels, and in addition they occur infrequently. Statistics and frequency filtering combine to yield cross-talk noise which is small compared with what one might be led to guess on superficial heuristic grounds.

THE SYSTEM

The system operates at a set of n_c equally spaced subcarrier frequencies

$$\omega_k = \omega_0 + k\Omega, \quad \omega_0 \gg \Omega \quad (1)$$

Each frequency provides for two channels in quadrature, with signals of the form

$$A_k(t) \cos(\omega_k t + \theta_k) \quad (2)$$

and

$$\bar{A}_k(t) \sin(\omega_k t + \theta_k) \quad (3)$$

Y-2

Each channel is operated in a biphasic mode. Ideally, $A_k(t)$ and $\bar{A}_k(t)$ would assume only the values $\pm C$, where C is a constant. Frequency multiplexing requires that the spectral content of $A(t)$ and $\bar{A}(t)$ be confined to a band $\Delta\omega$, where $\Delta\omega \ll \Omega$. The shapes of $A(t)$ and $\bar{A}(t)$ are therefore modified by appropriate filtering. It is assumed that the average power is equal in the different channels.

The total input signal $U(t)$ is a superposition of signals of the form (2) and (3). For simplicity, we put $\sin(\omega_k t + \theta_k) = \cos(\omega_k t + \theta_k + \pi/2)$ and write $U(t)$ as a sum of cosine form signals

$$U(t) = \sum_{k=1}^n A_k \cos(\omega_k t + \theta_k) \quad (4)$$

where n is the total number of channels and where each frequency appears in two terms of the sum.

THE NONLINEAR TRANSDUCER

We assume a nonlinear transducer (e.g., modulator) with a characteristic of sinusoidal shape. For an input $U(t)$, the output is given by

$$V(t) = V_c \sin(U(t)/U_c) \quad (5)$$

where V_c and U_c are constants. In the receiver, $V(t)$ is in turn split into separate channels, two for each frequency. In each channel the signal is represented in the form

$$B_k(t) \cos(\omega_k t + \theta_k) \quad (6)$$

We shall refer to the $A_k(t)$ as the transmitted signals and to the $B_k(t)$ as the received signals.

It is convenient to introduce the normalized variables

$$u(t) = U(t)/U_c \quad (7a)$$

$$a_k(t) = A_k(t)/U_c \quad (7b)$$

$$v(t) = V(t)/V_c \quad (7c)$$

$$b_k(t) = B_k(t)/V_c \quad (7d)$$

Equations (4) and (5), respectively, then assume the forms

$$u(t) = \sum_{k=1}^n a_k(t) \cos(\omega_k t + \theta_k) \quad (8)$$

and

$$v(t) = \sin u(t) \quad (9)$$

CROSS-TALK

Equation (9) can be expanded as a power series

$$\begin{aligned} v &= u - \frac{u^3}{3!} + \frac{u^5}{5!} \dots \\ &= v_1 + v_3 + v_5 + \dots \end{aligned} \quad (10)$$

The linear term, v_1 , represents a faithful reproduction of the signal u . The higher terms produce distortion and cross-talk.

The received signals b_k can be similarly represented in the form

$$b_k = b_{1k} + b_{3k} + b_{5k} + \dots \quad (11)$$

where b_{1k} equals the transmitted signal a_k .

We shall deal initially only with the third-order term $v_3 = -\frac{u^3}{3!}$. We shall show later that this term is indeed the only significant one in any reasonable regime of operation.

Using Eq. (8) we find

$$v_3 = -\frac{1}{6} \sum_{kjm} a_k a_j a_m \cos(\omega_k t + \theta_k) \cos(\omega_j t + \theta_j) \cos(\omega_m t + \theta_m). \quad (12)$$

Consider the trigonometric relation

$$\cos \alpha \cos \beta \cos \gamma = \frac{1}{4} [\cos(\alpha + \beta + \gamma) + \cos(\alpha + \beta - \gamma) + \cos(\alpha - \beta + \gamma) + \cos(-\alpha + \beta + \gamma)]. \quad (13)$$

In our case, in view of Eq. (1), terms of the form $\alpha + \beta + \gamma$ correspond to a frequency $3\omega_0 + k\Omega$ which lies outside the band of operation. Terms of the form $\alpha + \beta - \gamma$ correspond, on the other hand, to frequencies $\omega_0 + k\Omega$, which may coincide with one of the subcarrier frequencies. Considering only these types of terms [of which there are three in Eq. (13)], we find

$$v_3 = -\frac{1}{8} \sum_{kjm} a_k a_j a_m \cos[(\omega_k + \omega_j - \omega_m)t + \theta_k + \theta_j - \theta_m] \quad (14)$$

If we collect together all terms corresponding to a given frequency, this can be put in the form

$$v_3 = \sum b_{3p}(t) \cos(\omega_p t + \theta_p) \quad (15)$$

where b_{3p} is some linear combination of triple products $a_k a_j a_m$ with

$$\omega_p = \omega_k + \omega_j - \omega_m \quad (16)$$

In the receiver, v_3 is again separated into channels corresponding to the subcarrier frequencies ω_k . The spectrum of b_{3p} occupies a maximum bandwidth of $3\Delta\omega$, where $\Delta\omega$ is the bandwidth of $a_k(t)$, or an effective bandwidth of $\sqrt{3}\Delta\omega$. Let us assume for the moment that this bandwidth is smaller than the channel frequency Ω , and also smaller than the bandwidth of the receiver channel. Then $b_{3p}(t)$ represents the third-order contribution to the signal amplitude in the p th channel. It represents both distortion (i.e., change in the mean received signal) and statistical fluctuations (i.e., noise).

In order to evaluate $b_{3p}(t)$, it is necessary to regard the coefficients $a_k(t)$ as independent random variables with identical distributions. Assuming that $a_k(t)$ has a zero mean, i.e., is as likely to be positive as negative, then the same is true of the triple product $a_k a_j a_m$. Let us now consider the triplets contributing to a particular channel ω_p . These obey Eq. (16). Among these triplets, we may distinguish one special kind, namely, those where $k = p$ and $j = m$ or $j = p$ and $k = m$. These triplets have the form $a_k^2 a_p$ and are therefore proportional to the first-order signal a_p , with a positive coefficient. There are $2n$ such terms in the sum in Eq. (14). They contribute to a change in the average received value of

$$\Delta a_p = -\frac{n}{4} \langle a^2 \rangle a_p \quad (17)$$

where $\langle a^2 \rangle$ is the expected value of a_k^2 . The product $n \langle a^2 \rangle$ is proportional to the total input power.

The remaining triplets are not correlated to a_p nor are they correlated among themselves, except for the fact that each triplet with $k \neq j$ appears twice in the summation. For large n , according to the central limit theorem, the sum of these triplets yields a normally distributed parameter $g_p = b_p - \langle b_p \rangle$ with variance

$$\langle g_p^2 \rangle = \frac{1}{128} N(p) \langle a_p^2 \rangle^2 \quad (18)$$

The coefficient $1/128$ is composed of a factor $1/64$, which is simply the square of the numerical coefficient in Eq. (14), and an additional factor of $1/2$ since there are two channels at each frequency. The term $N(p)$ is the effective number of channels obeying Eq. (16) for a fixed p . In determining $N(p)$, we must take into account the equivalence of $a_k a_j a_m$ and $a_j a_k a_m$. The exact expression for $N(p)$ is elaborate and depends on the relative position of ω_p within the subcarrier manifold. For large n ,

$$N(p) = 2\alpha n^2 \quad (19)$$

where α varies from approximately $1/2$ at the edge of the manifold to $3/4$ at the center.

Combining Eqs. (18) and (19),

$$\langle g_p^2 \rangle = \frac{1}{64} \alpha n^2 \langle a^2 \rangle^3 \quad (20)$$

The received signal, b_k , at the frequency ω_k can thus be represented up to third-order terms in the form

$$b_k = a_k + \Delta a_k + g_k \quad (21)$$

where Δa_k , given by Eq. (17), represents a distortion, and g_k represents a random noise term.

We would like to reexpress this result in terms of the transmitted and received signal powers. To this end, we put the transmitted signal power at ω_k in the form

$$P_t(k) = P_C \langle a^2 \rangle \quad (22)$$

where P_C is a constant equal to the power corresponding to $\langle a^2 \rangle = 1$. The received power is put into similar form. Thus,

$$P_{r1}(k) = C \langle a^2 \rangle \quad (23)$$

Y-7

represents the received signal power in the absence of distortion, where C is a constant, and

$$P_{r2}(k) = C \langle (a_k + \Delta a_k)^2 \rangle \quad (24)$$

is the received power for the distorted signal. Similarly,

$$P_n(k) = C \langle g_k \rangle^2 \quad (25)$$

is the average "noise power" associated with cross-talk.

With the help of these definitions, we can put Eq. (17) in the form

$$\frac{\Delta a_k}{a_k} = -\frac{1}{4} \frac{P_{tot}}{P_C} \quad (26)$$

where $P_{tot} = nP_t(k)$ is the total transmitted power. Equation (20) assumes the form

$$\frac{P_n}{P_{r1}} = \frac{\alpha}{64} \frac{P_{tot}^2}{P_C^2} \quad (27)$$

and Eq. (28) the form

$$\frac{P_n}{P_r} = \frac{\alpha}{64} \frac{P_{tot}^2}{P_C^2} \left/ \left(1 - \frac{1}{4} \frac{P_{tot}}{P_C} \right)^2 \right. \quad (28)$$

Examples.

Consider a modulator-detector system with an overall characteristic given by Eq. (5).

Example 1. Let the total input power $P_{\text{tot}} = P_C$. This power corresponds to an input normalized amplitude of $a = 1$, or a modulation index of 83%. In this case, we obtain from Eq. (28) a ratio of noise to signal power

$$\frac{P_n}{P_r} < \frac{1}{48} \sim 0.02$$

where we have put $\alpha < 3/4$.

Example 2. Let $P_{\text{tot}} = \frac{3}{2} P_C$. This corresponds to a modulation index of 95% and a ratio of noise to signal power

$$\frac{P_n}{P_r} < 0.067$$

THE EFFECT OF FILTERING

As defined by Eq. (15), $b_{3k}(t)$ is contained in a bandwidth of $3\Delta\omega$. However, the effective bandwidth is more properly given by $\sqrt{3}\Delta\omega$. Now, we can safely assume that the transmitted channel bandwidth $\Delta\omega$ is the minimum bandwidth determined by the requirements of the detection and decision system, since there is no point in transmitting spectral components that are rejected in the receiver. Hence, filtering at the receiver can reduce cross-talk noise only by a relatively insignificant factor.

HIGHER ORDER NONLINEAR TERMS

The analysis for v_5 and v_7 can be performed along lines analogous to those that we have followed for v_3 . The counting procedures can become quite complex, but for high n reasonably simple approximate relations are easily obtained. For a given

order $s = 2r + 1$, we find

$$\frac{\Delta_s a_k}{a_k} = (-1)^r \frac{1}{2^{s-1}} \left(\frac{P_{\text{tot}}}{P_C} \right)^r$$

and

$$\frac{P_{ns}}{P_{lk}} = \frac{\alpha_s}{2^{2s-1} r! (r+1)!} \left(\frac{P_{\text{tot}}}{P_C} \right)^{s-1}$$

Here $\Delta_s a_k$ is the mean change in a_k resulting from v_s , P_{ns} is the corresponding cross-talk noise power, and α_s is a number smaller than 1. For $P_{\text{tot}} = P_C$, we find that these terms decrease rapidly with increasing s and that only the third-order term is significant.

DISCUSSION OF RESULTS

It is seen from the examples in Section 3 that operation of the electrooptic modulator at a modulation index approaching unity will cause an appreciable amount of intermodulation noise to appear in each of the channels of a frequency-multiplexed system. This noise will, of course, be superimposed on noise from other sources such as photodetector shot current and amplifier noise. Therefore, intermodulation will tend to increase the bit error rate, or, equivalently, to decrease the link power margin. Because the analysis assumes that the number of frequency-multiplexed channels is large, whereas usually it will be small, the results of the analysis do not apply in detail. Nevertheless, similar intermodulation effects can be anticipated. Therefore, it is important to consider means by which intermodulation effects can be reduced.

The most obvious approach is to improve the linearity of the input-output signal transfer function. Here we will consider only the nonlinearity in the baseline system due to the instantaneous transfer function of the electrooptic modulator-photodetector combination, $v(t) = \sin u(t)$, as given by Eq. (9). This nonlinearity is fundamental to the

optical modulation method adopted for the baseline system, but at least one alternative electrooptic modulation/demodulation method is known that can be made substantially linear in its input-output transfer function. Moreover, the theory needed for the design of such a linearized system has been worked out.* In this case, the electrooptic modulator is modified slightly so that it produces pure frequency modulation (rather than polarization modulation). Then, at the receiver, a special form of birefringent frequency discriminator is used to convert the phase modulation to intensity modulation. It appears that this scheme would be applicable to the present problem, and hence evaluation of this approach is indicated.

Another approach to reducing intermodulation noise is exemplified by the Interplex multiplexing technique developed by the Jet Propulsion Laboratory.** In this scheme, the signals to be multiplexed are first passed through a special nonlinear processor prior to transmission. The nonlinearity of the processor is adjusted to produce an intermodulation signal that is just equal to but opposite to that produced later in the nonlinear transmission system. Under proper conditions, the two sources of intermodulation noise can be made to cancel.

It has not yet been demonstrated that the nonlinear signal processing required by the Interplex system could be carried out in the case of the bandwidth signals that must be handled by the baseline system. Therefore, it is thought that the Interplex technique (or some variation thereof) might better be regarded as a supplement to other linearization approaches than as a primary approach. From a practical standpoint, design and construction of a linearized electrooptic modulator-demodulator seems more attractive; but both approaches should be examined further before a decision is made as to whether one or both should be pursued.

*S. E. Harris et al., "Optical Network Synthesis Using Birefringent Crystals," J. Opt. Soc. Am., Vol. 54, Oct 1964, pp. 1267 - 1279.

**S. Butman and A. Timor, "Interplex Modulation," J. P. L. Quart. Tech. Rev., Vol. 1, pp. 97 - 105.

Appendix Z

RECOMMENDED ADDITIONAL STUDIES

Dr. R. F. Whitmer

LOCKHEED PALO ALTO RESEARCH LABORATORY
LOCKHEED MISSILES & SPACE COMPANY
A GROUP DIVISION OF LOCKHEED AIRCRAFT CORPORATION

The following is an outline of additional efforts that should be performed in order to prescribe more accurately the final design of the QPSK system and also to predict its performance better. * LMSC is currently pursuing some of this work as in-house-funded efforts. However, expanded and supplemental studies are needed to examine fully the many detailed considerations which should be made. Having the results of such efforts would contribute directly to the success of the forthcoming Brassboard Demonstration and would also contribute to, and probably shorten the time required for, the Final Design phase of the program.

It is suggested that efforts in the following areas should be initiated as soon as possible:

- (1) Studies to extend the performance predictions of the QPSK system
 - Analyze the effects of bandlimiting in the transmitter and receiver on the following system characteristics:
 - Spectral density of signals applied to the optical modulator
 - Bit error rate
 - Analyze intersymbol and cross-channel interference and its effects on the system bit error rate
 - Evaluate intermodulation effects occurring in frequency division multiplexing (FDM) operation. The following causes should be considered:
 - Amplitude limiting in modulator driver or receiver electronics
 - Nonlinear transfer function of electrooptical modulator-photodetector combination
 - Establish stability and timing precision requirements of receiver local oscillator and bit synchronizer clock; determine effect of data timing errors on bit-error probability
 - Determine effect on bit error probability of non-Poisson, non-Gaussian statistics in avalanche photodetectors. Also, examine effect of departure from Poisson statistics for high-background conditions

*Since many of the unresolved questions have been clearly pointed out by the Aerospace Corporation evaluation team, we have attempted to reflect their recommendations in this appendix.

- (2) Investigation of new approaches and techniques for improving system performance
- Evaluate and extend techniques for reducing intermodulation effects during FDM operation. Emphasize improvement of linearity of modulation-demodulation processes, and especially the electrooptical modulator-photodetector combination. (See Appendix Y, Section 6.) Also consider means of minimizing intermodulation effects in electronic circuits
 - Develop LOS as a laser candidate to take advantage of the potential 3 to 5 improvement in overall efficiency.

Appendix AA

MODERN THERMAL DESIGN REQUIREMENTS
FOR SPACECRAFT ELECTRONICS

by

Dr. L. Fried

Mr. H. Cohan

LOCKHEED PALO ALTO RESEARCH LABORATORY
LOCKHEED MISSILES & SPACE COMPANY
A GROUP DIVISION OF LOCKHEED AIRCRAFT CORPORATION

Introduction

The environment in which most spaceborne equipment must survive and function is unique, and, to many designers, novel. Unlike the conditions for which almost all earth-surface based and airborne equipment are designed, the situation in which the package may be placed in service in an unmanned spacecraft is usually completely dependent on radiation and conduction to maintain proper control of temperatures.

The objective of spacecraft thermal design is to control the temperatures of the components of the vehicle in such a fashion as to accomplish the mission successfully. Electronic equipment represents a major part of those space vehicle components which require thermal control. It is apparent to the authors that good communication does not always exist between equipment designers and those responsible for spacecraft systems integration and design. The former are often unaware of the environmental and operational demands which will be placed on their products, the latter are all too frequently faced with an equipment design which is a fait accompli whose incompatibility with spacecraft requirements invokes excessive penalties. These penalties can appear as low reliability, which is unacceptable, additional weight, or operational restrictions on the space vehicle. Much of this difficulty can be resolved before final design of the equipment has proceeded too far if the package designer is made aware of the nature of the problems, and if he and the spacecraft thermal analyst can be brought together.

The Space Vehicle Environment

The spacecraft on orbit, or in transit to another planet, is in a radiation thermal energy balance with the universe. Its external surfaces receive heat from the sun, primarily in the visible spectrum. If orbiting close to a planet it also receives reflected sunlight, called albedo, which is also visible, as well as some energy in the infrared (because a planet is a warm body). Additional heat may be generated on board, for example as battery-stored electrical energy or energy from a nuclear source. Essentially all this heat energy is radiated away to space, a sink whose temperature is close to absolute zero. The average temperature of a solid, homogenous body without internal thermal resistance is that which satisfies the radiation energy balance.

$$q_{\text{out}} = \sigma \epsilon T^4 = q_{\text{in}} \quad (1)$$

where σ is the Stefan-Boltzmann constant and ϵ the emissivity.

The heat flow rate into the body can be controlled to considerable degree by the thermal-optical properties of the outer surfaces. If sunlight only is considered, then the solar absorptance, α_s , determines what proportion of the impinging energy is absorbed.

$$q_{\text{in}} = \alpha_s S \quad (2)$$

where S is the solar constant, approximately 123 watts/ft² at the orbit of earth.

The unabsorbed heat is reflected. Table I shows values for several materials in current use. The sun is so much hotter than the body that body temperature has no measurable effect on heat absorption. Energy is radiated from the body, however, at infrared wavelengths, and thus equation (1) is rearranged to determine the temperature.

$$T = \left[\frac{1}{\sigma} \frac{\alpha_s}{\epsilon} S \right]^{1/4}$$

It can be seen that the values of infrared emittance, ϵ , are equally important as α_s . It is not always possible to obtain optimum combinations of these values, thus one sees the mosaic-like patterns used on spacecraft.

TABLE I
TYPICAL PROPERTIES OF THERMAL CONTROL MATERIALS

Material	Solar Absorptance α_s	Emittance ϵ
White Paint	.20	.87
Black Paint	.9	.9
Aluminum Paint	.35	.4
Aluminum Foil	.15	.04
Gold Deposit	.4	.12

Even a radiator on a spacecraft skin must ultimately reject its heat to space by the radiation mechanism. Only in special cases when mass can be expended is any other rejection mode utilized, usually a water boiler or sublimator. These latter special cases will not be considered in this paper.

The space vehicle orbiting earth is not in a steady-state condition with respect to heat inputs, however. The vehicle will pass cyclically through sunlight and the darkness of the earth's shadow once per orbit pass. The relative times in sun and shade depend upon orbit geometry and altitude. A craft injected into polar or near-polar orbit, with inclination angle near 90°, i. e., an orbit lying in a plane containing the earth's axis, may spend anywhere from slightly more than half to all its time in the sun, depending on the angle β between the orbit plane and the solar vector. In a "noon" orbit, $\beta = 0^\circ$ and the vehicle spends almost half its time in shadow (at low altitude). In a "twilight" orbit, β is 70° to 90°, and the vehicle is always in the sun.

Consider now a space vehicle maintained in an earth-oriented non-spinning attitude. At $\beta = 0$, it is seen that the sun will appear to move across the skyward side of the vehicle from nose to tail, as the vehicle orbits. The top will receive much energy, the sides very little. The bottom, earth-facing surfaces, will receive albedo and infrared energy. Thus the skins will exhibit a non-uniform temperature distribution, as well as time-dependent cycling. The vehicle in twilight orbit will have a very large temperature gradient, but it can be seen that it will be constantly heated on the sunward side while constantly losing heat to space on the dark side, so that the temperatures are steady. Figure 1 shows orbit average heat inputs on a symmetrical cylindrical shape in noon and twilight orbits. To show the large excursions of temperature in a thin skin due to orbital variations, Fig. 2 presents instantaneous temperatures for a horizontal cylinder in a noon orbit, at relatively low altitude.

Altitude, too, will influence the energy inputs. For β angles less than twilight, the higher the orbit, the less portion of total time the vehicle will spend in the shade. At higher altitudes, however, albedo and earth-shine effects are less important.

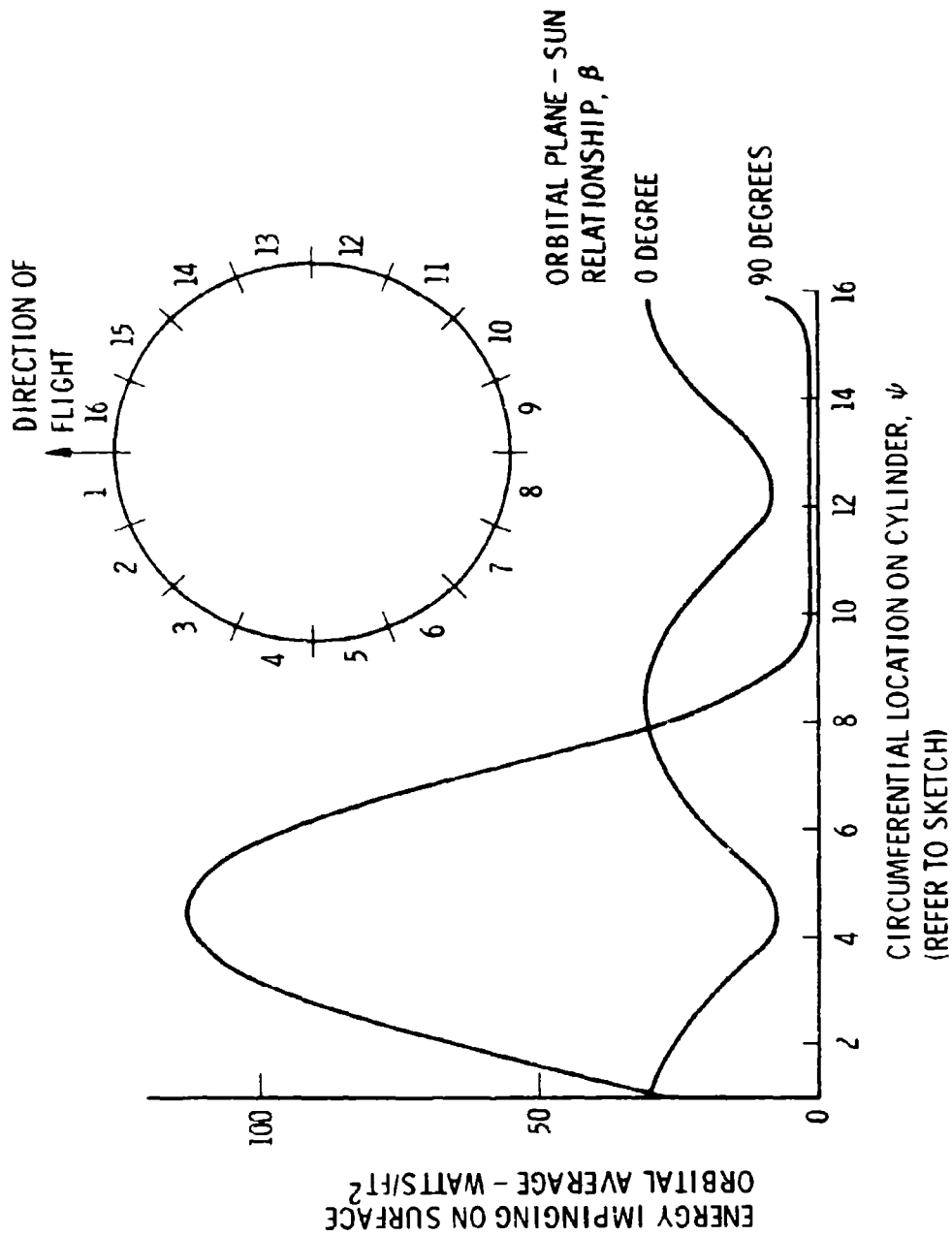


Fig. 1. Orbital average energy impinging on various portions of a cylindrical spacecraft in near-earth orbit.

The Mission Sets the Requirements

The two cases described above, $\beta = 0^\circ$ and $\beta = \pm 90^\circ$, are the extremes which bound all cases. All spacecraft orbital geometries fall between these limits. The nature of the mission determines the required orbital parameters, and thus the energy environment imposed on the spacecraft.

The spacecraft thermal designer will attempt to control the operating temperatures of the vehicle first by choice of the external and internal coatings and finishes and the arrangement of spacecraft elements -- passively -- and, only in the inability to achieve passive control, by use of active techniques, such as shutters, louvers, electrical heaters, heat pipes, and other active devices. The motivation is simple and direct. Nonpassive methods are, very likely, heavier and less reliable than passive, as well as more expensive.

It must be noted, however, that the temperature environment may not be entirely in control of the thermal designer. The spacecraft mission often requires a launch window requiring flight within a range of β angles, using one thermal control design. The orbital geometry may result in precession or regression of the orbit plane so that the β angle shifts from day to day.

The thermal environment imposed on electronic equipment, then, is the result of a number of compromises. The electronics designer must recognize these facts if his product is to be technically competitive in the long term.

The Space Vehicle Design

The real spacecraft cannot be treated as a simple single homogeneous lump. It is a complex structure, required by its mission to be structured of many thin, low mass elements which provide a housing and mounting for the electronics packages, power sources, and other equipment. With few exceptions, the structure is not pressurized. Figure 3 shows a typical spacecraft arrangement. Heat transfer within the geometric complex is entirely radiative and conductive.

A review of the usual procedure in arriving at an equipment arrangement may be helpful. Obviously, any design is a series of compromises. Before arriving on orbit the space vehicle must survive ground handling, countdown, launch and ascent accelerations and vibration, and aerodynamic heating.

Starting with the general outline and internal construction of the spacecraft, the thermal designer places the equipment in those locations which best appear to match the operational requirement. This is decided on the basis of the known thermal characteristics of the equipment, such as power dissipation, duty cycles, weight, temperature limitations, thermal finishes and possibly special requirements. The nature of the mission and the type of orbit strongly affect the placement of equipment. The location of some components is influenced by function; for example, horizon sensors must be located so they can see the horizon. Conflicting requirements frequently arise because of the needs of the power system, guidance system, attitude control system and others and because of desires to keep wiring short and to balance equipment mass. For the most part, an iterative procedure takes place as preliminary design proceeds. The spacecraft designer and the thermal analyst, working from experience, develop trial layouts, examine them, modify, analyze, and eventually produce a design that appears to be satisfactory. At this time, the thermal-mathematical model is built. This is a mathematical representation of the vehicle and equipment. The structure is divided into finite nodes, or lumps. Each equipment item is treated as one or more nodes. The thermal capacity of these nodes is the analogy of electrical capacitance. Nodes are connected by thermal resistors, again represented by their electrical counterparts. A network is thus constructed to simulate the spacecraft section. It is not unusual for a model to consist of 500 to 700 nodes. Digital computer programs of the most sophisticated type are used to solve for the transient temperature histories of all nodes. Inputs must include power

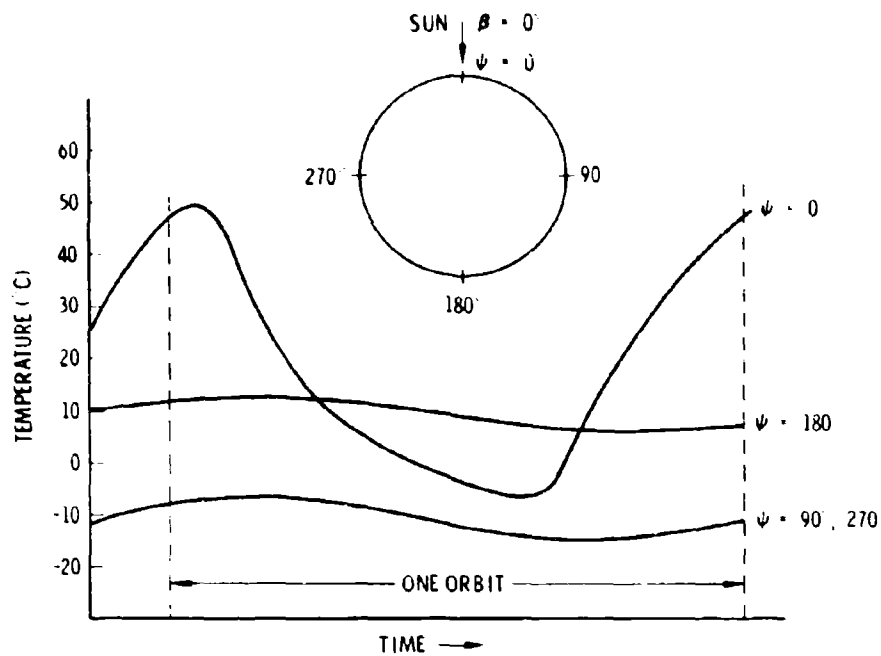


Fig. 2. Instantaneous skin temperatures, noon orbit, cylindrical vehicle.

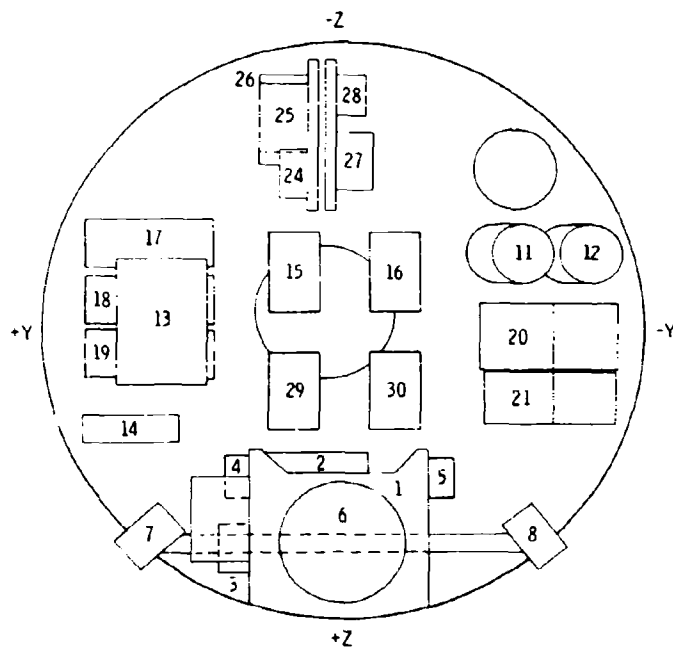


Fig. 3. View of typical spacecraft equipment mounting.

dissipation figures, anticipated duty cycles, package surface characteristics, spacecraft orbit geometries, and many others.

It is easily seen that no piece of equipment in the spacecraft is independent of its environment. Similarly, each item influences the environment to an extent determined by its power dissipation, duty cycle, thermal mass, shape, and so forth. Table II shows these influences. The table refers to the equipment of Fig. 3. It is noted that some components experience temperature rises almost half those of the equipment whose power dissipation is being increased.

TABLE II
THE INFLUENCE OF ELECTRONIC EQUIPMENT DISSIPATION
UPON ITS OWN ENVIRONMENT

For Each Watt Increase In Dissipation In Box	Its Own Temperature Increases	And The Temperature of Adjacent Boxes Increase:			
#14 (5.5w)	.95°C	#13 .17°C	#19 .25°C	#4 .11°C	
#2 (1.0w)	1.0	#5 .17°	#6 .22	#14 0.55	#21 .11
#15 (5.1w)	2.2	#16 .28	#29 .11	#24 .055	#13 .055
#25 (1w)	.78	#17 .11	#26 .33	#24 .33	#28 .28

Figures in parentheses are nominal power dissipations

The first computer runs of the thermal model normally point out the problem areas. Further dialogue ensues to modify the design to a point which will provide an acceptable complete entity. Parametric studies are made, to investigate all possible choices.

A result of this thermal and mechanical design is the design requirement. This document, which sets forth the conditions under which electronic equipment must operate, contains a thermal section. The restrictions are the results of the thermal analysis already completed, previous experience, and knowledge of the peculiarities of the electronics.

The Environment Seen By Electronic Equipment

In developing the design of an electronic equipment, the modes of interaction between the equipment and its environment are determined by the heat transfer mechanisms available.

- Ground-based and airborne electronics are cooled predominantly by flowing fluids and to a much lesser extent by thermal radiation and conduction. The influence of adjoining equipment is generally of secondary importance.
- Spacecraft electronics, because of the absence of air, are cooled by thermal radiation and conduction exclusively.

Here is a new situation for the electronics designer who is accustomed to having air inside and outside his boxes. He can take maximum advantage of the available heat transfer mechanisms by proper design or he can suffer the ignominy of having his equipment work well on the laboratory bench, but fail in a vacuum chamber test or in flight.

Environmental Effects on Boxes

The extent to which the environment dominates the temperature level of equipment may be seen by referring to Fig. 4. This figure shows time-averaged temperatures of an electrically passive equipment in the interior of a cylinder in near earth orbit. The effects of β angle and emittance are apparent. The example is hypothetical, but the conclusions to be drawn are representative. As shown previously, the mission controls the temperature level of the spacecraft itself. This is reflected to the electronics through the effects of the constantly changing β angle with the result that the equipment temperature level can be shifted greatly during the time the spacecraft is in orbit.

The spacecraft thermal designer also exerts his influence upon the electronics temperature level. The designer in his search for the optimum thermal control of the spacecraft, as described previously, will select the external thermal-optical properties of the space vehicle, and in addition will use internal emittances within the range shown to obtain results similar to those shown in Fig. 4.

It is evident, therefore, that the electronic equipment must be able to survive in an environment over which the designer has little or no control -- an environment which is highly variable, which seldom can be fully specified at the time the box is designed and, most importantly, which is quite different from that existing in the development laboratory.

A further complication is offered by the adjacent equipment, which can modify the gross environment and thereby modify the heat flow inside the box. Certainly, the ratios of internal dissipation to heat flow shown in Table II are influenced by the surrounding equipment. Consequently, Fig. 4 represents a highly simplified case, which demonstrates environmental effects, but only for a single item of equipment.

Figure 3 is more representative of real configurations in which each box is in close proximity to other equipment and subject to various conductive and radiative interrelationships. One of the boxes dissipates 1800 times as much heat as it receives from its environment, while another dissipates one-tenth as much heat as it receives.

"Defensive" Electronics Design

Method of Mounting

The overall temperature level of any box will be determined by circumstances outside the box. The method of interface with the environment - the conductive and radiative coupling - is beyond control of the electronics designer. The mounting of electronic equipment in the spacecraft determines whether the primary heat transfer mode will be conductive or radiative. This is largely controlled by the detailed design of the spacecraft structure with its necessary strong emphasis on weight reduction. Defensive design, then, is design which not only brings components to desired temperatures but which makes the thermal performance of the equipment as nearly independent of the method of attachment as possible.

In order to clarify this concept it is well to consider the consequences of not making the thermal performance of the equipment nearly independent of the method of attachment.

Consider an electronic box that has been designed properly for a typical aircraft application in which it is to be firmly attached to a cold-plate and to which it is to transfer all its heat dissipation by conduction. For the sake of simplicity, assume the box to be an isothermal mass (uniform temperature throughout) and the cold-plate to be held at 70°C. Figure 5 illustrates the situation which this box is placed into a typical spacecraft, where the box can

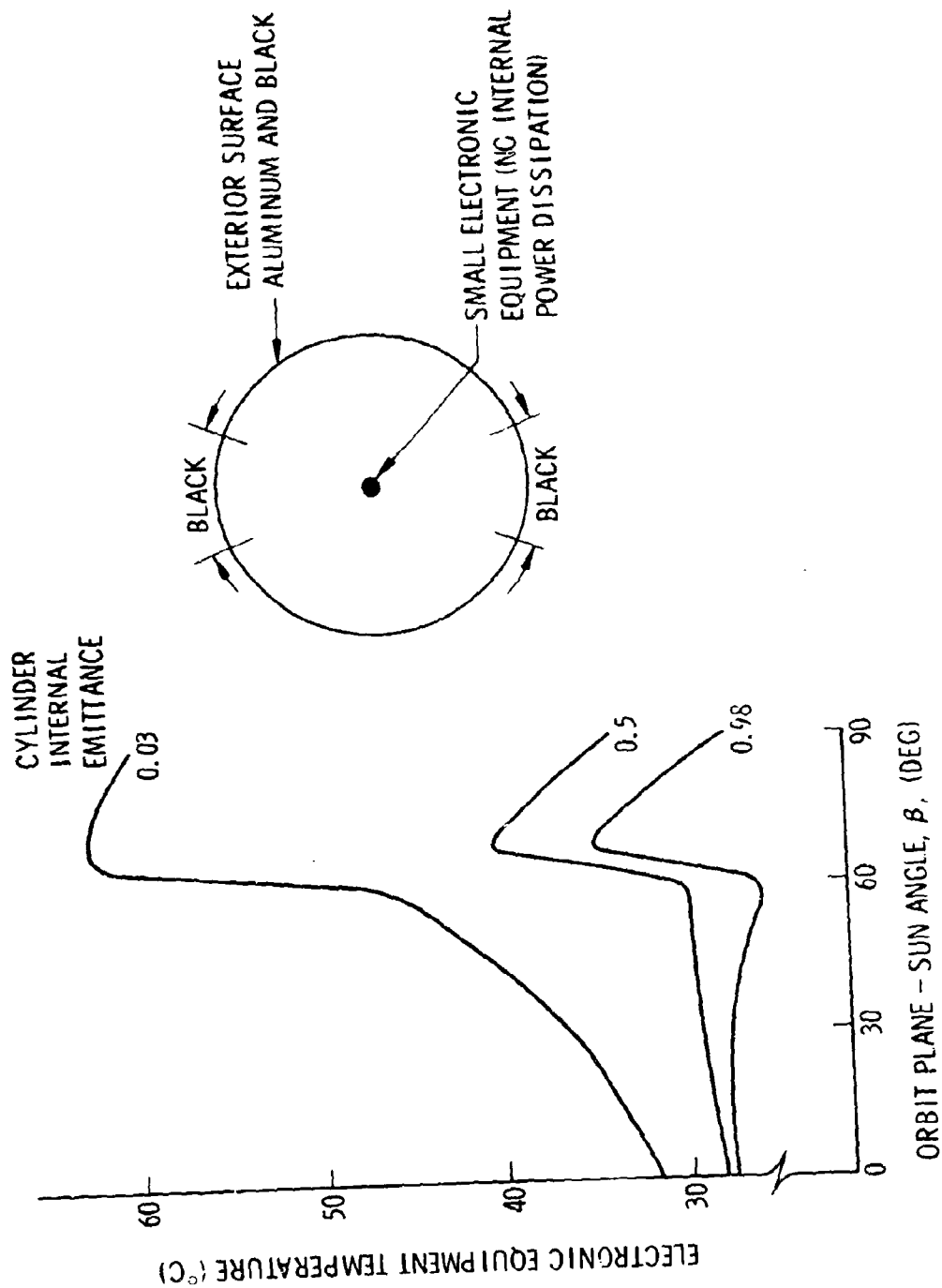


Fig. 4. Hypothetical spacecraft with electronic package.

transfer only part of its heat dissipation by conduction.

The abscissa in Fig. 5 is the surface temperature, which for this isothermal case represents the temperature of the entire box. The ordinate represents the method of attachment. For the case of cold-plate attachment this is 100%. The parameter is the ratio of the power dissipated in the box to the total surface area of the box (P/A) which is a convenient concept for discussing radiation heat transfer.

The magnitude of the problem becomes apparent from inspection of Fig. 6. The heat removal mechanism is shown for a small sample of spacecraft electronics. A larger sample would undoubtedly show an even wider range in both P/A and in the percentage of heat conducted away. One box is shown at over 100%, this arises from a radiating environment which is warmer than the box, so that more heat is conducted out the bottom than is dissipated in the box.

The significance of Fig. 6 to our hypothetical box may now be seen in Fig. 5, where the operating temperature of the equipment is seen to rise considerably when it is subjected to typical spacecraft installations, over what might have been expected in the original cold-plate design.

It is obvious that equipment designed to be cooled by conduction to a cold-plate is likely to suffer when used in a spacecraft environment. Equipment designed to be cooled by forced air is likely to suffer even more. On rare occasions the spacecraft thermal designer is forced into completely conduction-isolating a box, in this case the box can indeed be in trouble.

Defensive design would have avoided the foregoing problem. Suppose the box had been designed originally to function with only a small fraction, say 10%, of the total heat load to be conducted to the spacecraft. Then, any change in the conduction path to the environment over that designed for is likely to be beneficial and will result in lowered box temperatures.

A Design Example

The temperature of the surface of a box is, of course, of secondary interest, it is the temperatures of individual components that determine the success of the thermal design. Figure 7a shows a sketch of a hypothetical box designed for cooling by means of a cold-plate. The box has a surface area of 1 sq. ft. and is placed in a 70°C environment. The interior consists of a series of identical component boards. The center board carries most of the heat dissipated, in six components dissipating 0.555 watts each. The heat conduction paths are closely connected to the base of the box. 1.67 watts are dissipated uniformly on the remaining boards of the box to yield a P/A of 5 watts/ft². For the higher ratios shown, all dissipations are increased proportionately.

The dashed lines of Fig. 8 show the temperature of the hottest component as functions of box mounting. It is evident that substantial component temperature rises can occur, particularly for the minimum-conduction mountings which are often encountered in spacecraft.

Now let us redesign the hypothetical box of Fig. 7a for cooling predominantly by radiation, under the following constraints:

- Box outline to remain similar
- No increase in weight
- No major change in electronics layout
- No change in power dissipation distribution
- No increase in percentage of board covered by conductive paths

One of many possible redesigns is shown in Fig. 7b. There has been no attempt at optimization. The weight of the baseplate has merely been redistributed and the conduction

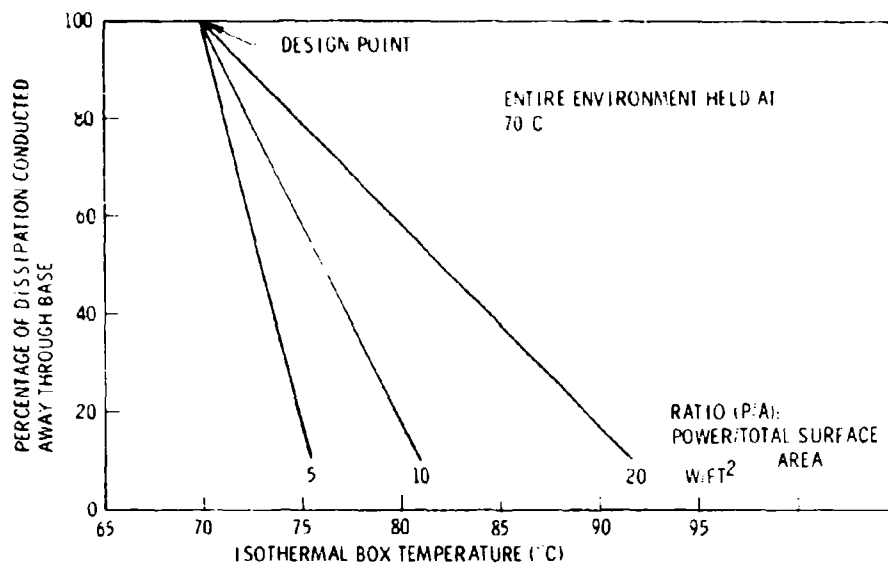


Fig. 5. Effect of mounting cold-plate designed equipment into typical spacecraft.

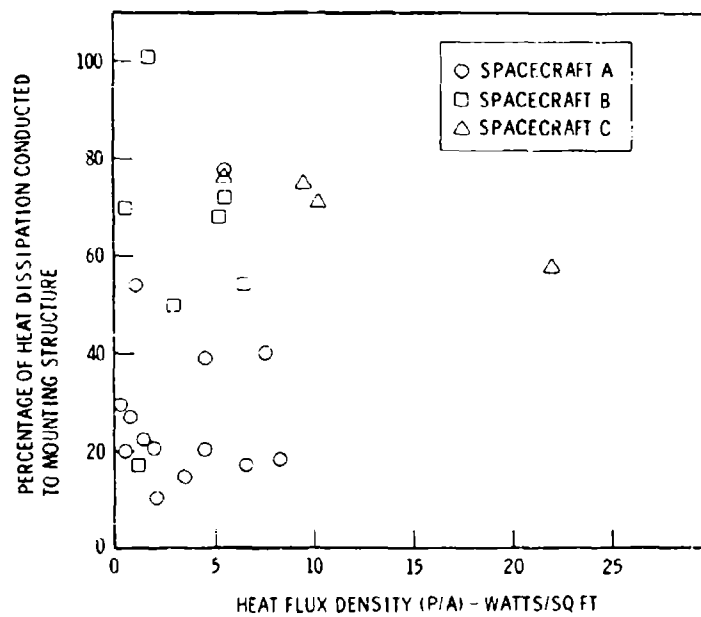


Fig. 6. Heat dissipation modes, spacecraft equipments.

paths inside the box have been realigned, with the results depicted by the solid lines of Fig. 8. Contrary to what might have been expected, a substantial temperature reduction has been achieved under all conditions, even when the equipment is mounted directly to a cold plate. Whether results such as these can be expected in all cases is not known, but this example at least shows that defensive design does not necessarily result in a weight or volume penalty, and does not handicap the design in other ways.

Design Procedures and Suggestions

Inspection of typical spacecraft equipment reveals that most electronics thermal design is still oriented toward cold-plate cooling. This is desirable in those spacecraft which utilize cold plates, but it unnecessarily stresses components in the many spacecraft which rely largely upon radiation heat transfer. In the latter it is obviously desirable to achieve the closest possible coupling between components and the environment to which the box is radiating. This is achieved by several means.

Low-Resistance Conduction Paths from Components to Cover.

Since covers are frequently quite thin, it is best to go directly to the cover, rather than to try to conduct to a baseplate first and from there to a poorly-conducting cover.

Couple closely by conduction from the component to its support. Consider bonding components (particularly cylindrical ones) to the support. Conformal coatings can be used to close gaps.

Keep the conductive path from the component support to the interface with the environment (say, the box cover) as short and "fat" as possible. Even the copper on printed circuit boards can be of some help.

Minimize thermal contact resistances. Note that contact resistances may increase in high vacuum. Values measured in air may be meaningless in vacuum. Grease is a better conductor than literally nothing in the interstice.

Low-Resistance Radiation Paths from Components to Cover.

Such paths are established by utilizing high-emittance surfaces on components and on the inside of the box cover -- and by making the "view" of the cover or other cooler surfaces by the critical components as good as possible. It is surprising that equipment with bare metal internal cover surfaces is still encountered.

High Emittance on the External Surfaces of the Cover.

The temperatures shown in Figs. 5 and 8 would be higher if the box surfaces had low emittances.

Check Effects of High-Wattage Components on Adjacent Components.

Merely derating a component is insufficient if an adjacent hot component brings the operating temperature above that allowable. Consider that radiation may cause overheating of a sensitive component.

Keep Temperature-Sensitive Circuit Elements Away From Components Experiencing Wide Temperature Swings.

Although a circuit may be very stable under continuous-duty operation, spacecraft electronics are frequently operated under highly variable, cyclic conditions but seldom long enough to achieve stable temperatures.

BOX 4.4 x 4.4 x 6 IN. LONG

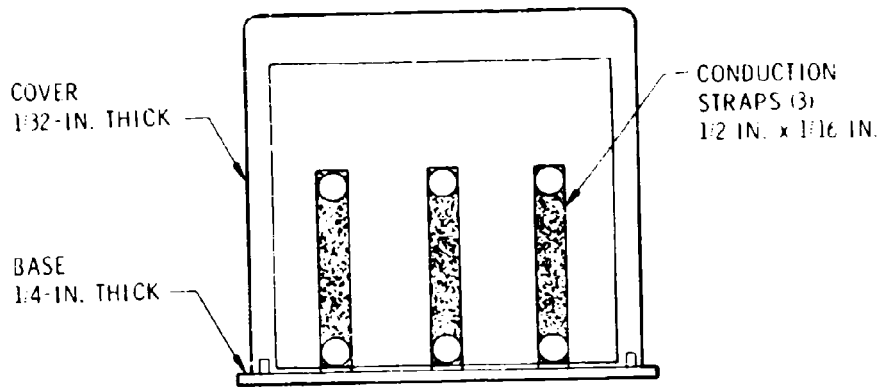


Fig. 7(a). Box designed for cold-plate mounting.

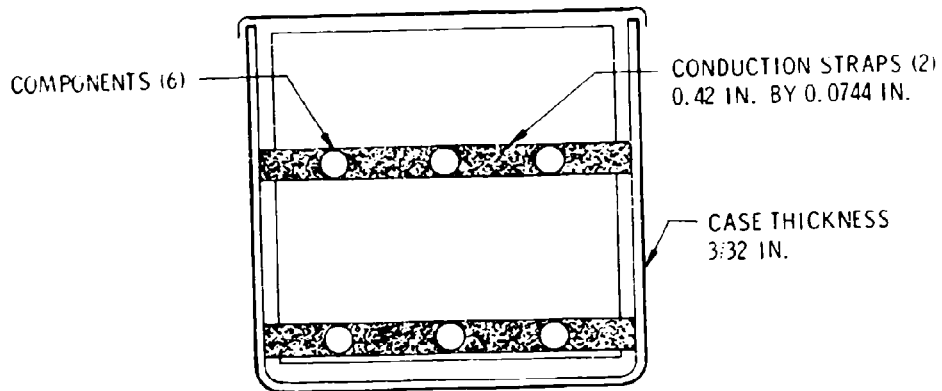


Fig. 7(b). Box redesigned for radiative cooling.

Use the Structure of the Box to Reduce Component Temperature Excursions in Cyclic Operation.

Make Allowance for Variations in Power Dissipation in Presumably Identical Components.

The foregoing suggestions are oriented toward the high-temperature end of the operating range, because this is where most problems seem to occur. Where low-temperature operation is critical, special attention must be paid to thermal design at both ends of the operating temperature range. At low temperatures, equipment that is predominantly radiation-coupled to the spacecraft will increase in temperature considerably more than equipment which is strongly connected conductively.

Verification of Design Adequacy

The ultimate proof of a successful design is obtained when the equipment functions successfully in space. Before this event, equipment is usually subjected to a series of tests on the ground to establish design adequacy. It is to the interest of both electronic equipment and spacecraft designers that these tests simulate the space environment as closely as possible. Certain relevant facts may be recalled at this point:

- . The final equipment mounting in the spacecraft may have any degree of conduction isolation. The exact degree is generally unknown until the completion of spacecraft design - and even then is subject to change.
- . The internal heat transfer mechanisms are altered considerably for non-pressurized equipment as the spacecraft ascends and the air bleeds out.
- . The spacecraft thermal designer usually treats electronic equipment as black boxes or homogeneous "lumps" in a thermal analytical model.
- . Equipment is subjected to a highly variable environment, and to variable duty cycles on itself and on adjacent equipment.

Therefore, the tests must be performed in a manner that will assure successful operation of the equipment throughout its lifetime no matter how it is applied in the spacecraft. Of course, a realistic set of equipment performance requirements must also be supplied to the electronics designer.

Tests that will provide a quite realistic and conservative simulation of spacecraft application can now be designed. They involve the following features:

- . For high-temperature conditions, the equipment is to be mounted so that nearly all (say 90%) of its power dissipation is transmitted to the environment by thermal radiation, when considering the box to be an isothermal mass.
- . For low-temperature tests, the equipment is to be mounted in intimate thermal contact with the mounting base. The mounting base must be kept at the required temperature.
- . The entire environment including mounting plate is to be at a uniform temperature. (The test chamber walls need not be held at this temperature, because an intermediate shroud can provide the environment.) This may not simulate any specific installation, but seems to be the only reasonable approach to a generalized environment.
- . Equipment shall be operated under cyclic or continuous conditions, as planned for the application.

Enough instrumentation should be provided to determine the thermal behavior of the equipment and the temperature patterns within the equipment.

Relationship of Spacecraft and Equipment Designers

It has been true in the past that very little information transfer has existed between the spacecraft thermal designer and the electronic equipment thermal designer. This paper is an attempt to inform the equipment designer of the general principles and design considerations applying to electronic equipment in spacecraft. It is hoped that design of adequately performing equipment will be aided by utilizing this information. On-orbit performance can be enhanced, however, where it is possible to transfer thermal information between the engineers. Unless a special situation exists, the spacecraft engineer generally prefers equipment that does not have to be "babied" and that can be placed anywhere in the spacecraft without special constraints. This makes the initial design of the electronics more difficult but probably improves overall equipment reliability as well as making the equipment more attractive in the competitive sense.

The electronic equipment engineer, however, has valuable information to transmit. He knows which are the critical portions of his design, where the best locations for test and flight thermocouples are, which faces of the box he might prefer for heat transfer, and the transient response of critical components. This kind of information can be used beneficially in spacecraft layout and may help substantially in improving the overall performance of the equipment. It also helps the spacecraft engineer in evaluating orbital behavior.

Summary

The space environment is sufficiently different from environments encountered by electronic equipment designed for ground-based or aircraft operation that thermal design should be specifically tailored for it. Design concepts developed for other environments need to be drastically modified to produce satisfactory results in space. Equipment can, however, be designed to function successfully in space when the unique conditions of space flight are taken into account during the design process. Adequate specifications and design for operational requirements, well-planned testing, and information transfer between the spacecraft and electronics thermal designers result in equipment that is successful in meeting mission requirements.

Acknowledgments: The authors wish to thank F. Verlot and D. Frank for their help in preparing part of the data.

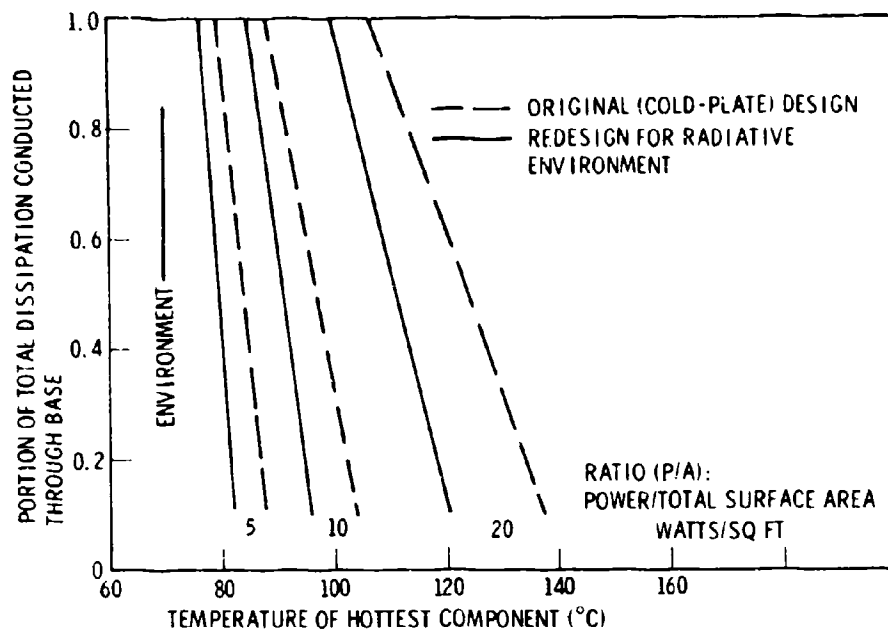


Fig. 8. Temperature of hottest component.

UNCLASSIFIED

Security Classification

DOCUMENT CONTROL DATA - R & D

Security classification of title, body of abstract and indexing and data must be entered when the report is classified.

1. ORIGINATOR'S ACTIVITY or corporate authority Lockheed Missiles & Space Company, Inc. A Subsidiary of Lockheed Aircraft Corporation Palo Alto, California 94304		2. REPORT NUMBER UNCLASSIFIED (Vol. I and II) 1 (Vol. II only)	
3. REPORT TITLE LASER COMMUNICATION PRELIMINARY SUBSYSTEM DESIGN FOR THE SPACE DATA RELAY SUBSYSTEM (U). VOL. I: EXECUTIVE SUMMARY. VOL. II: TASK REPORTS. VOL. III: APPENDIXES			
4. DESCRIPTIVE NOTES: Type of report and inclusive dates Final Report - 19 April 1971 through 19 October 1971			
5. AUTHOR(S): First name, middle initial, last name R. F. Whitmer et al.			
6. REPORT DATE 19 November 1971	7a. TOTAL NO. OF PAGES 1549	7b. NO. OF FIGS. 161	
8a. CONTRACT OR GRANT NO. F04701-71-C-0329	9a. ORIGINATOR'S REPORT NUMBER LMSC-B290200-1, -II, -III		
8b. PROJECT NO. FY76167103574	9b. OTHER REPORT NO(S) (Any other numbers that may be assigned this report) SAMSO TR 71-252		
10. DISTRIBUTION STATEMENT Distribution limited to U.S. Government agencies only; test and evaluation; 19 November 1971. Other requests for this document must be referred to SAMSO (SYAX).			
11. SUPPLEMENTARY NOTES None		12. SPONSORING MILITARY ACTIVITY Department of the Air Force, Headquarters Space and Missiles Systems Organization (AFSC) Los Angeles, California 90045	
13. ABSTRACT A preliminary design for a laser communication subsystem (LCS) for a Satellite Data Relay Subsystem is presented in three volumes. The LCS design includes a 1-Gbit/sec data relay system, a 20-kbit/sec command and control system, a ranging system, and the acquisition and tracking system for pointing a 2.4- μ rad beam. Communication links between ground/aircraft/low-orbit satellites and a synchronous relay satellite, between two synchronous relay satellites, and between a synchronous relay satellite and aircraft/ground terminals are treated. The baseline design uses quadriphase-shift-keying of a microwave subcarrier to modulate a 0.53- μ m Nd:YAG laser beam for the high-data-rate subsystem, modulation of a HeNe laser beam for command and control and ranging signals, and a Q-switched Nd:YAG laser for initial acquisition. The optical subsystem design includes 24-in.-diameter and 6-in.-diameter telescopes. The critical components requiring development are evaluated, and a plan and schedule are presented.			

DD FORM 1473

UNCLASSIFIED

Security Classification

UNCLASSIFIED

Security Classification

14	KEY WORDS	LINK A		LINK B		LINK C	
		ROLE	WT	ROLE	WT	ROLE	WT
	Lasers Communications Satellites Data relay Command and control Ranging systems Acquisition and tracking Nd:YAG laser HeNe laser						

UNCLASSIFIED

Security Classification